To the Graduate Council:

I am submitting herewith a dissertation written by Sameer Ranjan Paital entitled "Laser Textured Calcium Phosphate Bio-Ceramic Coatings on Ti-6Al-4V for Improved Wettability and Bone Cell Compatibility" I have examined the final electronic copy of this dissertation for form and content and recommend that it be accepted in partial fulfillment of the requirements for the degree of Doctor of Philosophy, with a major in Materials Science and Engineering.

Narendra B. Dahotre, Major Professor

We have read this dissertation

and recommend its acceptance:

Wei He

Roberto S. Benson

Syed K. Islam

Acceptance for the council:

Carolyn R. Hodges

Vice provost and Dean of the Graduate School

(Original signatures are on file with official student records.)

Laser Textured Calcium Phosphate Bio-Ceramic Coatings on Ti-6Al-4V for Improved Wettability and Bone Cell Compatibility

A Dissertation

Presented for the

Doctor of Philosophy

Degree

The University of Tennessee, Knoxville

Sameer Ranjan Paital

August 2010

Dedicated to

My Parents

And

Teachers

Copyright © 2010 by Sameer Ranjan Paital
All rights reserved.

Acknowledgements

I would like to take this opportunity to thank all contributors who have helped me in this research and putting together this dissertation. At first, I would like to thank my major research advisor Professor Narendra B. Dahotre, for his tremendous support and guidance and giving me the opportunity to work in an exciting interdisciplinary research project related to surface modification of biomaterials by laser engineering. I am also very thankful to my second research advisor Dr. Wei He for her valuable technical input and collaborative research support on work related to cell culture and cell differentiation studies. I would also like to extend my gratitude to Dr. Roberto S. Benson and Dr. Syed K. Islam for agreeing to serve on my doctoral committee and also providing valuable comments and suggestion during proposal defense. My special thanks to Dr. Claus Daniel for his help and the Industrial Technologies Program for the office of energy efficiency and renewable energy under DOE (Department of Energy) contract DE-AC05-00OR22725 for sponsoring the work related to laser interference patterning at Oak Ridge National Laboratory. My sincere acknowledgement and thanks to Nancy Bunce, research scientist at University of North Texas, Denton for the help and contribution related to XPS and FTIR studies. Special thanks to my lab mates and friends at University of Tennessee, Knoxville for helping me with experimentation and fruitful technical discussions. I would also like to thank my parents, friends and relatives for encouraging me to come to USA and join the PhD programme in Materials Science and Engineering at The University of Tennessee, Knoxville.

Lastly, I would like to acknowledge the financial support from the Center for Laser Applications (CLA) at The University of Tennessee Space Institute, Tullahoma, TN and the

Department of Materials Science and Engineering at The University of Tennessee, Knoxville, TN for providing graduate research and teaching assistantships.

Abstract

The interaction at the surfaces of load bearing implant biomaterials with tissues and physiological fluids is an area of crucial importance to all kinds of medical technologies. To achieve the best clinical outcome and restore the function of the diseased tissue, several surface engineering strategies have been discussed by scientific community throughout the world. In the current work, we are focusing on one such technique based on laser surface engineering to achieve the appropriate surface morphology and surface chemistry. Here by using a pulsed and continuous wave laser direct melting techniques we synthesize three dimensional textured surfaces of calcium phosphate (Ca-P) based surface chemistry on Ti-6Al-4V. The influence of each processing type on the micro texture and phase evolution and thereby its associated effect on wettability, in vitro bioactivity, and in vitro biocompatibility are systematically discussed.

For samples processed using the pulsed laser, it was realized that with increasing laser scan speed and laser pulse frequency there was a transition from surface textures with sharp circular grooves to surface textures with radial grooves and thereby improved hydrophilicity. For CW laser processing the results demonstrated improved hydrophilicity for the samples processed at 100 μm line spacing as compared to the samples processed at 200 μm line spacing.

Owing to the importance of Si for cartilage and hard tissue repair, a preliminary effort for synthesizing Ca-P-SiO_2 composite coating on Ti-6Al-4V surface were also conducted. As a future potential technique we also explored the Laser Interference Patterning (LIP) technique to achieve the textured surfaces and developed understanding on their wetting behavior.

In the current work, by adjusting the laser processing parameters we were able to synthesize textured coatings with biocompatible phases. The in vitro bioactivity and in vitro

biocompatibility of the coatings were proved by the precipitation of an apatite like phase following immersion in simulated body fluid (SBF), and increased proliferation and spreading of the MC3T3-E1 like cells. The results and understanding of the current research is encouraging in terms of looking at other bio-ceramic precursor compositions and laser process parameter window for synthesizing better textured biocompatible coatings.

Extended Abstract

The interaction at the surfaces of load bearing implant biomaterials with tissues and physiological fluids is an area of crucial importance to all kinds of medical technologies. To achieve the best clinical outcome and restore the function of the diseased tissue, several engineering strategies for these implant biomaterials have been discussed by scientific community throughout the world. Among these strategies, surface modification or surface engineering techniques for load bearing implant materials have been the subject of aggressive marketing and research. Most of these techniques are aimed to achieve the appropriate surface morphology and surface chemistry and thereby provide favorable biomechanical and biochemical functionalities at the interface.

In the current work, we are focusing on one such technique based on laser surface engineering to achieve the appropriate surface morphology and surface chemistry. Here by using a laser direct melting technique we synthesize three dimensional textured surfaces of calcium phosphate (Ca-P) based surface chemistry on Ti-6Al-4V. To achieve the above goal two different laser processing techniques i.e. pulsed laser direct melting and continuous wave (CW) laser direct melting were used to synthesize the textured Ca-P coatings. The influence of each processing type on the micro texture and phase evolution are studied. Finally, the effects of surface textures and phase evolution on wettability, in vitro bioactivity, and in vitro biocompatibility are systematically discussed. For samples processed using the pulsed laser, two different laser processing parameters i.e. the laser scan speed and laser pulse frequency were varied to achieve the textured morphology. Within the set of parameters employed in the current research work, it was realized that with increasing laser scan speed and laser pulse frequency

there was a transition from surface textures with sharp circular grooves to surface textures with radial grooves and thereby improved hydrophilicity. For samples processed using the CW laser two different surface textures were achieved by varying the line spacings (100 μm and 200 μm) between two consecutive laser tracks. The results demonstrated improved hydrophilicity for the samples processed at 100 μm line spacing as compared to the samples processed at 200 μm line spacing.

Following our established understanding of synthesis of textured Ca-P coatings using a pulsed laser, preliminary efforts for synthesizing Ca-P-SiO_2 composite coating on Ti-6Al-4V surface were also conducted. The effects of SiO_2 doping on wetting behavior, in vitro bioactivity, and in vitro biocompatibility were studied. As a future potential technique we also explored the Laser Interference Patterning (LIP) technique to achieve the textured surfaces and developed understanding on their wetting behavior.

In the current work, via laser based surface engineering approach, we therefore demonstrated the potential to synthesize textured biocompatible coatings with improved wettability. The laser process parameters were controlled to synthesize beneficial biocompatible phases such as $CaTiO_3$, TiO_2, α-TCP and $Ca_5(OH)(PO_4)_3$ within the coatings. The in vitro bioactivity and in vitro biocompatibility of the coatings were proved by the precipitation of an apatite like phase following immersion in simulated body fluid (SBF), and increased proliferation and spreading of the MC3T3-E1 like cells respectively. The results and understanding of the current research is encouraging in terms of looking at other bio-ceramic precursor compositions and laser process parameter window for synthesizing better textured biocompatible coatings. Further, the laser process parameters can also be controlled to achieve 3-

dimensional topographic cues mimicking the actual length scale of the bone cells and thereby provide tailored coatings for improved wettability, bioactivity and biocompatibility.

Table of Contents

Chapter 1 **Materials and Clinical Concerns of Load Bearing Orthopedic Implant Biomaterials……1**

1.1 Introduction……...1

1.2 Load bearing orthopedic implants and devices……1

1.3 Materials for load bearing implants and devices……...2

1.3.1 Metallic materials……....2

1.3.1.1 Stainless steels……5

1.3.1.2 Cobalt alloys……...5

1.3.1.3 Titanium and titanium alloys……..7

1.3.2 Polymers……...10

1.3.3 Ceramics……...10

1.3.4 Composites……...15

1.4 Clinical concerns with orthopedic implant biomaterials…….....15

1.4.1 Mechanical failures……...16

1.4.2 Failure due to corrosion……....18

1.4.3 Failures due to surface properties……19

1.5 Prospective for improvement……..20

1.5.1 Surface science and engineering of load bearing orthopedic implant biomaterials……..23

1.5.1.1 Morphological modifications……...23

1.5.1.2 Physiochemical modifications……..26

1.5.1.3 Biological modifications……..29

1.5.2 Ca-P based bioactive coatings……..31

Chapter 2 **Scope and Objective of Current Work……..34**
Chapter 3 **Experimental Work……40**
3.1 Materials selection and sample preparation……40
3.2 Surface modification via pulsed laser direct melting……..42
3.3 Surface modification via CW laser direct melting……..45
3.4 Surface modification via LIP……..48
3.5 Surface characterization……..50
3.5.1 Microstructural characterization……...50
3.5.2 Elemental analysis……50
3.5.3 Phase analysis……...51
3.5.4 Morphological evolution……...51
3.6 Mechanical characterization……....52
3.7 Contact angle and surface energy……....53
3.8 In vitro bioactivity……...56
3.9 In vitro biocompatibility……..57
3.9.1 Cell viability……..57
3.9.2 Cell morphology and cell cytoskeleton…….....58
3.9.3 Data analysis……59
Chapter 4 **Pulsed Laser Induced Ca-P Textured Coating on Ti-6Al-4V…….……60**
4.1 Introduction…….....60
4.2 Variation of laser scan speed……..…….……....60
4.2.1 Microstructure and morphology of coating……..…61
4.2.2 Phase evolution…….……65

4.2.3 Mechanical response…….67

4.2.4 Wettability of textured coatings……...……71

4.2.5 Mechanism and kinetics of HA precipitation

on the textured coating……..……77

4.3 Variation of laser pulse frequency…….……..89

4.3.1 Microstructure, morphology, and phase analysis…….89

4.3.2 Effects of phase and morphology on wettability……..92

4.3.3 In vitro bioactivity and mineralization…….….96

4.3.4 In vitro biocompatibility…….....114

Chapter 5 **Continuous Wave Laser Induced Ca-P Textured Coating on Ti-6Al-4V……120**

5.1 Introduction……...120

5.2 Microstructure, morphological, phase and

elemental analysis of the CW textured coatings……...120

5.3 Effects of surface roughness on wettability……..…125

5.4 Bioactivity and mineralization kinetics…….....131

5.5 In vitro biocompatibility……....148

Chapter 6 **Promising New Developments…….....153**

6.1 Pulsed Nd:YAG laser textured HA-SiO_2

composite coating on Ti-6Al-4V…….……..153

6.1.1 Phase evolution……...153

6.1.2 Wettability and in vitro bioactivity……155

6.1.3 In vitro biocompatibility……157

6.2 Laser interference patterning on Ti-6Al-4V…….…….162

6.2.1 Surface morphology of the samples……....162

6.2.2 Wetting behavior of the samples……....166

Chaptre 7 **Conclusions and Scope for Further Work…….……174**

7.1 Conclusions…….…..174

7.2 Scope for further work……..……175

List of References……...……177

Appendix……...…..188

Appendix A: List of Publications……...……..189

Appendix B: Reprints of Published Works……...…...193

Vita……..……389

List of Tables

Tables		Pages
Table 1.1	Mechanical properties and clinical applications of Ti-based etallic materials **[2, 3].**	9
Table 1.2	Chemical name, mineral name and composition of various Ca-P based ceramics **[32]**.	13
Table 3.1	Laser processing parameters used for coating using pulsed Nd:YAG laser.	44
Table 3.2	Laser processing parameters used for coating using a CW laser **[72]**.	47
Table 3.3	Surface energy components of the standard liquids (units mJ m^{-2}) **[89, 90]**.	56
Table 4.1	Experimental results of contact angle of SBF and the texture parameter (σ_A/λ) on the Ca-P coated sample obtained at various laser scan speeds **[70]**.	73
Table 4.2	Experimentally measured physical parameters related to surface texture **[71]**.	96
Table 4.3	Elemental composition and semi-quantitative analysis of Ca and P in terms of atomic concentration for the pulsed laser processed samples.	113

Table 5.1 Experimental results of contact angles of test liquids, texture parameter (σ_A/λ), surface energy components and surface energy as a function of sample processing conditions **[72]**. 128

Table 5.2 Contact angles and corresponding light optical images of the liquid droplet shadow on the laser processed samples and on the control (untreated Ti-6Al-4V) **[72]**. 132

Table 5.3 Elemental composition and semi-quantitative analysis of Ca and P in terms of atomic concentration for the CW laser processed samples. 147

Table 6.1 Contact angle with SBF, and surface energy of the samples **[120].** 156

Table 6.2 Process power and corresponding height of the groove/pillar pattern and contact angle related to interference-patterned samples **[80].** 165

List of Figures

Figures		Pages
Figure 1.1	Orthopedic Implant devices used for load bearing applications: (a) Hip Implant. (Reprinted from **[4]** with permission from source: www.zimmer.com), (b) Knee Implant (Reprinted from **[5]** with permission from source: http://thehipkneesurgeon.com/jointKnee.php) (c) Shoulder Implant (Reprinted from**[6]** with permission from source: http://www.djosurgical.com/products/shoulder/rsp/index.htm) (d) Elbow implant (Reprinted from **[4]** with permission from source: www.zimmer.com).	3
Figure 1.2	Biomaterials market statistics (a) world biomaterials market statistics (b) orthopedic biomaterials market share of different countries (c) USA biomaterials market statistics **[7]**.	4
Figure 1.3	SEM micrograph of 316L stainless steel wire surface with two different surface chemistries under both in vivo and in vitro conditions (a) 316L wire surface coated with an amorphous oxide layer (AO), and (b) as received 316L stainless steel wire surface (AS). The inset in the upper left hand side in figure (a) reveals a clean and free of pitting damage after anodic polarization test for the (AO) sample, whereas the inset in upper left hand side figure (b) reveals severe pitting degradation for the (AS) sample. Further the inset at the bottom in figure (a) reveals	

absence of proteins, fibrins and a clean surface for the coils passivated with amorphous oxide film, and the inset in bottom of figure (b) clumps of platelets, red cells, and fibrin under in vivo conditions. *(Reprinted from **[9]** and **[17]** with permission from Elsevier.)* 6

Figure 1.4 As cast Co-Cr-Mo alloys revealing (a) carbide separation in interdendrites and (b) abnormally long bands of interdendritic carbides near grain boundary. *(Reprinted from **[18]** with permissions from Springer.)* 8

Figure 1.5 Microstructure of a hot isostatic pressed (HIP) Co-Cr-Mo alloy. *(Reprinted from **[20]** with permission from Elsevier.)* 8

Figure 1.6 Microstructure of Ti-6Al-4V (a) under as received and annealed condition and (b) after cold working by equal channel angular pressing (ECA) technique. *(Reprinted from **[21]** and **[22]** with permission from Elsevier.)* 9

Figure 1.7 Figure illustrating the use of UHMWPE as a bearing metal for (a) hip joint *(Reprinted from **[28]** and **[29]** with permission from sources: www.devicelink.com and http://www.genesis-tech.ch/company/ respectively)*, and (b) knee joint prosthesis *(Reprinted from **[30]** and **[31]** with permission from sources: http://tc.engr.wisc.edu/UER/uer01/author1/content.html and http://www.jri-ltd.co.uk/total_knee_replacement.asp respectively*. 11

Figure 1.8 Fluorescence microscopy images of U-937 cells cultured on (a, b) TCP, and (c, d) HA, with VD_3 and PDBu for 21 days. *(Reprinted from **[33]** with permission from Elsevier.)* 14

Figure 1.9 Fatigue fracture surface morphology of Ti-6Al-4V. ((a) overall fracture surface; (b) crack initiation site taken from area "I"; (c) crack propagation site taken from area "II" ; (d) overload site taken from area "III"). *(Reprinted from **[41]** with permission from Elsevier.)* 17

Figure1.10 Schematic representation of the hierarchical organization of bone at different length scales. *(Reprinted from **[50]** with permissions from American Association for the Advancement of Science (AAAS).)* 22

Figure 1.11 SEM image of sand blasted and acid etched titanium surface. *(Reprinted from **[55]** with permissions from Institute of Physics Publishing (IOP).)* 24

Figure 1.12 SEM image of human osteoblast on the sand blasted and acid etched surface after seven days of incubation at different magnification. (A) 100× and (B) 700×. *(Reprinted from **[55]** with permissions from Institute of Physics Publishing (IOP).)* 25

Figure 1.13 Schematic illustrations of cross-sections of surface-modified layers of titanium specimens with and without calcium-ion-

implantation. *(Reprinted from **[57]** with permission from Elsevier.)* 27

Figure 1.14 Scanning electron micrographs of unimplanted titanium (a) and calcium-ion-implanted titanium (b) immersed in Hank's solution for 30 days. *(Reprinted from **[57]** with permission from Elsevier.)* 28

Figure 1.15 Figure illustrating immobilization of phosphorycholine polymers on to titanium surface controlled by a vinyldimethylsilane (VDMS) monolayer. *(Reprinted from **[62]** with permission from Elsevier.)* 31

Figure 2.1 Schematic illustration of the sequential reactions that take place after the implantation of a biomaterial into a living system **[2]**. 35

Figure 2.2 Schematic illustration of a textured surface morphology **[70-73]**. 37

Figure 2.3 Flow chart of proposed goal and approach of current research work. 39

Figure 3.1 Schematic representation of the output power delivery with time in a pulsed laser. 42

Figure 3.2 Different steps involved in evolution of the surface morphology at various times ($t_1 < t_2 < t_3$) for a single laser beam **[80]**. 43

Figure 3.3 Schematic of laser texturing process using pulsed Nd:YAG laser **[71]**. 44

Figure 3.4 Schematic representation of the output power delivery with time in a CW laser. 46

Figure 3.5 Schematic of laser texturing using CW laser **[72]**. 47

Figure 3.6 A schematic of the laser based interference patterning technique **[73]**. 49

Figure 3.7 Schematic of intensity distribution and corresponding surface profile obtained by two beam laser interference patterning. 49

Figure 3.8 Schematic of a wear testing set up **[87]**. 54

Figure 4.1 Sample processed at a laser scan speed of 36 cm/min: (a) optical cross sectional view and (b) SEM of the coating surface revealing a porous morphology with wide pore size distribution **[97]**. 63

Figure 4.2 Low magnification optical microscopic images of the surfaces of coatings obtained at laser scan speed of (a) 36 cm. min^{-1}, (b) 48 cm. min^{-1}, (c) 78 cm. min^{-1} and (d) 102 $cm.min^{-1}$ **[70]**. 64

Figure 4.3 XRD patterns of the samples processed at varying laser scan speeds using a pulsed Nd:YAG laser **[70]**. 66

Figure 4.4 Nanoindentation data: (a) characteristic loading and unloading curves for the coating and substrate and, (b) variation in E and H of the coatings as function of laser scan speed **[97]**. 69

Figure 4.5 Cumulative weight loss for the sample processed at varying laser scan speed and bare Ti-6Al-4V in a SBF environment **[97]**. 70

Figure 4.6 Optical microscopic image of the wear tracks on (a) bare Ti-6Al-4V and (b) Ca-P coatings processed at a laser scan speed of 102 cm/min **[97]**. 70

Figure 4.7 Schematic showing the variation in surface profiles with varying laser scan speed **[70]**. 74

Figure 4.8 Schematic showing the wetting behavior of a liquid drop on a rough surface having (a) circular grooves and (b) radial grooves **[70]**. 76

Figure 4.9 XRD analysis of the sample (processed at laser scan speed of 36 cm/min) (a) prior to immersion in SBF and after immersion in SBF for (b) 24 hours, (c) 48 hours, (d) 72 hours and (e) 96 hours **[70]**. 79

Figure 4.10 XRD analysis of the sample (processed at laser scan speed of 48 cm/min) (a) prior to immersion in SBF and after immersion in SBF for (b) 24 hours, (c) 48 hours, (d) 72 hours and (e) 96 hours **[70]**. 79

Figure 4.11 XRD analysis of the sample (processed at laser scan speed of 78 cm/min) (a) prior to immersion in SBF and after immersion in SBF for (b) 24 hours, (c) 48 hours, (d) 72 hours and (e) 96 hours **[70]**. 80

Figure 4.12 XRD analysis of the sample (processed at laser scan speed of 102 cm/min) (a) prior to immersion in SBF and after immersion in

SBF for (b) 24 hours, (c) 48 hours, (d) 72 hours and (e) 96 hours **[70]**. 80

Figure 4.13 SEM micrographs revealing the formation of globular apatite like layer following immersion in SBF for different time periods and the inset showing the corresponding EDS spectra for (a) 24 hours (b) 48 hours (c) 72 hours (d) 96 hours. (For samples processed at laser scan speed of 102 cm/min) **[70]**. 83

Figure 4.14 Schematic illustrations demonstrating (a) the favored mechanism for formation of more OH^- ion groups on the surface of sample processed at higher laser scan speed and (b) the mechanism of apatite formation on such a surface **[70]**. 85

Figure 4.15 Dependence of Ca and P atomic concentration and Ca/P atomic ratio on SBF immersion time for the samples processed at laser scan speed of (a) 36 $cm.min^{-1}$, (b) 48 $cm.min^{-1}$, (c) 78 $cm.min^{-1}$, and (d) 102 $cm.min^{-1}$ **[70].** 87

Figure 4.16 Deposition of HA in grams on Ca-P coated samples (laser textured at various laser scan speeds) and bare Ti-6Al-4V substrate from the SBF solution as a function of immersion time **[70]**. 88

Figure 4.17 Low-magnification optical microscopic images of the surface of coatings processed at laser pulse frequencies of (a) 10 Hz, (b) 20 Hz, (c) 30 Hz, and (d) 40 Hz **[71]**. 90

Figure 4.18 (a) Cross-sectional SEM images of the sample processed at 40 Hz and (b) XRD spectra for the laser processed samples at varying pulse frequencies **[71]**. 93

Figure 4.19 (a) The 3-dimensional confocal microscopic images of the surface of coatings and (b) contact angle variation and corresponding shadow images of the SBF droplets on laser processed sample and control (untreated Ti-6Al-4V) **[71]**. 95

Figure 4.20 SEM micrographs of laser processed samples following immersion in SBF for different time periods. Scale bar in the figure is equivalent to 10 μm **[71]**. 98

Figure 4.21 XRD spectra of laser textured samples following immersion in SBF for various immersion periods **[71]**. 100

Figure 4.22 Mineralization of laser textured samples in terms of (a) variation in apatite crystallite size with SBF immersion time and (b) logarithmic weight change with SBF immersion time **[71]**. 103

Figure 4.23 FTIR spectra of laser processed samples (a) 10 Hz, (b) 20 Hz, (c) 30 Hz and (d) 40 HZ following immersion in SBF for different time periods. 105-107

Figure 4.24 XPS spectra of laser processed samples (a) 10 Hz, (b) 20 Hz, (c) 30 Hz and (d) 40 HZ following immersion in SBF for different time periods. 108-111

Figure 4.25 Morphology of MC3T3-E1 osteoblast-like cells after 7 day culture on the samples processed at laser pulse frequency of (a) 10 Hz, (b) 20 Hz, (c) 30 Hz, (d) 40 Hz and (e) control (untreated Ti-6Al-4V). Arrows in the inset of Figure 9 (a), (b), (c), and (e) indicate the de-bonding or lack of proper adhesion of the MC3T3-E1 osteoblast-like cells on the substrate material **[71]**. 115

Figure 4.26 Fluorescence microscopic images showing the proliferation of the MC3T3-E1 osteoblast-like cells after 1 day and 7 day of culture on the laser processed and control (untreated Ti-6Al-4V) **[71]**. 117

Figure 4.27 (a) Cytoskeleton assessment of the MC3T3-E1 osteoblast-like cells after 7day culture on the laser processed samples and the control (untreated Ti-6Al-4V) and (b) cell shape index and cell area as a function of the samples processing conditions. ★ denotes the laser processed group is significantly higher than the control **[71]**. 118

Figure 5.1 Low magnification SEM images of the surface of coatings processed at (a) 137 J/cm^2, 100 μm line spacing, (b) 191 J/cm^2, 100 μm line spacing, (c) 137 J/cm^2, 200 μm line spacing, and (d), 191 J/cm2,_200 μm line spacing **[72]**. 122

Figure 5.2 Cross-sectional SEM images of the sample processed at 137 J/cm^2 and 100 μm line spacing: (a) revealing the textured coating

(b) revealing the sound metallurgical bonding at the interface and (c) a higher magnification of the coating and the inset showing the EDS pattern from the white precipitates **[72]**. 124

Figure 5.3 (a) XRD pattern and (b) corresponding EDS spectra of the laser processed samples **[72]**. 126

Figure 5.4 3-dimensional confocal microscopic images of surface of the coatings processed at (a) 137 J/cm^2, 100 μm line spacing (b) 191 J/cm^2, 100 μm line spacing, (c) 137 J/cm^2, 200 μm line spacing, and (d) 191 J/cm^2, 200 μm line spacing **[72]**. 127

Figure 5.5 Variation in surface roughness parameters as a function of laser processing conditions **[72]**. 128

Figure 5.6 (a) XRD spectra of the samples processed at 137 J/cm^2, 100 μm line spacing and (b) corresponding magnified spectra (2θ ~ 30°-32°) following immersion in SBF **[72]**. 134

Figure 5.7 (a) XRD spectra of the samples processed at 191 J/cm^2, 100 μm line spacing and (b) corresponding magnified spectra (2θ ~ 30°-32°) following immersion in SBF **[72]**. 135

Figure 5.8 XRD spectra of the samples processed at 137 J/cm^2, 200 μm line spacing following immersion in SBF **[72]**. 136

Figure 5.9 XRD spectra of the samples processed at 191 J/cm^2, 200 μm line spacing following immersion in SBF **[72]**. 137

Figure 5.10 SEM images of the sample processed at 137 J/cm^2, 100 μm line spacing following immersion in SBF for (a) 1 day, (b) 3 days,(c) 5 days, and (d) 7 days **[72]**. 139

Figure 5.11 FTIR spectra of laser processed samples (a) 215W, 0.1 mm, (b) 300W, 0.1 mm, (c) 215W, 0.2 mm, and (d) 300W, 0.2 mm following immersion in SBF for different time periods. 141-142

Figure 5.12 XPS spectra of laser processed samples (a) 215W, 0.1 mm, (b) 300W, 0.1 mm, (c) 215W, 0.2 mm, and (d) 300W, 0.2 mm following immersion in SBF for different time periods. 143-146

Figure 5.13 Cell morphology of MC3T3-E1 osteoblast-like cells after culture for 1 day on (a) control (untreated Ti-6Al-4V), and samples processed at (b) 137 J/cm^2 , 100 μm line spacing, (c) 191 J/cm^2, 100 μm line spacing, (d) 137 J/cm^2, 200 μm line spacing, and (e) 191 J/cm^2, 200 μm line spacing **[72]**. 149

Figure 5.14 Fluorescent micrographs for cytoskeleton assessment of adherent MC3T3-E1 osteoblast-like cells after culture for 1 day on (a) control (untreated Ti-6Al-4V substrate) and samples processed at (b) 137 J/cm^2, 100 μm line spacing, (c) 191 J/cm^2, 100 μm line spacing, (d) 137 J/cm^2, 200 μm line spacing, and (e) 191 J/cm^2, 200 μm line spacing **[72]**. 151

Figure 5.15 Graphical representation of the cell spreading area as a function of sample processing conditions. ★ denotes that the laser

processed group is significantly higher than the control Ti-6Al-4V ($p < 0.05$). Cell spreading area measurements were taken from 30 different cells **[72]**. 152

Figure 5.16 WST-1 assay of the MC3T3-E1 osteoblast-like cells following culture for 1, 3, and 5 days as a function of samples processing conditions. ★ denotes that the laser processed group is significantly higher than the control Ti-6Al-4V ($p < 0.05$) **[72]**. 152

Figure 6.1 XRD patterns of Ti-6Al-4V, 25 wt. % SiO_2-HA and 100 wt. % HA coated sample **[119]**. 155

Figure 6.2 SEM morphological analysis and corresponding EDS results on (a) 100 wt.% HA sample, and (b) 25 wt.% SiO_2-HA sample after 7 days immersion in SBF **[120]**. 158

Figure 6.3 Live/dead staining of MC3T3-E1 cells after 4 h of incubation on (a) Ti-6Al-4V, (b) 25 wt. % SiO_2-HA coating, (c) 100 wt. % HA coating; and (d) number of cells attached to Ti control, 25 wt. % SiO_2-HA coating, and 100 wt. % HA coating within observation areas after 4 h seeding; results are expressed as percentage of cells attached on Ti control (n=3). * denotes that the cell number on untreated Ti-6Al-4V is significantly lower than laser cladded Ti ($p < 0.05$), scale bars correspond to 100 μm **[119]**. 160

Figure 6.4 SEM images for cell morphology after 1 and 7 days of proliferation on Ti-6Al-4V (a and b), 25 wt. % SiO_2-HA coating

(c and d), and 100 wt. % HA coating (e and f). Scale bars in (a), (c), and (e) are 10 μm; and in (b), (d), and (f) in large images and in insets are 100 μm and 5 μm, respectively **[119]**. 161

Figure 6.5 Groove pattern on Ti-6Al-4V by laser interference technique (3.82 W laser power). (a) 2-dimensional morphological evolution, (b) 3-dimensional morphological evolution, and (c) variation in height and width (across the line scan) of the features obtained using a one step irradiation **[80]**. 164

Figure 6.6 Pillar pattern on Ti-6Al-4V by laser interference technique (3.82 W laser power). (a) 2-dimensional morphological evolution (b) 3-dimensional morphological evolution, and (c) variation in height and width at FWHM (across the line scan) of the features obtained using a two step irradiation **[80]**. 167

Figure 6.7 Light optical images of the distilled water droplet shadow on (a) flat Ti-6Al-4V, (b) groove patterned Ti-6Al-4V, and (c) pillar patterned Ti-6Al-4V; and light optical images of the SBF droplet shadow on (d) flat Ti-6Al-4V, (e) grove patterned Ti-6Al-4V, and (f) pillar patterned Ti-6Al-4V **[80]**. 169

Figure 6.8 Schematic illustration of liquid invasion in a (a) groove pattern and (b) pillar pattern **[80]**. 172

Figure 6.9 (a) variation in roughness factor, R_f and (b) critical wetting angle, θ_c with laser fluence for interference patterned samples **[80]**. 173

Chapter 1
Materials and Clinical Concerns of Load Bearing Orthopedic Implant Biomaterials

1.1 Introduction

Biomaterials are synthetic or natural materials intended to function appropriately in a bio environment. In particular, they are expected to integrate with the surrounding tissue to restore adequate function, without releasing harmful chemical products or significantly modifying the local electrical and mechanical environment **[1].** In light of this, some potential biomaterials that are being developed over the past few decades and are currently being used to restore function inside a human body include (1) orthopedic implant materials, (2) cardiovascular systems, (3) ophthalmics, (4) dental implants, (5) wound healing materials, and (6) drug delivery systems. Among these various potential biomaterials, load bearing orthopedic implant materials, to heal skeletal defects caused due to trauma, old age, and injury are in great demand. With increasing ageing population, war, and sports related injuries the demand for these materials has further gone up in a scalable manner during the recent times. Hence, a detailed study of their applications, as implants and devices for use inside a human body, to restore the function of a damaged organ or tissue is quite essential.

1.2 Load bearing orthopedic implants and devices

Orthopedic implants and devices are mostly used for fracture fixation and replacement of load bearing joints, which are subjected to high level of mechanical stresses, wear, and fatigue in the course of normal activity **[2, 3]**. The implants used for joint fixation include prosthesis for hip

(Figure 1.1(a)) **[4]**, knee (Figure 1.1(b)) **[5]**, ankle, shoulder (Figure 1.1(c)), **[6]** and elbow joints (Figure 1.1(d)) **[4].** The fracture fixation devices include spinal fixation devices, wires, pins, screws, and fracture plates. Their market share can very well exemplify the overwhelming success of these orthopedic biomaterials nationally and internationally (Figure 1.2) **[7]**. It can be observed that among all kinds of biomaterials, orthopedic biomaterials dominated the world market in the year 2009 with a market capture of 38 % (Figure 1.2 (a)) **[7]**. Further among all the counties, USA alone is responsible for 50 % of the world orthopedic biomaterials market (Figure 1.2 (b)) **[7]**. Also, within USA in the year 2009, statistical data showed that hip and knee implants (Figure 1.2 (c)) accounted to be the major consumer products among the orthopedic biomaterials. Because of the clinical success of total joint replacement procedures for knees and hips, demand for total joint replacement of other joints, such as the shoulder and elbow is also likely to grow in the coming years. Additionally, because of the stiff competition between manufacturers and requisite attention to marketing, there also has been a significant thrust in developing new materials systems for the fabrication of these implants and devices.

1.3 Materials for load bearing implants and devices

The different classes of materials used for the fabrication of load bearing orthopedic implants and devices can be broadly classified as (1) metallic materials, (2) polymers (3) ceramics and (4) composites.

1.3.1 Metallic materials

As the principal function of the long bones at the lower part of the body is to act as load- bearing members, it was hence reasonable that the initial materials introduced to replace damaged hip and knee were made up of metallic materials **[3]**. Apart from being used as hip and knee prosthe-



Figure 1.1 Orthopedic Implant devices used for load bearing applications: (a) Hip Implant. (Reprinted from **[4]** with permission from source: www.zimmer.com), (b) Knee Implant (Reprinted from **[5]** with permission from source: http://thehipkneesurgeon.com/jointKnee.php) (c) Shoulder Implant (Reprinted from **[6]** with permission from source: http://www.djosurgical.com/products/shoulder/rsp/index.htm) (d) Elbow implant (Reprinted from **[4]** with permission from source: www.zimmer.com).

sis, they are also used for manufacturing fracture fixation wires, pins, screws, and plates. The most commonly used metals and alloys for these applications include stainless steel, cobalt-based alloys, and commercially pure titanium and its alloys **[3]**.

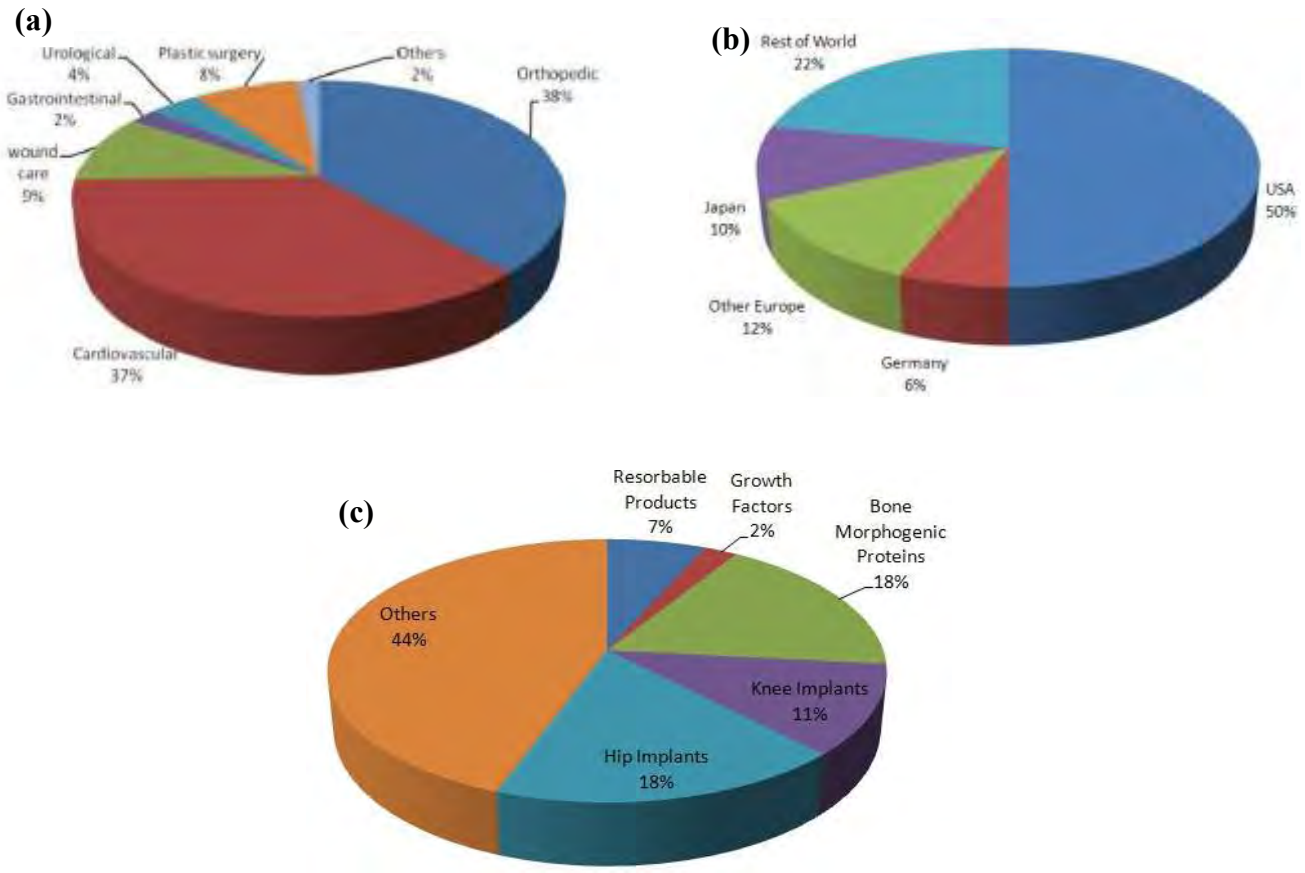


Figure 1.2 Biomaterials market statistics (a) world biomaterials market statistics (b) orthopedic biomaterials market share of different countries (c) USA biomaterials market statistics **[7]**.

1.3.1.1 Stainless steels

Stainless steels are iron-base alloys with a minimum of 10.5 % Cr as an alloying element, needed to prevent the formation of rust. Stainless steel was first used as an orthopedic implant material in the year 1926. However, it was not until 1943, when ASTM 304 was recommended as a standard implant alloy material **[3]**. Although there are several types of stainless steels in use for medical applications, 316L (18 wt% Cr-14 wt% Ni-2.5 wt% Mo) single phase austenitic (FCC) stainless steel is the most popular one for load bearing implant applications **[3, 8-16]**. The "L" in the designation denotes its low carbon content and as a result it has high corrosion resistance under in vivo conditions. Shih and coworkers studied the effect of surface treatment on the in vitro corrosion resistance and in vivo biocompatibility of 316L stainless steel **[9, 17]**. They demonstrated that passivation with an amorphous oxide layer has excellent corrosion resistance and low degree of thrombosis (Figure 1.3) than the as received sample.

1.3.1.2 Cobalt alloys

Co-Cr-based alloys are the most commonly used representative Co alloys for orthopedic applications as (a) fracture fixation plates and screws and (b) hip and knee prosthesis **[8].** The presence of Cr imparts the corrosion resistance and the addition of small amounts of other elements` such as iron, molybdenum, or tungsten can give very good high temperature properties and abrasion resistance **[8]**. The most commonly used Co-Cr alloys for orthopedic implant applications are Co-Cr-Mo (ASTM F75), Co-Cr-W-Ni (ASTM F90) and Co-Ni-Cr-Mo-Ti (ASTM F562) **[2, 3]**. Casting of these alloys for implant fabrication is not preferred as they result in large dendritic grains during solidification with casting defects such as such as inclusions and micro pores (Figure 1.4) **[18]**. Therefore, powder metallurgical techniques such as hot isostatic

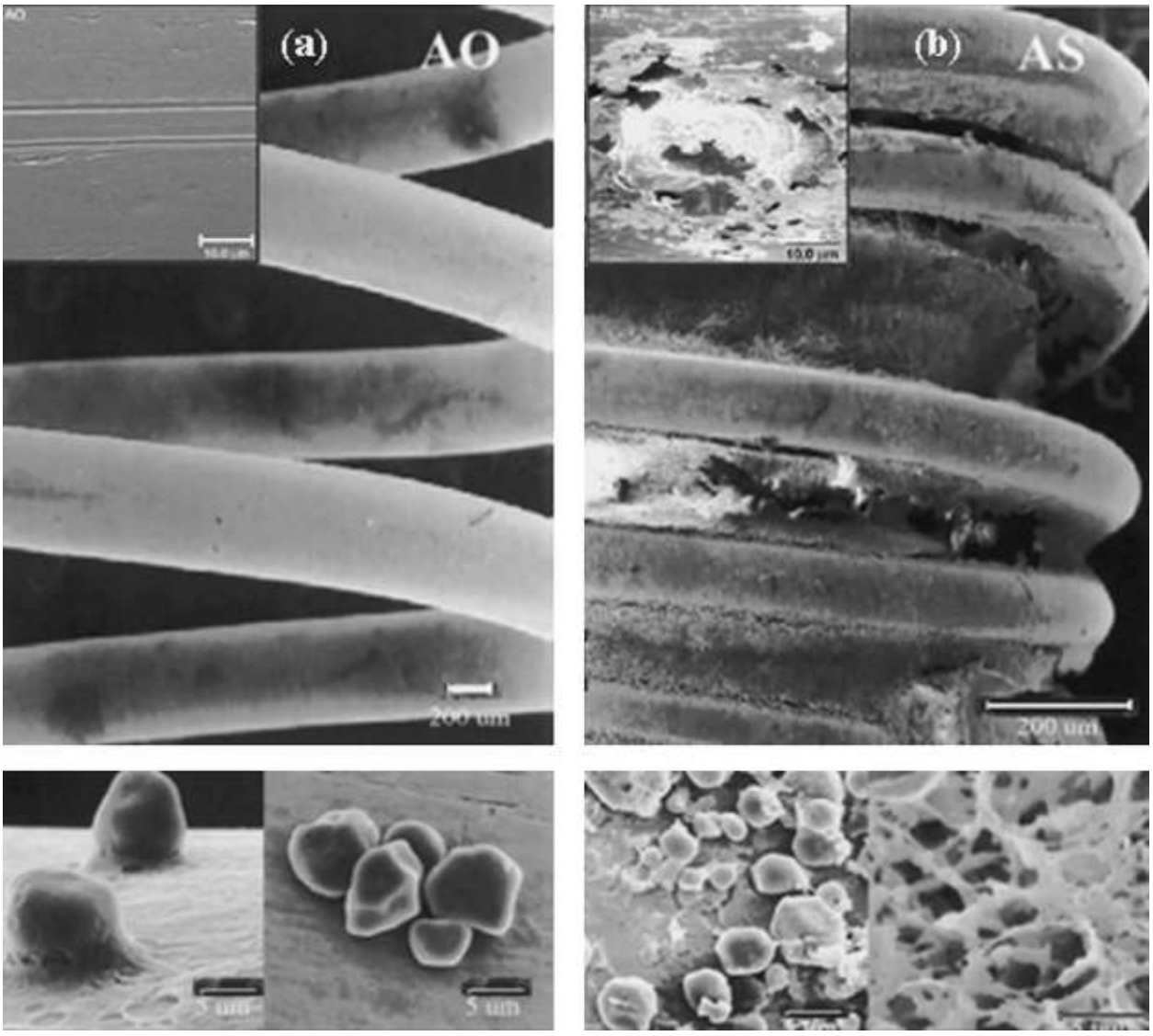


Figure 1.3 SEM micrograph of 316L stainless steel wire surface with two different surface chemistries under both in vivo and in vitro conditions (a) 316L wire surface coated with an amorphous oxide layer (AO), and (b) as received 316L stainless steel wire surface (AS). The inset in the upper left hand side in figure (a) reveals a clean and free of pitting damage after anodic polarization test for the (AO) sample, whereas the inset in upper left hand side figure (b) reveals severe pitting degradation for the (AS) sample. Further the inset at the bottom in figure (a) reveals absence of proteins, fibrins and a clean surface for the coils passivated with amorphous oxide film, and the inset in bottom of figure (b) clumps of platelets, red cells, and fibrin under in vivo conditions. *(Reprinted from **[9]** and **[17]** with permission from Elsevier.)*

pressing (HIP) followed by forging **[19]** have been used for fabrication of implants using these materials. This results in improved mechanical properties and corrosion resistance pertaining to the finer grain size (Figure 1.5) **[20]** and reduction in segregation of the alloying elements obtained by this technique.

1.3.1.3 Titanium and titanium alloys

Titanium as a pure metal was implanted for the first time into laboratory animals in 1940 by Bothe, Beaton, and Davenport **[2, 3, 8]**. From their studies, the authors concluded titanium as a better biocompatible material as compared to stainless steel and Co-Cr based alloys under in vivo conditions. The two most commercially used specifications for orthopedic implant applications are Pure Ti (ASTM F67) and Ti-6Al-4V (ASTM F136) **[3]**. These alloys have driven a lot of interest for load bearing implants due to its superior mechanical properties (tensile strength and fatigue strength), chemical stability (corrosion resistance), and biocompatibility under in vivo conditions **[2, 3]**. Commercially pure Ti is selected for applications where corrosion resistance is of prime importance than its mechanical properties. Ti-6Al-4V (ASTM F136) is an alpha-beta alloy, the microstructure (Figure 1.6) **[21-23]**, mechanical behavior, and chemical stability of which depend upon the type of heat treatment and mechanical working. In the recent past, however, there has been a great concern on the dissolution of aluminum and vanadium ions into the body fluid and the possibility of any toxic effects, as a result of the passivation layer break down during wear in Ti-6Al-4V **[24]**. Consequently, other titanium alloys such as Ti-6Al-7Nb and Ti-13Nb-13Zr are under study in terms of their corrosion rate, mechanical properties, and biocompatibility as compared to Ti-6Al-4V **[25-27]**. Table 1.1 **[2, 3]** lists the mechanical properties and the clinical applications of these compositions.

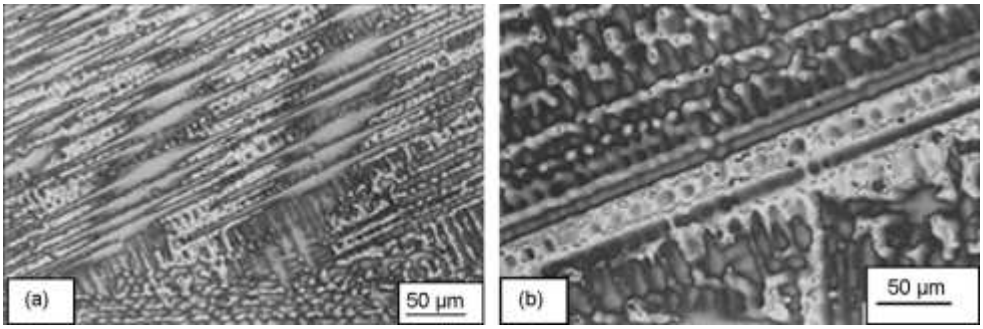


Figure 1.4 As cast Co-Cr-Mo alloys revealing (a) carbide separation in interdendrites and (b) abnormally long bands of interdendritic carbides near grain boundary. *(Reprinted from **[18]** with permissions from Springer.)*

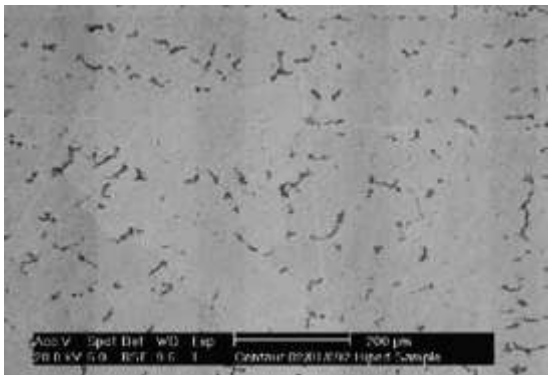


Figure 1.5 Microstructure of a hot isostatic pressed (HIP) Co-Cr-Mo alloy. *(Reprinted from **[20]** with permission from Elsevier.)*

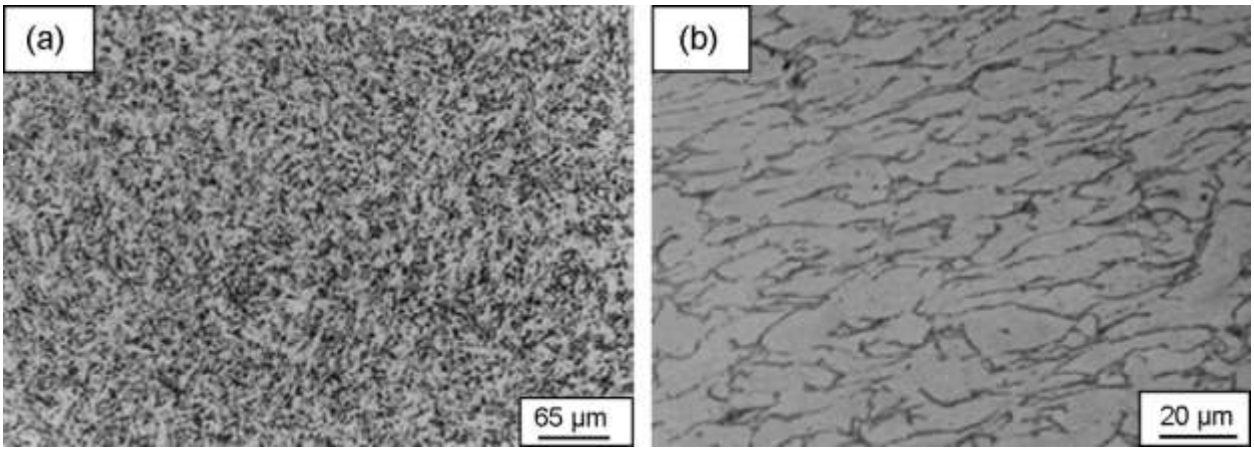


Figure 1.6 Microstructure of Ti-6Al-4V (a) under as received and annealed condition and (b) after cold working by equal channel angular pressing (ECA) technique. *(Reprinted from **[21]** and **[22]** with permission from Elsevier.)*

Table 1.1 Mechanical properties and clinical applications of Ti-based metallic materials **[2, 3].**

Alloy designation	Elastic modulus (GPa)	0.2 % offset yield strength (MPa)	Ultimate tensile strength (MPa)	Elongation (%)	Clinical applications
Pure Ti	102-110	170-480	240-550	15-24	dental implants, maxillofacial and craniofacial implants, screws and staples for spinal surgery
Ti-6Al-4V	110	860	930	10-15	total joint replacement arthroplasty primarily for hips and knees
Ti-6Al-7Nb	105	795	860	10	femoral hip stems, fracture fixation plates, spinal components, fasteners, nails, rods, screws and wire.
Ti-13Nb-13Zr	79-84	836-908	973-1037	10-16	orthopedic implants

1.3.2 Polymers

Polymers are long chain molecules consisting of large number of small repeating units known as monomers. They belong to the family of macromolecules and represent the largest class of biomaterials **[3]**. They are mostly used in orthopedics as articulating bearing surfaces of joint replacements **[3]**. Owing to their low coefficient of friction and low wear rates they are the preferred choice of materials for use in articulating contact with the opposing surface, which is generally a metal or ceramic **[2, 3]**. Among the various types of polymers available, ultrahigh molecular-weight polyethylene (UHMWPE) due to its high creep resistance, corrosion resistance, wear resistance, and in vivo compatibility is most commonly used as an inside lining or articulating material for femoral and acetabular cup. Figure 1.7 **[28-31]** shows the use of UHMWPE as a bearing material under acetabular metal shell and femoral head for hip joint and knee joint prostheses respectively.

1.3.3 Ceramics

Ceramics are inorganic compounds of metallic or nonmetallic materials, with interatomic bonding as ionic or covalent and are generally formed at elevated temperatures. A class of such materials used for skeletal or hard tissue repair is commonly referred to as bioceramics. These bioceramics may be bioinert (alumina, zirconia), bioresorbable (tricalcium phosphate), bioactive (hydroxyapatite (HA), bioactive glasses, and glass ceramics), or porous for tissue in growth (hydroxyapatite coating, and bioglass coating on metallic materials) **[2, 3]**. Their success depends on their ability to induce bone regeneration and bone in growth at the tissue implant interface without the intermediate fibrous tissue layer. The featured clinical applications include

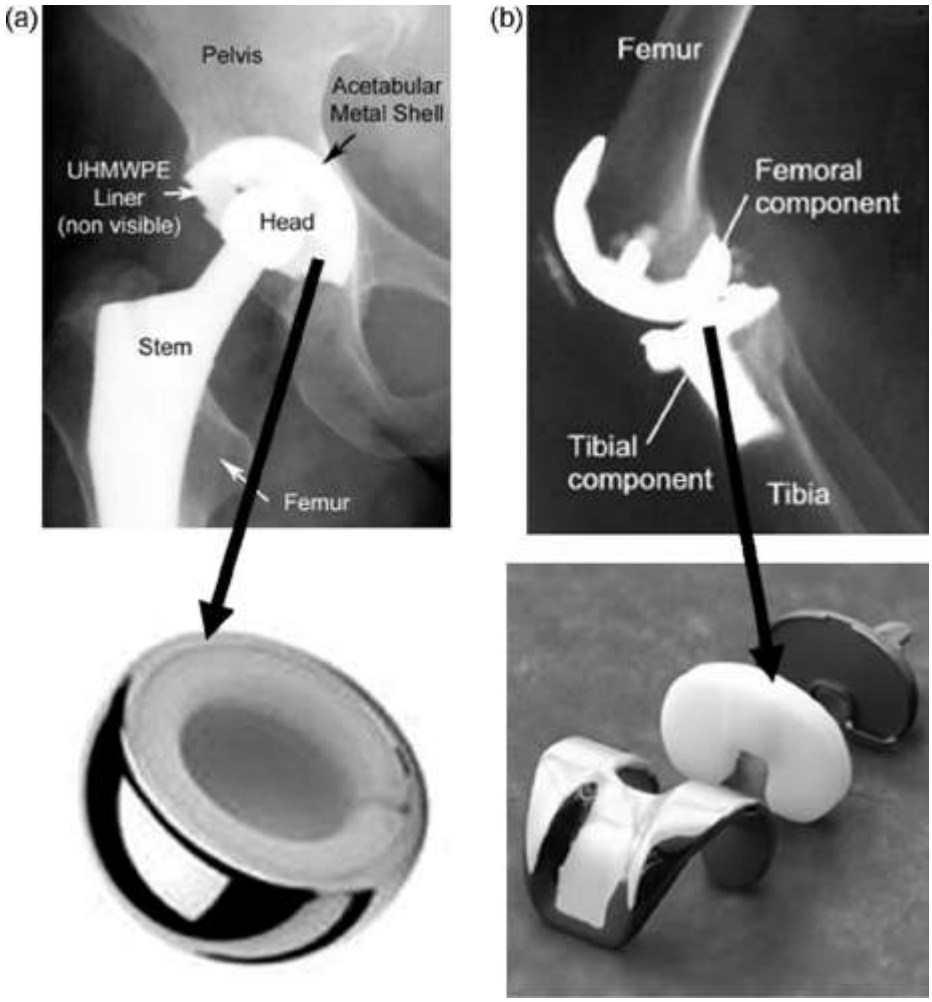


Figure 1.7 Figure illustrating the use of UHMWPE as a bearing metal for (a) hip joint *(Reprinted from* ***[28]*** *and* ***[29]*** *with permission from sources: www.devicelink.com and http://www.genesis-tech.ch/company/ respectively)*, and (b) knee joint prosthesis *(Reprinted from* ***[30]*** *and* ***[31]*** *with permission from sources: http://tc.engr.wisc.edu/UER/uer01/author1/content.html and http://www.jri-ltd.co.uk/total_knee_replacement.asp respectively*.

their use in orthopedics as (a) bone plates and screws, (b) total and partial hip components, (c) coatings on metal prosthesis for controlled implant or tissue interfacial response, (d) space fillings of diseased bone, and (e) vertebra prostheses, vertebra spacers, iliac crest prostheses, etc. Among the various types of bioceramics, bioactive ceramics such as HA ($Ca_{10}(PO_4)_6(OH)_2$), and bioglass ($CaO\text{-}SiO_2\text{-}P_2O_5\text{-}Na_2O$) are materials of major interest for load bearing implant applications.

As, HA based bioceramics mimic the naturally occurring bone mineral in terms of their chemical composition and crystallographic structure it allows for direct bone bonding by attachment, proliferation, and differentiation of bone forming cells. Therefore, there has been a tremendous interest in using synthetically derived HA for regenerating bone at the defect sites. HA can be synthesized from biological skeletal carbonate by hydrothermal exchange as per the following reaction **[8]**:

$$10CaCO_3 + 6(NH_4)_2 + 2H_2O \rightarrow Ca_{10}(PO_4)_6(OH)_2 + 6(NH_4)_2CO_3 + 4H_2CO_3 \quad \text{.....C1.1}$$

It also gets mineralized in situ on implants made of tricalcium phosphate and tetra calcium phosphate, due to interactions with the serum as per the following reactions **[8]**:

$$H_2O + 4Ca_3(PO_4)_2 \rightarrow Ca_{10} + (PO_4)_6(OH)_2 + 2Ca^{++} + 2HPO_4 \quad \text{.....C1.2}$$

$$3H_2O + 3Ca_4P_2O_9 \rightarrow Ca_{10}(PO_4)_6(OH)_2 + 2Ca^{++} + 4OH^- \quad \text{.....C1.3}$$

It is, however, realized that scaffolds fabricated using calcium phosphate salts (Table 1.2) **[32]**, with $1 \leq Ca/P \leq 2$ are not encapsulated by a fibrous tissue and allows for bone in growth to the implant surface **[8]**.

Several authors have studied the bioactivity and biocompatibility of such salts **[33-36]**. Detsch et. al **[33]** studied the response of osteoclast-like cells derived from human leukoma monocytic lineage on sintered tricalcium phosphate (TCP) and hydroxyapatite (HA). Their

studies showed that the osteoclast-like U-937 cells responded in a different manner to HA and TCP (Figure 1.8) **[33]**. Sintered HA plates favored giant cell formation with pronounced actin rings (Figure 1.8 (a), (b)) and therefore larger lacunas as compared to TCP (Figure 1.8 (c), (d)). The authors, therefore, proposed that calcium phosphate based ceramics as a bone substitute material must be chosen either for their fast degradation (TCP) or for the slow remodeling of the biomaterial (HA). The choice of ceramic depends on the location and size of the bone defect and the patient's personal characteristics.

Table 1.2 Chemical name, mineral name and composition of various Ca-P based ceramics **[32]**.

Ca/P	Formula	Name/mineral	Abbreviation
1.0	$CaHPO_4.2H_2O$	Hydrated calcium phosphate/brushite	DCP
1.0	$CaHPO_4$	Anhydrous calcium phosphate/Monetite	ADCP
1.33	$Ca_8H_2(PO_4)_6.5H_2O$	Octacalcium phosphate	OCP
1.5	$Ca_3(PO_4)_2$	Tricalcium phosphate/Whitlockite	TCP
1.67	$Ca_{10}(PO_4)_6F_2$	Flourapatite	FA
1.67	$Ca_{10}(PO4)_6(OH)_2$	Hydroxyapatite	HA
2.0	$CaO.Ca_3(PO_4)_2$	Tetracalcium phosphate/ Hilgenstockite	TTCP

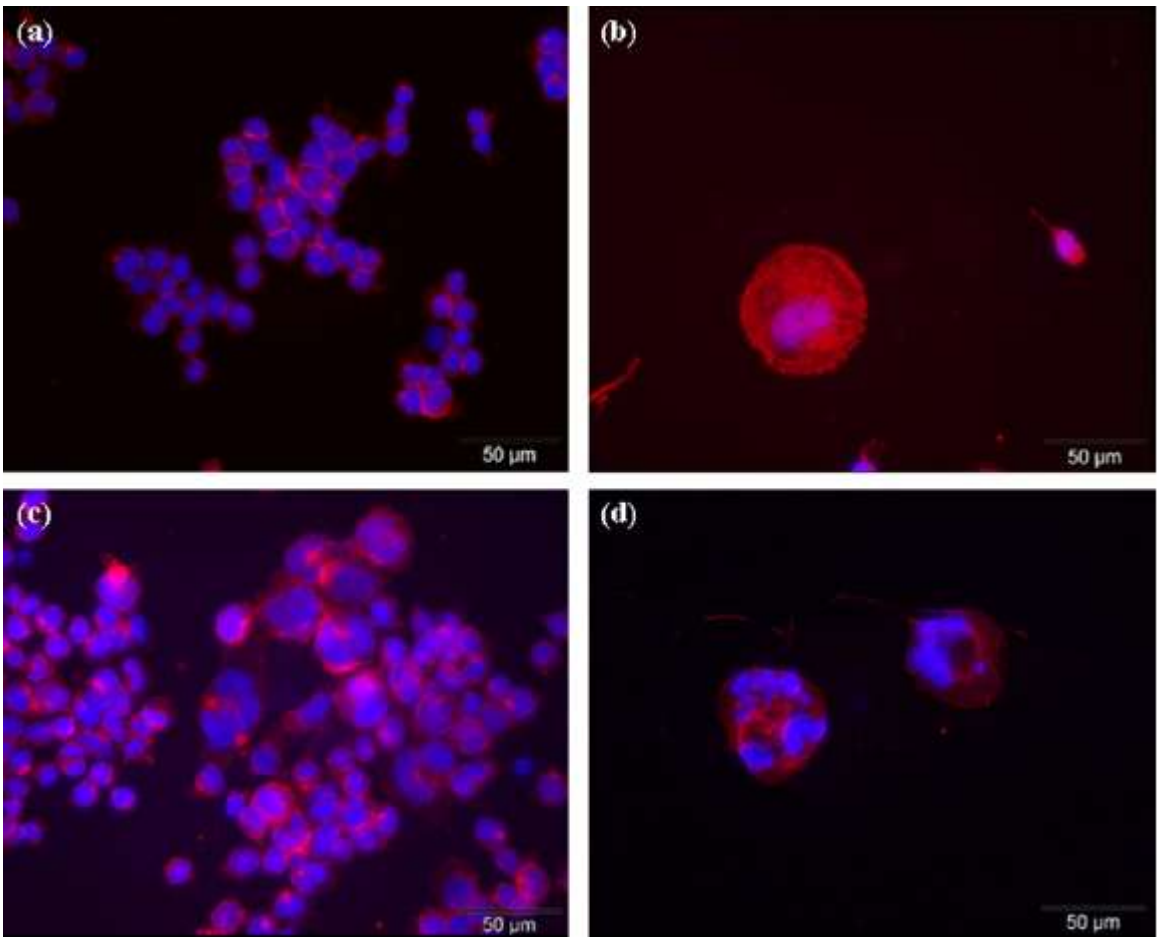


Figure 1.8 Fluorescence microscopy images of U-937 cells cultured on (a, b) TCP, and (c, d) HA, with VD_3 and PDBu for 21 days. *(Reprinted from **[33]** with permission from Elsevier.)*

1.3.4 Composites

A composite consists of two or more materials each with distinct physical or chemical properties and is designed to have a combination of best characteristic of each component materials. Biomedical composites are often designed to provide superior mechanical and biological compatibility. Some promising orthopedic applications of biomedical composites include their use in total joint replacements, spine rods, discs, plates, screws, and ligaments. They can be classified based on the matrix material or on the bioactivity of the composites. Considering matrix material as the basis for classification, there are three different types of biomedical composites **[37]**:

- Polymer matrix composites, e.g., carbon/PEEK (polyetheretherketone), HA/ HDPE.
- Metal matrix composites, e.g., HA/Ti, HA/Ti-6Al-4V.
- Ceramic matrix composites, e.g., stainless steel/HA, glass/HA.

Considering bioactivity of the composite as the basis for classification, there are three different types of biomedical composites **[37]**:

- Bioinert composites, e.g., carbon/carbon, carbon/ PEEK.
- Bioactive composites, e.g., stainless steel/Bioglass, HA/HDPE, HA/Ti-6Al-4V.
- Bioresorbable composites, e.g., tricalcium phosphate (TCP)/ poly lactic acid (PLA), TCP/ polyhydroxybutyrate (PHB).

1.4 Clinical concerns with orthopedic implant biomaterials

Despite their overwhelming success for long term performance, orthopedic biomaterials still have been associated with adverse local and remote tissue responses and bulk failure due to normal activity of patient. Hence, there has been a significant clinical concern in terms of improving the properties of these materials for their longevity and thereby restore the quality of life. The bulk failures of the load bearing orthopedic implant material are mostly associated with its mechanical behavior and chemical stability under in vivo conditions. Whereas failures due to adverse local and remote tissue responses is mostly due to the surface properties of the material.

1.4.1 Mechanical failures

The types of mechanical failures that are mostly common to these kind of medical devices are (a) failure due to high elastic modulus, (b) failure due to fatigue, and (c) failure due to wear. A material with high elastic modulus is not ideal for load bearing implants as insufficient load transfer from an artificial implant to the adjacent remodeling bone results in bone resorption and eventual loosening of the prosthetic device **[38]**. Failures caused due to repetitive or fluctuating stress cycles are called fatigue failures. Owing to the brittle nature of ceramics, fatigue may be a major area of concern for implants coated with bioactive and biocompatible ceramics as it may result in wear debris generated due to the fatigue process. This in turn may invoke adverse host-tissue response at the interface. Fatigue failure is also a common phenomenon in medical grade UHWMPE used as a bearing surface in total joint replacement **[39]**. Cyclic loading on polymeric materials such as UHWMPE may lead to softening accompanied by reduction in elastic modulus and yield stress. Fatigue is also often considered as a prime cause of failure for titanium base load bearing implant materials. Cyclic loading on Ti based metallic materials may result in alternating plastic deformation of microscopically small zones of stress concentrations produced by notches or microstructural inhomogenities **[40]**. These small zones of stress concentrations are the regions where the crack initiates, propagates, and finally fractures due to prolonged cyclic loading. Figure 1.9 **[41]** shows the fatigue fracture surface morphology with regions representing crack initiation, propagation, and overload site due to cyclic loading on Ti-6Al-4V.

Wear may be defined as a surface damage or material removal process resulting from two surfaces in contact and in motion with each other. In general, higher the mutual solid solubility between two materials in contact, higher is the wear. Hence, wear is generally higher for similar

materials in contact than for dissimilar materials. In contrast, for biomaterials used inside a human body wear may be extremely high for dissimilar metallic materials. This is due to the fact that dissimilar materials in contact in saline or aqueous environment form a galvanic cell and result in corrosion, which may further exacerbate the wear phenomena. This is a very common experience in hip implant prostheses where a metal or ceramic femoral head articulates with an UHMWPE acetabular cup **[42-46]**. Wear debris generated from such joint replacements enters the periprost-

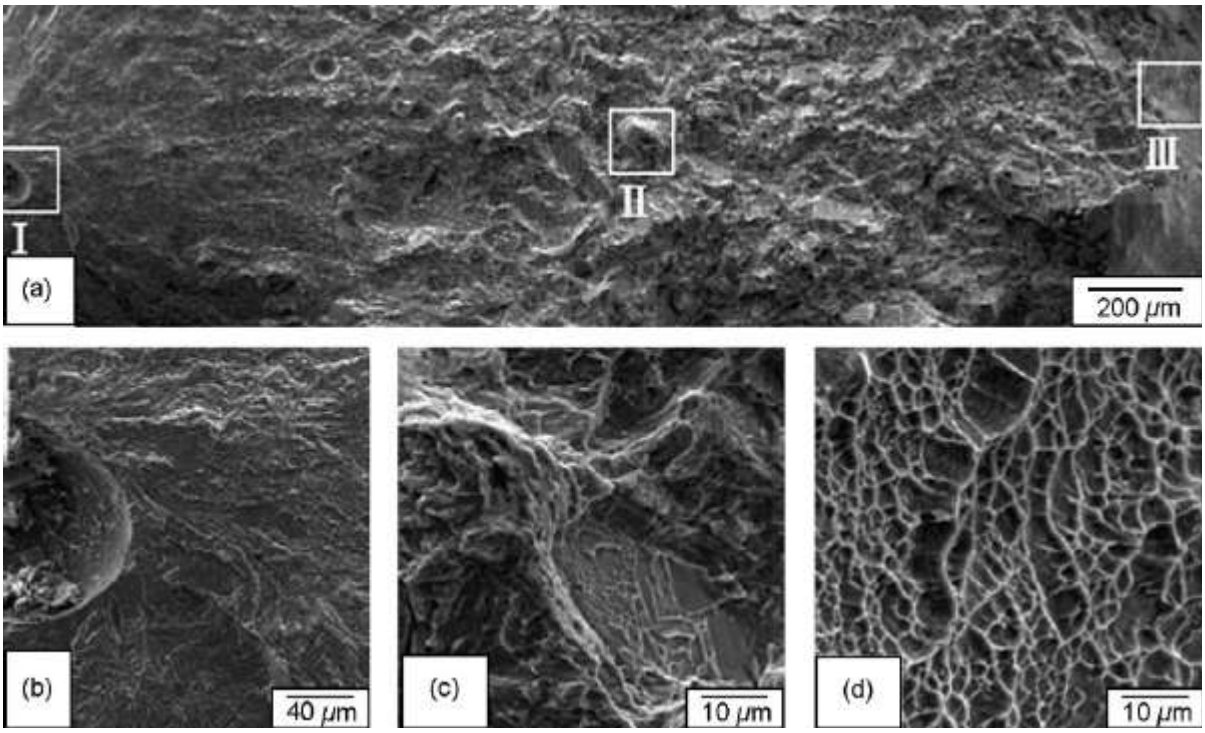


Figure 1.9 Fatigue fracture surface morphology of Ti-6Al-4V. ((a) overall fracture surface; (b) crack initiation site taken from area "I"; (c) crack propagation site taken from area "II"; (d) overload site taken from area "III"). *(Reprinted from **[41]** with permission from Elsevier.)*

hetic tissue and is phagocytosed by macrophages. These macrophages then release pro-inflammatory cytokines and other mediators of inflammation that stimulates osteoclastic bone resorption, leading to osteolysis and eventual loosening of the device **[46]**. Therefore, there has been a significant interest in developing metal-on-metal and ceramic-on-ceramic bearing surfaces for hip joint prostheses **[47-49]**.

1.4.2 Failure due to corrosion

Load bearing orthopedic metallic implant materials used inside a human body are generally exposed to a harsh aqueous environment containing various anions ($Cl^-, HCO_3^-, HPO_4^{2-}$), cations ($Na^+, K^+, Ca^{2+}, Mg^{2+}$), organic substances, and dissolved oxygen **[2, 3]**. Hence, metallic implant materials are prone to aqueous corrosion. The mechanism of corrosion for metallic implant materials is based on the following fundamental reactions **[2, 3]**:

$M \rightarrow M^{n+} + n(electrons)$ ……Anodic dissolution……...C1.4

$O_2 + 2H_2O + 4e \rightarrow 4OH^-$ ……...Cathodic reduction……...C1.5

$M^+ + OH^- \rightarrow M(OH)$ ……Corrosion product……....C1.6

The metallic components of the alloy are initially oxidized to their ionic forms and release a free electron. The dissolved oxygen in the aqueous environment then react with the water molecule and free electron to form hydroxyl ions. These hydroxyl anions then react with the metallic cations to form a corrosion product. The various factors upon which the above reaction process depends can be listed as follows: (a) geometric variables (e.g., taper crevices in modular component hip prosthesis), (b) metallurgical variables (e.g., surface microstructure, oxide layer, and composition), (c) mechanical variables (e.g., stress and/or relative motion), (4) solution

variables (e.g., pH, solution proteins, enzymes), and (5) the mechanical loading environment (e.g., degree of movement and contact forces) **[3]**.

1.4.3 Failures due to surface properties

The three most important surface parameters that dictate the biological response to implant surfaces are surface morphology, surface wettability, and surface chemical composition. The above three parameters control the first phase of cell/material interactions i.e. attachment, adhesion, and spreading of osteoblast cells and thereby influence its capacity to proliferate and differentiate on contact with the implant. Surface morphological features in the form of surface roughness or 3-D surface topographic cues act as anchorage points for bone tissue integration by bone ingrowth. However, if there is no such features it results in zero mechanical stimulation around the surrounding bone and hence bone loss during the early days of implantation **[2]**. Further, on smooth non textured surfaces the bone cells grow in a random manner without contact guidance and hence differentiate less as compared to the cells on a textured surface **[2]**. This, therefore, results in mineralized tissues which are less dense and substandard in mechanical properties.

Bone cells very well differentiate alterations in surface chemistry and are sensitive to the presence of chemical species available on the surface of a material. Depending on the type of species available and its exposure, the biomolecules may have different affinities for various surfaces. Further, at a microscopic level, a biomaterial surface may have patches, or domains, of different functionality and these patches or domains can interact differently with the biomolecules. For example metallic materials mostly exist in more than one phase. Ti-6Al-4V a commonly used orthopedic implant material consists of two different phases, i.e. the α- and β-

phase. Not only these different phases but also the grain boundaries may have a different chemical composition and thereby a different interaction with biomolecules. In polymers, segregation resulting from folding of macromolecular chains can provide various microstructural domains. Depending on the chemical species present within these domains, proteins may have different interaction with each phase. Hence, modulation of surface chemistry of implant biomaterials to provide better in vivo response is an area of extensive research. The lack of appropriate surface chemistry affects the recruitment of cell binding proteins and its orientation under in vivo conditions. This in turn ultimately affects the binding of cells to the implant material and its further differentiation to form a hard mineralized tissue.

Finally wetting is an important aspect for load bearing orthopedic implant devices, as it influences the initial interaction with physiological fluids under in vivo conditions. This further controls the adsorption of proteins followed by attachment of cells to the implant surface. Hence, surface wettability is considered as an important criterion that can dictate the biocompatibility of the implant material. The three most important factors that affect the wettability of a surface are its chemical composition, microstructural topography and surface charge. For all load bearing implant devices it is ideal for their surface to be hydrophilic to the surrounding body plasma. If the surface is hydrophobic the serum constituents do not interact with the implant and hence there will be no protein adsorption resulting in the formation of a fibrous capsule at the interface.

1.5 Prospective for improvement

Orthopedic implant materials currently available, therefore, lack one or more of the above discussed properties and result in failure under in vivo conditions. If most of these biomaterials have the required mechanical properties for a defined implantation site, they do not all possess

necessary bioactivity and biocompatibility for cell attachment and tissue integration. In order for new improved load bearing implant materials to address the above issues, there should be some understanding of the interrelationship between the structure and properties of the natural tissues that are being replaced. A detailed understanding and appreciation of the form-function relationship in calcified tissues like bone will help provide insight into factors determining implant design as well as deciding which are the materials of choice to meet a specific need **[3]**.

Human body essentially consists of several different calcified tissues and each of them can be categorized in a different way. However, most of these calcified tissues essentially consist of a principal protein component, collagen, small amounts of organic phases, and a major portion of inorganic component as hydroxyapatite (HA) **[2, 3]**. In the present context, we are only concerned about the hard calcified tissue that is compact bone. A compact cortical bone is composed of 20 wt-% collagen, 69 wt-% calcium phosphate, 9 wt-% water and the rest as organic materials such as proteins, polysaccharides and lipids **[2, 3]**. It is organized in a hierarchical manner at different length scales ranging from nanoscale to mesoscale **[2, 3]**. A schematic representation of such an organization is illustrated in Figure 1.10 **[50]**.

As discussed above it can be realized that a significant portion of the bone is composed of collagen. Hence, in addition to being anisotropic and inhomogeneous, bone is also viscoelastic like all other biological tissues **[3]**. Therefore, mimicking such properties in a long lasting synthetic biomaterial remains an unrealized goal of orthopedic biomaterials where the history of implant development has been characterized by the elimination of various available materials based on their poor performance rather than production of biocompatible synthetic bone-mimetic materials **[3]**. Nonetheless, to achieve the best clinical outcome by mimicking properties as close

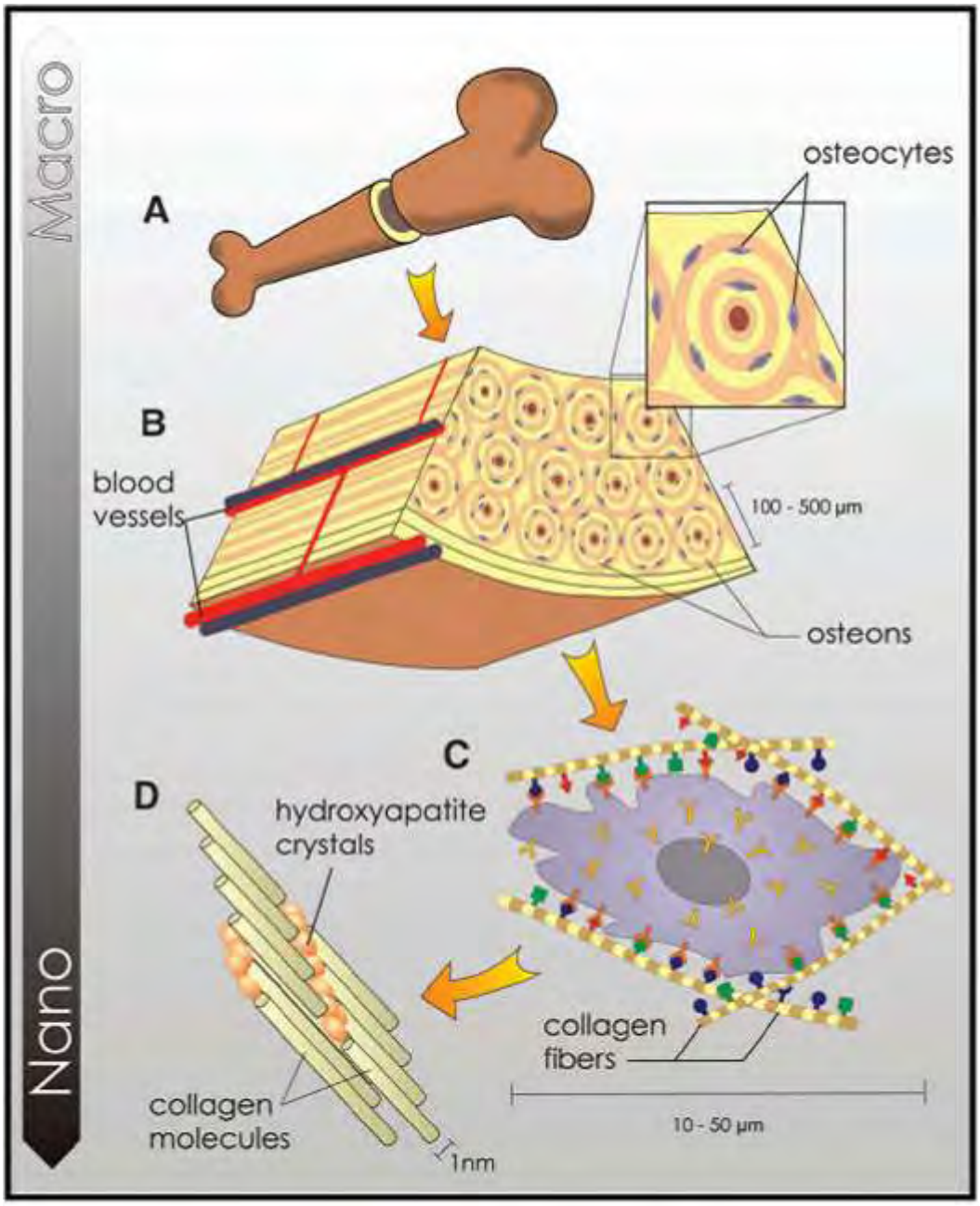


Figure1.10 Schematic representation of the hierarchical organization of bone at different length scales. *(Reprinted from* ***[50]*** *with permissions from American Association for the Advancement of Science (AAAS).)*

as possible to the natural organization, several engineering strategies have been carried out by scientists and researchers world wide. Among these various strategies, surface modification or surface engineering techniques for load bearing implant materials has been the subject of tremendous interest.

1.5.1 Surface science and engineering of load bearing orthopedic implant biomaterials

Surface modification or surface engineering for biomaterials offers the ability to selectively modify material and biological responses through changes in surface properties while still maintaining the bulk properties of the implant material. Surface modification for biomaterials can be classified according to the way the surface properties being altered, e.g., morphological, physiochemical, and biological modifications.

1.5.1.1 Morphological modifications

Morphological modification of biomaterial surfaces are aimed at creating three dimensional features in the form of pores, gratings, columns, dots, pits, and random surface roughness **[1, 51-55]**. These three dimensional features mimic the extra cellular matrix (ECM), a natural cell environment which possesses complicated nano and macro architecture. This can be achieved by various techniques such as ion beam etching, chemical etching, plasma etching, electron beam lithography, photolithography, surface coatings, freeze casting, sintering, UV-irradiation, mechanical roughening, etc.

Kim and coworkers studied a sand blasted and acid etched titanium surface (Figure 1.11) **[55]** for its biocompatibililty and osseointegration. This technique has the advantage of both sand blasting and acid-etching and thereby creating both macro-roughness and micro pits on the

surface. Human osteoblast cells grown on the sand blasted and acid etched titanium surface shows very good adherence and spread over the surface after seven days of incubation (Figure 1.12) **[55]**. In vivo evaluations of the samples were carried out using a screw shaped sand blasted and acid etched titanium implants. The implants were placed in New Zealand white rabbits in each proximal tibial metaphysic after giving them a general anesthesia. After 4 weeks of healing period the rabbits were sacrificed and histological evaluation demonstrated a very good bone bonding and bone formation at the interface **[55]**.

Since naturally occurring bone is a porous material, there is also a physiological rationale for the use of porous scaffolds for its replacement at defect sites. Apart from just mimicking the natural organization of a bone a porous structure also helps in the supply of blood and oxygen to the implant interface **[2]**. Porous Ca-P based composite scaffolds and porous Ca-P coatings are being widely used for load bearing hip and knee implants **[2]**.

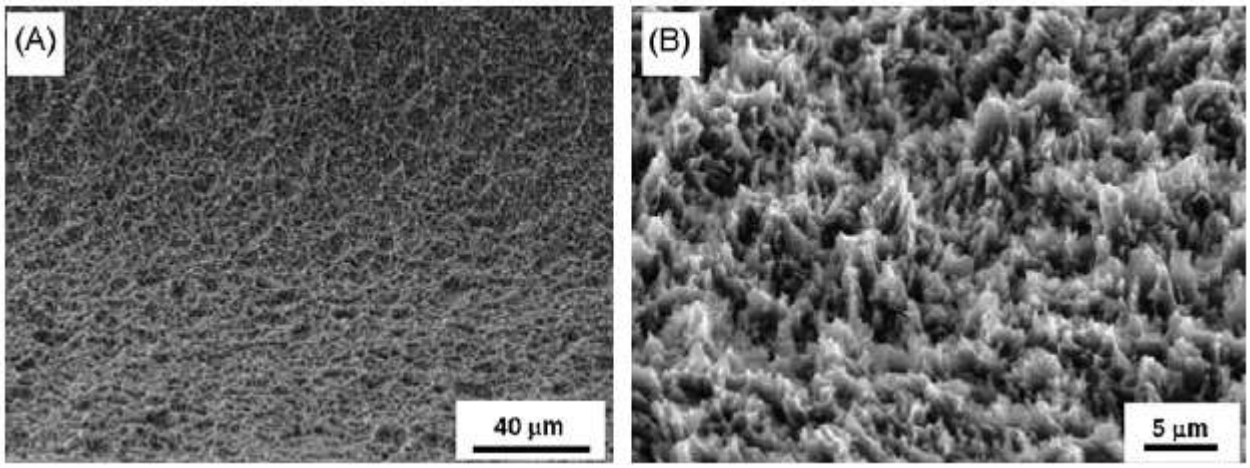


Figure 1.11 SEM image of a sand blasted and acid etched titanium surface. *(Reprinted from **[55]** with permissions from Institute of Physics Publishing (IOP).)*

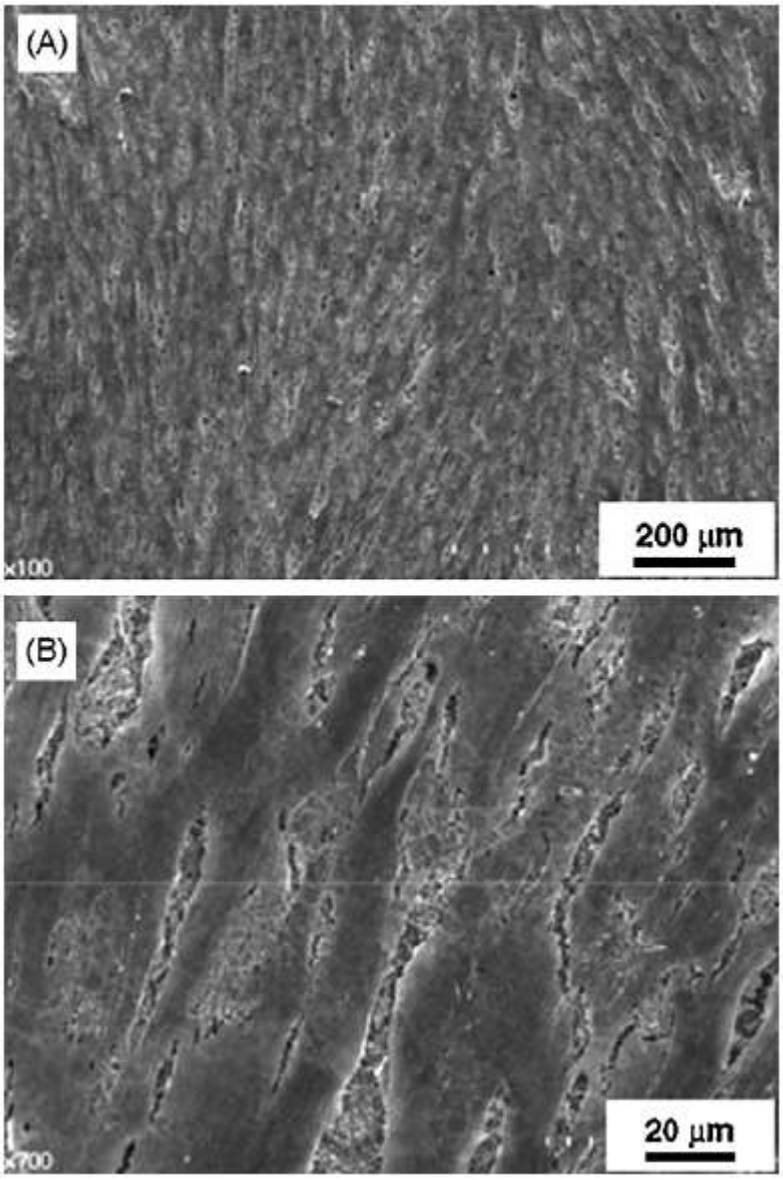


Figure 1.12 SEM image of human osteoblast on the SLA surface after seven days of incubation at different magnification. (A) 100× and (B) 700×. *(Reprinted from **[55]** with permissions from Institute of Physics Publishing (IOP).)*

1.5.1.2 Physiochemical modifications

Material and biological responses can be altered by changing physiochemical characteristics such as surface energy, surface charge, and surface composition. This can be achieved by various techniques such as glow discharge, ion implantation, grafting, and surface coatings.

Glow discharge involves the exposure of surface to a highly energized inert gas such as plasma **[56]**. Plasma glow discharge is most commonly used to sterilize the surface of biomedical devices and surgical instruments used for clinical applications. The energetic species in the plasma can easily kill a broad range of bacteria by generating oxygen, hydroxyl free radicals and other active species. This further improves the wettability of the implant material or its hydrophilicity. It has got several advantages compared to other sterilization techniques and can be listed as follows **[56]**:

- It is a nontoxic and fast procedure.
- Since plasma sterilization is similar to plasma etching it not only kills the bacteria, but also removes them from the surface.
- It is inexpensive and relatively a safe technique.

Ion implantation involves the bombardment of highly energetic ionic species to the surface of a material. The ions penetrate the surface and thereby bring significant changes in chemical composition and structure at the near surface region. This further improves the wear resistance, corrosion resistance, and biocompatibility of implant materials. For example calcium ions implanted into the surface of titanium can improve its bone conductivity. Penetration and phase changes at the surface of titanium following varying dosages of Ca ion implantation are schematically illustrated in Figure 1.13 **[57]**. Calcium titanate is formed at the surface when Ca

ions are implanted at the rate of 10^{16} and 10^{17} ions/cm^2 and both calcium oxide and calcium titanate are formed when ions are implanted at 10^{18} ions/cm^2. Figure 1.14 **[57]** shows the scanning electron micrographs of unimplanted titanium (a) and calcium-ion-implanted titanium (b) after immersion in a SBF for 30 days. It is observed that the surface of calcium ions implanted titanium is modified and a layer of calcium phosphate precipitation has taken place following immersion.

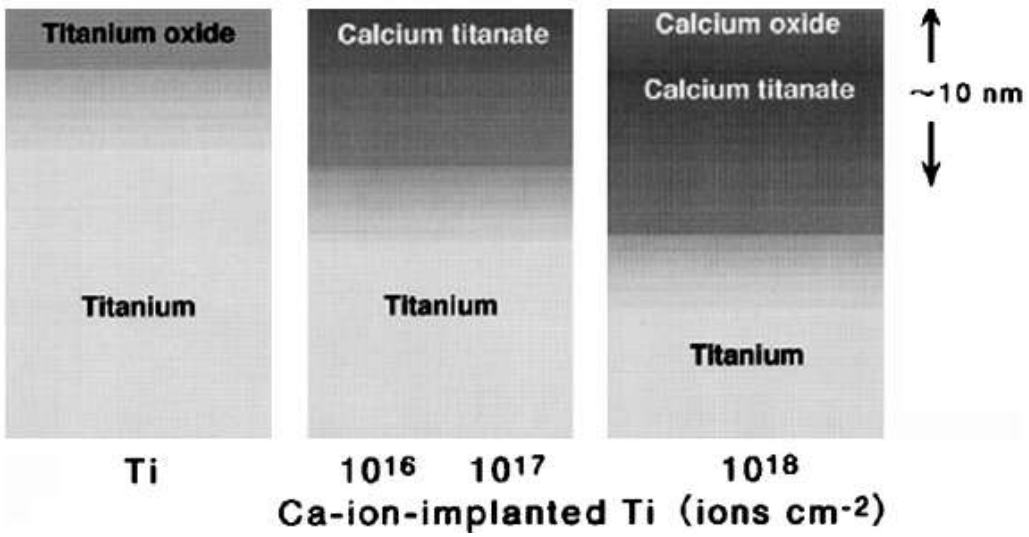


Figure 1.13 Schematic illustration of cross-sections of surface-modified layers of titanium specimens with and without calcium-ion-implantation. *(Reprinted from* ***[57]*** *with permission from Elsevier.)*

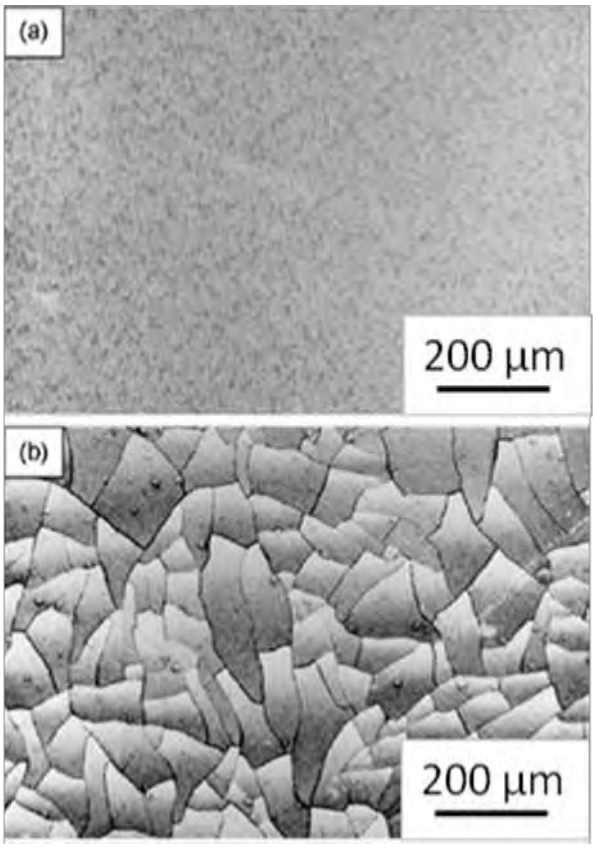


Figure 1.14 Scanning electron micrographs of unimplanted titanium (a) and calcium-ion-implanted titanium (b) immersed in Hank's solution for 30 days. *(Reprinted from **[57]** with permission from Elsevier.)*

Grafting involves the attachment of specific functional groups (mostly polymeric chains) onto the surface of a biomaterial **[58-60]**. This can be achieved by graft polymerization technique provided that the surface active sites or free radicals are available to react with a monomer. If reactive groups are available on the surface, the desired polymer can be attached through free radical graft polymerization of a monomer or through chemical reaction of a polymer with functional end groups. If there are no reactive groups available on the surface then plasma, γ-ray, and UV light induced graft polymerization is a useful technique.

Surface coatings can also be used to provide surface composition chemically different from the substrate. For orthopedic implant applications, engineered bio coatings of alumina, zirconia, bioactive glasses (glass ceramics), and calcium phosphate based (Ca-P) ceramics on Ti base alloys is a common practice. Alumina and zirconia are considered as boinert as they do not induce the formation of a fibrous tissue at the interface and direct bonding with the surrounding tissues. Bioactive glasses and Ca-P based ceramics are considered as bioactive as they form a direct chemical bonding with the bone. Ca-P based ceramics are widely used as bioactive coatings as they possess similarity with the mineral phase hydroxyapatite present in the human bone and teeth. Ion beam assisted deposition, plasma spray coating, pulsed laser physical vapor deposition, magnetron sputtering, etc. are among the several types of coating methodologies that are being employed to achieve such a surface.

1.5.1.3 Biological modifications

In the last few years, there has been a major shift in the design criteria for modern synthetic biomaterials. An understanding of cell and molecular biology has led biologists, chemists, and material scientists to design biomaterials equipped with molecular cues mimicking certain

aspects of structure or function of natural extra-cellular microenvironments **[1-3]**. Hence, biological surface modification is aimed at controlling cell and tissue response to an implant by immobilizing biomolecules representing such molecular cues on the surface of biomaterials. Adsorption, entrapment, and covalent attachment are the three mechanisms by which biomolecules are immobilized on the surface of a biomaterial. The most commonly used biomolecules for immobilization on load bearing implant surfaces include purified protein components such as fibronectin, laminin, and collagen. Purified protein components such as collagens from animal tissues are advantageous because of their inherent properties of biological recognition, presentation of receptor binding ligands, and susceptibility to cell triggered degradation and remodeling **[61]**.

Biological surface modifications can also be aimed at producing surfaces resistant to biofouling, protein and cell adhesion and thereby improve its blood compatibility. The outer membrane of intact blood cells consists mainly of phosphorycholine containing phospholipids that provide a nonthrombogenic surface. Hence, phosphorycholine polymers can, therefore, be grafted on to biomaterial surfaces to mimic the phospholipid head groups of the cell surface and thereby improve its biocompatibility. Figure 1.15 **[62]** shows the immobilization of phosphorycholine polymers on a titanium surface controlled by a vinyldimethylsilane (VDMS) monolayer.

Although all of the above surface modification techniques have demonstrated significant promise in terms of improving the bioactivity and biocompatibility of the implant materials, most of them are only restricted to lab scale experiments and yet to be fully practiced for large scale production and manufacturing. The most commonly used surface modification technique for load

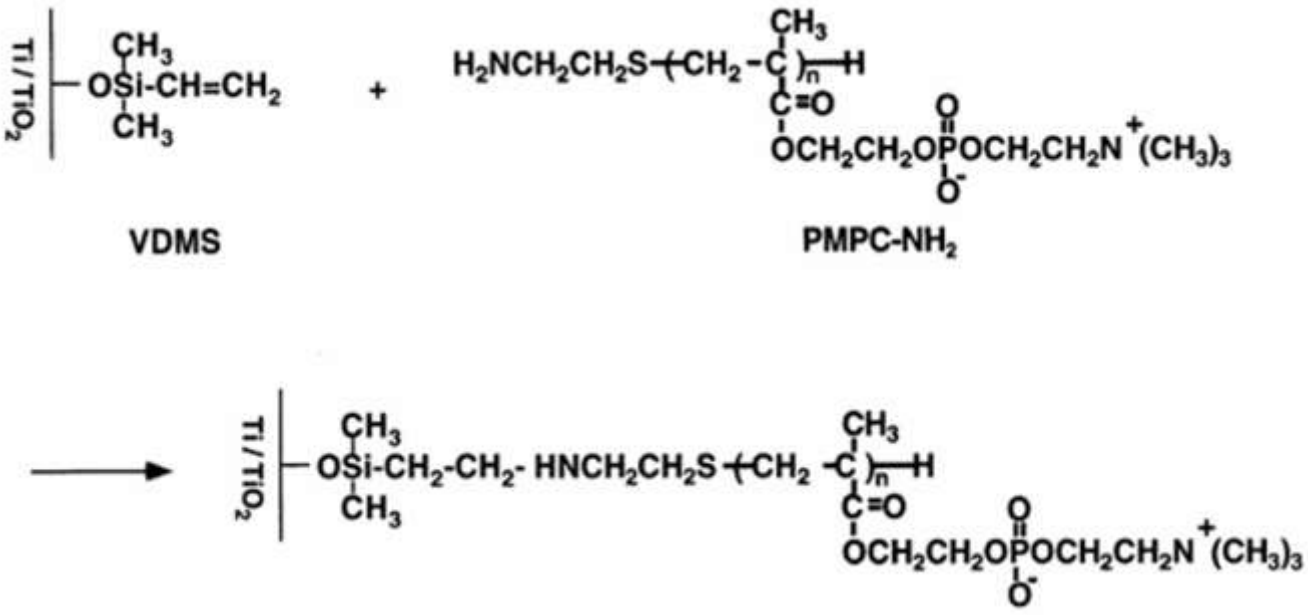


Figure 1.15 Figure illustrating the immobilization of phosphorycholine polymers on to titanium surface controlled by a vinyldimethylsilane (VDMS) monolayer. *(Reprinted from **[62]** with permission from Elsevier.)*

bearing orthopedic implant materials is the physiochemical surface coatings of Ca-P based bioactive ceramics on Ti based metallic alloys.

1.5.2 Ca-P based bioactive coatings

A variety of surface coating methodologies such as ion beam assisted deposition, plasma spray deposition, electrophoretic deposition, pulsed laser physical vapor deposition, micro-arc oxidation, magnetron sputtering, sol-gel derived coatings, etc. are being currently employed to deposit Ca-P on Ti based alloys. Most of these techniques are aimed to enhance short- and long-term performance of implants by encouraging bone ingrowth and provide enhanced fixation. Further, coatings of these bioceramics on Ti based alloys also provide appropriate surface

chemistry for tissue compatibility without altering the bulk mechanical properties of the material. Among the above surface coating methodologies plasma spray deposition is the most commercially used technique for orthopedics and dental implants. However, this method suffers from certain draw backs such as poor adherence of the coating to the substrate, low fracture toughness of the ceramic coating, lack of uniformity of the coating thickness, biodegradation, and fatigue and third body wear of the coating **[2, 63]**. The higher coating thickness (> 100 μm) associated with plasma spraying technique poses a major problem as it can cause failure due to fatigue under tensile loading conditions **[63]**. Also with increasing thickness the residual stresses within the coatings increase and its energy release may promote cracking at the substrate/coating interface **[63]**. To address these issues, a variety of thin film based surface coating techniques such as pulsed laser physical vapor deposition, magnetron sputtering, ion beam assisted deposition, etc. are being employed to deposit Ca-P coatings on metallic substrates **[63]**. Nonetheless, none of these thin film based coating techniques is able to synthesize a sound metallurgical bonding between the Ca-P coating and the substrate and unable to create a regular three dimensional topographic cues on the surface. The lack of a sound metallurgical bonding often results in loosening of the ceramic coating and release of foreign elements into the body environment. In order to improve the bonding strength between the coatings and substrate, several researchers tried the laser based melting technique **[64-69]**.

Potential of the laser based melting technique for load bearing orthopedic implant applications has already been demonstrated in the work by Cheng **[64]**, Lusquiños **[65],** and Wang **[67]**. Cheng and co-authors **[64],** directly melted pre-placed HA-Ti composite powders on Ti alloy substrate using a Nd:YAG laser. The authors characterized the mechanical properties of

the coatings using Vickers and nano indentation techniques. The higher values of hardness, elastic modulus, and resistance to crack growth as obtained using the above techniques proved for the sound interfacial toughness of the coatings. Lusquiños and co-authors **[65]** used a laser based cladding technique where a high power laser beam was used to melt the substrate (Ti-6Al-4V), and a simultaneous jet of precursor (HA powder) was blown by a carrier gas on to the molten cloud to form the coating. The authors showed the presence of sound bonding and minimum dilution of the clad layer into the matrix of the substrate using SEM and XRD analysis of the cross-sectioned specimens. A laser based cladding technique using calcium carbonate and calcium hydrogen phosphate as the precursor material to synthesize HA coating on Ti substrate was demonstrated by Wang et al. **[67]**. Using SEM and XRD analysis the authors showed the presence of sound bonding at the interface with cellular dendritic structure and the presence of phases HA, α-$Ca_2P_2O_7$, CaO, and $CaTiO_3$ within the coating **[67]**. Although, all of the above works proved the feasibility of a sound metallurgical bonding via laser based melting technique, none of these techniques could achieve a regular three dimensional topographic cue for contact guidance and adhesion of bone forming cells. In light of the above drawbacks associated with the present surface modification techniques, a laser based surface engineering approach was researched in the current work to simultaneously synthesize a metallurgically bonded textured Ca-P coating on Ti-6Al-4V substrate.

Chapter 2

Scope and Objective of the Current Work

A textured Ca-P bioceramic coating on Ti-6Al-4V substrate is expected to replicate the functionality and natural organization of the hard tissue to the best proximity. Following implantation of such a biomaterial, the various phenomena that may occur at the interface under in vivo conditions is sequential and can be best illustrated by the schematic shown in Figure 2.1 **[2]**. Initially, owing to the appropriate surface chemistry and textured morphology the proteins respond to the implant surface and within few seconds to minutes a thin layer of protein film is formed on the surface. Since cells respond to the proteins, this protein film then controls the subsequent bioreaction. The cells attached to the proteins get contact guided by the textured morphology, differentiate, and multiply to form complex tissues. Therefore, the initial adsorption of proteins plays a vital role in determining the nature of the tissue-implant interface. Further, as an alteration in surface morphology and surface chemistry affects the wetting behavior of the implant material under in vivo conditions, it is this wetting characteristic (hydophilicity or hydrophobicity) of the material that finally controls the adsorption of proteins to the implant surface. An understanding of the mechanism of wetting will help in tailoring the surfaces for more hydrophilic behavior to physiological fluids and thereby help recruit proteins and bone cells from the surrounding to the implant surface swiftly.

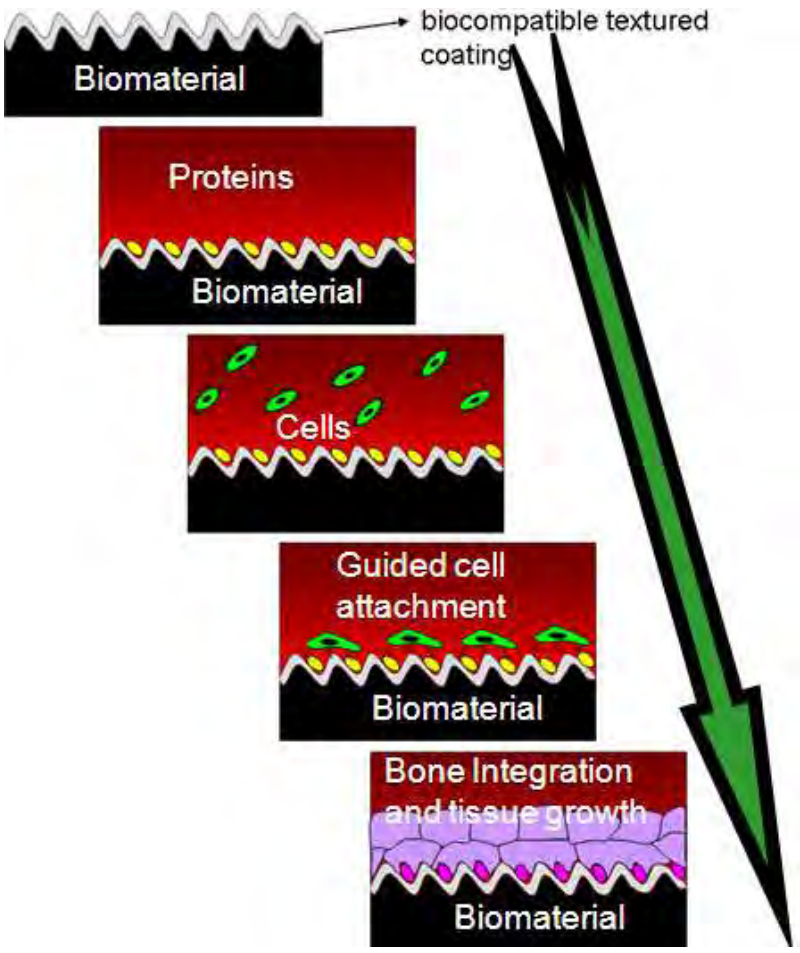


Figure 2.1 Schematic illustration of the sequential reactions that take place after the implantation of an biomaterial into a living system **[2]**.

Keeping in mind the above advantageous features associated with a textured coating for load bearing orthopedic implant biomaterials, the goals or objectives of the current research were set as follows:

- Develop a technique to synthesize simultaneously a textured biocompatible coating with appropriate topographic cues and surface chemistry.
- Study the microstructure and morphological and phase evolutions in the textured coatings as a function of processing parameters.
- Calculate the surface energy components of the textured surfaces for gaining enhanced understanding of the mechanisms and the effects of textured coating on the wetting behavior to both simulated body and standard testing liquids.
- Study the in vitro bioactivity of the textured coating by immersing the samples in a solution with ionic concentrations equal to that of the human blood plasma and analyzing the precipitation of HA.
- Correlate the precipitation kinetics or the mineralization behavior of HA to both the wetting and varying surface morphology.
- Study the biocompatibility of the textured coatings in terms of cell viability and cell differentiation by culture of bone cells.
- Make a qualitative assessment of the proliferation and cytoskeleton organization of the bone cells on the textured surfaces.

In the current work, we used a laser based direct melting technique to achieve textured coating. Here by controlling the laser process parameters, surfaces with appropriate topographic cues and

phases were aimed to be synthesized for improved wettability, in vitro bioactivity, and in vitro biocompatibility. Further, in order to only understand the effect of morphological features on the wetting dynamics, the laser process parameters were controlled to achieve surfaces with different morphologies and same beneficial (Ca-P) phases. The textured surfaces obtained by this approach were assumed to simulate a cosine profile (Figure 2.2) **[70-73]** with a Gaussian distribution of amplitude. They were then characterized in terms of the roughness parameters i.e. the standard deviation of amplitude (σ_A) and wavelength (λ) and their ratio (σ_A/λ) was taken as a measure of texture parameter. Based on the texture parameter value, the surface textures were characterized as radial type grooves and sharp circular type grooves **[70-73]**. Finally, the effect of laser processing parameters on the texture parameter (σ_A/λ) and thereby its influence on wettability**,** in vitro bioactivity, and in vitro biocompatibility is systematically discussed. As a future surface engineering approach, a laser based optical interference patterning technique (LIP)

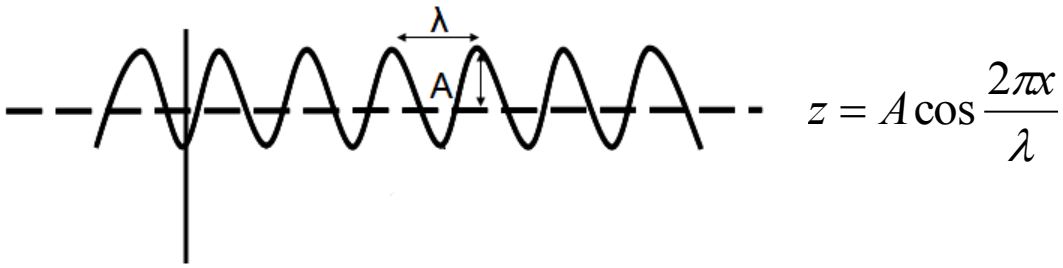


Figure 2.2 Schematic illustration of a textured surface morphology **[70-73]**.

technique to synthesize 3-dimensional regular topographic cues on Ti-6Al-4V was also touched upon. Preliminary efforts were made towards understanding the wetting behavior on interference patterned samples and thereby analyzed its potential for load bearing implant applications. Based on the wetting results obtained on the samples processed by laser direct melting and LIP, an attempts were made to understand the textured coating and simply textured surface (uncoated). Finally, the above proposed goal and approach of the current research can also be very well summarized in the following illustration (Figure 2.3).

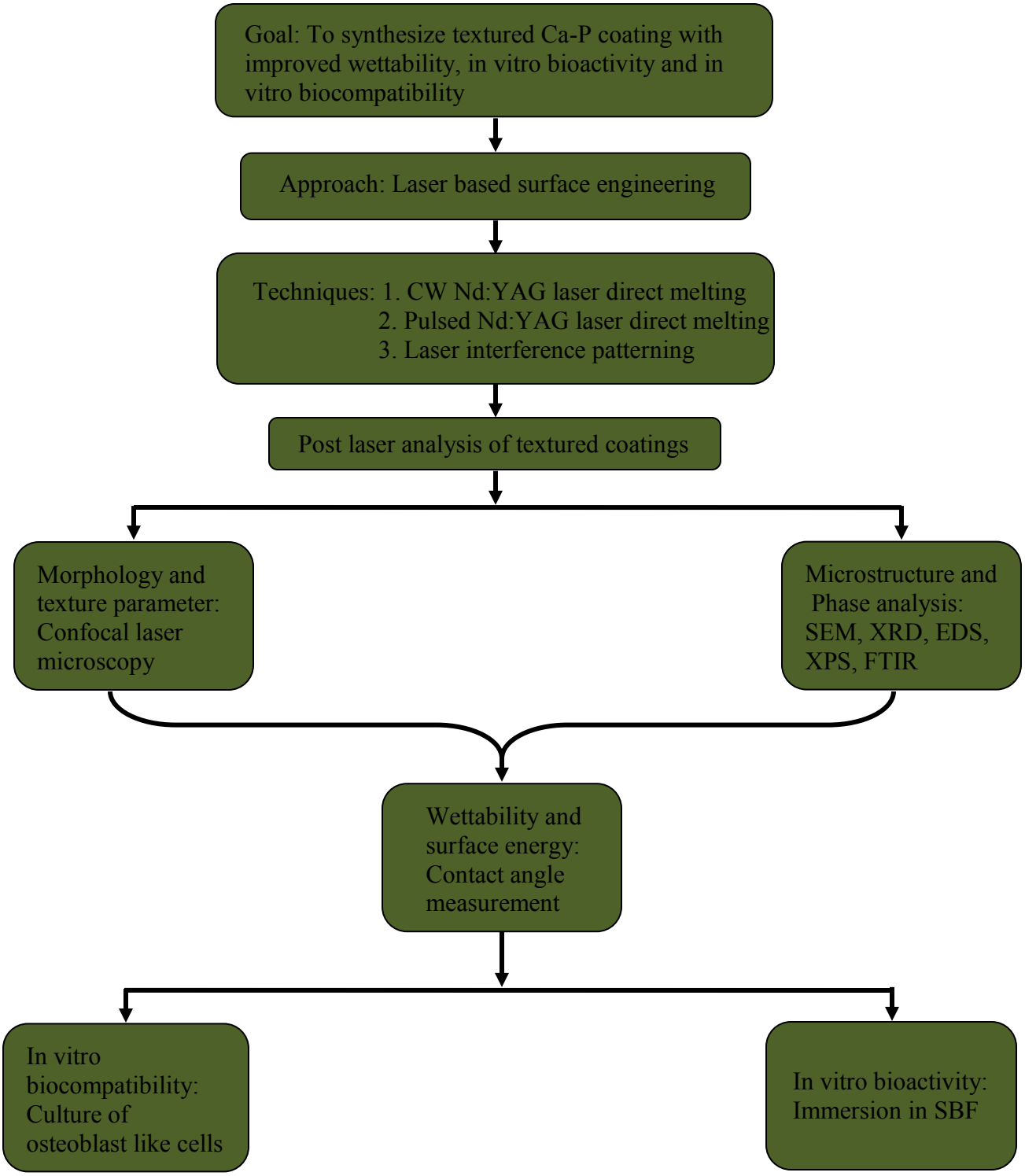


Figure 2.3 Flow chart of proposed goal and approach of current research work.

Chapter 3

Experimental Work

3.1 Materials selection and preparation

Understanding from the natural organization of the hard calcified tissue and service requirement of an orthopedic implant biomaterial, it can be realized that the synthetic material chosen to function at the damaged site should have appropriate mechanical behavior and in vivo biocompatibility. However, it is difficult to achieve both these properties in a single material. Hence, a striking balance had to be brought by integrating a substrate material having good mechanical properties with a coating material exhibiting superior biocompatibility. Because of its superior mechanical properties and chemical stability under in vivo conditions, Ti-6Al-4V was selected as the substrate material. Further, to provide the tissue/implant interface with the best biocompatible surface, Ca-P based HA ($Ca_{10}(PO_4)_6(OH)_2$) powders were used as the precursor coating material. The importance of HA in providing a bioactive surface and thereby enabling a chemical bonding at the tissue/implant interface has been discussed in chapter 1. In spite of the bioactive and biocompatible nature of HA, some of the recent studies on HA coatings have limited their scope for implant applications, owing to the adverse reactions found in vitro and in vivo **[74]**, low bonding strength between the HA and substrate, and poor mechanical properties of the coating. Hence, to overcome these limitations there has been a considerable interest in developing new bioactive ceramic coatings based on bioglass compositions such as Na_2O-CaO-SiO_2-P_2O_5 [**75]**, wollastonite ($CaSiO_3$) [**76]**, and dicalcium silicate (Ca_2SiO_4) **[77]**.

In most of the above compositions, the presence of SiO_2 is found to be in common, since SiO_2 can easily form a Si-OH functional layer under in vivo and in vitro conditions and there by enhance the mineralization of an apatite like phase at the interface between the bioceramic coating and hard tissue. Another reason for SiO_2 being used as the basement of above systems is that it can directly act in the mineralization process, where aqueous Si, in the form of orthosilicic acid ($Si(OH)_4$), is able to induce the precipitation of HA from electrolyte solutions in the presence of proteins that normally inhibit its precipitation **[78, 79]**. Due to the above beneficial properties of SiO_2 in biomaterials, preliminary efforts with HA-SiO_2 as a composite precursor material were also conducted for coating on Ti-6Al-4V and studied for its wettability, in vitro bioactivity, and in vitro biocompatibility.

The Ti-6Al-4V substrate coupons were obtained from Techcut10 ™ Allied High Tech Products Inc and the HA and SiO_2 precursor powders were obtained from Fischer Scientific. The HA and SiO_2 precursor powders had a spherical morphology with a unimodal distribution in the range of ~10 to 30 μm. To start with the sample preparation, the Ti-6Al-4V substrate coupons of dimensions 100 mm×50 mm×3 mm were cut from the rolled sheets using an abrasive cutter. Before being coated with the precursor, all substrate coupons were polished using a 30 μm grit SiC emery paper and then rinsed with acetone to get a clean surface free from rust and oxides. The pure HA precursor and the thoroughly blended HA-SiO_2 (the ratio of SiO_2 to HA is fixed as 1:3 in weight %) precursor were mixed separately in a water-based organic solvent (LISI W 15853) obtained from Warren Paint and Color Company (Nashville, TN, USA) and mechanically stirred for 25 minutes to get a viscous slurry. Each slurry was then sprayed onto the polished and clean substrate coupons using an air pressurized spray gun. The sprayed coupons were dried in

air to remove the moisture. The thickness of the precursor deposit was maintained at 80 μm for all samples. The dried coupons were then scanned under a laser beam to obtain a textured coating. For interference patterning, the Ti-6Al-4V (100mm×50mm×3mm) cut coupons were prepared by polishing with emery papers of different grits ranging from 200 μm to 1000 μm in succession followed by disc polishing with colloidal silica of 0.3 μm and 0.05 μm to get a mirror finished surface. Here, no precursor powders were used, and the LIP was carried directly on the polished Ti-6Al-4V sample.

3.2 Surface modification via pulsed laser direct melting

A pulsed laser is characterized by the short pulse duration (Figure 3.1) in the range of femto seconds to mili seconds, high peak power, and intermittent delivery of the laser beam. During the impact of such ultra short pulses a fine layer of material is melted and then is vaporized at the surface forming a vapor jet. This jet induces a recoil pressure and the liquid metal underneath is pushed towards the edges of the impact. After the end of the laser pulse the liquid metal solidif-

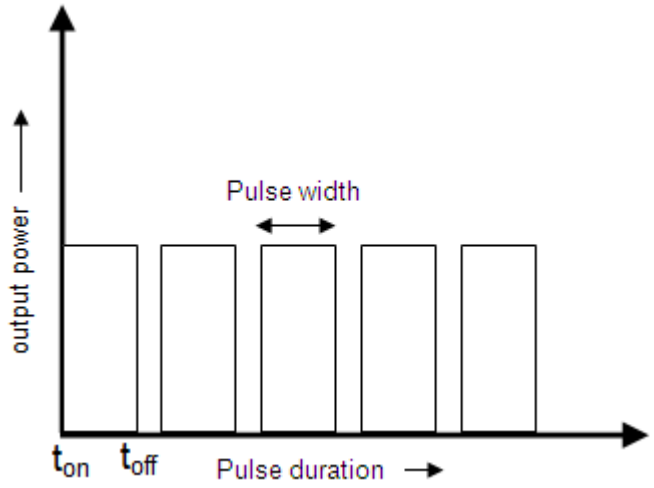


Figure 3.1Schematic representation of the output power delivery with time in a pulsed laser.

ies and forms a crater on the surface of a metal. The presence of such a crater due to pulsed laser irradiation generates a physical texture on the surface of a material (schematically shown in Figure 3.2 **[80]**) and can be considered as a 3-dimensional topographic cue for contact guidance and cell adhesion. The presence of short duration pulses also results in high cooling rate and thereby meta-stable phases suitable for bio-application. These beneficial effects were explored with the Ti-6Al-4V samples pre-sprayed with HA and HA-25 wt% SiO_2 precursor.

The pre-sprayed samples were scanned using a JK701 model pulsed Nd:YAG laser to obtain a metallurgical bonded textured coating. The schematic of the laser coating experimental set up used for the coating process is shown in Figure 3.3 **[71]**. The laser was equipped with a fiber optic beam delivery system to transfer the laser beam from the laser head to the material. The output coupler is equipped with a 120 mm focal length convex lens which gives a spot diameter of approximately 240 μm at focus. The focused spot is kept at approximately 0.8 mm above the surface of the sample so as to have a spot size of approximately 900 μm on the surface. The laser processing parameters used for the coating process is listed Table 3.1.

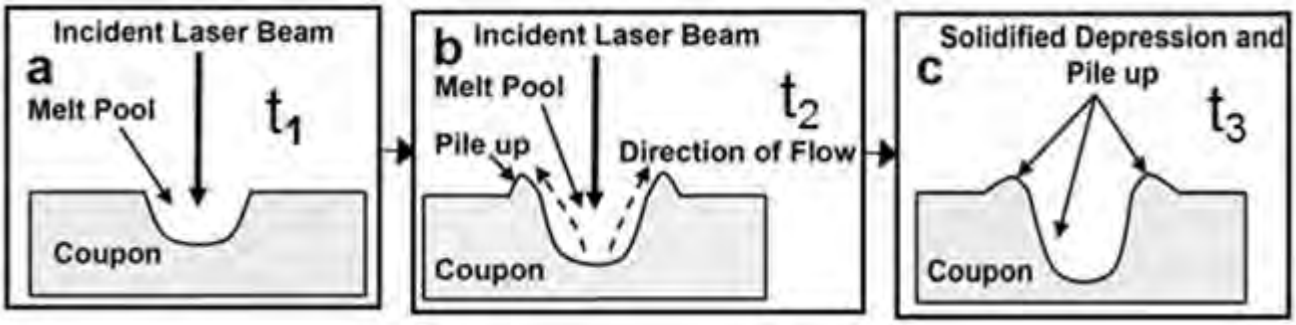


Figure 3.2 Different steps involved in evolution of the surface morphology at various times ($t_1 < t_2 < t_3$) for a single laser beam **[80]**.

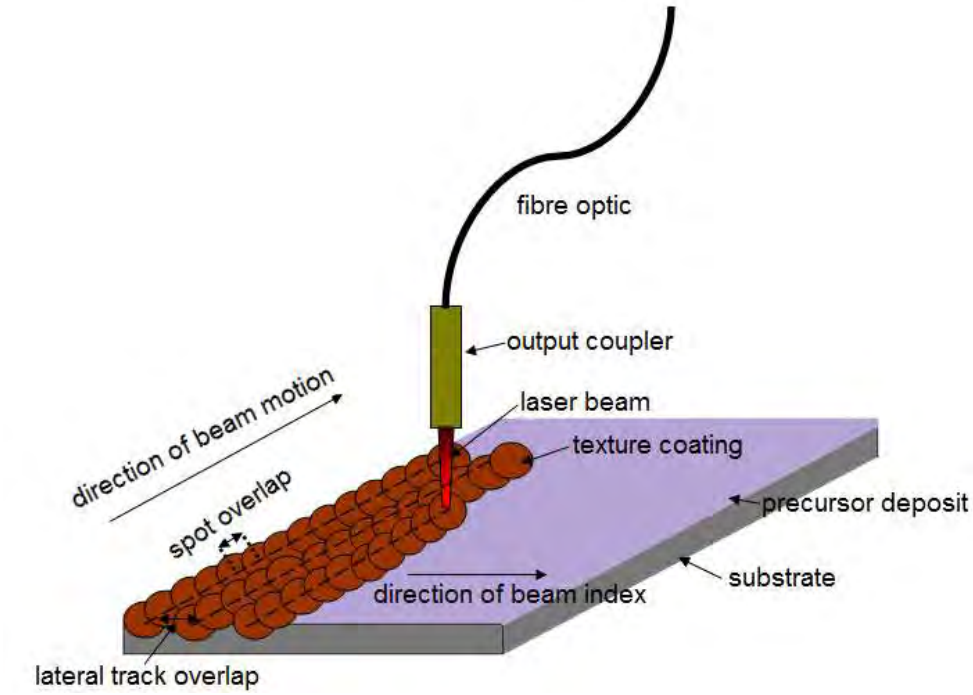


Figure 3.3 Schematic of laser texturing process using pulsed Nd:YAG laser **[71]**.

Table 3.1 Laser processing parameters used for coating using pulsed Nd:YAG laser.

Laser parameters	HA precursor		HA-25 wt% SiO_2 precursor
	Experiment 1	Experiment 2	
Pulse width	0.5 ms	1 ms	1ms
Pulse energy	4J	4J	4J
Pulse repetition rate (*f*)	20 Hz	10, 20, 30, 40 Hz	30 Hz
Laser scan speed (*V*)	36, 48, 78, 102 cm/min	50 cm/min	75 cm/min
Focus position	0.8 mm above the surface of the sample	0.8 mm above the surface of the sample	0.8 mm above the surface of the sample
Spot diameter on the surface (*D*)	900 μm	900 μm	900 μm
Pulse shape	rectangular	Rectangular	rectangular

From the table 3.1 above, it can be realized that for experiment 1 the laser scan speed was varied keeping the rest of the parameters constant, whereas for experiment 2 the pulse frequency was varied keeping the rest of the parameters constant. The scan speed (V) and the pulse frequency (f) can be related to the laser spot overlap (S_x) by the following equation **[70-71]**:

$$s_x = 1 - \frac{V}{f\,D} \quad \text{.....3.1}$$

For experiment 1 the spot overlap decreased with increasing laser scan speed and a spot overlap of 65, 55, 28 and 5.5% were obtained for the laser scan speed of 36, 48, 78 and 102 cm/min respectively. In contrast for experiment 2, the spot overlap increased with increasing pulse frequency and a spot overlap of 6, 53, 69 and 76 % were obtained for pulse frequency of 10, 20, 30 and 40 Hz, respectively. As only preliminary efforts were made for the HA-25 wt% SiO_2 precursor, a single suitable parameter based on past experience was selected to synthesize a textured coating.

3.3 Surface modification via CW laser direct melting

In a CW laser, the output power of the laser beam is constant with time (Figure 3.4). Hence, direct melting using a CW laser is likely to produce more uniform thermal conditions within the beam-substrate interaction region. Further, as the beam is delivered in a continuous mode, direct melting and simultaneous scanning of a material surface result in a line pattern rather than a crater as in the case of a pulsed mode operation. The laser scanning process in this case can be programmed to achieve line patterns with varying lateral track spacing and hence micro-textured patterns at varying length scales can be obtained. The formation of such line patterned Ca-P surface is expected to provide contact guidance for directional attachment of bone forming cells and thereby improve its biocompatibility. Keeping the above potential advantages in mind, the

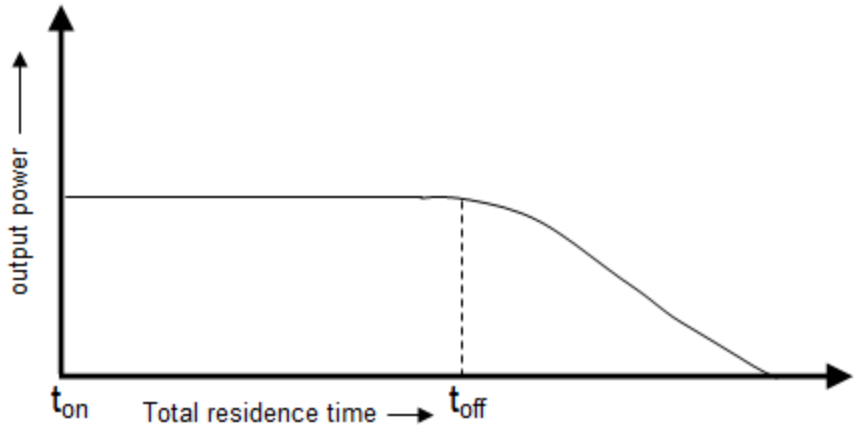


Figure 3.4 Schematic representation of the output power delivery with time in a CW laser.

HA pre-sprayed samples were scanned under a CW Nd:YAG laser equipped with a fiber optic beam delivery system to obtain a metallurgically bonded textured Ca-P coating. The schematic of laser coating experimental set up used for the coating process is shown in Figure 3.5 **[72]**. The fiber equipped with the laser system is interfaced with an end effector that houses a set of spherical and cylindrical lenses which are used to shape the laser beam output. The laser operates in the infrared region with a wavelength of 1064 nm. The laser processing parameters used for coating process are presented in Table 3.2 **[72]**. It can be observed (Table 3.2) that two different laser powers 215 W and 300 W were used for each side ways line spacing (100 µm and 200 µm). A lateral spacing of 100 µm and 200 µm is chosen so as to match the length scale of the naturally occurring three dimensional extra cellular matrix (ECM) present in the human bone **[50]**. Hence four different samples with a varying combination of laser power and surface topography were generated for the study.

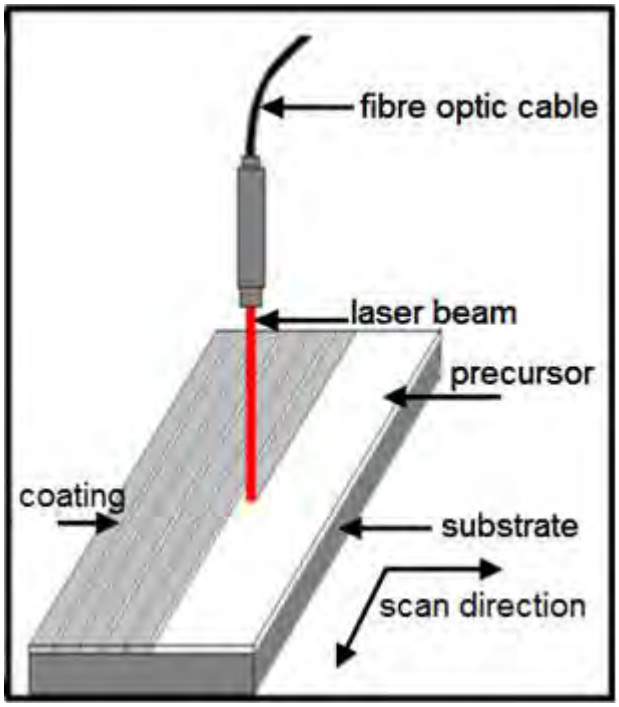


Figure 3.5 Schematic of laser texturing using CW laser **[72]**.

Table 3.2 Laser processing parameters used for coating using a CW laser **[72]**.

Stand of distance	356 mm above the sample surface
Laser spot shape	Circular
Laser spot diameter	400 μm
Laser scan speed	3000 cm/min
Average output power	215 W, 300 W
Laser fluence or energy density of the laser beam	137 J/cm^2, 191 J/cm^2
Line spacing	100 μm, 200 μm

3.4 Surface modification via LIP

The polished Ti-6Al-4V samples were surface treated using a linear polarized third harmonic of a Q-switched Nd:YAG laser (Coherent Infinity, Santa Clara, USA). In this technique, the primary laser beam was split into two coherent sub-beams that were guided using an optical system to produce interference at the sample surface. This allows the creation of periodic surface textures at length scales ranging from the micro to nano in a single step process. A detailed schematic set-up of the process is illustrated in Figure 3.6 **[73].** The geometry of the pattern depends on the wavelength and angles between the laser beams. The two interfering laser beams create a sinusoidal intensity distribution with high-and-low intensity lines (Figure 3.7). The distance, *w* between the high intensity spots (periodicity) can be varied with the angle (β) between the beams as per the following Bragg equation **[81, 82]**:

$$w = \frac{\pi}{2\sin\left(\frac{\beta}{2}\right)} \quad \text{.....3.2}$$

In this preliminary work, the pulse duration and repetition rate used to create the patterns were 2.5 ns and 10 Hz, respectively. The area irradiated by the laser beam was approximately 0.5024 cm^2. The samples were irradiated under three different laser fluences of 362.26, 525.47, and 760.35 mJ/cm^2, while keeping the number of pulses as 5. Two different surface patterns (i.e. the groove and pillar-like) were obtained under each laser fluence. In order to generate pillar-like features, the sample once irradiated was rotated 90° and irradiated again with 5 pulses. Hence, it was a two-step process, with the effective number of pulses being doubled compared with the groove-like features.

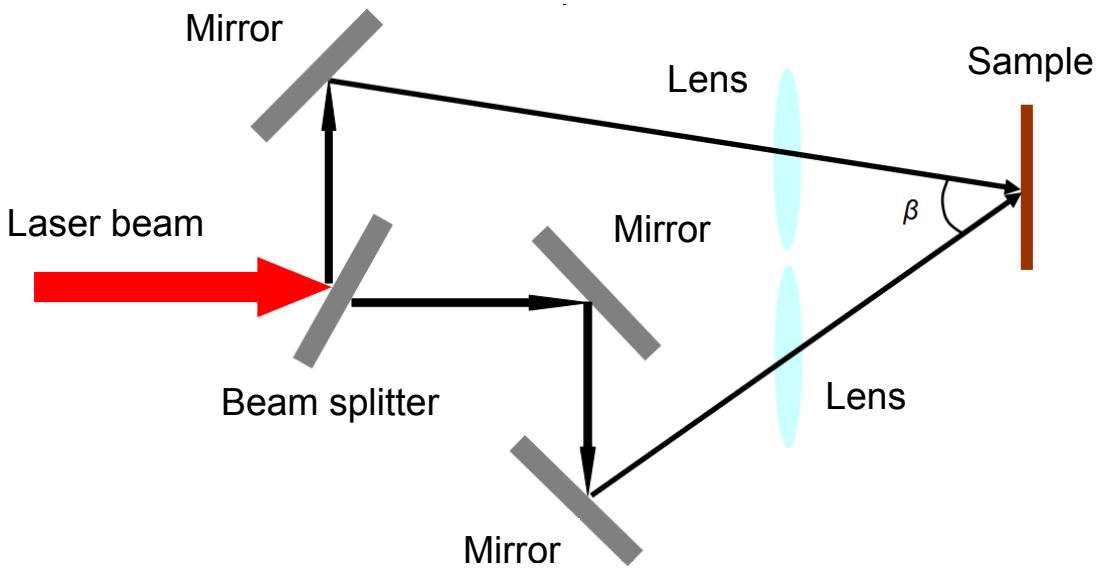


Figure 3.6 A schematic of the laser based interference patterning technique **[73]**.

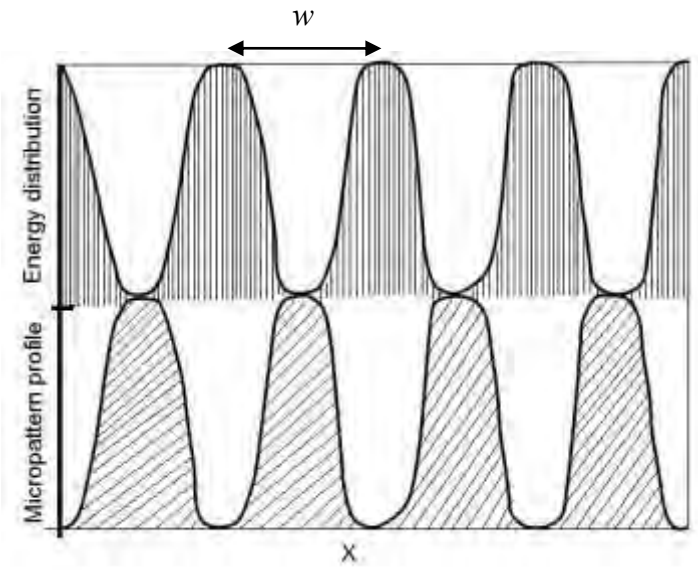


Figure 3.7 Schematic of intensity distribution and corresponding surface profile obtained by two beam laser interference patterning.

3.5 Surface characterization

3.5.1 Microstructural characterization

The characterization of surface and cross-section microstructure of the textured coated specimens, were carried out using both a LEO 1525 scanning electron microscope (SEM) and Leica optical microscope as per convenience and requirement. The samples in cross-section were prepared by polishing with emery papers of different grits ranging from 200 μm to 1000 μm in succession followed by disc polishing with colloidal silica of 0.3 μm and 0.05 μm to get a polished surface. The polished samples were then cleaned with acetone and etched with 5 vol % HF, 3 vol % HNO_3 and 92 vol % H_2O for 10-20 s by immersion etching to reveal the microstructural features.

3.5.2 Elemental analysis

The elemental analysis was conducted using both energy dispersive spectroscopy (EDS) and X-ray photoelectron spectroscopy (XPS) techniques. The EDS unit was attached to a JEOL1525 SEM system and the elemental analysis was obtained from a selective location while looking under the SEM. As the depth of probe using an EDS is in the range of micron scale (0.5 - 3μm depending on the energy of the electron beam), elemental data collected using this technique does not truly provide the near surface elemental composition. Hence, an XPS was also used in conjunction to quantify the surface elemental compositions.

A VersaProbe™ 5000 Scanning XPS Microprobe instrument was used here for the surface elemental analysis study. A monochromatic aluminum X-ray beam source at 1486.6 eV and 49.3 W was used to scan upon the sample surface. A high flux X-ray source with Aluminum anode was used for X-ray generation, and a quartz crystal monochromator was used to focus and

scan the X-ray beam on sample. The X-ray beam diameter used was 200 μm and the chamber was sputter cleaned and operated at a vacuum pressure of 5 x 10^{-6} Pascal for the study. The samples used for XPS studies were cleaned with distill water and dried in a vacuum desicator prior to analysis.

3.5.3 Phase analysis

The phase evolution was studied using both X-ray diffraction (XRD) and Fourier transform infrared (FTIR) spectroscopic technique. A Philips Norelco XRD system with Cu-Kα radiation of wavelength 1.5418 Å was used to study the phase evolution. The XRD system was operated at 20 kV and 10 mA in a 2θ range of 20° to 100° using a step size of 0.02° and count time of 1s.

The FTIR analysis was carried using a Nicolet FTIR Continuum Infrared Microscope, configured for operation under reflectance and transmission mode. In the current study the solid samples were analyzed under the reflectance mode and the samples were placed on an aluminum coated slide for the background. The spectra were obtained at 4.00 cm^{-1} resolution averaging 100 sample scans and 32 background scans. The acquisition range used was 650 cm^{-1} to 4000 cm^{-1}.

3.5.4 Morphological evolution

The 3-dimensional morphological evolutions, surface roughness, and texture parameter of the textured coated samples were studied using a Leica confocal laser microscope. The laser beam was scanned across a surface area of 1500 μm × 1500 μm to obtain the 3-dimensional surface morphology. The roughness values are recorded in the form of R_a (defined as the arithmetic average of all points of the profile also called the center line average height), R_z (arithmetic average of vertical distances between the highest peak and deepest valley within a sampling length) and R_{max} (maximum individual roughness depth). A total of 5 random scans were carried

out across each sample to get an average and standard deviation within these roughness values. In order to have a precise understanding of the effect of 3-dimensional topographic cues on wettability the rough surfaces were assumed to hold a Gaussian profile with a cosine distribution of amplitude as proposed by Zhou and De Hosson **[83]**. Hence, in the present work, the surface texture was characterized in terms of the roughness parameters σ_A (the standard deviation of amplitude of random points on the surface from a line drawn through the trace such that cross-sectional areas of the asperities above and below the grooves are equal) and λ (the periodicity of the profile or the distance between any two successive crests or troughs), and their ratio (σ_A/λ) was used as a measure of surface texture. A total of 5 random scans were chosen on each sample and the sampling showed that both parameters (σ_A and λ) could be defined with an accuracy of 2-4 %.

As the surface features for the LIP samples are in the nano to submicron scale, 3-dimensional morphological features such as width *d* at full width half maxima (FWHM), height *h,* and the periodicity *w* of the patterns were measured using a Zygo laser interferometer setup.

3.6 Mechanical characterization

The mechanical integrity of the coated samples was evaluated using nanoindentation and wear performance in a simulated body environment. A Hysitron® Triboindenter (Minneapolis, MN, USA) with a 100 nm radius Berkovich pyramidal tip was used for nanoindentation studies. Load-cycle involved peak load of 2000 μN ramped at 10 s, followed by a 3-second hold at the peak load, and consequent unloading in 10 seconds. The peak load was automatically adjusted by nanoindenter to keep the segment times constant for loading, dwell, and unloading. A minimum of 10 indentations were performed across the polished cross section for each sample and thereby

extracting data from three different locations with a test-area of 20 μm x 10 μm. Young's modulus and hardness were calculated from the load-displacement curve using Oliver-Pharr analysis **[84-86]**.

Wear performance of the coated samples in simulated body environment was studied using pin on disc wear tester with an arrangement for immersion of the pin and sample in SBF contained in a test cell attached to the tester (Figure 3.8) **[87]**. Since alumina (Al_2O_3) is used as a ceramic acetabular component which comes in contact with the femoral head, a 50 mm long and 3 mm diameter alumina pin was used to slide against the textured coated specimens. The coated specimens were cleaned with acetone in an ultrasonic bath to remove any dirt or grease from the surface of the sample. The tip of the pin was polished flat to have a close contact with the sample and the SBF solution was maintained all time in the cell so that the specimen remains immersed throughout the test. The test was conducted at a normal load of 8.8N and the wear cell rotating at a speed of 100 rpm or equivalent linear speed of 32 m/min. The total duration of the test was 100 minutes and the weight loss for the sample was noted down for every 10 minutes.

3.7 Contact angle and surface energy

Contact angle studies were carried out by a static sessile drop technique using a CAM-Plus^R contact angle goniometer (Cheminstruments, Inc. Fairfield, Ohio), equipped with a fiber optic light source and Video camera for imaging. A liquid droplet of volume 3 μl (droplet diameter of 2 mm) was placed on the thoroughly cleaned sample by a hypodermic syringe and the advancing contact angle was taken as a measure of wettability. The liquid drop placed on the sample was allowed to stabilize for 10 seconds before the reading was taken. The test was conducted at room

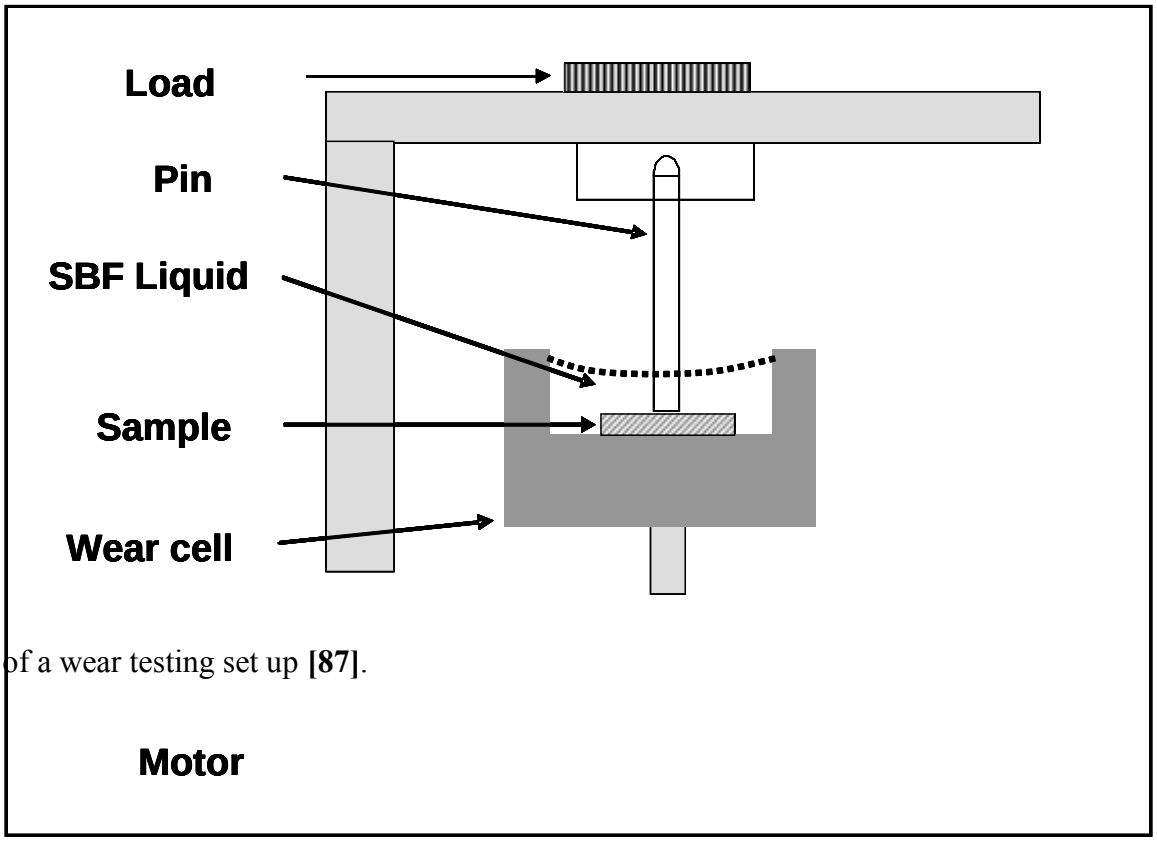


Figure 3.8 Schematic of a wear testing set up **[87]**.

temperature (26 °C) and a minimum of 10 contact angle readings were taken on each sample to minimize error in the measurement. Further, the measurement was based on the patented half angle method (US Patent 5268733) which eliminates the errors associated with the arbitrary tangential alignment.

The surface energy calculations were made according to the Van Oss **[88]** approach using the following equation:

$$(1+\cos\theta)\gamma_L = 2\left\{(\gamma_S^{LW}\gamma_L^{LW})^{1/2} + (\gamma_S^{+}\gamma_L^{-})^{1/2} + (\gamma_S^{-}\gamma_L^{+})^{1/2}\right\} \quad \text{.....3.3}$$

According to their approach the surface energy or surface energy of a solid γ_S (or a liquid γ_L) can be divided into the Lifshitz-van der Waals surface energy (γ_S^{LW}) and Lewis acid-base surface energy (γ_S^{AB}) components as described below:

$$\gamma_S = \gamma_S^{LW} + \gamma_S^{AB} \quad \text{.....3.4}$$

$$\gamma_S^{AB} = 2\sqrt{\gamma_S^{+}\gamma_S^{-}} \quad \text{.....3.5}$$

Here γ_S^{+} is the Lewis acidic or the electron-acceptor component, γ_S^{-} is the Lewis basic or the electron-donor component and θ is the contact angle of liquid *L* and solid *S*. The surface energy components of three well characterized test liquids (Table 3.3) **[89, 90]** i.e. one apolar (dioiodomethane) and two polar liquids (water and formamide) were used in equation 3.3 to solve for γ_S. In order to correlate the surface energy calculations to the mineralization behavior of the samples, contact angle measurements were also performed using both a SBF and cell culture medium. The composition and preparation of SBF and cell culture medium are discussed in the following sections.

Table 3.3 Surface energy components of the standard liquids (units mJ/m^2) **[89, 90]**.

Material	(γ_L^{LW})	γ_L^+	γ_L^-	γ_L^{AB}	γ_L
Water	21.8	25.5	25.5	51.0	72.8
Formamide	39.0	2.28	39.6	19.0	58.0
Dioiodomethane	51.0	0	0	0	51.0

3.8 In vitro bioactivity

In vitro bioactivity and mineralization kinetics of the laser processed samples were studied by soaking the samples in a SBF. The SBF solution was prepared by dissolving the reagent grade chemicals in the following order: NaCl (8.026 g), $NaHCO_3$ (0.352 g), KCl (0.225 g), $K_2HPO_4 \cdot 3H_2O$ (0.230 g), $MgCl_2 \cdot 6H_2O$ (0.311 g), $CaCl_2$ (0.293 g) and Na_2SO_4 (0.072 g) into distilled water (700 ml). The fluid was then buffered to pH = 7.4 at 37 °C with tri-hydroxymethyl-aminomethane (6.063 g) and 1.0-M hydrochloric acid (40 ml) **[70-73, 80]**. Plastic containers were used to soak the samples in SBF for different time periods. The solution was refreshed every 24 h to maintain a pH of 7.4, and the temperature was maintained at 37 °C during the course of the test. The samples were removed from the solution at specified time intervals followed by rinsing with distilled water and air drying for further analysis. Scanning electron microscopy (SEM) was used to observe the microstructure and morphological evolutions of mineralized samples. The phase analysis of the mineralized samples was conducted using XRD and FTIR technique.

3.9 In vitro biocompatibility

In vitro biocompatibility of textured coated samples was evaluated through cell attachment and cell morphology during cell culture studies using the mouse pre-osteoblast MC3T3-E1 (subclone 14) cell line, obtained from American Type Cell Culture Collection (ATCC, Manassas, VA, USA). The cells were maintained in a tissue culture flask using the cell culture medium at 37 °C under 5% CO_2 and 95% air in a humidified incubator. The culture medium was replaced every 3 days and confluent cells were trypsinized and replated (0.25% trypsin-EDTA, Invitrogen, USA) to maintain the cell line.

3.9.1 Cell viability

The textured coated samples and the control (untreated Ti-6Al-4V) of size 4 mm × 4 mm were cleaned with 70% ethanol and then UV sterilized prior to cell culture. The pre-osteoblast cells were then seeded on the surfaces of UV sterilized samples placed in 24-well culture plates at a density of 1.25×10^5 cells/cm^2 and stored in the CO_2 incubator (maintained at 37 °C under 5% CO_2 and 95% air) for different time periods. As, the seeding density of the pre-osteoblast cells were extremely high (1.25×10^5 cells/cm^2), only 2 or 3 different time periods were chosen to study the cell proliferation. To quantify the number of viable cells attached post-seeding, WST-1 assay was performed. WST-1 is a colorimetric assay where the absorbance at 450 nm is directly proportional to the amount of mitochondrial dehydrogenases activity in the cells. Briefly, samples were incubated with culture medium containing 10% WST-1 reagent (Roche, USA) for 4 h at 37 °C. After incubation, a 100 µl aliquot from each well was transferred to a 96-well plate and the absorbance at 450 nm was measured using a microplate reader (1420 Multilabel Counter,

Wallac Victor 2). Blank wells containing only culture medium and WST-1 reagent were also prepared and used as background control for sample absorbance reading correction.

3.9.2 Cell morphology and cell cytoskeleton

The osteoblast cells suspended in 300 µl cell culture medium were seeded on the UV sterilized samples at a lower density (1×10^4 cells/cm^2) and incubated for different time periods at 37 °C under 5% CO_2 and 95% air in a humidified incubator. For cell morphology analysis using SEM, cells cultured on the samples were fixed with 3% glutaraldehyde in 0.1 M cacodylate for 1 h and rinsed three times with phosphate buffered saline (PBS). The samples were further processed in 2% osmium tetroxide in 0.1 M cacodylate for 1 h, dehydrated with a series of increasing concentration of ethanol (25%, 50%, 70%, 95%, and 100%), critical point dried, and sputter-coated with gold for SEM observation. For immunocytochemical staining of the actin filament and focal adhesion, the cells cultured on the samples were fixed with 4% paraformaldehyde (Sigma-Aldrich, USA) in 1x PBS for 30 min at 4 °C. After washing with PBS, the samples were permeabilized with 0.1% Triton X-100 (Fisher Scientific, USA) in 1x PBS for 5 min, blocked with 1% bovine serum albumin (BSA, Sigma-Aldrich, USA) for 30 min, and incubated in the primary antibody mouse anti-vinculin (Chemicon, 0.2%) for 1 hr. After rinsing, the samples were incubated with 0.5% goat anti-mouse IgG Alexa Fluor 488 and 2% Alexa Fluor 594-conjugated phalloidin (Invitrogen, USA) that labels the cytoskeleton F-actin filaments. Cell nuclei were counterstained with 0.1% 4', 6 – Diamidino-2-phenylindole (DAPI, Chemicon, USA) in 1x PBS for 5 min. Samples were washed three times with 0.05% Tween-20 (Sigma) in 1x PBS before and after the staining steps. All the staining procedures were carried out at room temperature. High resolution fluorescence images were captured using an upright fluorescence

microscope (Nikon). Once the images were captured, a representative image was selected for quantitative analysis of cell spreading area (A), and cell shape index (Ø). A total of 30 cells were randomly selected for each sample, manually outlined, and the cell areas (A) were calculated using the ImageJ image analysis software. The morphology of the cells described by the cell shape index (Ø) was calculated using the following equation **[91]**:

$$\text{Ø} = \frac{4\pi A}{p^2} \quad \text{.....3.6}$$

Here A is the cell spreading area and p the perimeter of the cell. For a perfect circular morphology the cell shape index is 1, whereas for line morphology the shape index is 0. Previous studies **[92]** have demonstrated a correlation between the cell shape index and cell fate and function, thereby offering the potential to tailor biomaterial surfaces to control cell fate and function through control of cell spreading.

3.9.3 Data analysis

For a particular time period of seeding a total of 4 samples were used from each laser processing parameters and the control (untreated Ti-6Al-4V). The results were expressed as the mean of 4 replicates ±SD (standard deviation). Statistical analysis carried out using a student t-test was applied to determine the statistical significance observed between the groups and $P<0.05$ were considered statistically significant.

Chapter 4

Pulsed Laser Induced Ca-P Textured Coating on Ti-6Al-4V

4.1 Introduction

A systematic organization of Ca-P coating on Ti-alloy substrate can be synthesized directly by effectively controlling the thermo physical interactions during pulsed Nd:YAG laser processing. Proper adjustment of the pulsed Nd:YAG laser parameters can be carried out to achieve textured surface coatings by direct melting without any major ablation or material vaporization. Both macro and micro/nano scale features can be obtained by such pulsed laser induced direct melting. The micro/nano scale features produced due to temporal and spatial variation of energy distribution within the beam can induce protein interaction, attachment, and alignment with the substrate where as the macro scale features such as troughs, valleys, and pores obtained by laser spot overlap may aid towards cell attachment and bone ingrowth **[50, 93-96]**. Due to the shorter pulse width, the associated cooling rate is extremely high as compared to a continuous wave operation. This may be helpful in retaining some metastable or amorphous phases of Ca-P beneficial for bio applications.

In the present work, such feasibility of simultaneous synthesis of a textured and bioactive Ca-P coating on Ti-6Al-4V substrate using a pulsed Nd:YAG system has been demonstrated by varying both the laser scan speed and laser pulse frequency.

4.2 Variation of laser scan speed

Different textures were obtained by varying the laser spot overlap with change in laser scan speed. X-ray diffraction studies revealed the formation of α-TCP, TiO_2, Ti and Al as the major phases. Wear studies in a simulated biofluid (SBF) environment demonstrated an increased wear

resistance of the coated samples as compared to the bare Ti-6Al-4V. Surface roughness measurements of the textured coatings carried out using a white light interferometer indicated a decrease in roughness with increasing laser scan speed. Wettability of the coated samples measured using a static sessile drop technique demonstrated an increased hydrophilicity with increasing laser scan speed. The influence of such textures and the associated surface roughness on the precipitation kinetics of hydroxyapatite (HA) during immersion in a simulated body fluid (SBF) was the prime focus of the present work. The mineralized samples obtained after immersion in SBF were characterized using X-ray diffraction (XRD), energy dispersive spectroscopy (EDS) and scanning electron microscopy (SEM) to understand the kinetics of HA precipitation.

4.2.1 Microstructure and morphology of coating

In designing this experiment, the laser scan speeds are chosen in such a way that each of them provide a completely different spot overlap and thereby a different texture morphology. Further, under each of these laser scan speeds, the laser fluence or the input energy density was adjusted so that there is complete melting of both the precursor and substrate material and a metallurgical bonding is achieved at the interface. An optical microscope image (Figure 4.1 (a)) **[97]** of the cross-section of the sample processed at a laser scan speed of 36 cm/min indicated a sound interface between the coating and substrate material. A higher magnification SEM image of the surface of the coating demonstrated a porous morphology with wide pore size distribution (Figure 4.1 (b)) **[97]**. Low magnification optical microscopic images (Figure 4.2) **[70]** of the surfaces of the coated samples clearly demonstrate the effect of varying laser scan speed on the texture evolution. The laser scan speed influences the input energy density and the laser spot

overlap. These two parameters in turn, therefore, greatly influence the surface morphology or the texture evolution in the coating. Each pulse of a laser produces a solidified crater with a defined boundary and a flat region at the center (Figure 4.2). Hence, as the laser scan speed is increased the laser spot (crater) overlap is decreased as per Equation 3.1 which in turn modifies the crater area as well as the surface texture. Also with increasing laser scan speed the input energy density (fluence) decreased, and resulted in reduced surface melting or less thermal effect at the surface. Thus, variation of laser processing parameters produced variable thermodynamic conditions resulting in creation of different physical surface textures (Figure 4.2) **[70]**. The presence of these different surface textures will provide different level of surface roughness and thereby affect the wettability and in vitro bioactivity behavior. A major part of the succeeding studies in this current experiment will be dedicated towards understanding this phenomenon.

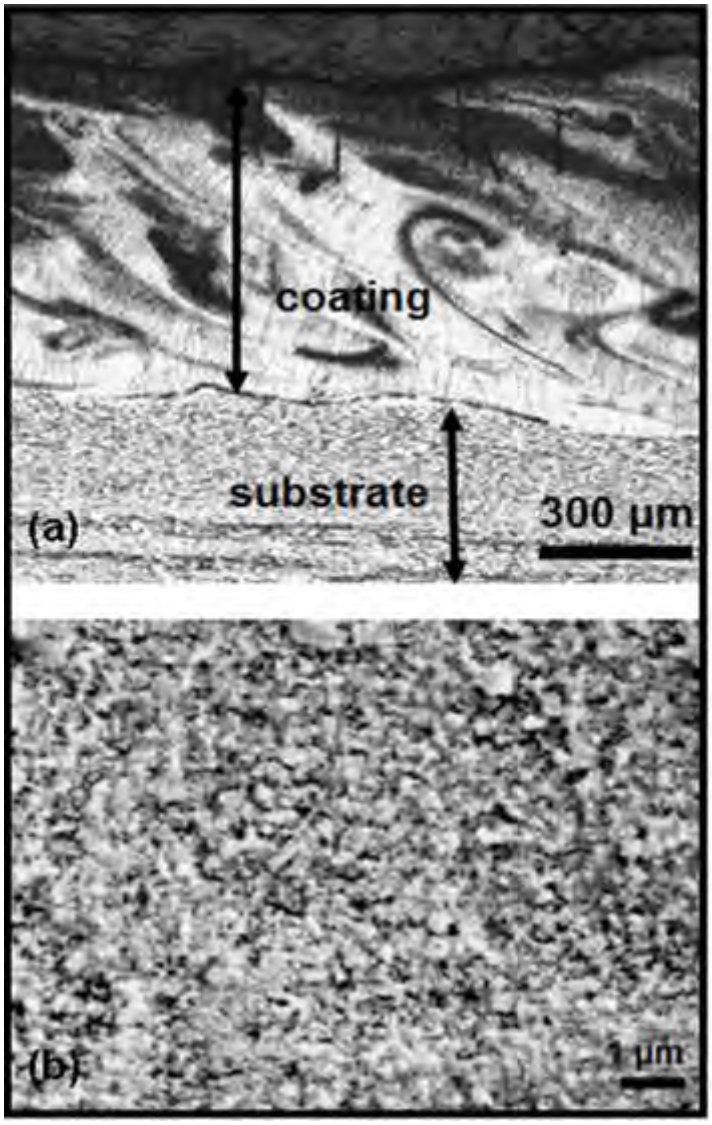


Figure 4.1 Sample processed at a laser scan speed of 36 cm/min: (a) optical cross sectional view and (b) SEM of the coating surface revealing a porous morphology with wide pore size distribution **[97]**.

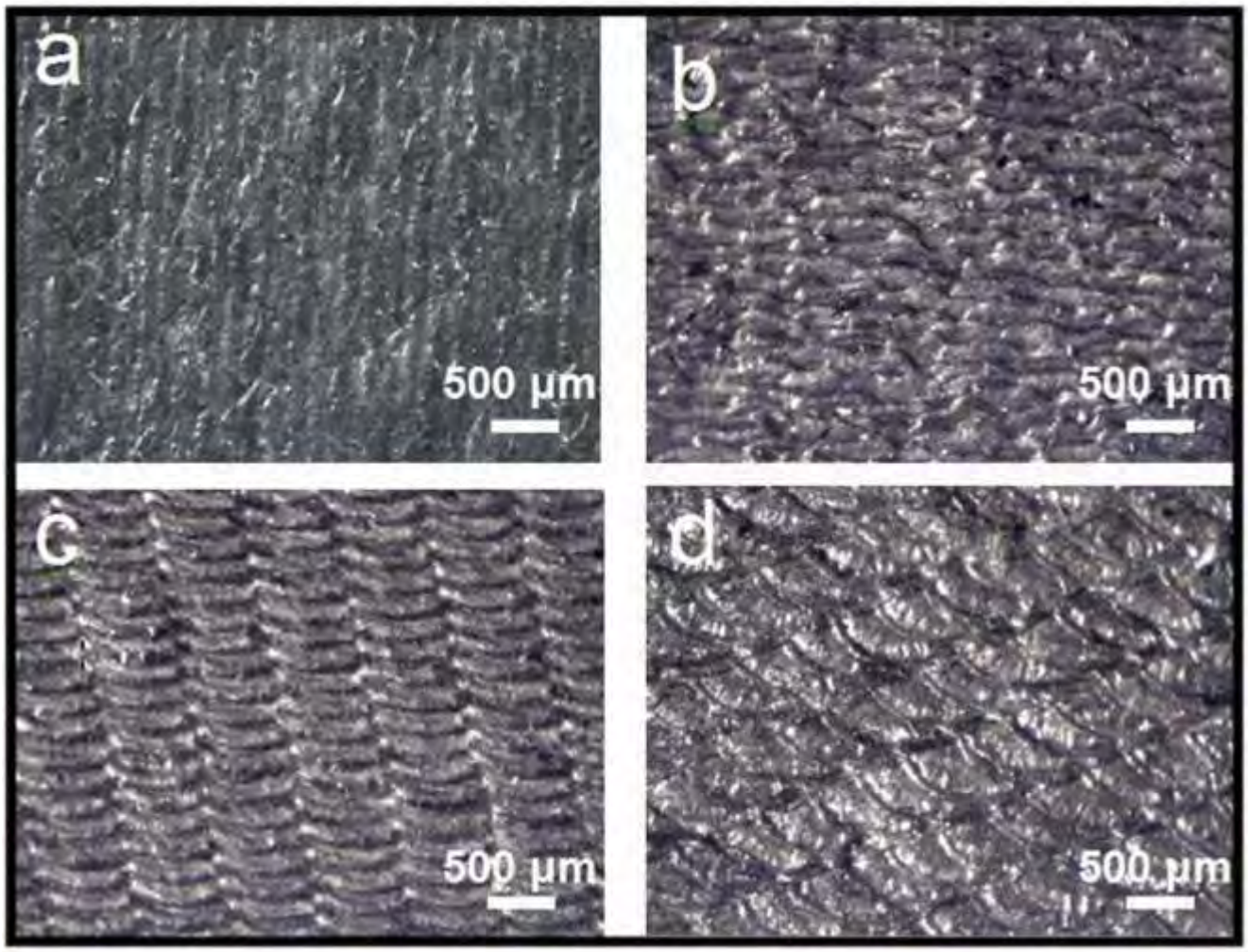


Figure 4.2 Low magnification optical microscopic images of the surfaces of the coatings obtained at laser scan speed of (a) 36 cm/min, (b) 48 cm/min, (c) 78 cm/min and (d)102 cm/min **[70]**.

4.2.2 Phase evolution

Apart from the spot overlap, the laser scan speed also influences the input energy density (laser fluence) and hence with varying laser scans speed the thermo-physical interaction and thereby the composition of the coating is expected to vary. To understand this effect XRD studies were carried out on the laser processed samples for phase analysis. The variation in thermodynamic conditions under the range of laser scanning speeds, (fluences: 1887, 1415, 871, 666 J/cm^2) employed in the present work appeared to have no detectable influence on type and amount of phase evolution in the modified surface region. All samples processed using these laser speeds (fluences) demonstrated the evolution of same phases (Figure 4.3) **[70]**. Such major phases identified within the detectable limits of the instrument are α-tricalcium phosphate (TCP), TiO_2 (rutile and anatase), Ti, and Al. The formation of α-TCP is mostly due to the dehydration of the $Ca_5(OH)(PO_4)_3$ precursor during laser processing. This is a biocompatible phase as it can hydrolyze under physiological conditions to form a calcium deficient hydroxyapatite **[93]**. The formation of TiO_2 is attributed to the oxidation of the underlying substrate as the samples were processed under ambient conditions at extreme laser fluence of the order of 10^5 to 10^6 W/cm^2. TiO_2 being a hard and chemically stable ceramic phase, it is expected to contribute towards enhanced beneficial corrosion and wear resistance under in vivo conditions. The existence of

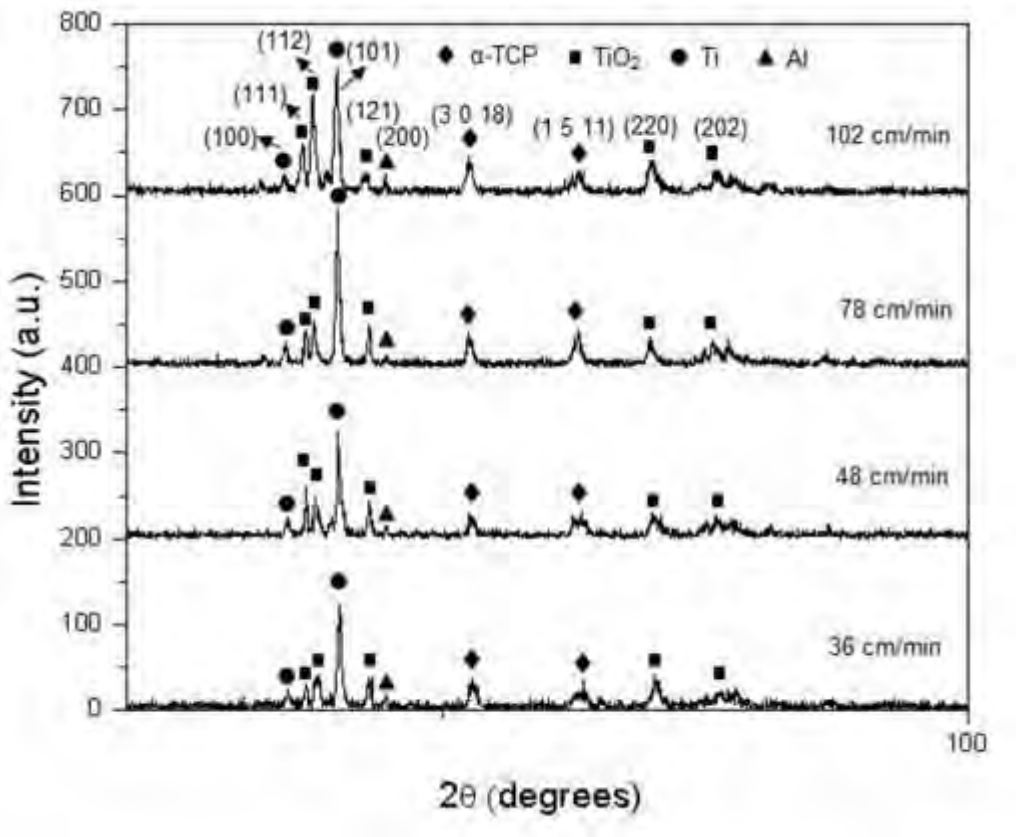


Figure 4.3 XRD patterns of the samples processed at varying laser scan speeds using a pulsed Nd:YAG laser **[70]**.

$CaTiO_3$ phase is detected only at the higher laser scan speed (102 cm/min) within the range of speeds employed in the present work. This may be attributed to the interaction between the Ca-rich phases such as Calcium Phosphate Tribasic and TiO_2 as per the reaction C4.1 **[93]**

$$2[Ca_5(OH)(PO_4)_3]_{(l)} + TiO_2 \rightarrow CaTiO_3 + 3\alpha\text{-}TCP + H_2O_{(g)} \uparrow \quad \text{.....C4.1}$$

The formation of $CaTiO_3$ during laser cladding of HA on Ti-6Al-4V is also previously reported **[66]**. Furthermore, the evolution of CaO may also take place through the partial decomposition of α-TCP as per the intermediate reactions C4.2 and C4.3 **[66]**:

$$\alpha\text{-}TCP + TiO_2 \rightarrow CaTiO_3 + \alpha\text{-}Ca_2P_2O_7 \quad \text{.....C4.2}$$

$$\alpha\text{-}Ca_2P_2O_7 + Ti \rightarrow CaTiO_3 + CaO + P_2O_{3(g)} \uparrow \quad \text{.....C4.3}$$

Although the formation of CaO was highly anticipated during laser direct melting of the calcium phosphate tribasic powder, in the present case the presence of such a phase was not observed from the XRD peaks (Figure 4.3) **[70]**. Since CaO is a water soluble through the formation of hydrade ($Ca(OH)_2$) **[98]** and the samples were thoroughly cleaned prior to XRD studies the absence of such a phase was greatly justified. The removal of CaO from the coating by water rinsing is desired to avoid its entering into the body fluid. Similar dissolution nature of the CaO phase was also previously reported in the work done by Kurella *et al.* **[93]** and Gu *at al.* **[99]** during the studies related to Ca-P coatings on Ti-alloy substrate for bioapplication.

4.2.3 Mechanical response

Under in vivo conditions the coated implants are expected to sustain against severe mechanical loading and wear from the surrounding body tissue. Hence, physical stability of the coating when it comes in contact with the body plasma was important. Nanoindentaton and wear in a SBF

environment were carried out to assess the mechanical behavior of the coatings. The characteristic nanoindentation loading and unloading curves for different scan speeds and the variation in elastic modulus (E) and hardness (H) with varying laser scan speed for the coatings presented in Figure 4.4 **[97]** and in its inset respectively. In general, all coatings possessed higher elastic modulus (~ 145 GPa) and hardness (~ 4.4 GPa) compared to the substrate material (E ~ 120 GPa and H ~ 2.20 GPa) and they do not differ substantially from each other (E: ±20 GPa and H: ±0.59 GPa). Such minor variation in these mechanical properties can be attributed to similar types of phases evolved in the coating under the processing parameters employed in the present work (Figure 4.3) **[70]**.

A good bioceramic coating is expected to exhibit resistance to attack by the body fluids and low metal ion release. The metal ions released through the chemical intereactions and the metal particles separated through wear mechanism are perceived as foreign elements in the body environment and may lead to osteolysis. Osteolysis results in loosening of the implant and creation of a fibrous capsule at the interface. Hence, evaluating a wear performance of the coatings in a SBF environment was vital. It is observed (Figure 4.5) **[97]** that the cumulative weight loss of the bare Ti-6Al-4V after 100 minutes of wear test is 3-10 folds (0.0035 g) higher compared to the Ca-P coatings (ranging from 0.00034 g to 0.00098 g for laser scan speeds varying from 36 cm/min to 102 cm/min respectively). The cumulative weight loss among various laser treated coatings varied between ±4 times (Figure 4.5) **[97]**. Such a large variation may be due to the variation in the nature of interfacial bond between the coating and substrate.

Optical microscopy images (Figure 4.6) **[97]** of the wear tracks on bare Ti-6Al-4V and Ca-P coated Ti-6Al-4V illustrate the severity of damage on both surfaces. The typical appearan-

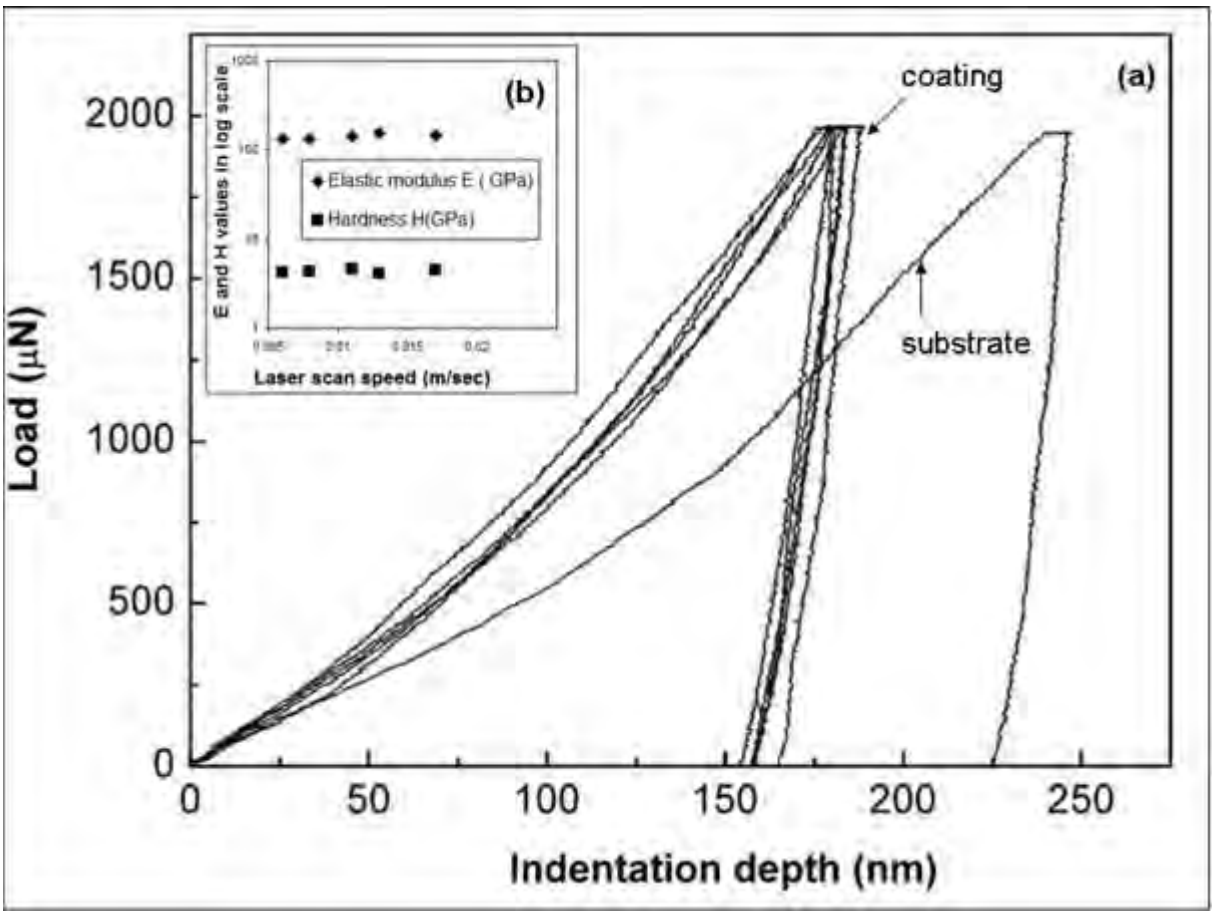


Figure 4.4 Nanoindentation data: (a) characteristic loading and unloading curves for the coating and the substrate and, (b) variation in E and H of the coatings as function of laser scan speed **[97]**.

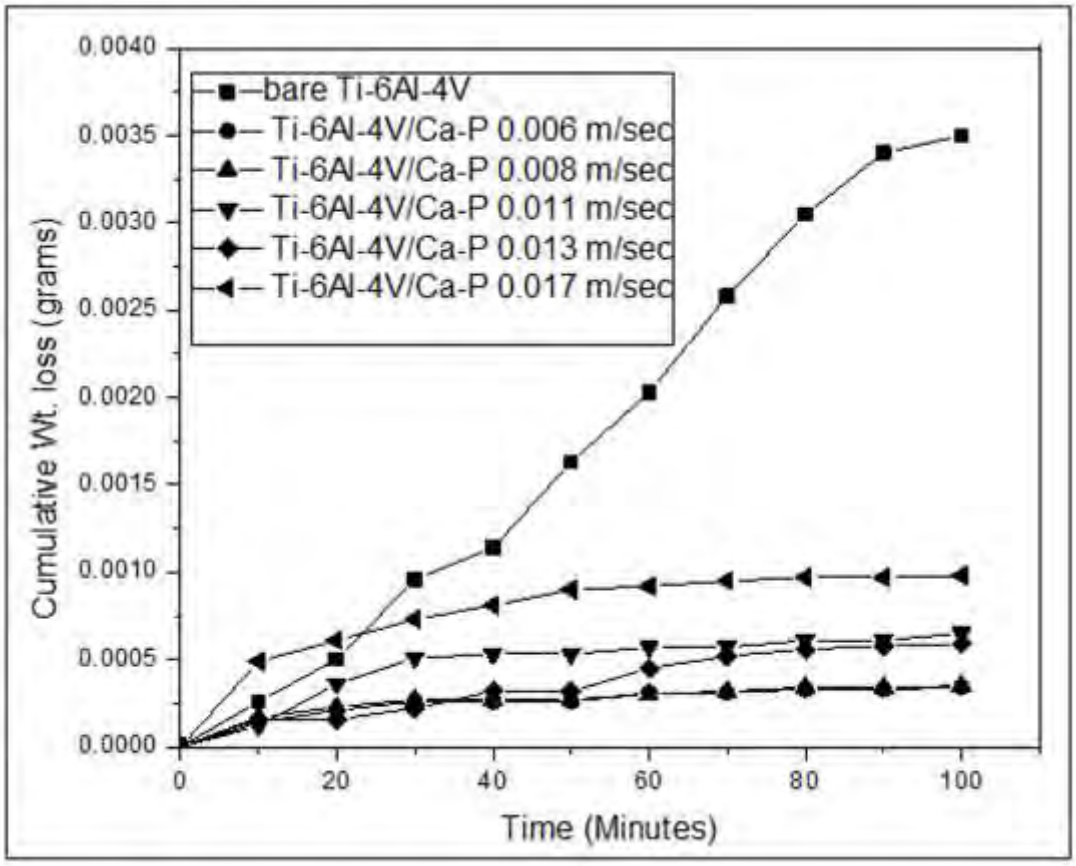


Figure 4.5 Cumulative weight loss for the sample processed at varying laser scan speed and bare Ti-6Al-4V in a SBF environment **[97]**.

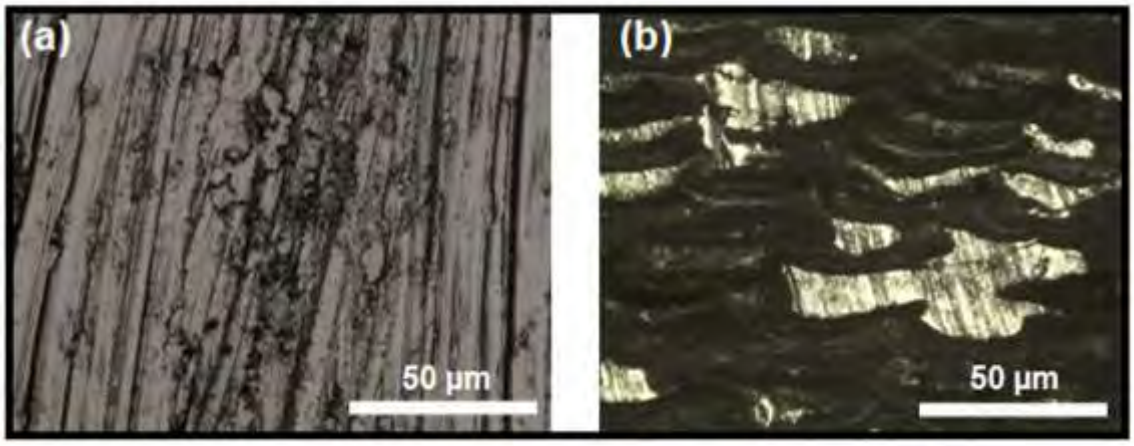


Figure 4.6 Optical microscopic image of the wear tracks on (a) bare Ti-6Al-4V and (b) Ca-P coatings processed at a laser scan speed of 102 cm/min **[97]**.

ce of surface damage in bare Ti-6Al-4V can be attributed to a mixed effect of adhesion and abrasion wear mechanisms. The flat mating surfaces of the pin and bare Ti-6Al-4V would have resulted in adhesion and cohesion at the interface due to sliding and/or vibratory motions. As a result, damage due to adhesive wear would result in the transfer of adhesively bound particles from one surface to the other. Progressive accumulation and strong adhesion of more material finally lead to increased abrasive wear and more material removal by ploughing. Thus, the significant cumulative weight loss or low sliding wear resistance of bare Ti-6Al-4V can be associated with this mutual effect of wear mechanism. On the other hand, the appearance of surface damage in Ca-P coating is characteristic of an abrasion wear mechanism. In addition to the presence of hard ceramic phase on the surface, the physical texture also contributed to high sliding wear resistance of Ca-P coating. It is known that introduction of surface textures in the form of depressions and undulations can improve the tribological properties **[100]**. In that case, the textured Ca-P coating acts as a reservoir for the SBF and reduces the contact between the two surfaces. Thus, the only wear mechanism associated with textured coating is slight ploughing of the material when the pin comes in contact with the undulations. For all these reasons, the textured Ca-P coatings exhibited very low cumulative weight loss or high sliding wear resistance.

4.2.4 Wettability of textured coatings

The presence of identical phases (Figure 4.3) **[70]** in the coatings of all laser processed samples is expected to provide minimal or no variation on the wetting characteristics during SBF immersion. However, as stated in the following section, all the coatings in presence of these phases and with the varying surface topographic cues have demonstrated significant increase in

wetting compared to uncoated Ti-6Al-4V alloy. The variation in surface roughness (texture) of coated samples with varying laser scan speed was evaluated using a white light interferometer. As defined earlier, the roughness parameters such as standard deviation in amplitude, σ_A and wavelength, λ are obtained from five random locations on each sample and presented as mean value with related scatter in Table 4.1 **[70]**. The corresponding mean values of σ_A/λ along with the related scatter as a measure of surface texture are also included in Table 4.1 **[70]**. The correlation between the experimental observations (Figure 4.2) **[70]** and measurement of roughness parameters (Table 4.1) **[70]** indicate that the decreasing values of σ_A/λ ratio corresponded with increasing values of laser scan speed. In other words, the surface roughness transitioned from circular grooves to radial grooves with increasing laser scan speed. A schematic of such a process is illustrated in Figure 4.7 **[70]**. The above transition or smoothening effect can be attributed to the fact that as the linear scan speed is increased the number of pulses per unit area (pulse overlap) and thereby the input energy density is reduced. As stated earlier, this in turn resulted in less thermal effects and reduced melting on the surface and therefore a low σ_A/λ value.

It is also well understood that wetting of a surface by a liquid is significantly affected by its surface roughness **[83, 101-104]**. Table 4.1 **[70]** lists the experimental contact angles (θ) or the apparent contact angles subtended by an SBF drop and corresponding texture parameter (σ_A/λ) for uncoated and coated Ti-6Al-4V samples. The texture parameter (σ_A/λ) and the experimental contact angle (θ) for coated samples can be seen to have significantly lower values compared to that for uncoated sample, indicating the influence of various phases evolved during laser processing. On the contrary, within the set of laser coated samples it can be noticed that

with increasing laser scan speed the texture parameter (σ_A/λ) and the experimental contact angle (θ) both decrease, indicating the influence of various surface textures and the same phases (α-TCP, TiO_2, Ti and Al) evolved during laser processing. Therefore, the surface becomes more wettable with increasing laser scan speed and decreasing σ_A/λ value, as schematically illustrated in Figure 4.8 **[70]**. At higher laser scan speeds the surface topographic features with smaller σ_A/λ value resembled a radial type groove morphology. When a liquid drop is placed on a surface with radial grooves (smaller σ_A/λ value), it can easily overcome the energy barriers associated with such surface to completely wet it. Thus, an equilibrium state of wetting is achieved when the grooves are radial. Hence, applying an energy minimum condition a relationship between the experimental contact angle affected by the radial grooves (θ_{rad}) and the theoretical contact angle (θ_{th}) can be obtained as follows **[83]**:

$$\cos\theta_{rad} = D\,(1 - F)\cos\theta_{th} - F \quad \text{.....4.1}$$

where D is defined as the average area ratio of real contacted interface to its projected part, and F

Table 4.1 Experimental results of contact angle of SBF and the texture parameter (σ_A/λ) on the Ca-P coated sample obtained at various laser scan speeds **[70]**.

Sample	Standard deviation of amplitude σ_A (μm)	Wavelength λ (μm)	Texture parameter σ_A/λ	Contact angle θ (degrees)
Bare Ti-6Al-4V	12.56 ± 0.37	2.79± 0.08	4.38 ± 0.04	60.5 ±0.85
Ti-6Al-4V/Ca-P 36 cm/min	5.384 ± 0.053	2.6 ± 0.026	2.28 ± 0.06	22±0.44
Ti-6Al-4V/Ca-P 48 cm/min	16.2 ± 0.024	9.46 ± 0.14	1.80 ± 0.036	19.5±0.48
Ti-6Al-4V/Ca-P 78 cm/min	12.93 ± 0.3235	7.98± 0.1995	1.14± 0.0171	18 ± 0.21
Ti-6Al-4V/Ca-P 102 cm/min	14.033 ± 0.18	12.52 ± 0.25	0.78 ± 0.0195	15±0.45

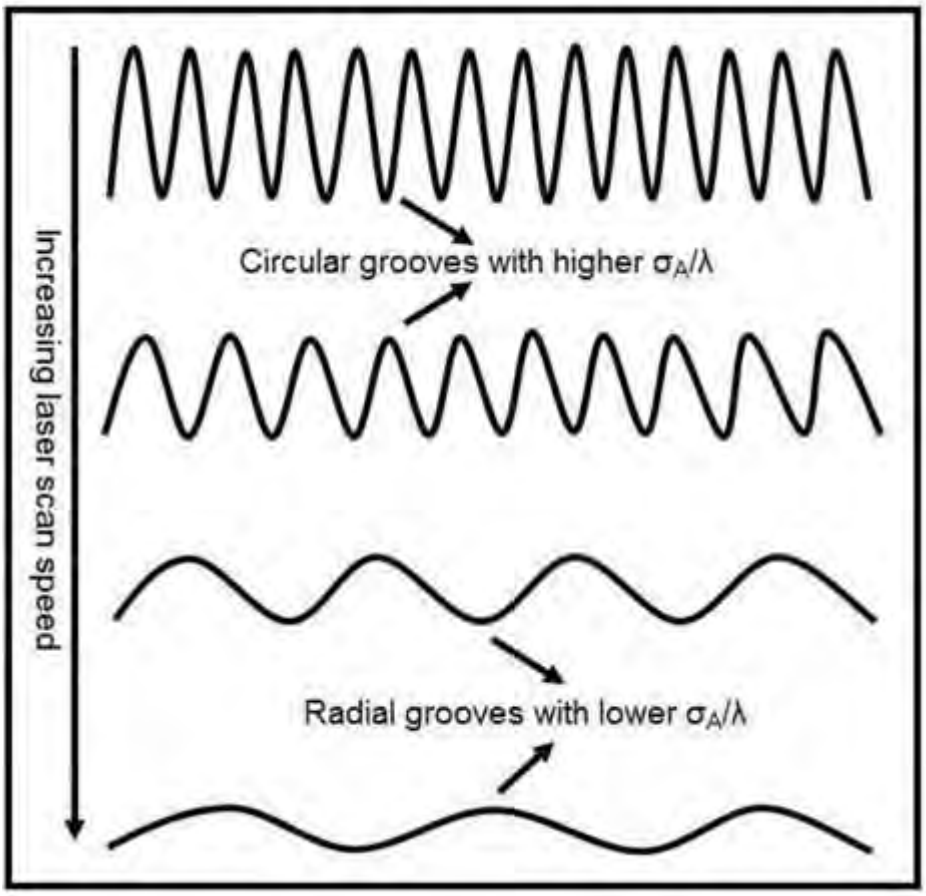


Figure 4.7 Schematic showing the variation in surface profiles with varying laser scan speed **[70]**.

is the area fraction of an uncontacted solid-liquid interface on solid (Figure 4.8) **[70]** . The theoretical contact angle θ_{th} is defined as: $Cos\theta_{th} = (\gamma_s - \gamma_{ls})/\gamma_l$, where γ_s, γ_{ls}, and γ_l are the interface energies between solid-vapor, liquid-solid, and liquid-vapor interfaces, respectively. For a radial groove, both D and F are constants and since, the rough surface is assumed to distribute as a cosine profile with a Gaussian distribution, they are both a function of σ_A/λ **[83]**. Hence, through this energy minimum route it can be clearly understood that the decrease in contact angle is due to formation of radial grooves (smaller σ_A/λ value) on a surface.

In contrast, when the surface features are sharp (higher σ_A/λ value) at lower laser scan speed they are termed as circular grooves. The intrinsic energy associated with the liquid drop may not be sufficient enough to overcome the energy associated with the sharp features or circular grooves. Hence, when a liquid drop is placed on such a surface an equilibrium state of wetting could never be achieved. In such case, the contact angles affected by the circular grooves can be related to the theoretical contact angle as per the following equation **[83]**.

$$\theta_{cir} = \theta_{th} + \left(\frac{\sqrt{8\pi}}{\lambda}\sigma_A\right) \quad \text{.....4.2}$$

Therefore, from the above equation it can be clearly explained that a circular or sharp groove with higher σ_A/λ value always results in an increase in contact angle and thereby a decrease in wettability (Figure 4.8) **[70]**.

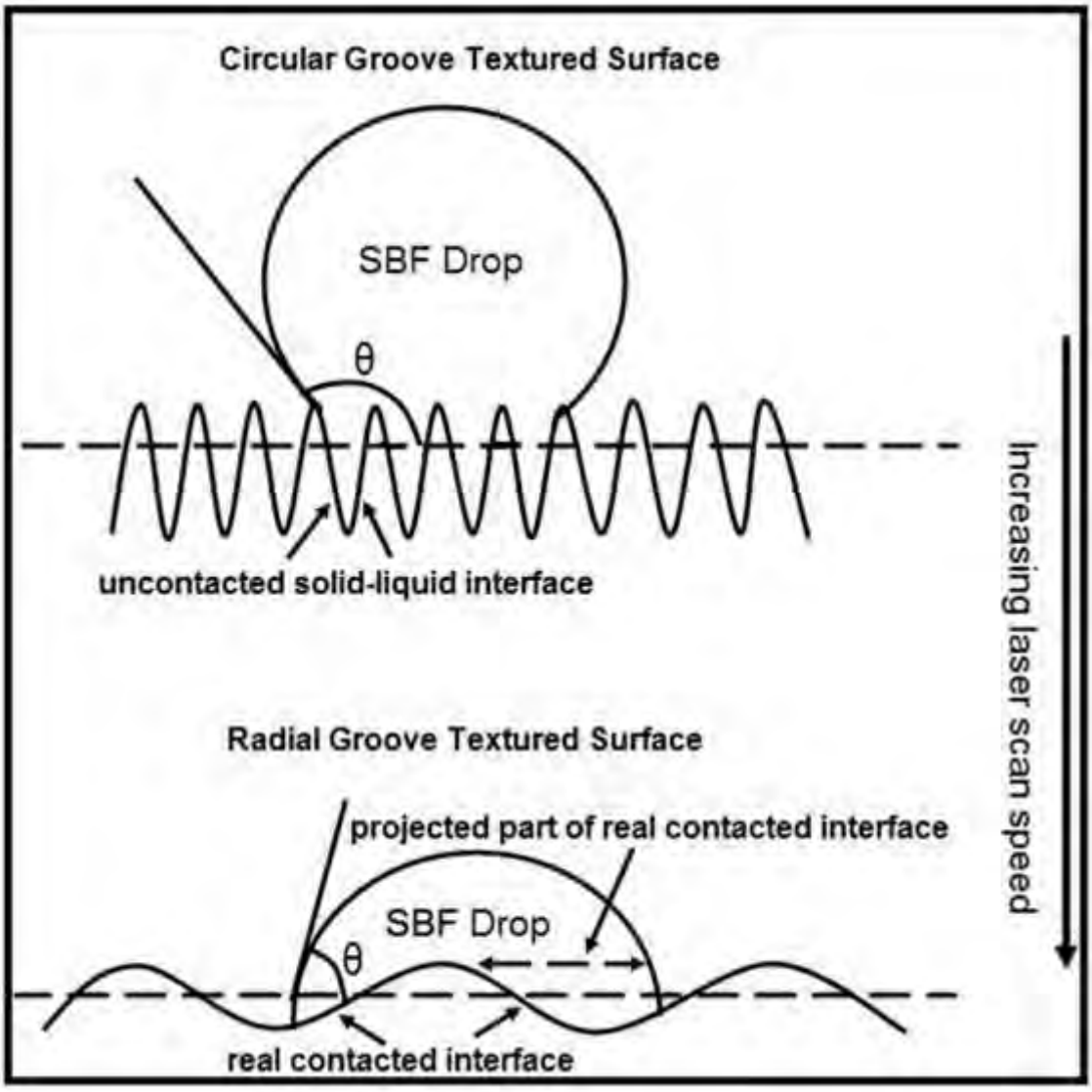


Figure 4.8 Schematic showing the wetting behavior of a liquid drop on a rough surface having (a) Circular grooves and (b) radial grooves **[70]**.

4.2.5 Mechanism and kinetics of HA precipitation on textured coating

The influence of texture parameter (σ_A/λ) and wettability on the mineralization behavior of samples are studied by immersing them in a SBF. An understanding of the above phenomena will provide insight for the in vitro bioactivity behavior of the coatings and also thereby help predict for the biocompatibility of the coatings. Figures 4.9-4.12 **[70]** represent the XRD studies prior to and after immersion in SBF (for different time periods) for samples processed at laser scan speeds of 36, 48, 78 and 102 cm.min^{-1}, respectively. In each of these, the base spectrum (prior to immersion in SBF) is included for comparison purpose. As discussed earlier, since there was no detectable change in surface phase composition (Figure 4.3) **[70]** in all samples processed using the set of laser parameters employed in the present work, it was inferred that surface roughness (textures) is the only controlling factor that has influenced the precipitation kinetics of HA on the sample surface during immersion in a supersaturated SBF. However, as explained later, in comparison, the precipitation kinetics is expected to be significantly different in uncoated and coated samples due to the influence of both surface phase composition and surface texture.

For the samples processed at laser scan speeds of 36 and 48 cm/min (Figure 4.9, 4.10) **[70]**, a maximum attributed to the apatite phase at 2θ =31.75° corresponding to the plane (211) was detected only after 48 hours immersion of the samples in SBF. On the contrary, for the sample processed at laser scan speed of 78 cm/min (Figure 4.11) **[70]** the same peak was observed soon after 24 hours of immersion in SBF. In addition to the above peak (2θ = 31.75°), two more apatite peaks appeared at 2θ ~22.0° and 22.9° corresponding to planes (200) and (111)

respectively, for the sample processed at laser scan speed of 102 cm/min (Figure 4.12) **[70]**. It, therefore, clearly indicates that the sample processed at laser scan speed of 102 cm/min has a pronounced biomineralization compared to all other samples. It can also be observed that there is an increased crystallographic texturing along the planes (2 0 0) and (2 1 1) with increasing immersion time. Such a phenomenon may be attributed to both the increase in volume fraction of the apatite-like phase and crystal growth along the c-axis.

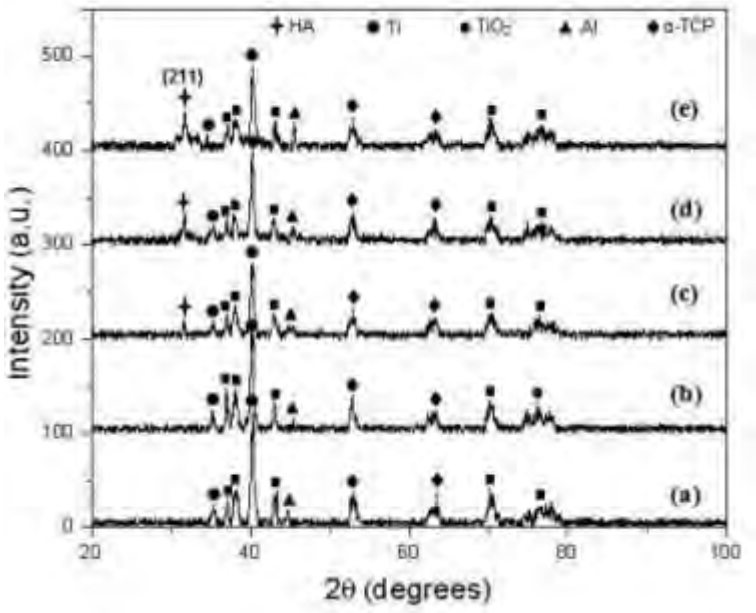


Figure 4.9 XRD studies of the sample (processed at laser scan speed of 36 cm/min) (a) prior to immersion in SBF and after immersion in SBF for (b) 24 hours, (c) 48 hours, (d) 72 hours and (e) 96 hours **[70]**.

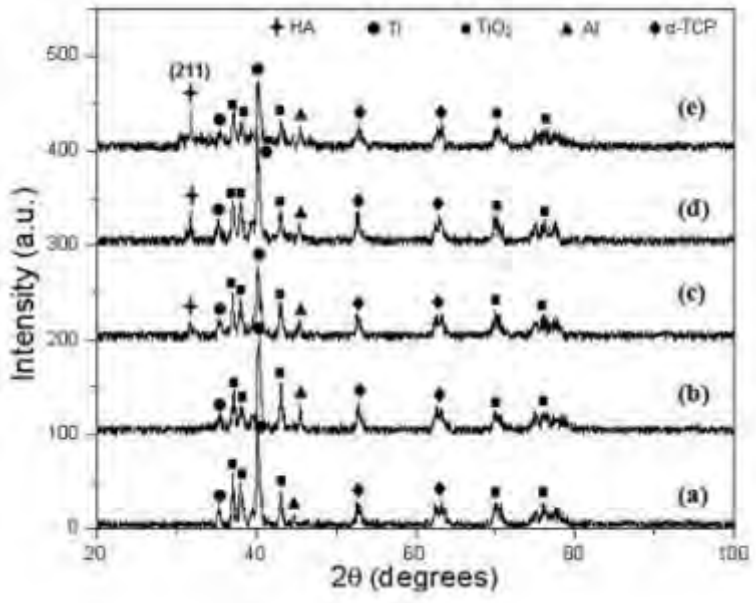


Figure 4.10 XRD studies of the sample (processed at laser scan speed of 48 cm/min) (a) prior to immersion in SBF and after immersion in SBF for (b) 24 hours, (c) 48 hours, (d) 72 hours and (e) 96 hours **[70]**.

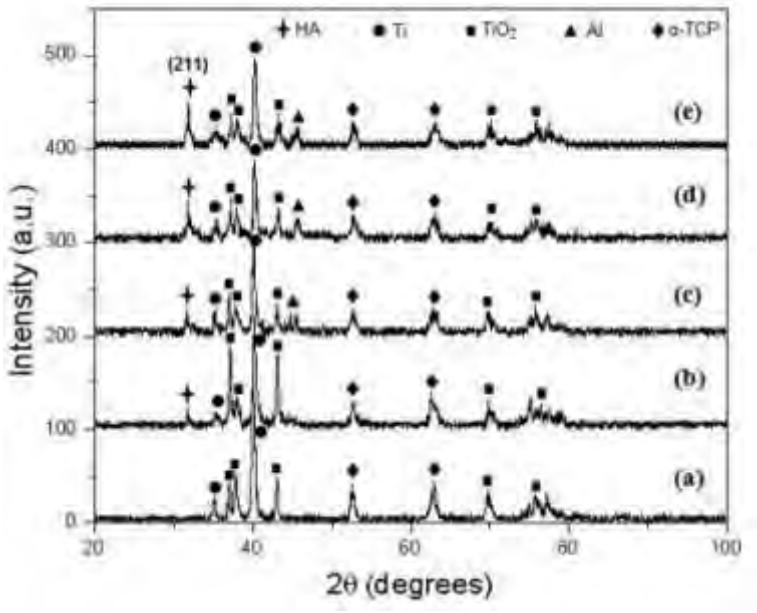


Figure 4.11 XRD studies of the sample (processed at laser scan speed of 78 cm/min) (a) prior to immersion in SBF and after immersion in SBF for (b) 24 hours, (c) 48 hours, (d) 72 hours and (e) 96 hours **[70]**.

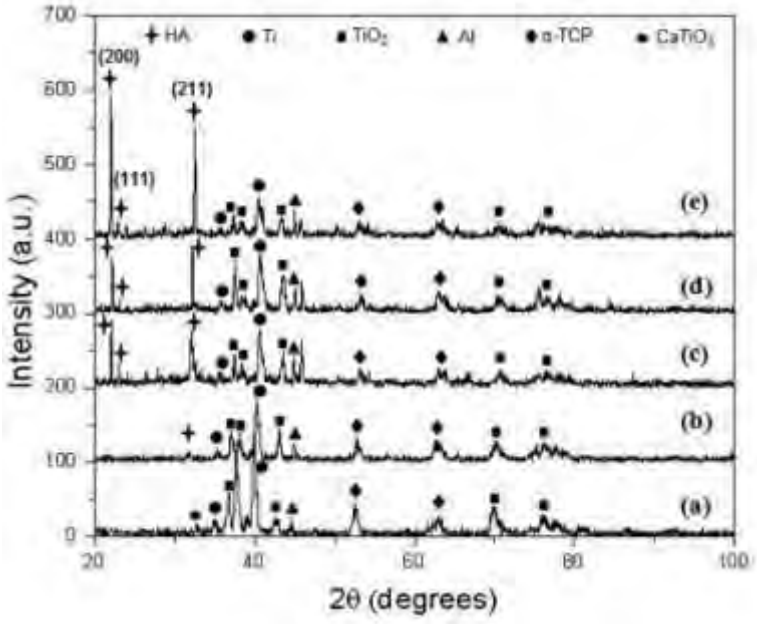


Figure 4.12 XRD studies of the sample (processed at laser scan speed of 102 cm/min) (a) prior to immersion in SBF and after immersion in SBF for (b) 24 hours, (c) 48 hours, (d) 72 hours and (e) 96 hours **[70]**.

SEM observations for the sample processed at laser scan speed of 102 cm/min demonstrated (Figure 4.13) **[70]** the formation of a globular apatite like layer, following immersion in SBF for different time periods. The formation of cracks within the thin apatite like layer was attributed to the removal of moisture during drying. Further, it can be concluded from the reduced dimensions of islands between cracks that, with increasing immersion time, there is an increased accumulation of an apatite like layer or enhancement in biomineralization. The thickness of this apatite layer varied from 8 to 15 μm with increasing immersion time. From the EDS spectra (presented as inset within the SEM images) it can be observed that there is a strong presence of Ca and P atoms following immersion in SBF, and also an increased intensity of both Ca and P with increasing immersion time. These studies, therefore, further complement to earlier findings from XRD studies (Figure 4.9-4.12) **[70]**. Apart from Ca and P, a small amount of Na and Cl precipitated from the SBF solution can also be observed in the EDS spectra. This enhancement in mineralization or bioactivity for the sample processed at laser scan speed of 120 cm/min, is as explained in earlier sections, a result of its improved wettability with SBF solution due to the textured surface produced during laser processing.

The mechanism for improvement in mineralization can also be explained as per the schematic illustrations presented in Figure 4.14 **[70]**. As explained earlier, when the laser scan speed is increased the coated surface undergoes a transition from surface features with circular grooves (high σ_A/λ value) to surface features with radial grooves (low σ_A/λ value) and thereby improves its wettability to SBF. This improvement in wetttability, therefore, enhances the reaction of water molecules present in the SBF with TiO_2 and α-TCP phases present on the surface of the sample as per the following reactions **[105-107]**:

$TiO_2 + 2H_2O \rightarrow Ti(OH)_4$.....C4.4

$3\alpha\text{-}Ca_3(PO_4)_2 + H_2O \rightarrow Ca_9HPO_4(PO_4)_5OH$.....C4.5

The above reactions (C4.4 and C4.5) on the samples processed at higher laser scan speeds (low σ_A/λ value) leads to the precipitation of more OH^- ions in stage 1 and thereby increased negative charge density on the surface of the sample (Figure 4.14 a) **[70]**. It has been widely reported that the presence of a negatively charged surface enhances the formation of apatite on the substrate **[108, 109]**. Following the precipitation of OH^- ions in stage 1 (Figure 4.14a) **[70]**, in stage 2 of this mechanism, calcium ions (Ca^{2+}) from the SBF are attracted towards the negatively charged (OH^-) surface (Figure 4.14b) **[70**] to form calcium hydroxide. In stage 3, the calcium hydroxide, therefore, reacts with phosphate ions (PO_4^{3-}) present in the SBF and consequently in stage 4 the apatite nuclei on surface are formed as per the reaction C4.6 (Figure 4.14b) **[110]**:

$10Ca(OH)_2 + 6H_3PO_4 \rightarrow Ca_{10}(PO_4)_6(OH)_2 + 18\ H_2O$.....C4.6

As the immersion time is increased, a large amount of calcium and phosphate ions are attracted towards the surface (stage 4) and thick layer of apatite is finally formed on the surface (stage 5, Figure 4.14b) **[70]**.

Further, the nature of precipitation kinetics was evaluated for HA stoichiometry through EDS analysis of all the samples for each immersion period. A total of five readings were taken from different locations on each sample. It can be observed (Figure 4.15) **[70]** that there is an increase in Ca and P atomic concentration with increasing immersion time for all the samples. This can be attributed to the presence of already formed apatite nuclei (stage 4, Figure 4.14b) **[70]** which act as nucleating sites for the deposition of more Ca and P ions from the SBF. From Figures 4.15a and 4.15b **[70]**, for the samples processed at laser scan speed of 36 and 48 cm/min respectively, the Ca/P atomic ratio following 24 hours of SBF immersion was more than 2 and

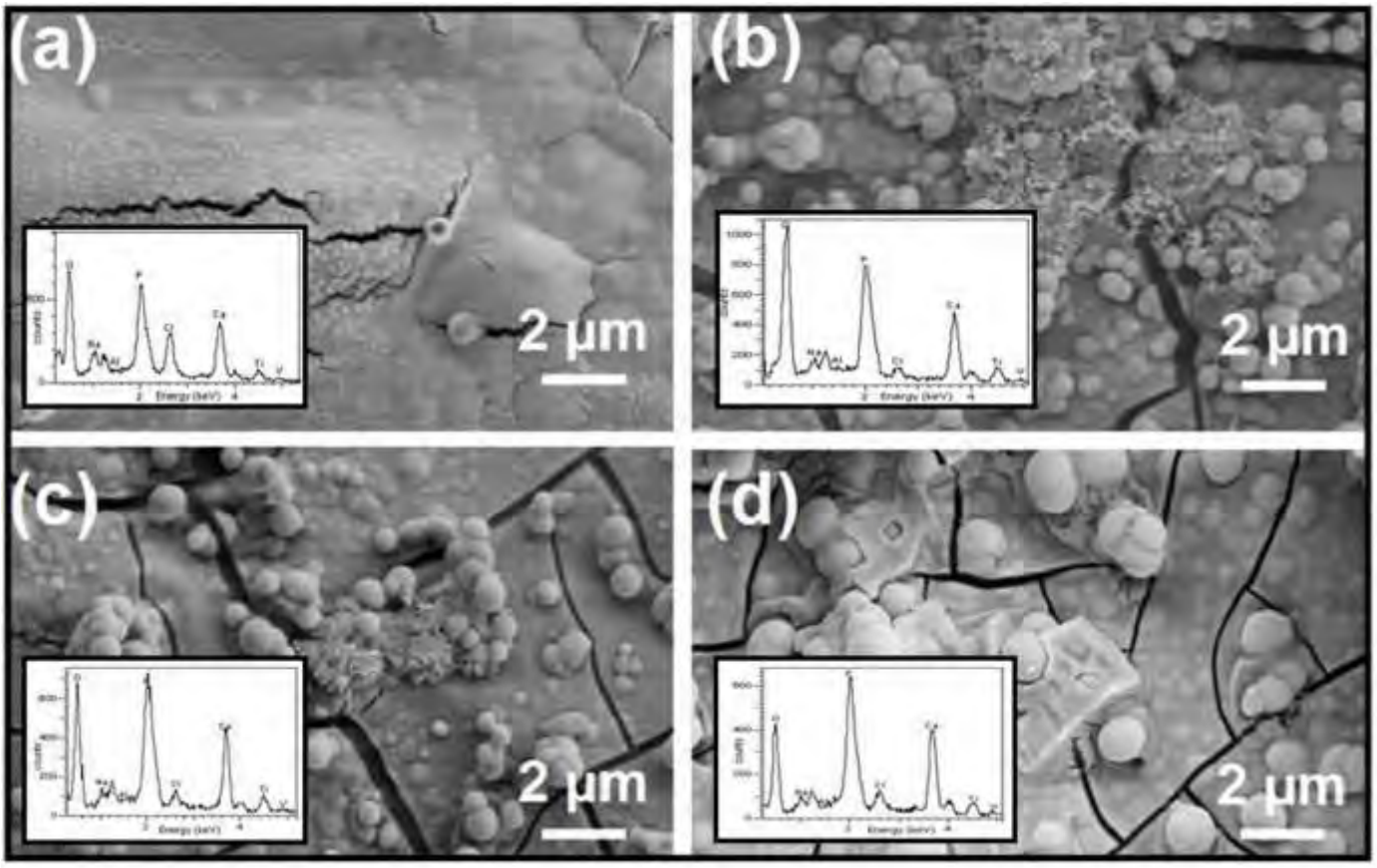


Figure 4.13 SEM micrographs revealing the formation of globular apatite like layer following immersion in SBF for different time periods and the inset showing the corresponding EDS spectra (a) 24 hours (b) 48 hours (c) 72 hours (d) 96 hours. (For samples processed at laser scan speed of 102 cm/min) **[70]**.

dropped to ~1.67 (the Ca/P atomic ratio for HA) after 48 hours immersion and remained the same during 72 hours and 96 hours of immersion time. In contrast, for the samples processed at laser scan speed of 78 and 102 cm/min (Figure 4.15c, and 4.15d) **[70]**) the Ca/P atomic ratio immediately reached ~1.67 during 24 hours of SBF immersion and remained the same with increasing immersion time (48, 72, and 96 hours). Such rapid saturation of Ca/P atomic ratio to the value of the atomic ratio for HA (~ 1.67) at higher processing speeds (78 and 102 cm/min) compared to at lower speeds (36 and 48 cm/min) further indicates the transition of surface texture from circular grooves to radial grooves and associated increased wettability.

Finally, the effects of surface phase and surface texture (roughness) on the growth kinetics of HA, on the bare Ti-6Al-4V and the samples processed at different laser scan speeds was studied by measuring the increase in weight following immersion in SBF for different time periods. The Ca-P coated samples processed at higher laser scan speeds (78 and 102 cm/min) have pronounced biomineralization compared to the samples processed at lower laser scan speeds (36 and 48 cm/min) and uncoated Ti-6Al-4V (Figure 4.16) **[70]**. Also, for the uncoated Ti-6Al-4V (Figure 4.16) it can be observed that there is a slight weight loss initially flowed by an increase after 96 hours of immersion. This initial weight loss may be attributed to the reaction between the reactive species (Na^+ and Cl^- ions) present in SBF solution and the uncoated Ti-6Al-4V. As, there is no ceramic coating, the Na^+ and Cl^- ions present in the SBF solution easily corrode the Ti-6Al-4V metallic surface, thereby resulting in a decrease in weight. However, as the apatite precipitation starts taking place, it forms a barrier between the Ti-6Al-4V metallic surface and the reactive species (Na^+ and Cl^- ions) and thereby results in an increase in weight at longer

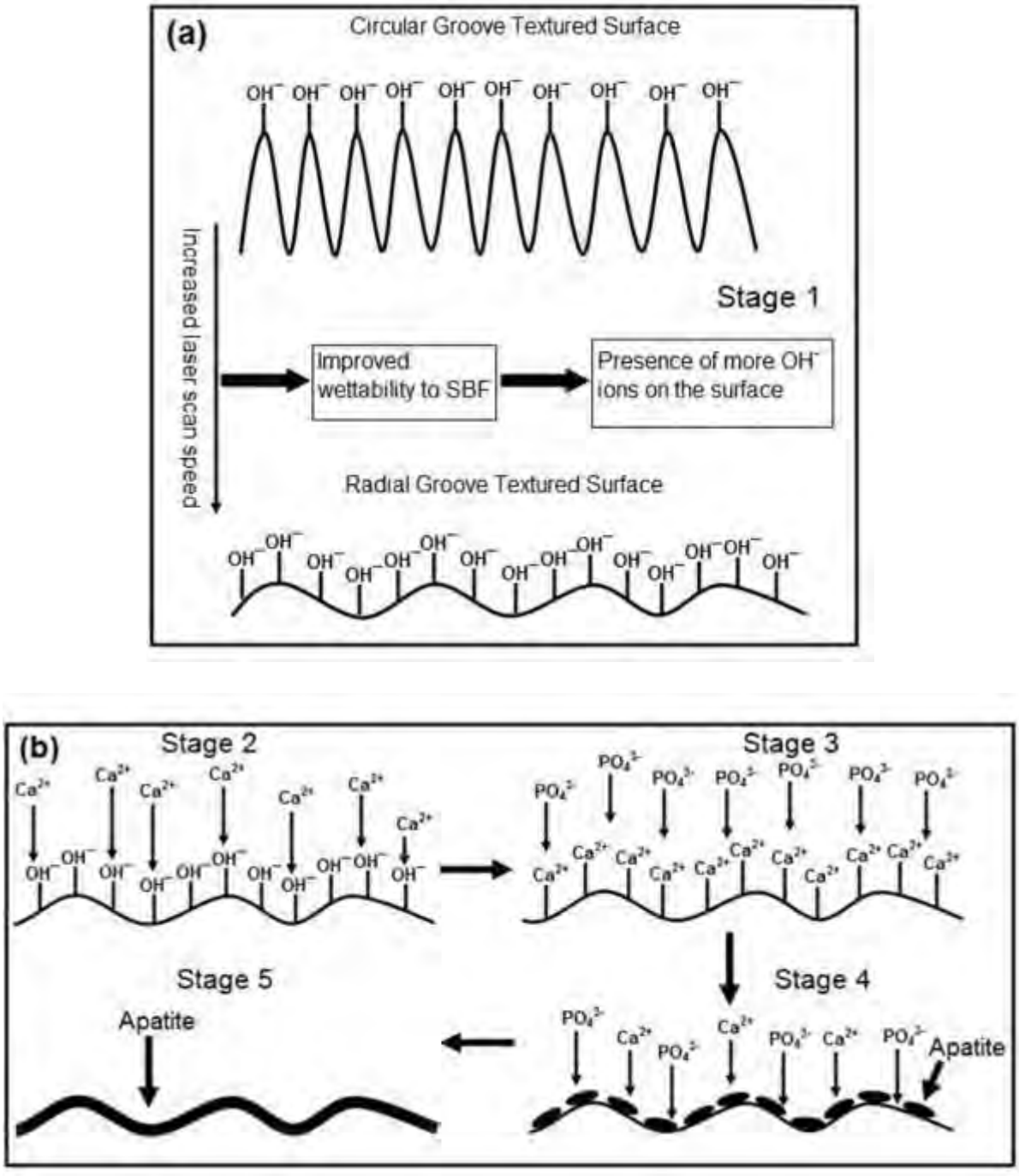


Figure 4.14 Schematic illustrations demonstrating (a) the favored mechanism for the formation of more OH^- ion groups on the surface of the sample processed at higher laser scan speed and (b) the mechanism of apatite formation on such a surface **[70]**.

immersion times. The growth kinetics of HA on the samples was studied by curve fitting and determining the kinetic constants. The weight increase for bare Ti-6Al-4V and the samples processed at laser scan speed of 36 and 48 cm/min followed a linear relationship with immersion time as per the following equation:

$$W = K(t) + A \quad \ldots\ldots 4.3$$

In contrast, the weight increase for samples processed at laser scan speed of 78 and 102 cm/min followed a power relationship with immersion time as per the following equation:

$$W = A(t)^{K} \quad \ldots\ldots 4.4$$

Here, W is the growth rate (grams/hour), A and K are the kinetic constants and t is the immersion time (hours). The kinetic constants A and K obtained from the curve fits are listed as an inset in Figure 4.16 **[70]**. These constitutive relationships and corresponding kinetic constants clearly define the nature of biomineralization and the effects of surface phase and surface texture on wettability as function of laser processing parameter (scan speed).

The above results therefore clearly demonstrated that by varying the laser scan speed, bioactive Ca-P coatings with varying surface textures can be synthesized on Ti-6Al-4V substrates. The presence of appropriate phase and surface textures resulted in an improvement in wettabilty and in vitro bioactivity for the textured coatings as compared to the untreated Ti-6Al-4V samples. Further, within the laser processed samples it can be observed that with increasing laser scan speed the surface textures assumed to have radial type morphology and thereby resulting in an improvement in wettability and its mineralization under in vitro conditions.

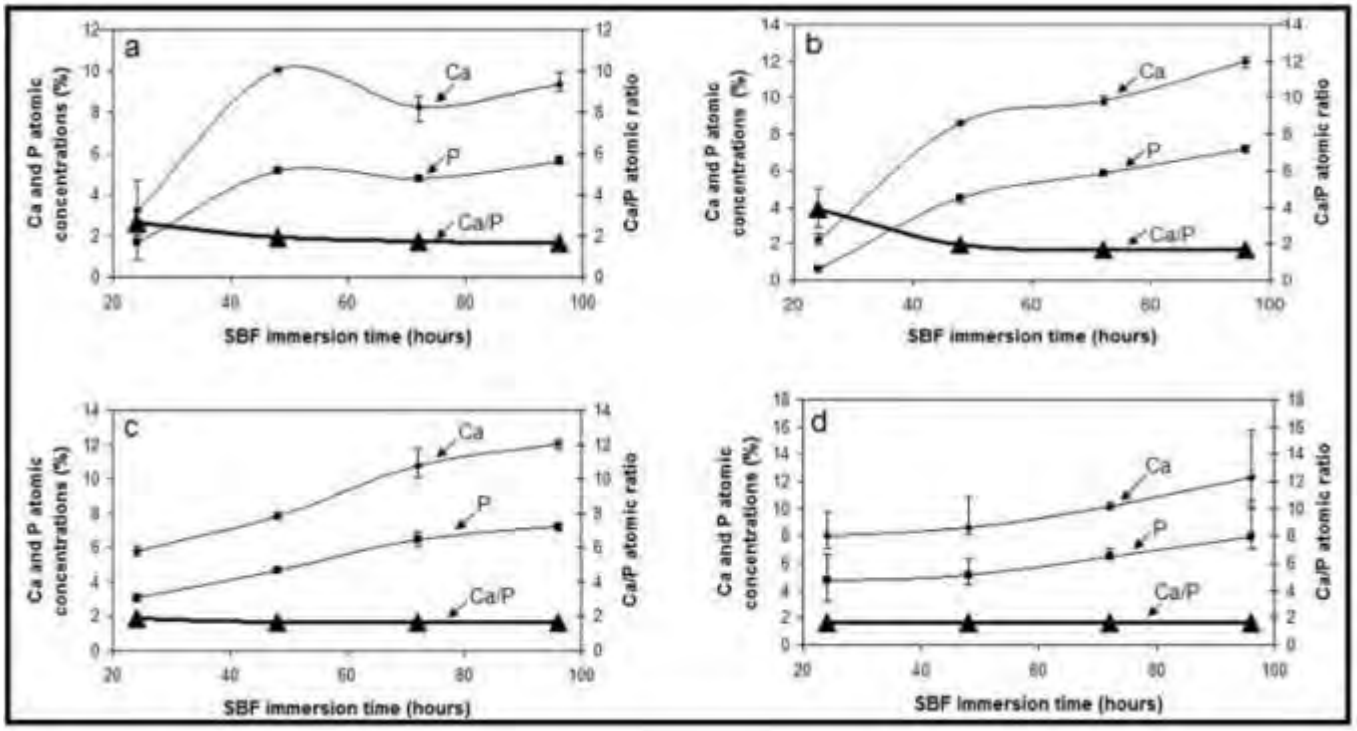


Figure 4.15 Dependence of Ca and P atomic concentration and Ca/P atomic ratio to SBF immersion time for the samples processed at laser scan speed of (a) 36 cm/min, (b) 48 cm/min, (c) 78 cm/min, and (d) 102 cm/min **[70]**.

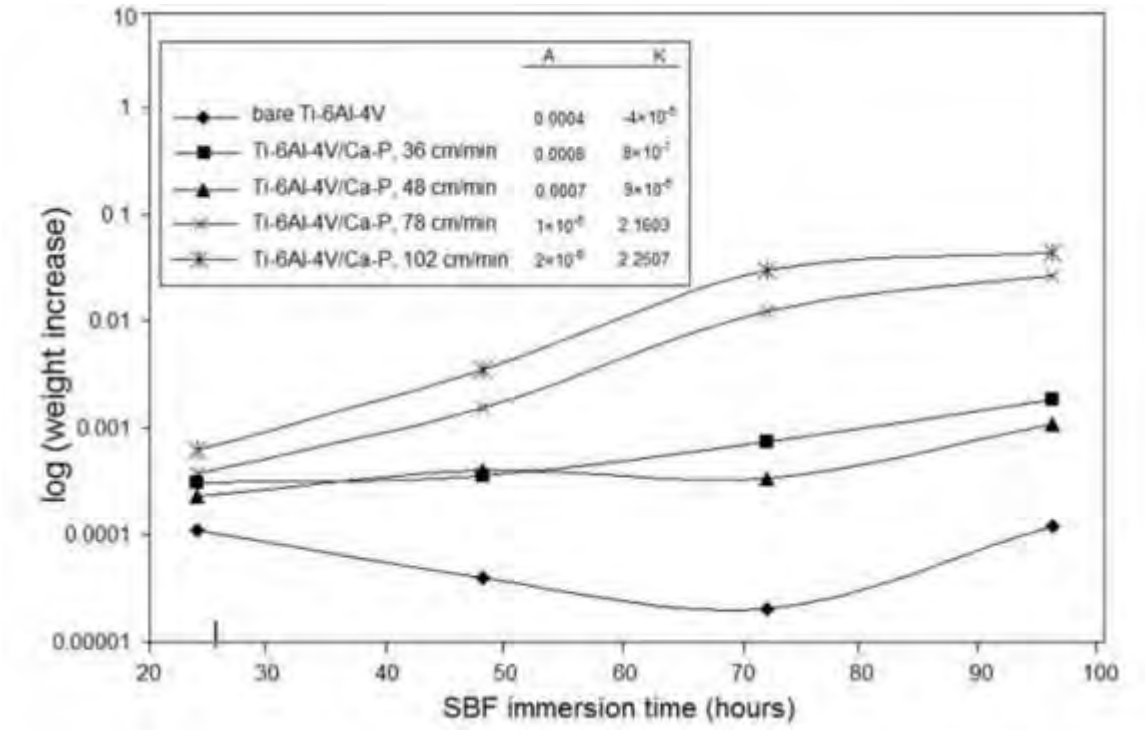


Figure 4.16 Deposition of HA in grams on Ca-P coated samples (laser textured at various laser scan speeds) and bare Ti-6Al-4V substrate from the SBF solution as a function of immersion time **[70]**.

4.3 Variation of laser pulse frequency

The process parameters used in earlier attempts with variation in laser scan speed (higher laser fluence in the range 666 mJ cm^{-2} – 1887 mJ cm^{-2}) resulted in oxidation of the underlying substrate and severe reaction between both the precursor (HA) and substrate (Ti-6Al-4V) material due to melting. This resulted in phases such as TiO_2 and α-TCP with almost no retention of HA on the surface. Hence, to retain cetain amount of the precursor (HA) material, the laser parameters are adjusted to operate with varying laser pulse frequency and laser pulse width (1 ms) to obtain the textured coating. Also, it was to our interest to see how a variation in laser pulse frequency, affects the texture morphology and thereby its wetting, in vitro bioactivity, and in vitro biocompatibility. Finally, in this current work, apart from X-ray diffraction, the SBF immersed samples are also characterized using FTIR and XPS for elemental and phase composition analysis of the precipitates.

4.3.1 Microstructure, morphology, and phase analysis

The low-magnification optical microscopic images (Figure 4.17) **[71]** of the surfaces of laser textured samples clearly demonstrate the effect of varying laser pulse frequency on the texture evolution. From equation 3.1 it can be observed that with increasing laser pulse frequency the laser spot overlap increases. This in turn results in more crater overlap with increasing pulse frequency and thereby contributes towards surfaces with varying textured morphology as observed in Figure 4.17 **[71]**. The cross-sectional SEM image (Figure 4.18a) **[71]** of the sample processed at 40 Hz is clearly an indicative of the sound metallurgical bonding between the coating and substrate (Ti-6Al-4V). A sound bonding of the bioceramic coating to the substrate

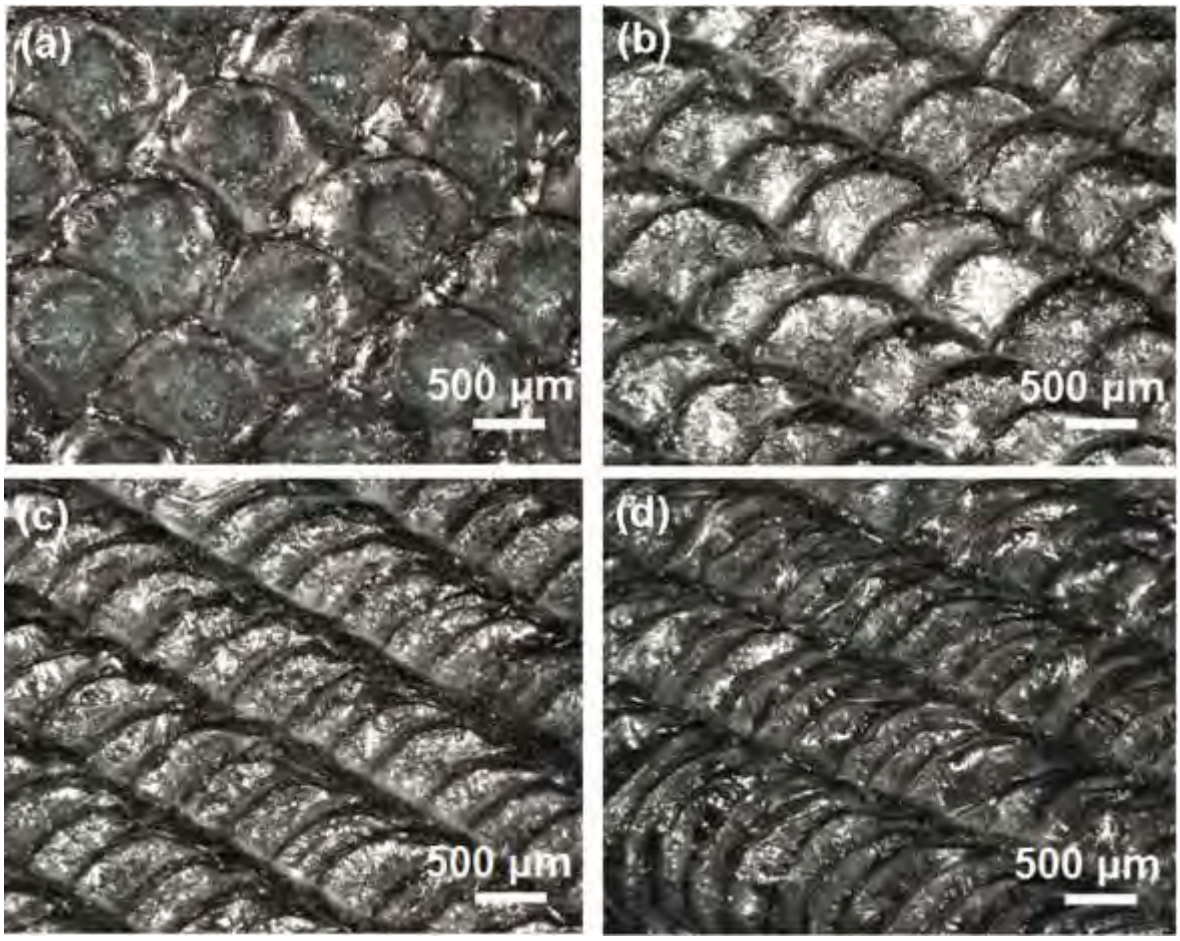


Figure 4.17 Low-magnification optical microscopic images of the surface of coatings processed at laser pulse frequencies of (a) 10 Hz, (b) 20 Hz, (c) 30Hz, and (d) 40 Hz **[71]**.

material is expected to reduce the delamination of the ceramic layer and thereby avoid the risk of dissolving metallic ions into the body plasma and problem of osteolysis.

The variable thermodynamic conditions resulting from the varying pulse frequency within the range employed in the present work only influenced the texture evolution and no detectable variation in the evolution of types of phases (Figure 4.18b) **[71]** is observed. The major phases identified within the detectable limits of the XRD instrument are HA ($Ca_{10}(PO_4)_6(OH)_2$), $CaTiO_3$, TiO_2 (Rutile and Anatase), $Ca_3(PO_4)_2$, and Al_2O_3. Although, there is no major variation in the types of phases evolved, the variation in peak intensities is clearly an indication of the variation in amounts of these phases with increasing pulse frequency. As the pulse frequency was increased from 10 to 40 Hz there is a decrease in peak intensities of $Ca_{10}(PO_4)_6(OH)_2$ and $CaTiO_3$ phases along (3 0 0) and (1 2 3) planes, respectively (Figure 4.18b) **[71]**. On the contrary, with increasing pulse frequency there is an increase in peak intensities of the TiO_2 (Rutile) and TiO_2 (Anatase) phases along (0 0 2) and (1 0 5) planes, respectively. The above observations can be attributed to the fact that with increase in laser pulse frequency from 10 to 40 Hz, there was an increase in the laser input energy density. Such increased input energy was likely to raise the temperature of laser material interaction zone to the level leading to the substantial amount of coating precursor material evaporation followed by oxidation of the substrate material for formation of more amount of TiO_2 and Al_2O_3. Although the identical phases are present in the coatings of all laser processed samples, as stated in the following sections, during SBF immersion these samples with varying surface topographic cues demonstrated varying wetting response and significant hydrophilicity with SBF compared to uncoated Ti-6Al-4V.

4.3.2 Effects of phase and morphology on wettability

The effect of laser pulse frequency (within the range employed in the present study) on three dimensional surface morphology of the coatings recorded using a confocal laser microscopy is presented in Figure 4.19a **[71]**. The sample processed at 10 Hz possesses a relatively rough morphology compared to the samples processed at 20, 30, and 40 Hz. As described earlier, due to only 6% overlap associated with 10 Hz frequency, the craters produced were least affected by the subsequent pulses. On the contrary, the frequencies of 20, 30, and 40 Hz provided substantially increased overlap of 53%, 69%, and 76% respectively. This increased spot overlap resulted in re-melting of the major portion of prior crater leading to smoothening of the coating. The values of σ_A, λ, and their ratio σ_A/λ were obtained from 5 random locations on each sample and are presented as mean values with related scatter in Table 4.2 **[71]**. All laser processed samples are associated with a significantly smaller value of σ_A/λ compared to the control (untreated Ti-6Al-4V). Also for all laser processed samples, with an increase in pulse frequency (in the range employed in the present study) there is a decrease in the σ_A/λ value. This further agrees with earlier visual observations that an increasing surface smoothening creeps in with increasing pulse frequency.

It has been well established that wetting of a surface by liquid is significantly affected by its surface roughness **[70, 83]**. The chart in Figure 4.19 b **[71]** provides the experimental contact angle subtended by the SBF drop on laser processed sample and the control Ti-6Al-4V. All laser processed samples except the sample processed at 10Hz depict an improved hydrophilic behavior compared to the control Ti-6Al-4V. Among the laser processed samples, the sample processed at 40 Hz possesses the maximum hydrophilicity to SBF with a contact angle of approximately 40°.

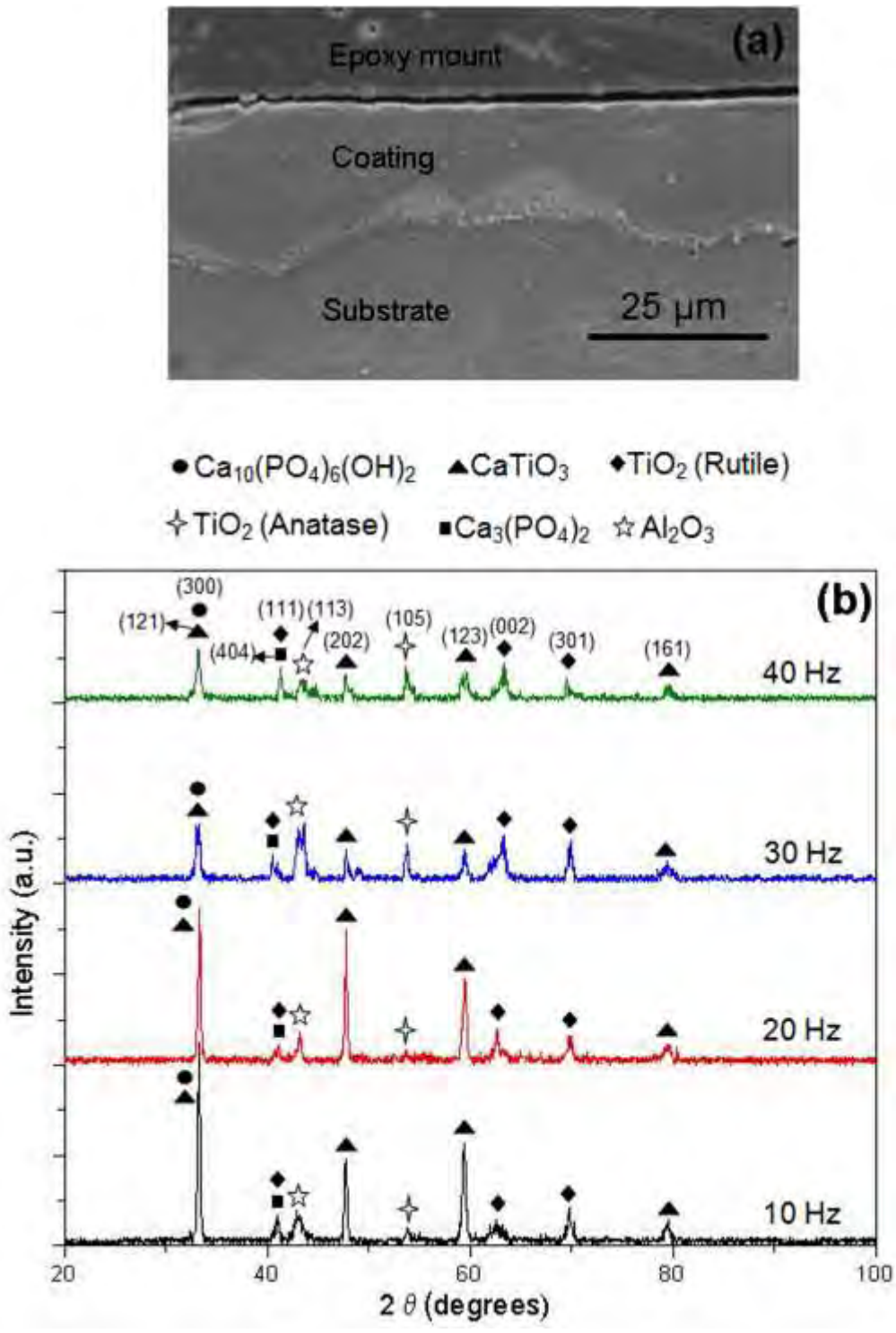


Figure 4.18(a) Cross-sectional SEM images of the sample processed at 40 Hz and (b) XRD pattern for the laser processed samples at varying pulse frequencies **[71]**.

The shadow image of SBF droplet (Figure 4.19b) **[71]** also shows the spreading of the SBF drop on the samples processed at 40Hz. Thus, there is a decrease in the experimental contact angle with decreasing texture parameter (σ_A/λ) (Table 4.2 and Figure 4.19b) **[71]**. This improved hydrophilic behavior of laser processed samples is attributed to the influence of surface texture and the types of phases (HA, $CaTiO_3$, $Ca_3(PO_4)_2$, TiO_2 (Anatase), and TiO_2 (Rutile)) evolved during laser processing. From equations 4.1 and 4.2 based on the model by Zhou and De Hosson, optical microscopy observations (Figure 4.17a) **[71]**, and confocal microscopy images (Figure 4.19a) **[71]** it is clearly evident that a laser pulse frequency of 10 Hz and associated minimal spot overlap produced a deep and circular groove morphology on the surface. This in turn resulted in a higher σ_A/λ value, leading to unstability in wetting and increased contact angle as per Equation 4.2. However, when the pulse frequency increased to 20, 30, and 40 Hz there was increased remelting due to increased spot overlap which in turn resulted in a relatively smoothly textured surface with lower σ_A/λ values. Therefore, the samples processed at these higher pulse frequencies are dominated by radial grooves that lead to improved wettability. As stated earlier, wetting is an important phenomenon which influences the mineralization, cell attachment, and cell proliferation. In light of this, the above preliminary efforts and corresponding understanding are further used to see how the texture parameter and associated wettability affect in vitro bioactivity and in vitro biocompatibility.

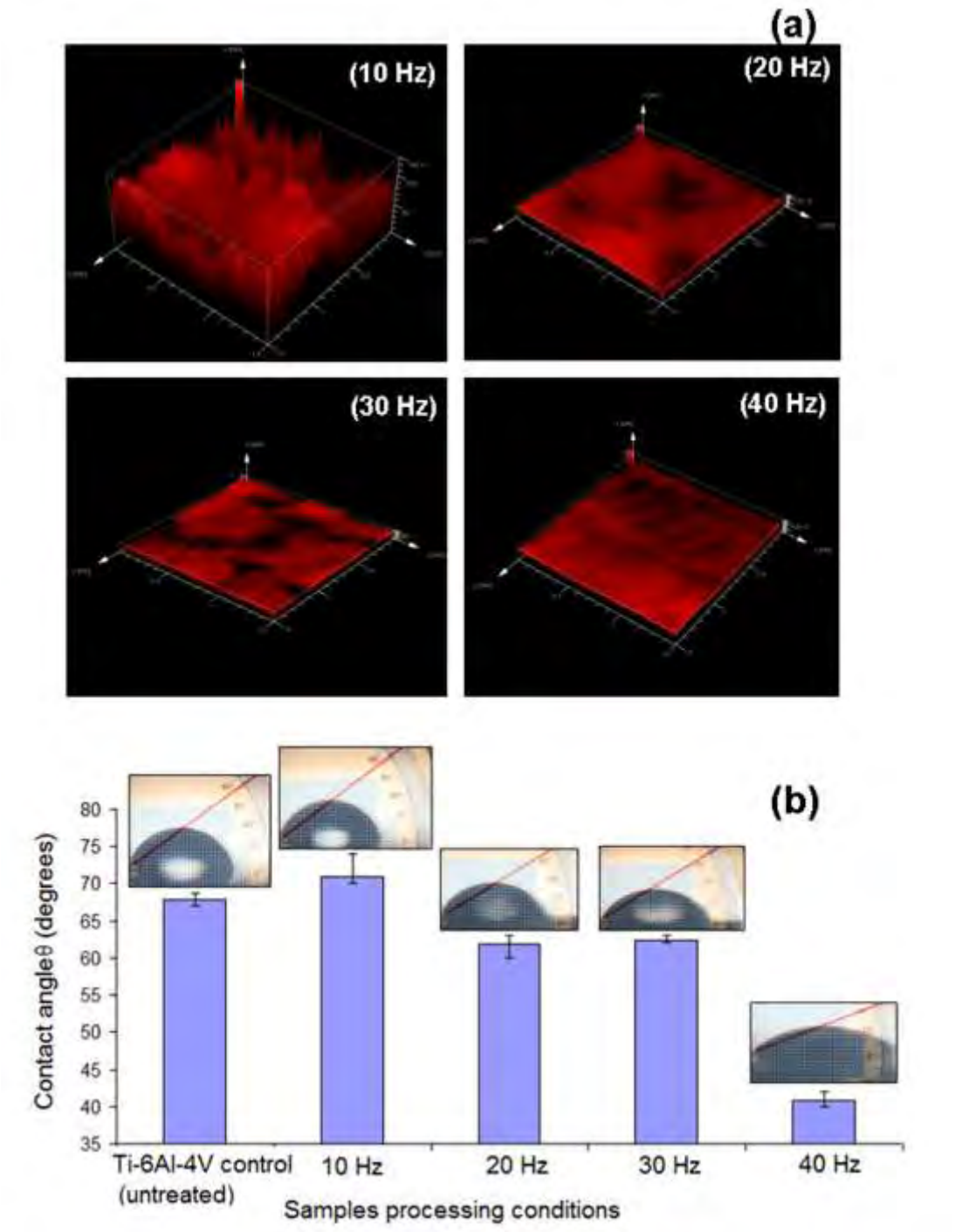


Figure 4.19 (a) The 3-dimensional confocal microscopic images of surface of the coatings and (b) contact angle variation and their corresponding shadow images of the SBF droplet on laser processed sample and control (untreated Ti-6Al-4V) **[71]**.

Table 4.2 Experimentally measured physical parameters related to surface texture **[71]**.

Sample	Frequency (Hz)	Standard deviation of amplitude σ_A (μm)	Wavelength λ (μm)	Texture parameter σ_A/λ
Bare Ti-6Al-4V	----	12.56 ± 0.17	2.79 ± 0.08	4.38 ± 0.04
Ti-6Al-4V/Ca-P	10	23.05 ± 0.023	0.9 ± 0.016	0.05655 ± 0.016
Ti-6Al-4V/Ca-P	20	19.41 ± 0.014	0.6 ± 0.104	0.0385 ± 0.0101
Ti-6Al-4V/Ca-P	30	15.4 ± 0.0123	0.4 ± 0.1095	0.03235 ± 0.026
Ti-6Al-4V/Ca-P	40	11.31 ± 0.018	0.2 ± 0.0125	0.025655 ± 0.016

4.3.3 In vitro bioactivity and mineralization

The laser textured surfaces demonstrated the precipitation of a whisker-like apatite phase (Figure 4.20) **[71]** soon after 24 hours of immersion in SBF. This improved mineralization compared to that in the samples treated earlier with variation in scanning speed might be attributed to the presence of HA phase on the surface of the coating. The whisker like morphology may be due to heterogeneous nucleation of the hexagonal close packed (HCP) apatite crystal (on the substrate material) and subsequent growth of this HCP structure along the c-axis (perpendicular to the close packed atomic plane) by the adsorption of Ca^{2+} and PO_4^{3-} ions from the super-saturated SBF solution. For longer immersion times this equilibrium morphology (whisker like apatite phase) due to its surface energy and modified Ca^{2+} and PO_4^{3-} concentrations within the surrounding SBF solution in turn control the further nucleation process and there by the change

in morphology of the newly precipitated apatite crystals. Irrespective of the laser processing conditions (varying σ_A/λ value) a transition from whisker-like apatite phase to refined submicron size HA with increasing immersion time are observed in all samples. To better understand the structural change in the apatite phase with increasing immersion time, XRD studies were carried out on the SBF immersed samples and the crystallite size (*S*) in a direction perpendicular to the surface of the specimen were measured from a highly resolved apatite peak using the Scherrer equation:

$$S = \frac{0.9\lambda_x}{B\cos\theta} \quad \text{.....4.5}$$

Where, λ_x is the wavelength of the X-ray source (1.54 A), θ is the half of the reported peak centroid and *B* is the broadening or the full width half maxima (FWHM) of the reported peak.

XRD studies of all laser textured samples following immersion in SBF for different time periods, indicated the presence of an apatite phase as evident from the characteristic HA peaks at 2θ ~22.0° and 31.75° corresponding to the planes (2 0 0) and (2 1 1) respectively (Figure 4.21) **[71]**. All samples (irrespective of the processing parameters and varying σ_A/λ value) following 24 hours of immersion in SBF, demonstrated intense peaks at 2θ ~22.0° and 31.75° that are attributed to the apatite phase. However, with increased immersion time these apatite peaks are either broadened with a reduction or sharpened with an increase in intensity. To precisely understand this phenomenon and thereby its influence on the crystallite size the highly resolved apatite peak corresponding to the plane (2 1 1) at 2θ ~31.75° was used for calculations in Equation 4.5. Figure 4.22a **[71]** shows the variation in apatite crystallite size with increasing SBF immersion time for all laser textured samples. All laser textured samples except the sample processed at 10 Hz experience decrease in the apatite crystallite size with increasing SBF immer-

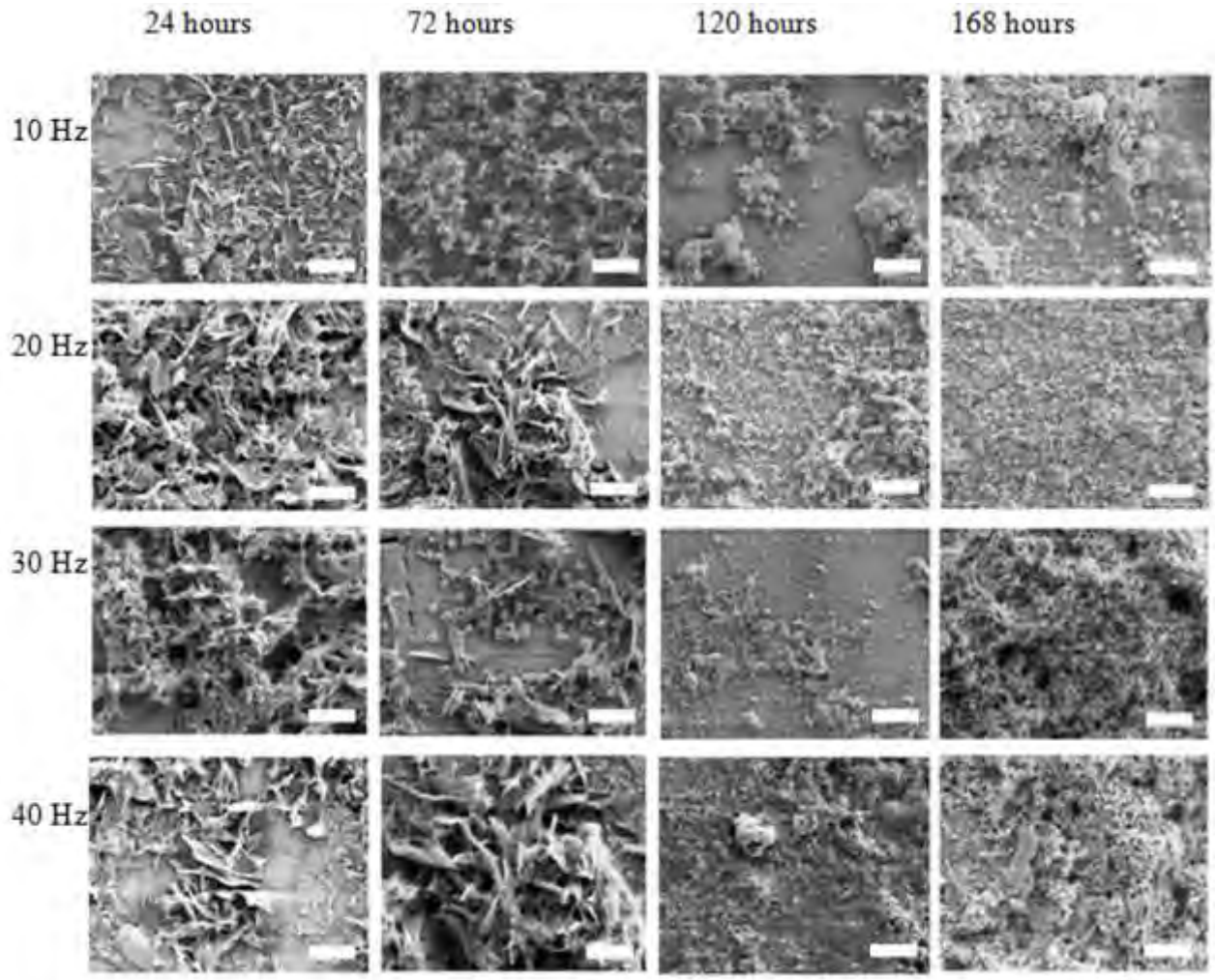


Figure 4.20 SEM micrographs of laser processed samples following immersion in SBF for different time periods. Scale bar in the figure is equivalent to 10 μm **[71]**.

sion time (Figure 4.22a) **[71]**. For the sample processed at 40 Hz, precipitated apatite crystallites were the smallest and the average crystallite size was approximately 1.02 nm during the first 72 hours of SBF immersion time, and decreased to 0.6795 nm as the immersion time is increased to 120 hours and 168 hours. The precipitation of such submicron size crystallites may be due to increased heterogeneous nucleation sites of the ionic species (Ca^{2+} and PO_4^{3-} ions from the SBF) on the substrate material owing to its improved wettability. This in turn may have resulted in reduction of Ca^{2+} and PO_4^{3-} ions concentration in the SBF leading to the growth arrest of HCP habit plane. On the contrary, the reduced hydrophilic nature of 10 Hz sample may have resulted in the less number of heterogeneous nucleation sites and hence the availability of more Ca^{2+} and PO_4^{3-} ions from SBF to nucleate on to the apatite crystal.

It is well known that as the apatite nucleation takes place under in vitro conditions, it modifies the initial surface layer and this in turn can control the subsequent precipitation. Hence, as a matter of interest we studied the mineralization behavior in terms of weight change with increasing SBF immersion time. The logarithmic weight increase with increasing SBF immersion time for all the laser processed samples is presented in Figure 4.22b **[71]**. As observed in the present study, the mineralization on the control (untreated Ti-6Al-4V) was not of detectable amount, hence its mineralization behavior with increasing SBF immersion time is not included. The mineralization increased with increasing SBF immersion time and followed the same trend for all laser textured samples with varying σ_A/λ values. Also, with an increase in pulse frequency (decrease in σ_A/λ value) there is an increase in HA precipitation for each SBF immersion time and the sample processed at 40 Hz (smaller σ_A/λ value) experienced the maximum weight change. This improved mineralization on laser processed samples is attributed

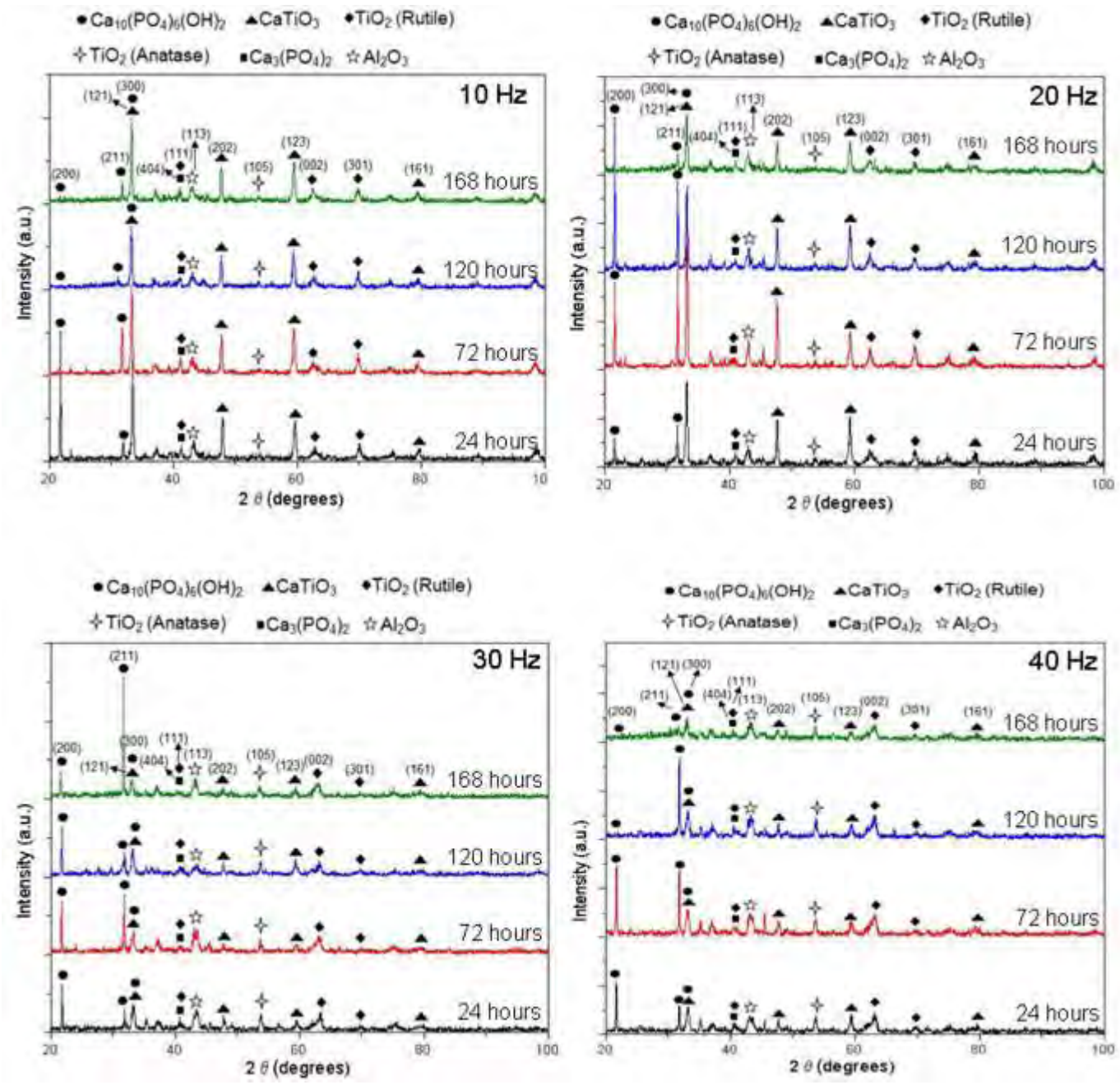


Figure 4.21 XRD spectra of pulsed laser textured samples following immersion in SBF for various immersion periods **[71]**.

to improved wettability (Figure 4.19b) **[71]** as a result of the appropriate surface textures (smaller σ_A/λ value, Table 4.2 **[71]**) and the types of phases (HA, $CaTiO_3$, $Ca_3(PO_4)_2$, TiO_2 (Anatase), and TiO_2 (Rutile), Figure 4.18b) **[71]** evolved during laser processing. Also, as described earlier, among all laser processed samples the precipitates formed on the sample processed at 40 Hz were the smallest for all immersion times (Figure 4.22a) **[71]**. The presence of such smaller crystallites provides increased surface energy for increased nucleation of HA on the surface of sample and thereby improves its mineralization under in vitro conditions.

Further, within the range of processing parameters employed in the current work, it can be concluded that by increasing the laser scan speed and laser pulse frequency there is always an improvement in biomineralization (Figure 4.16 and Figure 4.22b). Also, not much difference in weight change was observed by varying these two laser processing parameters. However, an improvement in wettability and thereby improved biomineralization was achieved by laser surface engineering. Comparing the XRD results for the SBF immersed samples (Figure 4.9-4.12 and Figure 4.21) it can be observed that for the sample processed at varying laser pulse frequency, the presence of apatite peaks corresponding to the (2 0 0) and (2 1 1) planes are evident soon after 24 hours of immersion. In contrast, for the samples processed at varying laser scan speed, the apatite peaks corresponding to only the (2 1 1) plane was evident after 24 hours of immersion. However, at higher laser scan speed (102 cm/min) with an improvement in wettability, the presence of extra apatite peaks corresponding to (2 0 0) and (1 1 1) planes were evident soon after 48 hours of immersion. The better mineralization behavior of the samples

processed at varying laser pulse frequency can be attributed to the retainment of HA precursor (Figure 4.18b) following laser processing.

The XRD results (Figure 4.21) **[71]** obtained above are further confirmed for the HA precipitation using FTIR and XPS studies. The FTIR absorbance spectra of the mineralized samples following immersion in SBF for different time periods are represented in Figure 4.23. The spectrum after each immersion period for all the laser processing conditions (Figure 4.23a, 4.23b, 4.23c and 4.23d) confirmed all functional groups associated with HA and carbonated HA such as OH^-, PO_4^{3-} and CO_3^{2-}. It is known that carbonate ions occupy two different sites in the carbonated apatite: peaks in the region of 1650 to 1300 cm^{-1} are due to v_3 vibrational mode carbonate ion and the peak at 873 cm^{-1} is due to v_2 vibrational mode**.** These carbonate bands in the region of 1650–1300 cm^{-1} are assigned to the surface carbonate ions rather than to the carbonate ions in the lattice of phosphate ions. Further, as the samples processed at 40 Hz had the highest mineralization behavior, the surfaces became extremely rough with deposits, and hence a lot of noise was recorded (Figure 4.23d) while collecting the FTIR data in the reflectance mode. This also further gave an indication of the improved mineralization behavior for the samples processed at 40Hz.

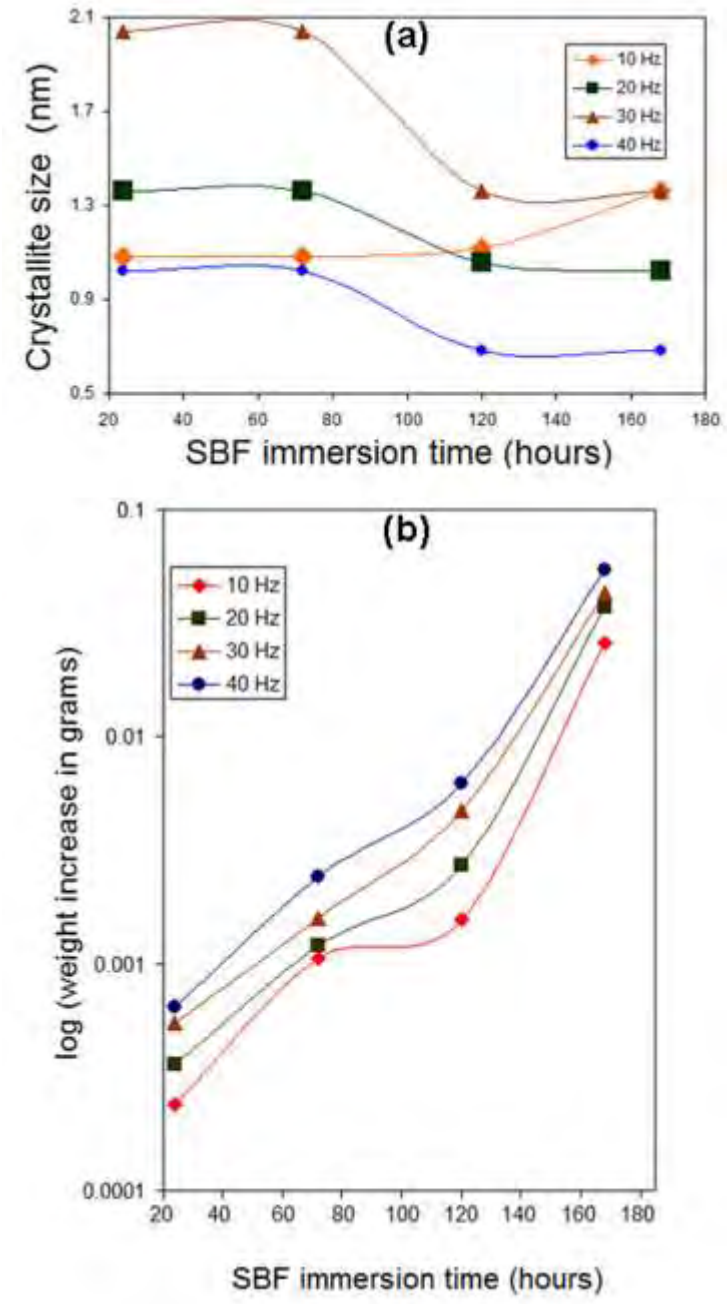
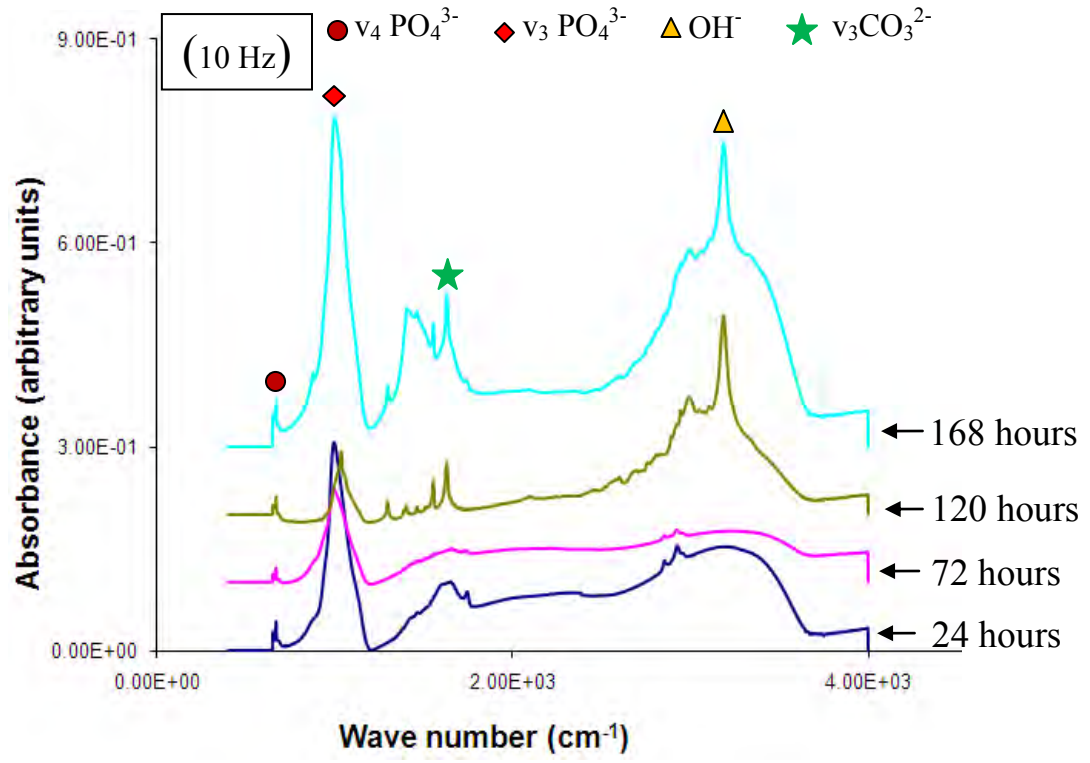
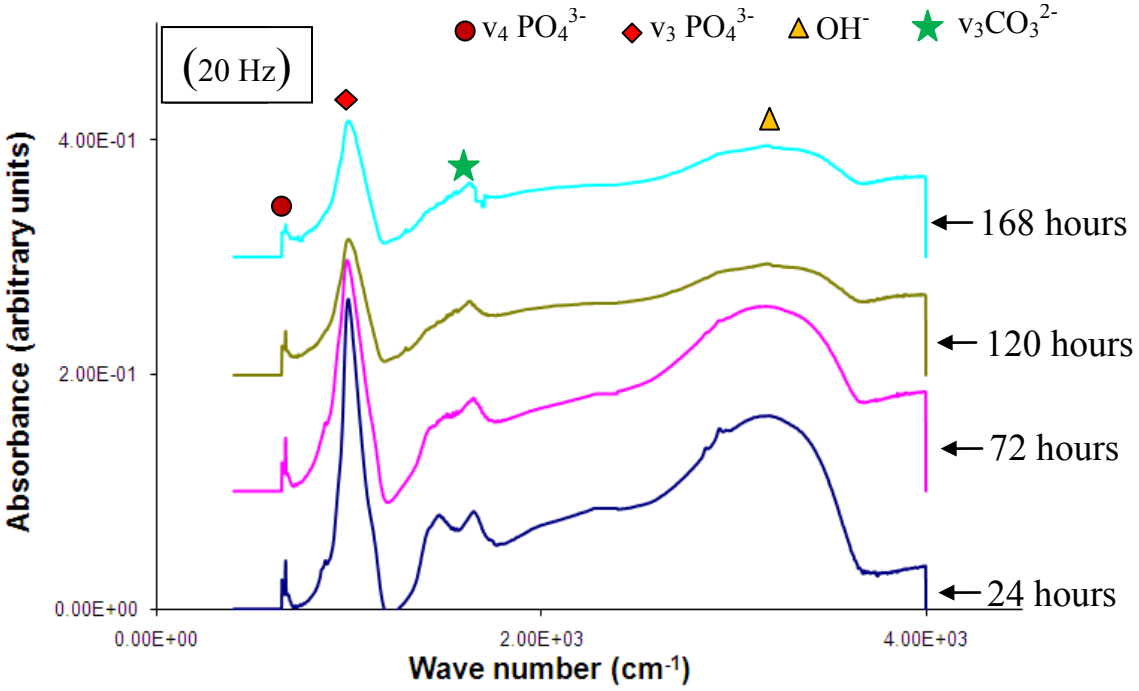
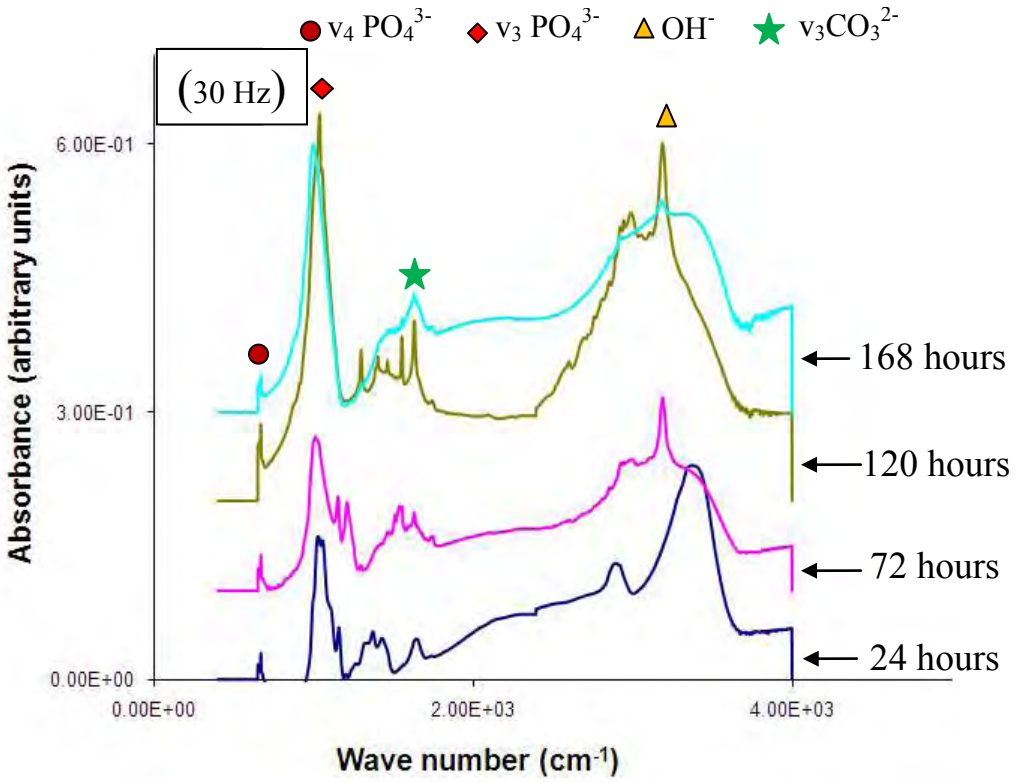


Figure 4.22 Mineralization of laser textured samples in terms of (a) variation in apatite crystallite size with SBF immersion time and (b) logarithmic weight change with SBF immersion time **[71]**.

Semi-quantitative elemental analysis of the laser textured coated samples prior to and after immersion in SBF was obtained using an XPS and is presented in Figure 4.24. It can be observed that within the processing parameters used in the current work, the laser processed samples prior to immersion in SBF demonstrated the presence of Ti2s, Ti2p3, Ca2s, Ca2p3, O1s and C1s level peaks. This further confirmed with earlier XRD observations (Figure 4.18b) indicating the presence of oxide phases such as $CaTiO_3$ and TiO_2 within the coating and at the surface region. However, following immersion in SBF, it can be observed that there is a strong presence of additional peaks such as MgKLL, P2s and P2p. The presence of the above additional peaks following immersion in SBF, was attributed to the precipitation of the mineralized apatite layer as a result of the reaction between the surface of the coatings and surrounding supersaturated SBF solution.


(10 Hz)
v4 PO4 3-
v3 PO4 3-
OH-
v3CO3 2-
9.00E-01
6.00E-01
3.00E-01
0.00E+00
Absorbance (arbitrary units)
168 hours
120 hours
72 hours
24 hours
0.00E+00
2.00E+03
4.00E+03
Wave number (cm-1)


(20 Hz)
v4 PO4 3-
v3 PO4 3-
OH-
v3CO3 2-
4.00E-01
2.00E-01
0.00E+00
Absorbance (arbitrary units)
168 hours
120 hours
72 hours
24 hours
0.00E+00
2.00E+03
4.00E+03
Wave number (cm-1)


v4 PO4 3-
v3 PO4 3-
OH-
v3CO3 2-
(30 Hz)
6.00E-01
3.00E-01
0.00E+00
Absorbance (arbitrary units)
0.00E+00
2.00E+03
4.00E+03
Wave number (cm-1)
168 hours
120 hours
72 hours
24 hours

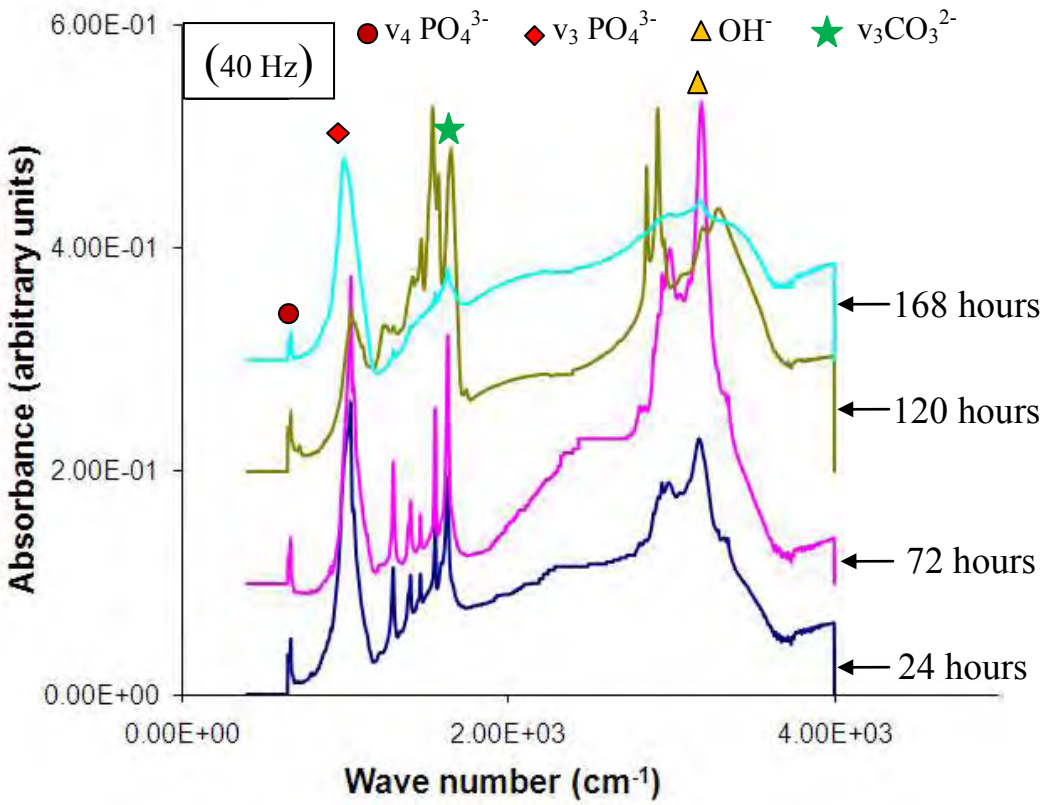
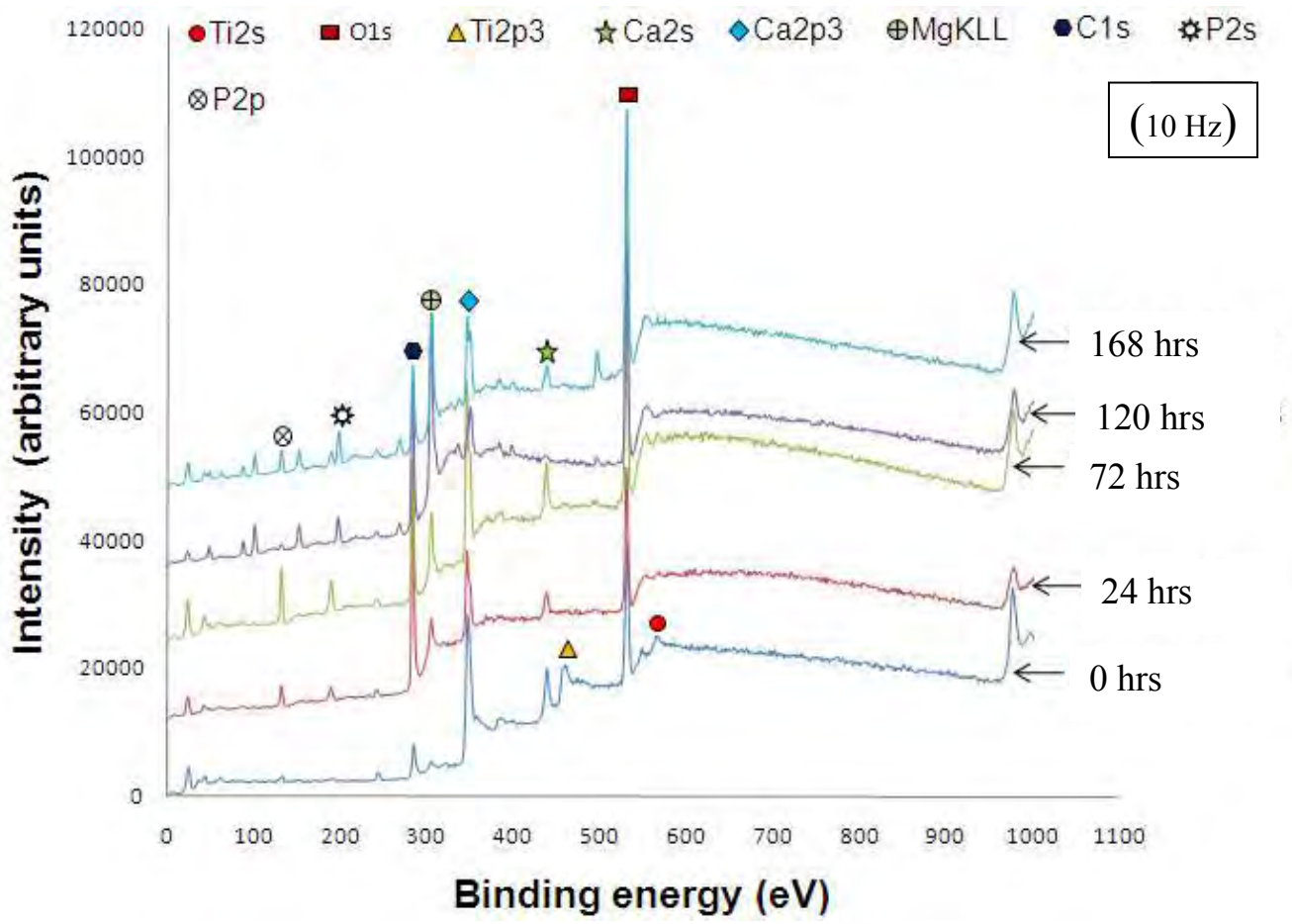
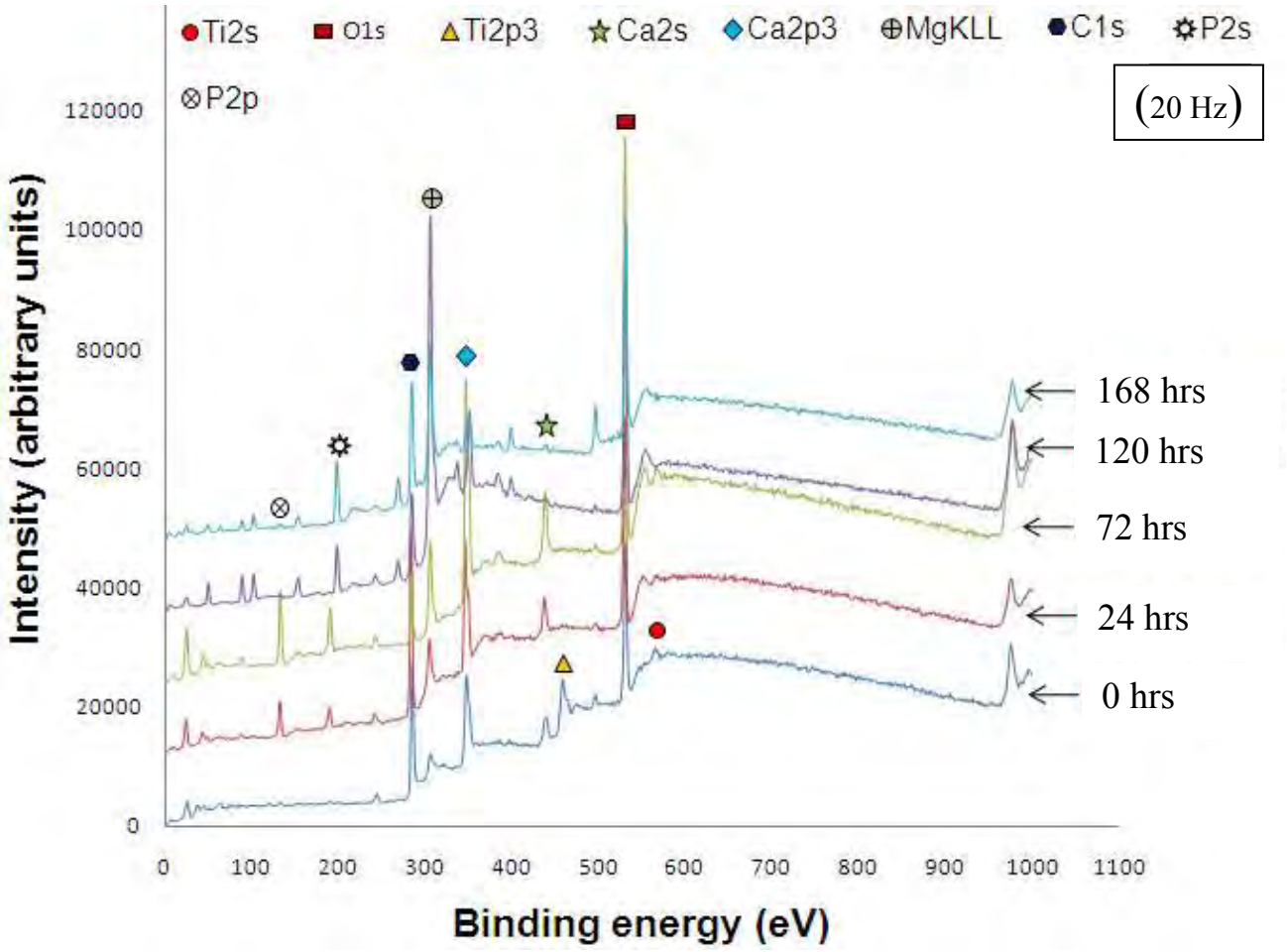
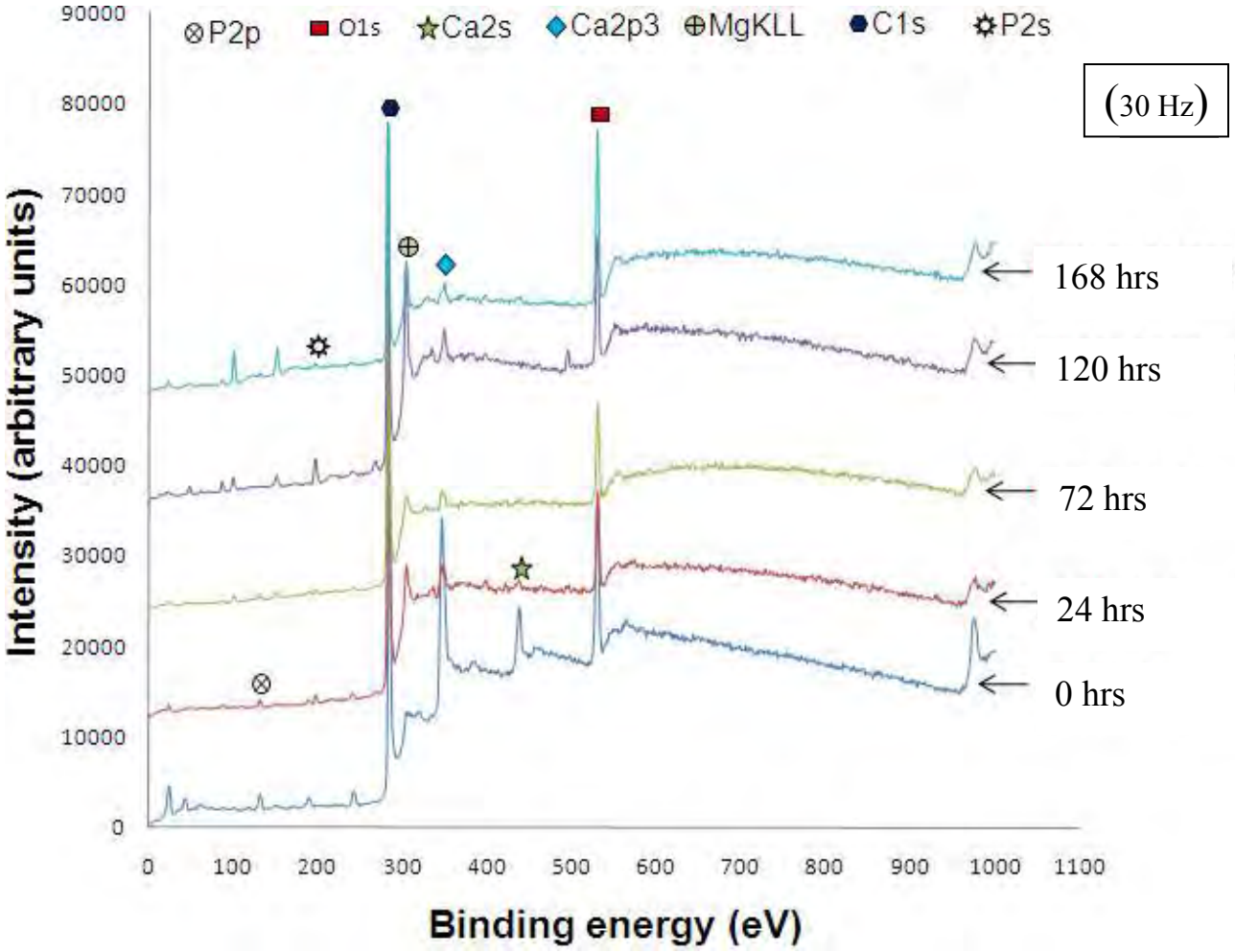


Figure 4.23 FTIR spectra of laser processed samples following immersion in SBF for different time periods.


Ti2s
O1s
Ti2p3
Ca2s
Ca2p3
MgKLL
C1s
P2s
P2p
(10 Hz)
168 hrs
120 hrs
72 hrs
24 hrs
0 hrs
Intensity (arbitrary units)
Binding energy (eV)
120000
100000
80000
60000
40000
20000
0
0
100
200
300
400
500
600
700
800
900
1000
1100


Ti2s
O1s
Ti2p3
Ca2s
Ca2p3
MgKLL
C1s
P2s
P2p
(20 Hz)
Intensity (arbitrary units)
120000
100000
80000
60000
40000
20000
0
0
100
200
300
400
500
600
700
800
900
1000
1100
Binding energy (eV)
168 hrs
120 hrs
72 hrs
24 hrs
0 hrs


⊗P2p
O1s
☆Ca2s
◆Ca2p3
⊕MgKLL
●C1s
✡P2s
(30 Hz)
168 hrs
120 hrs
72 hrs
24 hrs
0 hrs
Intensity (arbitrary units)
Binding energy (eV)
90000
80000
70000
60000
50000
40000
30000
20000
10000
0
0
100
200
300
400
500
600
700
800
900
1000
1100

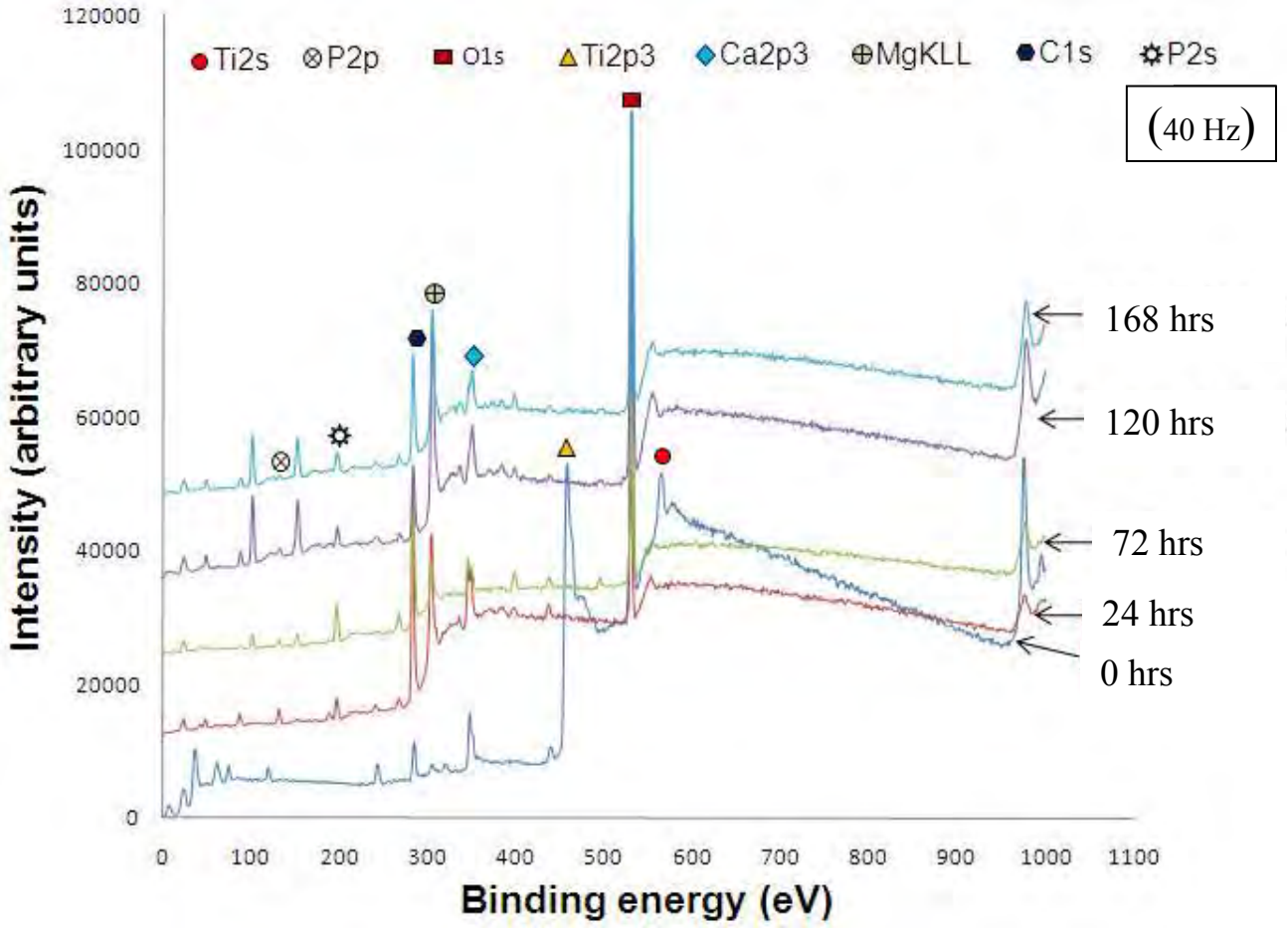


Figure 4.24 XPS spectra of laser processed samples following immersion in SBF for different time periods.

The semi-quantitative results in terms of the atomic concentrations of Ca and P, and their ratio (Ca/P) were calculated and tabulated in Table 4.3. It can be observed that prior to immersion in SBF the Ca/P atomic ratio was in the range of 3 to 11. In contrast, following immersion in SBF the Ca/P atomic ratio was in the range of 1.4 to 1.8 which is very close to the Ca/P atomic ratio of stoichiometric HA (~ 1.67). This rapid decrease in Ca/P ratio to a ratio close to that of HA might be attributed to the nucleation of PO_4^{3-} and CO_3^{2-} ions on the surface of the samples and thereby resulting in the precipitation of HA phase. Further, the presence of such nucleation on the surface of the textured coated samples can be thought of made possible owing to the presence of appropriate phases and surface textures following laser surface engineering. Hence, from the above XPS and FTIR results it can further be confirmed once again that the mineralized precipitates on the surface of the samples were of HA composition. Therefore using the pulsed Nd:YAG laser based texturing technique surfaces with improved in vitro bioactivity were achieved.

Table 4.3 Elemental composition and semi-quantitative analysis of Ca and P in terms of atomic concentration for the pulsed laser processed samples.

Sample	SBF immersion time in hours	Elements present	Ca atomic concentration (at %)	P atomic concentration (at %)	Ca/P atomic ratio
10 Hz	0	O, C, Ti, Ca, P	20.4	1.8	11.3
	24	O, C, Ca, P, Mg	6.1	3.7	1.65
	72	O, C, Ca, P, Mg	10.3	6.7	1.54
	120	O, C, Ca, P, Mg	3.6	2.4	1.5
	168	O, C, Ca, P, Mg	7.8	4.2	1.85
20 Hz	0	O, C, Ti, Ca, P	7.9	1.1	7.2
	24	O, C, Ca, P, Mg	8.4	5.6	1.5
	72	O, C, Ca, P, Mg	14.2	9.5	1.49
	120	O, C, Ca, P, Mg	5.5	3.0	1.83
	168	O, C, Ca, P, Mg	2.7	1.5	1.8
30 Hz	0	O, C, Ca, P,	9.2	2.1	4.4
	24	O, C, Ca, P, Mg	1.6	0.9	1.77
	72	O, C, Ca, P	1.0	0.7	1.43
	120	O, C, Ca, P, Mg	1.5	0.9	1.66
	168	O, C, Ca, P, Mg	1.4	0.8	1.75
40 Hz	0	O, C, Ti, Ca	3.6	1.2	3
	24	O, C, Ca, P, Mg	4.5	2.5	1.8
	72	O, C, Ca, P, Mg	3.2	1.8	1.77
	120	O, C, Ca, P, Mg	3.8	2.1	1.81
	168	O, C, Ca, P, Mg	3.1	1.9	1.63

4.3.4 In vitro biocompatibility

The surface mineralization kinetics and the in vitro bioactivity of the laser processed samples are further correlated to its biocompatibility by the culture of mouse MC3T3-E1 osteoblast-like cells. Cell morphology on laser processed and control (untreated Ti-6Al-4V) samples after 7 day culture of MC3T3-E1 osteoblast-like cells was assessed by SEM and the results are presented in Figure 4.25 **[71]**. Surfaces of all laser processed samples (Figures 4.25a, 4.25b, 4.25c, and 4.25d) **[71]** and the control (untreated Ti-6Al-4V, Figure 4.25e) **[71]** were confluent with the MC3T3-E1 osteoblast-like cells after 7 day of culture period. However, for the control (untreated Ti-6Al-4V) and samples processed at 10, 20, and 30 Hz most of the osteoblast-like cells appeared to de-bond from the surface of the coatings. In contrast, the osteoblast-like cells appeared to be flattened, spread out uniformly, and strongly adhered with an elliptical and circular morphology on the sample processed at 40 Hz.

The proliferation of the osteoblast-like cells after 1 day and 7 day of culture on the laser processed and control (untreated Ti-6Al-4V) samples were studied qualitatively using a fluorescence microscope (Figure 4.26) **[71]**. After 1 day of culture there are very few cells in the image fields of all laser processed samples and the control (untreated Ti-6Al-4V). The MC3T3-E1 osteoblast-like cells have a triangular morphology with the lamellipodia trying to extend along the surface of sample. In contrast, after 7 days of culture, the osteoblast-like cells are confluent over the entire surfaces of all samples and exhibit either elliptical or polygonal like morphology. Especially, for the sample processed at 40 Hz, the osteoblast-like cells are more confluent with well stressed actin filaments and are very much comparable to the control (untreated Ti-6Al-4V).

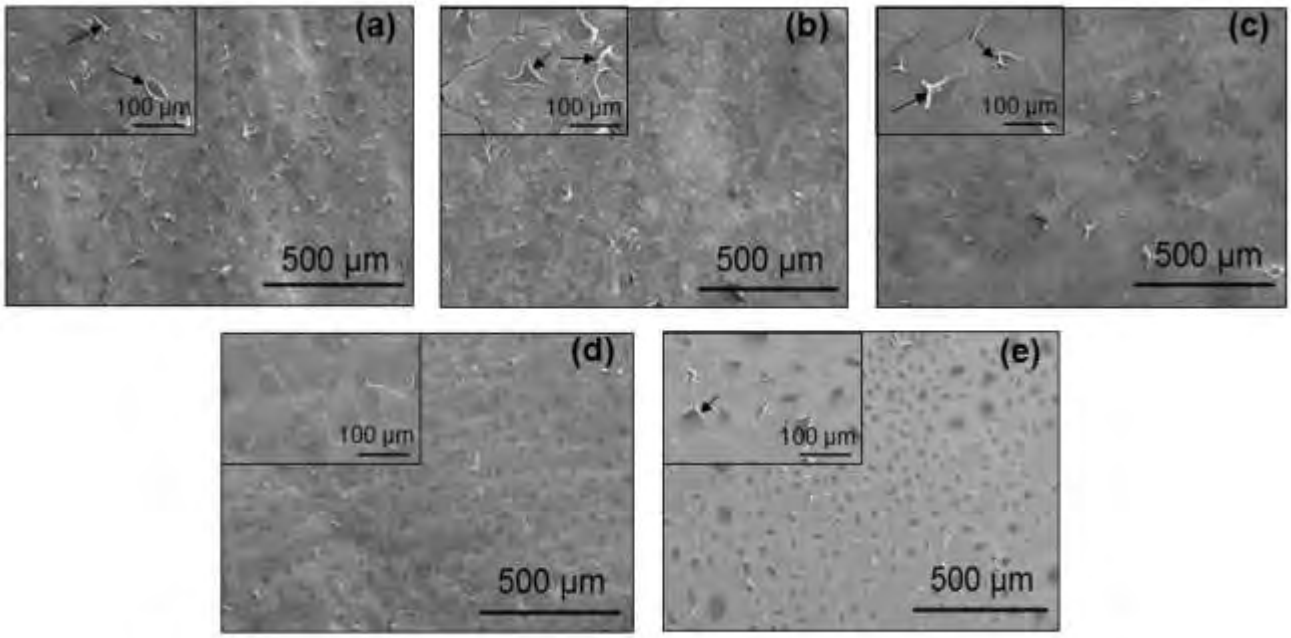


Figure 4.25 Morphology of MC3T3-E1 osteoblast-like cells after 7 day culture on the samples processed at laser pulse frequency of (a) 10 Hz, (b) 20 Hz, (c) 30 Hz, (d) 40 Hz and (e) control (untreated Ti-6Al-4V). Arrows in the inset of Figure 9 (a), (b), (c), and (e) indicate the de-bonding or lack of proper adhesion of the MC3T3-E1 osteoblast-like cells on the substrate material **[71]**.

The focal adhesion area, cellular extensions and cytoskeleton architecture of the MC3T3-E1 osteoblast-like cells are studied for its bone forming ability on the laser processed samples and control (untreated Ti-6Al-4V). The cytoskeletal organization of the MC3T3-E1 osteoblast-like cells on the control (untreated Ti-6Al-4V) and laser processed samples after 7 days culture are presented in Figure 4.27a **[71]**. All the samples indicate stressed actin filaments with well developed network of focal adhesion contacts. Also it can be qualitatively observed that for the sample processed at 40 Hz, the foot print area or the cell spreading is relatively more compared to the rest of laser processed samples and control (untreated Ti-6Al-4V). The cell shape index (Ø $= \frac{4\pi A}{p^2}$)_after 7 days culture of MC3T3-E1 osteoblast-like cells, calculated using the cell spreading area (A) and the perimeter (p) of the cell, provided a higher value for the sample processed at 40 Hz (Figure 4.27b) **[71]** as compared to the control (untreated Ti-6Al-4V) and the sample processed at 10, 20, and 30 Hz. This, therefore, indicated the uniform spreading and circularity of the osteoblast-like cells on the sample processed at 40 Hz. The above results therefore clearly indicated the improved osteoblast-substrate anchorage with an improvement in wettability following laser surface engineering of the Ti-6Al-4V substrate.

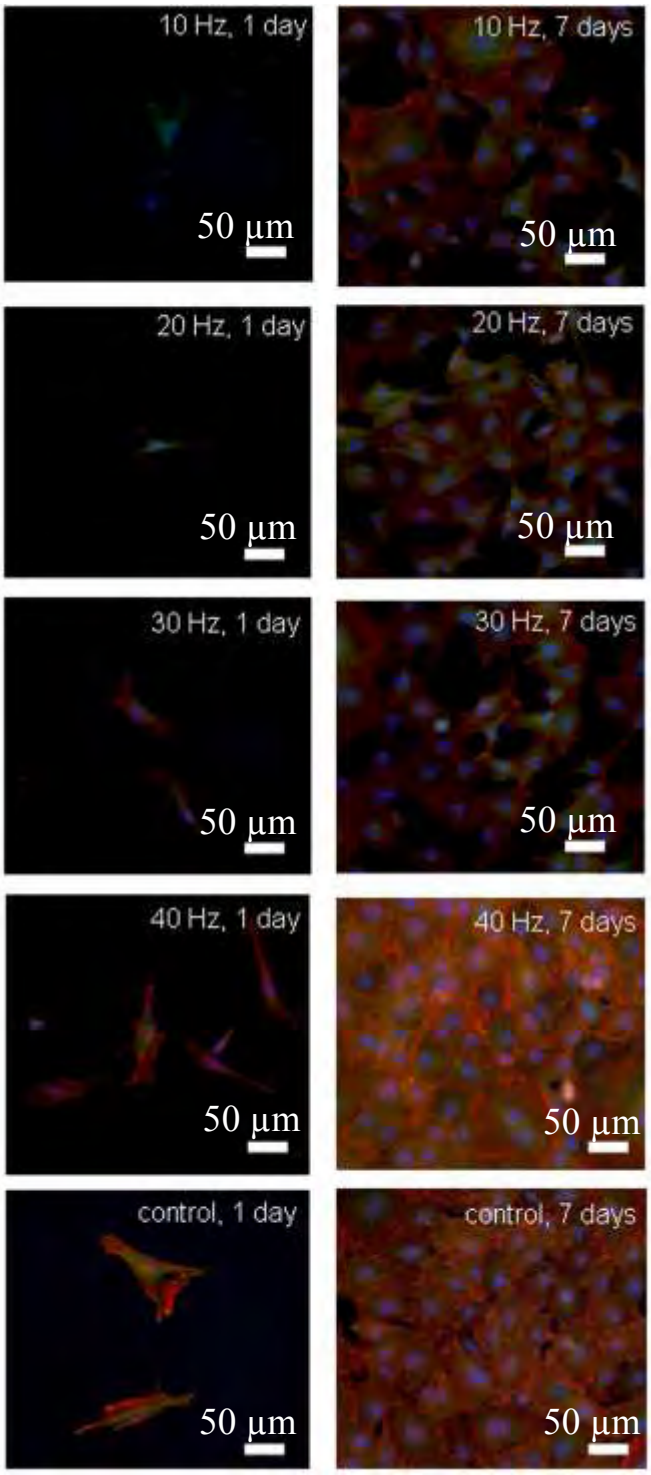


Figure 4.26 Fluorescence microscopic images showing the proliferation of the MC3T3-E1 osteoblast-like cells after 1 day and 7 day of culture on the laser processed and control (untreated Ti-6Al-4V) **[71]**.

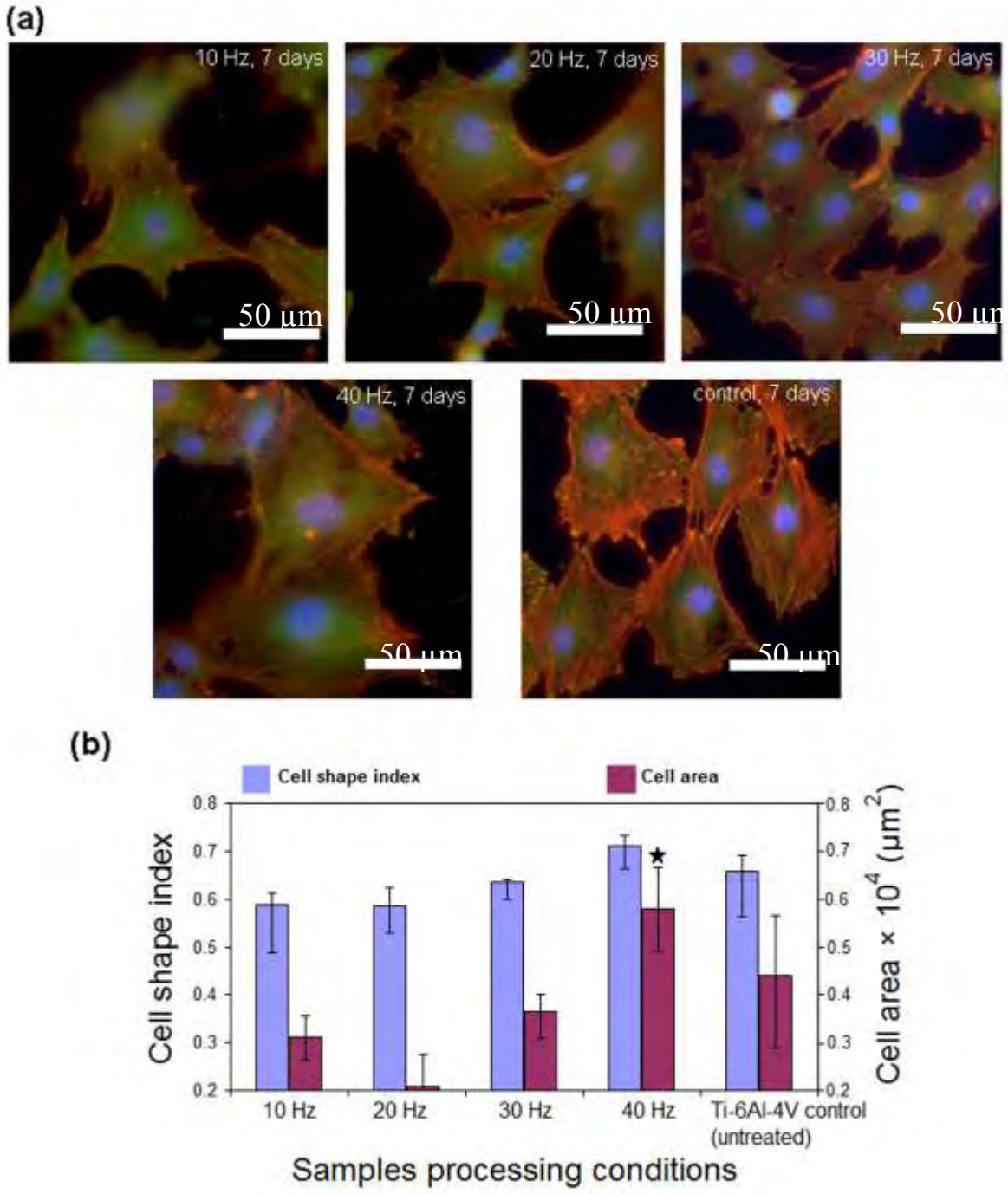


Figure 4.27(a) Cytoskeleton assessment of the MC3T3-E1 osteoblast-like cells after 7day culture on the laser processed samples and the control (untreated Ti-6Al-4V) and (b) Cell shape index and cell area as a function of the samples processing conditions. ★ denotes the laser processed processed group is significantly higher than the control **[71]**.

Although all laser processed samples (10 Hz, 20 Hz, 30 Hz, and 40 Hz) produced the same types of phases (HA, $CaTiO_3$, $Ca_2(PO_4)_2$, TiO_2 (Rutile), and TiO_2 (Anatase)) and physical textures with smaller values of σ_A/λ on the surface for substantially improved wettability compared to the control (untreated Ti-6Al-4V), only the sample processed at 40 Hz demonstrated reasonably improved biocompatibility in terms of cell morphology, cell proliferation, and cell shape index compared to the control. Thus these observations indicate that in general, the processing approach holds a promise in producing the attributes (surface composition and surface texture) suitable for improved biocompatibility.

Chapter 5

Continuous Wave Laser Induced Ca-P Textured Coating on Ti-6Al-4V

5.1 Introduction

Line patterned textured surfaces of Ca-P based phases were synthesized on Ti-6Al-4V using a CW Nd:YAG laser. Unlike the pulsed laser operation, the laser fluences used here to synthesize the textured coatings were extremely low (137 J cm^{-2} and 191 J cm^{-2}). Hence, loss of precursor due to evaporation and violent mixing in the melt pool (due to melting of both precursor and substrate) is expected to be minimized. Further, as the patterns obtained here had a line morphology unlike the dotted morphology obtained with pulsed Nd:YAG laser, their influence on wettability, in vitro bioactivity, and in vitro biocompatibility became a subject of interest.

5.2 Morphological, microstructure, phase and elemental analysis of coatings

As discussed earlier in Chapter 3, here the textured coatings are synthesized by directly melting both the precursor (HA) and substrate (Ti-6Al-4V) material using a laser energy source (CW laser) capable of delivering a constant energy with time. The surface physical textures in the current work are achieved by varying the lateral track overlap, and a lateral spacing of 100 μm and 200 μm are chosen in the current work so as to mimic the length scale of the three dimensional ECM present in human bone. Because of the CW mode operation and lateral over scanning technique, the thermo-physical interaction resulting in the microstructure, phase evolution and surface physical texture are going to be completely different from that obtained

using a pulsed laser melting. Hence the characterization of the above features prior to other studies is an essential part of the work. Low magnification SEM (Figure 5.1) **[72]** of the surface of the coatings clearly shows the effect of laser track overlap on the surface morphology. By varying the laser track overlap in the lateral direction two different periodic line patterns with 100 μm (Figures 5.1a and 5.1b) **[72]** and 200 μm (Figures 5.1c and 5.1d) **[72]** line spacings are obtained at two different laser energy inputs (J/cm^2). Since cells are sensitive to micron scale features such micro-textured topography is expected to provide an instructive background to guide their behavior towards tissue growth **[111-114]**.The cross-sectional SEM image (Figure 5.2a) **[72]** of the sample processed at 137 J/cm^2 and 100 μm line spacing also clearly demonstrates the textured topography due to the lateral laser beam track overlap. This textured topography can induce a mechanical stimulation on the surrounding bone during the early days of implantation and help in quick fixation. This mechanical stimulation is attributed to the improved shear strength at the interface and mechanical interlocking when bone grows into the textured morphology **[115]**. A higher magnification SEM image (Figure 5.2b) **[72]** of the interface between the coating and substrate is clearly an indicative of the sound metallurgical bonding between the coating and the substrate (Ti-6Al-4V). A sound bonding of bioceramic coating to the substrate material is expected to reduce the delamination of ceramic layer and thereby avoid complications associated with osteolysis. The microstructural evolution within the coating (Figure 5.2c) clearly shows the presence of HA phase infiltrated in the matrix of Ti. The Ca/P atomic ratio of ~ 1.64 as obtained from the EDS spectra (presented as inset in Figure 5.2c) also further confirms the near HA composition. Due to the inherent rapid cooling the laser treat-

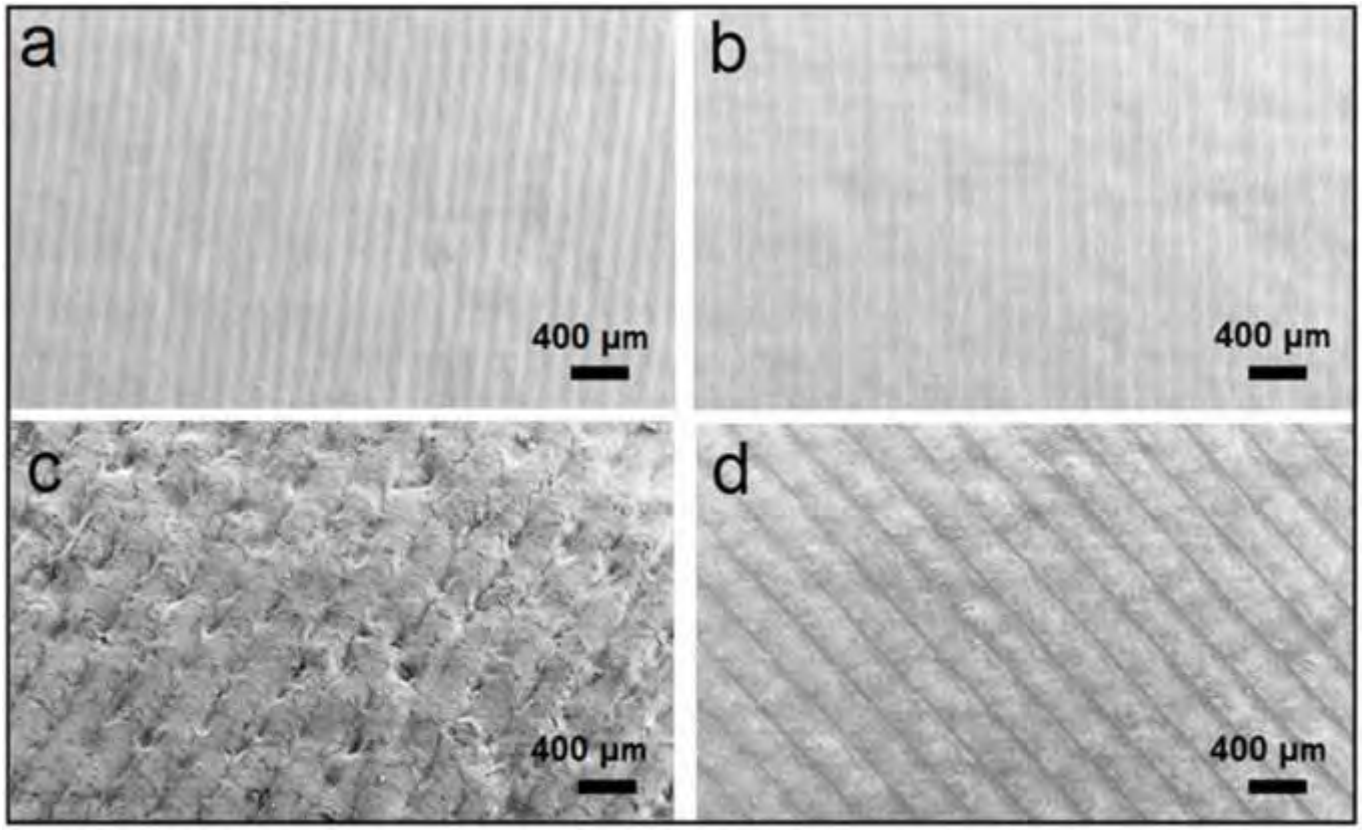


Figure 5.1 Low magnification SEM images of the surface of coatings processed at (a) 137 J/cm^2, 100 µm line spacing, (b) 191 J/cm^2, 100 µm line spacing, (c) 137 J/cm^2, 200 µm line spacing, and (d), 191 J/cm^2, 200 µm line spacing **[72]**.

ment has produced acicular α-Ti in the melt region. Under the set of laser parameters employed in the present study the HA based precursor and a part of the substrate Ti-6Al-4V has undergone rapid melting and mixing in the melt pool thereby forcing the infiltration of precursor (HA) into the molten volume of the substrate.

Unlike our previous studies **[70, 97, 106]** where there was no retainment of precursor (HA phase) following laser processing, in the present work the presence of such a phase after laser processing was clearly evident from the XRD pattern (Figure 5.3a) **[72]**. Under a varying combination of laser fluence and track overlap used in the present study it can be observed from the composite of the XRD patterns (Figure 5.3a) that there is no major change in the types of phases evolved and HA, $CaTiO_3$, $Ca_3(PO_4)_2$, TiO_2 (Anatase), TiO_2 (Rutile), and Ti are the major phases present within the coatings. However, from the variation in peak intensities, it can be realized that, although there is no change in the phase constituents, a variation in the amount of these phases with varying laser processing parameters exists. With an increase in laser fluence from 137 J/cm^2 to 191 J/cm^2, there is an increase in intensity of the Ti and the Al_2O_3 phase along the (1 0 1) and (1 1 0) planes respectively. The intense presence of the above phases (Ti and Al_2O_3) at higher laser fluence of 191 J/cm^2 (used in the present study) can be attributed to the fact that at these laser processing conditions a substantial amount of the substrate (Ti-6Al-4V) material undergoes rapid melting and as a result float on the surface of the melt pool. Also, as the processing is carried out in an ambient atmosphere using argon as the cover gas a certain amount of oxidation of the melt pool constituents is expected to take place leading to precipitation of a small amount of Al_2O_3 at the surface. With an increase in laser fluence there is also an increase in the cooling rate **[116, 117]**, and hence the constituents present in the melt pool are expected to

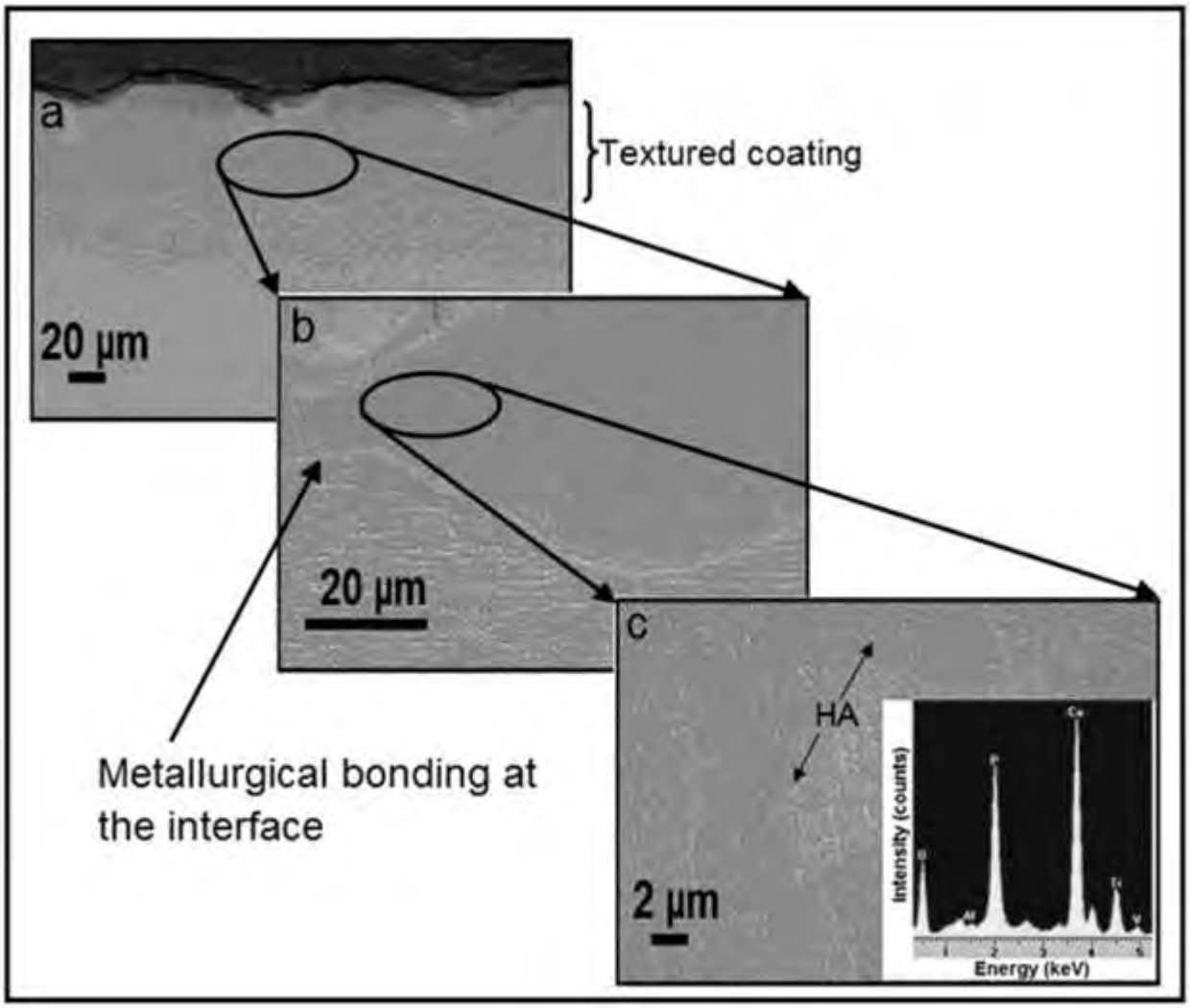


Figure 5.2 Cross-sectional SEM images of the sample processed at 137 J/cm^2 and 100 µm line spacing: (a) revealing the textured coating (b) revealing the sound metallurgical bonding at the interface and (c) A higher magnification of the coating and the inset showing the EDS pattern from the white precipitates **[72]**.

be retained without vaporization and precipitation Ti on the surface of the coating. The EDS spectra (Figure 5.3b) from a random location on the surface of the coating indicated the strong presence of Ca, P, Ti, Al, V, and O peaks. From the composite of EDS spectra (Figure 5.3b), it can be observed that there is an increase in intensity of the Ti and V peaks for the sample processed at 191 J/cm^2. This further complements with our earlier observations from the XRD studies proving the fact that a certain amount of dilution has taken place owing to the partial melting of the substrate material.

5.3 Effects of surface roughness on wettability

The effect of laser track overlap on the 3-dimensional surface morphology of the coatings obtained using a confocal microscope is shown in Figure 5.4 **[72]**. Irrespective of the laser fluence, the samples processed at 100 μm line spacing (Figure 5.4a and 5.4b) have a smoother surface finish as compared to the samples processed at 200 μm spacing (Figure 5.4c and 5.4d). The quantitative variation in surface roughness owing to varying combination of laser fluence and line spacing (track overlap) was also evaluated using a confocal laser microscopy. The samples processed for 100 μm line spacing (irrespective of the laser fluence) have significantly lower values of R_a, R_z, and R_{max} compared to the samples processed for 200 μm line spacing (Figure 5.5) **[72]**. With reduced track overlap or line spacing there is an increase in the spot overlap (spot diameter ~ 400 μm) in the lateral direction leading to remelting of a predominant amount of the previously melted layer. This remelting of the ceramic layer in turn smoothens the surface of coating. Further, to correlate the effects of surface roughness on wettability, two additional surface roughness parameters, standard deviation of amplitude (σ_A) and periodicity (λ) are defined earlier in section 2.2. Their ratio (σ_A/λ) is taken as a measure of surface texture. As

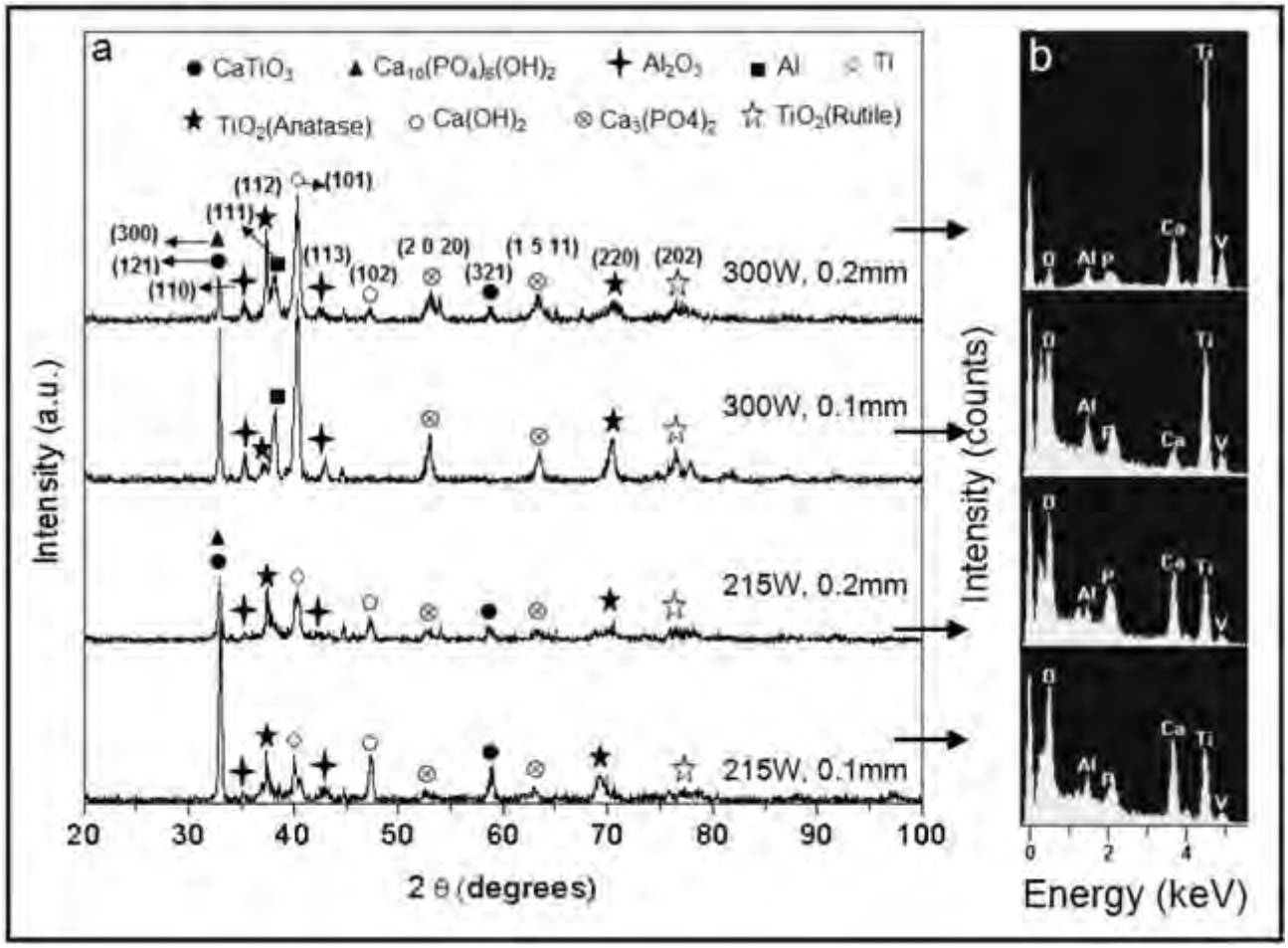


Figure 5.3(a) XRD pattern and (b) corresponding EDS spectra for the laser processed samples **[72]**.

discussed earlier, the values of σ_A and λ were taken from 5 random locations on each sample and are presented as mean values with related scatter in Table 5.1 **[72]**. The corresponding mean values of σ_A/λ and its related scatter as a measure of surface texture are also included in Table 5.1 **[72]**. It can be observed that the laser processed samples have a significantly smaller value of σ_A/λ as compared to the control (untreated Ti-6Al-4V). Further, within the laser processing parameters employed in the present study, the samples processed at 100 μm line spacing have a notably smaller value of σ_A/λ as compared to the samples processed at 200 μm line spacing. This further complements to our results from the roughness parameters R_a, R_z and R_{max} (Figure 5.5) **[72]**.

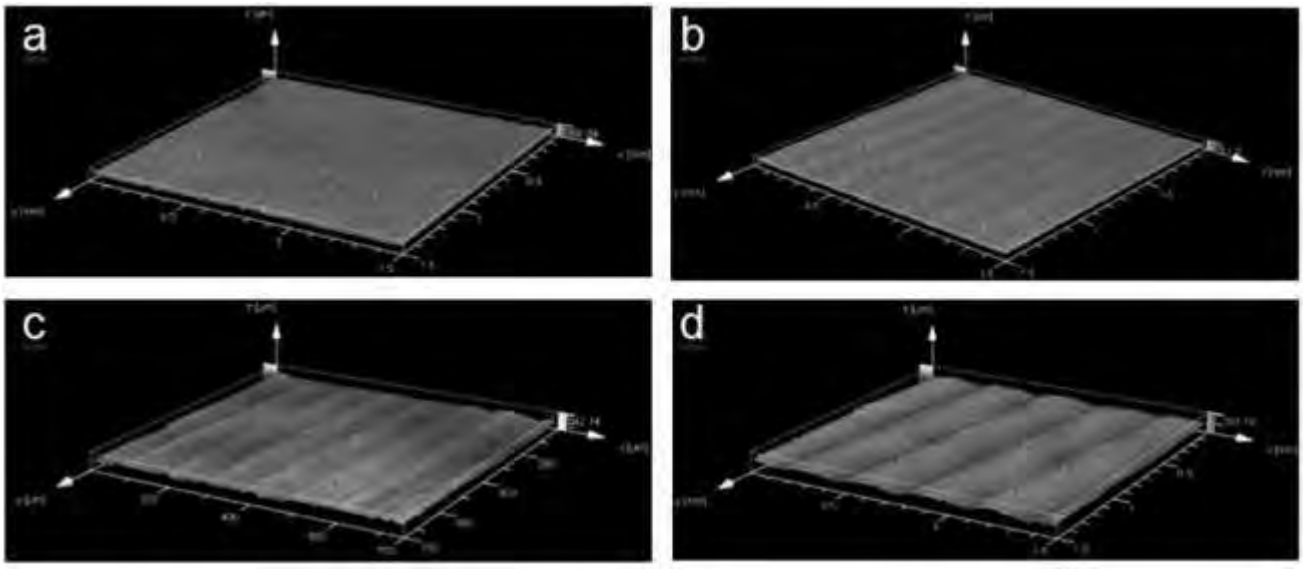


Figure 5.4 The 3-dimensional confocal microscopic images of surface of the coatings processed at (a) 137 J/cm^2, 100 μm line spacing (b) 191 J/cm^2, 100 μm line spacing (c) 137 J/cm^2, 200 μm line spacing and (d) 191 J/cm^2, 200 μm line spacing **[72]**.

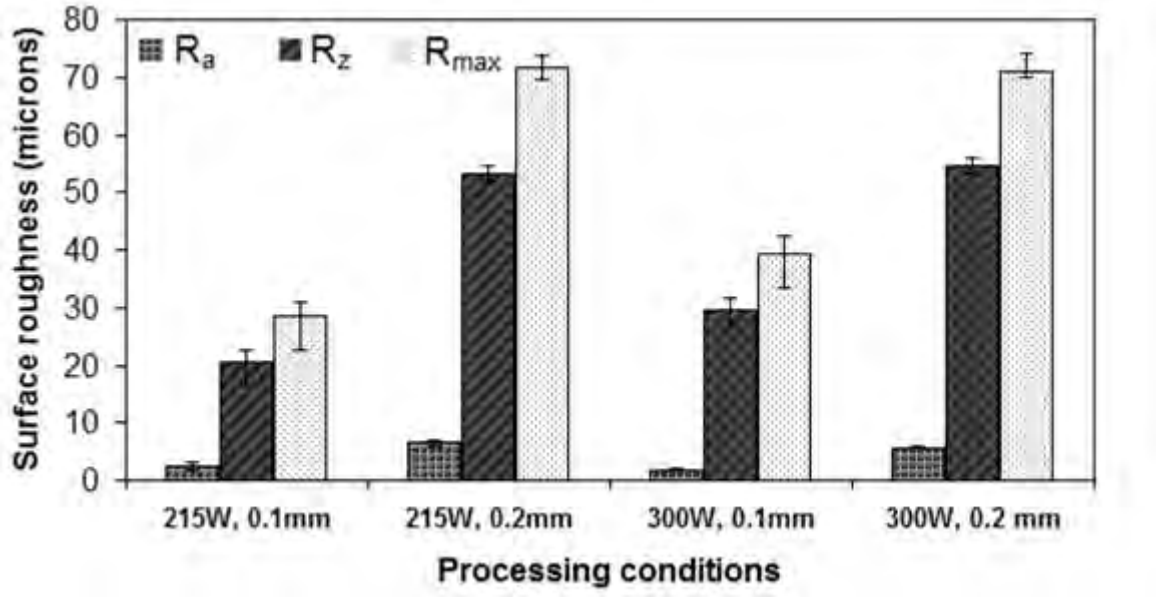


Figure 5.5 Variation in surface roughness parameters as a function of laser processing conditions **[72]**.

Table 5.1 Experimental results of contact angles of test liquids, texture parameter (σ_A/λ), surface energy components and surface energy as function of sample processing conditions **[72]**.

Samples processing conditions	σ_A (μm)	λ (μm)	σ_A/λ	Contact angle			γ_s^{LW}	γ_s^{AB}	γ_s
				distilled water	formamide	dioiodo-methane			
Ti-6Al-4V control	12.56 ±0.37	2.79 ±0.08	4.38 ±0.04	82.6 ±0.08	57.4 ±0.06	53 ±0.04	29.87 ±0.004	4.27 ±0.03	34.19 ±0.04
137 J/cm^2, 0.1mm	3.024 ±0.114	150.6 ±0.44	0.0171 ±0.0001	53.7 ±0.16	31.9 ±0.10	29.4 ±0.08	43.97 ±0.002	8.08 ±0.02	52.05 ±0.03
137 J/cm^2, 0.2mm	7.926 ±0.081	401.4 ±0.92	0.0203 ±0.0002	71.8 ±0.11	35.9 ±0.12	39.3 ±0.07	39.81 ±0.018	6.43 ±0.04	46.25 ±0.04
191 J/cm^2, 0.1mm	2.528 ±0.033	133.3 ±0.44	0.0189 ±0.0002	62.4 ±0.05	32.4 ±0.06	31.6 ±0.08	44.80 ±0.008	7.01 ±0.02	51.82 ±0.01
191 J/cm^2, 0.2mm	8.858 ±0.025	397.5 ±0.85	0.0223 ±0.0001	73.4 ±0.15	37.9 ±0.12	39.9 ±0.09	40.11 ±0.003	5.65 ±0.05	45.77 ±0.04

From our earlier work **[70]** and the work by Zhou and De Hosson **[83]**, it was clear that the texture parameter (σ_A/λ) significantly affects the wetting behavior of a liquid. Table 5.1 **[72]** lists the experimental contact angles subtended by three different liquids (water, formamide, and dioiodomethane) on each of these surfaces. With a decrease in σ_A/λ value there is a decrease in the experimental contact angles for three test liquids (Table 5.1) **[72]**. Further, all the laser processed samples have a significantly smaller value of experimental contact angle (for the three testing liquids) compared to the control (Ti-6Al-4V). This improved hydrophilic behavior for the laser processed samples is attributed to the influence of surface texture and the same phases (HA, $CaTiO_3$, $Ca_3(PO_4)_2$, TiO_2 (Anatase), TiO_2 (Rutile), and Ti) evolved during laser processing. Also within the laser processing parameters employed in the present study, the samples processed at 100 μm line spacing have a significantly smaller value of experimental contact angle (for the three testing liquids) compared to the samples processed at 200 μm line spacing. The improved wetting behavior for the laser processed samples, and the correlation between texture parameter (σ_A/λ) and experimental contact angles can be explained as follows. Based on SEM (Figure 5.1) and confocal microscopic (Figure 5.4) images along with smaller σ_A/λ value (Table 5.1) **[72]**, the textures generated in the present study are confirmed to be of radial groove type **[70, 83]**. Hence, when a liquid drop is placed on such a surface (smaller σ_A/λ value), it can easily overcome the energy barriers associated with it and completely wet it. Thus, an equilibrium state of wetting is achieved when the grooves are radial. Further it can also be conditioned that as the σ_A/λ value increases there is an increase in the contact angle and vice versa thereby further confirming our results (Table 5.1) **[72]**.

The surface energy calculations obtained using Equations 3.3-3.5 further showed compatibility with our previous observations on surface roughness (R_a, R_z and R_{max}), texture parameter (σ_A/λ), and contact angle. Accordingly, the laser processed samples have a higher surface energy value (~45.77 mJ/m^2 – 52.05 mJ/m^2) compared to the Ti-6Al-4V control (~34.19 mJ/m^2). This increase in the surface energy (γ_s) for laser processed samples is mostly contributed from the higher value of the Lifshitz-Vander Waals surface energy (γ_S^{LW}) component compared to the Lewis acid-base surface energy (γ_S^{AB}) component (Table 5.1) **[72]**. Further within the laser processed samples, the samples processed at 100 μm line spacing (having lower value of R_a, R_z, R_{max}, and σ_A/λ and being hydrophilic) have higher γ_S^{LW}, γ_S^{AB}, and γ_s (mJ/m^2) compared to the samples processed at 200 μm line spacing. This, therefore, clearly demonstrates the effect of laser processing in producing controlled topographic cues with appropriate surface chemistry, which in turn significantly increased the values of the surface energy components and thereby the value of γ_S.

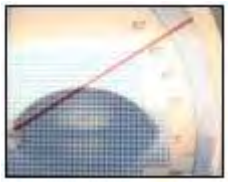
The contact angle measurements for SBF and cell culture media can provide an understanding of the effect of surface energy on their wetting behavior and thereby their bioactivity (following immersion in SBF) and cell viability. Table 5.2 **[72]** presents the contact angles and corresponding light optical images of the liquid droplet shadow on the laser processed samples and the control (untreated Ti-6Al-4V). The results (Table 5.2) **[72]** demonstrated a more hydrophilic behavior (improved wettability) for the laser processed samples compared to the control (untreated Ti-6Al-4V). Also, as discussed earlier, within the laser processing parameters employed in the present work, the samples with lower σ_A/λ value and higher surface energy γ_s

(100 μm line spaced) demonstrated more hydrophilic nature for both liquids (SBF and culture media) compared to the samples with higher σ_A/λ value and lower surface energy γ_s (200 μm line spaced). This is attributed to the fact that when a liquid drop is placed on a surface with higher surface energy, it tries to reduce its energy and come back to an equilibrium state by interacting with the molecules present in the liquid drop and there by resulting in the spreading and an improved wettability.

5.4 Bioactivity and mineralization kinetics

Within the detectable limits of the XRD instrument, compared to the laser surface treated samples, no HA formation on control (untreated Ti-6Al-4V) is realized after 1 day immersion in SBF. Hence, the XRD spectra corresponding to the control (untreated Ti-6Al-4V) are not included in the present study. However, for all the laser processed samples following immersion in SBF for each soaking period, the presence of an apatite phase is evident from the characteristic HA peaks at $2\theta \sim 21.82°$ and 31.75° corresponding to the planes (2 0 0) and (2 1 1) respectively (Figures 5.6 - 5.9) **[72]**. For the samples processed at 100 μm line spacing (having

Table 5.2 Contact angles and corresponding light optical images of the liquid droplet shadow on the laser processed samples and on the control (untreated Ti-6Al-4V) **[72]**.

Samples processing conditions	Contact angle	
	Growth media ($\theta_{growth\ media}$)	Simulated body fluid (θ_{SBF})
Ti-6Al-4V control (untreated)	79.2±1.84 	62.5±0.85 
137 J/cm^2, 0.1mm	69.91±0.74 	50.82±2.5 
137 J/cm^2, 0.2mm	74±1.2 	59.46±1.2 
191 J/cm^2, 0.1mm	70.42±0.8 	55.91±1.07 
191 J/cm^2, 0.2mm	78.58±1.21 	60.16±0.7 

lower value of R_a, R_z , R_{max}, and σ_A/λ and increased wettability) following 1 day immersion in SBF, XRD spectra (Figures 5.6a and 5.7a) demonstrated a highly intense peak attributable to the apatite phase at $2\theta \sim 31.75°$ corresponding to the plane (2 1 1). In contrast, the intensity of this peak is low for the samples processed at 200 μm line spacing (having lower value of R_a, R_z , R_{max} and σ_A/λ and increased wettability) (Figures 5.8 and 5.9) **[72]**. Also for the samples processed at 100 μm line spacing after 3 and 5 days of immersion in SBF, the apatite peak (at $2\theta \sim 31.75°$) becomes broadened with a reduction in intensity (Figures 5.6b and 5.7b). This gives an indication that there is a rapid transformation from a highly crystallized HA phase to a near amorphous or fine crystallite sized HA phase. However, after 7 days immersion (Figure 5.6a and 5.7a) the characteristic apatite peak (at $2\theta \sim 31.75°$) again recrystallized. There is also an additional peak at $2\theta \sim 22.0°$ corresponding to the plane (2 0 0). Such a rapid transformation from a highly crystallized HA phase (following 1 day immersion in SBF) to a near amorphous HA phase (following 3 and 5 days of immersion in SBF) and again thereafter undergoing recrystallization is not observed for the samples processed at 200 μm line spacing. Further considering the XRD results of the pulsed laser processed samples (Figure 4.9-4.12, processed with varying laser scan speed), it can be observed that there is an increase in intensity of the characteristic apatite peaks with increasing SBF immersion time. Hence, these samples are not associated with the rapid transformation to an amorphous apatite phase unlike the CW laser processed samples. As far as the samples processed at varying laser pulse frequency is concerned (Figure 4.21), not much difference in their mineralization kinetics are observed as compared to the CW laser processed samples (Figure 5.6 – 5.9). The better mineralization of the pulsed laser

processed samples (varying laser pulse frequency) and the CW laser processed samples might be attributed to the retainment of the HA precursor within the coating following laser processing.

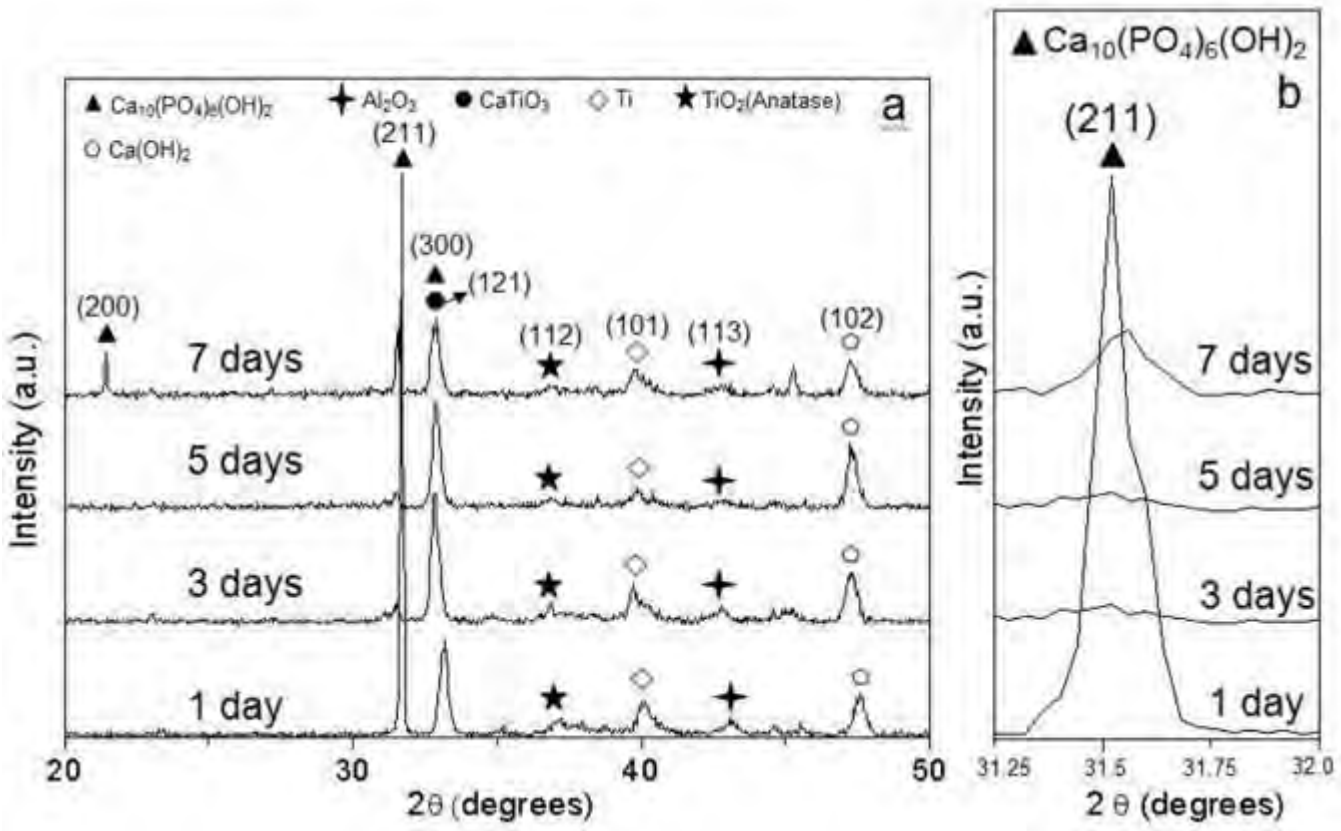


Figure 5.6(a) XRD spectra of the samples processed at 137 J/cm^2, 100 μm line spacing and (b) corresponding enlarged spectra (2θ ~ 30°-32°) following immersion in SBF**[72]**.

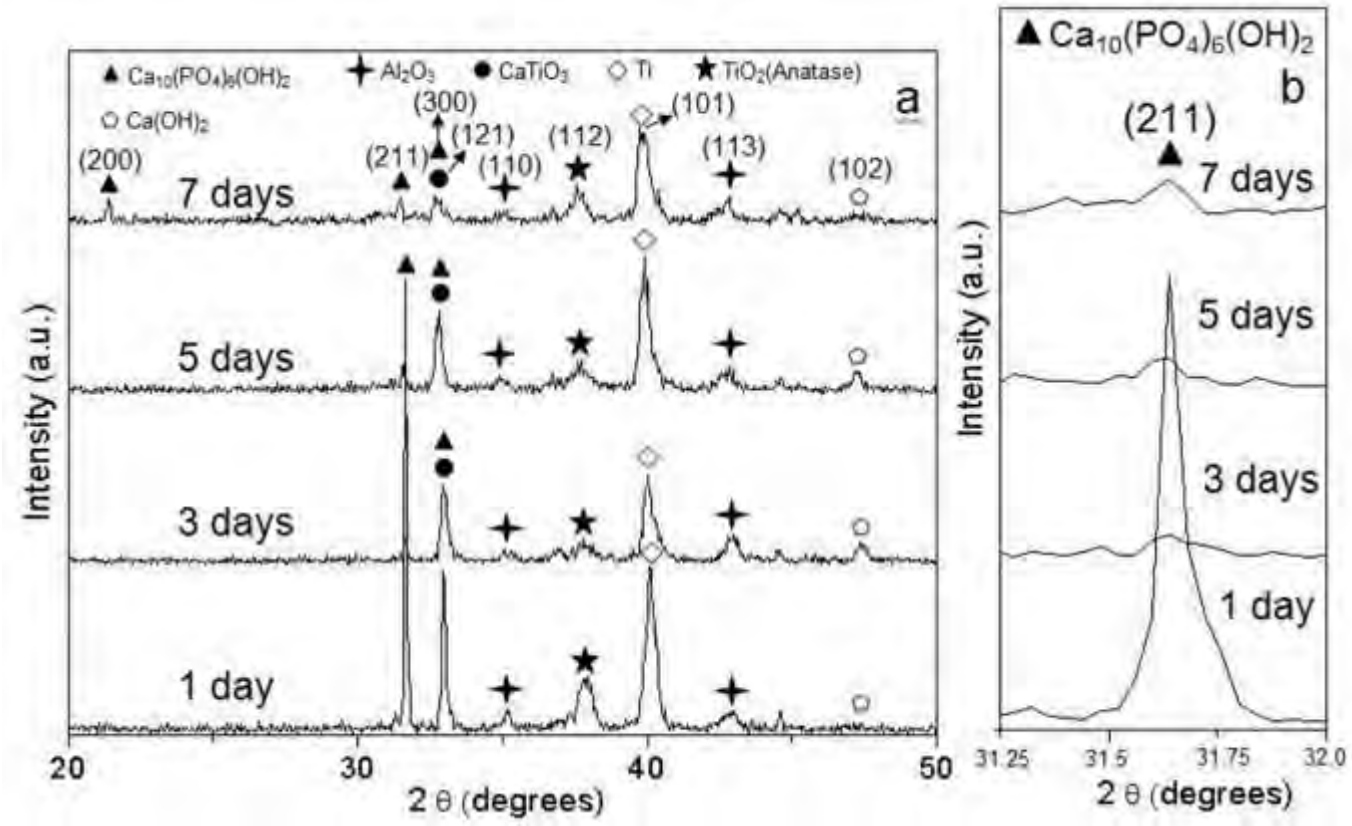


Figure 5.7(a) XRD spectra of the samples processed at 191 J/cm^2, 100 μm line spacing and (b) corresponding enlarged spectra (2θ ~ 30°-32°) following immersion in SBF **[72]**.

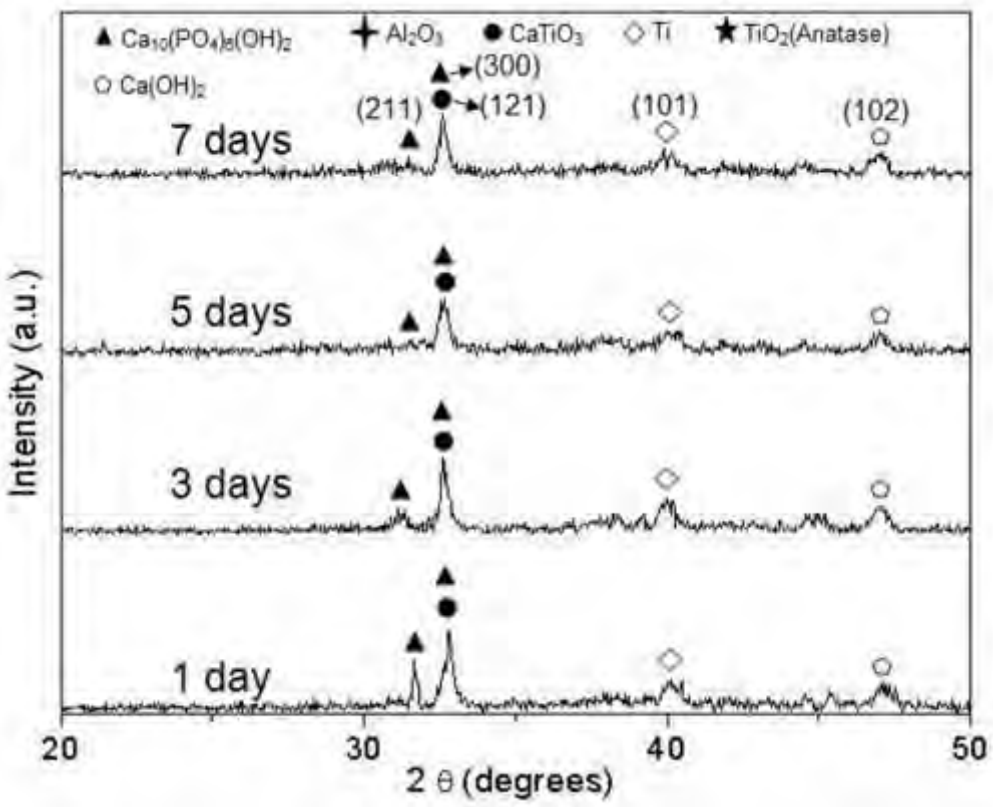


Figure 5.8 XRD spectra of the samples processed at 137 J/cm^2, 200 μm line spacing following immersion in SBF **[72]**.

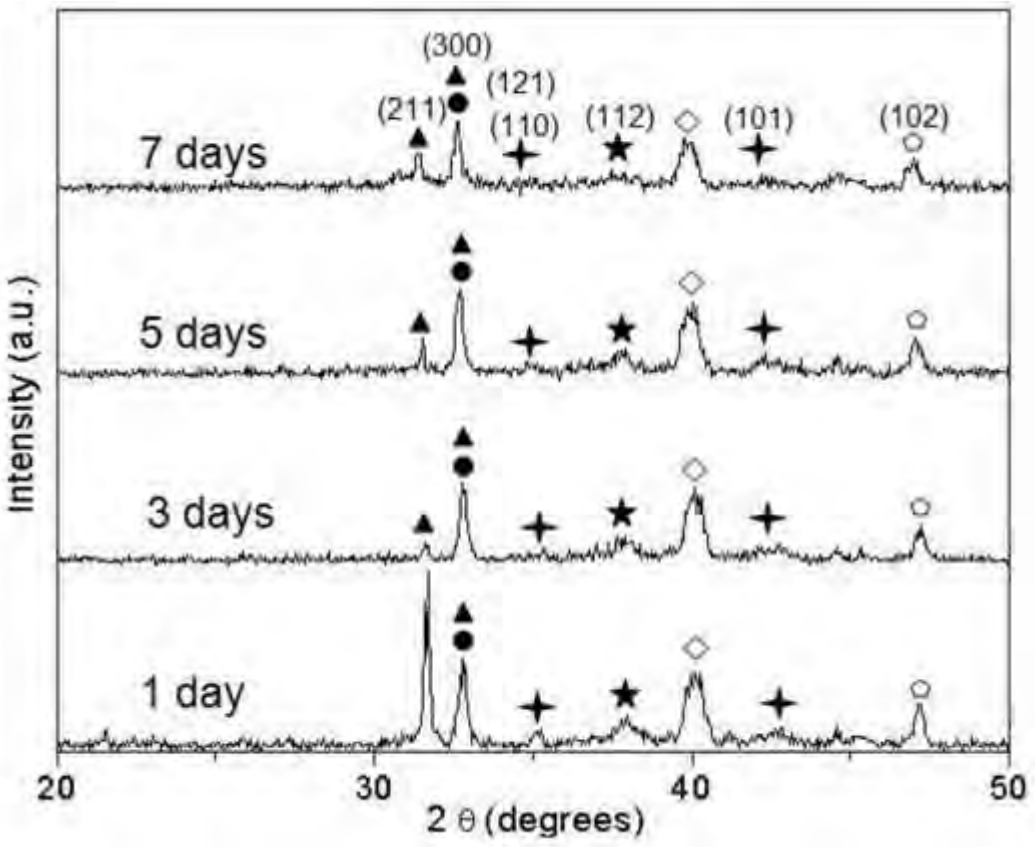


Figure 5.9 XRD spectra of the samples processed at 191 J/cm^2, 200 μm line spacing following immersion in SBF **[72]**.

From the XRD studies (Figures 5.6 - 5.9) **[72]** it is evident that both the samples processed at 100 μm line spacing irrespective of the laser fluence used (137 and 191 J/cm^2) demonstrated the same superior mineralization kinetics compared to the samples processed at 200 μm line spacing following immersion in SBF. Hence, SEM analysis (Figure 5.10) **[72]** is only done for the sample processed at 100 μm line spacing and 137 J/cm^2 laser fluence. It can be observed (Figure 5.10a) that after 1 day immersion in SBF, characteristic whisker-like apatite crystals are nucleated on the surface of sample. As the immersion time is increased to 3 days the whisker-like feature seems to have covered by another mixed layer of whisker-like and nano HA crystals (Figure 5.10b). After 5 day immersion the layer is completely covered with nano crystallites of HA (Figure 5.10c) and at the end of 7 days there is a thick mineralized layer of HA on the surface of the sample (Figure 5.10d). These observations further demonstrated a strong agreement with our XRD results (Figure 5.6 and 5.7) **[72]** obtained earlier. This rapid modification and mineralization kinetics of HA on the surface of samples processed at 100 μm line spacing (following immersion in SBF) is attributed to the higher surface energy and increased hydrophilicity as a result of the of appropriate surface textures (lower σ_A/λ value) and the same phases (HA, $CaTiO_3$, $Ca_3(PO_4)_2$, TiO_2 (Anatase), TiO_2 (Rutile) and Ti) evolved during laser processing.

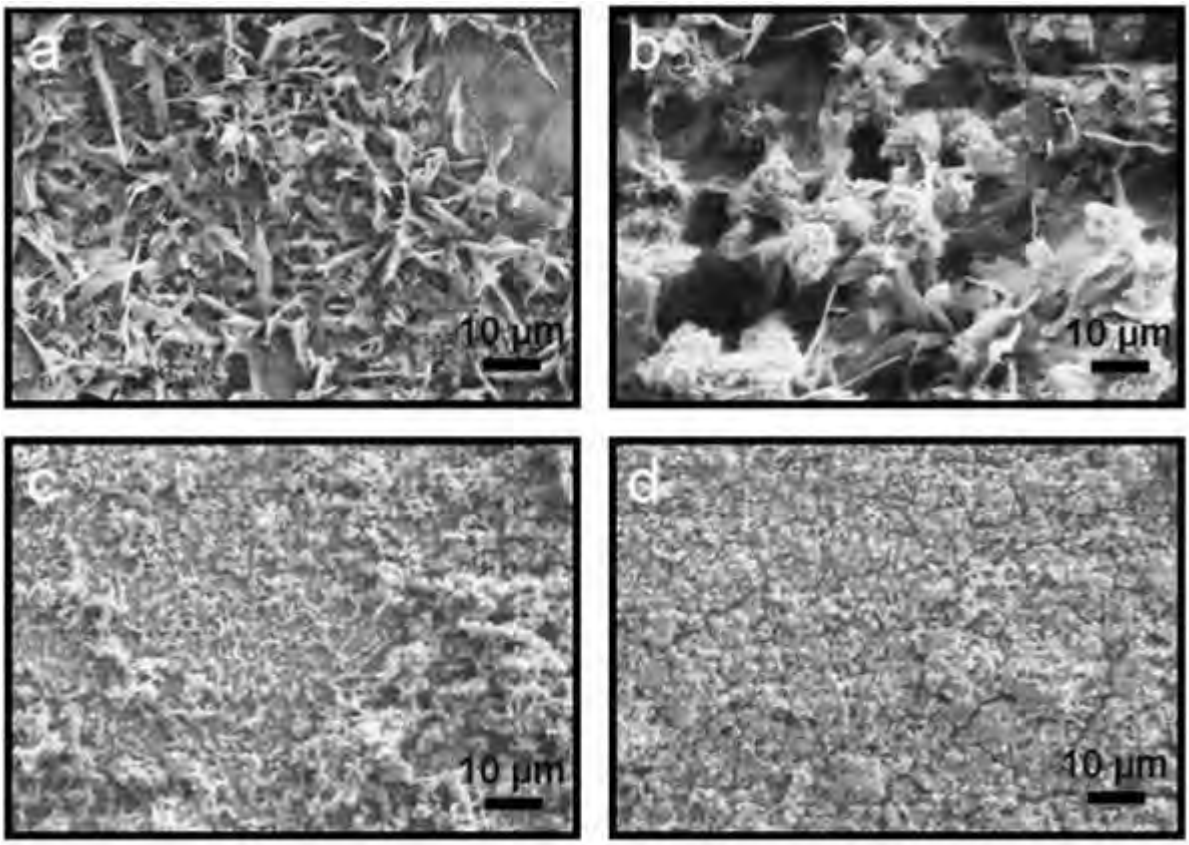
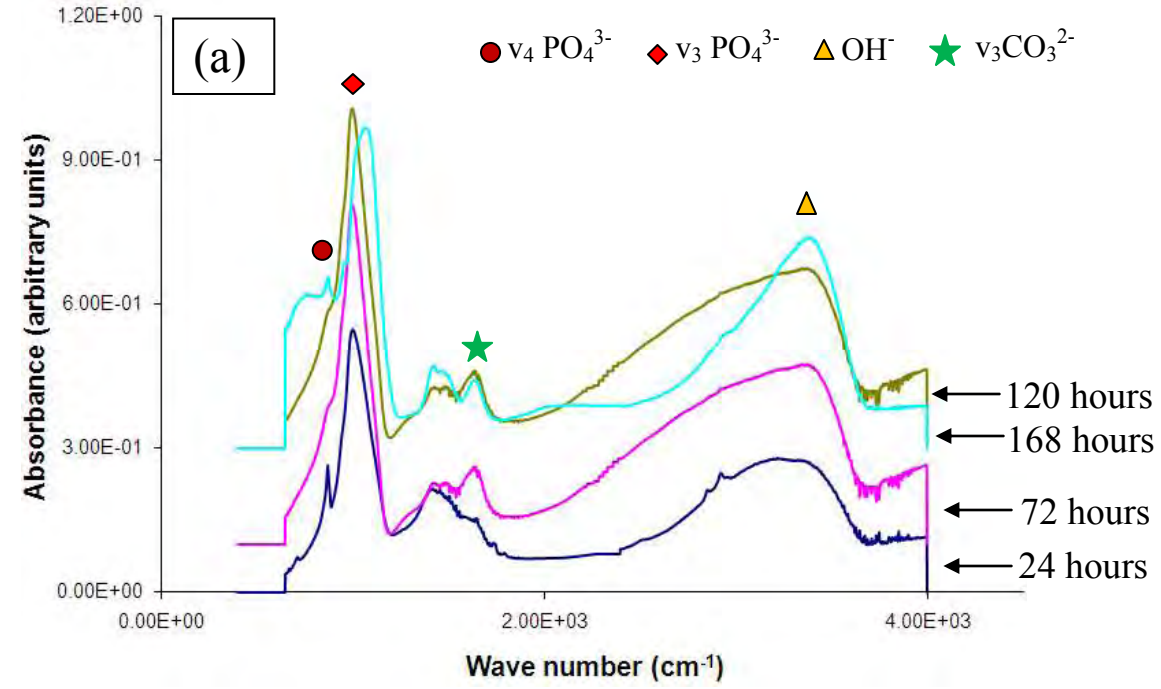
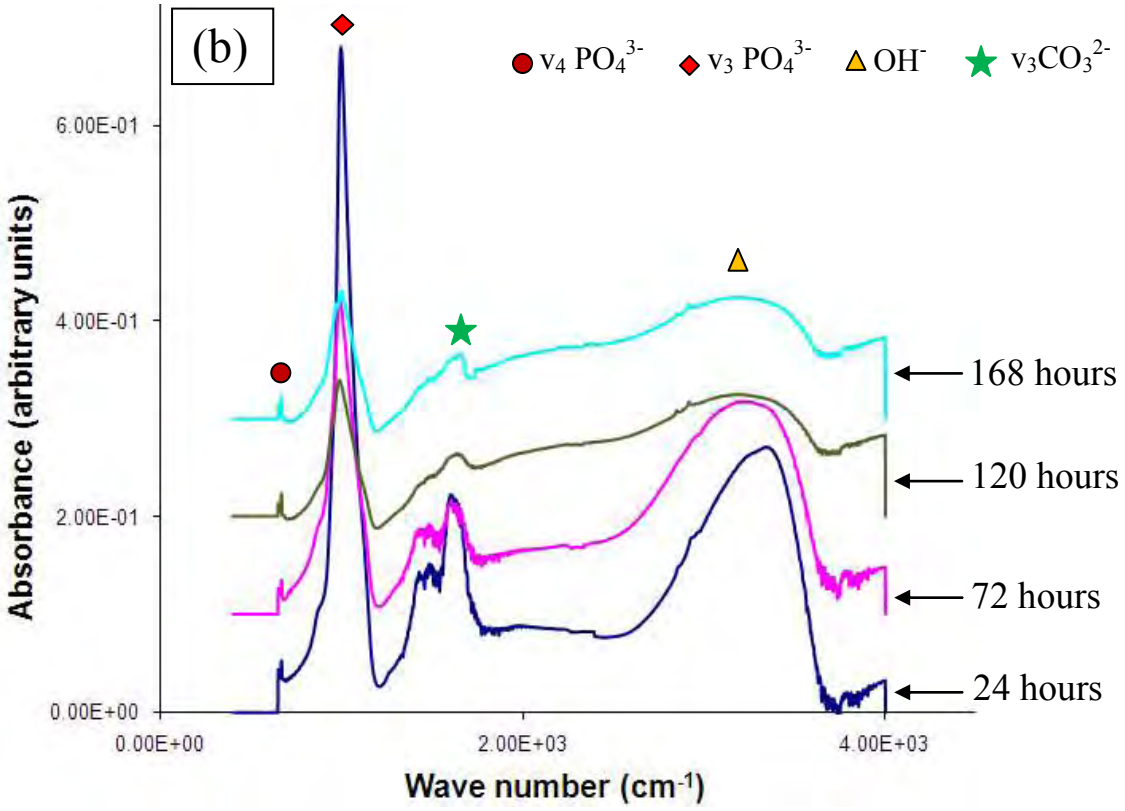


Figure 5.10 SEM images of the sample processed at 137 J/cm^2, 100 µm line spacing following immersion in SBF for (a) 1 day (b) 3 days (c) 5 days and (d) 7 days **[72]**.

The precipitated HA phase observed using the XRD studies (Figure 5.6, Figure 5.7, Figure 5.8, and Figure 5.9) **[72]** was also further confirmed using the FTIR analysis. The FTIR absorbance spectra of the laser textured samples following immersion in SBF for different time periods are presented in Figure 5.11. In the spectra, the band at 3570 cm^{-1} corresponds to the vibration of the hydroxyl ion (OH^-). The band at 667 cm^{-1} is the characteristic band of the phosphate bending vibration, while the band at 990 cm^{-1} is attributed to the phosphate stretching vibration. The band at 1630 cm^{-1} is indicative of the carbonate ion substitution. The analysis of the above bands further confirmed that the spectra shown belong to HA. Further with increased SBF immersion time, it can be observed that the phosphate band around 990 cm^{-1} demonstrated an increased intensity. This further confirmed for the increased mineralization behavior of the textured coatings with immersion times.

XPS analysis of the elements present on the surface of the samples following immersion in SBF for different time periods are recorded and presented in Figure 5.12. It can be observed that with increasing SBF immersion times there is an increase in the Ca2s, Ca2p3, P2s and P2p peaks for all laser textured samples. This further confirms the precipitation and improved mineralization of a Ca-P phase under in vitro conditions. To understand the composition of the Ca-P phase, semi-quantitative Ca and P atomic concentration and its ratio (Ca/P) was measured using area under the peak technique and tabulated in Table 5.3. It can be observed that all the laser processed samples following immersion in SBF demonstrated a reduction in the Ca/P atomic ratio and it was approximately in the range of 1.5 to 1.65, which is very close to the Ca/P atomic ratio of stoichiometric HA. Hence, it is confirmed that the Ca-P phase precipitated on the surface of the sample was that of HA.


(a)
v4 PO4 3-
v3 PO4 3-
OH-
v3CO3 2-
1.20E+00
9.00E-01
6.00E-01
3.00E-01
0.00E+00
Absorbance (arbitrary units)
0.00E+00
2.00E+03
4.00E+03
Wave number (cm-1)
120 hours
168 hours
72 hours
24 hours


(b)
v4 PO4 3-
v3 PO4 3-
OH-
v3CO3 2-
6.00E-01
4.00E-01
2.00E-01
0.00E+00
Absorbance (arbitrary units)
0.00E+00
2.00E+03
4.00E+03
Wave number (cm-1)
168 hours
120 hours
72 hours
24 hours

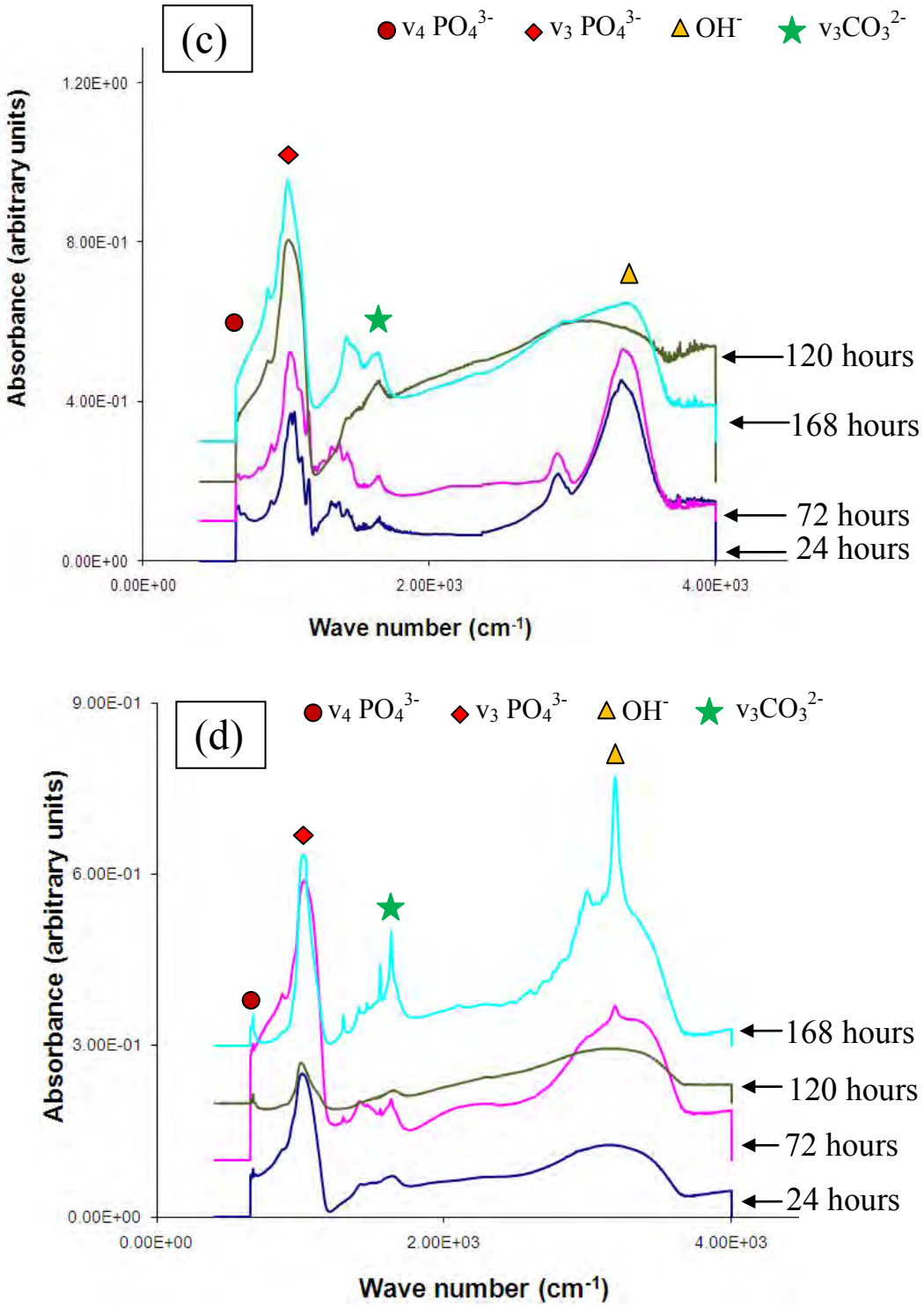
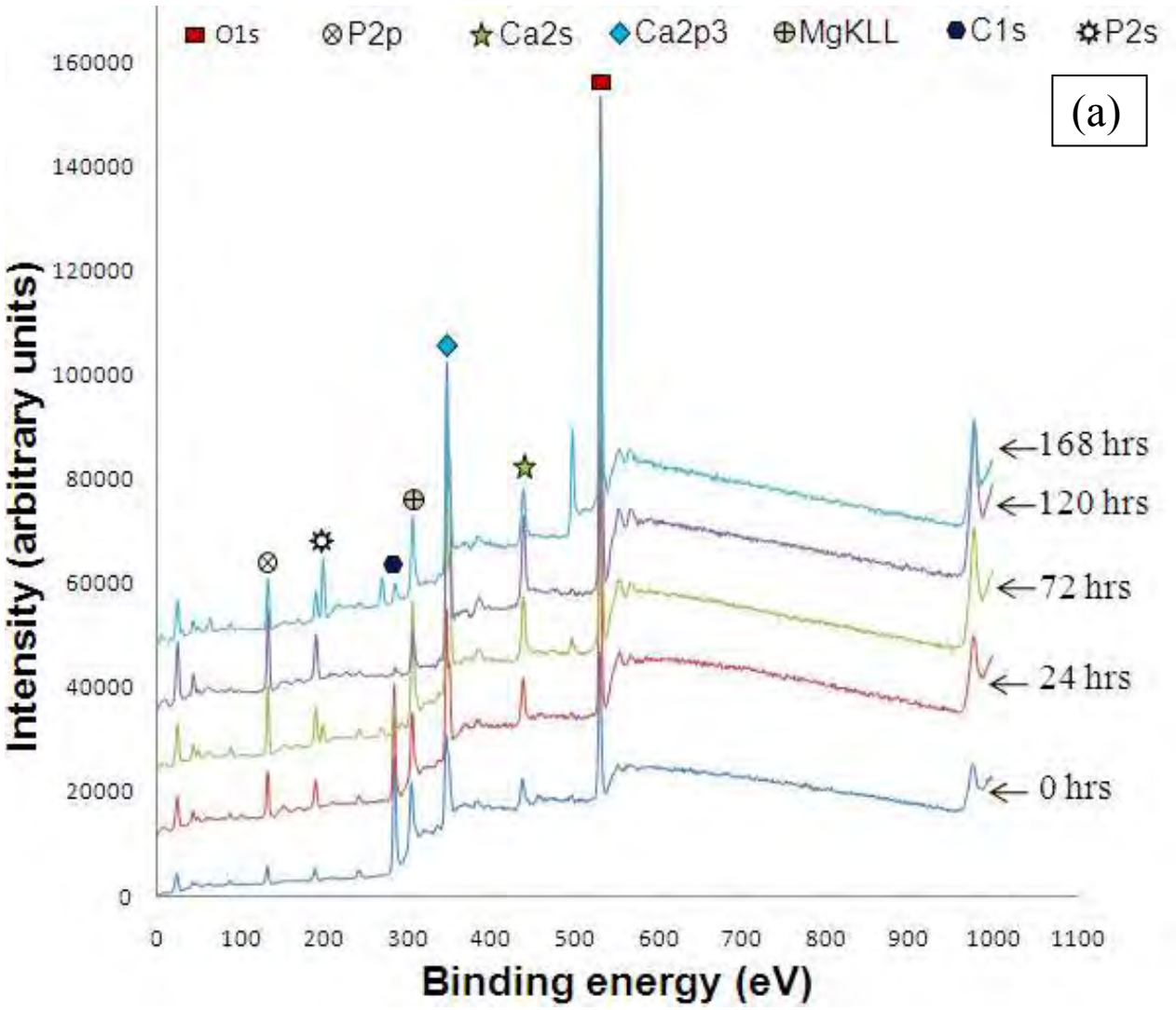
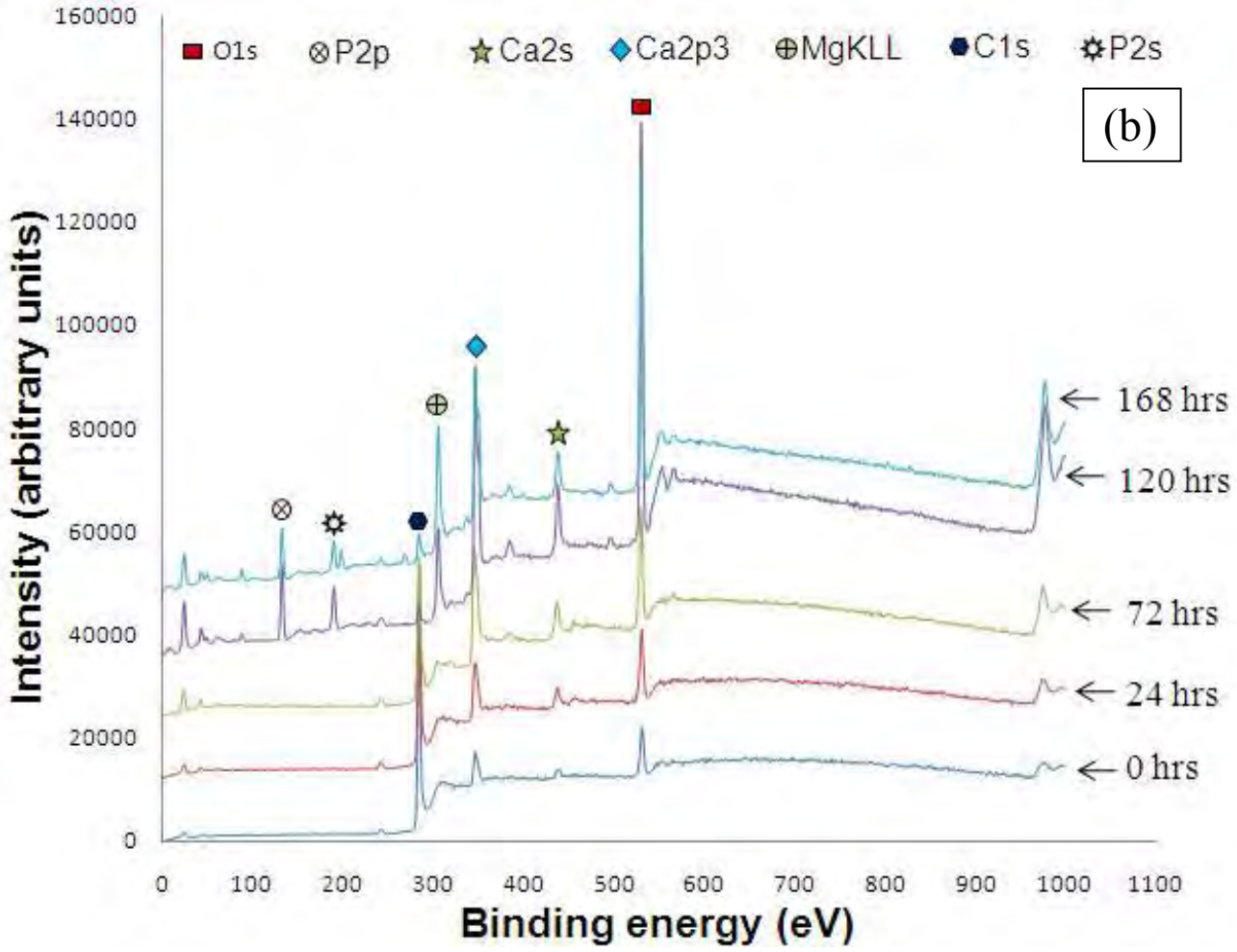
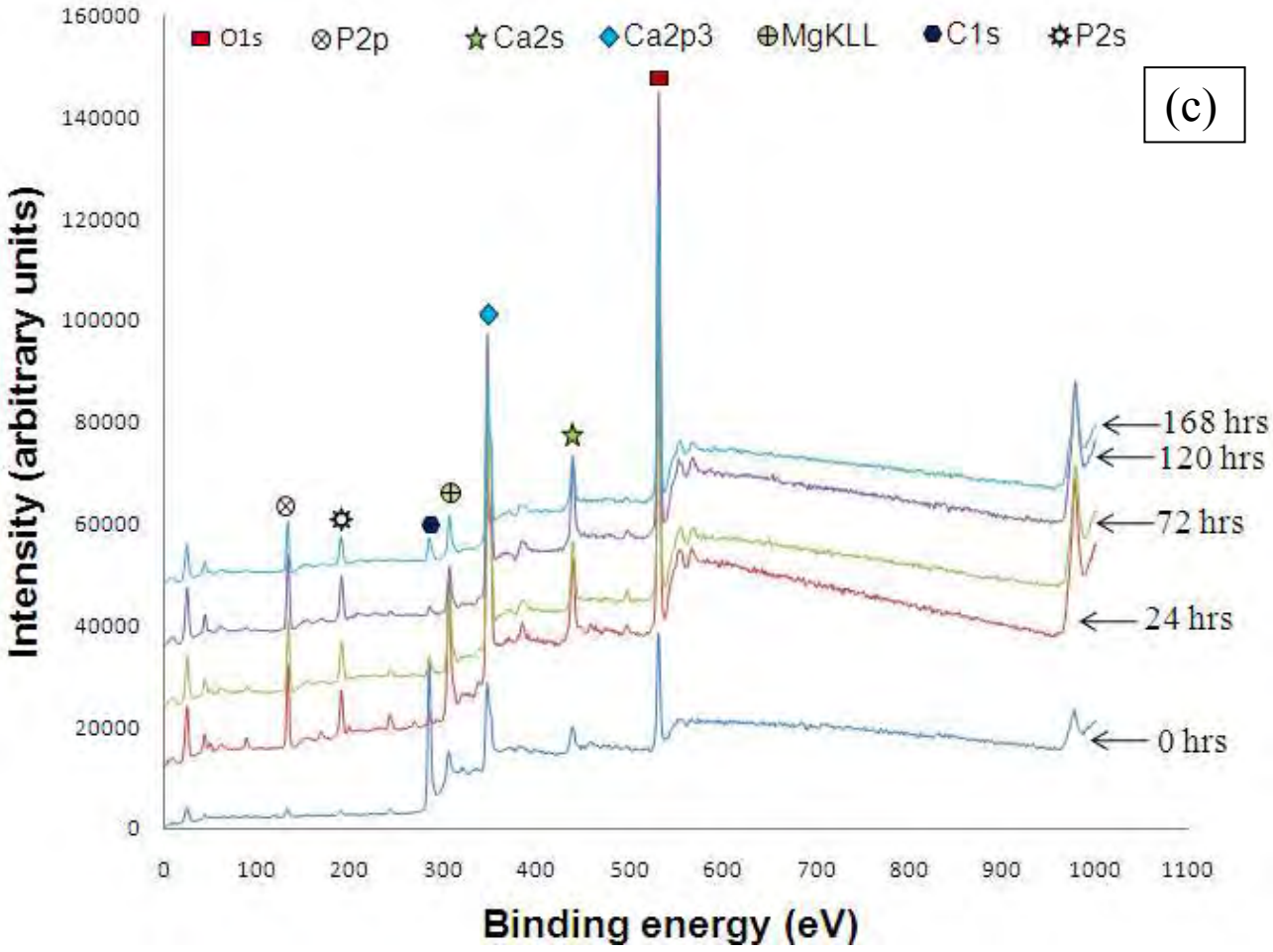


Figure 5.11 FTIR spectra of laser processed samples (a) 215W, 0.1 mm (b) 300W, 0.1 mm (c) 215W, 0.2 mm and (d) 300W, 0.2 mm following immersion in SBF for different time periods.


O1s
P2p
Ca2s
Ca2p3
MgKLL
C1s
P2s
(a)
Intensity (arbitrary units)
160000
140000
120000
100000
80000
60000
40000
20000
0
0
100
200
300
400
500
600
700
800
900
1000
1100
Binding energy (eV)
168 hrs
120 hrs
72 hrs
24 hrs
0 hrs


O1s
P2p
Ca2s
Ca2p3
MgKLL
C1s
P2s
(b)
Intensity (arbitrary units)
160000
140000
120000
100000
80000
60000
40000
20000
0
0
100
200
300
400
500
600
700
800
900
1000
1100
Binding energy (eV)
168 hrs
120 hrs
72 hrs
24 hrs
0 hrs


O1s
P2p
Ca2s
Ca2p3
MgKLL
C1s
P2s
(c)
Intensity (arbitrary units)
Binding energy (eV)
168 hrs
120 hrs
72 hrs
24 hrs
0 hrs
0
20000
40000
60000
80000
100000
120000
140000
160000
0
100
200
300
400
500
600
700
800
900
1000
1100

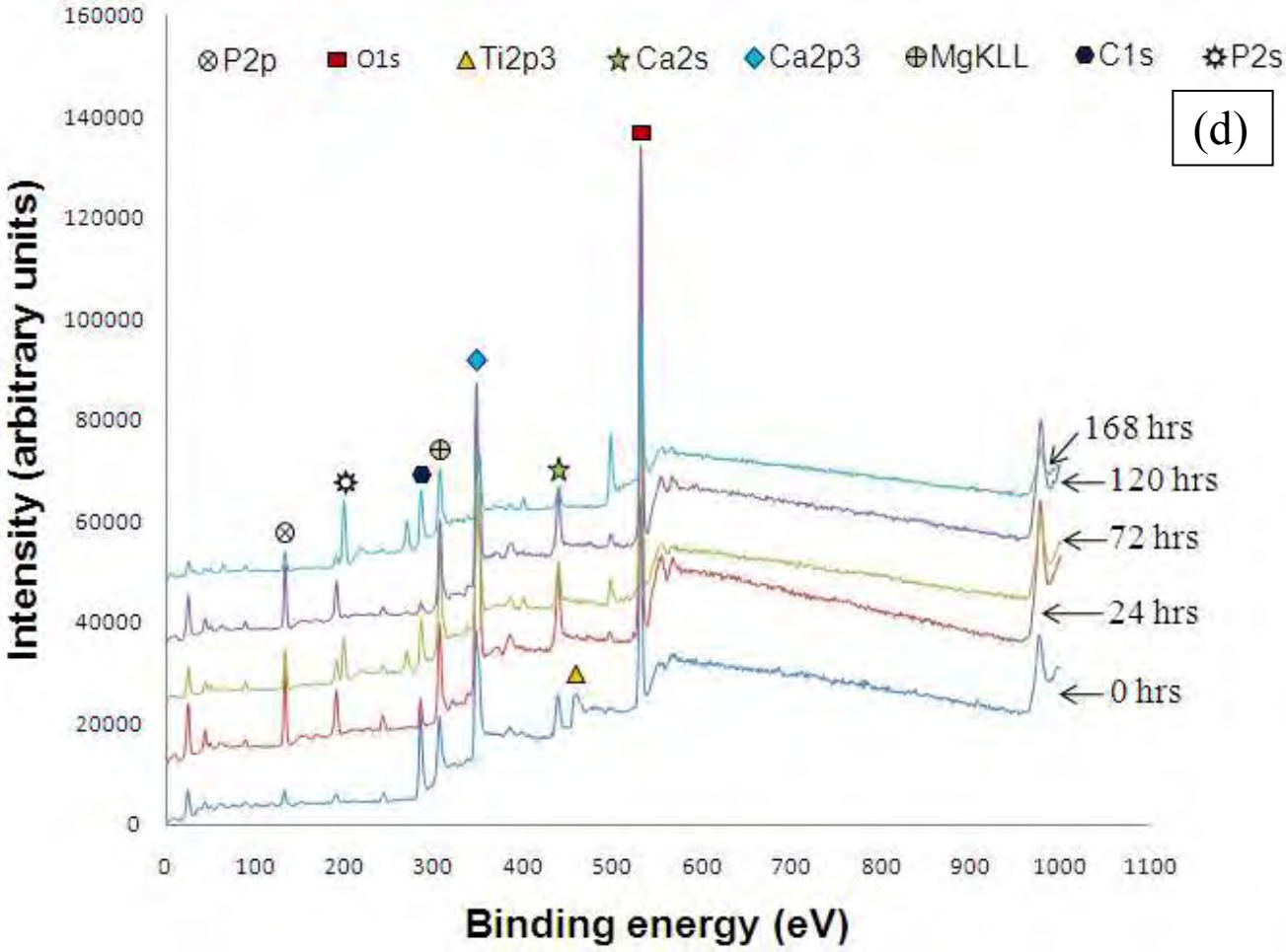


Figure 5.12 XPS spectra of laser processed samples (a) 215W, 0.1 mm (b) 300W, 0.1 mm (c) 215W, 0.2 mm and (d) 300W, 0.2 mm following immersion in SBF for different time periods.

Table 5.3 Elemental composition and semi-quantitative analysis of Ca and P in terms of atomic concentration for the CW laser processed samples.

Sample	SBF immersion time in hours	Elements present	Ca atomic concentration (%)	P atomic concentration (%)	Ca/P atomic ratio
215W, 0.1 mm	0	O, C, Ca, P	8.7	3.9	2.23
	24	O, C, Ca, P, Mg	10.2	6.7	1.52
	72	O, C, Ca, P, Mg	15.3	10.0	1.53
	120	O, C, Ca, P, Mg	18.0	11.0	1.63
	168	O, C, Ca, P, Mg	15.3	10.0	1.53
300W, 0.1 mm	0	O, C, Ca, P	3.1	1.2	2.58
	24	O, C, Ca, P, Mg	15.4	10.0	1.54
	72	O, C, Ca, P, Mg	14.5	9.5	1.53
	120	O, C, Ca, P, Mg	15.8	10.5	1.50
	168	O, C, Ca, P, Mg	14.1	9.0	1.57
215W, 0.2 mm	0	O, C, Ca, P	7.7	2.0	3.85
	24	O, C, Ca, P, Mg	16.9	11.0	1.54
	72	O, C, Ca, P, Mg	16.6	12.0	1.4
	120	O, C, Ca, P, Mg	17.5	12.4	1.41
	168	O, C, Ca, P, Mg	15.0	10.2	1.47
300W, 0.2 mm	0	O, C, Ti, Ca, P	11.5	3.0	3.83
	24	O, C, Ca, P, Mg	16.7	11.0	1.52
	72	O, C, Ca, P, Mg	12.2	7.4	1.65
	120	O, C, Ca, P, Mg	15.9	10.6	1.5
	168	O, C, Ca, P, Mg	8.5	5.3	1.60

5.5 In vitro biocompatibility

The textured coated samples are tested for its in vitro biocompatibility by the culture of mouse MC3T3-E1 osteoblast-like cells and characterizing for its spreading, morphology and cytoskeleton organization. Based on these findings, an understanding is drawn on the effect of line spacing and appropriate phases on wettability and thereby its concomitant effect on biocompatibility. Cell morphology for the laser processed and control (untreated Ti-6Al-4V) samples after 1 day culture of MC3T3-E1 osteoblast-like cells was assessed by SEM and the results are presented in Figure 5.13 **[72]**. The MC3T3-E1 osteoblast-like cells show a triangular morphology (Figure 5.13a) on the control (untreated Ti-6Al-4V) samples and have a rectangular and elongated morphology on the laser processed samples (Figure 5.13a, 5.13b, 5.13c, 5.13d, and 5.13e). Their sound adhesion especially on the laser processed samples is characterized by the lamellipodia trying to extend and adhere along the grooves. In contrast, no such adhesion is observed on the control (untreated Ti-6Al-4V) sample. Also from the SEM images (Figure 5.13) **[72]** it can be observed that the number of cells on the control (untreated Ti-6Al-4V) sample is significantly less compared to the laser processed samples. Such a difference in cell spreading and adherence on these samples is attributed to both the varying surface chemistry and surface roughness as a result of laser processing. Further, the laser processed samples also provided the appropriate length scale surface morphologies (micro textured surface patterns with 100 μm and 200 μm line spacing) for the cells to interact and spread on these surfaces.

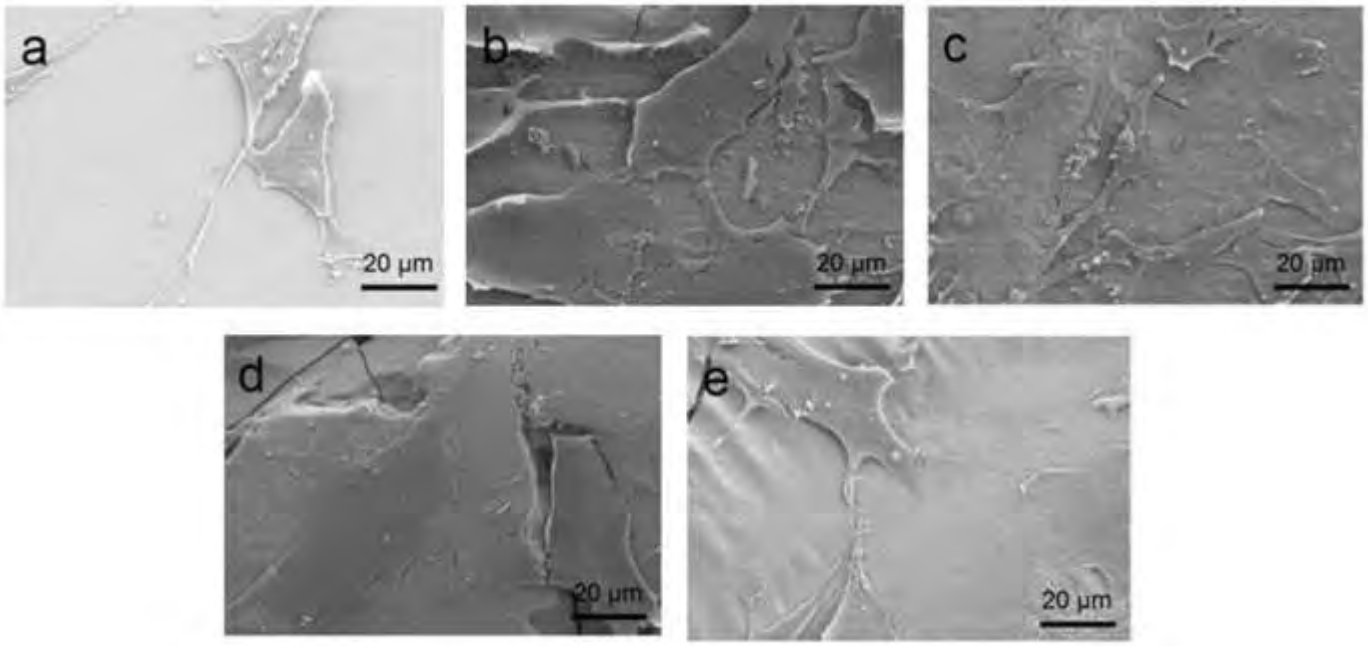


Figure 5.13 Cell morphology of MC3T3-E1 osteoblast-like cells after culture for 1 day on (a) control (untreated Ti-6Al-4V), and samples processed at (b) 137 J/cm^2 , 100 µm line spacing, (c) 191 J/cm^2, 100 µm line spacing, (d) 137 J/cm^2, 200 µm line spacing, and (e) 191 J/cm^2, 200 µm line spacing **[72]**.

The fibril networks and spreading of the MC3T3-E1 osteoblast-like cells on the laser textured samples and control (untreated Ti-6Al-4V) are studied from its cytoskeleton organization. The cytoskeletal organization of the cells on the control (untreated Ti-6Al-4V) and laser processed samples after 1 day culture are presented in Figure 5.14 **[72]**. The cells are more confluent with well stressed actin filaments on the laser processed samples compared to the control (untreated Ti-6Al-4V). The quantified area of the cells measured using the ImageJ software indicated more spreading of the cell on the sample processed at 100 μm line spacing compared to the control (untreated Ti-6Al-4V) and the sample processed at 200 μm line spacing (Figure 5.15) **[72]**. This improved cytoskeletal organization and spreading of the cells on the 100 μm line spaced sample is attributed to the higher surface energy as a result of the appropriate surface texture (lower $\sigma_A/\ \lambda$ value) and the same phases (HA, $CaTiO_3$, $Ca_3(PO_4)_2$, TiO_2 (Anatase), TiO_2 (Rutile) and Ti) evolved during laser processing. The number of viable cells on the laser processed samples and control (untreated Ti-6Al-4V) was evaluated using WST-1 assay after 1, 3 and 5 day of culture of the cells. For the three different time periods the number of viable cells appeared to be more for the samples processed at 100 μm line spacing compared to the control (untreated Ti-6Al-4V) and the sample processed at 200 μm line spacing (Figure 5.16) **[72]**. The absorbance for the control (untreated Ti-6Al-4V) and the 200 μm line spaced samples is comparable for the three different time periods. This improved behavior of the 100 μm line spaced sample further complemented to all our results and observations made earlier.

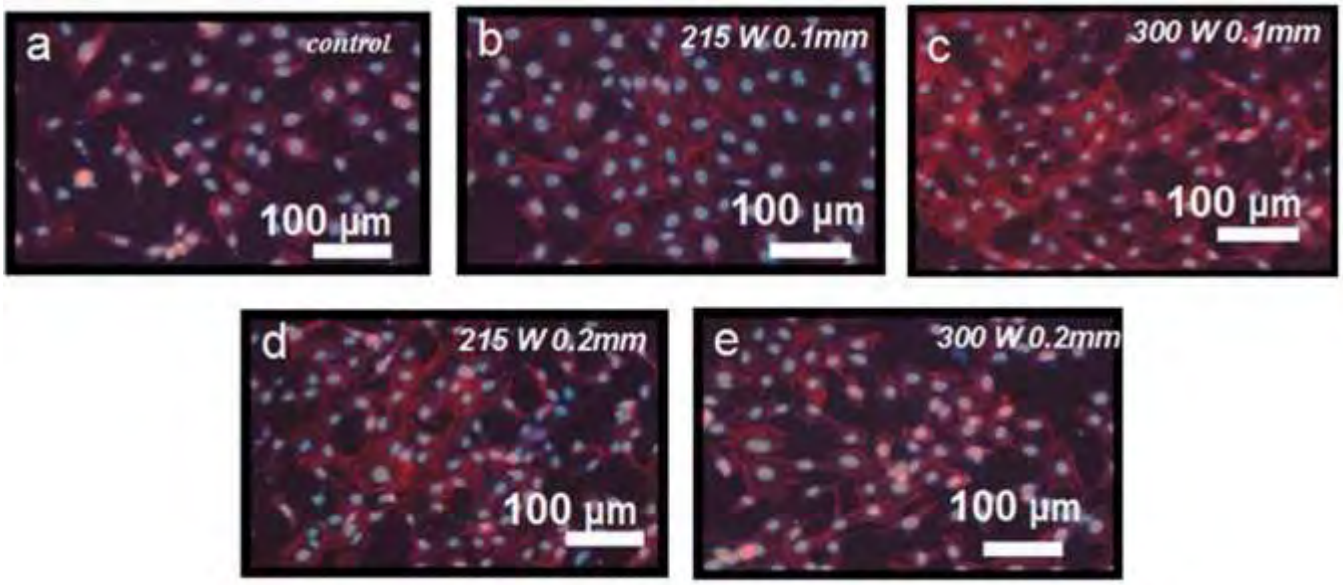


Figure 5.14 Fluorescent micrographs for cytoskeleton assessment of adherent MC3T3-E1 osteoblast-like cells after culture for 1 day on (a) control (untreated Ti-6Al-4V substrate) and samples processed at (b) 137 J/cm^2, 100 µm line spacing, (c) 191 J/cm^2, 100 µm line spacing, (d) 137 J/cm^2, 200 µm line spacing, and (e) 191 J/cm^2, 200 µm line spacing **[72]**.

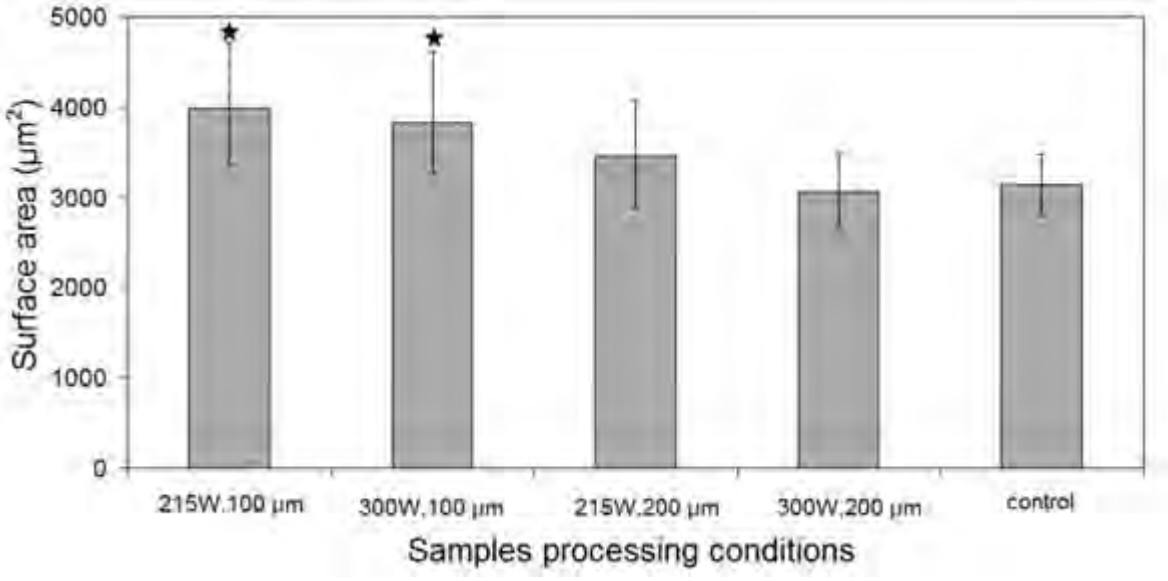


Figure 5.15 Graphical representation of the cell spreading area as a function of sample processing conditions. ★ denotes that the laser processed group is significantly higher than the control Ti-6Al-4V ($p < 0.05$). Cell spreading area measurements were taken from 30 different cells **[72]**.

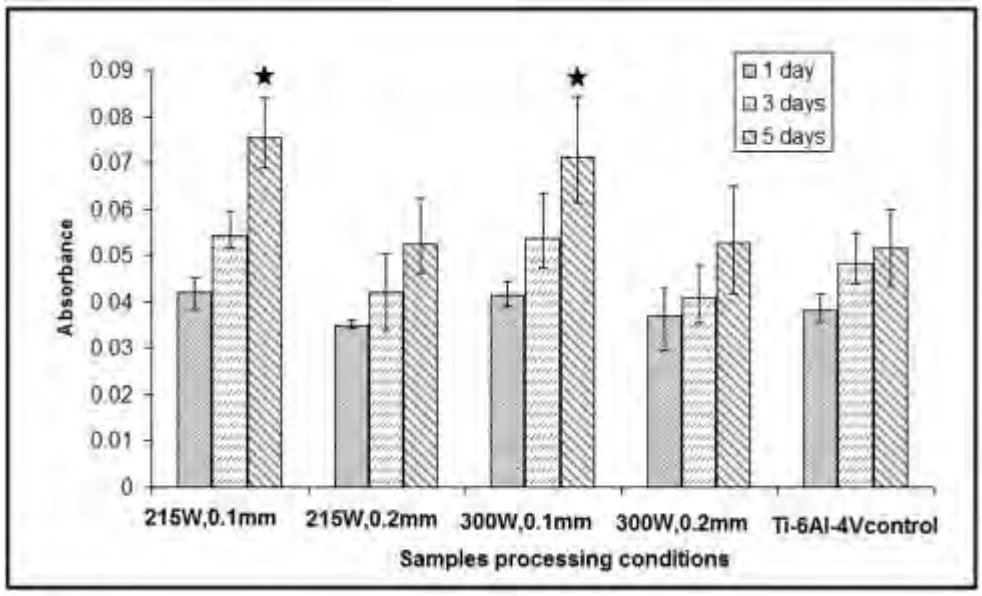


Figure 5.16 WST-1 assay of the MC3T3-E1 osteoblast-like cells following culture for 1, 3, and 5 days as a function of samples processing conditions. ★denotes that the laser processed group is significantly higher than the control Ti-6Al-4V ($p < 0.05$) **[72]**.

Chapter 6

Promising New Developments

6.1 Pulse Nd:YAG laser textured SiO_2-HA composite coating

In the last decade, researchers have intensely devoted towards synthesizing doped Ca-P coatings to improve the ostegenesis, bioreasorption rate, strength and phase composition of the resulting bioceramics. In particular Si has been found to be essential for normal bone and cartilage growth and development. It was found that synthetic Ca-P based materials with trace level of Si substitution in their structures demonstrate markedly increased biological performance in comparison to stoichiometric counterparts **[118]**. Furthermore, Si is also present at a trace level of 100 ppm in the bone and 200-600 ppm in cartilage and other connective tissue **[119]**. Owing to the above beneficial effects associated with Si, a Si doped Ca-P based textured bioceramic coating on Ti-6Al-4V substrate was targeted in the current work. Here, 100 wt.% hydroxyapatite (HA) precursor and 25 wt.%SiO_2-HA precursors were used to prepare bioactive coatings on Ti-6Al-4V substrates by a pulsed laser induced direct melting technique. The effects of SiO_2 on phase constituents, wettability, in vitro bioactivity and in vitro biocompatibility was studied in the preliminary efforts. Furthermore, on the basis of these results, the effects and roles of SiO_2 substitution in HA were systematically discussed.

6.1.1 Phase evolution

XRD studies were carried out on Ti-6Al-4V, 25 wt.% SiO_2-HA and 100 wt.% HA coated samples (Figure 6.1) **[119]**. From Figure 6.1**[119]** it can be observed that, compared to bare Ti-6Al-4V, some new phases, specifically $CaTiO_3$, $Ca_3(PO_4)_2$, Ca_2SiO_4, and TiO_2, were formed

during laser processing of 25 wt.% SiO_2-HA and 100 wt.% HA precursors. Main phases on the 25 wt.% SiO_2-HA precursor sample include $CaTiO_3$, $Ca_3(PO_4)_2$, Ca_2SiO_4, and minor phase TiO_2, but for 100 wt.% HA precursor samples, TiO_2 is the main phase together with some $CaTiO_3$ and minor $Ca_3(PO_4)_2$. However, no HA was detected in any sample laser processed using a set of parameters employed in the present work. Due to the higher laser fluence employed in the present work (10^3 J/cm^2) interactions between Ti-6Al-4V substrate and HA or SiO_2-HA precursor material was expected to take place. The possible reactions between HA and Ti-6Al-4V due to melting by the laser beam can be characterized as follows **[68]**:

$Ti + O_2 \rightarrow TiO_2$ (ΔG= - 864.09kJ/mol).....C6.1

$HA + TiO_2 \rightarrow CaTiO_3 + 3TCP + H_2O$ (ΔG= - 7312.39kJ/mol).....C6.2

$TCP + TiO_2 \rightarrow CaTiO_3 + \alpha\text{-}Ca_2P_2O_7$ (ΔG= - 41.51kJ/mol).....C6.3

$\alpha\text{-}Ca_2P_2O_7 + Ti \rightarrow CaTiO_3 + CaO + P_2O_3\,(g)\uparrow$ (ΔG= - 1247.46kJ/mol) C6.4

Further, the possible reaction between HA-SiO_2 precursor and Ti-6Al-4V substrate material can be given as:

$2CaO + SiO_2 \rightarrow Ca_2SiO_4$ (ΔG= -122.17 kJ/mol).....C6.5

All the above reactions clearly suggest that the chemical compositions of the laser textured coating depend on the precursor compositions and the reactions among them. Same phases such as TiO_2, $CaTiO_3$, $Ca_3(PO_4)_2$ (TCP) were detected both in laser cladded 100 wt.% HA and 25 wt.% SiO_2-HA coatings based on the above C6.1-C6.4 reactions. Due to the absence of SiO_2 in 100 wt. % HA precursor, reaction (C6.5) will not occur, and instead it led to the retention of CaO in laser cladded 100 wt.% HA coating. On the contrary, in laser cladded 25 wt.% SiO_2-HA coating, reaction (5) occurred, and led to the formation of additional phase of Ca_2SiO_4.

6.1.2 Wettability and in vitro bioactivity

Contact angle measurements obtained from SBF liquid provided an understanding of the effect of SiO_2 addition on the wetting behavior. Table 6.1 **[120]** represents the contact angle measurements and corresponding light optical images of the liquid droplet shadow on 100 wt.% HA samples, 25 wt.% SiO_2-HA samples, and the control (untreated Ti-6Al-4V). The results (Table 6.1) **[120]** demonstrated improved wettability and thereby higher surface energy for the laser processed samples (100 wt.% HA and 25 wt.% SiO_2-HA samples) compared to the control (untreated Ti-6Al-4V). Furthermore, compared to 100 wt.% HA samples, 25 wt.% SiO_2-HA samples indicated a more hydrophilic behavior (better improved wettability). Thus, the

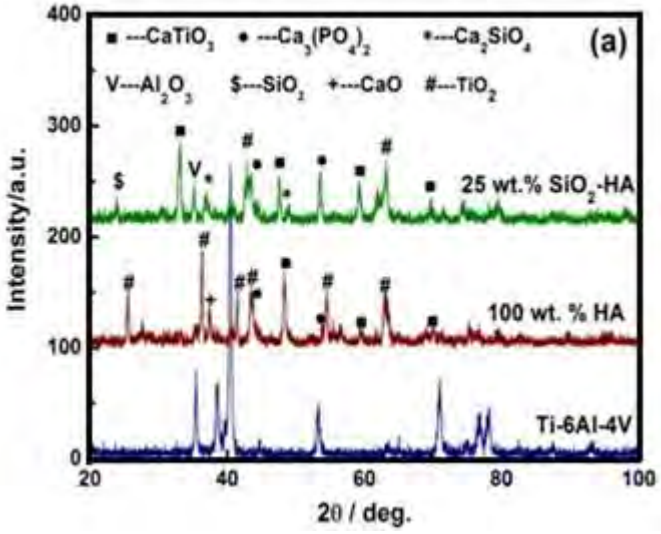
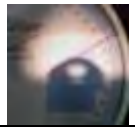


Figure 6.1 XRD patterns of Ti-6Al-4V, 25 wt.% SiO_2-HA and 100 wt.% HA coated sample **[119]**.

Table 6.1 Contact angle with SBF, and surface energy of the samples **[120].**

Precursor	Laser scan speed cm/min	SBF contact angle	Surface energy (mJ/m^2)
25 wt. % SiO_2-HA	75	26.4±1.3 	55.94±0.87
100 wt. % HA	75	32.8±1.9 	48.01±0.92
Ti-6Al-4V control		55.7±1.6 	34.19±0.05

addition of SiO_2 not only influenced the phase constituents, but also contributed to increase in the surface energy and thereby the hydrophilic behavior of the coatings.

The wettability of the coatings was finally correlated to its mineralization or in vitro bioactivity by immersing the samples in SBF and analyzing for the precipitation of an apatite like phase. The mineralized layer or the precipitate on the 100 wt.% HA sample and 25 wt.% SiO_2-HA sample after 7 day immersion in SBF is shown in Figure 6.2 **[120]**. The presence of a cuboidal like apatite crystallites can be clearly seen on the surfaces of 100 wt.% HA and 25 wt.% SiO_2-HA samples (Figure 6.2a and Figure 6.2b respectively). The EDS spectrum from a selected region indicates the presence of various elemental species such as Ca, P, Na, Cl, Al, O, Ti and V in the precipitated layer. The EDS spectra from the mineralized surface of 100 wt% HA demonstrated for a small amount of Ca and P with a Ca/P atomic ratio of 0.62. In contrast, the

selected region EDS spectrum of the mineralized layer on 25 wt% SiO_2-HA demonstrated strong presence of Ca and P with a Ca/P atomic ratio of 1.68 which is close to the stoichiometric HA (1.67). This improved mineralization of the 25 wt% SiO_2-HA coated samples was attributed to the presence of SiO_2 addition, which in turn improved the hydrophilicity and the in vitro bioactivity of the coatings.

6.1.3 In vitro biocompatibility

Live/dead staining results (Figure 6.3a - 6.3c) **[119]** indicated that cells attached well on the substrates after 4 hours of incubation with very few dead/disrupted cells. This suggested good initial adhesion and high viability of cells exposed to modified surfaces. Quantitatively, the total number of cells attached after 4 hours on the 25 wt.% SiO_2-HA and 100 wt.% HA coated samples were significantly higher than the Ti-6Al-4V control (Figure 6.3d). Cell morphology after 1 day and 7 days of proliferation was assessed by SEM, with resulting images shown in Figure 6.4 **[119]**. From Figure 6.4c and 6.4e, it can be seen that the normal individual MC3T3-E1 osteoblasts on laser cladded sample (25 wt. % SiO_2-HA and 100 wt. % HA) surfaces mostly had a triangular form, with an average size of around 20 μm in width and 60-80 μm in length. This exhibits that good adhesion was obtained by laser cladding 25 wt. % SiO_2-HA and 100 wt. % HA precursor on Ti-6Al-4V substrate. Their good adhesion can be characterized by the presence of lamellipodia, i.e. large front projections, which strongly adhere to the substrate and draw the cellular body by cytoplasmic contraction. It is also found that several multiple microvilli exists on the surface, and fine cytoplasmic extensions in multiple directions were formed. Those cultured on 25 wt. % SiO_2-HA and 100 wt. % HA samples also revealed greater spreading with large lamellipodia, indicating active cell migration. On untreated Ti-6Al-4V

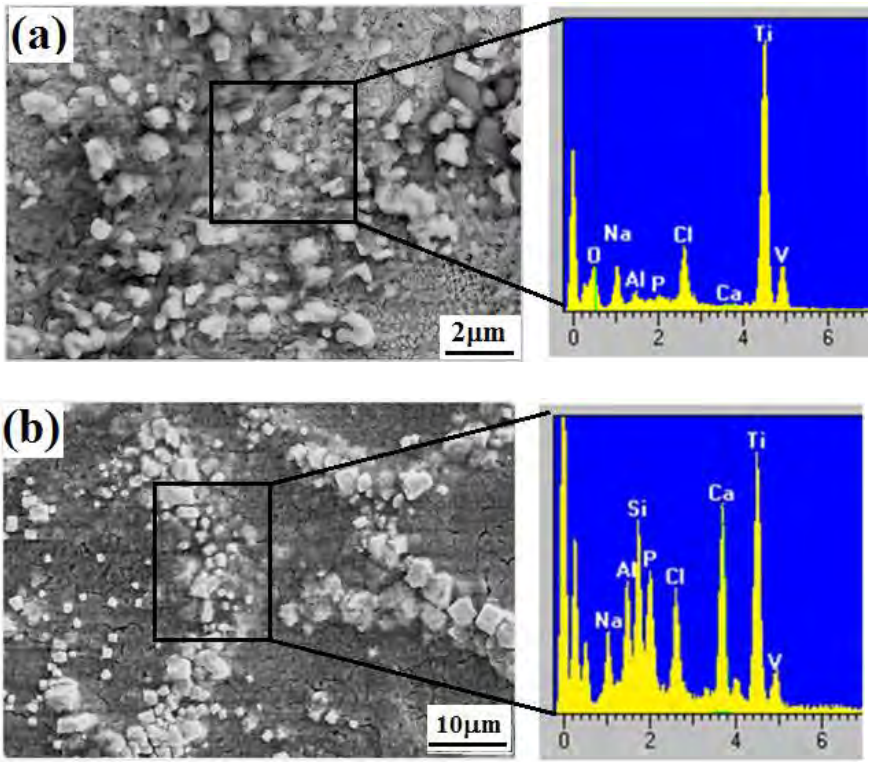


Figure 6.2 SEM morphological analysis and corresponding EDS results on (a) 100 wt.% HA sample, and (b) 25 wt.% SiO_2-HA sample after 7 days immersion in SBF **[120]**.

sample, however, the osteoblasts showed a polygonal form (Figure 6.4a). The cell surface features were less-developed on untreated Ti-6Al-4V than those on 25 wt. % SiO_2-HA and 100 wt. % HA. In addition, the numbers of filopodia and cytoplasmic extensions were also less on cells grown on bare Ti-6Al-4V alloy.

Figure 6.4b, 6.4d and 6.4f illustrate the cell morphology after 7 days of proliferation. It is clear that after proliferation for 7 days, the cells distributed evenly and compactly on the sample surfaces. The higher magnification inset indicated excellent cell spreading and cell-cell interaction after 7 days of proliferation. The improved osteoblast cell attachment and cell morphology on the samples processed with 25 wt.% SiO_2-HA precursor can be attributed to the improved hydrophilicity as a result of SiO_2 doping into the HA phase.

Here in this preliminary work, the role of SiO_2 doping in improving the wettability, and thereby its in vitro bioactivity and in vitro biocompatibility of the HA coatings has been clearly demonstrated. However, further investigation to understand the exact mechanism by which SiO_2 doping is improving the hydrophilicity of the coatings still needs to be explored.

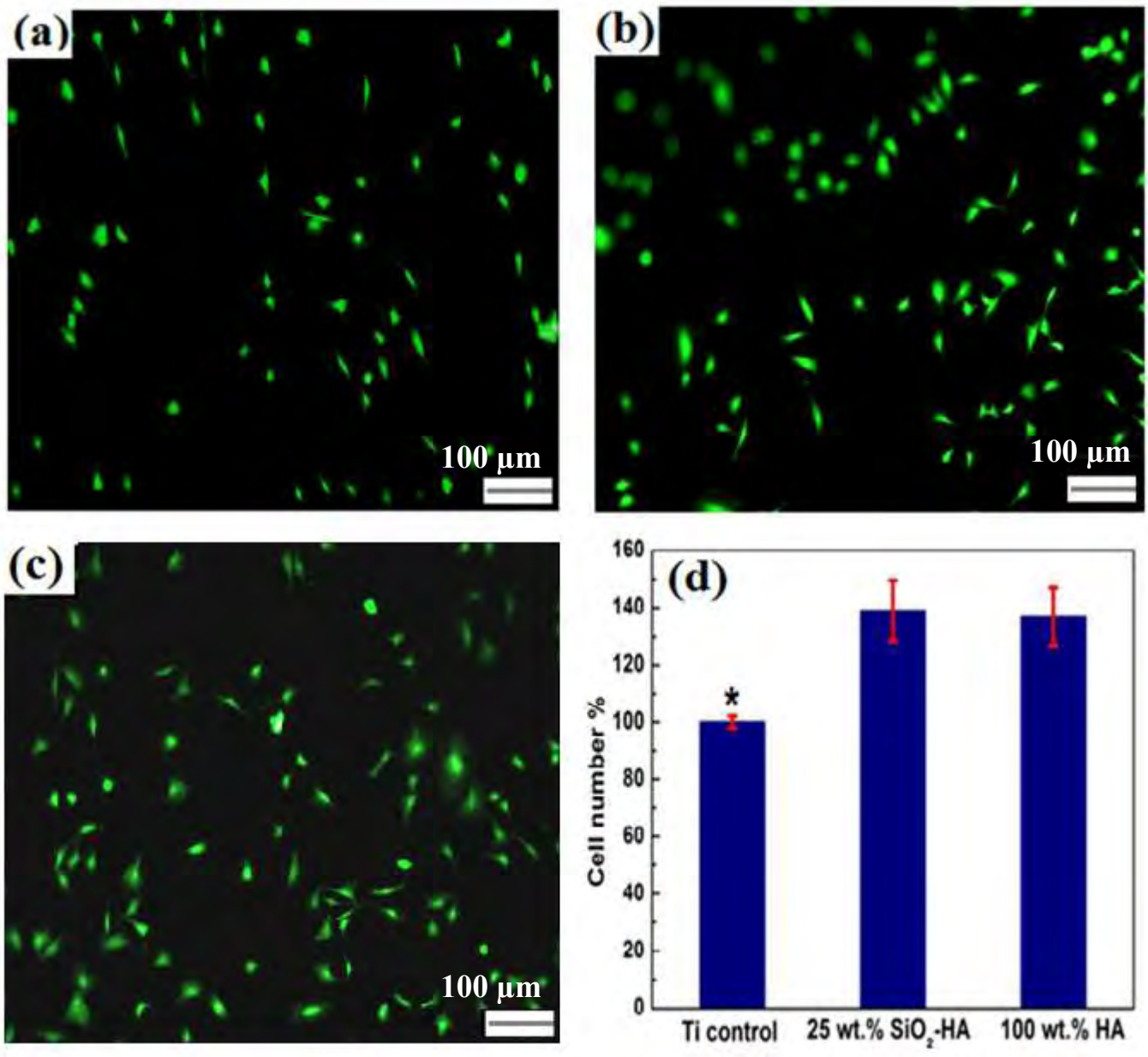


Figure 6.3 Live/dead staining of MC3T3-E1 cells after 4 h of incubation on (a) Ti-6Al-4V, (b) 25 wt.% SiO_2-HA coating, (c) 100 wt.% HA coating; and (d) cell numbers attached to Ti control, 25 wt. % SiO_2-HA coating, and 100 wt. % HA coating within observation areas after 4 h seeding; results are expressed as percentages of cells attached on Ti control (n=3). * denotes that the cell number on untreated Ti-6Al-4V is significantly lower than laser cladded Ti ($p < 0.05$) **[119]**.

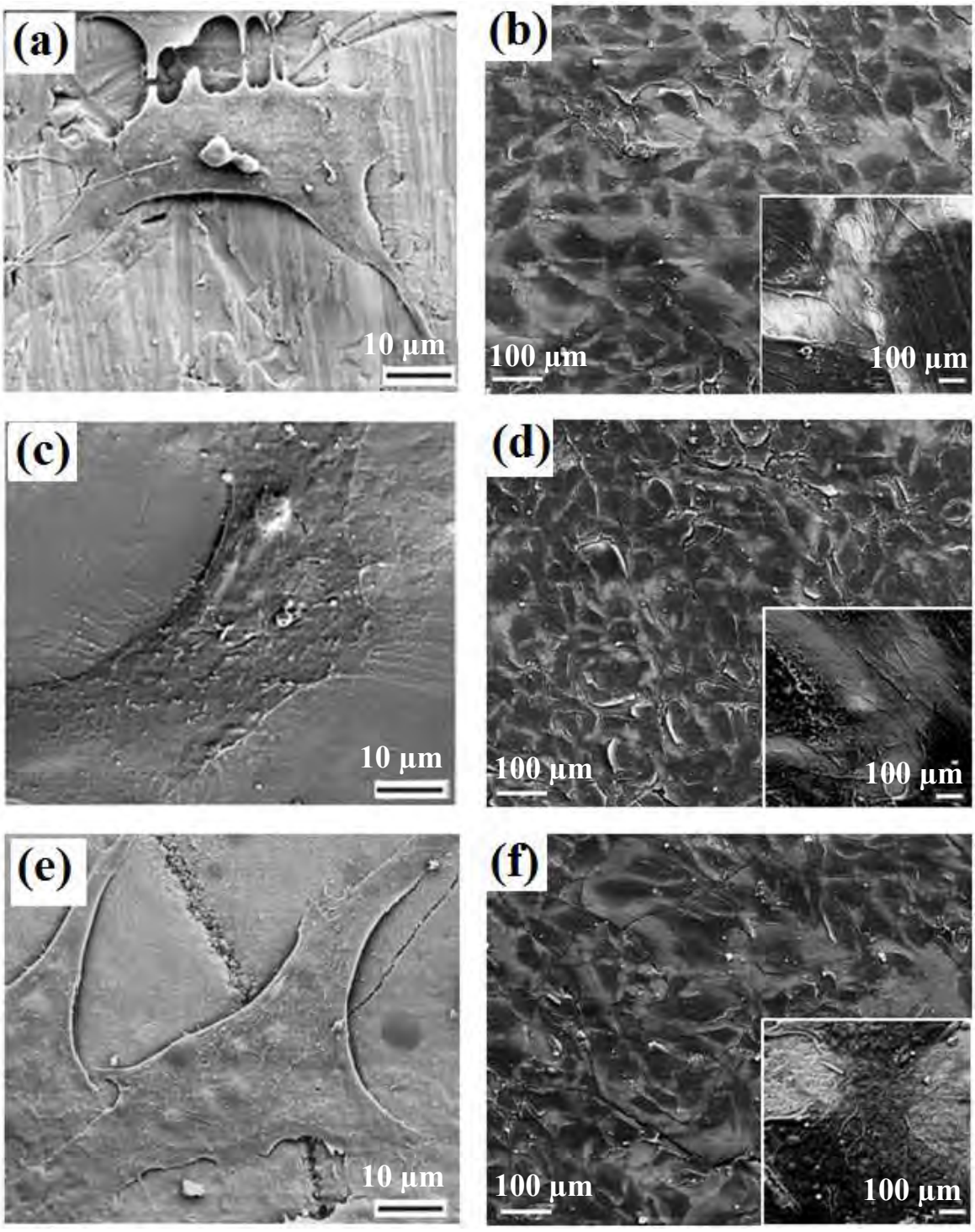


Figure 6.4 SEM images for cell morphology after 1 and 7 days of proliferation on Ti-6Al-4V (a and b), 25 wt. % SiO_2-HA coating (c and d), and 100 wt. % HA coating (e and f) **[119]**.

6.2 Laser interference patterning on Ti-6Al-4V

Most of the above discussed experiments until now are associated with multiple step process such as precursor spraying, drying and laser melting to achieve a textured coating. Also the length scale of the features (surface textures) obtained using this technique are at the micron and submicron scale. To upgrade the current technique a single step process know as laser interference patterning is explored to synthesize nano scale features. In this preliminary work, laser interference patterned surface textures were obtained on Ti-6Al-4V samples and their influence on wettability was studied.

6.2.1 Surface morphology of the samples

Using the laser-based optical interference patterning technique, textured surfaces with groove- and pillar-like features were obtained on the flat Ti-6Al-4V sample by varying the laser power. The 2-dimensional and 3-dimensional morphological evolution of the groove like features generated using a one-step irradiation under a laser fluence of 760.35 mJ/cm^2 are presented in Figure 6.5a **[80]** and Figure 6.5b **[80],** respectively. From the Figure 6.5a (2-dimensional morphological evolution) and Figure 6.5b (3-dimensional morphological evolution) it can be observed that the spacing or the periodicity, *w* (equivalent to the width of the depression or width of the melt pool) of the pattern is approximately 2.5 μm. Further, the ratio of total scanned distance (across the grooves in x-direction) to the number of grooves within the scanned length (Figure 6.5c) also clearly proved the width *w* to be approximately 2.5 μm. As discussed earlier, since the angle, β between the beams (Figure 3.6) is kept constant in this process throughout the experiment, there was no change in the periodicity or width, *w* of the patterns. On the contrary, with varying laser fluence only the feature size, *h* in the z-direction is varied and an increase in

feature size is realized with increasing laser fluence (Table 6.2) **[80]**. This is attributed to the fact that with increase in laser fluence there is an increase in volume of the molten pool and thereby an increased temperature gradient across the vertical direction probably resulting in greater Marangoni forces. The Marangoni forces may have resulted in extensive surface tension gradients across the border, expelling substantial amount of the liquid melt from the pool and thereby resulting in a groove with increased depth at higher laser power.

In order to generate pillar like features, the sample once irradiated was rotated 90° and irradiated again with 5 pulses. Hence, it was a two step process, with the effective number of pulses being doubled compared to the groove like features. The 2-dimensional and 3-dimensional morphological evolution of the pillar like features obtained under a laser fluence of 760.35 J/cm^2 are presented in Figure 6.6a **[80]** and Figure 6.6b **[80],** respectively. From a line scan across the sample (Figure 6.6c) **[80]** it was observed that the width, *d* at full-width-half-maxima (FWHM) and the periodicity, *w* of the pillar were approximately 1.04 μm and 2.5 μm respectively. Again, the periodicity is dependent upon the angle, β between the beams (Figure 3.6). Therefore, in the pillar patterns also the only physical feature that was varied with varying laser fluence was the height, *h* of the pillar. It was observed that there is an increase in pillar height, *h* with increasing laser fluence (Table 6.2) **[80]** as per earlier discussion.

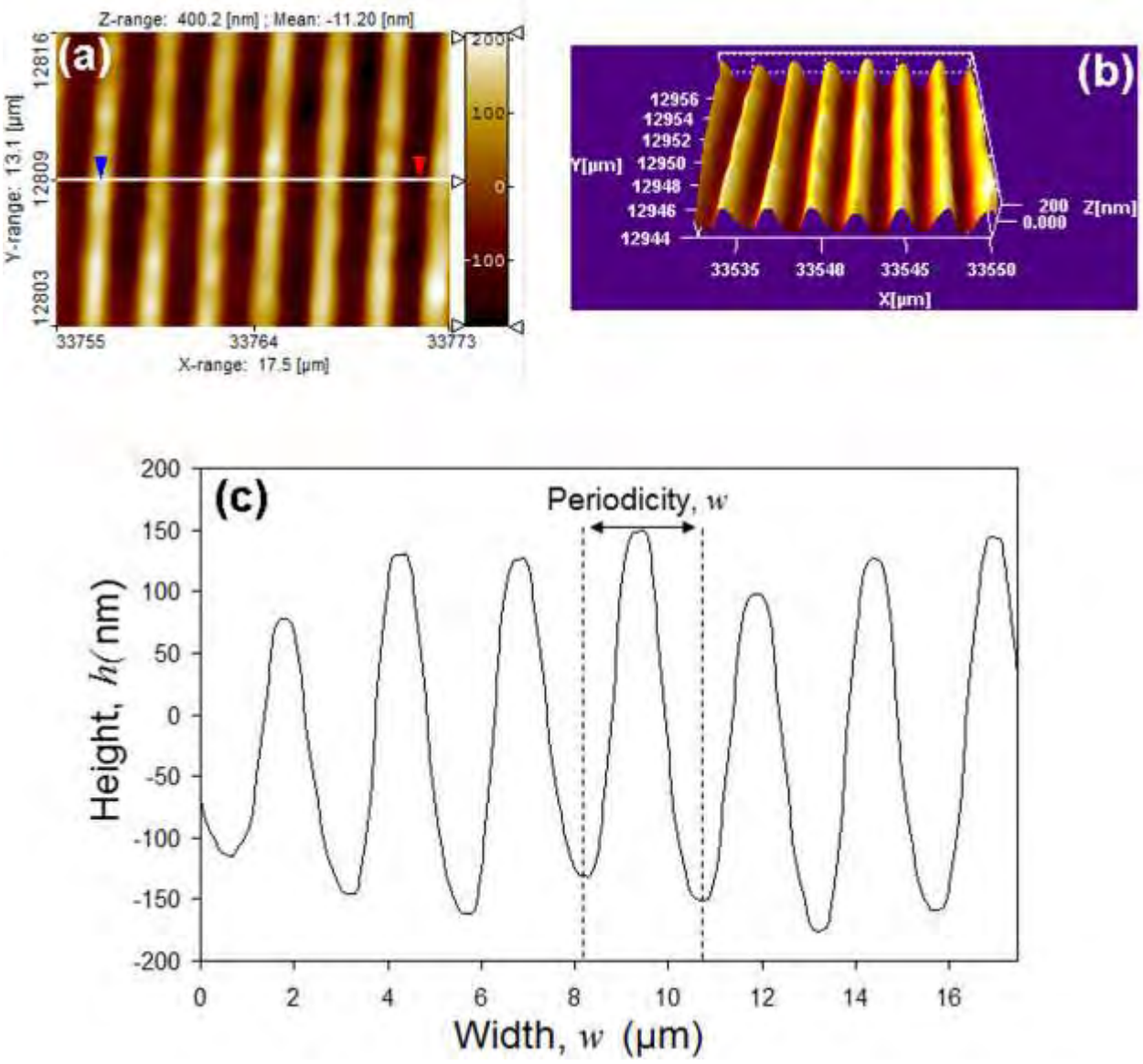


Figure 6.5 Groove pattern on Ti-6Al-4V obtained by LIP technique using a laser fluence of 760.35 J/cm^2.(a) 2-dimensional morphological evolution, (b) 3-dimensional morphological evolution, and (c) variation in height and width (across the line scan) of the features obtained using a one step irradiation **[80]**.

Table 6.2 Process power and corresponding height of the groove/pillar pattern and contact angle related to interference-patterned samples **[80].**

Sample	Laser fluence (mJ/ cm^2)	Height, h (nm)	Apparent contact angle, θ^* (°)	
			Distilled water	SBF
Groove pattern on Ti-6Al-4V	760.35	208.08±0.08	78.55±0.45	67.4±0.60
	525.47	71.35±0.02	73.45±0.55	64.2±0.80
	362.26	68.08±0.02	70.7±0.30	60.2±0.80
Pillar pattern on Ti-6Al-4V	760.35	77.65±1.07	78.45±0.55	66.8±0.20
	525.47	44.14±1.04	77.45±0.55	66.6±0.40
	362.26	36.68±1.03	77.9±0.10	67.1±0.90
Ti-6Al-4V Control	-	-	Chemical angle θ (°)	
			Distilled water	SBF
			67.98±0.02	59.2±0.80

6.2.2 Wetting behavior of the samples

Contact angle measurements on both the groove and pillar patterns were conducted using distilled water and SBF. Selected images of the droplet shadow on the goniometer are presented in Figure 6.7 **[80]**. It can be observed that the distilled water droplet (Figure 6.7a, 6.7b, and 6.7c corresponding to flat, grove patterned, and pillar patterned Ti-6Al-4V, respectively) subtended a higher contact angle compared to the SBF droplet (Figure 6.7d , 6.7e, and 6.7f corresponding to flat, grove patterned, and pillar patterned Ti-6Al-4V respectively). The chemical angle or the Young angle, θ on the flat Ti-6Al-4V averaged around 67.98° for distilled water and 59.2° for SBF (Table 6.2) **[80]**. Further, it was observed that there was a decrease in the apparent contact angle (contact angle affected by both the surface chemistry and surface topography), θ^* (using SBF and distilled water) with decreasing laser power for the groove like pattern, however, no such distinct trend was observed for the pillar pattern. This disparity is mostly due to their geometrical structure (groove and pillar feature) and can be justified based on the Cassie and Baxter model. According to the Cassie and Baxter model, the apparent contact angle, θ^* on a surface with chemical patch work or rough features entrapped with air is given as **[121].**

$$\cos\theta^* = f_1 \cos\theta_1 + f_2 \cos\theta_2 \quad \text{.....6.1}$$

Here f_1 and f_2 represents the surface area fraction of the liquid in contact with the solid and air respectively and θ_1 and θ_2 represents their corresponding contact angles. Hence, according to their model, when a liquid drop is placed on a composite surface with solid and air patches in it, the liquid does not follow the surface contours and sits upon the composite surface as it is pushed by the air. As the grooves in the groove pattern are bridged by certain amount of material, air entrapment within them is more feasible. Also with increasing laser fluence there is an increase

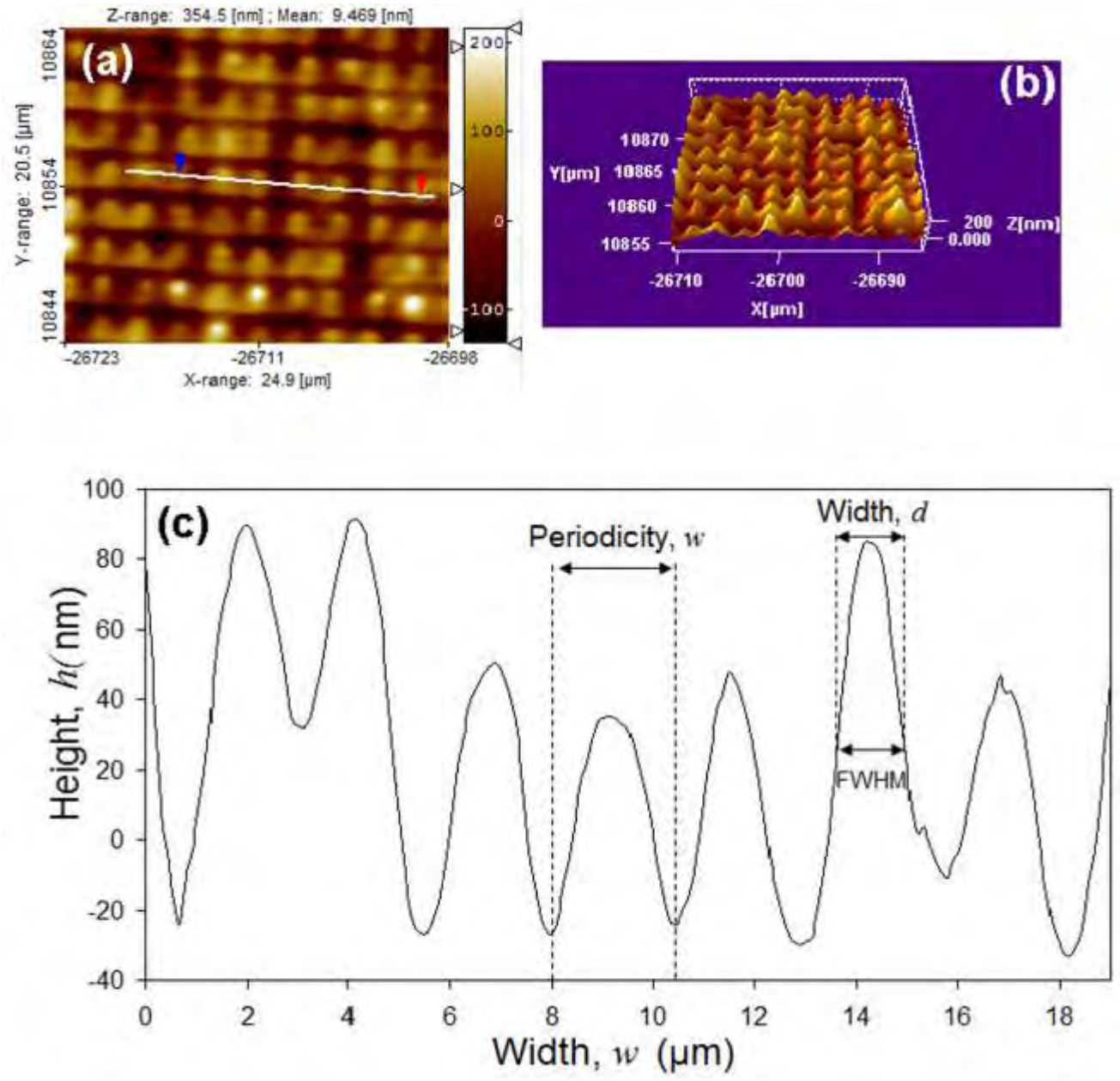


Figure 6.6 Pillar pattern on Ti-6Al-4V by laser interference technique (3.82 W laser power)(a) 2-dimensional morphological evolution (b) 3-dimensional morphological evolution and (c) variation in height and width at FWHM (across the line scan) of the features obtained using a two step irradiation **[80]**.

in the height, h of the groove (width, w of the groove is constant) and thereby an increased volume of trapped air pockets resulted in an increase in apparent contact angle, θ^*. In contrast, for the pillar pattern, there is an open volume within the pillars and hence air entrapment may not be possible. Further, as there is not much variation in the height, h of the pillar (width, d and periodicity, w of the pillars being constant) with increasing laser power, their roughness factor $R_f = 1+ 2\frac{h}{d}$ (ratio of the solid area to its projected area as explained later) did not vary much and hence, a noticeable change in the apparent contact angle could not be expected.

Also from the droplet shadow images (Figure 6.7) **[80]** and from Table 6.2 **[80]** it can be realized that there is an increase in apparent contact angle, θ^* for the interference patterned samples compared to the chemical angle (contact angle subtended on a non textured polished sample and is only a function of the surface chemistry) on the flat sample. Therefore, the presence of groove and pillar features generated using laser interference technique with the present set of processing parameters (Table 6.2) resulted in tuning the surface towards a less hydrophilic behavior. This reduced wettability on the patterned samples can further be explained with the thermodynamic models as discussed below.

Here for the ease of calculations, based on energy balance equations, the grooves are approximated to be of triangular type (Figure 6.8a) **[80]** and pillars to be of cylindrical type (Figure 6.8b) **[80]**. Applying an energy minimum condition it can be hypothesized that liquid progression into a groove like pattern is favorable if the apparent contact angle θ^* or chemical

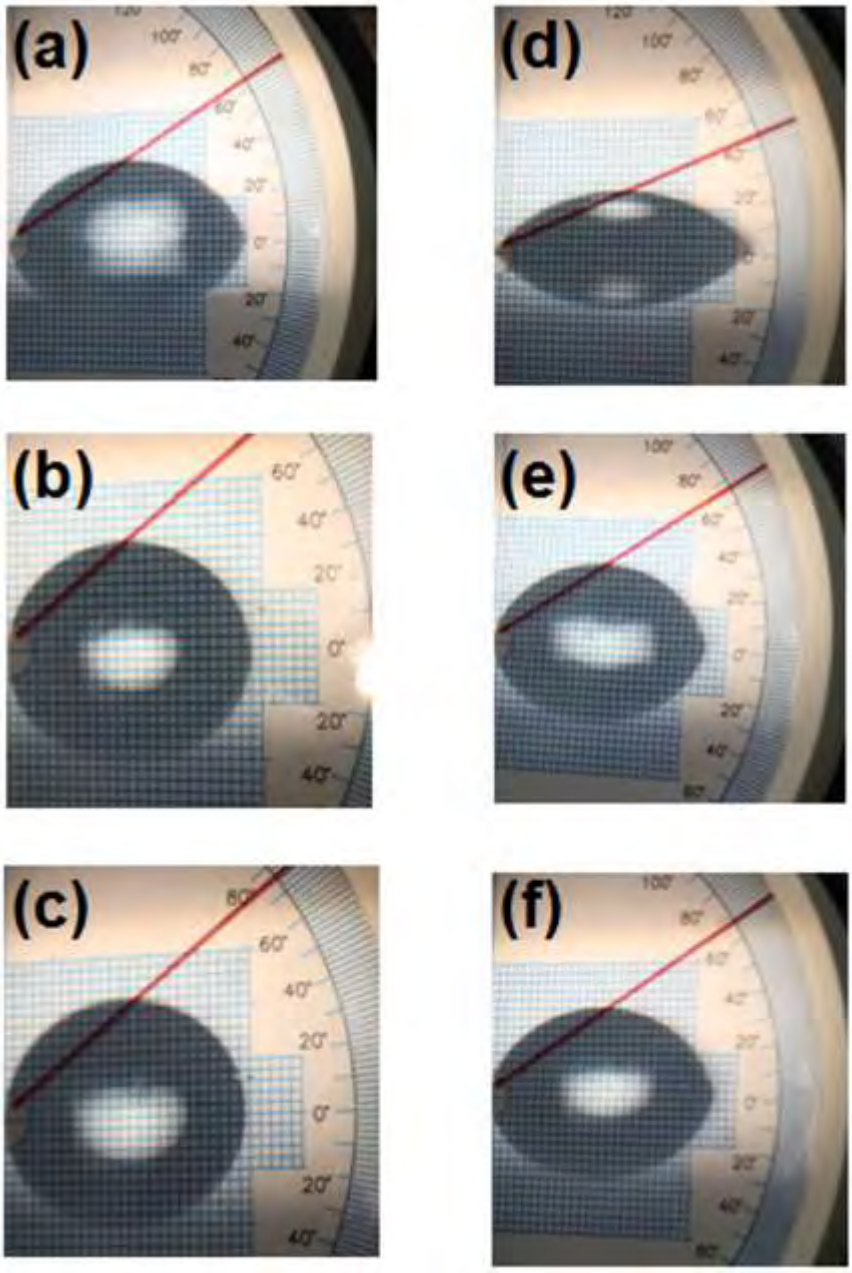


Figure 6.7 Light optical images of the distilled water droplet shadow on (a) flat Ti-6Al-4V, (b) groove patterned Ti-6Al-4V, and (c) pillar patterned Ti-6Al-4V; and light optical images of the SBF droplet shadow on (d) flat Ti-6Al-4V, (e) grove patterned Ti-6Al-4V, and (f) pillar patterned Ti-6Al-4V **[80]**.

angle θ is smaller than the critical angle θ_c for wetting, where θ_c is given as **[122]**:

$$\cos\theta_c = \frac{w}{2(h^2 + \frac{w^2}{4})^{\frac{1}{2}}} = \frac{1}{\sqrt{1+\frac{4h^2}{w^2}}} \quad \text{.....6.2}$$

Therefore, for groove texture the critical angle for wetting depends on the roughness factor R_f $= \sqrt{1+\frac{4h^2}{w^2}}$ (ratio of the actual surface area to apparent surface area).

In contrast, a surface with an assembly of pillar-like patterns (Figure 6.8b) is characterized by Φ_s (solid fraction remaining dry) and roughness factor $R_f = 1 + 2\frac{h}{d}$ (ratio of the actual solid area to its projected area). The critical angle θ_c for wetting on such a surface is given as **[122]**:

$$\cos\theta_c = \frac{1-\phi_S}{R_f - \phi_S} \quad \text{.....6.3}$$

The roughness factor R_f was calculated for both groove and pillar patterns from the geometrical parameters (w, h, and d) of the features obtained using laser based interference technique, and plotted as a function of laser fluence (Figure 6.9a) **[80]** . It can be observed (Figure 6.9a) that there is a slight increase in R_f with increasing laser fluence for both the groove and pillar patterns, and R_f is higher for the pillar patterns compared to the groove pattern. This increased value of roughness factor (R_f >1) for the pillar pattern is attributed to reduced width, d of the features as a result of the two step processing involved in this technique. Further, the critical wetting angle (θ_c) based on the above equations (6.2 and 6.3) was calculated for both the groove and pillar patterns and plotted as a function of laser fluence (Figure 6.9b) **[80]**. The critical wetting angle (θ_c) increased with increasing laser fluence for both the patterns and the values of critical wetting angle (ranging from 3° to 48°) are smaller compared to the chemical or the Young angles (θ, measured on the flat Ti-6Al-4V samples) using both distilled water and SBF.

As a result the condition for wetting (θ^* or $\theta < \theta_c$) is not satisfied in both the cases (pillar and groove) and hence, the liquid dewets on both the patterns due to an increase in apparent contact angle (θ^*). Owing to the above reasons the samples were not further tested for its in vitro bioactivity and in vitro biocompatibility. However, there are an ongoing efforts to identify appropriate combinations of laser interference processing parameters to obtain surface textures at appropriate length scales and thereby improve its wettability.

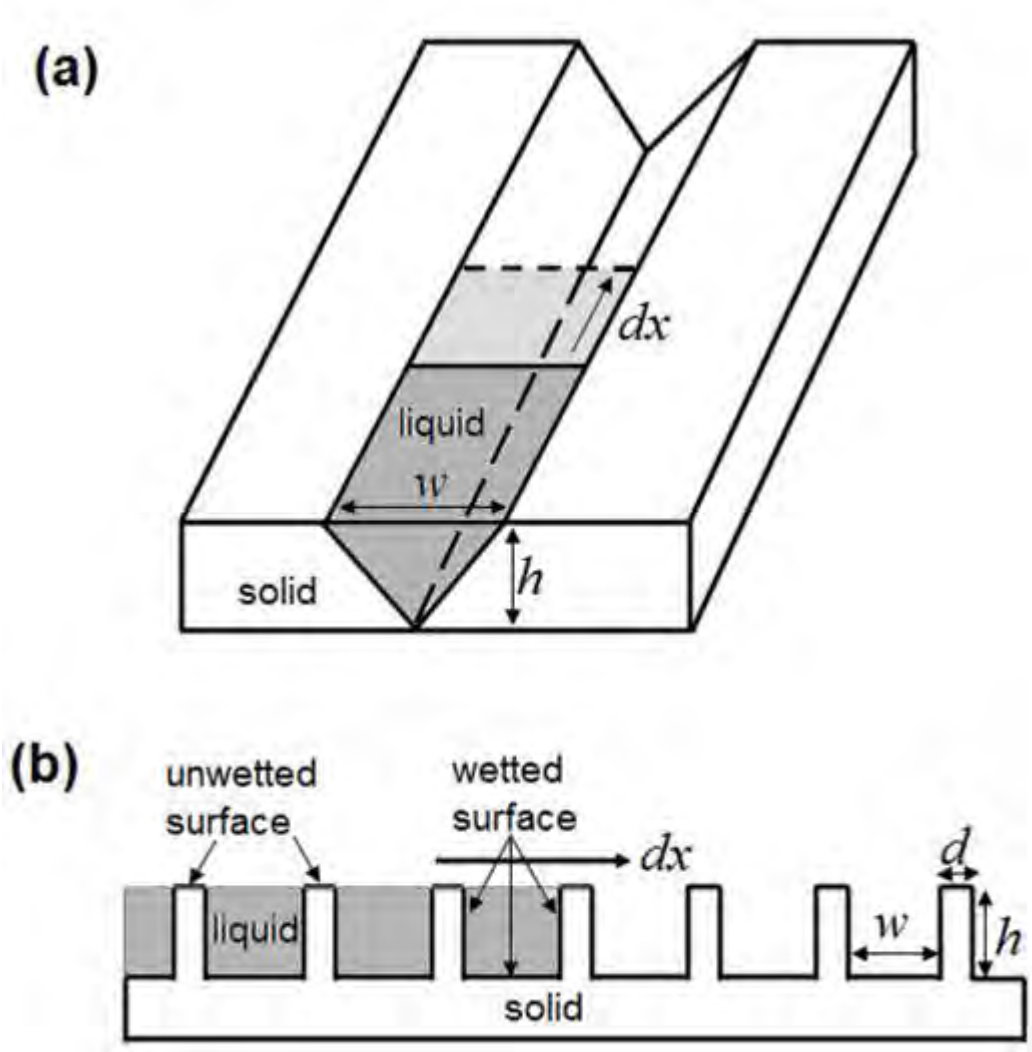


Figure 6.8 Schematic illustration of liquid invasion into a (a) groove pattern and (b) pillar pattern **[80]**.

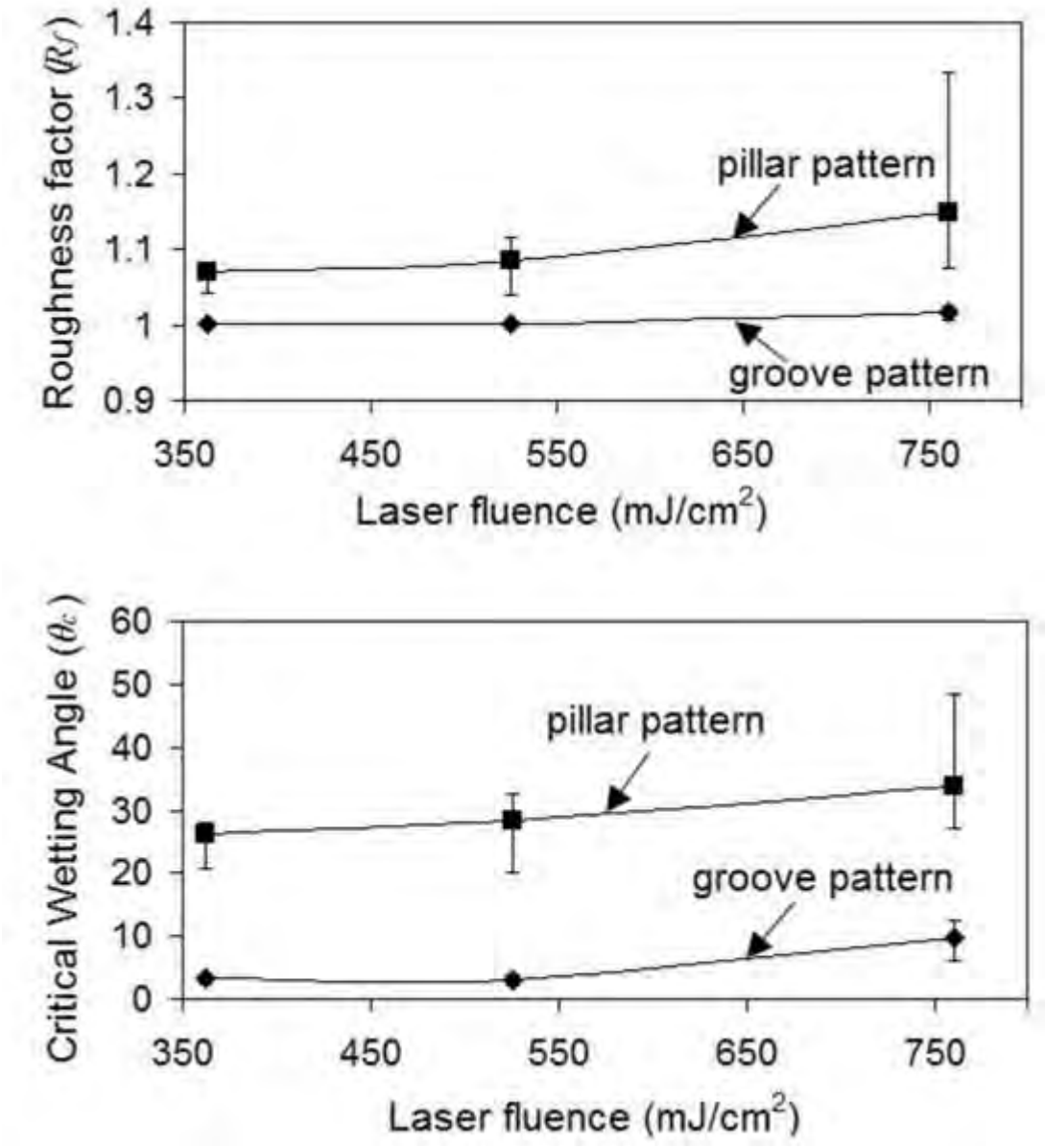


Figure 6.9 (a) variation in roughness factor,R_f and (b) critical wetting angle, θ_c with laser fluence for interference patterned samples **[80]**.

Chapter 7

Conclusions and Scope for Further Work

7.1 Conclusions

- Laser textured Ca-P coatings demonstrated improved wettability to physiological fluids.
- With a decrease in texture parameter (σ_A/λ) there is an increase in surface energy and improved wettability for the laser textured Ca-P coatings.
- XRD studies of the laser textured samples showed the presence of presence of beneficial biocompatible phases such as $CaTiO_3$, TiO_2, α-TCP and $Ca_5(OH)(PO_4)_3$ within the coatings.
- Improved bioactivity of the textured coatings was proved by the formation of an apatite like phase following immersion in SBF.
- XPS and FTIR analysis of the mineralized samples confirmed for the presence of HA on the surface of the sample.
- Improved in vitro biocompatibility on the textured coated samples was characterized by the increased proliferation and spreading of the mouse MC3T3-E1 osteoblast-like cells.
- In a preliminary effort, the role of SiO_2 doping in improving the wettability, and thereby it's in vitro bioactivity and in vitro biocompatibility of the HA coatings was demonstrated.
- To upgrade the above laser based melting technique, a newer technique based on a single step process known as LIP is also introduced.

- The groove and pillar patterns obtained using the LIP technique resulted in an increase in apparent contact angle.
- The nano scale features (grooves and pillars) obtained using the LIP technique created pinning effects on the liquid drop and thereby resulted in the decrease in critical wetting angle.
- Hence a concomitant change in surface morphology along with appropriate topographical cues is necessary to improve the wettability and thereby the in vitro bioactivity and in vitro biocompatibility.
- For pulsed laser processing, with increasing laser scan speed and laser pulse frequency there is always an improvement in biomineralization and not much difference in weight change following immersion in SBF is observed by varying these two processing parameters.
- As compared to the pulsed laser direct melting technique, the retainment of precursor HA within the coating was much viable under CW laser direct melting process.
- Under the set of laser processing parameter employed in the current work the improvement in wettability was better for the samples processed using the direct melting technique as compared to the LIP technique.

7.2 Scope for further work

- Long term cell culture studies to study the cell viability and cell differentiation.
- Culture of mesenchymal stem cells on the textured coated samples and quantify its differentiation to form bone cells (osteoblasts).
- Revise the interference patterning technique to provide surfaces with better wettability.

- Study the mineralization kinetics or in vitro bioactivity of the interference patterned samples.
- Understand the MC3T3-E1 osteoblast-like cell interaction mechanism on the groove and pillar like patterns.

List of References

1. K.C. Dee, D.A. Puleo, R. Bizios. Tissue biomaterial interactions, 2nd edition, chapter 1, New York, Wiley-Liss, 2008.
2. S.R. Paital, N.B. Dahotre. Calcium phosphate coatings for bio-implant applications: Materials, performance factors and methodologies, Materials Science and Engineering R, 66, 1-70, 2009.
3. B. D. Ratner, A. S. Hoffman, F J. Schoen, J. E. Lemons. Biomaterials science: An introduction to Materials in Medicine, 2nd edition, Chapter 7, San Diego, California, Elsevier academic press, 2004.
4. Source: www.zimmer.com
5. Source: http://www.thehipkneesurgeon.com/jointKnee.php
6. Source: http://www.djosurgical.com/products/shoulder/rsp/index.htm
7. Source: Med Market diligence
8. David F. Williams. Biocompatibility of Clinical Implant Materials, CRC Press, 1st edition, 1981.
9. Chun-Che Shih, Chun-Ming Shih, Yea-Yang Su, Mau-Song Chang and Shin-Jong Lin. Characterization of thrombogenic potential of surface oxides on stainless steel for implant purposes, Applied Surface Science, 219, 347-362, 2003.
10. I. Ozbek, B.A. Konduk, C. Bindal, A.H. Ucisik. Characterization of borided AISI 316L stainless steel implant, Vacuum, 65, 521-525, 2002.

11. J. Beddoes and K. Bucci. The influence of surface condition on the localized corrosion of 316L stainless steel orthopaedic implants, Journal of materials science: materials in medicine, 10, 389-394, 1999.
12. David R. Haynes, Tania N. Crotti and Michael R. Haywood. Corrosion of and changes in biological effects of cobalt chrome alloy and 316L stainless steel prosthetic particles with age, Journal of Biomedical Materials Research, 49, 167-175, 2000.
13. Karim Bordji, Jean-Yves Jouzeau, Didier Mainard, Elisabeth Payan, Jean-Pierre Delagoutte and Patrick Netter. Evaluation of the effect of three surface treatments on the biocompatibility of 316L stainless steel using human differentiated cells, Biomaterials, 17, 491-500, 1996.
14. T.M. Sridhar, U. Kamachi Mudali and M. Subbaiyan. Preparation and characterization of electrophoretically deposited hydroxyapatite coatings on type 316L stainless steel, Corrosion Science, 45, 237-252, 2003.
15. J. Walczak, F. Shahgaldi and F. Heatley. In vivo corrosion of 316 L stainless-steel hip implants: morphology and elemental composition of corrosion products, Biomaterials, 19, 229-237, 1998.
16. Jeong Sik Choi and Duk Yong Yoon. The temperature dependence of abnormal grain growth and grain boundary faceting in 316L stainless steel, ISIJ International, 41, 478-483, 2001.
17. Chun-Che Shih, Chun-Ming Shih, Yea-Yang Su, Lin Hui Julie Su, Mau-Song Chang, and Shin-Jong Lin. Effect of surface oxide properties on corrosion resistance of 316L stainless steel for biomedical applications, Corrosion science, 46, 427-441, 2004.

18. L.Z. Zhuang and E.W. Langer. Effects of cooling rate control during the solidification process on the microstructure and mechanical properties of cast Co-Cr-Mo alloy used for surgical implants, Journal of Materials Science, 24, 381-388, 1989.
19. Mitsuo Ninomi. Recent metallic materials for biomedical applications, Metallurgical and Materials Transactions A, 33A, 477-486, 2002.
20. J. Cawley, J.E.P. Metcalf, A.H. Jones, T.J. Band, and D.S. Skupien. A tribological study of cobalt chromium molybdenum alloys used in metal-on-metal resurfacing hip arthroplasty, Wear, 255, 999-1006, 2003.
21. T. Seshacharyulu, S.C. Medeiros, W.G. Frazier, and Y.V.R.K. Prasad. Hot working of commercial Ti-6Al-4V with an equiaxed α-β microstructure: materials modeling considerations. Materials Science and Engineering A, 284, 184-194, 2000.
22. Y.G. Ko, W.S. Jung, D.H. Shin, and C.S. Lee. Effects of temperature and initial microstructure on the equal channel angular pressing of Ti-6Al-4V alloy, Scripta Materialia, 48, 197-202, 2003.
23. S.L. Semiatin, V. Seetharaman, and I.Weiss. Flow behavior and globularization kinetics during hot working of Ti-6Al-4V with a colony alpha microstructure, Materials Science and Engineering A, 263, 257-271, 1999.
24. Black J. Does corrosion matter?, J bone and joint surgery 70B, 517-520, 1988.
25. A. Choubey, R. Balasubramaniam, and B.Basu. Effect of replacement of V by Nb and Fe on the electrochemical and corrosion behavior of Ti-6Al-4V in simulated physiological environment, Journals of Alloys and Compounds, 381, 288-294, 2004.
26. M.A. Khan, R.L. Williams, and D.F. Williams. The corrosion behavior of Ti-6Al-4V, Ti-6Al-7Nb and Ti-13Nb-13Zr in protein solutions, Biomaterials, 20, 631-637, 1999.
27. M.C. Bottino, P.G. Coelho, M. Yoshimoto, B. König Jr., V.A.R. Henriques, A.H.A. Bressiani, and J.C. Bressiani. Histomorphologic evaluation of Ti-13Nb-13Zr alloys processed via powder metallurgy. A study in rabbits, Materials Science and Engineering C, 28, 223-227, 2008.
28. Source: www.devicelink.com
29. Source: http://www.genesis-tech.ch/company/
30. Source: http://tc.engr.wisc.edu/UER/uer01/author1/content.html
31. Source: http://www.jri-ltd.co.uk/total_knee_replacement.asp
32. K de Groot, J G C Wolke, and J A Jansen. Calcium phosphate coatings for medical implants, Proceedings Institute of Mechanical Engineers, 212, 137-147, 1998.

33. R. Detsch, H. Mayr, and G.Ziegler. Formation of ostoclast-like cells on HA and TCP ceramics, Acta Biomaterialia, 4, 139-148, 2008.
34. E.Gyorgy, S.Grigorescu, G.Socol, I.N. Mihailescu, D.Janackovic, A. Dindune, Z.Kanepe, E. Palcevskis, E.L. Zdrentu, and S.M. Petrescu. Bioactive glass and hydroxyapatite thin films obtained by pulsed laser deposition, Applied Surface Science, 253, 7981-7986, 2007.
35. Hae-Won Kim, Hyoun-E Kim, Vehid Salih, and Jonathan C.Knowles. Dissolution control and cellular responses of calcium phosphate coatings on zirconia porous scaffold. Journal of Biomedical Materials Research, 68A, 522-530, 2004.
36. L. Clέries, J.M. Fernάndez-Pradas, and J.L. Morenza. Bone growth and resorption of calcium phosphate coatings obtained by pulsed laser deposition, Journal of Biomedical Materials Research, 49, 43-52, 2000.
37. Min Wang. Developing bioactive composite materials for tissue replacement, Biomaterials, 24, 2133-2151, 2003.
38. J.R. Davis (2003). Handbook of materials for medical devices, 1st edition, ASM International.
39. Lissa A. Pruitt. Deformation, yielding, fracture and fatigue behavior of conventional and highly cross-linked ultra high molecular weight polyethylene, Biomaterials, 26, 905-915, 2005.
40. Marc Long, and H.J. Rack. Titanium alloys in total joint replacement- a materials science perspective, Biomaterials, 19, 1621-1639, 1998.
41. Chia-Wei Lin, Chien-Ping Ju, and Jiin-Huey Chern Lin. A comparison of the fatigue behavior of cast Ti-7.5 Mo with c.p. titanium, Ti-6Al-4V and Ti-13Nb-13Zr alloys, Biomaterials, 26, 2899-2907, 2005.
42. P. Bills, L. Blunt, and X. Jiang. Development of a technique for accurately determining clinical wear in explanted total hip replacements, Wear, 263, 1133-1137, 2007.
43. M. Semlitsch and H.G. Willert. Clinical wear behavior of ultra-high molecular weight polyethylene cups paired with metal and ceramic ball heads in comparison to metal-on-metal pairings of hip joint replacements, Processing Institute of Mechanical Engineers, 211, 73-88, 1997.
44. J. Nevelos, E. Ingham, C. Doyle, R. Streicher, A. Nevelos, W.Walter, and J. Fisher. Microseparation of the centers of alumina-alumina artificial hip joints during simulator testing

produces clinically relevant wear rates and patterns, The journal of arthroplasty, 15, 793-795, 2000.

45. Manuela Teresa Raimondi, and Riccardo Pietrabissa. The in-vivo wear performance of prosthetic femoral heads with titanium nitride coating, Biomaterials, 21, 907-913, 2000.
46. E. Ingham, and J. Fisher. Biological reactions to wear debris in total joint replacement, Processing Institute of Mechanical Engineers, 214, 21-37, 2000.
47. S. Affatato, M.Goldoni, M.Testoni, and A. Toni. Mixed oxides prosthetic ceramic ball heads. Part 3: effect of the ZrO2 fraction on the wear of ceramic on ceramic hip joint prostheses. A long-term in vitro wear study, Biomaterials, 22, 717-723, 2001.
48. M.A.L. Hernández-Rodríguez, R.D. Mercado-Solís, A.J. Pérez-Unzueta, D.I. Martinez-Delgado, and M.Cantú-Siuentes. Wear of cast metal-metal pairs for total replacement hip prostheses, Wear, 259, 958-963, 2005.
49. A.Wang, S. Yue, J.D. Bobyn, F.W. Chan, and J.B. Medley. Surface characterization of metal-on-metal hip implants tested in a hip simulator, Wear, 225-229, 708-715, 1999.
50. Molly M. Stevens and Julian H. George. Exploring and engineering the cell surface interface, Science, 310, 1135-1138, 2005.
51. Yoshihiro Ito. Surface micropatterning to regulate cell functions, Biomaterials, 20, 2333-2342, 1999.
52. E.Wintermantel, J.Mayer, J. Blum, K.L. Eckert, P. Lüscher, and M. Mathey. Tissue engineering scaffolds using superstructures, Biomaterials, 17, 83-91, 1996.
53. F.H. Jones. Teeth and bones: applications of surface science to dental materials and related biomaterials, Surface Science Reports, 42, 75-205, 2001.
54. Matthew Tirrell, Efrosini Kokkoli, and Markus Biesalski. The role of surface science in bioengineered materials, Surface Science, 500, 61-83, 2002.
55. Hyeongil Kim, Seong-Ho Choi, Jae-Jun Ryu, Seung-Yong Koh, Ju-Han Park, and In-Seop Lee. The biocompatibility of SLA-treated titanium implants, Biomedical Materials, 3, 1-6, 2008.
56. B.O. Arronson, J. Lausmaa, and B. Kasemo. Glow discharge plasma treatment for surface cleaning and modification of metallic biomaterials. Journal of Biomedical Materials Research, 35, 49-73, 1997.
57. Takao Hanawa. In vivo metallic biomaterials and surface modification, Materials Science and Engineering A, 267, 260-266, 1999.

58. Zhen-Mei Liu, Zhi-Kang Xu, Jian-Qin Wang, Jian Wu, and Jun-Jie Fu. Surface modification of polypropylene microfiltration membranes by graft polymerization of N-vinyl-2-pyrrollidone, European Polymer Journal, 40, 2077-2087, 2004.
59. Fu Zhang, E.T. Kang, K.G. Neoh, Peng Wang, and K.L. Tan. Surface modification of stainless steel by grafting of poly (ethylene glycol) for reduction in protein adsorption, Biomaterials, 22, 1541-1548, 2001.
60. Inn-Kyu Kang, Oh Hyeong Kwon, Young Moo Lee, and Yong Kiel Sung. Preparation and functional characterization of functional group-grafted and heparin-immobilized polyurethanes by plasma glow discharge, Biomaterials, 17, 841-847, 1996.
61. Joerg C. Tiller, Gary Bonner, Li-Chun Pan, and Alexander M. Klibanov. Improving biomaterials properties of collagen films by chemical modification, Biotechnology Bioengineering, 73, 246-252, 2001.
62. Yasuhiko Iwasaki and Nobuyuki Saito. Immobilization of phosphorylcholine polymers to Ti-supported vinyldimethylsilyl monolayers and reduction of albumin adsorption, Colloids and Surfaces B: Biointerfaces, 32, 77-84, 2003.
63. B. León and J.A. Jansen. Thin calcium phosphate coatings for medical implants, Springer, 2nd edition, New York, USA, 2009.
64. G.J. Cheng, D. Pirzada, M. Cai, P. Mohanty, A. Bandyopadhyay. Bioceramic coating of hydroxyapatite on titanium substrate with Nd:YAG laser. Mater. Sci. Eng. C, 25, 541-547, 2005.
65. F. Lusquiños, J. Pou, J.L. Arias, M. Boutinguiza, M. Pérez-Amor, B. León, F.C.M. Driessens. Production of calcium phosphate coatings on Ti6Al4V obtained by Nd:yttrium-aluminum-garnet laser cladding. Journal of Applied Physics, 90, 4231-4236, 2001.
66. F. Lusquiños, A. De Carlos, J. Pou, J.L. Arias, M. Boutinguiza, B. León, M. Pérez-Amor, F.C.M. Driessens, K. Hing, I. Gibson, S. Best, W. Bonfield. Calcium phosphate coatings obtained by Nd:YAG laser cladding: Physicochemical and biologic properties. Journal of Biomedical Materials Research, 64A,630-637, 2003.
67. D. Wang, C. Chen, J. Ma, G. Zhang. In situ synthesis of hydroxyapatite coating by laser cladding. Colloids and Surfaces B: Biointerfaces, 66, 155-162, 2008.

68. M. Roy, B.V. Krishna, A. Bandyopadhyay, S. Bose. Laser processing of bioactive tricalcium phosphate coating on titanium for load-bearing implants. Acta Biomaterialia, 4, 324-333, 2008.
69. Y. Zhang, J. Gao, J. Tan, Z. Zou. Laser surface coating of a bioceramic composite layer. Surface and Coatings Technology, 58, 125-127, 1993.
70. S.R. Paital, N.B. Dahotre. Wettability and kinetics of hydroxyapatite precipitation on a laser-textured Ca-P bioceramic coating. Acta Biomaterialia, 5, 2763-2772, 2009.
71. S.R. Paital, W. He, N. B. Dahotre. Laser pulse dependent micro textured calcium phosphate coatings for improved wettability and cell compatibility. Accepted to Journal of Materials Science: Materials in Medicine, 2010, doi: 10.1007/s10856-010-4085-6
72. S.R. Paital, Z. Cao, W. He, N. B. Dahotre. Wetting effects on in vitro bioactivity and in vitro biocompatibility of laser micro-textured Ca-P coating. Biofabrication, 2 ,2010, doi:1758-5082/10/000000+14
73. S.R. Paital, W. He,C. Daniel, N. B. Dahotre. Laser process effect on the texture evolution and wetting behavior in implantable Ti-6Al-4V alloys. Accepted to Journal of Materials JOM, 2010.
74. J. Weng, Q. Liu, J.G.C. Wolke, X.D. Zhang, K. de Groot. Formation and characteristics of the apatite layer on plama-sprayed hydroxyapatite coatings in simulated body fluid. Biomaterials, 18, 1027-1035, 1997.
75. H.G. Bang, S.J. Kim, S.Y. Park. Biocompatibility and the physical properties of bio-glass ceramics in the Na2O-CaO-SiO2-P2O5 system with CaF2 and MgF2 additives. Journal of Ceramic Processing Research, 9,588-590, 2008.
76. J.H. Hristov, B.I. Bogdanov, I.G. Chomakov, I.G. Markov, I.G. Markovska. Drawing standard curve for quantitative determination of the crystalline phase in wollastonite glass ceramics. Journal of the Balkan Tribological Association, 15, 347-354, 2009.
77. S.W. Choi, S.H. Hong, Y.J. Kim. Characterization of Ca_2SiO_4: Eu2+ phosphors synthesized by Polymeric Precursor Process. Journal of the American Ceramic Society, 92,2025-2028, 2009.

78. Y. Tanizawa, T. Suzuki. Effects of silicate ions on the formation and transformation of calcium phosphates in neutral aqueous solutions. J Chem Soe Faraday Trans, 91, 3499-3503, 1995.
79. J. Damen, J. Ten Cate. Silica-induced precipitation of calcium phosphate in the presence of inhibitors of hydroxyapatite formation. J Dent Res, 71,453-457, 1992 .
80. N.B. Dahotre, S.R. Paital, Anoop N. Samant, Claus Daniel. Wetting behavior of laser synthetic surface micro textures on Ti-6Al-4V for bioapplication. Philosophical Transactions of the Royal Society A, 2010, doi: 10.1098/rsta. 2010.0003.
81. A. Lasagni, M. Nejati, R. Clasen and F. Mucklich. Periodical surface structuring of metals by laser interference metallurgy as a new fabrication method of textured solar selective absorbers. Advanced Engineering Materials, 8, 580-584, 2006.
82. C. Daniel, F.Mucklich and Z. Liu. Periodical micro-nano-structuring of metallic surfaces by interfering laser beams. Applied Surface Science, 208-209, 317-321, 2003.
83. X.B. Zhou, and J.Th.M. De Hosson. Influence of surface roughness on the wetting angle. Journal of Materials Research, 10, 1984-1992, 1995.
84. G.M. Pharr. Measurement of mechanical properties by ultra low indentation. Materials Science and Engineering A, 253, 151-159, 1998.
85. Xiaodong Li and Bharat Bhusan. A review of nanoindentation continuous stiffness measurement technique and its applications. Materials Characterization, 48, 11-36, 2002.
86. Xi Chen, Jin Yan and Anette M. Karlsson. On the determination of residual stress and mechanical properties by indentation. Materials Science and Engineering A, 416, 139-149, 2006.
87. R. Singh, A. Kurella, and N. B. Dahotre. Laser surface modification of Ti-6Al-4V: Wear and corrosion characterization in simulated biofluid, Journal of Biomaterial Applications, 21, 49-73, 2006
88. C.J. Van Oss, R.J. Good, M.K. Chaudhury. Additive and non additive surface tension components and the interpretation of contact angles. Langmuir, 4, 884-891, 1988.

89. L.K. Randeniya, A. Bendavid, P.J. Martin, M.S. Amin, E.W. Preston, F.S.M. Ismail, S. Coe. Incorporation of Si and SiO_x into diamond-like carbon films: Impact on surface properties and osteoblast adhesion. Acta Biomaterialia, 5, 1791-1797, 2009.
90. C.J. Van Oss, R.F. Giese Jr., R.J. Good. Reevaluation of the surface tension components and parameters of polyacetylene from contact angle of liquids. Langmuir, 6,1711-1713, 1990.
91. B.Ø. Palson, S.N. Bhatia. Tissue Engineering, 1st edition, Pearson Prentice Hall, New Jersey, p 252-255, 2004.
92. C.S. Chen, M. Mrksich, S. Huang, G.M. Whitesides, D.E. Ingber. Geometric control of cell life and death. Science, 276, 1425-1428, 1997.
93. A. Kurella and N. B. Dahotre. Laser induced hierarchical calcium phosphate structures. Acta Biomaterialia, 2, 677-683, 2006.
94. B. Kasemo. Biological Surface Science. Surface Science, 500, 656-677, 2002.
95. H. Assender, V. Bliznyuk, K. Porfyrakis. How surface topography relates to materials properties. Science, 297, 973-976, 2002.
96. M. P. Lutolf, J. A. Hubbell. Synthetic biomaterials as instructive extracellular microenvironments for morphogenesis in tissue engineering. Nature biotechnology, 23, 47-55, 2005.
97. S.R. Paital, K. Balani, A. Agarwal, N.B. Dahotre. Fabrication and evaluation of a pulse laser-induced Ca-P coating on a Ti alloy for bioapplication. Biomaedical Materials, 4, 1-10, 2009.
98. S.W. Bang, R.M. Lec, J.M. Genco, J.C. Ransdell. Acoustic emission chemical sensor. IEEE Ultrasonics Symposium Proc, 439-443, 1993.
99. Y.W. Gu, K.A. Khor, and P. Cheang. In-vitro studies of plasma sprayed hydroxyapatite/Ti-6Al-4V composite coating in simulated body fluid (SBF). Biomaterials, 24, 1603-1611, 2003.
100. U. Pettersson and S. Jacobson. Influence of surface texture on boundary lubricated sliding contacts. Tribology International, 36, 857-864, 2003.
101. K.C. Baker, J.Drelich, I. Miskioglu, R.Israel, H.N. Herkowitz. Effect of polyethylene pretreatments on the biomimetic deposition and adhesion of calcium phosphate films. Acta Biomaterialia, 3, 391-401, 2007.

102. S.J. Hitchcock, N.T. Carroll, M.G. Nicholas. Some effects of substrate roughness on wettability. Journal of Materials Science, 16, 714-732, 1981.
103. J.F. Oliver, S.G. Mason. Liquid spreading on rough metal surfaces. Journal of Materials Science, 15, 431-437, 1980.
104. J.D. Miller, S. Veeramasuneni, J. Drelich, M. R. Yalamanchili, G. Yamauchi. Effect of roughness as determined by atomic force microscopy on the wetting properties of PTFE thin films. Polymer Engineering and Science, 36, 1849-1855, 1996.
105. J. E. Ellingsen. A study on the mechanism of protein adsorption to TiO_2. Biomaterials, 12, 593-596, 1991.
106. S. R. Paital, N. B. Dahotre. Laser surface treatment for porous and textured Ca-P bio-ceramic coating on Ti-6Al-4V. Biomedical Materials, 2, 274-281, 2007.
107. Y. E. Greish, P. W. Brown. Phase evolution during the formation of stoichiometric hydroxyapatite at 37.4 °C. Journal of Biomedical Materials Resesarch Part B: Applied Biomaterials, 67B, 632-637, 2003.
108. X. Liu, C. Ding, P. K. Chu. Mechanism of apatite formation on wollastonite coatings in simulated body fluids. Biomaterials, 25, 1755-1761, 2004.
109. K. Yamashita, N. Oikawa, Takao Umegaki. Acceleration and deceleration of bone-like crystal growth on ceramic hydroxyapatite by electric poling. Chemistry of Materials, 8, 2697-2700, 1996.
110. M. Karanjai, R. Sundaresan, T. R. R. Mohan, B. P. Kashyap. Evaluation of growth of Ca-P ceramics on sintered Ti-Ca-P composites. Materials Science and Engineering C, 28, 1401-1407, 2008.
111. G. Zhao, A.L. Raines, M. Wieland, Z Schwartz, B.D. Boyan. Requirement for both micron-and submicron scale structure for synergistic responses of osteoblasts to substrate surface energy and topography. Biomaterials, 28, 2821-2829, 2007.
112. X. Zhu, J. Chen, L. Scheideler, T. Altebaeumer, J. Geis-Gerstorfer, D Kern. Cellular reactions of osteoblasts to micron-and submicron scale porous structures of titanium surfaces. Cells Tissues Organs, 178, 13-22, 2004.
113. A.C. Duncan, F. Weisbuch, F. Rouais, S. Lazare, Ch. Baquey. Laser microfabricated model surfaces for controlled cell growth. Biosensors and Bioelectronics, 17, 413-426, 2002.

114. S.N. Bhatia, C.S. Chen. Tissue engineering at the microscale. Biomedical Microdevices, 2, 1387-2176, 2004.
115. S. Hansson, M. Norton. The relation between the surface roughness and interfacial shear strength for bone-anchored implants: A mathematical model. Journal of Biomechanics, 32, 829-836, 1999.
116. S.P. Harimkar, A.N. Samant, N.B. Dahotre. Temporally evolved recoil pressure driven melt infiltration during laser surface modifications of porous alumina ceramic. Journal of Applied Physics, 101, 054911,2007.
117. S.P. Harimkar, A.N. Samant, A.A. Khangar, N.B. Dahotre. Prediction of solidification microstructures during laser dressing of alumina based grinding wheel material. Journal of Physics D: Applied Physics, 39, 1642-1649, 2006.
118. M. Vallet-Regi, D. Acros. Silicon substitution hydroxyapatites. A method to upgrade calcium phosphate based implants. Journal of Materials Chemistry, 15, 1509-1516, 2005.
119. Y. Yang, K. Serpersu, W. He, S.R. Paital, N.B. Dahotre. Osteoblast interaction with laser cladded HA and SiO_2- HA coatings on Ti-6Al-4V. Submitted to Biomedical Materials.
120. Y. Yang, S.R. Paital, N.B. Dahotre. Effect of SiO_2 substitution on wettability of laser deposited Ca-P biocoating on Ti-6Al-4V. Accepted to Journal of Materials Science: Materials in Medicine, 2010.
121. C. Ishino, K. Okumura, D. Quéré. Wetting transitions on rough surfaces. Electrophysics Letters, 68, 419 – 425, 2004.
122. J. Bico, U. Thiele, D. Quéré. Rough wetting. Electrophysics Letters, 55, 214 – 220, 2001.

Appendix

Appendix A: List of Publications

List of accepted peer-reviewed journal publications

- **Sameer R. Paital,** Wei He, Narendra B. Dahotre. "Laser pulse dependent micro textured calcium phosphate coatings for improved wettability and cell compatibility" Accepted to Journal of Materials Science: Materials in Medicine, (2010), doi:10.1007/s10856-010-4085-6
- **Sameer R. Paital**, Zheng Cao, Wei He, Narendra B. Dahotre. "Wetting effects on in vitro bioactivity and in vitro biocompatibility of laser micro-textured Ca-P coating" Biofabrication, 2 (2010), doi:1758-5082/10/000000+14
- **Sameer R. Paital,** Wei He, Claus Daniel, Narendra B. Dahotre. "Laser process effect on the texture evolution and wetting behavior in implantable Ti-6Al-4V alloys" Accepted to Journal of Materials JOM, (2010).
- Narendra B. Dahotre, **Sameer R. Paital**, Anoop N. Samant, Claus Daniel. "Wetting behavior of laser synthetic surface micro textures on Ti-6Al-4V for bioapplication" Philosophical Transactions of the Royal Society A, (2010), doi: 10.1098/rsta. 2010.0003.
- Yuling Yang, **Sameer R. Paital**, Narendra B. Dahotre. "Effect of SiO_2 substitution on wettability of laser deposited Ca-P biocoating on Ti-6Al-4V" Accepted to Journal of Materials Science: Materials in Medicine, (2010).
- **Sameer R. Paital**, Narendra B. Dahotre. "A thermal model for laser interaction with thick dielectric film on metallic substrate: Application to Ca-P layer on Ti alloy" Journal of Alloys and Compounds, 487 (2009), doi:10.1016/j.jallcom.2009.07.162.
- **Sameer R. Paital,** Narendra B. Dahotre. "Calcium phosphate coatings for bio-implant applications" Materials, performance factors, and methodologies" Materials Science and Engineering R, 66 (2009), doi:10.1016/j.mser.2009.05.001.
- **Sameer R. Paital**, Narendra B. Dahotre. "Wettability and kinetics of hydroxyapatite precipitation on a laser-textured Ca-P bioceramic coating" Acta Biomaterialia, 5 (2009), doi:10.1016/j.actbio.2009.03.004.

- **Sameer R. Paital**, Kantesh Balani, Arvind Agarwal, Narendra B. Dahotre. "Fabrication and evaluation of a pulse laser-induced Ca-P coating on a Ti alloy for bioapplication" Biomedical Materials, 4 (2009), doi:10.1088/1748-6041/4/1/015009.
- **Sameer R. Paital**, Narendra B. Dahotre. "Review of laser based biomimetic and bioactive Ca-P coatings" Materials Science and Technology, 24 (2008), doi: 10.1179/174328408X341825.
- **Sameer R. Paital**, Narendra B. Dahotre. "Laser surface treatment for porous and textured Ca-P bio-ceramic coating on Ti-6Al-4V" Biomedical Materials, 2 (2007), doi:10.1088/1748-6041/2/4/011.
- Yuling Yang**, Sameer R. Paital**, Narendra B. Dahotre. "Wetting and in vitro bioactivity of laser processed Ca-P coating with presence and variation of SiO_2 on Ti-6Al-4V" (Accepted to the special issue of Materials Technology Journal and under review).

Journal publications under review/preparation

- Yuling Yang, Kaan Serpersu, Wei He, **Sameer R. Paital**, Narendra B. Dahotre. "Osteoblast Interaction with Laser Cladded HA and SiO_2-HA Coatings on Ti-6Al-4V" (Under preparation).

Conference oral and poster presentations

- **Sameer R. Paital**, Wei He, Claus Daniel, Narendra B. Dahotre."Wetting behavior of laser synthetic surface micro textures on Ti-6Al-4V for bioapplication" Oral presentation at The Minerals, Metals and Materials Society (TMS) 2010, Seattle, WA, USA.
- **Sameer R. Paital**, Yuling Yang, Zheng Cao, Wei He, Claus Daniel, Narendra B. Dahotre. "Wetting and corollary biocompatibility of laser synthetic surface microtextures for bone tissue engineering" Poster presentation at The Minerals, Metals and Materials Society (TMS) 2010, Seattle, WA, USA.
- **Sameer R. Paital**, G. Wang, Peter K. Liaw, Narendra B. Dahotre. "Generation of geometric crystalline patterns within amorphous matrix of iron based bulk metallic glass foils via laser melting" Poster presentation at ASM meeting, Oak Ridge Chapter, November 2009, Oak Ridge, Tennessee, USA.

- **Sameer R. Paital**, Yuling Yang, Zheng Cao, Wei He, Claus Daniel, Narendra B. Dahotre. "Wetting and corollary biocompatibility of laser synthetic surface microtextures for bone tissue engineering" Poster presentation at ASM meeting, Oak Ridge Chapter, November 2009, Oak Ridge, Tennessee, USA.
- Sandip Harimkar, Ashish Singh, **Sameer R. Paital**, Narendra Dahotre. "Spark plasma sintering of Fe-based amorphous alloys" Oral presentation at Powder Metallurgy Processing and Products: Advanced Sintering/Consolidation Processes, MS&T 2009, Pittsburgh, USA.
- **Sameer R. Paital**, Zheng Cao, Wei He, and Narendra B. Dahotre. " Mineralization and cell interaction on laser textured Ca-P coatings" Oral presentation at Next Generation Biomaterials symposium, MS&T 2009, Pittsburgh, USA.
- **Sameer R. Paital**, and Narendra B. Dahotre. "Wettability and kinetics of hydroxyapatite precipitation on laser textured Ca-P bioceramic coating" Oral presentation at Surface Structures at Multiple Length Scales Symposium, The Minerals, Metals and Materials Society (TMS) 2009, San Francisco, California, USA.
- **Sameer R. Paital**, Zheng Cao, Wei He, and Narendra B. Dahotre. "Laser Textured Ca-P Coatings for Hard Tissue Replacement" Poster presentation at Biological Materials Science symposium, The Minerals, Metals and Materials Society (TMS) 2009, San Francisco, California, USA.
- **Sameer R. Paital**, Zheng Cao, Wei He and Narendra B. Dahotre. "Laser textured Ca-P bioceramic coatings for hard tissue replacement" Oral presentation at Biological Materials Science symposium, The Minerals, Metals and Materials Society (TMS) 2009, San Francisco, California, USA.
- Josh Burgess, **Sameer R. Paital**, Gongyao Wang, Elena Garlea, Jonathan S. Morell, Doug Fielden, Greg Jones, P. Liaw, Narendra B. Dahotre and T. Meek. Laser surface treatment of metallic glasses, Poster presentation at ASM meeting, Oak Ridge Chapter, November 2008, Oak Ridge, Tennessee, USA.
- **Sameer R. Paital**, and Narendra B. Dahotre. Laser induced Ca-P biomimetic coating on Ti-6Al-4V substrate, Poster presentation at ASM meeting, Oak Ridge Chapter, November 2008, Oak Ridge, USA.

- **Sameer R. Paital**, and Narendra B. Dahotre. "Pulsed laser induced Ca-P coatings on Ti-6Al-4V for bio-implant applications" Oral presentation at Biological Materials Science symposium, MS&T 2008, Pittsburgh, USA.
- **Sameer R. Paital**, and Narendra B. Dahotre. Laser synthesis of porous and textured Ca-P bio-ceramic coating on Ti-6Al-4V, Poster presentation at General Poster Session, The Minerals, Metals and Materials Society (TMS) 2008, New Orleans, USA.
- **Sameer R. Paital**, and Narendra B. Dahotre. Laser induced Ca-P biomimetic coating on Ti-6Al-4V substrate, Poster presentation at Biological Materials Science symposium, The Minerals, Metals and Materials Society (TMS) 2008, New Orleans, USA.
- **Sameer R. Paital**, and Narendra B. Dahotre. Microstructure and Bioactivity of laser induced geometrically textured and porous Ca-P coatings on Ti-6Al-4V, Oral presentation at Biological Materials Science symposium, The Minerals, Metals and Materials Society (TMS) 2008, New Orleans, USA.
- **Sameer R. Paital**, Peter E. Murray, Franklin Gracia-Godoy and Narendra B. Dahotre. Laser induced biomimetic and biocompatible Ca-P coatings on Ti-6Al-4V, Poster presentation at ASM meeting, Oak Ridge Chapter, November 2007, Oak Ridge, Tennessee, USA.

Appendix B: Reprints of Published Works

Peer-reviewed journal publications

J Mater Sci: Mater Med
DOI 10.1007/s10856-010-4083-6

Laser pulse dependent micro textured calcium phosphate coatings for improved wettability and cell compatibility

Sameer R. Paital · Wei He · Narendra B. Dahotre

Received: 2 December 2009 / Accepted: 15 April 2010
© Springer Science+Business Media, LLC 2010

Abstract Surface wettability of an implant material is an important criterion in biological response as it controls the adsorption of proteins followed by attachment of cells to its surface. Hence, micro-textured calcium phosphate coatings with four length scales were synthesized on Ti–6Al–4V substrates by a laser cladding technique and their effects on wettability and cell adhesion were systematically evaluated. Microstructure and morphological evolutions of the coatings were studied using scanning electron and light optical microscopes respectively. The surface texture of coating defined in terms of a texture parameter was correlated to its wetting behavior. The contact angle of simulated body fluid measured by a static sessile drop technique, demonstrated an increased hydrophilicity with decreasing value of texture parameter. The influence of such textures on the in vitro bioactivity and in vitro biocompatibility were studied by the immersion of the samples in simulated body fluid and mouse MC3T3-E1 osteoblast-like cell culture respectively.

1 Introduction

Bone graft procedures to heal skeletal defect is an area of active research as there exists millions of cases each year requiring such treatments [1]. These defects arise from several reasons including trauma, old age, congenital deformity, tumor resection, and injury and thus exist in a wide range of shapes, sizes, and functional locations [1]. The two most commonly used treatments to heal such defects are the autologous bone graft procedure and bone tissue engineering. Bone tissue engineering provides an attractive method than the autologous bone graft procedure as the latter is associated with the drawbacks such as limited supply of donor bone, risk of morbidity at the donor site, and risk of disease transmission and immune reaction arising from the donor site [2, 3]. The use of a solid artificial scaffold biomaterial that can support the bone cells and thereby provide anchorage for newly mineralized hard tissue is the most commonly used strategy for bone tissue engineering.

Among the various types of scaffold materials used, Hydroxyapatite (HA) and other calcium phosphate (CaP) bioceramics are being widely accepted owing to their similarity to the minerals in the natural bone, and their excellent bioactivity, biocompatibility, and osteoconduction [3–8]. When implanted inside a body these bioactive ceramics provide an ideal environment for cellular reaction, osteoblast colonization, and mineralized tissue integration to the implant surface. However, these CaP based ceramic materials possess inferior mechanical properties (low plasticity, fatigue, and creep resistance) and hence cannot be used as a stand alone implant material for hard tissue replacement. To overcome this issue, several researchers have emphasized on the coatings of CaP based bioceramics on titanium alloys [9–15]. Titanium being a bio-inert and biocompatible material, it does not elicit any harmful reaction and also provides appropriate mechanical properties for its long term stability inside the body. Hence, coating the surfaces of these implant materials (titanium alloys) by a CaP based chemistry can elicit favorable

S. R. Paital · W. He · N. B. Dahotre (✉)
Department of Materials Science and Engineering, The University of Tennessee, Knoxville, TN 37996, USA
e-mail: ndahotre@utk.edu

W. He
Department of Mechanical, Aerospace and Biomedical Engineering, The University of Tennessee, Knoxville, TN 37996, USA

Published online: 13 May 2010

biological and chemical responses on the surfaces, thereby enabling to mimic the reactions occurring in the natural tissue without losing the bulk mechanical properties such as long term durability and inertness.

The most commonly used coating technique that has been explored both in academic research and also largely practiced in the industry is the thermal spray coating technique [16]. However, this method suffers from certain drawbacks such as poor adherence of the coating to the substrate material, lack of uniformity of the coating, low fracture toughness of the ceramic layer, excess thickness of the coating, biodegradation, fatigue, third body wear, and absence of appropriate topographical cues mimicking the naturally occurring 3 dimensional extra cellular matrix (ECM) [16–18]. These attributes often result in loosening of the CaP ceramic coating due to non uniform load distribution and wear at the implant/defect tissue interface. The release of these foreign elements in the body environment can cause the problem of osteolysis. Further, the absence of appropriate topographical cues limits the anchoring of bone cells by contact guidance and hence, promotes weak bonding between the newly mineralized tissue and the scaffold material. The higher coating thickness ($\geq$1 mm) associated with plasma spraying technique also poses a major problem as it can cause failure due to fatigue under tensile loading conditions [16]. Also with increasing thickness the residual stresses within the coating increase and corresponding energy release may promote cracking at the substrate/coating interface [16]. To address the above issues a variety of thin film-based coating techniques such as pulsed laser physical vapor deposition [19], magnetron sputtering [11], ion beam assisted deposition [10], etc. are being explored to deposit CaP coatings on metallic substrates. Nonetheless, none of these coating techniques is able to synthesize a sound metallurgical bonding between the CaP coating and the substrate and unable to create a regular three dimensional topographic cues on the surface. In order to improve the bonding strength between the coatings and the substrate, several researchers also tried upon the laser based melting technique [20–25]. In the work by Cheng and coauthors [20] a metallurgical bonding was achieved by directly melting the pre-placed HA-Ti composite powders on Ti alloy substrate using a Nd:YAG laser. The authors characterized the mechanical properties of the coatings using Vickers and nano indentation techniques. The higher values of hardness, elastic modulus and resistance to crack growth as obtained using the above techniques proved for the sound interfacial toughness of the coatings [20]. Lusquiños and co-authors [21, 22] used a laser based cladding technique where a high power laser beam was used to melt the substrate (Ti–6Al–4V), and a simultaneous jet of precursor (HA powder) was blown by a carrier gas on to the molten cloud to form the coating. The authors showed the presence of a sound bonding and minimum dilution of the clad layer into the matrix of the substrate using SEM and XRD analysis of the cross-sectioned specimens [21]. A laser based cladding technique using calcium carbonate and calcium hydrogen phosphate as the precursor material to synthesize HA coating on Ti substrate was demonstrated by Wang et al. [23]. Using SEM and XRD analysis the authors showed the presence of sound bonding at the interface with cellular dendritic structure and consisting of phases HA, α-$Ca_2P_2O_7$, CaO and $CaTiO_3$ within the coating [23]. Although, all of the above works proved for the feasibility of a sound metallurgical bonding via laser based melting technique, none of these techniques could achieve a regular three dimensional topographic cue for contact guidance and adhesion of the bone cells.

In light of the above drawbacks associated with the present coating techniques, a laser based direct melting technique was established by the current group to simultaneously synthesize a textured CaP coating on Ti–6Al–4V substrate [26–30]. In the previous effort by the group [26, 28] a textured CaP coating on Ti–6Al–4V substrate was produced by direct melting of HA precursor using a continuous wave (CW) Nd:YAG laser. Here a systematic organization of the CaP coating on the Ti–6Al–4V substrate was obtained by effectively controlling the thermophysical interactions during laser processing. On the contrary, in the current work such feasibility of simultaneous synthesis of a textured CaP coating on Ti–6Al–4V substrate was realized using a pulsed Nd:YAG laser. During pulsed operation of Nd:YAG laser, the energy is delivered through intermittent pulses and hence the individual pulses can be controlled for duty cycle (on-off time), frequency (number of pulses delivered per second), and energy. Such control over selection of pulse parameters allows more precise control over spatial and temporal modes of delivery of laser energy, which in turn can create far more different thermal conditions, microstructures, and phase features within the laser-substrate interaction region than are obtained in the samples processed using a CW laser.

Further, wetting is an important aspect for all load bearing implants, as it controls the adsorption of proteins followed by attachment of cells to the implant surface. The surface morphology, surface chemistry, and surface charge of an implant material significantly influence its wetting behavior when it comes in contact with the physiological fluids under in vivo conditions [30]. An understanding of the mechanism of wetting will help in tailoring the surfaces for more hydrophilic behavior to physiological fluids and thereby help recruit proteins and bone cells from the surrounding to the implant surface swiftly. However, for the rough surface with irregular topographic cues the wetting dynamics is difficult to understand due to a non equilibrium

state of wetting and hence, no surface roughness parameters can be adopted to relate such a phenomenon. In light of this, with the present pulsed Nd:YAG laser coating technique, the sets of laser parameters can be chosen to synthesize surfaces with varying regular topographic cues. Finally, as the basis of the present study is to delineate and understand the effect of micro-textured surface morphology on wettability, in vitro bioactivity, and in vitro biocompatibility, the laser parameters are chosen to synthesize surfaces of the same phase composition and thereby only have a change in the surface topography.

2 Materials and methods

2.1 Sample preparation and Ca–P coating

Ti–6Al–4V substrate coupons (100 mm × 50 mm × 3 mm) cut from the rolled sheets were polished using 30 μm grit SiC emery paper followed by rinsing with acetone. The HA ($Ca_{10}(OH)_2(PO_4)_6$) powder (Fisher Scientific, USA) was used as the precursor material. This precursor powder had a spherical morphology with a unimodal distribution in the range of 10–30 μm. The precursor was mixed with a water-based organic solvent LISI W 15853 (Warren Paint and Color Company, Nashville, TN, USA) and sprayed onto the substrate coupons using an air pressurized spray gun. This green body was air dried to remove the moisture and a uniform thickness of 80 μm was maintained for all precoating precursor deposits. The samples were then scanned using a 400 W average power, JK701 model pulsed Nd:YAG laser to obtain the coating. The schematic of the laser coating experimental set up used for the coating process is shown in Fig. 1. The processing parameters used for the above process are listed in Table 1. From the table it can be observed that

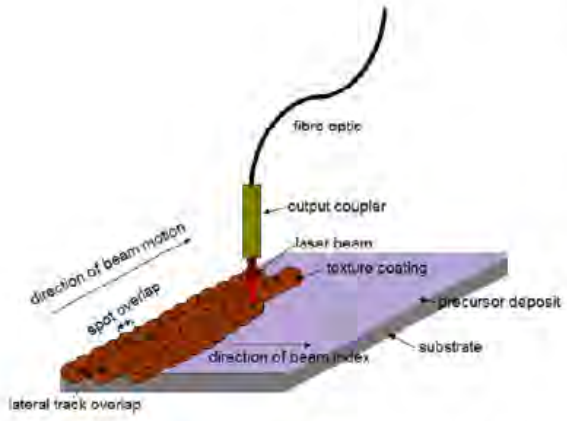


Fig. 1 Schematic of laser texturing process using pulsed Nd:YAG laser

Table 1 Laser parameters used in the study

Pulse width	1 ms
Pulse energy	4 J
Pulse repetition rate	10, 20, 30, 40 Hz
Laser scan speed	50 cm min^{-1}
Focus position	0.8 mm above sample surface
Spot diameter on the surface	900 μm
Pulse shape	Rectangular

only the laser pulse frequency was varied (10, 20, 30, and 40 Hz) keeping the rest of the parameters constant. This pulse frequency can be related to the spot overlap by the following equation [29, 30]:

$$(\text{Spot diameter}) \times (1 - \text{spot overlap}) \times (\text{pulse frequency}) = \text{linear scan speed}. \quad (1)$$

Hence, four different samples with spot overlap varying as 6, 53, 69 and 76% were obtained.

2.2 Surface characterization

The morphological evolutions of the surface of the coatings were characterized using low magnification Leica optical microscopes. The microstructure within the cross-section and the morphological evolution of the surface of coatings following immersion in a simulated body fluid (SBF) were characterized using a LEO 1525 scanning electron microscope (SEM). The samples in cross-section were prepared by polishing with emery papers of different grits ranging from 200 to 1,000 μm in succession followed by disc polishing with colloidal silica of 0.3 and 0.05 μm. The polished samples were then cleaned with acetone and etched with 5 vol% HF, 3 vol% HNO_3 and 92 vol% H_2O for 10–20 s by immersion etching to delineate the microstructural features.

Phase evolution within the coatings was studied using a Philips Norelco X-ray diffractometer (XRD) with Cu K_α radiation of wavelength 1.5418 Å. The system was operated at 20 kV and 10 mA in a 2θ range of 20° to 100° using a step size of 0.02° and count time of 1 s. In order to correlate the effects of surface roughness to wettability two roughness parameters such as standard deviation of amplitude (σ_A) and wavelength (λ) of the textured surface were measured using the Leica confocal laser microscope. Eventually, their ratio (σ_A/λ) defined as the texture parameter is used to reveal the effect of surface morphology on wettability. A total of 5 random scans were chosen on each sample and the sampling showed that the parameters can be defined with an accuracy of 2–4%.

2.3 Contact angle and in vitro bioactivity

Wettability of the coated samples with SBF was carried out by a static sessile drop technique using a CAM-Plus^R contact angle goniometer (Cheminstruments, Inc. Fairfield, Ohio) equipped with a fiber optic light source and Video camera for imaging. Prior to the contact angle measurements the samples were thoroughly cleaned with acetone and air dried. The SBF solution was prepared by mixing reagent grade chemicals in the following order: NaCl (8.026 g), $NaHCO_3$ (0.352 g), KCl (0.225 g), $K_2HPO_4 \cdot 3H_2O$ (0.230 g), $MgCl_2 \cdot 6H_2O$ (0.311 g), $CaCl_2$ (0.293 g) and Na_2SO_4 (0.072 g) into distilled water (700 ml). The fluid was then buffered to pH = 7.4 at 37°C with tri-hydroxymethyl-aminomethane (6.063 g) and hydrochloric acid (40 ml). A SBF droplet of volume 3 µl (droplet diameter of 2 mm) was placed on the thoroughly cleaned sample by a hypodermic syringe and the advancing contact angle was recorded as a measure of wettability. The liquid drop placed on the sample was allowed to stabilize for 10 s before the reading was taken. The test was conducted at room temperature (26°C) and a minimum of 10 contact angle readings were taken on each sample to minimize errors in the measurement. Further, the measurements were based on the patented half angle method (US Patent 5268733) which eliminates the errors associated with the arbitrary tangential alignment.

In vitro bioactivity and mineralization on the laser processed samples were studied by immersing a set of four samples from each processing condition in the SBF solution. Plastic containers were used to soak the samples in SBF for different time periods (24, 72, 120, and 168 h). The solution was refreshed every 24 h to maintain a pH of 7.4, and the temperature was maintained at 37°C during the course of the test. The samples were removed at regular intervals from the SBF solution and an increase in weight owing to the precipitation of HA was measured using a microbalance. The change in pH of the SBF solution was monitored using a Fisher Scientific FB-10 pH meter.

2.4 In vitro biocompatibility

In vitro biocompatibility of laser textured samples and control (untreated Ti–6Al–4V) was evaluated through cell attachment and cell morphology during cell culture studies using the mouse pre-osteoblast MC3T3-E1 (subclone 14) cell line, obtained from American Type Cell Culture Collection (ATCC, Manassas, VA, USA). The cells were maintained in a tissue culture flask using the cell culture medium at 37°C under 5% CO_2 and 95% air in a humidified incubator. The cell culture medium used in the present case was Alpha minimum essential medium (Invitrogen Corporation, USA) supplemented with 10% fetal bovine serum (Thermo Fisher Scientific Inc, USA) and 1% penicillin/streptomycin (Invitrogen Corporation, USA). The culture medium was replaced every 3 days and confluent cells were trypsinized and replated (0.25% trypsin-EDTA, Invitrogen, USA) to maintain the cell line.

2.4.1 Cell morphology and cell cytoskeleton

The osteoblast cells suspended in 300 µl cell culture medium were seeded on the UV sterilized samples at a lower density (1×10^4 cells cm^{-2}) and incubated for 24 and 168 h at 37°C under 5% CO_2 and 95% air in a humidified incubator. For cell morphology analysis using SEM, cells cultured on the samples were fixed with 3% glutaraldehyde in 0.1 M cacodylate for 1 h and rinsed three times with phosphate buffered saline (PBS). The samples were further processed in 2% osmium tetroxide in 0.1 M cacodylate for 1 h, dehydrated with a series of increasing concentration of ethanol (25, 50, 70, 95, and 100%), critical point dried, and sputter-coated with gold for SEM observation. For immunocytochemical staining of the actin filament and focal adhesion, the cells cultured on the samples were fixed with 4% paraformaldehyde (Sigma-Aldrich, USA) in 1× PBS for 30 min at 4°C. After washing with PBS, the samples were permeabilized with 0.1% Triton X-100 (Fisher Scientific, USA) in 1× PBS for 5 min, blocked with 1% bovine serum albumin (BSA, Sigma-Aldrich, USA) for 30 min, and incubated in the primary antibody mouse anti-vinculin (Chemicon, 0.2%) for 1 h. After rinsing, the samples were incubated with 0.5% goat anti-mouse IgG Alexa Fluor 488 and 2% Alexa Fluor 594-conjugated phalloidin (Invitrogen, USA) that labels the cytoskeleton F-actin filaments. Cell nuclei were counterstained with 0.1% 4′,6-Diamidino-2-phenylindole (DAPI, Chemicon, USA) in 1× PBS for 5 min. Samples were washed three times with 0.05% Tween-20 (Sigma) in 1× PBS before and after the staining steps. All the staining procedures were carried out at room temperature. High resolution fluorescence images were captured using an upright fluorescence microscope (Nikon). Once the images were captured, a representative image was selected for quantitative analysis of cell spreading area (A), and cell shape index (Ø). A total of 30 cells were randomly selected for each sample, manually outlined, and the cell areas (A) were calculated using the ImageJ image analysis software. The morphology of the cells described by the cell shape index (Ø) was calculated using the following equation [31]:

$$\varnothing = \frac{4\pi A}{p^2}. \tag{2}$$

Here A is the cell spreading area and p the perimeter of the cell. For a perfect circular morphology the cell shape index is 1, whereas for line morphology the shape index is 0.

Previous studies [32] have demonstrated a correlation between the cell shape index and cell fate and function, thereby offering the potential to tailor biomaterial surfaces to control cell fate and function through control of cell spreading.

2.4.2 Data analysis

For a particular time period of seeding a total of 4 samples were used from each laser processing parameters and the control (untreated Ti–6Al–4V). The results were expressed as the mean of 4 replicates ± SD (standard deviation). Statistical analysis carried out using a Student's t test was applied to determine the statistical significance observed between the groups and $P < 0.05$ were considered statistically significant.

3 Results and discussions

3.1 Microstructure, morphology, and phase analysis

The low-magnification optical microscopic images (Fig. 2) of the surfaces of laser textured samples clearly demonstrate the effect of varying laser pulse frequency on the texture evolution. The laser pulse frequency influences the input energy density [29], and the laser spot overlap as indicated by Eq. 1. Each single pulse of a laser beam on the surface of sample produces a solidified crater with a defined boundary and central flat region. Hence, when such craters are overlapped by varying the laser pulse frequency, surfaces with varying textures are obtained. Further, with increasing pulse frequency, the input energy density increases and this in turn also contributes to the texture evolution. The presence of such geometrically textured cues is expected to support bone cells and thereby induce bone in-growth from the surrounding tissue. The cross-sectional SEM image (Fig. 3a) of the sample processed at 40 Hz is clearly an indicative of the sound metallurgical bonding between the coating and the substrate (Ti–6Al–4V). A sound bonding of the bioceramic coating to the substrate material is expected to reduce the delamination of the ceramic layer and thereby avoid the risk of dissolving metallic ions into the body plasma and the problem of osteolysis.

The variable thermodynamic conditions resulting from the varying pulse frequency within the range employed in the present work only influenced the texture evolution and no detectable variation in the evolution of types of phases (Fig. 3b) is observed. The major phases identified within the detectable limits of the instrument are $Ca_{10}(PO_4)_6(OH)_2$, $CaTiO_3$, TiO_2 (Rutile and Anatase), $Ca_3(PO_4)_2$, and Al_2O_3.

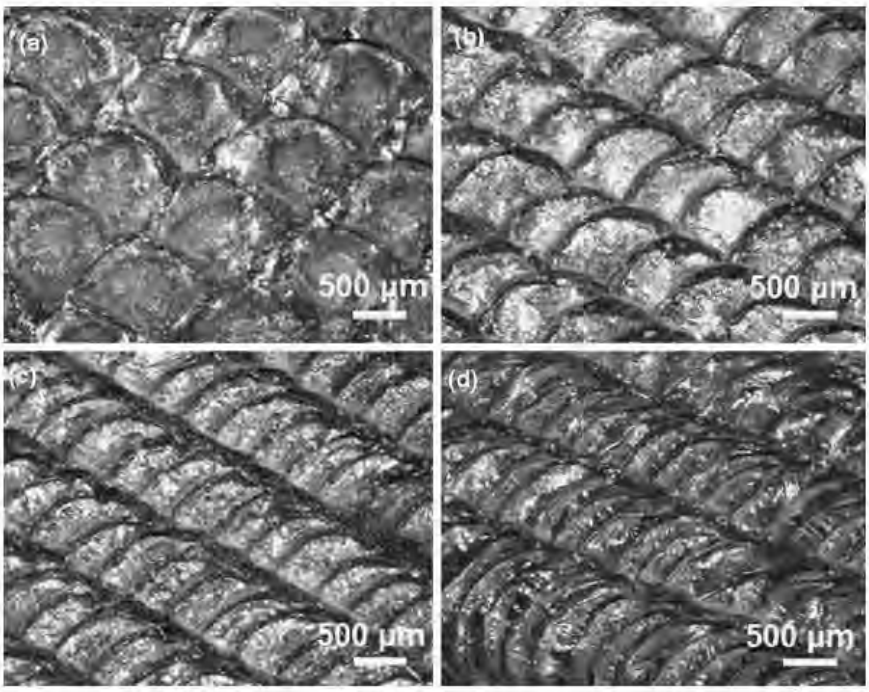


Fig. 2 Low-magnification optical microscopic images of the surface of coatings processed at laser pulse frequencies of **a** 10 Hz, **b** 20 Hz, **c** 30 Hz, and **d** 40 Hz

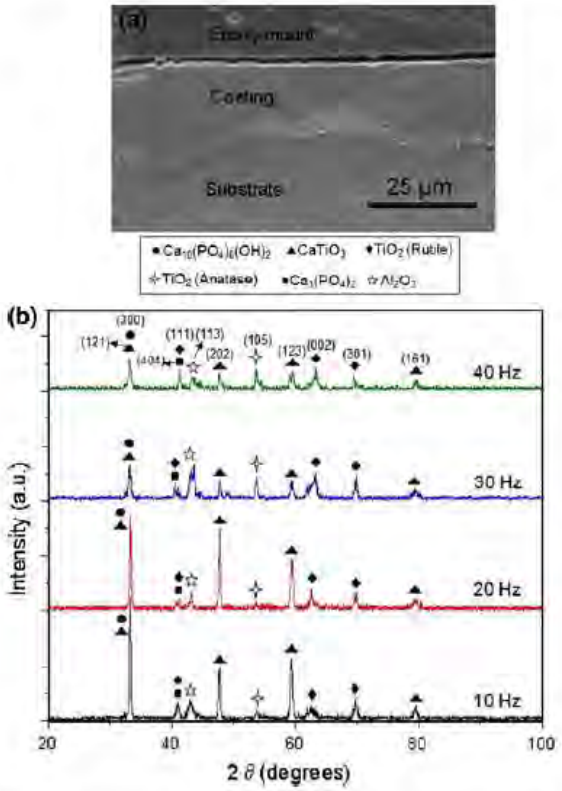


Fig. 3 **a** Cross-sectional SEM images of the sample processed at 40 Hz and **b** XRD pattern for the laser processed samples at varying pulse frequencies

Although, there is no major variation in the types of phases evolved, the variation in peak intensities is clearly an indication of the variation in amounts of these phases with increasing pulse frequency. As the pulse frequency was increased from 10 to 40 Hz there is a decrease in peak intensities of $Ca_{10}(PO_4)_6(OH)_2$ and $CaTiO_3$ phases along (300) and (123) planes respectively (Fig. 3b). Also, with increasing pulse frequency there is an increase in peak intensities of the TiO_2 (Rutile) and TiO_2 (Anatase) phases along (002) and (105) planes respectively. The above observations can be attributed to the fact that with increase in laser pulse frequency from 10 to 40 Hz, there was an increase in the laser input energy density. Such increased input energy was likely to raise the temperature of laser material interaction zone to the level leading to the substantial amount of coating precursor material evaporation followed by oxidation of the substrate material for formation of more amount of TiO_2 and Al_2O_3. Although the identical phases are present in the coatings of all laser processed samples, as stated in the following sections, during SBF immersion, these samples with varying surface topographic cues demonstrated varying wetting response and significant hydrophilicity with SBF compared to uncoated Ti–6Al–4V.

3.2 Effects of phase and morphology on wettability

The effect of laser pulse frequency (within the range employed in the present study) on three dimensional surface morphology of the coatings recorded using a confocal laser microscopy is presented in Fig. 4a. The sample processed at 10 Hz possesses a relatively rough morphology compared to the samples processed at 20, 30, and 40 Hz. As described earlier, due to only 6% overlap associated with 10 Hz frequency, the craters produced were least affected by the subsequent pulses. On the contrary, the frequencies of 20, 30, and 40 Hz provided substantially increased overlap of 53, 69, and 76% respectively. This increased spot overlap resulted in re-melting of the major portion of prior crater leading to smoothening of the coating. The values of σ_A, λ, and their ratio σ_A/λ were obtained from 5 random locations on each sample and are presented as mean values with related scatter in Table 2. All laser processed samples are associated with a significantly smaller value of σ_A/λ compared to the control (untreated Ti–6Al–4V). Also for all laser processed samples, with an increase in pulse frequency (in the range employed in the present study) there is a decrease in the σ_A/λ value. This further agrees with earlier visual observations that an increasing surface smoothening creeps in with increasing pulse frequency.

It has been well established that wetting of a surface by liquid is significantly affected by its surface roughness [30, 33]. The chart in Fig. 4b provides the experimental contact angles subtended by the SBF drop on laser processed samples and the control Ti–6Al–4V. All laser processed samples except the sample processed at 10 Hz depict an improved hydrophilic behavior compared to the control Ti–6Al–4V. Among the laser processed samples, the sample processed at 40 Hz possesses the maximum hydrophilicity to SBF with a contact angle of approximately 40°. The shadow image of SBF droplet (Fig. 4b) also shows the spreading of the SBF drop on the samples processed at 40 Hz. Thus, there is a decrease in the experimental contact angle with decreasing texture parameter (σ_A/λ) (Table 2; Fig. 4b). This improved hydrophilic behavior of laser processed samples is attributed to the influence of surface texture and the types of phases (HA, $CaTiO_3$, $Ca_3(PO_4)_2$, TiO_2 (Anatase), and TiO_2 (Rutile)) evolved during laser processing.

The wettability of laser processed sample, and the correlation between texture parameter (σ_A/λ) and experimental contact angle can be explained as per the wetting model on rough surfaces described by Zhou and De Hosson [33]. According to their model a practical rough surface is

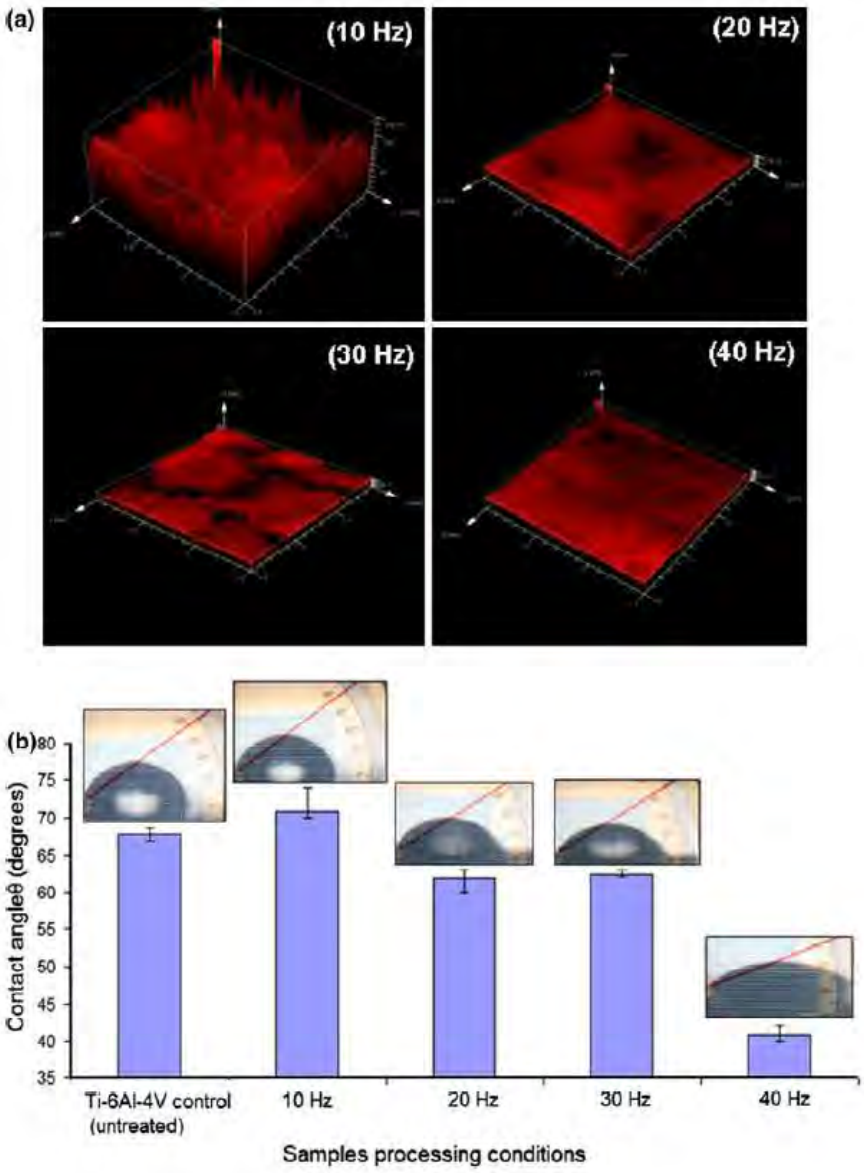


Fig. 4 **a** The 3-dimensional confocal microscopic images of surface of the coatings and **b** contact angle variation and their corresponding shadow images of the SBF droplet on laser processed sample and control (untreated Ti–6Al–4V)

Table 2 Experimentally measured physical parameters related to surface texture

Sample	Frequency (Hz)	Standard deviation of amplitude σ_A (μm)	Wavelength λ (μm)	Texture parameter (σ_A/λ)
Bare Ti–6Al–4V	–	12.56 ± 0.17	2.79 ± 0.08	4.38 ± 0.04
Ti–6Al–4V/Ca–P	10	23.05 ± 0.023	0.9 ± 0.016	0.05655 ± 0.016
Ti–6Al–4V/Ca–P	20	19.41 ± 0.014	0.6 ± 0.104	0.0385 ± 0.0101
Ti–6Al–4V/Ca–P	30	15.4 ± 0.01235	0.4 ± 0.1095	0.03235 ± 0.026
Ti–6Al–4V/Ca–P	40	11.31 ± 0.018	0.2 ± 0.0125	0.025655 ± 0.016

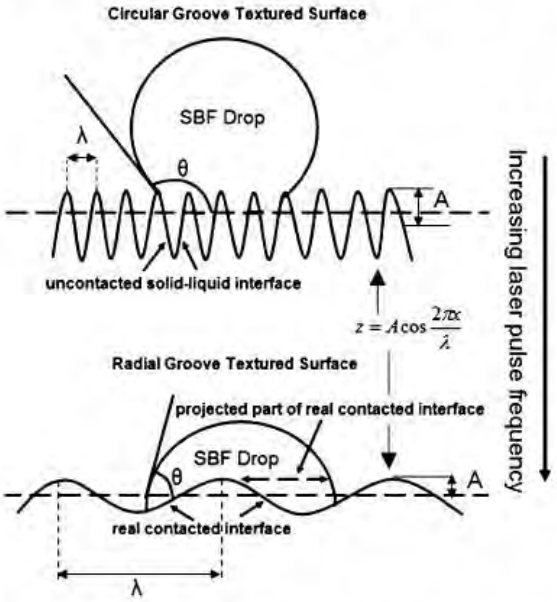


Fig. 5 Schematic of the wetting behavior of a liquid drop on a surface with **a** the circular grooves and **b** the radial grooves

assumed to have a cosine profile (Fig. 5) with a Gaussian distribution and is either of a radial or circular type grove. When a liquid is placed on the surface with only radial type groves, an equilibrium state of wetting is achieved and the relation between the experimental contact angle affected by the radial groves (θ_{rad}) and the theoretical contact angle (θ_{th}) is given by the following equation [33]:

$$\cos\theta_{rad} = D(1 - F)\cos\theta_{th} - F \quad (3)$$

where D is defined as the average area ratio of real contacted interface to its projected part, and F is the area fraction of an uncontacted solid–liquid interface on solid. The theoretical contact angle θ_{th} is defined as: $Cos\theta_{th} = (\gamma_S - \gamma_{LS})/\gamma_L$ where γ_S, γ_{LS}, and γ_L are the interface energies between solid–vapor, liquid–solid, and liquid–vapor interfaces respectively. For a radial groove, both D and F are constants and since, the rough surface is assumed to distribute as a cosine profile with a Gaussian distribution, they are both a function of σ_A/λ [33]. Hence, when a liquid drop is placed on such surface (smaller σ_A/λ value) it can easily overcome the energy barriers associated with it and completely wet it. Thus, an equilibrium state of wetting and thereby a smaller experimental contact angle is observed

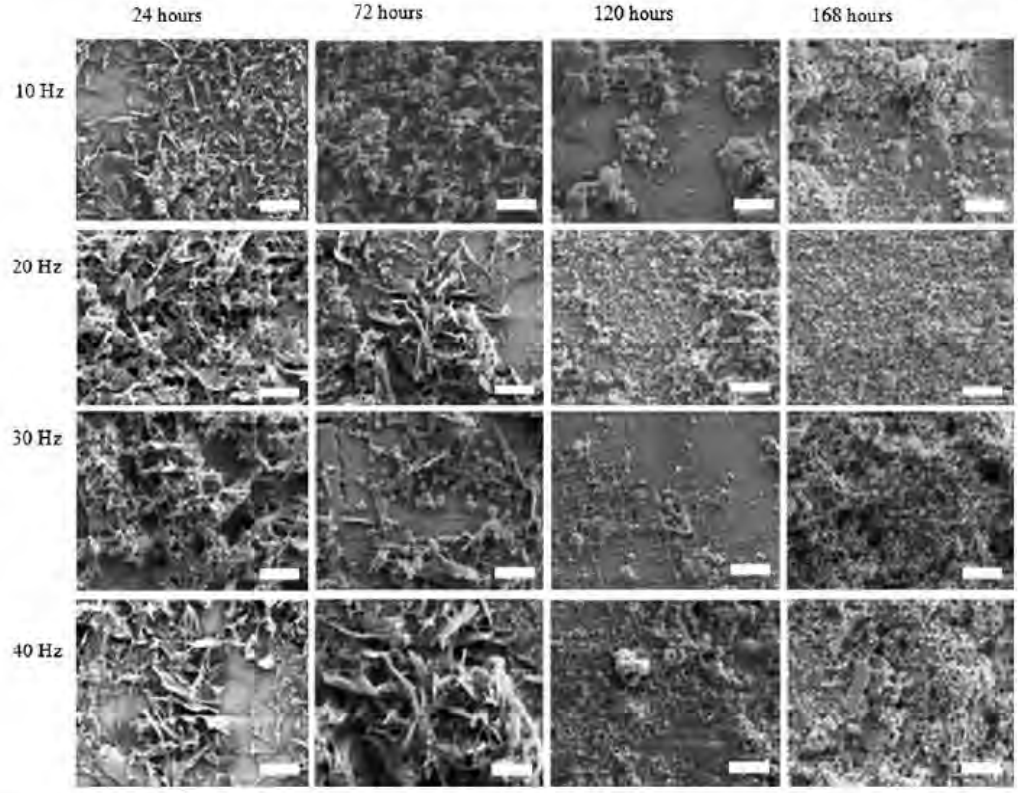


Fig. 6 SEM micrographs of laser processed samples following immersion in SBF for different time periods. *Scale bar* in the figure is equivalent to 10 μm

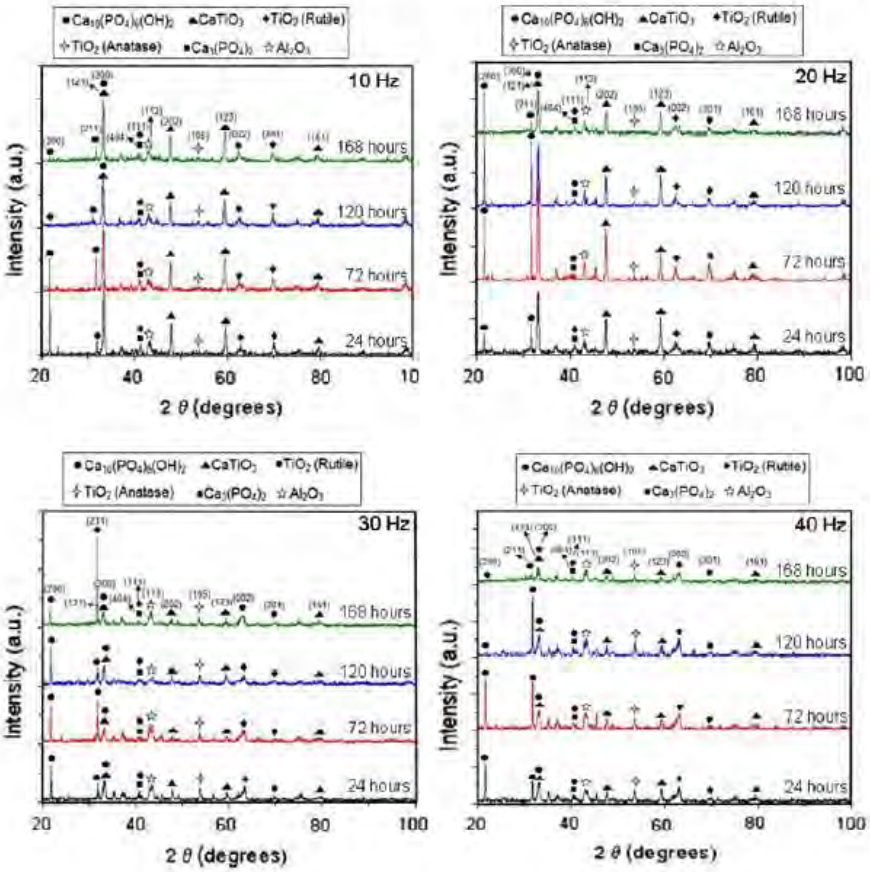


Fig. 7 XRD spectra of laser textured samples following immersion in SBF for various immersion periods

when the grooves are radial. In contrast, when the surface possesses sharp circular type features (higher σ_A/λ value) an equilibrium state of wetting could never be achieved. This type of sharp feature with higher σ_A/λ value contributes to the contact angle hysteresis and the experimental contact angle affected by these kinds of grooves (θ_{cir}) can be related to theoretical contact angle (θ_{th}) by the following equation:

$$\theta_{cir} = \theta_{th} + \left(\frac{\sqrt{8\pi}}{\lambda}\sigma_A\right). \quad (4)$$

From the above equation it is clear that a sharp circular type groove with higher σ_A/λ value can only result in a higher contact angle and thereby a reduced wettability. Hence, from the above equations based on the model by Zhou and De Hosson, optical microscopy observations (Fig. 2a), and confocal microscopy images (Fig. 4a) it is clearly evident that at a laser pulse frequency of 10 Hz and associated minimal spot overlap produced a deep and circular groove morphology on the surface. This in turn resulted in a higher σ_A/λ value, leading to unstability in wetting and increased contact angle as per Eq. 4. However, when the pulse frequency increased to 20, 30, and 40 Hz there was increased remelting due to increased spot overlap which in turn resulted in a relatively smoothly textured surface with lower σ_A/λ values. Therefore, the samples processed at these higher pulse frequencies are dominated by radial grooves that lead to improved wettability. As stated earlier, wetting is an important phenomenon which influences the mineralization, cell attachment, and cell proliferation. In light of this, the above preliminary efforts and corresponding understanding are further used to see how the texture parameter and associated wettability affect in vitro bioactivity and in vitro biocompatibility.

3.3 In vitro bioactivity and mineralization

In vitro bioactivity of laser textured samples and control (untreated Ti–6Al–4V) was assessed for precipitation of an apatite (HA, $[Ca_{10}(PO_4)_6(OH_2)]$) like mineral layer on the surface during immersion in SBF. The precipitation of such phase under in vivo conditions is beneficial as HA is a naturally occurring mineral component of the human bone laying along side the collagen fibrils. This layer, therefore, provides an appropriate surface chemistry for cell

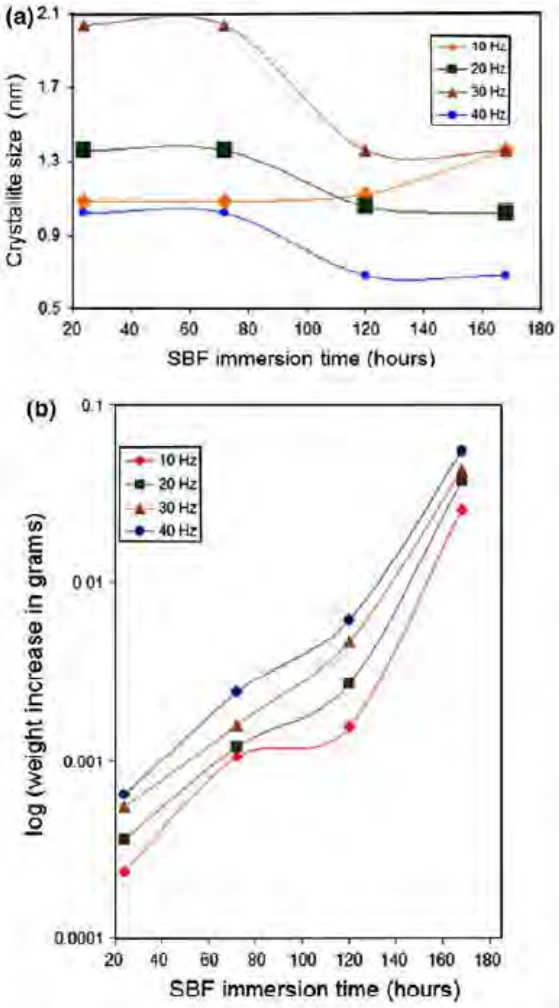


Fig. 8 Mineralization of laser textured samples in terms of **a** variation in apatite crystallite size with SBF immersion time and **b** logarithmic weight change with SBF immersion time

attachment and proliferation and minimizes the formation of a fibrous capsule at the interface.

As, there was no detectable amount of HA precipitation on the control (untreated Ti–6Al–4V) following 24 h of immersion in SBF, the SEM and XRD results pertaining to it are not included in the present study. However, the laser textured surfaces demonstrated the precipitation of a whisker-like apatite phase (Fig. 6) soon after 24 h of immersion in SBF. The presence of such morphology is attributed to heterogeneous nucleation of the hexagonal close packed (HCP) apatite crystal (on the substrate material) and subsequent growth of this HCP structure along the *c* axis (perpendicular to the close packed atomic plane) by the adsorption of Ca^{2+} and PO_4^{3-} ions from the super-saturated SBF solution. For longer immersion times this equilibrium morphology (whisker like apatite phase) due to its surface energy and modified Ca^{2+} and PO_4^{3-} ions concentration within the surrounding SBF solution in turn control the further nucleation process and thereby the change in morphology of the newly precipitated apatite crystals. Irrespective of the laser processing conditions (varying σ_A/λ value) a transition from whisker-like apatite phase to refined submicron size HA with increasing immersion time are observed in all samples (Fig. 6). To better understand the structural change in the apatite phase with increasing immersion time, XRD studies were carried out on the SBF immersed samples and the crystallite size (S) in a direction perpendicular to the surface of the specimen were measured from a highly resolved apatite peak using the Scherrer equation:

$$S = \frac{0.9\lambda}{\beta \cos\theta} \tag{5}$$

where λ is the wavelength of the X-ray source (1.54 A), θ is the half of the reported peak centroid and β is the broadening or the full width half maxima (FWHM) of the reported peak.

XRD studies of all laser textured samples following immersion in SBF for different time periods, indicated the presence of an apatite phase as evident from the characteristic HA peaks at $2\theta \sim 22.0°$ and 31.75° corresponding to the planes (200) and (211) respectively (Fig. 7). All samples (irrespective of the processing parameters and varying σ_A/λ value) following 24 h of immersion in SBF, demonstrated intense peaks at $2\theta \sim 22.0°$ and 31.75° that are attributable to the apatite phase. However, with increased immersion time these apatite peaks are either broadened with a reduction or sharpened with an increase in intensity. To precisely understand this phenomenon and thereby its influence on the crystallite size the highly resolved apatite peak corresponding to the plane (211) at $2\theta \sim 31.75°$ was used for calculations in Eq. 5. Figure 8a shows the variation in apatite crystallite size with increasing SBF immersion time for all laser textured samples. All laser textured samples except the sample processed at 10 Hz experience decrease in the apatite crystallite size with increasing SBF immersion time (Fig. 8a). For the sample processed at 40 Hz, precipitated apatite crystallites were the smallest and the average crystallite size was approximately 1.02 nm during the first 72 h of SBF immersion time, and decreased to 0.6795 nm as the immersion time is increased to 120 and 168 h. The precipitation of such submicron size crystallites may be due to increased heterogeneous nucleation sites of the ionic species (Ca^{2+} and PO_4^{3-} ions from the SBF) on the substrate material owing to its improved wettability. This in turn may have resulted in reduction of Ca^{2+} and

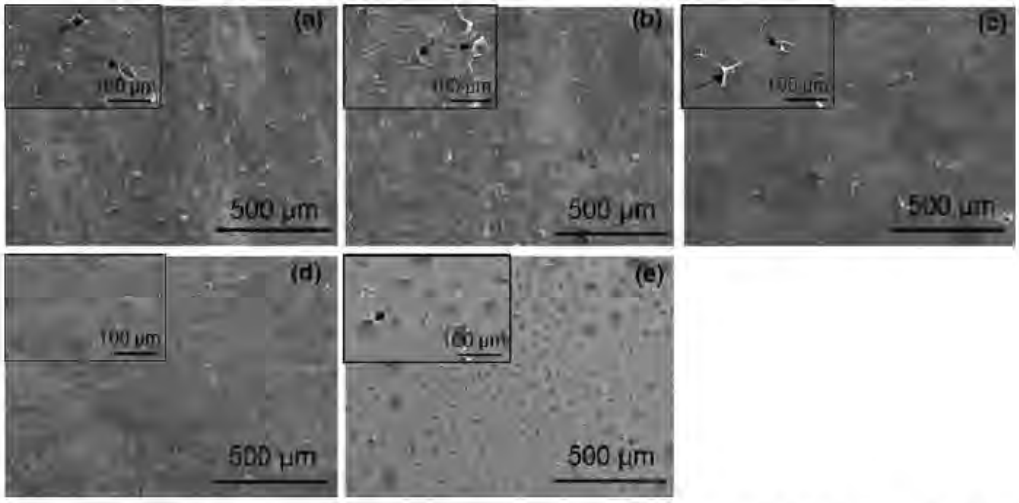


Fig. 9 Morphology of MC3T3-E1 osteoblast-like cells after 7 day culture on the samples processed at laser pulse frequency of **a** 10 Hz, **b** 20 Hz, **c** 30 Hz, **d** 40 Hz and **e** control (untreated Ti–6Al–4V). *Arrows* in the inset of Fig. 9**a**, **b**, **c**, and **e** indicate the de-bonding or lack of proper adhesion of the MC3T3-E1 osteoblast-like cells on the substrate material

PO_4^{3-} ions concentration in the SBF leading to the growth arrest of HCP habit plane. On the contrary, the reduced hydrophilic nature of 10 Hz sample may have resulted in the less number of heterogeneous nucleation sites and hence the availability of more Ca^{2+} and PO_4^{3-} ions from SBF to nucleate on to the apatite crystal.

It is well known that as the apatite nucleation takes place under in vitro conditions, it modifies the initial surface layer and this in turn can control the subsequent precipitation. Hence, it would be interesting to study the mineralization behavior in terms of weight change with increasing SBF immersion time. The logarithmic weight increase with increasing SBF immersion time for all the laser processed samples is presented in Fig. 8b. Also, as observed in our earlier work [30] as well as in the present study, the mineralization on the control (untreated Ti–6Al–4V) was not of detectable amount, hence its mineralization behavior with increasing SBF immersion time is not included in the present study. The mineralization increased with increasing SBF immersion time and followed the same trend for all laser textured samples with varying σ_A/λ values. Also, with an increase in pulse frequency (decrease in σ_A/λ value) there is an increase in HA precipitation for each SBF immersion time and the sample processed at 40 Hz (smaller σ_A/λ value) experienced the maximum weight change. This improved mineralization on laser processed samples is attributed to improved wettability (Fig. 4b) as a result of the appropriate surface textures (smaller σ_A/λ value, Table 2) and the types of phases (HA, $CaTiO_3$, $Ca_3(PO_4)_2$, TiO_2 (Anatase), and TiO_2 (Rutile), Fig. 3b) evolved during laser processing. Also, as described earlier, among all laser processed samples the precipitates formed on the sample processed at 40 Hz were the smallest for all immersion times (Fig. 8a). The presence of such smaller crystallites provides increased surface energy for increased nucleation of HA on the surface of sample and thereby improves its mineralization under in vivo conditions.

3.4 Biocompatibility assessment

Cell morphology on laser processed and control (untreated Ti–6Al–4V) samples after 7 day culture of MC3T3-E1 osteoblast-like cells was assessed by SEM and the results are presented in Fig. 9. Surfaces of all laser processed samples (Fig. 9a, b, c, and d) and the control (untreated Ti–6Al–4V, Fig. 9e) were confluent with the MC3T3-E1 osteoblast-like cells after 7 day of culture period. However, for the control (untreated Ti–6Al–4V) and samples processed at 10, 20, and 30 Hz most of the osteoblast-like cells appeared to de-bond from the surface of the coatings. In contrast, the osteoblast-like cells appeared to be flattened, spread out uniformly, and strongly adhered with an elliptical and circular morphology on the sample processed at 40 Hz.

The proliferation of the osteoblast-like cells after 1 and 7 day of culture on the laser processed and control (untreated Ti–6Al–4V) samples were studied qualitatively using a fluorescence microscope (Fig. 10). After 1 day of culture there are very few cells in the image fields of all laser processed samples and the control (untreated Ti–6Al–4V). The MC3T3-E1 osteoblast-like cells have a triangular

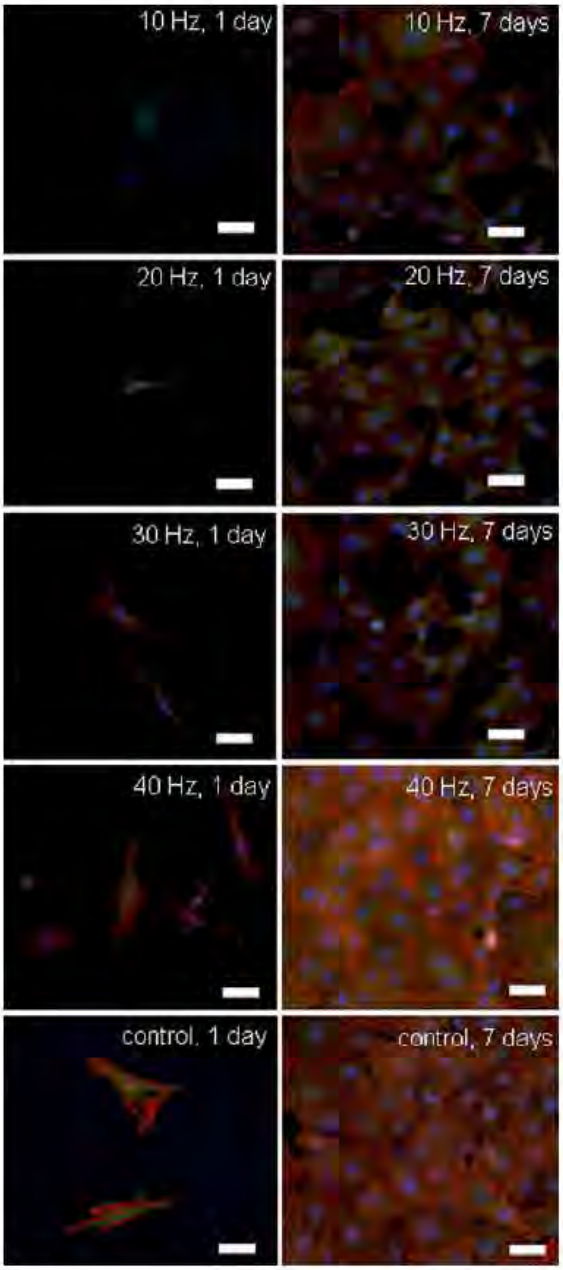


Fig. 10 Fluorescence microscopic images showing the proliferation of the MC3T3-E1 osteoblast-like cells after 1 and 7 day of culture on the laser processed and control (untreated Ti–6Al–4V). *Scale bar* in the figure is equivalent to 50 μm

morphology with the lamellipodia trying to extend along the surface of sample. In contrast, after 7 days of culture, the osteoblast-like cells are confluent over the entire surfaces of all samples and exhibit either elliptical or polygonal like morphology. Especially, for the sample processed at 40 Hz, the osteoblast-like cells are more confluent with well stressed actin filaments and are very much comparable to the control (untreated Ti–6Al–4V).

The cytoskeletal organization of the MC3T3-E1 osteoblast-like cells on the control (untreated Ti–6Al–4V) and laser processed samples after 7 days culture are presented in Fig. 11a. All the samples indicate stressed actin filaments with well developed network of focal adhesion contacts. Also it can be qualitatively observed that for the sample processed at 40 Hz, the foot print area or the cell spreading is relatively more compared to the rest of laser processed samples and control (untreated Ti–6Al–4V). The cell shape index (after 7 days culture of MC3T3-E1 osteoblast-like cells), calculated using the cell spreading area (A) and the perimeter (p) of the cell, provided a higher value for the sample processed at 40 Hz (Fig. 11b) as compared to the control (untreated Ti–6Al–4V) and the sample processed at 10, 20, and 30 Hz. This, therefore, indicated the uniform spreading and circularity of the osteoblast-like cells on the sample processed at 40 Hz.

Although all laser processed samples (10, 20, 30, and 40 Hz) produced the same types of phases (HA, $CaTiO_3$, $Ca_2(PO_4)_2$, TiO_2 (Rutile), and TiO_2 (Anatase)) and physical textures with smaller values of σ_A/λ on the surface for substantially improved wettability compared to the control (untreated Ti–6Al–4V), only the sample processed at 40 Hz demonstrated reasonably improved biocompatibility in terms of cell morphology, cell proliferation, and cell shape index compared to the control. Thus these observations indicate that in general, the processing approach holds a promise in producing the attributes (surface composition and surface texture) suitable for improved biocompatibility. In light of this, the efforts are on going to explore and extend the laser processing parameters for a larger matrix to produce samples of substantially improved biocompatibility. Further, long term cell culture studies in terms of cell viability and cell differentiation are in the process to understand its biocompatibility and the results pertaining to the above will be discussed in our subsequent journal communications.

4 Conclusions

The laser direct melting of HA precursor on the Ti–6Al–4V substrate resulted in formation of various phases such as, $CaTiO_3$, $Ca_3(PO_4)_2$, TiO_2 (Anatase), and TiO_2 (Rutile), within the coated regions. By varying the laser pulse frequency in combination of appropriate selection of other laser processing conditions only a variation in surface morphology was achieved keeping the phase composition same. The sample processed at a laser pulse frequency of 40 Hz is associated with a smallest texture parameter (σ_A/λ) leading to the maximum wettability with SBF. This

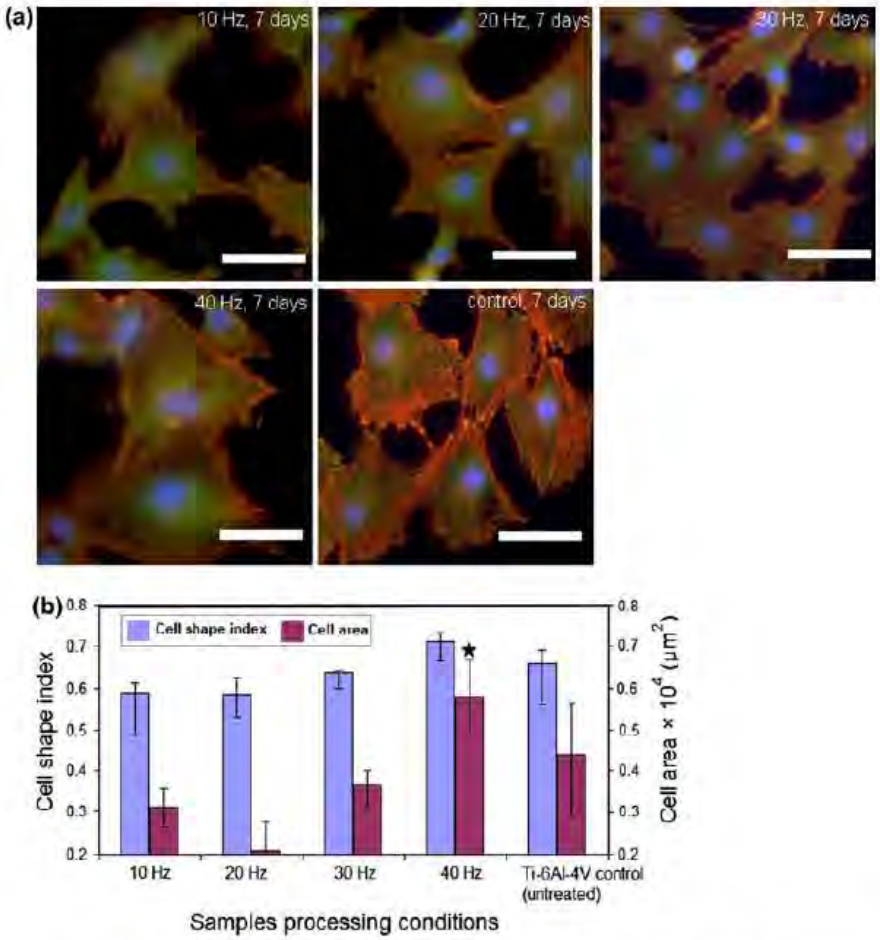


Fig. 11 **a** Cytoskeleton assessment of the MC3T3-E1 osteoblast-like cells after 7 day culture on the laser processed samples and the control (untreated Ti–6Al–4V) and **b** cell shape index and cell area as a function of the samples processing conditions. *Scale bar* in the figure is equivalent to 50 μm and ★ denotes the laser processed processed group is significantly higher than the control

improved hydrophilic behavior for the sample processed at 40 Hz also resulted in its enhanced mineralization (in vitro bioactivity) following immersion in SBF and improvement in in vitro biocompatibility characterized via increased proliferation and spreading of the MC3T3-E1 osteoblast-like cells.

Acknowledgments The authors would like to acknowledge Dr. John Dunlop of University of Tennessee, Knoxville in helping us preparing the samples for SEM observations, Lu Huang for cell culture, and Dr. Peter Liaw of University of Tennessee, Knoxville in providing the cell line.

References

1. Fisher JP. Tissue engineering. 1st ed. New York: Springer; 2006. p. 225.
2. Zhang ZY, Teoh SH, Chong WS, Foo TT, Chng YC, Choolani M, Chan J. A biaxial rotating bioreactor for the culture of fetal mesenchymal stem cells for bone tissue engineering. Biomaterials. 2009;30:2694–704.
3. Quan R, Yang D, Yan J, Li W, Wu X, Wang H. Preparation of graded zirconia-CaP composite and studies of its effect on rat osteoblast cells in vitro. Mater Sci Eng C. 2009;29:253–60.
4. Moreau JL, Xu HHK. Mesenchymal stem cell proliferation and differentiation on an injectable calcium phosphate-chitosan composite scaffold. Biomaterials. 2009;30:2675–82.
5. Mei HH, Phillips GJ, Mikhalovsky SV, Lloyd AW. In vitro cytotoxicity assessment of carbon fabric coated with calcium phosphate. New Carbon Mater. 2008;23:139–43.
6. Baker KC, Drelich J, Miskioglu I, Israel R, Herkowitz HN. Effect of polyethylene pretreatments on the biomimetic deposition and adhesion on calcium phosphate films. Acta Biomater. 2007;3:391–401.
7. Chou L, Marek B, Wagner WR. Effect of hydroxyapatite coating crystallinity on biosolubility, cell attachment efficiency and proliferation in vitro. Biomaterials. 1999;20:977–85.

8. Alcaide M, Serrano MC, Pagani R, Salcedo SS, Regi VM, Portoles MT. Biocompatibility markers for the study of interactions between osteoblasts and composite biomaterials. Biomaterials. 2009;30:45–51.
9. Shih WJ, Wang SH, Li WL, Hon MH, Wang MC. The phase transition of calcium phosphate coatings deposited on a Ti–6Al–4V substrate by an electrolytic method. J Alloys Compd. 2007;434–435:693–6.
10. Blalock T, Bai X, Rabiei A. A study on microstructure and properties of calcium phosphate coatings processed using ion beam assisted deposition on heated substrates. Surf Coat Technol. 2007;201:5850–8.
11. Boyd AR, Meenan BJ, Leyland NS. Surface characterization of the evolving nature of radio frequency (RF) magnetron sputter deposited calcium phosphate thin films after exposure to physiological solution. Surf Coat Technol. 2006;200:6002–13.
12. Wen HB, de Wijin JR, van Blitterswijk CA, de Groot K. Incorporation of bovine serum albumin in calcium phosphate coating on titanium. J Biomed Mater Res. 1999;46:245–52.
13. Ji H, Ponton CB, Marquis PM. Microstructural characterization of hydroxyapatite coating on titanium. J Mater Sci: Mater Med. 1992;3:283–7.
14. Habibovic P, Barrère F, van Blitterswijk CA, de Groot K, Layrolle P. Biomimetic hydroxyapatite coating on metal implants. J Am Ceram Soc. 2002;85:517–22.
15. Ramires PA, Romito A, Cosentino F, Milella E. The influence of titania/hydroxyapatite composite coatings on in vitro osteoblasts behavior. Biomaterials. 2001;22:1467–74.
16. Paital SR, Dahotre NB. Calcium phosphate coatings for bio-implant applications: materials, performance factors, and methodologies. Mater Sci Eng: R: Rep. 2009;66:1–70.
17. Campbell AA, Fryxell GE, Linehan JC, Graff GL. Surface-induced mineralization: a new method for producing calcium phosphate coatings. J Biomed Mater Res. 1996;32:111–8.
18. Gracía-Sanz FJ, Mayor MB, Arias JL, Pou J, León B, Pérez-Amor M. Hydroxyapatite coatings: a comparative study between plasma-spray and pulsed laser deposition techniques. J Mater Sci: Mater Med. 1997;8:861–5.
19. Clèries L, Fernández-Pradas JM, Morenza JL. Bone growth on and resorption of calcium phosphate coatings obtained by pulsed laser deposition. J Biomed Mater Res. 2000;49:43–52.
20. Cheng GJ, Pirzada D, Cai M, Mohanty P, Bandyopadhyay A. Bioceramic coating of hydroxyapatite on titanium substrate with Nd:YAG laser. Mater Sci Eng C. 2005;25:541–7.
21. Lusquiños F, Pou J, Arias JL, Boutinguiza M, Pérez-Amor M, León B, Driessens FCM. Production of calcium phosphate coatings on Ti6Al4V obtained by Nd:yttrium-aluminum-garnet laser cladding. J Appl Phys. 2001;90:4231–6.
22. Lusquiños F, De Carlos A, Pou J, Arias JL, Boutinguiza M, León B, Pérez-Amor M, Driessens FCM, Hing K, Gibson I, Best S, Bonfield W. Calcium phosphate coatings obtained by Nd:YAG laser cladding: physicochemical and biologic properties. J Biomed Mater Res. 2003;64A:630–7.
23. Wang D, Chen C, Ma J, Zhang G. In situ synthesis of hydroxyapatite coating by laser cladding. Colloids Surf B: Biointerfaces. 2008;66:155–62.
24. Roy M, Krishna BV, Bandyopadhyay A, Bose S. Laser processing of bioactive tricalcium phosphate coating on titanium for load-bearing implants. Acta Biomater. 2008;4:324–33.
25. Zhang Y, Gao J, Tan J, Zou Z. Laser surface coating of a bioceramic composite layer. Surf Coat Technol. 1993;58:125–7.
26. Kurella A, Dahotre NB. Laser induced hierarchical calcium phosphate structures. Acta Biomater. 2006;2:677–88.
27. Kurella A, Dahotre NB. A multi-textured calcium phosphate coating for hard tissue via laser surface engineering. J Miner, Met Mater Soc (JOM). 2006;58:64–6.
28. Paital SR, Dahotre NB. Laser surface treatment for porous and textured Ca–P bio-ceramic coating on Ti–6Al–4V. Biomed Mater. 2007;2:274–81.
29. Paital SR, Balani K, Agarwal A, Dahotre NB. Fabrication and evaluation of a pulse laser-induced Ca–P coating on a Ti alloy for bioapplication. Biomed Mater. 2009;4:1–10.
30. Paital SR, Dahotre NB. Wettability and kinetics of hydroxyapatite precipitation on a laser-textured Ca–P bioceramic coating. Acta Biomater. 2009;5:2763–72.
31. Palson BØ, Bhatia SN. Tissue engineering. 1st ed. New Jersey: Pearson Prentice Hall; 2004. p. 252–5.
32. Chen CS, Mrksich M, Huang S, Whitesides GM, Ingber DE. Geometric control of cell life and death. Science. 1997;276:1425–8.
33. Zhou XB, De Hosson JThM. Influence of surface roughness on the wetting angle. J Mater Res. 1995;10:1984–92.

TB, RMK, US, BF/337535, 5/02/2010

IOP PUBLISHING BIOFABRICATION

Biofabrication **2** (2010) 000000 (14pp) UNCORRECTED PROOF

Wetting effects on *in vitro* bioactivity and *in vitro* biocompatibility of laser micro-textured Ca-P coating

Sameer R Paital[1], Zheng Cao[1], Wei He[1,2] and Narendra B Dahotre[1,3]

[1] Department of Materials Science and Engineering, The University of Tennessee, Knoxville, TN 37996, USA

[2] Department of Mechanical, Aerospace and Biomedical Engineering, The University of Tennessee, Knoxville, TN 37996, USA

E-mail: Narendra.Dahotre@unt.edu

Received 11 November 2009
Accepted for publication 26 January 2010
Published DD MMM 2010
Online at stacks.iop.org/BF/2/000000

Abstract

Calcium phosphate (Ca-P) coating on the Ti-6Al-4V alloy enhances osteoblast adhesion and tissue formation at the bone implant interface. In light of this, in the current work a laser-based coating technique was used to synthesize two different micro-textured (100 μm and 200 μm spaced line patterns) Ca-P coatings on the Ti-6Al-4V alloy and its effect on wettability and osteoblast cell adhesion were systematically studied. X-ray diffraction (XRD) analysis of the coated samples indicated the presence of precursor material, $Ca_{10}(PO_4)_6(OH)_2$ (HA) and various other additional phases such as $CaTiO_3$, $Ca_3(PO_4)_2$, TiO_2 (Anatase) and TiO_2 (Rutile) owing to the reaction between the precursor (HA) and substrate (Ti-6Al-4V) during laser processing. Confocal laser scanning microscopy-based characterization of coated samples indicated that the samples processed at 100 μm line spacing demonstrated a reduced surface roughness and smaller texture parameter value as compared to the samples processed at 200 μm spacing. The surface energy and wettability of the 100 μm spaced samples measured using a static sessile drop technique demonstrated higher surface energy and increased hydrophilicity as compared to the control (untreated Ti-6Al-4V) and the samples processed at 200 μm spacing. The tendency of coated samples for mineralization through generation of an apatite-like phase during immersion in a simulated body fluid was indicative of their *in vitro* bioactive nature. In light of higher surface energy and increased hydrophilicity the *in vitro* biocompatibility of the samples with 100 μm line spacing was demonstrated through increased cell proliferation and cell adhesion of mouse MC3T3-E1 osteoblast-like cells.

1. Introduction

Biomaterials are often characterized by their interaction with biological molecules, cells and tissues. These biological responses on biomaterials depend on both the surface chemistry and surface topography of the implant material. An appropriate surface chemistry can affect the biological response by binding a specific receptor, stimulating cell migration to the interface, and thereby providing the desired mechanical properties to the remodeling tissue [1]. On the other hand, three-dimensional surface features of appropriate length scales can modulate the cell orientation and direct migration, and can affect tissue adhesion [1]. Hence, synthesis and fabrication of surface-engineered scaffold biomaterials mimicking the chemistry and three-dimensional extracellular matrix (ECM) of the naturally occurring tissue is an area of active research.

For load bearing implant applications such as hip joint prosthesis, knee joint prosthesis, dental implants, etc, several authors have tried to modulate the surface chemistry and surface topography of implant materials by direct deposition

[3] Author to whom any correspondence should be addressed.

 © 2010 IOP Publishing Ltd Printed in the UK

of Ca-P-based bioceramics on Ti alloys and studied their *in vitro* bioactivity and biocompatibility [2–5]. Here the bioceramic coating is expected to provide the desirable surface chemistry for cell attachment and tissue integration and the substrate Ti-6Al-4V the required mechanical properties for its long-term durability. Several coating methodologies that various researchers have studied till now include plasma spray deposition [6], magnetron sputtering [7], sol-gel-based coatings [8], pulsed laser deposition [9] and electrophoretic deposition [10]. Valereto and co-workers [11] studied the *in vitro* biocompatibility of plasma-sprayed hydroxyapatite (HA) coating on the Ti-6Al-7Nb alloy by culturing of osteoblast-like cells for 15 days. The presence of the extracellular matrix and bundle of collagen fibers on the coated specimen proved the *in vitro* biocompatibility and the biomineralization ability of the coated specimen. Ball *et al* [12] synthesized HA thin films on Ti substrates by a pulsed laser deposition technique and studied its *in vitro* biocompatibility by culturing of human osteoblast-like cells. The authors studied the effect of crystallinity and laser fluence on cell attachment. Their studies demonstrated enhanced cell attachment and proliferation with increasing laser fluence and crystallinity. This enhanced cell activity on the crystalline HA film was attributed to the less dissolution of the crystalline phase and thereby less release of Ca and P ions into the solution.

Although, most of these techniques are aimed to enhance short- and long-term performance of implants by encouraging bone in-growth and providing enhanced fixation, they suffer from certain drawbacks such as poor adherence of the coating to the substrate material, lack of uniformity, absence of appropriate topographical cues at the surface and absence of desirable chemistry. Hence, to address these issues, in the present experimental work a continuous wave (CW) laser-based coating technique will be used to synthesize micro-textured Ca-P coatings on the Ti-6Al-4V substrate. Here a highly intense laser beam will be used to melt both the precursor (HA) and the substrate (TI-6Al-4V) and thereby provides a metallurgical bonding at the interface, unlike the mechanical bonding achieved by various other techniques. Also as the laser scanning process is programmed to achieve line patterns with varying lateral track spacings (center to center distance between the laser tracks), micro-textured patterns at varying length scales can be obtained. Further, as the rationale behind the present study is to delineate and understand the effect of micro-textured surface morphology on wettability, *in vitro* bioactivity, and *in vitro* biocompatibility, the laser parameters are chosen to synthesize surfaces with the same chemistry and thereby only have a change in the surface topography. Finally, the three-dimensional surface morphology of the coated specimens is characterized in terms of the texture parameter σ_A/λ (ratio of the standard deviation of amplitude (σ_A) to periodicity (λ) of the roughness pattern), and thereby its effect on wettability, *in vitro* bioactivity and *in vitro* biocompatibility is systematically studied. An understanding of the above correlation between the texture parameter, wettability and cell compatibility will provide an insight into synthesis of tunable textured Ca-P coatings, for predictable cell response.

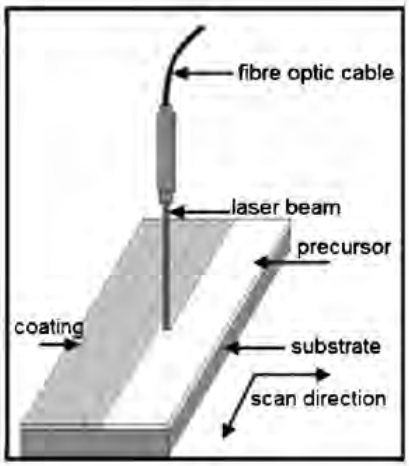


Figure 1. Schematic of the laser coating experimental setup.

2. Materials and methods

2.1. Sample preparation and Ca-P coating by a continuous wave (CW) laser

The substrates Ti-6Al-4V used for the coating (100 mm × 50 mm × 3 mm) were cut from the rolled sheets using an abrasive cutter. All substrate coupons were then prepared for coating by polishing on a 30 μm grit SiC emery paper followed by rinsing with acetone. Hydroxyapatite ($Ca_{10}(PO_4)_6(OH)_2$) powder obtained from Fischer Scientific was taken as the precursor material. This precursor powder had a spherical morphology with a unimodal distribution in the range of 10–30 μm. The precursor was mixed in a water-based organic solvent LISI W 15853 obtained from Warren Paint and Color Company (Nashville, TN, USA). The mixed slurry was then sprayed onto the preheated (~50 °C) substrate coupons using an air-pressurized spray gun. The sprayed coupons were air-dried to remove the moisture and a uniform thickness of 80 μm was maintained for all precoating deposits. Finally, the samples were scanned using a CW Nd:YAG laser equipped with a fiber optic beam delivery system to obtain a metallurgical bonding between the precursor and the substrate material. The schematic of the laser coating experimental setup used for the coating process is shown in figure 1. The fiber equipped with the laser system is interfaced with an end effector that houses a set of spherical and cylindrical lenses which are used to shape the laser beam output. The laser operates in the infrared region with a wavelength of 1064 nm. The laser processing parameters used for the coating process are presented in table 1. It can be observed (table 1) that two different laser output powers 215 W and 300 W corresponding to the laser fluences (energy density) of 137 J cm^{-2} and 191 J cm^{-2} were used for each side ways line spacing (100 μm and 200 μm). A lateral spacing of 100 μm and 200 μm is chosen so as to match the length scale of the naturally occurring three-dimensional extra cellular matrix (ECM) present in the human bone [13].

Table 1. The laser parameters.

Stand off distance	356 mm
Spot shape	Circular
Spot diameter	400 μm
Laser scan speed	500 mm s^{-1}
Average output power	215 W, 300 W
Laser fluence or energy density of the laser beam	137 J cm^{-2}, 191 J cm^{-2}
Line spacing	100 μm, 200 μm

Hence four different samples with a varying combination of laser fluence and surface topography were generated for the study.

2.2. Surface characterization

The surface microstructure, the microstructure across the cross section and the elemental analysis of the coated specimens were carried out using a LEO 1525 scanning electron microscope (SEM) coupled with an energy dispersive spectrometer (EDS). The samples in the cross section were prepared by polishing with emery papers of different grits ranging from 200 μm to 1000 μm in succession followed by disc polishing with colloidal silica of 0.3 μm and 0.05 μm to get a polished surface. The polished samples were then cleaned with acetone and etched with 5 vol % HF, 3 vol % HNO_3 and 92 vol % H_2O for 10–20 s by immersion etching to get the microstructural features. The phase evolutions within the processed samples were studied using an x-ray diffraction (XRD) technique. A Philips Norelco x-ray diffractometer with Cu-Kα radiation of wavelength 1.5418 Å was used for the XRD study. The XRD system was operated at 20 kV and 10 mA in a 2θ range of 0°–100° using a step size of 0.02° and a count time of 1 s.

The three-dimensional morphological evolutions, surface roughness and texture parameter of the coated samples were studied using a Leica confocal laser microscope, by scanning the laser beam across a surface area of 1500 μm × 1500 μm. The roughness values are recorded in the form of R_a (defined as the arithmetic average of all points of the profile also called the center line average height), R_z (arithmetic average of vertical distances between the highest peak and deepest valley within a sampling length) and R_{max} (maximum individual roughness depth). A total of five random scans were carried out across each sample to get an average and standard deviation within these roughness values. In order to have a precise understanding of the effect of three-dimensional topographic cues on wettability, the rough surfaces were assumed to hold a Gaussian profile with a cosine distribution of amplitude as proposed by Zhou and De Hosson [14]. Hence, in the present work, the surface texture was characterized in terms of the roughness parameters σ_A (the standard deviation of amplitude of random points on the surface from a line drawn through the trace such that cross-sectional areas of the asperities above and below the grooves are equal) and λ (the periodicity of the profile or the distance between any two successive crests or troughs), and their ratio (σ_A/λ) was used as a measure of surface texture. A total of five random scans were chosen on each sample and the sampling showed that both parameters (σ_A and λ) could be defined with an accuracy of 2–4%.

Table 2. Surface energy components of the standard liquids (units mJ m^{-2}) [16, 17].

Material	γ_L^{LW}	γ_L^+	γ_L^-	γ_L^{AB}	γ_L
Water	21.8	25.5	25.5	51.0	72.8
Formamide	39.0	2.28	39.6	19.0	58.0
Dioiodomethane	51.0	0	0	0	51.0

2.3. Contact angle and surface energy

Contact angle studies were carried out by a static sessile drop technique using a CAM-Plus^R contact angle goniometer (Cheminstruments, Inc. Fairfield, OH), equipped with a fiber optic light source and Video camera for imaging. A liquid droplet of volume 3 μl (droplet diameter of 2 mm) was placed on the thoroughly cleaned sample by a hypodermic syringe and the advancing contact angle was taken as a measure of wettability. The liquid drop placed on the sample was allowed to stabilize for 10 s before the reading was taken. The test was conducted at room temperature (26 °C) and a minimum of ten contact angle readings were taken on each sample to minimize errors in the measurement. Further, the measurement was based on the patented half angle method (US Patent 5 268 733) which eliminates the errors associated with the arbitrary tangential alignment.

The surface energy calculations were made according to the Van Oss [15] approach using the following equation:

$$(1+\cos\theta)\gamma_L = 2\left\{\left(\gamma_S^{LW}\gamma_L^{LW}\right)^{1/2} + \left(\gamma_S^+\gamma_L^-\right)^{1/2} + \left(\gamma_S^-\gamma_L^+\right)^{1/2}\right\}. \quad (1)$$

According to their approach the surface energy or surface energy of a solid γ_S (or a liquid γ_L) can be divided into the Lifshitz-van der Waals surface energy $\left(\gamma_S^{LW}\right)$ and Lewis acid-base surface energy $\left(\gamma_S^{AB}\right)$ components as described below:

$$\gamma_S = \gamma_S^{LW} + \gamma_S^{AB} \quad (2)$$

$$\gamma_S^{AB} = 2\sqrt{\gamma_S^+\gamma_S^-}. \quad (3)$$

Here γ_S^+ is the Lewis acidic or the electron-acceptor component, γ_S^- is the Lewis basic or the electron-donor component and θ is the contact angle of liquid L and solid S. The surface energy components of three well-characterized test liquids (table 2) [16, 17], i.e. one apolar (dioiodomethane) and two polar liquids (water and formamide) were used in equation (1) to solve for γ_S. In order to correlate the surface energy calculations to the mineralization behavior of the samples, contact angle measurements were also performed for both a simulated body fluid (SBF) and cell culture medium. The SBF solution was prepared by dissolving the reagent grade chemicals in the following order: NaCl (8.026 g), $NaHCO_3$ (0.352 g), KCl (0.225 g), $K_2HPO_4{\cdot}3H_2O$ (0.230 g), $MgCl_2{\cdot}6H_2O$ (0.311 g), $CaCl_2$ (0.293 g) and Na_2SO_4 (0.072 g) into distilled water (700 ml). The fluid was then buffered to pH = 7.4 at 37 °C with tri-hydroxymethyl-aminomethane (6.063 g) and 1.0-M hydrochloric acid

(40 ml). The cell culture medium used in the present case was Alpha minimum essential medium (Invitrogen Corporation, USA) supplemented with 10% fetal bovine serum (Thermo Fisher Scientific Inc., USA) and 1% penicillin/streptomycin (Invitrogen Corporation, USA).

2.4. In vitro bioactivity

To study the bioactivity and the mineralization kinetics, a set of four samples from each processing condition was immersed in the SBF solution. Plastic containers were used to soak the samples in SBF for different time periods (1, 3, 5 and 7 days). The solution was refreshed every 24 h to maintain a pH of 7.4, and the temperature was maintained at 37 °C during the course of the test. The samples were removed from the solution at specified time intervals followed by rinsing with distilled water and air drying for further analysis. Scanning electron microscopy (SEM) was used to observe the microstructure and morphological evolutions of mineralized samples. The phase analysis of mineralized samples was conducted using the XRD technique.

2.5. In vitro biocompatibility

In vitro biocompatibility of coated samples was evaluated through cell attachment and cell morphology during cell culture studies using the mouse pre-osteoblast MC3T3-E1 (subclone 14) cell line, obtained from American Type Cell Culture Collection (ATCC, Manassas, VA, USA). The cells were maintained in a tissue culture flask using the cell culture medium as described earlier at 37 °C under 5% CO_2 and 95% air in a humidified incubator. The culture medium was replaced every 3 days and confluent cells were trypsinized and replated (0.25% trypsin-EDTA, Invitrogen, USA) to maintain the cell line.

2.5.1. Cell viability. The coated samples and the control (untreated Ti-6Al-4V) of size 4 mm × 4 mm were cleaned with 70% ethanol and then UV sterilized prior to cell culture. The pre-osteoblast cells were then seeded on the surfaces of UV sterilized samples placed in 24-well culture plates at a density of 1.25×10^5 cells cm^{-2} and stored in the CO_2 incubator (maintained at 37 °C under 5% CO_2 and 95% air) for 1, 3 and 5 days. As, the seeding density of the pre-osteoblast cells were extremely high (1.25×10^5 cells cm^{-2}, only three different time periods, i.e. 1, 3 and 5 days were chosen to study the cell proliferation. To quantify the number of viable cells attached post-seeding, WST-1 assay was performed. WST-1 is a colorimetric assay where the absorbance at 450 nm is directly proportional to the amount of mitochondrial dehydrogenases activity in the cells. Briefly, samples were incubated with culture medium containing 10% WST-1 reagent (Roche, USA) for 4 h at 37 °C. After incubation, a 100 μl aliquot from each well was transferred to a 96-well plate and the absorbance at 450 nm was measured using a microplate reader (1420 Multilabel Counter, Wallac Victor 2). Blank wells containing only culture medium and WST-1 reagent were also prepared and used as background control for sample absorbance reading correction.

2.5.2. Cell morphology. The osteoblast cells were seeded on the UV sterilized samples at a lower density (1×10^4 cells cm^{-2}) and incubated for 24 h at 37 °C under 5% CO_2 and 95% air in a humidified incubator. For cell morphology analysis using SEM, cells cultured on the samples were fixed with 3% glutaraldehyde in 0.1 M cacodylate for 1 h and rinsed three times with phosphate buffered saline (PBS). The samples were further processed in 2% osmium tetroxide in 0.1 M cacodylate for 1 h, dehydrated with a series of increasing concentration of ethanol (25%, 50%, 70%, 95% and 100%), critical point dried and sputter-coated with gold for SEM observation. For immunocytochemical staining of the actin filament, the cells cultured on the samples were fixed with 4% paraformaldehyde (Sigma-Aldrich, USA) in 1× PBS for 30 min at 4 °C. After washing with PBS, the samples were permeabilized with 0.1% Triton X-100 (Fisher Scientific, USA) in 1× PBS for 5 min, blocked with 1% bovine serum albumin (BSA, Sigma-Aldrich, USA) for 30 min and stained with 2% Alexa 594 conjugated Phalloidin (Invitrogen, USA) fluorescent dye for 1 h. Cell nuclei were counterstained with 0.1% 4′, 6-diamidino-2-phenylindole (DAPI, Chemicon, USA) in 1× PBS for 5 min. Samples were washed three times with 0.05% Tween-20 (Sigma) in 1× PBS before and after the staining steps. All the staining procedures were carried out at room temperature. High-resolution fluorescence images were captured using an upright fluorescence microscope (Nikon). Once the images were captured, a representative image was selected for each processing parameter for quantitative analysis of cell spreading area. A total of 30 cells were randomly selected for each sample, manually outlined and the cell areas were calculated using the ImageJ image analysis software.

2.5.3. Data analysis. For a particular time period of seeding, a total of four samples were used from each laser processing parameters and the control (untreated Ti-6Al-4V). The results were expressed as the mean of four replicates ±SD (standard deviation). Statistical analysis carried out using a student *t*-test was applied to determine the statistical significance observed between the groups and $P < 0.05$ was considered statistically significant.

3. Results and discussions

3.1. Microstructure, morphological, phase and elemental analysis

Low magnification SEM (figure 2) of the surface of the coatings clearly shows the effect of laser track overlap on the surface morphology. By varying the laser track overlap in the lateral direction, two different periodic line patterns with 100 μm (figures 2(*a*) and (*b*)) and 200 μm (figures 2(*c*) and (*d*)) line spacings are obtained. Since cells are sensitive to micron scale features, such micro-textured topography is expected to provide an instructive background to guide their behavior toward tissue growth [18–21]. The cross-sectional SEM image (figure 3(*a*)) of the sample processed at 137 J cm^{-2} and 100 μm line spacing also clearly demonstrates

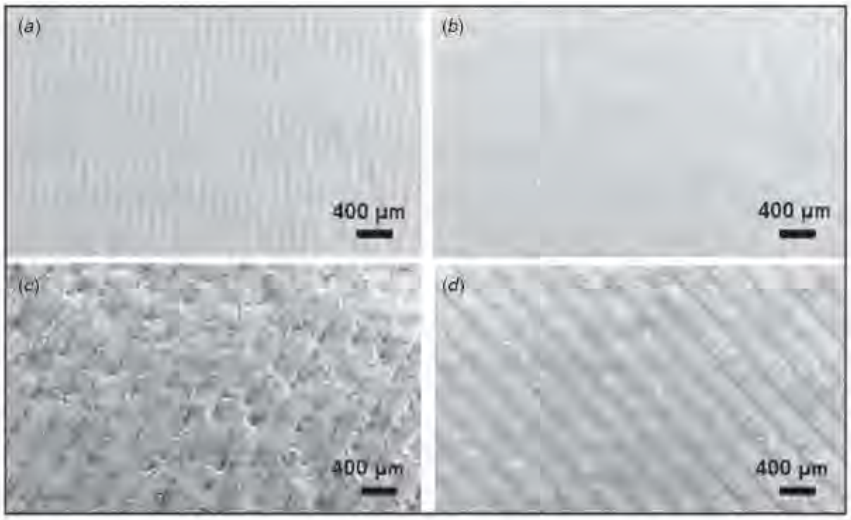


Figure 2. Low magnification SEM images of the surface of coatings processed at (*a*) 137 J cm^{-2}, 100 μm line spacing, (*b*) 191 J cm^{-2}, 100 μm line spacing, (*c*) 137 J cm^{-2}, 200 μm line spacing and (*d*) 191 J cm^{-2}, 200 μm line spacing.

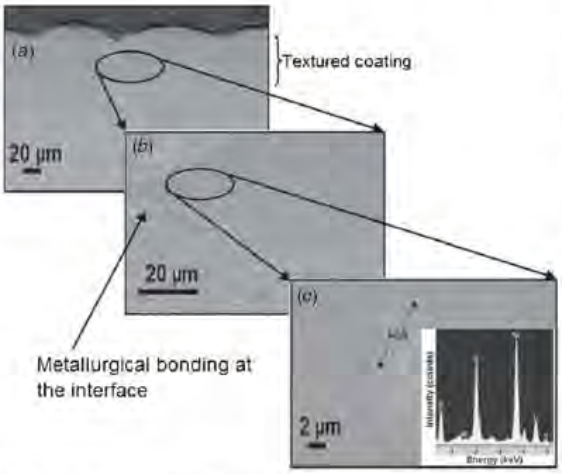


Figure 3. Cross-sectional SEM images of the sample processed at 137 J cm^{-2} and 100 μm line spacing: (*a*) revealing the textured coating, (*b*) revealing the sound metallurgical bonding at the interface and (*c*) a higher magnification of the coating and the inset showing the EDS pattern from the white precipitates.

the textured topography due to the lateral laser beam track overlap. This textured topography can induce a mechanical stimulation on the surrounding bone during the early days of implantation and help in quick fixation. This mechanical stimulation is attributed to the improved shear strength at the interface and mechanical interlocking when bone grows into the textured morphology [22]. A higher magnification SEM image (figure 3(*b*)) of the interface between the coating and the substrate is clearly an indicative of the sound metallurgical bonding between the coating and the substrate (Ti-6Al-4V). A sound bonding of bioceramic coating to the substrate material is expected to reduce the delamination of the ceramic layer and thereby avoids complications associated with osteolysis. The microstructural evolution within the coating (figure 3(*c*)) clearly shows the presence of the HA phase infiltrated in the matrix of Ti. The Ca/P atomic ratio of ~1.64 as obtained from the EDS spectra (presented as the inset in figure 3(*c*)) also further confirms the near HA composition. Due to the inherent rapid cooling the laser treatment has produced acicular α-Ti in the melt region. Under the set of laser parameters employed in the present study, the HA-based precursor and a part of the substrate Ti-6Al-4V has undergone rapid melting and mixing in the melt pool thereby forcing the infiltration of precursor (HA) into the molten volume of the substrate.

Unlike our previous studies [23–25] where there was no retainment of the precursor (HA phase) following laser processing, in the present work the presence of such a phase after laser processing was clearly evident from the XRD pattern (figure 4(*a*)). Under a varying combination of laser fluence and track overlap used in the present study, it can be observed from the composite of the XRD patterns (figure 4(*a*)) that there is no major change in the types of phases evolved and HA, $CaTiO_3$, $Ca_3(PO_4)_2$, TiO_2 (Anatase), TiO_2 (Rutile) and Ti are the major phases present within the coatings. From the variation in peak intensities, it can be realized that, although there is no change in the phase constituents, a variation in the amount of these phases with varying laser processing parameters exists. With an increase in laser fluence from 137 J cm^{-2} to 191 J cm^{-2}, there is an increase in intensity of the Ti and the Al_2O_3 phase along the (1 0 1) and (1 1 0) planes respectively. The intense presence of the above phases (Ti and Al_2O_3) at a higher laser fluence of 191 J cm^{-2} (used in the present study) can be attributed to the fact that at these laser processing conditions a substantial amount of the substrate (Ti-6Al-4V) material undergoes rapid melting and as a result float on the surface of the melt pool. Also, as the processing is carried

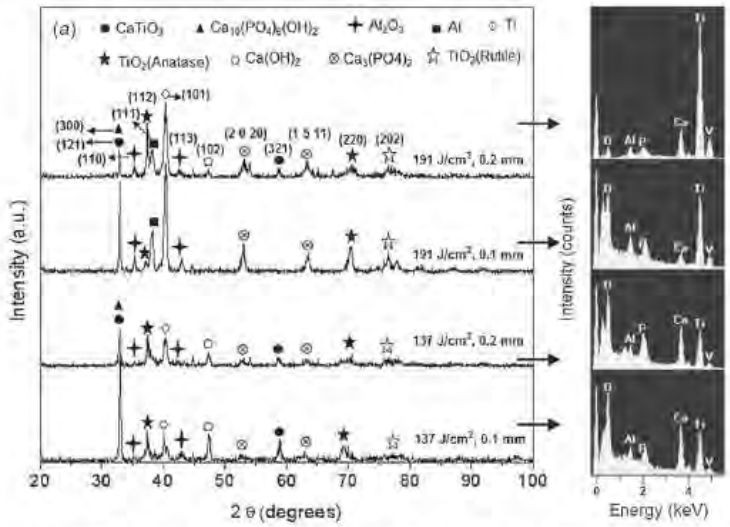


Figure 4. (*a*) XRD pattern and (*b*) corresponding EDS spectra for the laser processed samples.

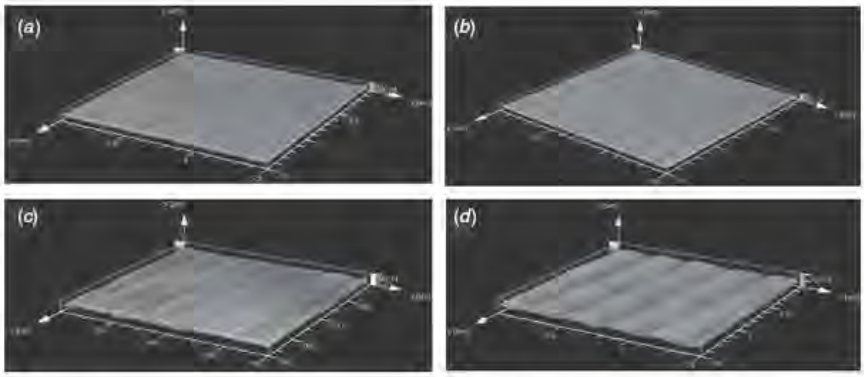


Figure 5. The three-dimensional confocal microscopic images of the surface of the coatings (surface area of 1500 μm × 1500 μm) processed at (*a*) 137 J cm^{-2}, 100 μm line spacing, (*b*) 191 J cm^{-2}, 100 μm line spacing, (*c*) 137 J cm^{-2}, 200 μm line spacing and (*d*) 191 J cm^{-2}, 200 μm line spacing.

out in an ambient atmosphere using argon as the cover gas, a certain amount of oxidation of the melt pool constituents is expected to take place leading to precipitation of a small amount of Al_2O_3 at the surface. With an increase in laser fluence, there is also an increase in the cooling rate [26, 27], and hence the constituents present in the melt pool are expected to be retained without vaporizing and precipitating Ti on the surface of the coating. The EDS spectra (figure 4(*b*)) obtained from a random location on the surface of the coating indicated the strong presence of Ca, P, Ti, Al, V and O peaks. From the composite of EDS spectra (figure 4(*b*)), it can be observed that there is an increase in intensity of the Ti and V peaks for the sample processed at 191 J cm^{-2}. This further complements with our earlier observations from the XRD studies proving the fact that a certain amount of dilution has taken place owing to the partial melting of the substrate material.

3.2. Effects of surface roughness and texture parameter on wettability

The effect of laser track overlap on the three-dimensional surface morphology of the coatings obtained using a confocal microscope is shown in figure 5. Irrespective of the laser fluence, the samples processed at 100 μm line spacing (figures 5(*a*) and (*b*)) have a smoother surface finish as compared to the samples processed at 200 μm spacing (figures 5(*c*) and (*d*)). The quantitative variation in surface roughness owing to varying combination of laser fluence and line spacing (track overlap) was also evaluated using a confocal laser microscopy. The samples processed for 100 μm line spacing (irrespective of the laser fluence) have significantly lower values of R_a, R_z, and R_{max} as compared to the samples processed for 200 μm line spacing (figure 6). With reduced track overlap or line spacing, there is an increase in the spot overlap (spot diameter ~400 μm) in the lateral direction

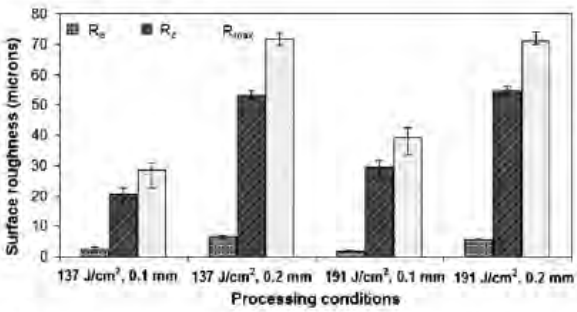


Figure 6. Variation in surface roughness parameters as a function of laser processing conditions.

leading to remelting of a predominant amount of the already melted layer. This remelting of the ceramic layer in turn smoothens the surface of coating. Further to correlate the effects of surface roughness on wettability, two additional surface roughness parameters, standard deviation of amplitude (σ_A) and periodicity (λ) are defined earlier in section 2.2. Their ratio (σ_A/λ) is taken as a measure of surface texture. As discussed earlier, the values of σ_A and λ were taken from five random locations on each sample and are presented as mean values with related scatter in table 3. The corresponding mean values of σ_A/λ and its related scatter as a measure of surface texture are also included in table 3. It can be observed that the laser processed samples have a significantly smaller value of σ_A/λ as compared to the control (untreated Ti-6Al-4V). Further, within the laser processing parameters employed in the present study, the samples processed at 100 μm line spacing have a notably smaller value of σ_A/λ as compared to the samples processed at 200 μm line spacing. This further complements to our results obtained from the roughness parameters R_a, R_z and R_{max} (figure 6).

From our earlier work [24] and the work by Zhou and De Hosson [14], it was clear that the texture parameter (σ_A/λ) significantly affects the wetting behavior of a liquid. Table 3 lists the experimental contact angles subtended by three different liquids (water, formamide and dioiodomethane) on each of these surfaces. With a decrease in the σ_A/λ value, there is a decrease in the experimental contact angles for three test liquids (table 3). Further, all the laser processed samples have a significantly smaller value of experimental contact angle (for the three testing liquids) as compared to the control (Ti-6Al-4V). This improved hydrophilic behavior for the laser processed samples is attributed to the influence of surface texture and the same phases (HA, $CaTiO_3$, $Ca_3(PO_4)_2$, TiO_2 (Anatase), TiO_2 (Rutile), and Ti) evolved during laser processing. Also within the laser processing parameters employed in the present study, the samples processed at 100 μm line spacing has a significantly smaller value of experimental contact angle (for the three testing liquids) compared to the samples processed at 200 μm line spacing.

The improved wetting behavior for the laser processed samples, and the correlation between texture parameter (σ_A/λ) and experimental contact angles can be explained as follows. Based on SEM (figure 2) and confocal microscopic (figure 5) images along with smaller σ_A/λ value (table 3), the textures generated in the present study are confirmed to be of radial groove type [14, 24]. As proposed by Zhou and De Hosson [14] the equilibrium relationship between the experimental contact angle affected by the radial grooves (θ_{rad}) and the theoretical contact angle (θ_{th}) can be described as follows:

$$\cos\theta_{rad} = D(1 - F)\cos\theta_{th} - F, \quad (4)$$

where D is defined as the average area ratio of real contacted interface to its projected part, and F is the area fraction of an uncontacted solid–liquid interface on solid. The theoretical contact angle θth is defined as $\mathrm{Cos}\theta_{th} = (\gamma_S - \gamma_{LS})/\gamma_L$ where γ_S, γ_{LS} and γ_L are the interface energies between solid–vapor, liquid–solid and liquid–vapor interfaces respectively. For a radial groove both D and F are constants and since, the rough surface is assumed to distribute as a cosine profile with a Gaussian distribution, they are both a function of σ_A/λ [14]. Hence, when a liquid drop is placed on such a surface (smaller σ_A/λ value), it can easily overcome the energy barriers associated with it and completely wet it. Thus, an equilibrium state of wetting is achieved when the grooves are radial. Further it can also be conditioned that as the σ_A/λ value increases there is an increase in the contact angle and vice versa thereby further confirming our results (table 3).

The surface energy calculations obtained using equations (1)–(4) further showed compatibility with our previous observations on surface roughness (R_a, R_z and R_{max}), texture parameter (σ_A/λ) and contact angle. Accordingly, the laser processed samples have a higher surface energy value (~45.77 mJ m^{-2}–52.05 mJ m^{-2}) compared to the Ti-6Al-4V control (~34.19 mJ m^{-2}). This increase in the surface energy (γ_s) for the laser processed samples is mostly contributed from the higher value of the Lifshitz–Vander Waals surface energy (γ_S^{LW}) component compared to the Lewis acid-base surface energy (γ_S^{AB}) component (table 3). Further within the laser processed samples, the samples processed at 100 μm line spacing (having lower value of R_a, R_z, R_{max}, and σ_A/λ and being hydrophilic) have a higher γ_S^{LW}, γ_S^{AB} and γ_s (mJ m^{-2}) compared to the samples processed at 200 μm line spacing. This, therefore, clearly demonstrates the effect of laser processing in producing controlled topographic cues with appropriate surface chemistry, which in turn significantly increased the values of the surface energy components and thereby the value of γ_S.

When an implant material is placed inside a human body, among the plethora of events that takes place, the first and the foremost one is the wetting of the implant material by the physiological fluids. This further controls the absorption of proteins followed by attachment of cells to the implant materials. Hence, understanding the wettability of SBF and culture media by contact angle measurements is also an important part of this work. The contact angle measurements obtained from these two liquids may also provide an understanding of the effect of surface energy on their wetting behavior and thereby its bioactivity (following immersion in SBF) and cell viability. Table 4 presents the contact angles and corresponding light optical images of the liquid droplet shadow on the laser processed samples and

Table 3. Experimental results of contact angles of test liquids, texture parameter (σ_A/λ), surface energy components and surface energy as function of sample processing conditions.

Samples	Standard deviation		Texture	Contact angle			Surface energy components		Surface
processing conditions	of amplitude σ_A (μm)	λ (μm) Periodicity	parameter (σ_A/λ)	Distilled water	Formamide	Dioiodomethane	γ_S^{LW}	γ_S^{AB}	energy γ_s (mJ m^{-2})
Ti-6Al-4V control	12.56 ± 0.37	2.79 ± 0.08	4.38 ± 0.04	82.6 ± 0.08	57.4 ± 0.06	53 ± 0.04	29.87 ± 0.004	4.27 ± 0.03	34.19 ± 0.045
137 J cm^{-2}, 0.1 mm	3.024 ± 0.114	150.6 ± 0.44	0.0171 ± 0.0001	53.7 ± 0.16	31.9 ± 0.10	29.4 ± 0.08	43.97 ± 0.002	8.08 ± 0.02	52.05 ± 0.039
137 J cm^{-2}, 0.2 mm	7.926 ± 0.081	401.4 ± 0.92	0.0203 ± 0.0002	71.8 ± 0.11	35.9 ± 0.12	39.3 ± 0.07	39.81 ± 0.018	6.43 ± 0.04	46.25 ± 0.041
191 J cm^{-2}, 0.1 mm	2.528 ± 0.033	133.3 ± 0.44	0.0189 ± 0.0002	62.4 ± 0.05	32.4 ± 0.06	31.6 ± 0.08	44.80 ± 0.008	7.01 ± 0.02	51.82 ± 0.015
191 J cm^{-2}, 0.2 mm	8.858 ± 0.025	397.5 ± 0.85	0.0223 ± 0.0001	73.4 ± 0.15	37.9 ± 0.12	39.9 ± 0.09	40.11 ± 0.003	5.65 ± 0.05	45.77 ± 0.047

Table 4. Contact angles and corresponding light optical images of the liquid droplet shadow on the laser processed samples and on the control (untreated Ti-6Al-4V).

Samples processing conditions	Contact angle	
	Growth media ($\theta_{growthmedia}$)	Simulated body fluid (θ_{SBF})
Ti-6Al-4V control (untreated)	79.2 ± 1.84 	62.5 ± 0.85 
137 J cm^{-2}, 0.1 mm	69.91 ± 0.74 	50.82 ± 2.5 
137 J cm^{-2}, 0.2 mm	74 ± 1.2 	59.46 ± 1.2 
191 J cm^{-2}, 0.1 mm	70.42 ± 0.8 	55.91 ± 1.07 
191 J cm^{-2}, 0.2 mm	78.58 ± 1.21 	60.16 ± 0.7 

on the control (untreated Ti-6Al-4V). The results (table 4) demonstrated a more hydrophilic behavior (improved wettability) for the laser processed samples compared to the control (untreated Ti-6Al-4V). Also, as discussed earlier, within the laser processing parameters employed in the present work, the samples with lower σ_A/λ value and higher surface energy γ_s (100 μm line spaced) demonstrated more hydrophilic nature for both liquids (SBF and culture media) as compared to the samples with higher σ_A/λ value and lower surface energy γ_s (200 μm line spaced). This is attributed to the fact that when a liquid drop is placed on a surface with higher surface energy, it tries to reduce its energy and come back to an equilibrium state by interacting with the molecules present in the liquid drop and there by resulting in the spreading and an improved wettability.

3.3. Bioactivity and mineralization kinetics

The *in vitro* bioactivity of the Ca-P coatings and control (untreated Ti-6Al-4V) is accessed for the precipitation of an apatite (HA, $[Ca_{10}(PO_4)_6(OH_2)]$)-like mineral layer on the surface during immersion in simulated body fluid (SBF). The precipitation of such a phase under *in vivo* conditions following insertion of the implant into the body is beneficial, as HA is a naturally occurring mineral component of the human bone laying along side the collagen fibrils [13–28]. Hence, this layer provides the appropriate chemistry and thereby acts as a bone bonding interface, where the cells can preferentially proliferate and differentiate into higher ordered structures such as bone [13].

Within the detectable limits of the XRD instrument, as compared to the laser surface treated samples, no HA formation on control (untreated Ti-6Al-4V) is realized after 1 day immersion in SBF. Hence, the XRD spectra corresponding to the control (untreated Ti-6Al-4V) are not included in the present study. However, for all the laser processed samples following immersion in SBF for each soaking period, the presence of an apatite phase is evident from the characteristic HA peaks at $2\theta \sim 21.82°$ and 31.75° and corresponding to the planes (2 0 0) and (2 1 1) respectively (figures 7–10). For the samples processed at 100 μm line spacing (having lower value of R_a, R_z, R_{max} and σ_A/λ and increased wettability) following 1 day after immersion in SBF, XRD spectra (figures 7(*a*) and 8(*a*)) demonstrated a highly

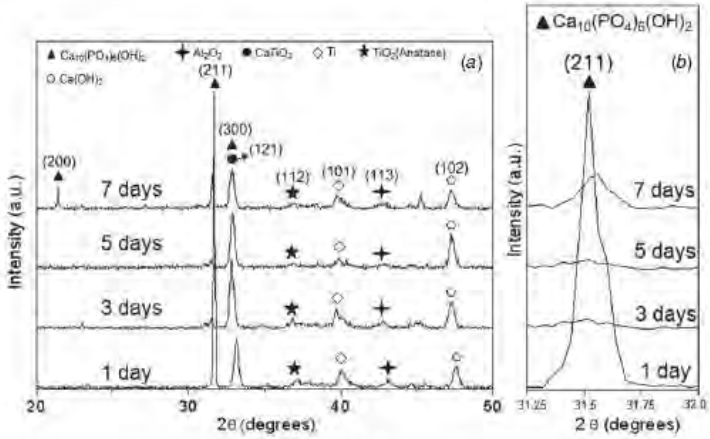


Figure 7. (*a*) XRD spectra of the samples processed at 137 J cm^{-2}, 100 μm line spacing and (*b*) corresponding enlarged spectra ($2\theta \sim 30°$–$32°$) following immersion in SBF.

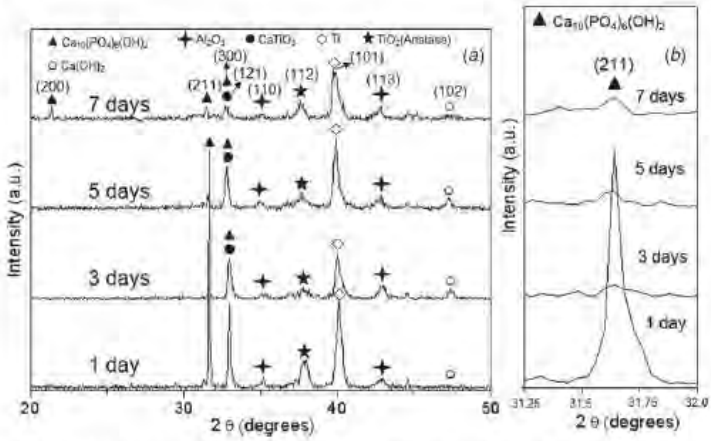


Figure 8. (*a*) XRD spectra of the samples processed at 191 J cm^{-2}, 100 μm line spacing and (*b*) corresponding enlarged spectra ($2\theta \sim 30°$–$32°$) following immersion in SBF.

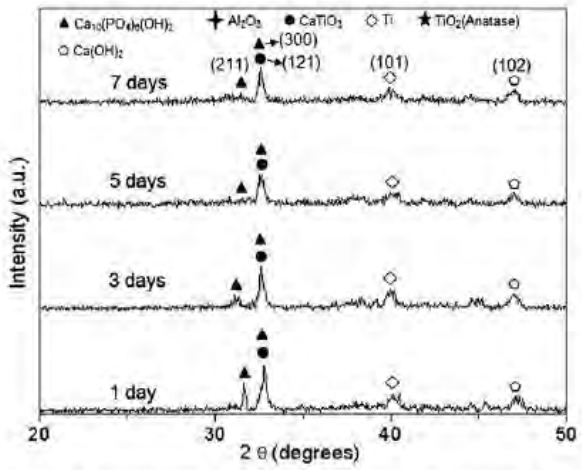


Figure 9. XRD spectra of the samples processed at 137 J cm^{-2}, 200 μm line spacing following immersion in SBF.

intense peak attributable to the apatite phase at $2\theta \sim 31.75°$ corresponding to the plane (2 1 1). In contrast, the intensity of this peak (figures 9 and 10) is low for the samples processed at 200 μm line spacing (having lower value of R_a, R_z, R_{max} and σ_A/λ and increased wettability). Also for the samples processed at 100 μm line spacing after 3 and 5 days of immersion in SBF, the apatite peak (at $2\theta \sim 31.75°$) becomes broadened with a reduction in intensity (figures 7(*b*) and 8(*b*)). This gives an indication that there is a rapid transformation from a highly crystallized HA phase to a near amorphous or low crystallite-sized HA phase. However, after 7 days immersion (figure 7(*a*) and 8(*a*)) the characteristic apatite peak (at $2\theta \sim 31.75°$) again recrystallized and there is also an additional peak at $2\theta \sim 22.0°$ corresponding to the plane (2 0 0). Such a rapid transformation from a highly crystallized HA phase (following 1 day immersion in SBF) to an near amorphous HA phase (following 3 and 5 days immersion in SBF) and again thereafter undergoing recrystallization is not observed for the samples processed at 200 μm line spacing.

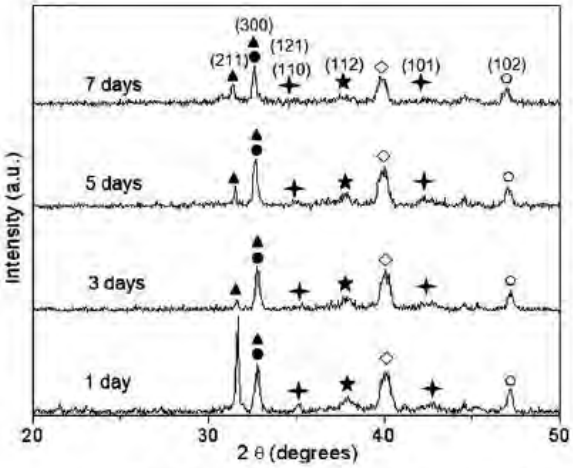


Figure 10. XRD spectra of the samples processed at 191 J cm^{-2}, 200 μm line spacing following immersion in SBF.

From the XRD studies (figures 7–10), it is evident that both the samples processed at 100 μm line spacing irrespective of the laser fluence used (137 and 191 J cm^{-2}) demonstrated the same superior mineralization kinetics as compared to the samples processed at 200 μm line spacing following immersion in SBF. Hence, SEM analysis (figure 11) is only done for the sample processed at 100 μm line spacing and 137 J cm^{-2} laser fluence. It can be observed (figure 11(*a*)) that after 1 day immersion in SBF, characteristic whisker-like apatite crystals are nucleated on the surface of the sample. As the immersion time is increased to 3 days, the whisker-like feature seems to have got covered by another mixed layer of whisker-like and nano HA crystals (figure 11(*b*)). After 5 day immersion, the layer is completely covered with nano crystallites of HA (figure 11(*c*)) and at the end of 7 days there is a thick mineralized layer of HA on the surface of the sample (figure 11(*d*)). These observations further demonstrated a strong agreement with our XRD results (figures 7 and 8) obtained earlier. This rapid modification and mineralization kinetics of HA on the surface of samples processed at 100 μm line spacing (following immersion in SBF) is attributed to the higher surface energy and increased hydrophilicity as a result of the of appropriate surface textures (lower σ_A/λ value) and the same phases (HA, $CaTiO_3$, $Ca_3(PO_4)_2$, TiO_2 (Anatase), TiO_2 (Rutile) and Ti) evolved during laser processing.

3.4. Biocompatibility

3.4.1. SEM observations for cell morphology. Cell morphology for the laser processed and control (untreated Ti-6Al-4V) samples after 1 day culture of MC3T3-E1 osteoblast-like cells was assessed by SEM and the results are presented in figure 12. The MC3T3-E1 osteoblast-like cells show a triangular morphology (figure 12(*a*)) on the control (untreated Ti-6Al-4V) samples and have a rectangular and elongated morphology on the laser processed samples (figures 12(*b*)–(*e*)). Their good adhesion especially on the laser processed samples is characterized by the lamellipodia trying to extend and adhere along the grooves. In contrast, no such adhesion is observed on the control (untreated Ti-6Al-4V) sample. Also from the SEM images (figure 12), it can be observed that the number of cells on the control (untreated Ti-6Al-4V) samples are significantly less compared to the laser processed samples. Such a difference in cell spreading and adherence on these samples is attributed to both the varying surface chemistry and surface roughness as a result of laser processing. Further, the laser processed samples also provided the appropriate length scales (micro-textured surface patterns with 100 μm and 200 μm line spacing) for the cells to interact and spread on these surfaces.

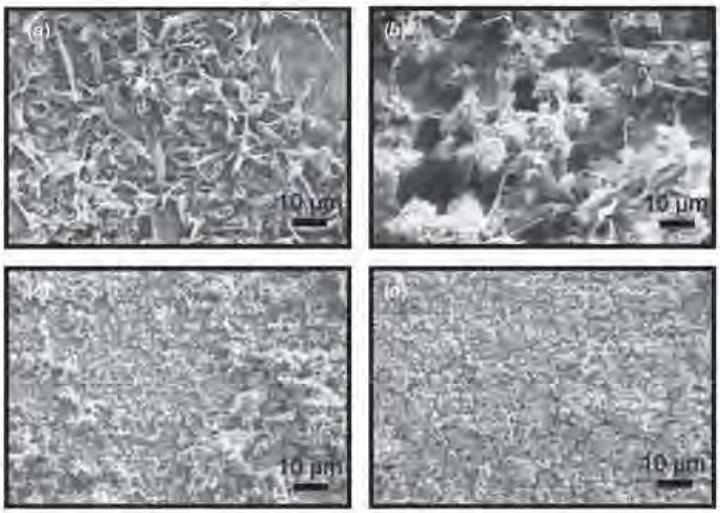


Figure 11. SEM images of the sample processed at 137 J cm^{-2}, 100 μm line spacing following immersion in SBF for (*a*) 1 day, (*b*) 3 days, (*c*) 5 days and (*d*) 7 days.

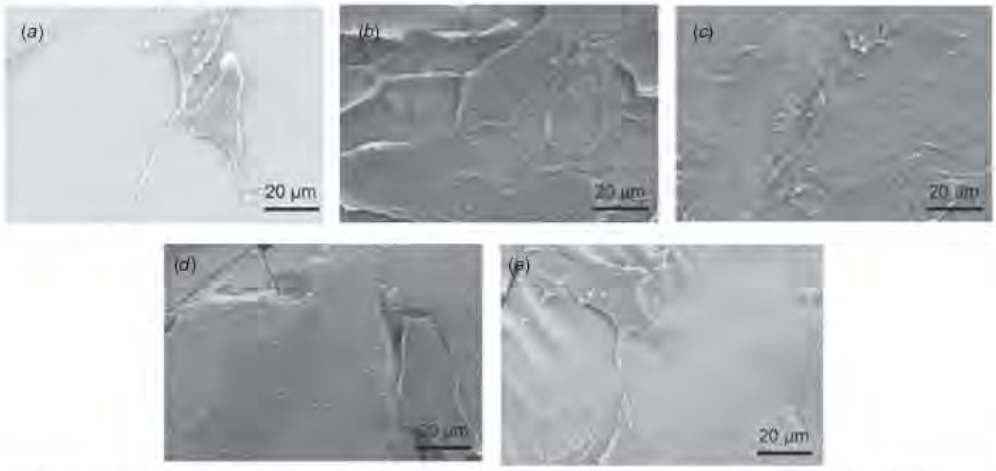


Figure 12. Cell morphology of MC3T3-E1 osteoblast-like cells after culture for 1 day on (*a*) control (untreated Ti-6Al-4V), and samples processed at (*b*) 137 J cm^{-2}, 100 μm line spacing, (*c*) 191 J cm^{-2}, 100 μm line spacing, (*d*) 137 J cm^{-2}, 200 μm line spacing, and (*e*) 191 J cm^{-2}, 200 μm line spacing.

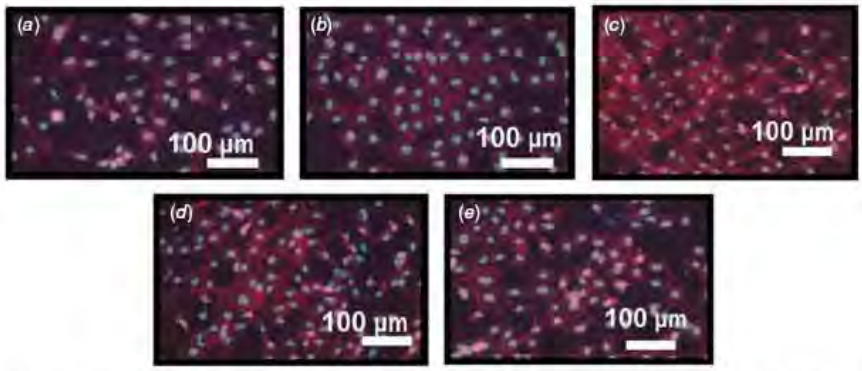


Figure 13. Fluorescent micrographs for cytoskeleton assessment of adherent MC3T3-E1 osteoblast-like cells after culture for 1 day on (*a*) control (untreated Ti-6Al-4V substrate) and samples processed at (*b*) 137 J cm^{-2}, 100 μm line spacing, (*c*) 191 J cm^{-2}, 100 μm line spacing, (*d*) 137 J cm^{-2}, 200 μm line spacing and (*e*) 191 J cm^{-2}, 200 μm line spacing.
(This figure is in colour only in the electronic version)

3.4.2. Cell cytoskeleton observation and cell spreading. The cytoskeletal organization of the cells on the control (untreated Ti-6Al-4V) and laser processed samples after 1 day culture are presented in figure 13. The cells are more confluent with well-stressed actin filaments on the laser processed samples as compared to the control (untreated Ti-6Al-4V). The quantified area of the cells measured using the ImageJ software indicated more spreading of the cell on the sample processed at 100 μm line spacing compared to the control (untreated Ti-6Al-4V) and the sample processed at 200 μm line spacing (figure 14). This improved cytoskeletal organization and spreading of the cells on the 100 μm line spaced sample is attributed to the higher surface energy as a result of the appropriate surface texture (lower σ_A/λ value) and the same phases (HA, $CaTiO_3$, $Ca_3(PO_4)_2$, TiO_2 (Anatase), TiO_2 (Rutile) and Ti) evolved during laser processing.

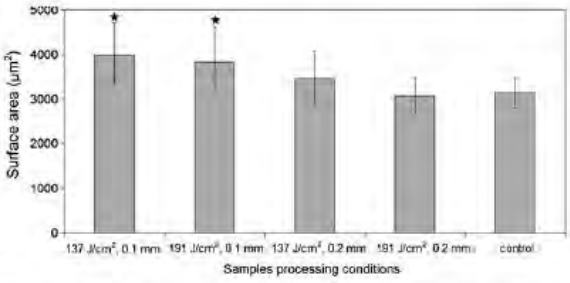


Figure 14. Graphical representation of the cell spreading area as a function of sample processing conditions. ⋆ denotes that the laser processed group is significantly higher than the control Ti-6Al-4V ($p < 0.05$). Cell spreading area measurements were taken from 30 different cells.

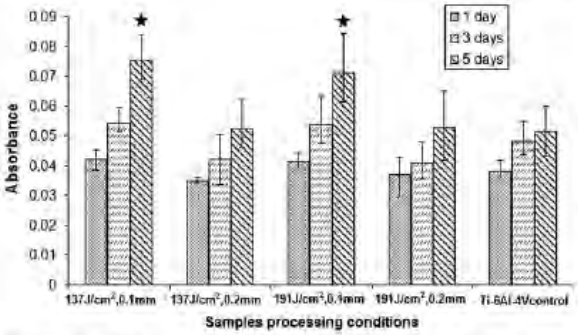


Figure 15. WST-1 assay of the MC3T3-E1 osteoblast-like cells following culture for 1, 3 and 5 days as a function of samples processing conditions. ⋆ denotes that the laser processed group is significantly higher than the control Ti-6Al-4V ($p < 0.05$).

3.4.3. Cell viability. The number of viable cells on the laser processed samples and control (untreated Ti-6Al-4V) was evaluated using WST-1 assay after 1, 3 and 5 day of culture of the cells. For the three different time periods, the number of viable cells appeared to be more for the samples processed at 100 μm line spacing as compared to the control (untreated Ti-6Al-4V) and the sample processed at 200 μm line spacing (figure 15). The absorbance for the control (untreated Ti-6Al-4V) and the 200 μm line spaced samples is comparable for the three different time periods. This improved behavior of the 100 μm line spaced sample further complemented to all our results and observations made earlier.

Finally as there was an indication of overall improved behavior with decrease in line spacing (from 200 μm to 100 μm), samples with still smaller line spacing (20–50 μm) may demonstrate much more improved characteristic in terms of hydrophilicity, *in vitro* bioactivity and *in vitro* biocompatibility. Hence, separate efforts are being made by the group to synthesize such smaller line spaced coatings with features as close to a typical osteoblast cells size as possible and thereby study their properties.

4. Conclusions

Using a laser-based coating technique, micro-textured Ca-P coatings with two different lines spacing (100 and 200 μm) are synthesized on the Ti-6Al-4V substrates. By appropriate selection of laser processing conditions only a variation in surface morphology is achieved keeping the chemistry same. With the decrease in the texture parameter (σ_A/λ) there is an increase in surface energy and hence the samples processed at 100 μm line spacing (irrespective of the laser fluence used in the present study) are associated with a higher surface energy as compared to the control (untreated Ti-6Al-4V) and the 200 μm line spaced samples. Owing to the higher surface energy, the 100 μm line spaced samples (smaller σ_A/λ) demonstrated increased hydrophilicity to SBF and culture media. As a result of this increased hydrophilicity, the 100 μm line spaced samples demonstrated enhanced mineralization (*in vitro* bioactivity) following immersion in SBF and improved *in vitro* biocompatibility characterized by the increased proliferation and spreading of the MC3T3-E1 osteoblast cells. These biocompatible Ca-P-based bioceramic coatings associated with their micro-textured surface topography are expected to induce improved osseointegration and bone mineralization at the tissue/implant interface.

References

[1] Palson B Ø and Bhatia S N 2004 *Tissue Engineering* 1st edn (NJ: Pearson Prentice-Hall) pp 252–5

[2] Chou L, Marek B and Wagner W R 1999 Effects of hydroxyapatite coating crystallinity on biosolubility, cell attachment efficiency and proliferation *in vitro Biomaterials* **20** 977–85

[3] Cui Z D, Chen M F, Zhang L Y, Hu R X, Zhu S L and Yang X J 2008 Improving the biocompatibility of NiTi alloy by chemical treatments: an *in vitro* evaluation in 3T3 human fibroblast cell *Mater. Sci. Eng.* C **28** 1117–22

[4] Kikuchi L, Park J Y, Victor C and Davies J E 2005 Platelet interactions with calcium-phosphate-coated surfaces *Biomaterials* **26** 5285–95

[5] Ramires P A, Romito A, Cosentino F and Milella E 2001 The influence of titania/hydroxyapatite composite coatings on *in vitro* osteoblasts behavior *Biomaterials* **22** 1467–74

[6] Ji H, Ponton C B and Marquis P M 1992 Microstructural characterization of hydroxyapatite coating on titanium *J. Mater. Sci., Mater. Med.* **3** 283–7

[7] Boyd A R, Meenan B J and Leyland N S 2006 Surface characterization of the evolving nature of radio frequency magnetron sputter deposited calcium phosphate thin films after exposure to physiological solution *Surf. Coat. Technol.* **200** 6002–13

[8] Haddow D B, James P F and Van Noort R 1998 Sol-gel derived calcium phosphate coatings for biomedical applications *J. Sol-Gel Sci. Technol.* **13** 261–5

[9] Nelea V, Ristoscu C, Chiritescu C, Ghica C, Mihailescu I N, Pelletier H, Mille P and Cornet A 2000 Pulsed laser deposition of hydroxyapatite thin films on Ti-5Al-2.5Fe substrates with and without buffer layers *Appl. Surf. Sci.* **168** 127–31

[10] Shirkhanzadeh M 1991 Bioactive calcium phosphate coatings prepared by electrodeposition *J. Mater. Sci. Lett.* **10** 1415–7

[11] Lavos-Vaalereto C, Wolynec S, Deboni M C Z and König B Jr 2001 *In vitro* and *in vivo* biocompatibility testing of Ti-6Al-7Nb alloy with and without plasma-sprayed hydroxyapatite coating *J. Biomed. Mater. Res. (Appl. Biomater.)* **58** 727–33

[12] Ball M D, Downes S, Scotchford C A, Antonov E N, Bagratashvili V N, Popov V K, Lo W J, Grant D M and Howdle S M 2001 Osteoblast growth on titanium foils coated with hydroxyapatite by pulsed laser ablation *Biomaterials* **22** 337–47

[13] Stevens M M and George J H 2005 Exploring and engineering the cell surface interface *Science* **310** 1135–8

[14] Zhou XB and De Hosson JThM 1995 Influence of surface roughness on the wetting angle *J. Mater. Res.* **10** 1984–92

[15] Van Oss CJ, Good RJ and Chaudhury MK 1988 Additive and nonadditive surface tension components and the interpretation of contact angles *Langmuir* **4** 884–91

[16] Randeniya L K, Bendavid A, Martin P J, Amin M S, Preston E W, Ismail F S M and Coe S 2009 Incorporation of Si and SiO_x into diamond-like carbon films: impact on surface properties and osteoblast adhesion *Acta Biomaterialia* **5** 1791–7

[17] Van Oss C J, Giese R F Jr and Good R J 1990 Reevaluation of the surface tension components and parameters of

polyacetylene from contact angle of liquids *Langmuir* **6** 1711–13

[18] Zhao G, Raines A L, Wieland M, Schwartz Z and Boyan B D 2007 Requirement for both micron- and submicron scale structure for synergistic responses of osteoblasts to substrate surface energy and topography *Biomaterials* **28** 2821–9

[19] Zhu X, Chen J, Scheideler L, Altebaeumer T, Geis-Gerstorfer J and Kern D 2004 Cellular reactions of osteoblasts to micron- and submicron scale porous structures of titanium surfaces *Cells Tissues Organs* **178** 13–22

[20] Duncan A C, Weisbuch F, Rouais F, Lazare S and Baquey Ch 2002 Laser microfabricated model surfaces for controlled cell growth *Biosens. Bioelectron.* **17** 413–26

[21] Bhatia S N and Chen C S 2004 Tissue engineering at the microscale *Biomed. Microdevices* **2** 1387–2176

[22] Hansson S and Norton M 1999 The relation between surface roughness and interfacial shear strength for bone-anchored implants: a mathematical model *J. Biomech.* **32** 829–36

[23] Paital S R, Balani K, Agarwal A and Dahotre N B 2009 Fabrication and evaluation of a pulse laser-induced Ca-P coating on a Ti alloy for bioapplication *Biomed. Mater.* **4** 1–10

[24] Paital S R and Dahotre N B 2009 Wettability and kinetics of hydroxyapatite precipitation on laser textured Ca-P Bioceramic coating *Acta Biomaterialia* **5** 2763–72

[25] Paital S R and Dahotre N B 2007 Laser surface treatment for porous and textured Ca-P bio-ceramic coating on Ti-6Al-4V *Biomed. Mater.* **2** 274–81

[26] Harimkar S P, Samant A N and Dahotre N B 2007 Temporally evolved recoil pressure driven melt infiltration during laser surface modifications of porous alumina ceramic *J. Appl. Phys.* **101** 054911

[27] Harimkar S P, Samant A N, Khangar A A and Dahotre N B 2006 Prediction of solidification microstructures during laser dressing of alumina based grinding wheel material *J. Phys. D: Appl. Phys.* **39** 1642–9

[28] Rho J Y, Kuhn-Spearing L and Zioupos P 1998 Mechanical properties and the hierarchical structure of bone *Med. Eng. Phys.* **20** 92–102

Laser Process Effects on Physical Texture and Wetting in Implantable Ti-Alloys*

Sameer R. Paital, Wei He, Claus Daniel, and Narendra B. Dahotre

Wetting is an important aspect for implantable biomaterials, as it affects the initial interaction with physiological fluids, which in turn dictates the protein adsorption, cell attachment, and tissue integration at the interface. In light of this in the present overview, surface engineering techniques based on laser processing of implantable titanium alloys for improved wettability and cell compatibility is discussed. Here three different laser processing techniques, Laser interference patterning, continuous wave laser direct melting, and pulsed laser direct melting and the influence of each type of processing on the micro-texture evolution are studied. Finally, the effect of micro-textures on the wettability and thereby its in vitro bioactivity and in vitro biocompatibility is systematically discussed.

INTRODUCTION

Surfaces and Interfaces for Bone Tissue Engineering

The interface between the implanted biomaterial and the living tissue is the site of a variety of dynamic biochemical processes and reactions.[1] These numerous atomic and molecular level events at the interface modulate the surface chemistry and morphology of the implant material, and which in turn influences its long-term durability and compatibility inside the body.[1] Under ideal situations, following implantation, a protein rich layer is supposed to be confirmed at the surface of an implant material as it further influences the cell attachment and tissue integration. The presence or the interaction of protein molecules depends on the wetting characteristic or the hydrophilicity of the implant material with the physiological fluids. The two most important factors that govern the wetting of the implant material with the physiological fluids are the surface chemistry and surface morphology of the implant material. Hence, there is a tremendous interest toward surface modification and effective design of such implantable materials so as to improve their hydrophilicity and thereby elicit a specific, desired, and timely response from the surrounding cells and tissues.

For bone tissue engineering applications, the most common design approach followed by various researchers is to mimic the functionality of the naturally occurring hierarchically organized hard tissue into the artificial implant material.[2–5] It has been well understood that human bone is rich in calcium and phosphorous based hydroxyapatite (HA) phase at the nanoscale, and have a three-dimensional (3-D) extra cellular matrix (ECM) to support bone cells at the sub-micrometer scale.[6,7] Hence, artificial biomaterials with biocompatible HA coatings on titanium based alloys, and engineered 3-D features at the meso-scale to support cells and tissue integration is becoming a reality. However, most of the surface engineering techniques[8–10] used are "line of sight" methods: they either provide the appropriate surface chemistry (calcium and phosphorous based) or the 3-D topographic cue and lack in ability to achieve both simultaneously. Hence, in the present overview we demonstrate the laser-based surface engineering approach by which both an appropriate surface chemistry and regular 3-D topographic cues can be achieved simultaneously. Also, the effect of laser processing parameters and laser operation mode on the morphological and phase evolution is going to be discussed.

Finally, as discussed above, since the surface morphology and surface chemistry of the implant material affects its wetting behavior under in vivo condi-

How would you...

...describe the overall significance of this paper?

This paper demonstrates the usage of high energy laser beams to synthesize biocompatible surfaces at various length scales for load bearing implant applications. It also demonstrates the significance of wetting phenomena for bioapplication and the use of laser surface engineering to achieve surfaces with tunable wetting characteristics.

...describe this work to a materials science and engineering professional with no experience in your technical specialty?

Fabricating and designing biomaterials to provide appropriate surface chemistry and surface morphology is a significant challenge for many materials scientists. To meet the above requirement we use a laser based direct melting and laser interference patterning technique. Here by using a high energy laser beam we provide calcium phosphate based bioactive textured coating on Ti-6Al-4V. This process only alters the surface chemistry without altering the bulk mechanical properties of the material.

...describe this work to a layperson?

Our work is mostly focused on synthesizing or designing artificial materials for load bearing implant applications. These materials are mostly used inside a body to replace a damaged hard tissue and thereby restore its function. Hence while designing these artificial materials for such applications, materials scientists are mostly concerned about mimicking the material as close as possible to the naturally occurring tissue and there by make it more biocompatible.

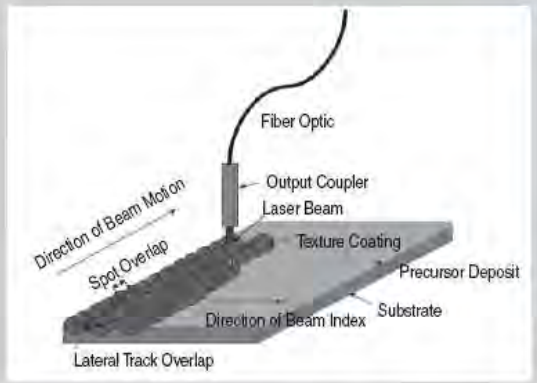


Figure 1. Schematic of a pulsed Nd:YAG laser set up.

Equations

$$w = \frac{\pi}{2\sin\left(\frac{\beta}{2}\right)} \quad (1)$$

$$\cos\theta_c = \frac{w}{2(h^2 + \frac{w^2}{4})^{\frac{1}{2}}} = \frac{1}{\sqrt{1 + \frac{4h^2}{w^2}}} \quad (2)$$

$$\cos\theta_c = \frac{1-\phi_s}{R_f - \phi_s} \quad (3)$$

tions, attempts are being made to better understand these findings by conducting wetting experiments on laser textured surfaces with varying surface morphology and surface chemistry.

PULSED LASER SYNTHESIS OF TEXTURED Ca-P COATING

A pulsed laser is characterized by the short pulse duration (femtoseconds to milliseconds), high peak power, and intermittent delivery of the laser beam. During the impact of such ultra-short pulses a fine layer of material is melted and then is vaporized at the surface, forming a vapor jet. This jet induces a recoil pressure and the liquid metal underneath is pushed toward the edges of the impact. After the end of the laser pulse the liquid metal solidifies and forms a crater on the surface of a metal. The presence of such a crater due to pulsed laser irradiation generates a physical texture on the surface of a material (schematically shown in Figure 1) and can be considered as a 3-D topographic cue for cell adhesion. The presence of short duration pulses also results in high cooling rate and thereby meta-stable phases suitable for bio-application. Their beneficial effects were explored in the samples presprayed with HA powder suspended in a water-based organic solvent (LISI) and scanned under a Lumonics JK701 model pulsed Nd:YAG laser. A metallurgical bonding at the coating/substrate interface and four different texture morphologies were obtained by varying the laser pulse frequency (10, 20, 30, and 40 Hz) and keeping the laser spot diameter (900 μm) and laser scan speed (50 cm min^{-1}) constant. These variations in frequency resulted in variations of 6%, 53%, 69%, and 76% crater overlap.

With an increase in pulse frequency there is an increase in crater overlap and hence varying surface textured morphology. Further, the 3-D morphological evolutions of the coatings (presented as insets in Figure 2) obtained using a confocal microscopic image indicate that the sample processed at 10 Hz possesses a relatively rough morphology as compared to the samples processed at higher frequencies. This is attributed to the fact that for the samples processed at higher frequencies the crater overlap was substantially high as compared to the sample processed at 10 Hz. This increased crater overlap resulted in remelting of the major portion of the prior crater thereby smoothing of the coating surface. The presence of such geometrically textured cues is expected to support bone cells and thereby induce bone in growth from the surrounding tissue.

The effect of surface morphology on its wetting behavior can be studied by the contact angle measurement of a simulated body fluid (SBF) subtended on these surfaces and by maintaining the SBF at 37°C and 7.4 pH. The composition and preparation of SBF solution was in accordance to References 11 and 12. The contact angle measurements carried out by a static sessile drop technique using a CAM Plus® contact angle goniometer (Cheminstruments, Inc. Fairfield, Ohio), indicated that all the laser-processed samples except for the sample processed at 10 Hz demonstrat-

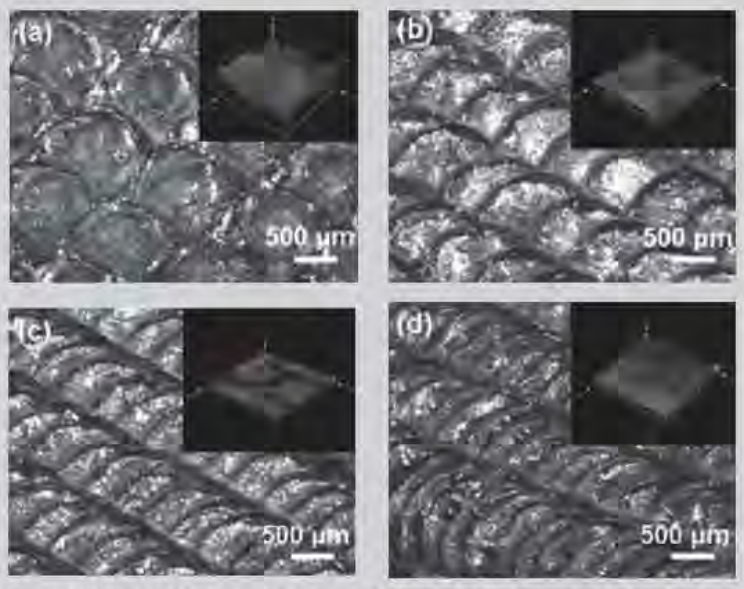
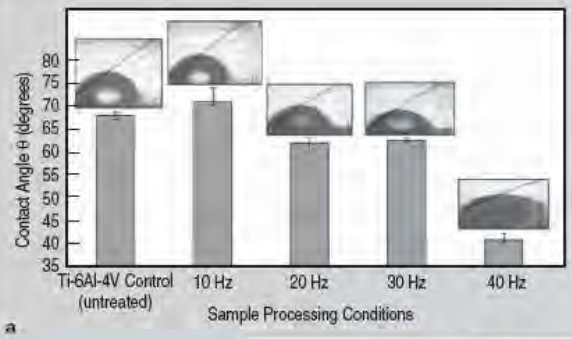
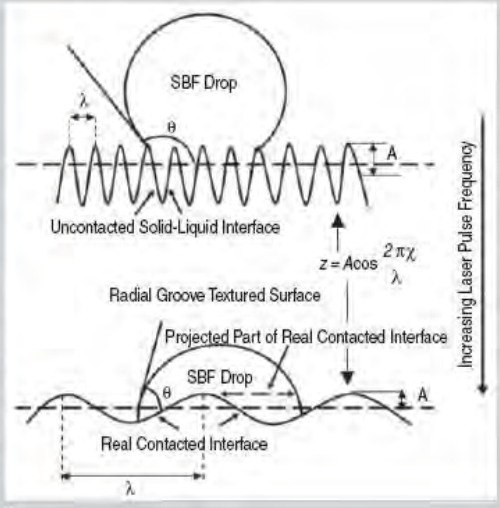


Figure 2. Low magnification optical microscopic images of the surface of the coatings and their corresponding 3-dimensional confocal microscopic images as inset obtained at laser pulse frequencies of (a) 10 Hz, (b) 20 Hz, (c) 30 Hz, and (d) 40 Hz.



a

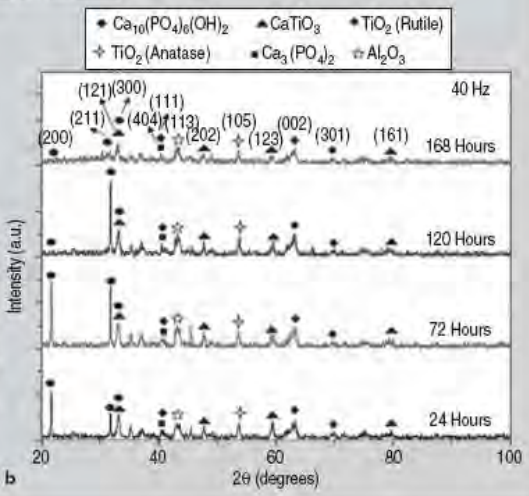


b

Figure 3. (a) Contact angle variations and corresponding shadow images of the SBF droplet on a laser processed sample and control (untreated Ti-6Al-4V); (b) schematic of the wetting behavior of a liquid droplet on a surface processed with increasing laser pulse frequency.



a

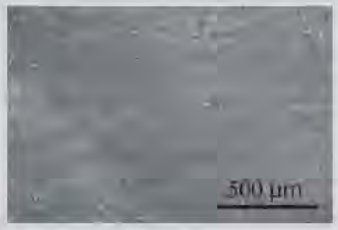


b

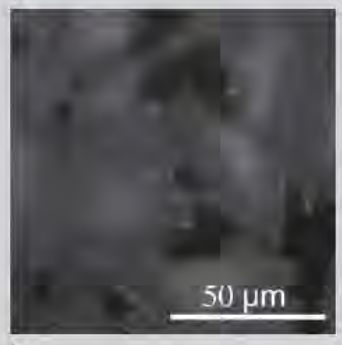
Figure 4. (a) An SEM micrograph of the 40 Hz processed sample revealing the precipitation of an whisker-like apatite phase following immersion in SBF for 1 day; (b) XRD spectra of the 40 Hz processed sample following immersion in SBF for different time periods.

ed an improved hydrophilic behavior as compared to the control Ti-6Al-4V (Figure 3). Within the laser-processed samples, the sample processed at 40 Hz showed the maximum hydrophilicity to SBF with a contact angle of approximately 40°.

The improvement in hydrophilicity with increasing laser pulse frequency can be explained as per the schematic shown in Figure 3b.[11] A practical rough surface is assumed to have a cosine profile with a Gaussian distribution and is characterized by the texture parameter (σ_A/λ), where σ_A is the standard deviation of amplitude and λ the distance between two successive crests or troughs.[11,13] From the confocal microscopy images (insets in Figure 2), it is clearly evident that at a laser pulse frequency of 10 Hz the surface had a rough morphology due to the minimal crater overlap. This resulted in a higher σ_A/λ value, leading to instability in wetting and increased contact angle. However, with an increase in laser pulse frequency there is increased remelting of the craters, resulting in a smoothing effect and lower σ_A/λ value. Hence when a liquid drop is placed on such a surface it easily overcomes the



a



b

Figure 5. (a) An SEM morphology of the MC3T3-E1 osteoblast-like cells, and (b) cytoskeletal organization of the MC3T3-E1 osteoblast-like cells after culture for 7 days on the sample processed at 40 Hz.

energy barriers associated with it and tries to wet it. Thus, an equilibrium state of wetting and thereby reduced contact angle is achieved on surfaces with lower σ_A/λ value.

As the samples processed at 40 Hz showed the maximum wettability, it was further studied for its in vitro bioactivity and in vitro biocompatibility. The in vitro bioactivity studies were carried out by soaking the sample in SBF and analyzing for the precipitation of an apatite ($Ca_{10}(PO_4)_6(OH)_2$) like mineral layer. Following 24 hours of immersion in SBF the sample indicated for the precipitation of a whisker-like apatite phase (Figure 4a). XRD studies of the samples (Figure 4b)[14] following immersion in SBF for different time periods indicated the presence of an apatite phase as evident from the characteristic HA maxima at $2\theta \sim 22.0°$ and 31.75° corresponding to the planes (200) and (211), respectively. The presence of whisker-like morphology following 24 hours of immersion was attributed to heterogeneous nucleation of the hexagonal close packed (HCP) apatite crystal and subsequent growth of this HCP structure along the c axis (perpendicular to the close packed atomic plane) by the adsorption of Ca^{2+} and PO_4^{3-} ions from the super-saturated SBF solution. Also, from the XRD results (Figure 4b) it can be observed that as the immersion time is increased to 168 hours there is a decrease in intensity for the apatite peaks indicating a rapid change in the apatite crystallite size and thereby its mineralization behavior. The above results obtained from the SEM and XRD analysis

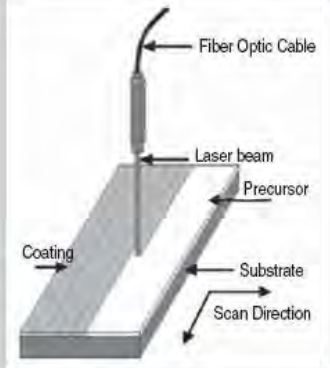


Figure 6. A schematic of a continuous wave Nd:YAG laser coating set up.

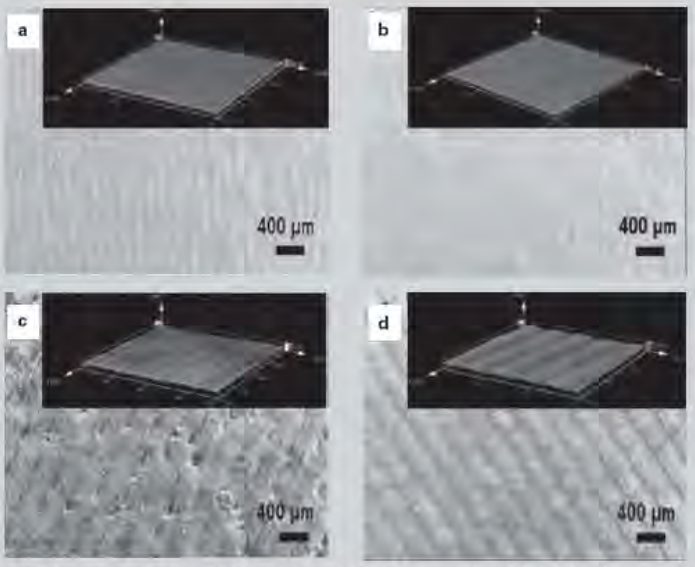


Figure 7. Low-magnification SEM images and their corresponding 3-D confocal microscopic images of the surface of coatings processed at (a) 137 J/cm², 100 µm line spacing, (b) 191 J/cm², 100 µm line spacing, (c) 137 J/cm², 200 µm line spacing, and (d), 191 J/cm², 200 µm line spacing.

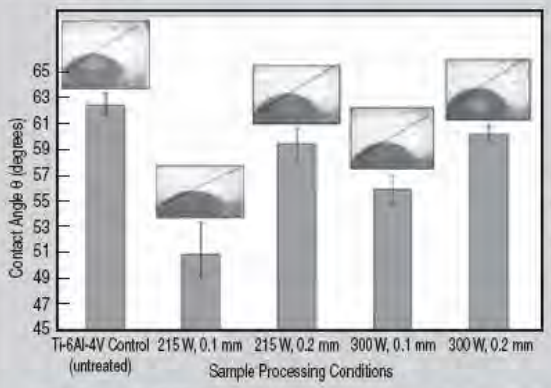


Figure 8. Contact angle variations and their corresponding shadow images of the SBF droplet on laser processed sample and control (untreated Ti-6Al-4V).

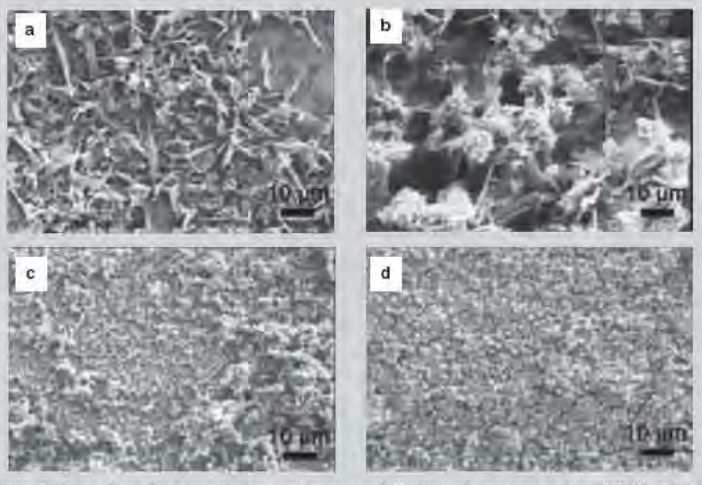


Figure 9. Scanning electron microscopy images of the sample processed at 137 J/cm², 100 µm line spacing following immersion in SBF for (a) 1 day, (b) 3 days, (c) 5 days, and (d) 7 days.

for the 40 Hz sample therefore proved for its in vitro bioactivity.

The in vitro biocompatibility of the sample was assessed by cell attachment and cell proliferation of mouse pre-osteoblast MC3T3-E1 (subclone 14) cell line obtained from American Type Cell Culture Collection (ATCC, Manassas, VA, USA). The cell culture procedure, cell fixation for cell morphology analysis using SEM, and cell fixation for cytoskeleton organization using fluorescence microscope can be obtained from our previously published work.[14] The morphology of the MC3T3-E1 osteoblast-like cells after 7 days of culture on the 40 Hz processed sample appeared to be flattened, spread out uniformly, and strongly adhered with an elliptical and circular morphology (Figure 5a). The cytoskeletal organization of the osteoblast-like cells after 7 days culture indicated stressed actin filaments with well developed network of focal adhesion contacts (Figure 5b). Therefore, the pulsed laser processing technique holds the promise to synthesize bioactive and biocompatible textured CaP coatings on Ti alloys.

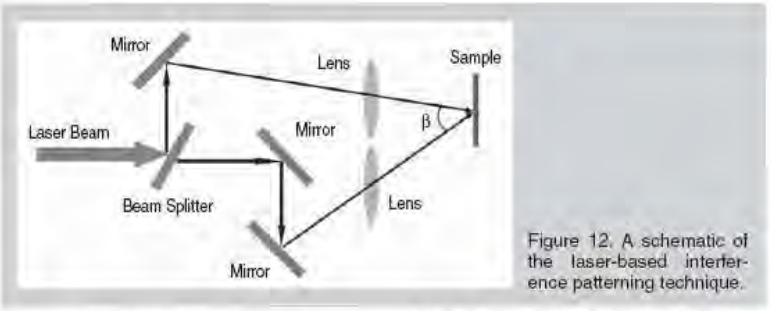


Figure 12. A schematic of the laser-based interference patterning technique.

CW LASER-INDUCED DIRECT MELTING FOR TEXTURED CaP COATING

In a CW laser, the output power of the laser beam is constant with time. Hence direct melting using a CW laser is likely to produce more uniform thermal conditions within the beam-substrate interaction region. Further, as the beam is delivered in a continuous mode, direct melting and simultaneous scanning of a material surface results in a line pattern rather than a crater as in the case of a pulsed mode operation. The laser scanning process in this case can be programmed to achieve line patterns with varying lateral track spacing and hence micro-textured patterns at varying length scales can be obtained. The schematic of such an operation is illustrated in Figure 6.[15] The formation of such line patterned CaP surface is expected to provide contact guidance for directional attachment of bone forming cells and thereby improve its biocompatibility.

Keeping the above potential advantages in mind, the pre-coated samples were scanned under a CW Nd:YAG laser equipped with a fiber optic beam delivery system to obtain a metallurgical bonding between the precursor ($Ca_{10}(PO_4)_6(OH)_2$) and the substrate (Ti-6Al-4V). In the current work, two different laser fluences of 137 J/cm^2 and 191 J/cm^2 were used for each sideways line spacing (100 μm and 200 μm). A lateral or sideways spacing of 100 and 200 μm were chosen so as to match the length scale of the naturally occurring 3-D extra cellular matrix (ECM) present in the human bone.[7] Irrespective of the laser fluence, the samples processed at 100 μm line spacing (Figure 7a and b) have a smoother surface finish as compared to the samples processed at 200 μm spacing (insets of Figure 7c and d)[15] due to the increased overlap of melted layers as a result of reduced line spacing.

The wetting behavior of the textured CaP surfaces and control (untreated Ti-6Al-4V) obtained by a static sessile drop measurement technique indicated that the laser textured CaP surface have a significantly smaller value of experimental contact angle to SBF as compared to the control (untreated Ti-6Al-4V) (Figure 8). This improved hydrophilic behavior of the laser textured surface is attributed to the influence of surface texture and the presence of CaP phases evolved during laser processing. Further, within the laser processed parameters, it can be observed that the samples processed at 100 μm line spacing (irrespective of the

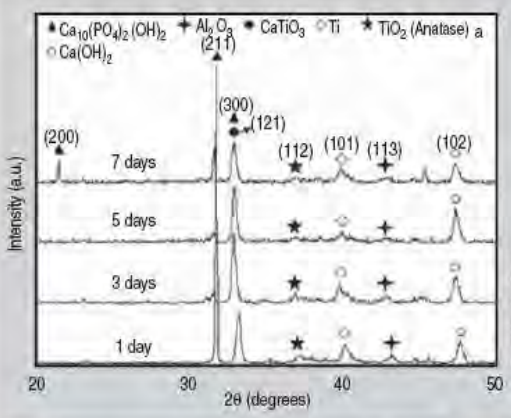


Figure 10. The XRD spectra of the samples processed at 137 J/cm^2, 100 μm line spacing following immersion in SBF for different time periods.

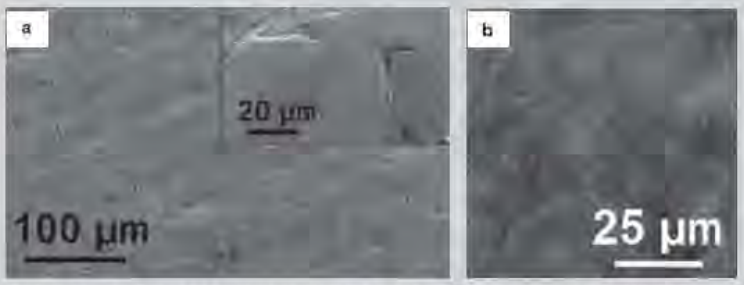


Figure 11. (a) The SEM morphology of the MC3T3-E1 osteoblast-like cells, and (b) cytoskeleton organization of the MC3T3-E1 osteoblast-like cells following culture for 1 day on the sample processed at 137 J/cm^2, 100 μm line spacing.

laser fluences) has a significantly smaller value of experimental contact angle compared to the 200 μm line spaced samples. The improved hydrophilicity of the 100 μm line spaced samples can also be due to the significant overlap within the melted regimes that resulted in a smoothening effect and smaller texture parameter ($\sigma_A/\lambda \sim 0.01$) value as compared to the samples processed with 200 μm line spacing ($\sigma_A/\lambda \sim 0.02$). With a smaller σ_A/λ value, there is certain amount invasion of the liquid along the textured surface and thereby improved wettability.

As, the sample processed at 137 J/cm² and 100 μm line spacing has the most significant hydrophilic behavior, it was further selected to study for its in vitro bioactivity and in vitro biocompatibility. SEM analysis of the samples following immersion in SBF for four different time periods (1, 3, 5, and 7 days) is shown in Figure 9.[15] After 1 day immersion in SBF (Figure 9a), characteristic whisker-like apatite crystallites are nucleated on the surface of the sample. As the immersion time is increased to 3 days the whisker-like crystallites gets covered with another mixed layer of whisker-like and nano HA crystallites (Figure 9b). After 5 day immersion in SBF the layer is completely covered with nano crystallites of HA (Figure 9c) and at the end of the 7 days there is a thick mineralized layer of HA on the surface of the sample (Figure 9d). X-ray diffraction studies of the mineralized layers following immersion in SBF for 1, 3, and 5 days, indicated the presence of characteristic HA peaks at $2\theta \sim 31.75°$ corresponding to the plane (211) (Figure 10).[15] As the immersion time is increased to 7 days an extra HA peak at $2\theta \sim 21.82°$ corresponding to the plane (200) is also evolved.

The morphology of the MC3T3-E1 osteoblast-like cells following culture for 1 day on the samples processed at 137 J/cm² and 100 μm line spacing is shown in Figure 11a. The good adhe-

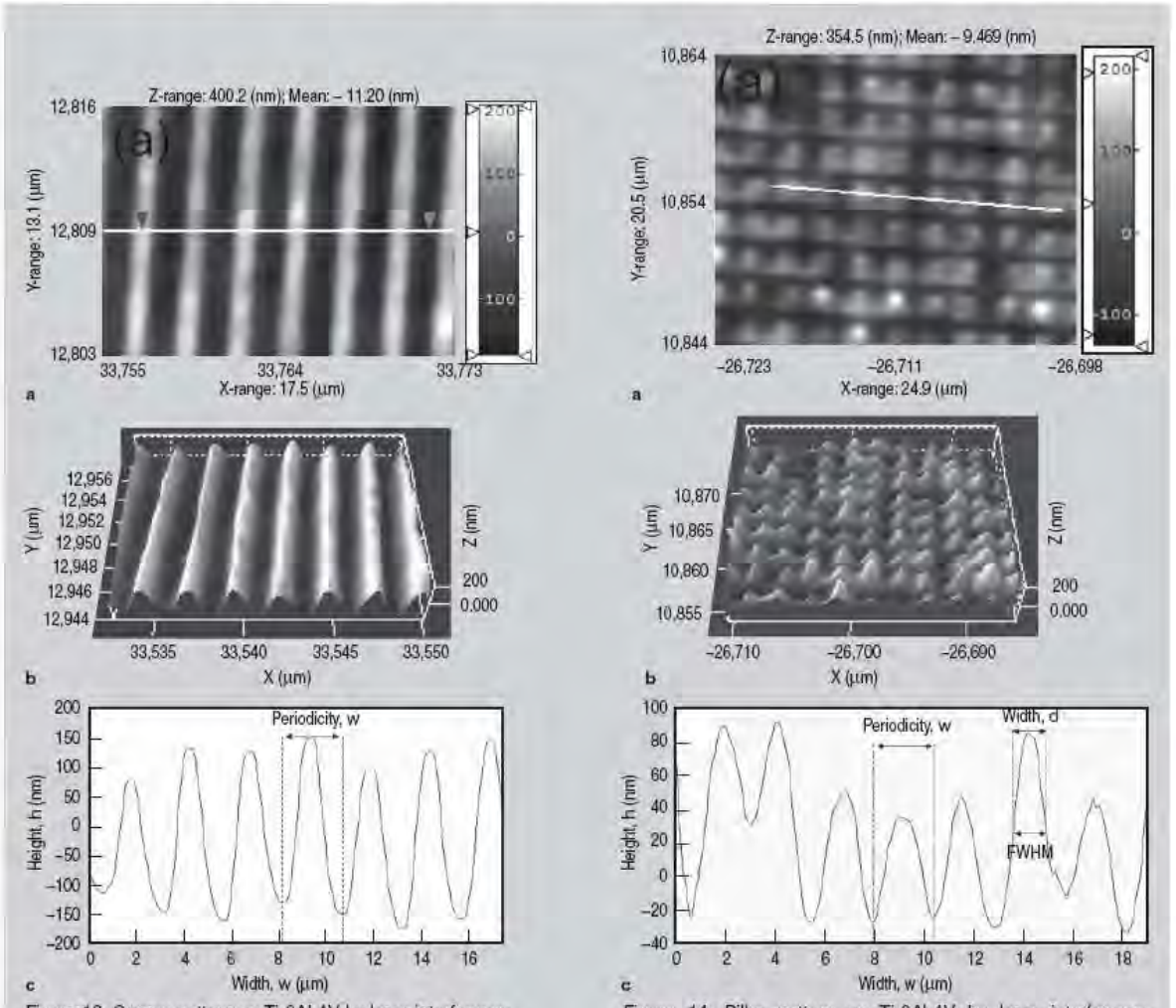


Figure 13. Groove pattern on Ti-6Al-4V by laser interference technique (760.35 mJ/cm²): (a) 2-D morphological evolution, (b) 3-D morphological evolution, and (c) variation in height and width (across the line scan) of the features obtained using a one-step irradiation.

Figure 14. Pillar pattern on Ti-6Al-4V by laser interference technique (760.35 mJ/cm²): (a) 2-D morphological evolution, (b) 3-D morphological evolution, and (c) variation in height and width at FWHM (across the line scan) of the features obtained using a two-step irradiation.

sion of the osteoblast-like cells were characterized by the lamelopodia trying to extend and adhere along the grooves (inset of Figure 11a). The cytoskeleton organization of the osteoblast-like cells demonstrated uniform spreading with stressed actin filaments. The network of focal adhesion contacts along their edges can also be further proved for their strong attachment to the laser textured surface. Therefore, using a CW laser, textured CaP coatings with appropriate length scales can be synthesized for improved wettability, in vitro bioactivity, and in vitro biocompatibility.

LASER INTERFERENCE TECHNIQUE FOR PATTERNING Ti-6Al-4V

In this technique, the primary laser beam is split into two coherent subbeams, which were then guided using an optical assembly to produce interference on the sample surface. The two interfering laser beams create a sinusoidal intensity distribution with high-and-low intensity lines. A detailed schematic setup of the interference patterning process is illustrated in Figure 12. The distance, w between the high intensity spots (periodicity) can be varied with the angle (β) between the beams as per the following Bragg equation (Equation 1 in the table.[16,17] The advantage associated with the present technique is that it creates periodic surface textures at length scales ranging from the micro to nano in a single-step process. Further, the process can also be controlled to mimic features close to size of the extra cellular matrix (ECM) or the pre-osteoblast cell size for their better adhesion and differentiation into bone cells.

In this preliminary work, laser interference patterned surface textures were obtained on Ti-6Al-4V samples and their influence on wettability was studied. The polished Ti-6Al-4V samples were interference patterned using a linear polarized third harmonic of a Q-switched Nd:YAG laser (Coherent Infinity, Santa Clara, CA, USA) operated at a wavelength of 355 nm. The pulse duration and repetition rate used in the present experiment were 2.5 ns and 10 Hz, respectively. The samples were irradiated under three different laser fluences of 362.26, 525.47, and 760.35 mJ/cm^2, while keeping the number of pulses as 5. Two different surface patterns i.e. the groove and pillar-like were obtained under each laser fluence. The two- and 3-D morphological evolution of the groove-like feature obtained under a laser fluence of 760.35 mJ/cm^2 and the variation in height (h) and periodicity (w) of the grooves across the sample in x-direction are presented in Figure 13 a, b, and c, respectively.[18] For obtaining the pillar-like features the samples irradiated with 5 pulses for a groove like pattern were rotated through 90° and irradiated once again with 5 pulses. Hence it was a two step process for the pillar-like pattern, with the effective number of pulses being doubled compared to the groove-like pattern. The 2- and 3-D morphological evolution of the pillar-like feature obtained under a laser

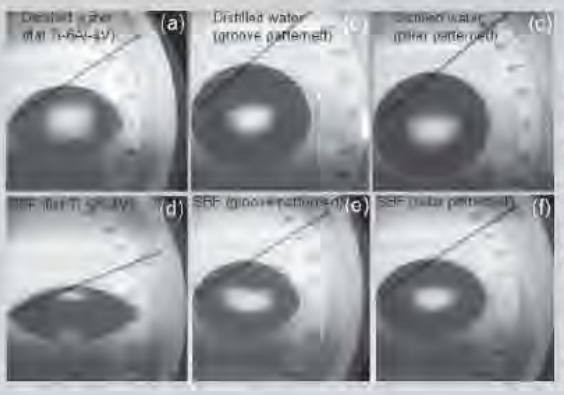


Figure 15. Light optical images of the distilled water droplet shadow on (a) flat Ti-6Al-4V, (b) grove patterned Ti-6Al-4V, (c) pillar patterned Ti-6Al-4V and light optical images of the SBF droplet shadow on (d) flat Ti-6Al-4V, (e) grove patterned Ti-6Al-4V, (f) pillar patterned Ti-6Al-4V.

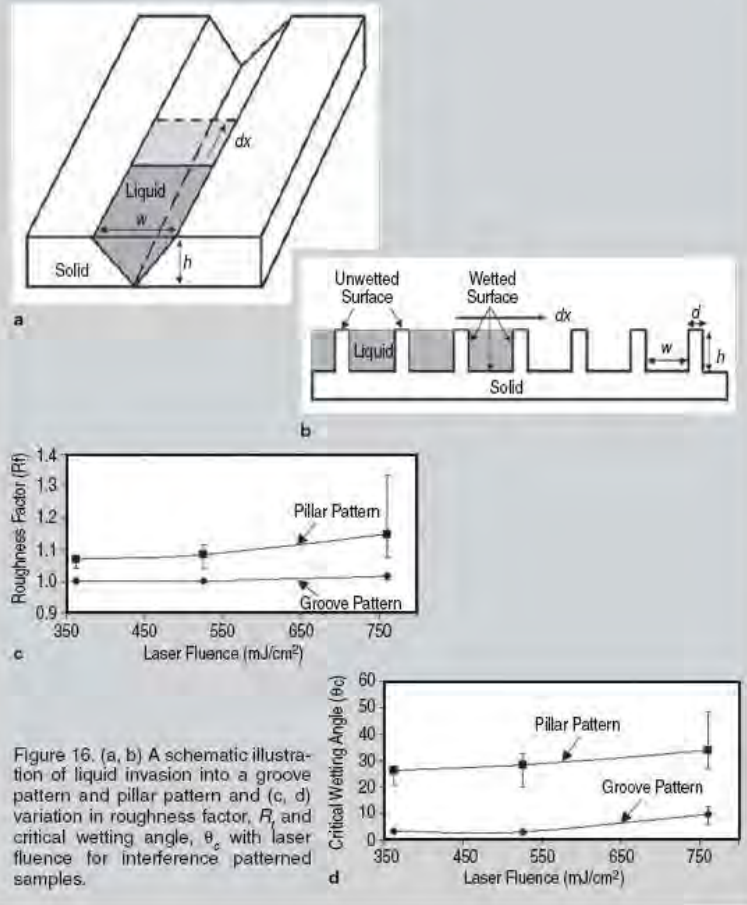


Figure 16. (a, b) A schematic illustration of liquid invasion into a groove pattern and pillar pattern and (c, d) variation in roughness factor, R_f and critical wetting angle, θ_c with laser fluence for interference patterned samples.

fluence of 760.35 mJ/cm^2 is presented in Figure 14a, b, respectively.[18] From a line scan across the sample (Figure 14c), it was observed that the width (d) at full-width-half-maxima (FWHM) and the periodicity (w) of the pillars were approximately 1.04 and 2.5 μm, respectively. As described earlier in Equation 1, the periodicity (w) only depends on the angle (β) between the beams and hence the only physical feature which varied with laser fluence was the height (h) of the pillars and the grooves.

Contact angle measurements on both the groove- and pillar-like patterns were conducted using distilled water and SBF. It can be observed that irrespective of the samples processing conditions, the distilled water droplet (Figure 15a–c) subtended a higher contact angle compared to the SBF droplet (Figure 15d–f).[18] Therefore, the presence of groove and pillar like features obtained using a laser interference technique with the present set of processing parameters resulted in tuning the surface towards a less hydrophilic behavior. This reduced wettability on the patterned surfaces can be explained based on the thermodynamic models as discussed below.

Here, for the ease of calculations, based on energy balance equations, the grooves are approximated to be of triangular type (Figure 16a)[18] and pillars to be of cylindrical type (Figure 16b).[18] Applying an energy minimum condition it can be hypothesized that liquid progression into a groove like pattern is favorable if the apparent contact angle θ^* or chemical angle θ is smaller than the critical angle θ_c for wetting, where θ_c is given as Equation 2.[19] Therefore, for groove texture the critical angle for wetting depends on the roughness factor $R_f = \sqrt{1+\frac{4h^2}{w^2}}$ (ratio of the actual surface area to apparent surface area).

In contrast, a surface with an assembly of pillar-like patterns (Figure 16b) is characterized by Φ_s (solid fraction remaining dry) and roughness factor $R_f = 1 + 2$ h/d (ratio of the actual solid area to its projected area). The critical angle θ_c for wetting on such a surface is given as Equation 3.[19] The roughness factor R_f was calculated for both groove and pillar patterns from the geometrical parameters (w, h, and d) of the features obtained using laser based interference technique, and plotted as a function of laser fluence (Figure 16c).[18] It can be observed (Figure 16c) that there is a slight increase in R_f with increasing laser fluence for both the groove and pillar patterns, and R_f is higher for the pillar patterns compared to the groove pattern. This increased value of roughness factor (R_f>1) for the pillar pattern is attributed to reduced width, d of the features as a result of the two step processing involved in this technique. Further, the critical wetting angle (θ_c) based on the above equations were calculated for the groove and pillar patterns respectively and plotted as a function of laser fluence (Figure 16d).[18] The critical wetting angle (θ_c) increased with increasing laser fluence for both the patterns and the values of critical wetting angle (ranging from 3° to 48°) are smaller compared to the chemical or the Young angles (θ, measured on the flat Ti-6Al-4V samples) obtained using both distilled water and SBF. As a result the condition for wetting (θ^* or $\theta < \theta_c$) is not satisfied in both the cases (pillar and groove) and hence, the liquid dewets on both the patterns due to an increase in apparent contact angle (θ^*). Owing to the above reasons the samples were not further tested for its in vitro bioactivity and in vitro biocompatibility. However, there is an ongoing efforts to identify appropriate combinations of the laser interference processing parameters to obtain surface textures at appropriate length scales and thereby improve its wettability.

CONCLUSIONS

Three different laser-based surface modification techniques have been demonstrated to hold tremendous promise for improving the wettability of load-bearing implant alloys (Ti-6Al-4V). The samples processed by the pulsed and CW laser-based direct melting technique demonstrated an improved wettability with the SBF as compared to the control (untreated Ti-6Al-4V). Within the range of processing parameters employed in the present work, it was observed that there is an improved hydrophilicity with increasing laser pulse frequency for the pulsed laser direct melting. On the other hand, for the CW laser direct melting the samples demonstrated improved wettability with decreasing lateral track overlap. This improved wettability was attributed to the presence of appropriate CaP-based surface chemistry and 3-D topographic cues obtained using this technique. This improved wettability resulted in the precipitation of an apatite like phase following immersion in SBF and the attachment and spreading of the MC3T3-E1 osteoblast-like cells following culture for 1 day. The pulsed and CW laser direct melted samples therefore proved for its in vitro bioactivity and in vitro biocompatibility as a result of the improved hydrophilicity. The groove and the pillar pattern obtained using the laser interference patterning technique with limited exploration of the parameters resulted in an increase in apparent contact angle. Such an increase was attributed to the decrease in the critical wetting angle as a result of the pinning effect created by the sharp grooves on the liquid drop. However, further exploration of combination of processing parameters hold tremendous potential for favorable outcome. However, further exploration of combination of the processing parameters hold tremendous potential for favorable outcome.

References

1. B.Ø. Palson and S.N. Bhatia, *Tissue Engineering,* 1st edition (New York: Pearson Prentice Hall, 2004), pp. 252–255.
2. D.A. Wahl and J.T. Czernuszka, *European Cells and Materials,* 11 (2006), pp. 43–56.
3. R.M. Streicher et al., *Nanomedicine,* 2 (6) (2007), pp. 861–874.
4. I. Sopyan et al., *Science and Technology of Advanced Materials,* 8 (1-2) (2007), pp. 116–123.
5. A. Kurella and N.B. Dahotre, *Acta Biomaterialia,* 2 (2006), pp. 677–683.
6. S.R. Paital and N.B. Dahotre, *Materials Science and Technology,* 24 (9) (2008), pp. 1144–1161.
7. M.M. Stevens and J.H. George, *Science,* 310 (18) (2005), pp. 1135–1138.
8. T. Blalock et al., *Surface and Coatings Technology,* 201 (12) (2007), pp. 5850–5858.
9. L. Clèries et al., *Journal of Biomedical Materials Research Part A,* 49 (1) (1999), pp. 43–52.
10. A.R. Boyd et al., *Surface and Coatings Technology,* 200 (20-21) (2006), pp. 6002–6013.
11. S.R. Paital and N.B. Dahotre, *Acta Biomaterialia,* 5 (7) (2009), pp. 2763–2772.
12. S.R. Paital and N.B. Dahotre, *Biomedical Materials,* 2 (2007), pp. 274–281.
13. X.B. Zhou and J.Th.M. DeHosson, *Journal of Materials Research,* 10 (1995), pp. 1984–1992.
14. S.R. Paital et al., *Journal of Materials Science: Materials in Medicine* (under review).
15. S.R. Paital et al., *Biofabrication* (accepted for publication).
16. C. Daniel et al., *Applied Surface Science,* 208-209 (2003), pp. 317–321.
17. A. Lasagni et al., *Advanced Engineering Materials,* 8 (2006), pp. 580–584.
18. N.B. Dahotre et al., *Philosophical Transactions of the Royal Society A* (in press).

19. J. Bico et al ., *Electrophysics Letters,* 55 (2001), pp. 214–220.

Sameer R. Paital, graduate student, and Narendra B. Dahotre, Chairman and Professor, are with the Laboratory for Laser Materials Synthesis and Fabrication; Wei He, assistant professor, is with the Mechanical Aerospace and Biomedical Engineering Department; and Claus Daniel, staff scientist, is with the Materials Science and Technology Division, Oak Ridge National Laboratory, Oak Ridge, TN 37831. All are with the Department of Materials Science and Engineering, University of Tennessee, Knoxville, TN 37996, USA. Dr. Dahotre can be reached at (865) 974-3609; fax (865) 974-4115; e-mail ndahotre@utk.edu.

PHILOSOPHICAL TRANSACTIONS OF THE ROYAL SOCIETY A

Phil. Trans. R. Soc. A (2010) **368**, 1863–1889
doi:10.1098/rsta.2010.0003

Wetting behaviour of laser synthetic surface microtextures on Ti–6Al–4V for bioapplication

By Narendra B. Dahotre[1,2,*], Sameer R. Paital[1,2], Anoop N. Samant[1,2] and Claus Daniel[2,3]

[1]*Laboratory for Laser Materials Synthesis and Fabrication, and* [2]*Department of Materials Science and Engineering, University of Tennessee, Knoxville, TN 37996, USA*

[3]*Materials Science and Technology Division, Oak Ridge National Laboratory, Oak Ridge, TN 37831, USA*

Wettability at the surface of an implant material plays a key role in its success as it modulates the protein adsorption and thereby influences cell attachment and tissue integration at the interface. Hence, surface engineering of implantable materials to enhance wettability to physiological fluid under *in vivo* conditions is an area of active research. In light of this, in the present work, laser-based optical interference and direct melting techniques were used to develop synthetic microtextures on Ti–6Al–4V alloys, and their effects on wettability were studied systematically. Improved wettability to simulated body fluid and distilled water was observed for Ca–P coatings obtained by direct melting technique. This superior wettability was attributed to both the appropriate surface chemistry and the three-dimensional surface features obtained using this technique. To assert a better control on surface texture and wettability, a three-dimensional thermal model based on COMSOL's multiphysics was employed to predict the features obtained by laser melting technique. The effect of physical texture and wetting on biocompatibility of laser-processed Ca–P coatings was evaluated in the preliminary efforts on culturing of mouse MC3T3-E1 osteoblast cells.

Keywords: interference patterning; direct melting; wettability; thermal modelling; simulated body fluid

1. Introduction

When an implant material is placed inside a human body, among the plethora of events that take place, the first and the foremost one is the wetting of the implant material by the physiological fluids. This further controls the adsorption of proteins, followed by attachment of cells to the implant surface. Hence, the surface wettability is considered to be an important criterion that can dictate the biocompatibility of the implant material. The three most important factors that affect the wettability of a surface are its chemical composition, microstructural topography and surface charge.

*Author for correspondence (narendra.dahotre@unt.edu).

One contribution of 14 to a Theme Issue 'Advanced processing of biomaterials'.

This journal is © 2010 The Royal Society

Keeping this in mind, several research groups have studied the interaction of different types of cultured cells or blood proteins with various solid substrates having different wettabilities to correlate the relationship between surface wettability and cell or blood compatibility (Yuehuei & Richard 1998; Jones *et al.* 2000; Wei *et al.* 2007). Wei *et al.* (2007) modelled the surfaces of hexamethyldisiloxane to different degrees of wettability and thereby studied their effects on cell attachment, cell proliferation and cell morphology. Plasma polymerization followed by O_2 plasma treatment was used to modify the surface of hexamethyldisiloxane. The authors concluded that, with an increase in O_2 plasma treatment duration, there was a decrease in the contact angle of distilled water and an increase in attachment of L929 cells on these surfaces. Such an improvement in biocompatibility was attributed to the introduction of more hydrophilic (−COOH) groups and a decrease in hydrophobic groups such as $-CH_3$ on the surface.

Adsorption of a protein to the surface of an implant material also modulates the surface roughness and thereby the wettability and cell adhesion. Fibronectin, a well-known extracellular matrix and cell-adhesive protein, was coated on Ti surfaces, and its effect on cell compatibility was studied by various researchers (Schneider & Burridge 1994; Sauberlich *et al.* 1999; Scheideler *et al.* 2003). Coating of Ti with this extracellular matrix protein enhanced the focal adhesion and spreading of osteoblast and gingival fibroblast on these surfaces (Schneider & Burridge 1994; Sauberlich *et al.* 1999; Scheideler *et al.* 2003). This *in vivo*-derived cell-adhesive protein gets adsorbed to the surfaces of the endosseous implants, as they are exposed to the patient's blood during surgery (Rupp *et al.* 2004). The osteoblast precursors then adhere to these proteins and thereby provide a matrix for cell adhesion through integrin-mediated mechanisms. Apart from influencing the wetting behaviour on the cellular level, biological responses such as orientation and migration of cells and the cellular production of organized cytoskeletal arrangements are also directly influenced by the surface topography (Flemming *et al.* 1999). Hence, it is well established that surface roughness plays an important role in determining successful osseointegration of Ti implants.

Until now, most surface modification techniques are aimed at achieving the appropriate surface chemistry and surface topography for enhanced bone-to-implant fixation and increased biomechanical interlocking with bone (Pilliar 1998; Cooper 2000; Perrin *et al.* 2002). There are only a few reports dealing with the initial interactions of these surfaces with the simulated body fluid (SBF) in terms of the wetting perspective (Hao *et al.* 2004, 2005; Lawrence *et al.* 2005; Paital & Dahotre 2009). However, recent reports on wetting behaviour of various types of morphologically textured surfaces have increased our understanding of which requirements a surface topography has to fulfil to induce a specific hydrophilicity or hydrophobicity during contact with a liquid phase (Bico *et al.* 2001, 2002; Palasantzas & De Hosson 2001; Ishino *et al.* 2004; Ma *et al.* 2005, 2007; Sheng *et al.* 2007; Bhusan *et al.* 2009; Yong & Zhang 2009). Hence, in the present work, attempts are being made to better understand these findings by conducting wetting experiments on defined surface morphologies and predicting the wetting behaviour based on theoretical thermodynamic models on arbitrarily structured surfaces. Laser-based optical interference patterning and direct melting techniques were employed to generate the surface morphologies on Ti–6Al–4V at two different length scales. Furthermore, a three-dimensional

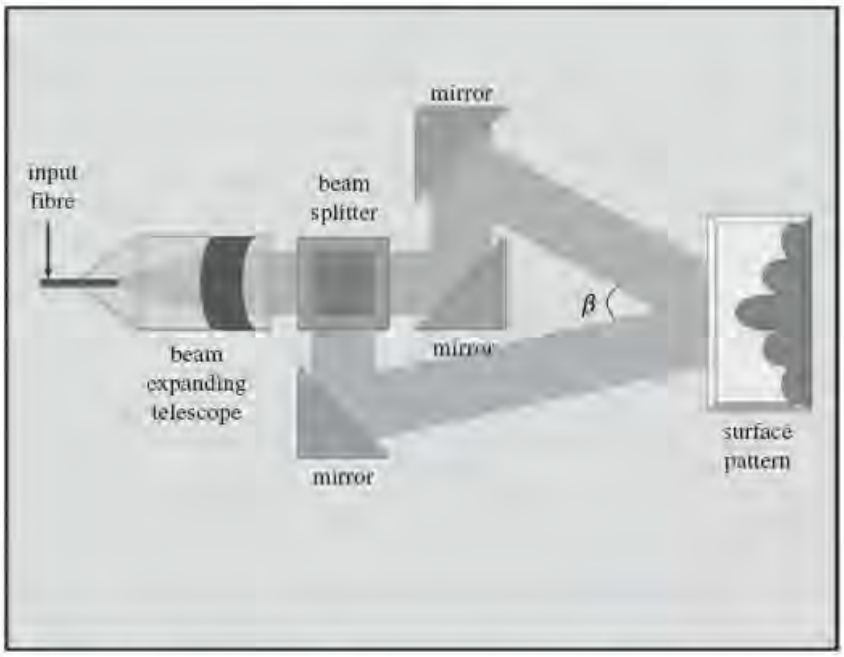


Figure 1. Schematic of a laser interferometer set-up (Engleman *et al.* 2005).

thermal model based on COMSOL's multiphysics was developed to predict the evolution of surface features, thereby asserting a better control on the laser processing parameters for tunable wettability. A preliminary, mouse MC3T3-E1 osteoblast cell culture study on Ca–P laser-coated Ti–6Al–4V was conducted to observe the effects of surface texture and wettability.

2. Laser microtexturing

(*a*) *Interference patterning*

The samples were surface treated using a linear polarized third harmonic of a Q-switched Nd:YAG laser (Coherent Infinity, Santa Clara, CA, USA). In this technique, the primary laser beam was split into two coherent sub-beams that were guided using an optical system to produce interference at the sample surface. This allows the creation of periodic surface textures at length scales ranging from micro to nano in a single-step process. A detailed schematic set-up of the process is illustrated in figure 1 (Engleman *et al.* 2005). The area irradiated by the laser beam was approximately $0.5024\,\mathrm{cm}^2$. The geometry of the pattern depends on the wavelength and the angles between the beams. The two interfering laser beams create a sinusoidal intensity distribution with high- and low-intensity lines. The distance w between the high-intensity spots (periodicity) can be varied with the angle (β) between the beams as per the following Bragg's equation (Daniel *et al.* 2003, 2005; Engleman *et al.* 2005; Lasagni *et al.* 2006, 2007):

$$w = \frac{\pi}{2\sin(\beta/2)}. \tag{2.1}$$

Table 1. Laser and material parameters used for the study.

	direct writing	interference patterning
laser parameters		
wavelength of laser beam (nm)	1064	355
pulse width	0.5 ms	2.5 ns
pulse energy (J)	4	—
pulse repetition rate (Hz)	20	10
laser power (W)	156, 131.2, 124, 80	3.82, 2.64, 1.82
laser scan speed ($cm\,min^{-1}$)	36, 48, 78, 102	—
laser fluence	1887, 1415, 871, 666 $J\,cm^{-2}$	760.35, 525.47, 362.26 $mJ\,cm^{-2}$
focus position	0.8 mm above the sample surface	at focus
laser spot diameter on the surface (μm)	900	8000
number of pulses for groove-like patterns	—	5
number of pulses for pillar-like patterns	—	10
pulse shape	rectangular	—
material parameters		
density of precursor (Ca–P tribasic)	3156 $kg\,m^{-3}$ (Dyshlovenko *et al.* 2004)	
density of substrate (Ti–6Al–4V)	4420 $kg\,m^{-3}$ (Boivineau *et al.* 2006)	
melting point of precursor (Ca–P tribasic)	1843 K (Dyshlovenko *et al.* 2004)	
melting point of substrate (Ti–6Al–4V)	1800 K (Boivineau *et al.* 2006)	
activation energy for Ti–6Al–4V	126 $kJ\,mol^{-1}$ (Dabhade *et al.* 2007)	
viscocity of precursor (Ca–P tribasic)	6.8 mPas (Li *et al.* 2007)	
surface tension precursor (Ca–P tribasic)	28 $mN\,m^{-1}$ (Li *et al.* 2007)	
latent heat of melting of precursor (Ca–P tribasic)	49.9 $kJ\,mol^{-1}$ (Dyshlovenko *et al.* 2004)	
latent heat of melting of substrate (Ti–6Al–4V)	290 $kJ\,mol^{-1}$ (Boivineau *et al.* 2006)	

In the present work, the patterns were obtained by varying the laser power. The pillar-like patterns were synthesized in a two-step process, in which the sample periodicity w was kept constant at 2.5 μm. Two different surface textures, i.e. groove- and pillar-like, were rotated 90° prior to the second irradiation. The processing parameters employed in laser interference patterning are listed in table 1.

(*b*) *Direct writing*

In the direct writing technique, the samples were scanned using a 400 W average power, JK701 model, pulsed Nd:YAG laser to obtain a metallurgical bonding between the precursor and the substrate material. The laser was equipped with a fibre-optic beam delivery system to transfer the laser beam from the laser head to the material. The control panel for the laser allows control of the pulse

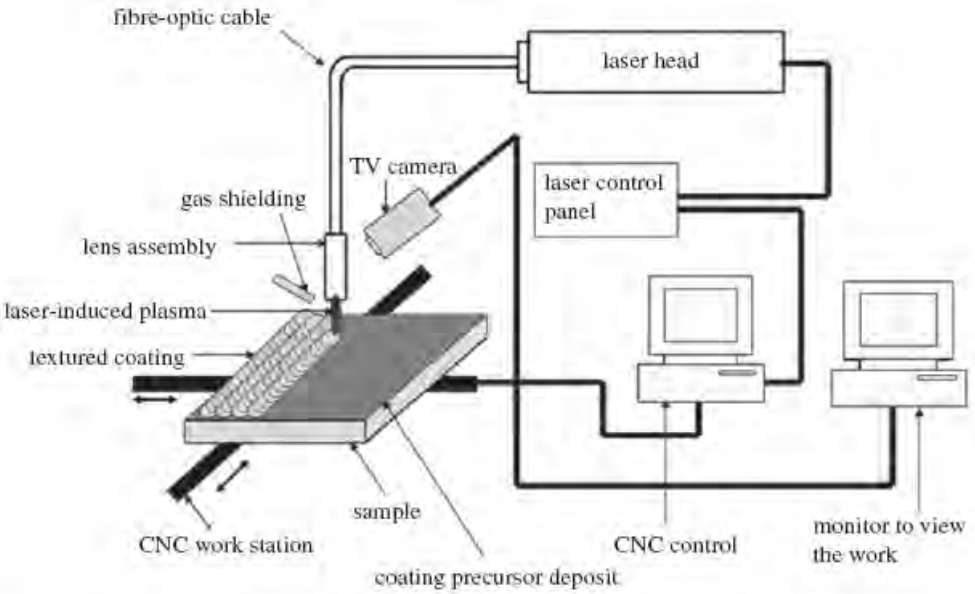


Figure 2. Schematic of the pulsed Nd:YAG laser system used for the coating process (Paital *et al.* 2009).

height, pulse width, pulse repetition rate and pulse shape. The lens assembly is equipped with a 120 mm focal length convex lens, which gives a spot diameter of approximately 240 µm at focus. The focused spot is kept at approximately 0.8 mm above the surface of the sample so as to have a spot size of approximately 900 µm on the surface. A schematic set-up of the laser system is shown in figure 2 (Paital *et al.* 2009). The processing parameters used for the above process are listed in table 1. From the table, it can be observed that only the linear scan speed was varied (36, 48, 78 and 102 cm min^{-1}), keeping the rest of the parameters constant. This linear scan speed can be related to the spot overlap (s_x) by the following equation (Paital & Dahotre 2009):

$$s_x = 1 - \frac{V}{2fR}, \tag{2.2}$$

where V is the laser scan speed, f the pulse repetition rate and R the beam radius. Hence, four different samples with spot overlap varying as 65, 55, 28 and 5.5 per cent were obtained.

(*c*) *Pre- and post-laser treatment surface preparation and characterization*

Substrate coupons of Ti–6Al–4V (100 × 50 × 3 mm) were cut from rolled sheets using an abrasive cutter. For interference patterning, the cut coupons were prepared by polishing with emery papers of different grits ranging from 200 to 1000 µm in succession, followed by disc polishing with colloidal silica of 0.3 and 0.05 µm to get a mirror-finished surface. For sample processing by the direct melting technique, substrate coupons of Ti–6Al–4V (100 × 50 × 3 mm)

were prepared for coating by initially polishing using a 30 µm grit silicon carbide emery paper, followed by rinsing with acetone. Calcium phosphate tribasic ($Ca_5(OH)(PO_4)_3$) powder obtained from Fisher Scientific was taken as the precursor material. This precursor powder had a spherical morphology with a unimodal distribution in the range of 10–30 µm. The precursor was mixed in a water-based organic solvent LISI W 15853 obtained from Warren Paint and Color Company (Nashville, TN, USA). The mixed slurry was then sprayed onto the pre-heated (approx. 50 °C) substrate coupons using an air-pressurized spray gun. The sprayed coupons were air-dried to remove the moisture, and a uniform thickness of 40 µm was maintained for all pre-coating deposits.

Surface roughness of the laser-treated samples was measured using a white light interferometer. Contact angles on the surface-modified Ti–6Al–4V and Ti–6Al–4V control (Ra) with distilled water and SBF were measured by a static sessile drop technique. The SBF solution was prepared by mixing reagent grade chemicals in the following order: NaCl (8.026 g), $NaHCO_3$ (0.352 g), KCl (0.225 g), $K_2HPO_4{\cdot}3H_2O$ (0.230 g), $MgCl_2{\cdot}6H_2O$ (0.311 g), $CaCl_2$ (0.293 g) and Na_2SO_4 (0.072 g) in distilled water (700 ml). The fluid was then buffered to pH = 7.4 at 37 °C with tri-hydroxymethyl-aminomethane (6.063 g) and hydrochloric acid (40 ml). A liquid droplet of volume 3 µl (droplet diameter of 2 mm) was placed on the thoroughly cleaned sample by a hypodermic syringe, and the advancing contact angle was taken as a measure of wettability. The test was conducted at room temperature, and a minimum of 10 contact angle readings were taken on each sample to minimize errors in the measurement. Further, the measurement was based on the patented half-angle method (US Patent no. 5268733), which eliminates the errors associated with the arbitrary tangential alignment.

For cell culture studies, mouse pre-osteoblast cell line MC3T3-E1 cells (subclone 14, American Type Culture Collection (ATCC)) were seeded on the surfaces of UV-sterilized samples placed in 24-well culture plates at a density of 1.25×10^5 cells cm^{-2}. The cells were cultured in α minimum essential medium (MEM) (Invitrogen, USA) supplemented with 10 per cent foetal bovine serum (Thermo Scientific) and 1 per cent penicillin/streptomycin (Invitrogen) at 37 °C under 5 per cent CO_2 in air in a humidified incubator.

For cell morphology analysis using SEM, cells cultured on the sample were fixed with 3 per cent glutaraldehyde in 0.1 M cacodylate for 1 h and rinsed three times with phosphate-buffered saline (PBS). The sample was further processed in 2 per cent osmium tetroxide in 0.1 M cacodylate for 1 h, dehydrated with a series of increasing concentrations of ethanol (25, 50, 70, 95 and 100%), critical point dried and sputter-coated with gold for SEM observation. For immunocytochemical staining of the actin filament, the cells cultured on the sample were fixed with 4 per cent paraformaldehyde (Sigma-Aldrich) in 1x PBS for 30 min at 4 °C. After washing with PBS, the sample was permeabilized with 0.1 per cent Triton X-100 (Fisher Scientific) in 1x PBS for 5 min, blocked with 1 per cent bovine serum albumin (Sigma-Aldrich) for 30 min and stained with 2 per cent Alexa 594 conjugated Phalloidin (Invitrogen) fluorescent dye for 1 h. Cell nuclei were counterstained with 0.1 per cent 4′,6-diamidino-2-phenylindole (Chemicon) in 1x PBS for 5 min. The sample was then washed three times with 0.05 per cent Tween-20 (Sigma) in 1x PBS before and after the staining steps. All the staining procedures were carried out at room temperature. High-resolution fluorescence images were captured using an upright fluorescence microscope (Nikon).

3. Computational model for predicting effects of laser parameters on surface morphology

As the geometry and design of surface structures strongly affect the wettability, it was vital to understand the different physical phenomena taking place during laser–material interaction and their effects on evolution of the surface morphology.

(*a*) *Laser–material interaction*

The excitation energy provided by the laser is rapidly converted into heat, and this is followed by various heat transfer processes such as conduction into the material, convection and radiation from the top and bottom surfaces. The temperature distribution within the material as a result of these heat transfer processes depends on the thermo-physical properties of the material (density, absorptivity, emissivity, thermal conductivity and specific heat), dimensions of the sample and the laser processing parameters (absorbed energy, processing speed and beam cross-sectional area). In light of this, the thermal predictions were modelled using COMSOL's transient heat transfer mode. In the case of the direct writing method, the processing was performed on a substrate (Ti–6Al–4V) with a precursor deposit (calcium phosphate tribasic) for textured coating. Hence, the precursor represented in the form of a slab was coupled with another slab representing the substrate. The laser parameters that were considered were pulse width, pulse repetition rate and pulse energy. In contrast, in the interference patterning technique, the original beam is split into two beams, which in turn are constructively superimposed to generate several intense lines. Analogous to a single beam, each of these intense lines simultaneously interacts with the substrate to generate corresponding thermal effects, thereby producing a physical texture on the surface. Unlike direct writing, the interference patterning technique was employed to produce a physical texture directly on the substrate (Ti–6Al–4V) without using a coating precursor.

The model described below predicts the surface morphological (physical) changes owing to the thermal effects under a single laser beam that can be further extended for subsequent multiple laser beam runs in the case of direct writing and for simultaneous multiple laser lines owing to a constructive interference in the case of interference patterning. The effective energy density input to the system affects the temperature evolution and is discussed in the next section.

The conduction of the heat into the material is in accordance with Fourier's second law of heat transfer,

$$\frac{\partial T(x,y,z,t)}{\partial t} = \frac{k(T)}{\rho C_{\mathrm{p}}(T)}\left[\frac{\partial^2 T(x,y,z,t)}{\partial x^2} + \frac{\partial^2 T(x,y,z,t)}{\partial y^2} + \frac{\partial^2 T(x,y,z,t)}{\partial z^2}\right], \tag{3.1}$$

where T is the temperature field, t is the time, x, y and z are the spatial directions, ρ, $C_{\mathrm{p}}(T)$ and $k(T)$ are the density, specific heat and thermal conductivity of the material, respectively. For improved accuracy of calculations, variation in the thermal conductivity and specific heat of the precursor and substrate was considered in the model to be a function of temperature (Dyshlovenko *et al.* 2004; Boivineau *et al.* 2006). The balance between the absorbed laser energy at the surface and the radiation losses is given by

$$-k(T)\left(\frac{\partial T(x,y,0,t)}{\partial x}+\frac{\partial T(x,y,0,t)}{\partial y}+\frac{\partial T(x,y,0,t)}{\partial z}\right)$$
$$=\delta aP-\varepsilon\sigma(T(x,y,0,t)^4-T_0^4),\quad \delta=1 \quad \text{if } 0\le t\le t_\mathrm{p} \text{ and } \delta=0 \quad \text{if } t>t_\mathrm{p}, \tag{3.2}$$

where P is the effective incident peak power density discussed in the next section, a is the absorptivity of the material (0.1; Guillot-Noël *et al.* 1996), ε is the emissivity of thermal radiation, T_o is the ambient temperature (300 K), t_p is the on-time for the laser discussed in the next section and σ is the Stefan–Boltzmann constant ($5.67\times10^{-8}\,\mathrm{W\,m^{-2}\,K^{-4}}$). The term δ takes a value of 1 when time t is less than laser on-time t_p and it is 0 when time t exceeds laser on-time. Thus, the value of δ depends on time t and ensures that the energy is input to the model only when the laser is on and cuts off the energy supply when the laser is switched off. The convection taking place is

$$-k(T)\left(\frac{\partial T(x,y,H,t)}{\partial x}+\frac{\partial T(x,y,H,t)}{\partial y}+\frac{\partial T(x,y,H,t)}{\partial z}\right)$$
$$=h(T)(T(x,y,H,t)-T_0), \tag{3.3}$$

where H is the thickness of the sample being processed and $h(T)$ is the temperature-dependent heat transfer coefficient (Incropera & Dewitt 1985).

(*b*) *Effective incident peak power density*

While scanning the material surface, several laser tracks are laid subsequently (direct writing technique) or simultaneously (interference patterning), and the length of a single track is equal to the distance between the centre of the first pulse and the centre of the last pulse. Furthermore, it is assumed that the morphology corresponding to an area equal to a single beam spot would be repeated for the entire length of the track. Within a single track, the overlap (s_x) between adjacent pulses is given by equation (2.2). The distance b travelled by the beam between two adjacent pulses is given by

$$b=2R(1-s_x). \tag{3.4}$$

As the laser beam moves with a constant velocity V, multiple laser pulses will be required to process an area equal to the beam spot diameter ($2R$), as shown in figure 3, and the number of pulses N required to process this area is given by (Samant 2009):

$$N=\frac{2R}{b}. \tag{3.5}$$

The corresponding overlap of each pulse over the spot area is given by

$$s_\mathrm{pulse}=\frac{2R-(n-1)b}{2R}, \tag{3.6}$$

where n is the number of the pulse ranging from 1 to N, b is the distance travelled by the laser beam between consecutive pulses and R is the beam radius. The values of s_x and N would depend on the beam radius and the laser scanning speed.

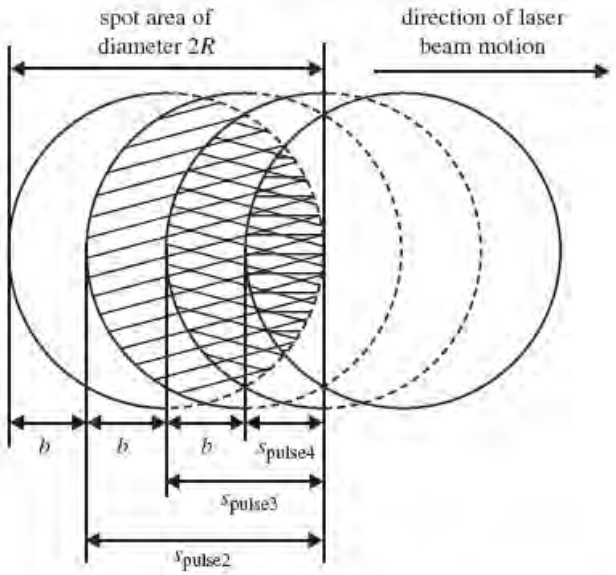


Figure 3. Overlap of successive laser pulses over a single spot area.

As shown in figure 3, the overlap s_{pulse} was different for each pulse (s_{pulse2}, s_{pulse3} and s_{pulse4}, corresponding to overlap of the second, third and fourth pulses, respectively, over the spot area of the first pulse). The contribution of each of these pulses to effective energy falling on every spot area (Incropera & Dewitt 1985) was $s_{\text{pulse}} \times \epsilon$, where ϵ is the energy of the individual laser pulse. The total effective energy Q incident on a spot area due to N pulses is given by

$$Q = \sum_{n=1}^{N} \left[\frac{2R - (n-1)b}{2R} \right] e. \tag{3.7}$$

As seen later, in this study, the beam radius will be varied and its effect on the evolved morphology will be studied. Assuming beam distribution in temporal and spatial evolution to be uniform, the corresponding effective peak power density P within a single spot area is given by equation (3.8) below, and this energy density would be incident for time t_{p} equal to $(N \times p)$ seconds, where p is the pulse width of each incident pulse,

$$P = \frac{Q}{N \times p \times A_{\text{beam}}} = \frac{\sum_{n=1}^{N} [(2R - (n-1)b)/2R]\epsilon}{NpA_{\text{beam}}}. \tag{3.8}$$

The energy density and time of incidence are input to the model described earlier, and it would govern the temperature evolution when the laser beam is incident on the material. The temperature evolution instigates Marangoni convection that affects the surface morphology, as seen in §3.3.

(c) Marangoni convection

The surface temperature evolves in accordance with equations (3.1–3.3), and a melt pool is formed when the temperature exceeds the melting point of the material. The melt depth z was obtained from the surface by tracking the melting point of the lowest melting component of the system Ti–6Al–4V (1800 K; Boivineau *et al.* 2006) for both direct writing and interference patterning. Similarly, the width of the melt pool w on the surface was predicted by tracking the melting point of Ca–P (1843 K; Dyshlovenko *et al.* 2004) for direct writing and of Ti–6Al–4V for interference patterning. For a given set of processing conditions, the surface temperature increases with an increase in energy density. Furthermore, the temperature is highest at the centre and lowest at the border of the molten pool. This temperature gradient in the vertical direction creates Marangoni forces and leads to the formation of a surface tension gradient towards the border of the molten pool (Carles *et al.* 1990; Zhang *et al.* 2008). The molten material is thus pulled towards the border of the molten pool, causing the material to pile up at the edge of the pool. At the end of laser on-time t_p, the balance melt (remaining after a portion is pulled towards the edge) and the pile-up material solidify because of the high cooling rates encountered in laser processing (of the order of 10^7–$10^8\,\mathrm{K\,s^{-1}}$), leading to the formation of a depression on the surface along with solidified pile-up material at the boundary of the depression.

The average velocity of displacement of the molten material (fluid) v_z from the hotter to the cooler regions is governed by the Navier–Stokes equation (expressed in cylindrical coordinates) as

$$v_z = \frac{1}{2\eta(T)r}\frac{\partial}{\partial r}\left(rz^2\frac{\partial\alpha(T)}{\partial r}\right), \tag{3.9}$$

where $\eta(T)$ and $\alpha(T)$ are the temperature-dependent dynamic viscosity and surface tension, respectively, of the melt, z is the melt depth from the surface and r is the radial coordinate. The origin of the cylindrical coordinate system is located on the surface of the sample and at the centre of the laser beam. The change in morphology of the fluid by the laser impact Δz is the integral of v_z (equation 3.9) over time and is given by (Schwarz-Selinger *et al.* 2001)

$$\Delta z = -\frac{1}{2\eta(T)r}\frac{\partial\alpha(T)}{\partial T}\frac{\partial}{\partial r}\left(r\langle z^2\rangle\frac{\partial I}{\partial r}\right), \tag{3.10}$$

where I and $\langle z^2\rangle$ are the integrated temperature and average melt depth, respectively, and are defined as

$$I = \int_{T_s > T_m} (T_s - T_m)\,\mathrm{d}t \tag{3.11}$$

and

$$\langle z^2\rangle I = \int_{T_s > T_m} z^2(T_s - T_m)\,\mathrm{d}t, \tag{3.12}$$

where T_s and T_m are the surface and melting temperatures, respectively. Furthermore, as the majority of the incident energy is absorbed by the latent heat of melting L, the melt depth z is approximately given by (Schwarz-Selinger *et al.* 2001)

$$z \sim \frac{a(Q - Q_{\mathrm{th}})}{A_{\mathrm{beam}} L}, \tag{3.13}$$

where L is the latent heat of melting and Q_{th} is the threshold energy required for melting, which is obtained by iterating the thermal model for different absorptivity values and selecting that value of incident energy for which the temperature at the surface is just equal to the melting point of the precursor calcium phosphate tribasic (1843 K; Dyshlovenko *et al.* 2004) or substrate Ti–6Al–4V (1800 K; Boivineau *et al.* 2006). Also, the temperature evolution is mainly governed by the melt depth and the thermal conductivity of the material, and the integrated temperature is given by

$$I \sim \frac{a(Q - Q_{\mathrm{th}})z}{A_{\mathrm{beam}} k(T)}. \tag{3.14}$$

Replacing differentials of r in equation (3.10) by the laser beam radius R, the evolution of morphology Δz is given by (Schwarz-Selinger *et al.* 2001)

$$\Delta z = a^4 \frac{\partial \alpha(T)}{\partial T} \frac{(Q - Q_{\mathrm{th}})^4}{A_{\mathrm{beam}}^4 \eta(T) L^3 k(T) R^2}. \tag{3.15}$$

As in the case of direct writing, the melt composed of both the precursor and the substrate, and the law of mixtures was used to determine the properties of the melt such as latent heat of melting, dynamic viscosity and surface tension of the melt based on the percentage contribution of the precursor and the substrate to the melt. In contrast, for interference patterning, in the absence of coating precursor, the properties of only Ti–6Al–4V are considered. When the melt depth z was greater than 40 µm, it was assumed that the entire precursor melted and the remaining depth $(z - 40)$ µm of the melt pool was contributed by the substrate. The dynamic viscosity of the substrate was assumed to be the same as Ti and was given by (Dabhade *et al.* 2007)

$$\eta = 0.49 \exp\left(\frac{Q_\eta}{R_{\mathrm{g}} T}\right) \mathrm{MPa\,s}, \tag{3.16}$$

where R_{g} is the gas constant and Q_η is the activation energy. The variation of the surface tension of the substrate as a function of temperature was given by (Schneider *et al.* 2002)

$$\alpha = 1.389 \pm 0.09 - 9.017 \times 10^{-4} \pm 5.64 \times 10^{-5}(T - 1933\,K)\,\mathrm{N\,m^{-1}}. \tag{3.17}$$

In general, the different steps involved in the evolution of the surface topography for an area equal to the spot diameter as a result of the above-mentioned effects are illustrated in figure 4.

The values of the laser beam radius were varied from 150 to 450 µm typically used in the present work, and the temperature evolution was predicted using the above-described model (equations 3.1–3.17). Furthermore, as mentioned earlier, the width of the melt pool w was also predicted by tracking the melting point of calcium phosphate tribasic for direct writing and of Ti–6Al–4V for interference patterning on the surface, and a correlation with the beam radius R was obtained. A relation of $w = R$, $w = 1.1R$ and $w = 2R$ was obtained for the beam radii of 150, 300 and 450 µm, respectively, and the corresponding evolution of morphology is

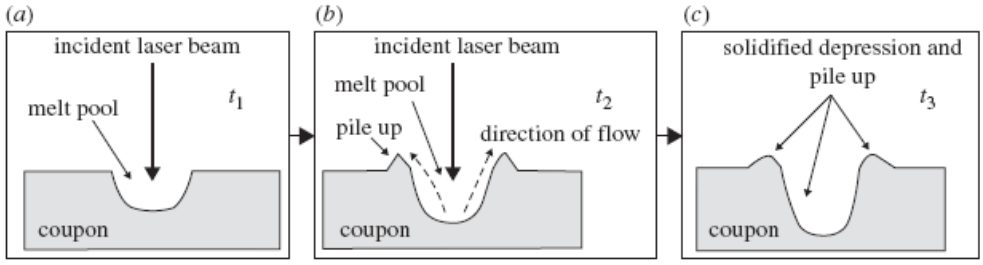


Figure 4. Different steps involved in the evolution of the surface morphology at various times ($t_1 < t_2 < t_3$) for a single laser beam.

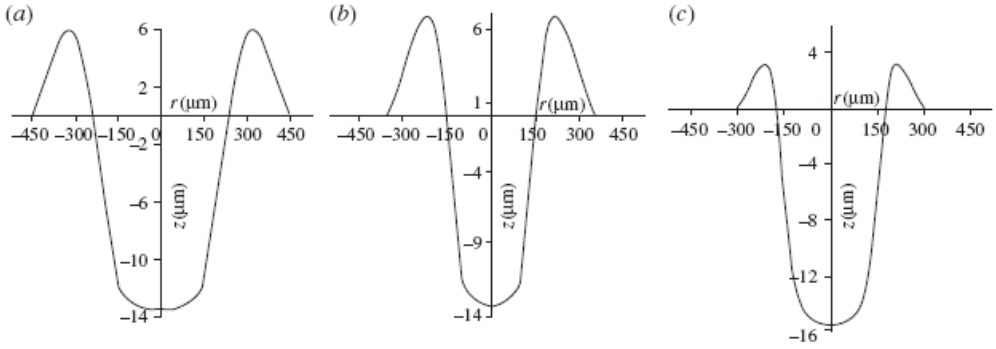


Figure 5. Surface evolution for laser beam radii of (*a*) 450 μm, (*b*) 300 μm and (*c*) 150 μm.

shown in figure 5. In this study, the capillary effects were neglected as they are not dominant when the thickness of coatings and/or the melt depth is of the order of a few microns (Schüssler *et al.* 1992).

As mentioned earlier, the process of formation of a depression and associated pile-up corresponding to an area equal to spot diameter repeats itself for successive laser runs and the sinusoidal morphology evolves as shown in figure 6, where w is the wavelength (width of depression or width of melt pool) and A is the amplitude (distance between the centre-line passing through the profile and the highest point on the surface). The amplitude A is representative of and proportional to the depth of depression or depth of melt pool. A flow chart representing the evolution of the surface topography starting with the laser processing conditions and material properties is shown in figure 7.

Since the invasion or the wetting behaviour of a liquid on a solid surface depends on the surface design and the above-mentioned geometrical parameters, an understanding of or the estimation of such parameters owing to laser–material interaction will provide a strong base for tuning wettability. Assuming a constant spot size, it can be realized from equation (3.15) that, with increasing effective input laser energy, the depth or the height of the features (depression) can be increased for a possible hydrophobic surface because of air entrapment. On the contrary, for improved wettability and desirable cell compatibility, the samples must be processed within the regime of lower effective laser energy.

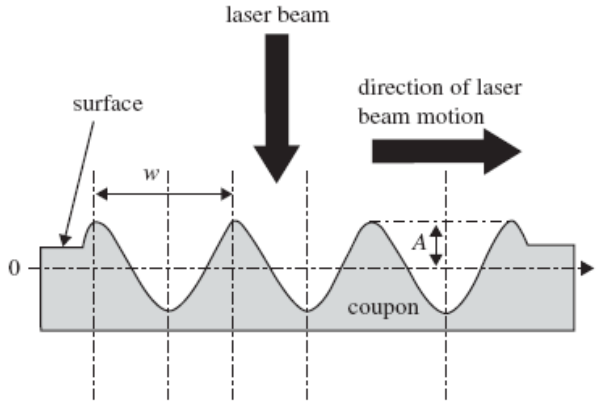


Figure 6. Combination of profiles generated by successive pulses defining the width w and amplitude A.

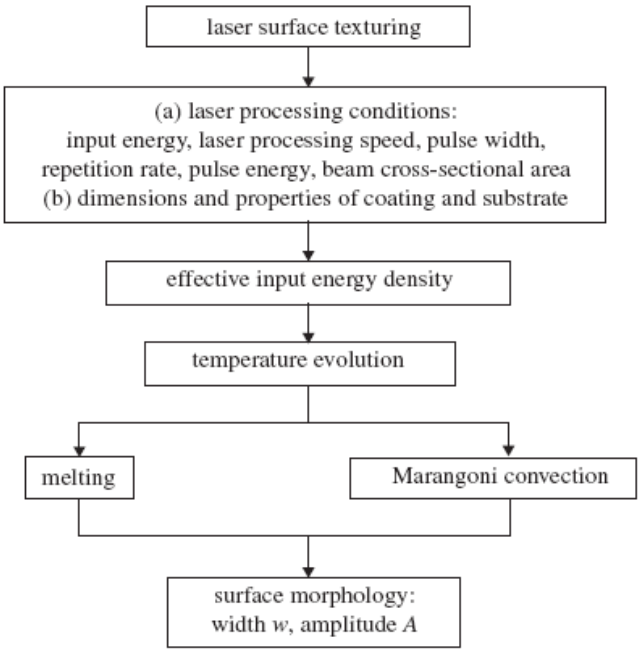


Figure 7. Flow chart illustrating the method to predict surface morphology starting with laser processing parameters and material geometry and properties.

4. The effects of surface morphology on wettability

Using the laser-based optical interference technique, textured surfaces with groove- and pillar-like features were obtained on the flat Ti–6Al–4V sample by varying the laser power. The two- and three-dimensional morphological evolution of the groove-like features obtained using a one-step irradiation under a laser power of 3.82 W is presented in figure 8*a*,*b*, respectively. From figure 8*a*,*b* (two- and three-dimensional morphological evolution, respectively), it can be observed

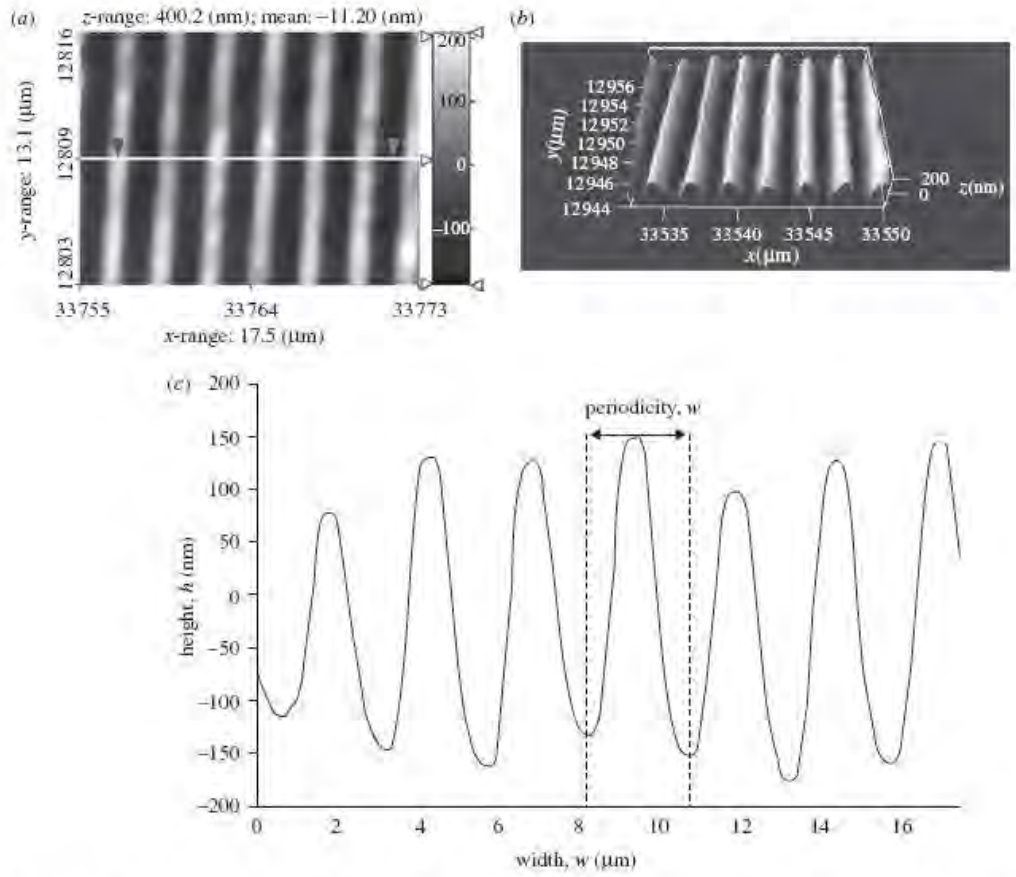


Figure 8. Groove pattern on Ti–6Al–4V by the laser interference technique (3.82 W laser power): (*a*) two-dimensional morphological evolution, (*b*) three-dimensional morphological evolution and (*c*) variation in height and width (across the line scan) of the features obtained using a one-step irradiation.

that the spacing or the periodicity w (equivalent to the width of the depression or width of the melt pool) of the pattern is approximately 2.5 μm. Further, the variation in height h of the grooves across the sample in x-direction (figure 8*c*) also clearly proved the width w to be approximately 2.5 μm. As discussed earlier, since the angle β between the beams is kept constant in this process throughout the experiment, there was no change in the periodicity or width w of the patterns. With varying laser power only, the feature size h is varied in the z-direction, and an increase in feature size is realized with increasing laser power (table 2). This is attributed to the fact that, with increasing laser power, there is an increase in molten pool and thereby an increased temperature gradient across the vertical direction, resulting in greater Marangoni forces. As discussed earlier, this Marangoni force may have resulted in extensive surface tension gradients across the border, expelling a substantial amount of the liquid melt from the pool and thereby resulting in a bigger groove at higher laser power.

Table 2. Process power and corresponding height of the groove/pillar pattern and contact angle related to interference-patterned samples.

sample	laser fluence ($mJ\,cm^{-2}$)	height, h (nm)	apparent contact angle, θ^* (°)	
			distilled water	SBF
groove pattern on Ti–6Al–4V	760.35	208.08 ± 0.08	78.55 ± 0.45	67.4 ± 0.60
	525.47	71.35 ± 0.02	73.45 ± 0.55	64.2 ± 0.80
	362.26	68.08 ± 0.02	70.7 ± 0.30	60.2 ± 0.80
pillar pattern on Ti–6Al–4V	760.35	77.65 ± 1.07	78.45 ± 0.55	66.8 ± 0.20
	525.47	44.14 ± 1.04	77.45 ± 0.55	66.6 ± 0.40
	362.26	36.68 ± 1.03	77.9 ± 0.10	67.1 ± 0.90
			chemical angle, θ (°)	
			distilled water	SBF
Ti–6Al–4V control	—	—	67.98 ± 0.02	59.2 ± 0.80

In order to generate pillar-like features, the sample once irradiated was rotated 90° and irradiated again with five pulses. Hence, it was a two-step process, with the effective number of pulses being doubled compared with the groove-like features. The two- and three-dimensional morphological evolution of the pillar-like features obtained under a laser power of 3.82 W is presented in figure 9*a*,*b*, respectively. From a line scan across the sample (figure 9*c*), it was observed that the width d at full-width-half-maxima (FWHM) and the periodicity w of the pillars were approximately 1.04 and 2.5 µm, respectively. Again, the periodicity is dependent on the angle β between the beams. Therefore, in the pillar patterns also, the only physical feature that was varied with varying laser power was the height h of the pillars. It was observed that there is an increase in the pillar height h with increasing laser power (table 2) as per earlier discussion.

Contact angle measurements on both the groove and pillar patterns were conducted using distilled water and SBF. Selected images of the droplet shadow on the goniometer are presented in figure 10. It can be observed that the distilled water droplet (figure 10*a–c* corresponding to flat, groove-patterned and pillar-patterned Ti–6Al–4V, respectively) subtended a higher contact angle than the SBF droplet (figure 10*d–f* corresponding to flat, groove-patterned and pillar-patterned Ti–6Al–4V, respectively). The chemical angle or the Young angle θ obtained on the flat Ti–6Al–4V averaged around 67.98° for distilled water and 59.2° for SBF (table 2). Furthermore, it was observed that there was a decrease in the apparent contact angle θ^* (using SBF and distilled water) with decreasing laser power for the groove-like patterns; however, no such distinct trend was observed for the pillar patterns. This disparity is mostly due to their geometrical structure (groove and pillar features) and can be justified based on the Cassie and Baxter model. According to the Cassie and Baxter model, the apparent contact angle θ^* on a surface with chemical patch work or rough features entrapped with air is given as (Ishino *et al.* 2004)

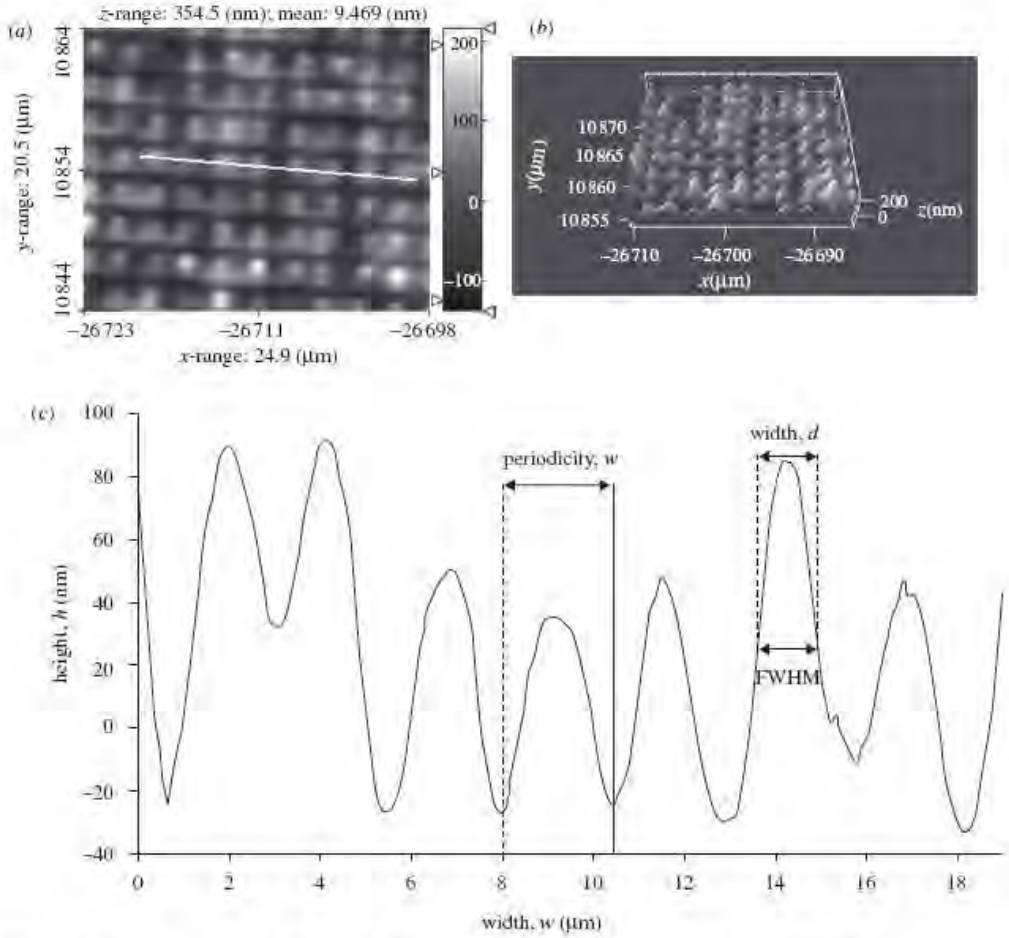


Figure 9. Pillar pattern on Ti–6Al–4V by the laser interference technique (3.82 W laser power): (*a*) two-dimensional morphological evolution, (*b*) three-dimensional morphological evolution and (*c*) variation in height and width at FWHM (across the line scan) of the features obtained using a two-step irradiation.

$$\cos\theta^* = f_1 \cos\theta_1 + f_2 \cos\theta_2, \tag{4.1}$$

where f_1 and f_2 represent the surface area fraction of the liquid in contact with the solid and air, respectively, and θ_1 and θ_2 represent their corresponding contact angles. Hence, according to their model, when a liquid drop is placed on a composite surface with solid and air patches in it, the liquid does not follow the surface contours and sits upon the composite surface as it is pushed by the air. As the grooves in the groove pattern are bridged by a certain amount of material, air entrapment within them is more feasible. Also, with increasing laser power, there is an increase in the height h of the grooves (width w of the grooves is constant) and thereby an increased volume of trapped air pockets resulted in an increase in apparent contact angle θ^*. In contrast, for the pillar patterns, there is an open volume within the pillars, and hence air entrapment may not

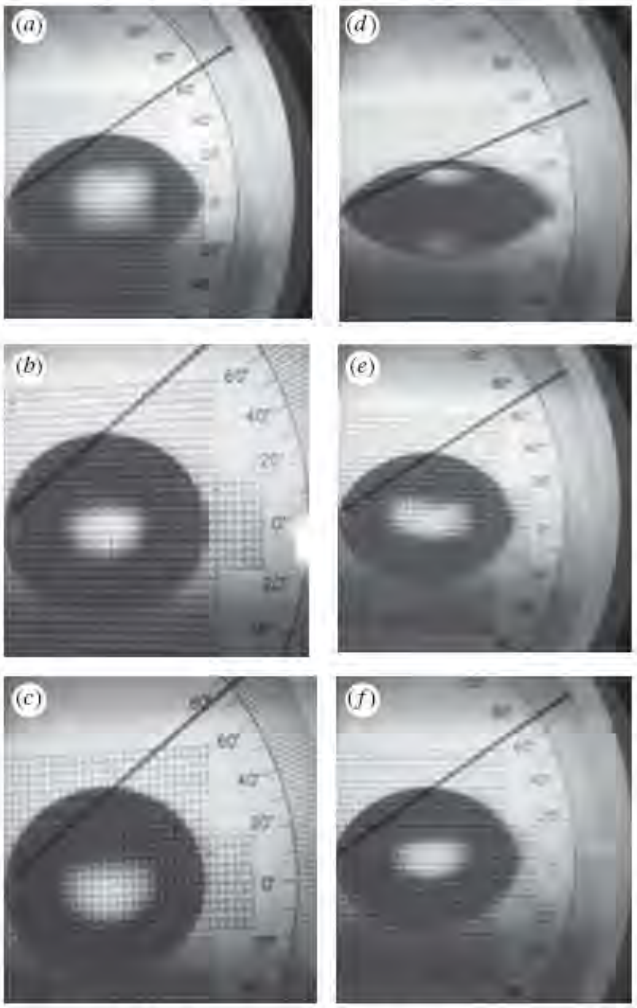


Figure 10. Light optical images of the distilled water droplet shadow on (*a*) flat Ti–6Al–4V, (*b*) groove-patterned Ti–6Al–4V and (*c*) pillar-patterned Ti–6Al–4V and those of the SBF droplet shadow on (*d*) flat Ti–6Al–4V, (*e*) groove-patterned Ti–6Al–4V and (*f*) pillar-patterned Ti–6Al–4V.

be possible. Further, as there is not much variation in the height h of the pillars (width d and periodicity w of the pillars being constant) with increasing laser power, their roughness factor $R_f = 1 + 2(h/d)$ (the ratio of the solid area to its projected area as explained later) did not vary much, and, hence, a noticeable change in the apparent contact angle could not be expected.

Also from the droplet shadow images (figure 10) and from table 2, it can be seen that there is an increase in the apparent contact angle θ^* for the interference-patterned samples compared with the chemical angle obtained on the flat sample. Therefore, the presence of groove and pillar features obtained using the laser interference technique with the present set of processing parameters

(table 1) resulted in tuning the surface towards a less hydrophilic behaviour. This reduced wettability on the patterned samples can further be explained with the thermodynamic models as discussed below.

It is well established that, when the solid is hydrophobic with rough features on it, a water drop deposited on such a surface remains extremely spherical (Bico *et al.* 2001, 2002; Ishino *et al.* 2004). This is attributed to the fact that the liquid is only in contact with the upper part of the relief and the roughness is mainly filled with air, leading to super-hydrophobicity. In contrast, for a hydrophilic solid such as Ti–6Al–4V, the presence of the surface texture leads to a certain amount of liquid invasion when brought in contact with a liquid phase. This invasion of the liquid depends on the geometric parameters of the surface design and is known as hemi-wicking (Bico *et al.* 2001). The process of hemi-wicking alters the contact angle, and, therefore, the critical angle (θ_c) below which a liquid can impregnate a textured surface can be calculated based on energy balance equations. For the ease of calculations based on the energy balance equations, the grooves were approximated to be of triangular type and the pillars to be of cylindrical type.

For spontaneous invasion of liquid into a groove pattern (figure 11*a*), the solid must lower its energy by being wet ($\gamma_{SL} < \gamma_{SA}$). The liquid/vapour interface at the top of the groove is assumed to be flat and corresponds to a minimum surface area. Therefore, if the liquid progression front advances by a distance dx, the change in the surface energy (dE) is given by the following equation (Bico *et al.* 2001):

$$dE = (\gamma_{SL} - \gamma_{SA})2\left(h^2 + \frac{w^2}{4}\right)^{1/2} dx + \gamma_{LA} w\, dx. \tag{4.2}$$

Here γ_{SL}, γ_{SA} and γ_{LA} are the interface energies between solid–liquid, solid–air and liquid–air interfaces, respectively, and are connected by an equation known as Young's equation,

$$\gamma_{SA} = \gamma_{SL} + \gamma_{LA}\cos\theta. \tag{4.3}$$

Here, θ is considered as the chemical angle of the solid assuming the surface to be molecularly flat. Substituting Young's equation (equation 4.3) into equation (4.2), it can be hypothesized that liquid progression is favourable ($dE < 0$) if θ^* or $\theta < \theta_c$, where θ_c is the critical angle for wetting and can be derived as (Bico *et al.* 2001)

$$\cos\theta_c = \frac{w}{2(h^2 + (w^2/4))^{1/2}} = \frac{1}{\sqrt{1 + (4h^2/w^2)}}. \tag{4.4}$$

Therefore, for groove texture, the critical angle for wetting depends on the roughness factor $R_f = \sqrt{1 + (4h^2/w^2)}$ (i.e. the ratio of the actual surface area to apparent surface area).

In contrast, a surface with an assembly of pillar patterns (figure 11*b*) is characterized by ϕ_S (solid fraction remaining dry) and roughness factor $R_f = 1 + 2(h/d)$ (i.e. the ratio of the actual solid area to its projected area). If on such a surface the progressive front of the liquid phase advances by a distance dx (figure 11*b*), the interfacial energies change by a quantity dE (per unit width of the sample) as per the following equation (Bico *et al.* 2001):

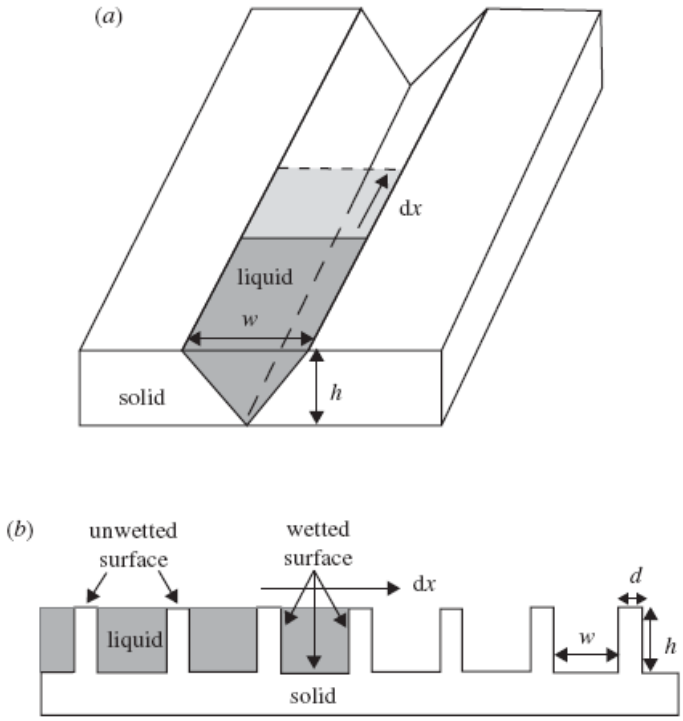


Figure 11. Schematic illustration of liquid invasion into (*a*) a groove pattern and (*b*) a pillar pattern.

$$\mathrm{d}E = (\gamma_{\mathrm{SL}} - \gamma_{\mathrm{SA}})(R_{\mathrm{f}} - \phi_{\mathrm{S}})\,\mathrm{d}x + \gamma_{\mathrm{LA}}(1 - \phi_{\mathrm{S}})\,\mathrm{d}x. \tag{4.5}$$

The first term on the right-hand side of the above equation is related to the replacement of a dry solid by a wet one and is proportional to the factor (R_{f}–ϕ_{S}). The second term is related to the creation of a liquid/vapour interface and is proportional to $(1 - \phi_{\mathrm{S}})$. The liquid progression is favourable if $\mathrm{d}E$ is negative and by introducing Young's equation gives the condition for wetting on such a surface as (Bico *et al.* 2001)

$$\theta^* \text{ or } \theta < \theta_{\mathrm{c}} \text{ with } \cos\theta_{\mathrm{c}} = \frac{1 - \phi_{\mathrm{s}}}{R_{\mathrm{f}} - \phi_{\mathrm{s}}}. \tag{4.6}$$

Therefore, the liquid invasion on the microtextured solids can be tuned by effectively modifying the structures.

Using the above relationships and experimentally measured geometrical parameters (w, h and d) of the features obtained using laser-based optical interference patterning technique, the roughness factor R_{f} was calculated for both groove and pillar patterns and plotted as a function of laser power (figure 12*a*). It can be observed (figure 12*a*) that there is a slight increase in R_{f} with increasing laser power for both the groove and pillar patterns, and R_{f} is higher for the pillar pattern than for the groove pattern. This increased value of roughness factor ($R_{\mathrm{f}} > 1$) for the pillar pattern is attributed to reduced width d of the features as a result of the two-step processing involved in this technique. Further, the

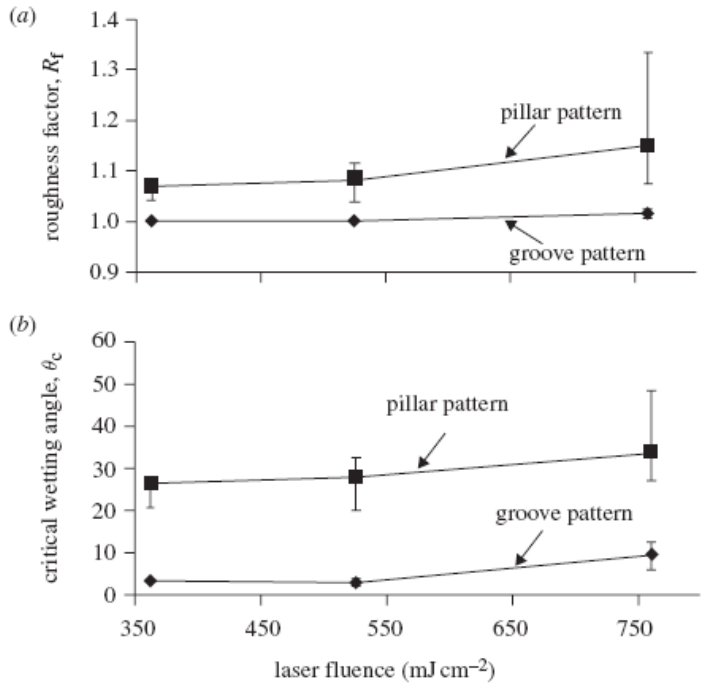


Figure 12. (*a*) Variation in roughness factor R_f and (*b*) critical wetting angle θ_c with laser fluence for interference-patterned samples.

critical wetting angle (θ_c) based on equations (4.4) and (4.6) was calculated for the groove and pillar patterns, respectively, and plotted as a function of laser power (figure 12*b*). Here, for the pillar patterns, the liquid is assumed to seep into the interpillar region with the top of pillars remaining dry, and therefore, ϕ_S (solid fraction remaining dry) is calculated from the geometry of the pillars (figure 11*b*). It can be observed (figure 12*b*) that there is an increase in the critical wetting angle (θ_c) with increasing laser power for both the patterns, and the values of the critical wetting angle (ranging from 3° to 48°) are subsequently smaller than the chemical or the Young angles (θ) obtained using both distilled water and SBF (table 2). As a result, the condition for wetting (θ^* or $\theta < \theta_c$) is not satisfied in both the cases (pillar and groove), and, hence, the liquid dewets on both the patterns owing to an increase in apparent contact angle (θ^*).

Keeping the above results in mind and understanding the limitations associated with the laser-based optical interference patterning technique in generating suitable surface features under a set of processing conditions employed in the present work, a modified technique based on laser direct writing was adopted. Here, to improve wettability, not only surface morphology but also surface chemistry was altered by directly melting calcium phosphate tribasic coating on Ti–6Al–4V substrate. Although in these coated samples diverse surface morphologies were generated within a set of laser processing parameters employed in the present work, no chemical phase variations were realized (Paital & Dahotre 2009). Hence, the wettability was observed as variation in the surface morphology.

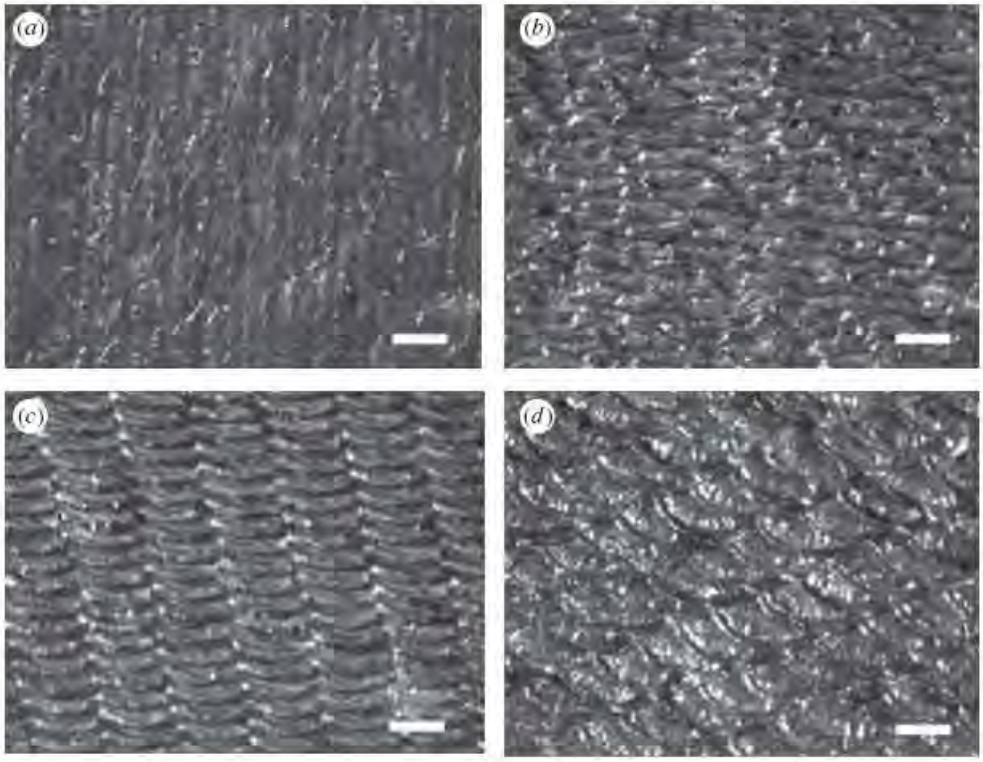


Figure 13. Low-magnification optical microscopic images of the surfaces of the coatings obtained at laser scan speed of: (*a*) 36 cm min^{-1}, (*b*) 48 cm min^{-1}, (*c*) 78 cm min^{-1} and (*d*) 102 cm min^{-1} (Paital & Dahotre 2009). Scale bar, (*a*–*d*) 500 µm.

Low-magnification optical microscopic images (figure 13) of the surfaces of samples coated using the laser direct writing technique clearly demonstrate the effect of varying laser scan speed on the texture evolution. The laser scan speed influences the input energy density (table 1) and the laser spot overlap. These two parameters in turn greatly influence the surface morphology or the texture evolution in the coating. As seen in figure 13, each pulse of a laser produces a solidified crater with a defined boundary and a flat region at the centre. Hence, as the laser scan speed is increased, the laser spot (crater) overlap is decreased as per equation (2.2), which in turn modifies the crater area as well as the surface texture. Also with increasing laser scan speed, the input energy density (fluence) decreased and resulted in reduced surface melting or less thermal effect at the surface. Thus, variation of laser processing parameters produced variable thermodynamic conditions, resulting in the creation of different physical surface textures (figure 13).

The two-dimensional morphological evolution (figure 14*a*) and the variation in height h of the features across a line scan (figure 14*b*) were obtained using the white light interferometer. It can be observed (figure 14*a*,*b*) that the features were similar to those of a groove-like pattern and are of higher length scales when compared with the similar type features obtained using the laser-based optical

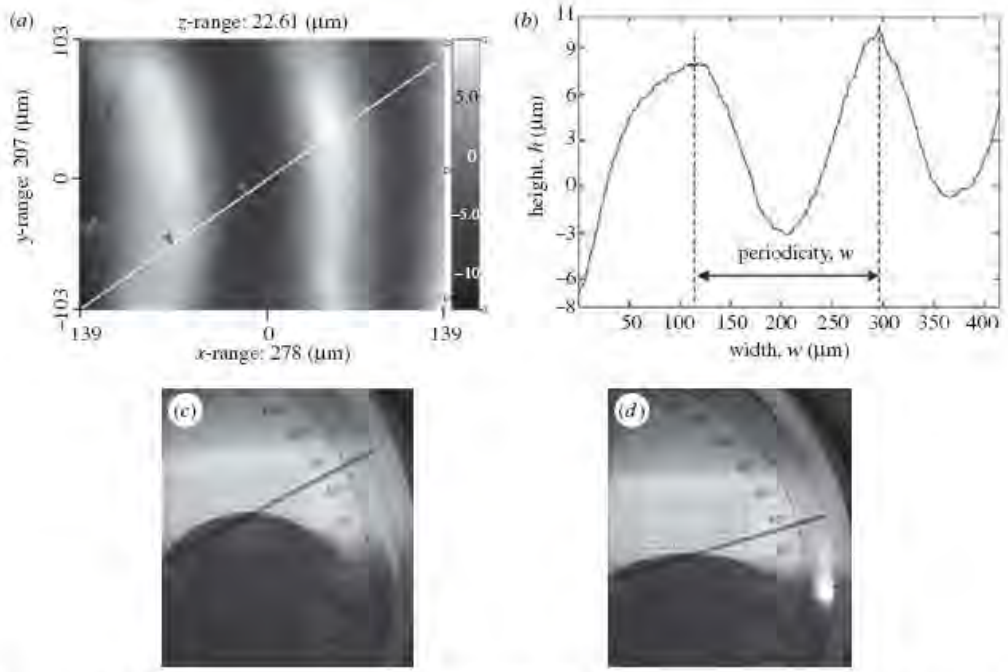


Figure 14. (*a*) Two-dimensional morphological evolution and (*b*) variation in height h and width w of the groove patterns (across the line scan). Light optical micrographs of (*c*) a distilled water droplet shadow and (*d*) a SBF droplet shadow on laser direct writing synthesized Ca–P-coated sample obtained at a laser power of 156 W.

interference patterning technique. Unlike the laser-based optical interference patterning technique, in the direct writing technique both the height h and width w of the grooves were varied with increasing laser power (table 3). Contact angle measurements using distilled water and SBF demonstrated a decrease in apparent contact angle (θ^*) with decreasing laser power (table 3). Furthermore, as observed previously in the laser-based optical interference patterning technique, in the present case also, within the processing parameters, the SBF demonstrated a lower contact angle than the distilled water (table 3). The images of droplets of the distilled water (figure 14*c*) and SBF (figure 14*d*) formed on a sample processed at 156 W also clearly support the above observations. The decrease in apparent contact angle (θ^*) for the processed samples (table 3) when compared with the chemical or Young angle (θ) obtained from the flat Ti–6Al–4V can be explained based on the calculation of the critical wetting angle (θ_c), as discussed earlier.

The roughness factor $R_f = \sqrt{1 + (4h^2/w^2)}$ (i.e. the ratio of the actual surface area to apparent surface area for the groove pattern) and the corresponding critical wetting angle (θ_c) based on equation (4.4) are plotted as a function of laser power (figure 15). The roughness factor R_f and the critical wetting angle θ_c increased with increasing laser power. The critical wetting angle varied from 75° to 82°, which is far greater than the range of apparent contact angle for both distilled water (38–44°) and SBF (15–22°) (table 3). Hence, as the criteria for

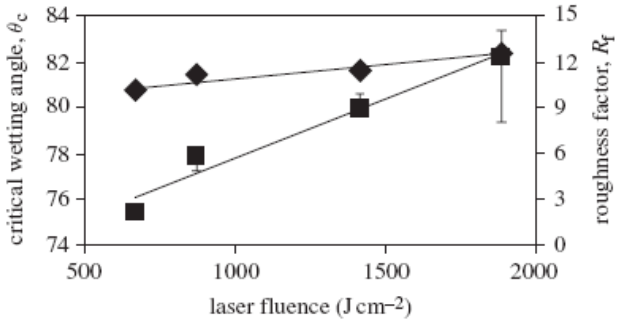


Figure 15. The variation in roughness factor R_f and critical wetting angle θ_c with laser fluence of Ca–P-coated samples obtained by the laser direct writing technique.

Table 3. Geometrical parameter and apparent contact angle measurement on laser direct writing synthesized Ca–P-coated Ti–6Al–4V samples.

				apparent contact angle, θ^* (°)	
sample	laser fluence	height, h (μm)	width, w (μm)	distilled water	SBF
Ca–P	1887	12.76	2.6 ± 0.02	44 ± 1.2	22 ± 0.44
	1415	38.4	9.46 ± 0.14	43 ± 1.5	19.5 ± 0.48
	871	31.86	7.98 ± 0.19	40 ± 1.4	18 ± 0.2
	666	24.06	12.52 ± 0.25	38 ± 2.1	15 ± 0.45

wettability or liquid invasion (θ^* or $\theta < \theta_c$) are satisfied, a liquid drop placed on such a surface is not being pinned by the defects and flows into the contours, thereby resulting in a reduced apparent contact angle (θ^*).

As the Ca–P-coated samples obtained by the laser direct writing technique demonstrated significant wettability to physiological fluids (SBF) compared with laser interference structured surfaces (on bare Ti–6Al–4V), a preliminary study on cell compatibility was carried out on a representative (Ca–P coated) sample. Further, since the sample processed at 156 W provided the maximum contact angle and thereby less wettability, it was chosen for the study of biocompatibility. Cell morphology for the sample after 1 day of culture was assessed by SEM, and the results are presented in figure 16. The MC3T3-E1 osteoblast cells possessed a triangular morphology, and they were well spread on the surface. Especially, their good adhesion was characterized by the lamellipodia trying to extend and adhere along the grooves. The cytoskeletal organization of the cells after 1 day of culture as observed using a fluorescence microscope is shown in figure 17. The presence of stressed actin filaments and a well-developed nucleus further proved the strong proliferation and good focal adhesion contact to the Ca–P-coated surfaces.

Unlike most research articles on wettability in which the prime focus was to improve hydrophobicity for self-cleaning (Bico *et al.* 2001, 2002; Palasantzas & De Hosson 2001; Ishino *et al.* 2004; Ma *et al.* 2005, 2007; Sheng *et al.* 2007;

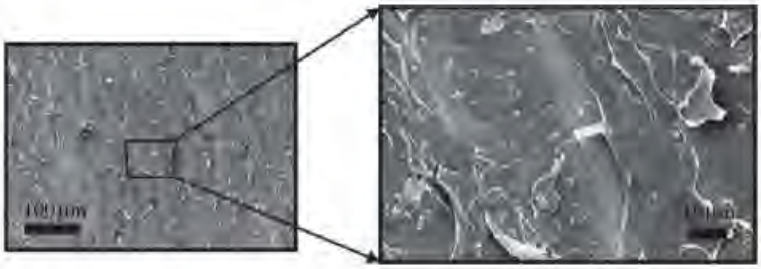


Figure 16. SEM micrographs revealing the morphology of the MC3T3-E1 osteoblast cells following culture for 1 day on a laser direct writing synthesized Ca–P-coated sample obtained at a laser power of 156 W.

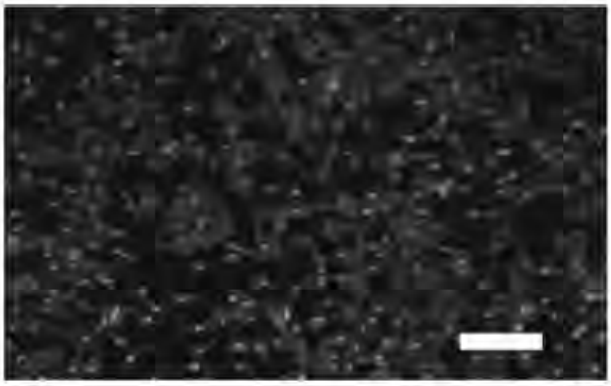


Figure 17. Fluorescent micrographs for cytoskeleton assessment of adherent MC3T3-E1 osteoblast cells after culture for 1 day on a laser direct writing synthesized Ca–P-coated sample obtained at a laser power of 156 W. Scale bar, 100 μm.

Bhusan *et al.* 2009; Yong & Zhang 2009), the above study was mostly focused on improving the wettability or hydrophilicity for load-bearing implants. Since implant materials when placed inside a human body come in contact with the physiological fluids, which then further governs the protein interaction followed by cell attachment and tissue integration at the interface, an improved hydrophilic behaviour was considered ideal for such surfaces. As the wettability or the contact behaviour of a liquid can be tuned by the surface morphology or surface textures, the techniques such as laser-based optical interference patterning and direct writing can be instrumental in creating the surface textures at different length scales on the Ti–6Al–4V surface. Furthermore, these techniques in integration with the computational model approach and fundamental understanding of involved physical phenomena can be important to control surface texture parameters such as width, height and periodicity in tuning the wettability for improved biocompatibility. Apart from load-bearing implant applications, the above understanding can also be used to design surfaces for corrosion prevention, self-cleaning (water repellent), energy conversion and conservation, biomimetics, etc.

5. Conclusions

A systematic study based on the laser-based surface modification technique to improve the wettability of the load-bearing implant alloys (Ti–6Al–4V) to physiological fluids is demonstrated. The surfaces were characterized based on the roughness factor and the apparent contact angle measurements. The groove and pillar patterns obtained using the interference patterning technique resulted in an increase in apparent contact angle. Such an increase was attributed to the decrease in the critical wetting angle as a result of the pinning effect created by the sharp grooves on the liquid drop. Owing to the limitations associated with the laser-based optical interference patterning technique in getting appropriate surface features, a modified technique based on laser-based direct writing was adopted. Here, to improve the wettability, both the surface morphology and the surface chemistry were altered by directly melting calcium phosphate tribasic on Ti–6Al–4V substrate. The groove features obtained using the direct writing technique demonstrated a significant decrease in the apparent contact angle. This improved wettability is concluded as a result of the increase in the critical wetting angle. The well-organized morphological evolution and the spreading of the MC3T3-E1 osteoblast cells after culture for 1 day on a representative Ca–P-coated sample further proved its biocompatibility.

The authors acknowledge the help from Sudarshan Phani in white light interferometry-based surface measurements. The authors also highly acknowledge the support and help from Dr Wei He and Zheng Cao in conducting cell culture measurements. A part of this research has been performed at Oak Ridge National Laboratory, managed by UT-Battelle, LLC, for the US Department of Energy under contract DE-AC05-00OR22725 and has been sponsored by the Industrial Technologies Program for the Office of Energy Efficiency and Renewable Energy.

References

Bhusan, B., Jung, Y. C. & Koch, K. 2009 Micro-, nano- and hierarchical structures for superhydrophobicity, self-cleaning and low adhesion. *Phil. Trans. R. Soc. A* **367**, 1631–1672. (doi:10.1098/rsta.2009.0014)

Bico, J., Tordeux, C. & Quéré, D. 2001 Rough wetting. *Electrophys. Lett.* **55**, 214–220. (doi:10.1209/epl/i2001-00402-x)

Bico, J., Thiele, U. & Quéré, D. 2002 Wetting of textured surfaces. *Colloid Surf. A Physiochem. Eng. Aspects* **206**, 41–46. (doi:10.1016/S0927-7757(02)00061-4)

Boivineau, M., Cagran, C., Doytier, D., Eyraud, V., Nadal, M.-H., Wilthan, B. & Pottlacher, G. 2006 Thermophysical properties of solid and liquid Ti–6Al–4V (TA6V) alloy. *Int. J. Thermophys.* **27**, 507–529. (doi:10.1007/s10765-005-0001-6)

Carles, P., Troian, S. M., Cazabat, A. M. & Heslot, F. 1990 Hydrodynamic fingering instability of driven wetting films: hindrance by diffusion. *J. Phys. Condens. Mater.* **2**, 477–482. (doi:10.1088/0953-8984/2/S/076)

Cooper, L. F. 2000 A role of surface topography in creating and maintaining bone at titanium endosseous implants. *J. Prosthet. Dent.* **84**, 522–534. (doi:10.1067/mpr.2000.111966)

Dabhade, V. V., Rama Mohan, T. R. & Ramakrishnan, P. 2007 Viscous flow during sintering of attrition milled nanocrystalline titanium powders. *Mater. Res. Bull.* **42**, 1262–1268. (doi:10.1016/j.materresbull.2006.10.008)

Daniel, C., Mucklich, F. & Liu, Z. 2003 Periodical micro-nano-structuring of metallic surfaces by interfering laser beams. *Appl. Surf. Sci.* **208–209**, 317–321. (doi:10.1016/S0169-4332(02)01381-8)

Daniel, C., Balk, T. J., Wubben, T. & Mucklich, F. 2005 Bio-mimetic scaling of mechanical behavior of thin films, coatings, and surfaces by laser interference metallurgy. *Adv. Eng. Mater.* **7**, 823–826. (doi:10.1002/adem.200500110)

Dyshlovenko, S., Pateyron, B., Pawlowski, L. & Murano, D. 2004 Numerical simulation of hydroxyapatite powder behavior in plasma jet. *Surf. Coat. Technol.* **179**, 110–117. (doi:10.1016/S0257-8972(03)00799-0)

Engleman, P. G., Kurella, A., Samant, A., Blue, C. A. & Dahotre, N. B. 2005 The application of laser-induced multi-scale surface texturing. *JOM J. Miner. Metal Mater. Soc.* **57**, 46–50. (doi:10.1007/s11837-005-0182-2)

Flemming, R. G., Murphy, C. J., Abrams, G. A., Goodman, S. L. & Nealey, P. F. 1999 Effects of synthetic micro- and nano-structured surfaces on cell behavior. *Biomaterials* **20**, 573–588. (doi:10.1016/S0142-9612(98)00209-9)

Guillot-Noël, O., Gomez-San Roman, R., Perrière, J., Hermann, J., Craciun, V., Boulmer-Leborgne, C. & Barboux, P. 1996 Growth of apatite films by laser ablation: reduction of the droplet areal density. *J. Appl. Phys.* **80**, 1803–1808. (doi:10.1063/1.362991)

Hao, L., Lawrence, J., Phua, Y. F., Chian, K. S., Lim, G. C. & Zheng, H. Y. 2004 Enhanced human osteoblast cell adhesion and proliferation on 316L stainless steel by means of CO_2 laser surface treatment. *J. Biomed. Mater. Res. B Appl. Biomater.* **73B**, 148–156. (doi:10.1002/jbm.b.30194)

Hao, L., Lawrence, J. & Li, L. 2005 Manipulation of the osteoblast response to a Ti–6Al–4V titanium alloy using a high power diode laser. *Appl. Surf. Sci.* **247**, 602–606. (doi:10.1016/j.apsusc.2005.01.165)

Incropera, F. P. & Dewitt, D. P. 1985 *Fundamentals of heat and mass transfer*, 2nd edn. New York, NY: Wiley.

Ishino, C., Okumura, K. & Quéré, D. 2004 Wetting transitions on rough surfaces. *Electrophys. Lett.* **68**, 419–425. (doi:10.1209/epl/i2004-10206-6)

Jones, M. I., McColl, I. R., Grant, D. M., Parker, K. G. & Parker, T. L. 2000 Protein adsorption and platelet attachment and activation, on TiN, TiC, and DLC coatings on titanium for cardiovascular applications. *J. Biomed. Mater. Res.* **52**, 413–421. (doi:10.1002/1097-4636(200011)52:2%3C413::AID-JBM23%3E3.0.CO;2-U)

Lasagni, A., Nejati, M., Clasen, R. & Mucklich, F. 2006 Periodical surface structuring of metals by laser interference metallurgy as a new fabrication method of textured solar selective absorbers. *Adv. Eng. Mater.* **8**, 580–584. (doi:10.1002/adem.200500261)

Lasagni, A., Holzapfel, C., Weirich, T. & Mucklich, F. 2007 Laser interference metallurgy: a new method for periodic surface microstructure design on multilayered metallic thin films. *Appl. Surf. Sci.* **253**, 8070–8074. (doi:10.1016/j.apsusc.2007.02.092)

Lawrence, J., Hao, L. & Chew, H. R. 2005 On the correlation between Nd:YAG laser-induced wettability characteristics modification and osteoblast cell bioactivity on a titanium alloy. *Surf. Coat. Technol.* **200**, 5581–5589. (doi:10.1016/j.surfcoat.2005.07.107)

Li, X., Huang, J., Ahmad, Z. & Edirisinghe, M. 2007 Electrohydrodynamic coating of metal with nano-sized hydroxyapatite. *Biomed. Mater. Eng.* **17**, 335–346.

Ma, M., Mao, Y., Gupta, M., Gleason, K. K. & Rutledge, G. C. 2005 Superhydrophobic fabrics produced by electrospinning and chemical vapor deposition. *Macromolecules* **38**, 9742–9748. (doi:10.1021/ma0511189)

Ma, M., Gupta, M., Li, Z., Zhai, L., Gleason, K. K., Cohen, R. E., Rubner, M. F. & Rutledge, G. C. 2007 Decorated electrospun fibers exhibiting superhydrophobicity. *Adv. Mater.* **19**, 255–259. (doi:10.1002/adma.200601449)

Paital, S. R. & Dahotre, N. B. 2009 Wettability and kinetics of hydroxyapatite precipitation on a laser-textured Ca–P bioceramic coating. *Acta Biomater.* **5**, 2763–2772. (doi:10.1016/j.actbio.2009.03.004)

Paital, S. R., Balani, K., Agarwal, A. & Dahotre, N. B. 2009 Fabrication and evaluation of a pulse laser-induced Ca–P coating on a Ti alloy for bioapplication. *Biomed. Mater.* **4**, 1–10. (doi:10.1088/1748-6041/4/1/015009)

Palasantzas, G. & De Hosson, J. Th. M. 2001 Wetting on rough surfaces. *Acta Mater.* **49**, 3533–3538. (doi:10.1016/S1359-6454(01)00238-5)

Perrin, D., Szmukler-Moncler, S., Echikou, C., Pointaire, P. & Bernard, J. P. 2002 Bone response to alteration of surface topography and surface composition of sandblasted and acid (SLA) implants. *Clin. Oral. Implant Res.* **13**, 465–469. (doi:10.1034/j.1600-0501.2002.130504.x)

Pilliar, R. M. 1998 Overview of surface variability of metallic endosseous dental implants: textured and porous surface-structured designs. *Implant Dent.* **7**, 305–314. (doi:10.1097/00008505-199807040-00009)

Rupp, F., Scheideler, F., Rehbein, D., Axmann, D. & Geis-Gerstorfer, J. 2004 Roughness induced dynamic changes of wettability of acid etched titanium implant modifications. *Biomaterials* **25**, 1429–1438. (doi:10.1016/j.biomaterials.2003.08.015)

Samant, A. N. 2009 Laser machining of structural ceramics: computational and experimental analysis. Doctoral dissertation, The University of Tennessee, Knoxville, TN.

Sauberlich, S., Klee, D., Richter, E. J., Hocker, H. & Spiekermann, H. 1999 Cell culture tests for assessing the tolerance of soft tissue to variously modified titanium surfaces. *Clin. Oral. Implant Res.* **10**, 379–393. (doi:10.1034/j.1600-0501.1999.100505.x)

Scheideler, L., Geis-Gerstorfer, J., Kern, D., Pfeiffer, F., Rupp, F., Weber, H. & Wolburg, H. 2003 Investigation of cell reactions to microstructured implant surfaces. *Mater. Eng. C* **23**, 455–459.

Schneider, G. & Burridge, K. 1994 Formation of focal adhesions by osteoblasts adhering to different substrata. *Exp. Cell. Res.* **214**, 264–269. (doi:10.1006/excr.1994.1257)

Schneider, S., Egry, I. & Seyhan, I. 2002 Measurement of the surface tension of undercooled liquid Ti90Al6V4 by the oscillating drop technique. *Int. J. Thermophys.* **23**, 1241–1248. (doi:10.1023/A:1019896321431)

Schüssler, A., Steen, P. H. & Ehrhard, P. 1992 Laser surface treatment dominated by buoyancy flows. *J. Appl. Phys.* **71**, 1972–1975. (doi:10.1063/1.351161)

Schwarz-Selinger, T., Cahill, D. G., Chen, S.-C., Moon, S.-J. & Grigoropoulos, C. P. 2001 Micron-scale modifications of Si surface morphology by pulsed-laser texturing. *Phys. Rev. B* **64**, 155 323. (doi:10.1103/PhysRevB.64.155323)

Sheng, Y. J., Jiang, S. & Tsao, H. K. 2007 Effects of geometrical characteristics of surface roughness on droplet wetting. *J. Chem. Phys.* **127**, 234 704. (doi:10.1063/1.2804425)

Wei, J., Yoshinari, M., Takemoto, S., Hattori, M., Kawada, E., Liu, B. & Oda, Y. 2007 Adhesion of mouse fibroblasts on hexamethyldisiloxane surfaces with wide range of wettability. *J. Biomed. Mater. Res. B Appl. Biomater.* **81**, 66–75. (doi:10.1002/jbm.b.30638)

Yong, X. & Zhang, L. T. 2009 Nanoscale wetting on groove-patterned surfaces. *Langmuir* **25**, 5045–5053. (doi:10.1021/la804025h)

Yuehuei, H. An. & Richard, J. F. 1998 Concise review of mechanics of bacterial adhesion to biomaterial surfaces. *J. Biomed. Mater. Res. Appl. Biomater.* **43**, 338–348. (doi:10.1002/(SICI)1097-4636(199823)43:3%3C338::AID-JBM16%3E3.0.CO;2-B)

Zhang, Z., Zhou, H., Ren, L., Tong, X., Shan, H. & Li, X. 2008 Surface morphology of laser tracks used for forming the non-smooth biomimetic unit of 3Cr2W8V steel under different processing parameters. *Appl. Surf. Sci.* **254**, 2548–2555. (doi:10.1016/j.apsusc.2007.09.102)

Effects of SiO_2 substitution on wettability of laser deposited Ca-P biocoating on Ti-6Al-4V

Yuling Yang · Sameer R. Paital · Narendra B. Dahotre

Received: 10 February 2010 / Accepted: 20 May 2010
© Springer Science+Business Media, LLC 2010

Abstract Silicon (Si) substitution in the crystal structure of calcium phosphate (CaP) ceramics has proved to generate materials with improved bioactivity than their stoichiometric counterpart. In light of this, in the current work, 100 wt% hydroxyapatite (HA) precursor and 25 wt% SiO_2-HA precursors were used to prepare bioactive coatings on Ti-6Al-4V substrates by a laser cladding technique. The effects of SiO_2 on phase constituents, crystallite size, surface roughness, and surface energy of the CaP coatings were studied. Furthermore, on the basis of these results, the effects and roles of SiO_2 substitution in HA were systematically discussed. X-ray diffraction analysis of the coated samples indicated the presence of various phases such as $CaTiO_3$, Ca_2SiO_4, $Ca_3(PO_4)_2$, TiO_2 (Anatase), and TiO_2 (Rutile). The addition of SiO_2 in the HA precursor resulted in the refinement of grain size. Confocal laser microscopy characterization of the surface morphology demonstrated an improved surface roughness for samples with 25 wt% SiO_2-HA precursor compared to the samples with 100 wt% HA precursor processed at 125 cm/min laser speed. The addition of SiO_2 in the HA precursor resulted in the highest surface energy, increased hydrophilicity, and improved biomineralization as compared to the control (untreated Ti-6Al-4V) and the sample with 100 wt% HA as precursor. The microstructural evolution observed using a scanning electron microscopy indicated that the addition of SiO_2 in the HA precursor resulted in the presence of reduced cracking across the cross-section of the bioceramic coating.

Y. Yang
Department of Physics, Northeastern University, Shenyang 110004, China

Y. Yang · S. R. Paital · N. B. Dahotre (✉)
Department of Materials Science and Engineering, The University of Tennessee, Knoxville, TN 37996, USA
e-mail: ndahotre@utk.edu; Narendra.Dahotre@unt.edu

Present Address:
N. B. Dahotre
Department of Materials Science and Engineering, University of North Texas, Denton, TX 76203, USA

1 Introduction

A significant amount of work has been performed on synthetic biomaterials due to their high demands for replacing damaged and degraded organs and tissues [1]. Among these various potential biomaterials, load bearing implant materials to heal skeletal defects caused due to trauma, old age, and injury are on the continuous rise. As a potential scaffold biomaterial, these materials are expected to provide mechanical support for bone tissue growth, enhancement in cell proliferation, and a tissue-specific differentiation at the interface [2–4]. In light of this, several researchers have synthesized CaP based bioactive hydroxyapatite ($Ca_{10}(PO_4)_6(OH)_2$, HA) coatings on Ti-6Al-4V substrates and studied their in vitro bioactivity and in vitro biocompatibility [5, 6]. These HA based bioceramics mimic the naturally occurring bone mineral in terms of their chemical composition and crystallographic structure and hence, allow for direct bone bonding by attachment, proliferation, and differentiation of bone forming cells. However, some of the recent studies on HA coatings have limited their scope for implant applications, owing to the adverse reactions found in vitro and in vivo [7], low bonding strength between the HA and substrate, and poor mechanical properties of the coating. Hence, to overcome these limitations there has been a considerable interest in developing new bioactive ceramic coatings based on bioglass compositions such as Na_2O–CaO–SiO_2–P_2O_5 [8],

UNCORRECTED PROOF

wollastonite ($CaSiO_3$) [9], and dicalcium silicate (Ca_2SiO_4) [10].

In most of the above compositions, the presence of SiO_2 is found to be in common, since SiO_2 can easily form a Si-OH functional layer under in vivo and in vitro conditions and there by enhance the mineralization of an apatite like phase at the interface between the bioceramic coating and hard tissue. The role of Si as an essential element for higher biological organisms was discovered in the 1970s through the studies by Carlisle [11], Schwarz [12], and Seaborne [13]. It was reported that Si is present at a level of ~1 ppm in the serum, 2–10 ppm in the liver, kidney, lung, and muscle, 100 ppm in the bone and ligaments, and 200–600 ppm in cartilage and other connective tissues [14]. Hence, Si in particular has been found to be essential for normal bone and cartilage growth and development [15]. Another reason for SiO_2 being used as the basement of above systems is that it can act directly in the mineralization process, where aqueous Si, in the form of orthosilicic acid ($Si(OH)_4$), is able to induce the precipitation of HA from electrolyte solutions in the presence of proteins that normally inhibit its precipitation [16, 17]. Due to the above beneficial properties of SiO_2 in biomaterials, SiO_2 (or Si) substitution in the CaP bioceramics has been an area of active research. The synthesis and characterization of SiO_2 or Si fortified HA and α-tricalcium phosphates have been the focus of many research efforts [15, 18–25]. In all of these works, the synthesis method, the phase composition, the effect of Si on biological activity, and the role of Si on the grain growth, were extensively studied. It was concluded that the phase composition of the materials highly depend on the Ca/(P + Si) and Ca/P ratios of the system, the level of Si addition, and the method of introducing Si to CaP [15]. Furthermore, Si tends to inhibit the grain growth to generate materials with fine structures [19, 23, 24]. The work by Patel et al. compared the biological activity of Si-HA and HA granules and reported a 14.5% increase in bone in-growth in Si-HA versus HA controls [25].

Most of the above studies on the composite coatings (SiO_2-HA or Si-HA) focus on the synthesis methodologies, the biological activity, the influence of SiO_2 or (Si) addition on the grain growth, and the biological response to an implant. There are not many efforts towards understanding effects of SiO_2 (or Si) addition on the wettability and surface energy of these composite (SiO_2-HA or Si-HA) ceramic coatings except the work by Thian et al. [26]. In their work, the authors [26] used an electrospraying technique to synthesize nano HA, carbonate substituted nano HA and silicon substituted nano HA on glass substrates. The authors demonstrated that the modification of nanoapatite by silicon resulted in improved hydrophilicity and thereby enhanced osteoblast cell attachment, proliferation and protein expression as compared to the nano HA coating and carbonate substituted nano HA coating. Hence, it is very important to critically study and understand the role of SiO_2 or (Si) addition on the wetting behavior of these composite ceramic coatings. Also, as implant materials when placed inside a human body initially come in contact with the body fluid, it further controls the adsorption of proteins followed by attachment of cells to the implant surface. Hence, an understanding of the above can aid in designing an appropriate precursor (SiO_2 or Si-HA composite) to enhance its wettability and thereby tune its bioactivity and biocompatibility efficiently.

Therefore, in the present effort the effect of SiO_2 addition on the wettability and bioactivity of laser deposited CaP coating on Ti-6Al-4V substrate has been discussed. Here, a highly intense laser beam was used to melt the precursor (HA and SiO_2-HA) and the Ti-6Al-4V substrate to get a micro-textured multi-phase coating and a metallurgical bonding at the interface. The effects of SiO_2 on the phase constituents, the crystallite size, the surface roughness, and the surface energy of the micro-textured CaP coating are studied. Furthermore, on the basis of these results, the effects and roles of SiO_2 addition in HA are systematically discussed.

2 Materials and methods

2.1 Sample preparation and laser processing

Ti-6Al-4V substrate coupons of dimensions 100 mm × 50 mm × 3 mm were cut from the rolled sheets using an abrasive cutter. Before being coated with the precursor, all substrate coupons were polished using a 30 μm grit SiC emery paper and then rinsed with acetone to get a clean surface free from rust and oxides. Hydroxyapatite ($Ca_{10}(PO_4)_6(OH)_2$) powder and silica (SiO_2) powder obtained from Fischer Scientific were taken as the precursor materials. The HA and SiO_2 precursor powders had a spherical morphology with an unimodal distribution in the range of 10–30 μm. The pure HA precursor and the thoroughly blended HA-SiO_2 (the ratio of SiO_2 to HA is fixed as 1:3 in weight %) precursor were mixed in a water-based organic solvent (LISI W 15853) obtained from Warren Paint and Color Company (Nashville, TN, USA) and mechanically stirred for 25 min to get a viscous slurry. The slurry was then sprayed onto the polished and clean substrate coupons using an air pressurized spray gun. The sprayed coupons were dried in air to remove the moisture. The thickness of the precursor deposit was maintained at 80 μm for all samples. The precoated samples were finally scanned using a pulsed Nd:YAG laser equipped with a fiber optic beam delivery system to achieve a metallurgical bonding

UNCORRECTED PROOF

Table 1 The laser parameters used for the study

Pulse width (ms)	1.0
Average power (W)	80
Spot shape	Rectangular
Spot diameter (μm)	900
Laser scan speed (cm/min)	25; 75; 125
Line spacing (mm)	0.1

between the precursor and the substrate. The pulsed Nd:YAG laser operates in the infrared region with a wavelength of 1064 nm. The processing parameters used for the above process are listed in Table 1. It can be seen from the table that three different laser scan speeds, 25, 75, and 125 cm/min were employed for processing each precursor component.

2.2 Surface characterization

Phase evaluations in the samples were studied using a Philips Norelco X-ray Diffractometer (XRD) with Cu Kα radiation of wavelength 0.15418 nm. The XRD system was operated at 20 kV and 10 mA in a 2θ range of 20–100° using a step size of 0.02° and a count time of 1 s. As laser based processing is often associated with extremely rapid cooling rates (>10^3°C/s), the resultant microstructure was expected to produce extremely refined grain structure. Hence, the crystallite size of the coated samples was calculated using the Scherrer formula [27]:

$$t = \frac{0.9\lambda}{B \cdot \cos\theta_B} \quad (1)$$

Here, t is the crystallite size of a particular phase, B is the broadening of diffraction line measured at half its maximum intensity (radians) at Bragg angle θ_B, and λ is the wavelength of Cu Kα radiation (0.15418 nm). The peaks used for calculating crystallite size were chosen to avoid too much overlapping from different phases. In the above equation, the instrumental broadening is not taken into account as our interest was only to see the effect of laser scan speed on the relative crystallite size.

For micro-structural observation across the cross-section the laser processed samples were sectioned perpendicular to the laser track using a low speed saw. The sectioned samples were then polished with emery papers of different grits ranging from 200 to 1000 μm in succession, followed by disc polishing with colloidal silica of 0.3 and 0.05 μm average particle sizes to get a smoothly polished surface. The polished samples were then etched with 5 vol% HF, 3 vol% HNO_3, and 92 vol% H_2O for 10–20 s by immersion etching to reveal the microstructural features. The microstructure observations across the cross-section were carried out using a LEO 1525 scanning electron microscope (SEM) coupled with energy dispersive spectrometer (EDS). The surface roughness of Ti-6Al-4V control and laser processed samples were measured using a Leica Confocal laser microscope. The roughness values are recorded in the form of R_a (defined as the arithmetic average of all points of the profile also called the center line average height), and RMS (root-mean-square deviation). Five random scans were done across each sample to get an average and standard deviation within these roughness values.

2.3 Contact angle and surface energy

Contact angle measurements were conducted by a static sessile drop technique using a CAM-Plus^R contact angle goniometer (Cheminstruments, Inc. Fairfield, Ohio), equipped with a fiber optic light source and Video camera for imaging. A 3 μl liquid droplet with the diameter of 2 mm was suspended from the tip of the hypodermic syringe on the thoroughly cleaned sample and the advancing contact angle was taken as a measure of wettability. The liquid droplet placed on the sample was allowed to stabilize for 10 s before the reading was taken. The test was conducted at room temperature (26°C) and a minimum of ten contact angle readings were taken from random locations on each sample to minimize the errors in the measurement. Further, the contact angle measurement used in the present case was based on the patented (US patent 5268733) half angle technique which also eliminates the errors associated with the tangential alignment. For surface energy calculations by the contact angle measurement technique, an apolar liquid (dioiodomethane) and two polar liquids (distilled water and formamide) were used and the calculations were made according to the Van Oss approach [28] using the following equation:

$$\gamma_L(1+\cos\theta) = 2\left[\left(\gamma_S^{LW}\gamma_L^{LW}\right)^{1/2} + \left(\gamma_S^{+}\gamma_L^{-}\right) + \left(\gamma_S^{-}\gamma_L^{+}\right)\right] \quad (2)$$

Here, θ is the contact angle of liquid L subtended on solid S, γ^{LW} is the apolar component of the surface energy, γ^{+} is the Lewis acid component (electron acceptor), and γ^{-} is the Lewis base component (electron donor). The surface energy components of three standard liquids used in this study are listed in Table 2 [29, 30]. The relationships

Table 2 Surface energy components of the standard liquids used in this study (units mJ/m^2)

Liquid	γ_L^{LW}	γ_L^{+}	γ_L^{-}	γ_L^{AB}	γ_L
Water	21.8	25.5	25.5	51	72.8
Formamide	39	2.28	39.6	19	58
Dioiodomethane	51	0	0	0	51

UNCORRECTED PROOF

between surface energy γ_s and these components are described below [28]:

$$\gamma_S = \gamma_S^{LW} + \gamma_S^{AB} \quad (3)$$

$$\gamma_S^{AB} = 2\sqrt{\gamma_S^+ \gamma_S^-} \quad (4)$$

The surface energy components of different precursor coated samples were calculated using the above equations.

Finally, in order to correlate the surface energy calculations to the mineralization behavior (bioactivity) of the samples, contact angle between the coated samples and simulated body fluid (SBF) and in vitro bioactivity of the coated samples following immersion in SBF was studied. The SBF solution was prepared by dissolving the reagent grade chemicals in the following order: NaCl (8.026 g), $NaHCO_3$ (0.352 g), KCl (0.225 g), $K_2HPO_4 \cdot 3H_2O$ (0.230 g), $MgCl_2 \cdot 6H_2O$ (0.311 g), $CaCl_2$ (0.293 g) and Na_2SO_4 (0.072 g) into distilled water (700 ml). The fluid was then buffered to pH = 7.4 at 37°C with tri-hydroxymethylaminomethane (6.063 g) and hydrochloric acid (40 ml). Following SBF immersion, the surfaces of the samples were analyzed using SEM equipped with EDS to study the morphology and elemental composition of the HA precipitates. The EDS analysis was carried out with an electron beam energy of 20 keV.

3 Results and discussions

3.1 Phase evolution

Prior to wettability assays, surface characterization of both 100 wt% HA and 25 wt% SiO_2-HA precursor-coated samples as well as uncoated Ti-6Al-4V control was carried out for several aspects, including phase analysis, surface roughness, microstructure, and surface energy.

Figures 1 and 2 show the X-ray diffraction patterns corresponding to 100 wt% HA and 25 wt% SiO_2-HA precursor samples, respectively, processed with different laser scan speeds of 25, 75, and 125 cm/min. There is no major change in the types of phases with varying laser scan speed for the samples processed with 100 wt% HA as precursor material (Fig. 1). Apart from the retention of original precursor (HA phase), the various other phases evolved are $CaTiO_3$, $Ca_3(PO_4)_2$, TiO_2 (Anatase), TiO_2 (Rutile), Al_2O_3, and CaO. Although there is no change in phase constituents, the peak intensities varied with varying laser scan speed. Unlike the XRD results of 100 wt% HA sample (Fig. 1), the phase constituents of 25 wt% SiO_2-HA samples (Fig. 2) show dependence on the laser scan speed. For the samples processed with higher laser speed of 75 and 125 cm/min, although the peak intensities varied no major change in the types of phases evolved. The main

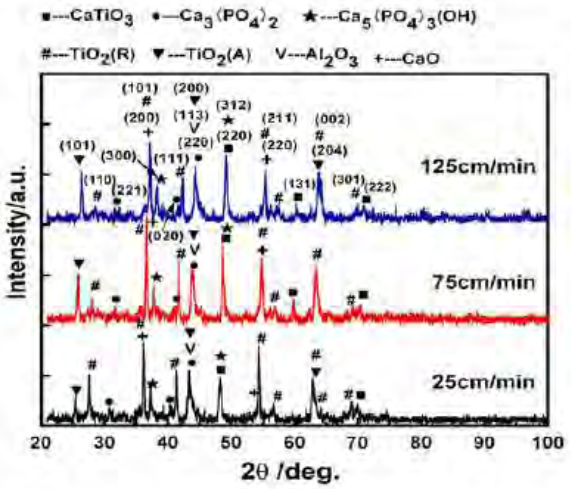


Fig. 1 XRD pattern of 100 wt% HA precursor after processed with different laser scan speed

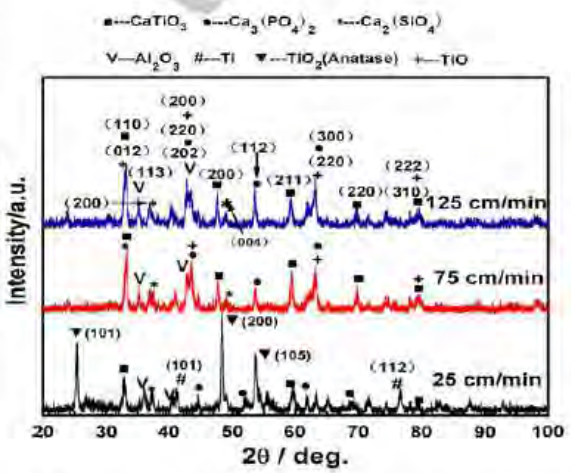


Fig. 2 XRD pattern of 25 wt% SiO_2-HA precursor after processed with different laser scan speed

phases are identified as $CaTiO_3$, $Ca_3(PO_4)_2$, Ca_2SiO_4, Al_2O_3, and TiO. On the contrary, for the samples processed with slower speed of 25 cm/min, the major phase presented in the coating is TiO_2 (Anatase), and the peak intensities corresponding to such phases as $CaTiO_3$, $Ca_3(PO_4)_2$, and Ca_2SiO_4 are relatively weak. Thus, it appeared that at higher range of laser scan speed (75–125 cm/min), the phase constituent is minimally affected by the speed for both 100 wt% HA and 25 wt% SiO_2-HA precursor samples. Where as at slower laser scan speed (<25 cm/min) the laser beam residence time on the sample surface being longer, the surface temperature rises to the level possibly leading to substantial amount of coating precursor material

evaporation followed by oxidation of the substrate material for formation of more amount of TiO_2. Also, as the laser processing is carried out in an ambient atmosphere under higher energy laser beam, a small portion of the substrate material (Ti-6Al-4V) always gets melted and oxidized to form Al_2O_3 for both the precursor material compositions.

The effect of addition of SiO_2 in HA precursor is further realized through the absence of HA and CaO in laser processed 25 wt% SiO_2-HA samples (Fig. 2) compared to laser processed 100 wt% HA samples (Fig. 1). This phenomenon can be explained on the basis of the following possible primary and intermediate reactions between the material systems employed in the present work.

$$Ca_{10}(PO_4)_6(OH)_2 = 3Ca_3(PO_4)_2 + CaO + H_2O\uparrow \quad (\Delta G = -1333.75\ \text{kJ/mol}) \tag{5}$$

$$Ti + O_2 = TiO_2\ (\text{Anatase or Rutile}) \quad (\Delta G = -864.09\ \text{kJ/mol}) \tag{6}$$

$$2Ti + O_2 = 2TiO\ (\text{inadequate reaction}) \quad (\Delta G = -492.52\ \text{kJ/mol}) \tag{7}$$

$$4Al + 3O_2 = 2Al_2O_3 \quad (\Delta G = -1586.57\ \text{kJ/mol}) \tag{8}$$

$$TiO_2 + CaO = CaTiO_3 \quad (\Delta G = -80.90\ \text{kJ/mol}) \tag{9}$$

$$2CaO + SiO_2 = Ca_2SiO_4 \quad (\Delta G = -122.17\ \text{kJ/mol}) \tag{10}$$

From the above equations, it is clear that the retention of HA precursor phase depends on the Eqs. 5, 6, 9, and 10. The more HA takes part in Eq. 5, the less it will be retained in the coating. From Eqs. 9 and 10 it is clear that for 100 wt% HA samples, only TiO_2 react with CaO, where as in 25 wt% SiO_2-HA samples SiO_2 addition will consume more CaO resolved from HA. This is likely to accelerate the resolving process of HA, and the reaction process between CaO and SiO_2, leading to less or no retention of HA or SiO_2 in the coating. The above intermediate reactions (Eqs. 9, 10) during laser processing of 25 wt% SiO_2-HA precursor, therefore, results in generation of Ca_2SiO_4 in the coating (Fig. 2).

The average crystallite size of 100 wt% HA and 25 wt% SiO_2-HA samples was calculated using the Scherrer formula as stated in Eq. 1. The results are presented in Fig. 3. It is obvious that the crystallite size in 25 wt% SiO_2-HA samples is significantly smaller ($\sim$28%) than that of 100 wt% HA samples, which indicates the effect of SiO_2 addition on grain refinement. SiO_2 has long been added to $BaTiO_3$ to reduce the grain size [31]. In the work by M.A.Zubair et al. [32], it was reported that SiO_2 addition can develop the grain boundaries and reduce the grain size. Kaishu Guan et al. [33] have studied the enhanced effect and mechanism of SiO_2 addition in super-hydrophilic property of TiO_2 film. The authors reported that the grain

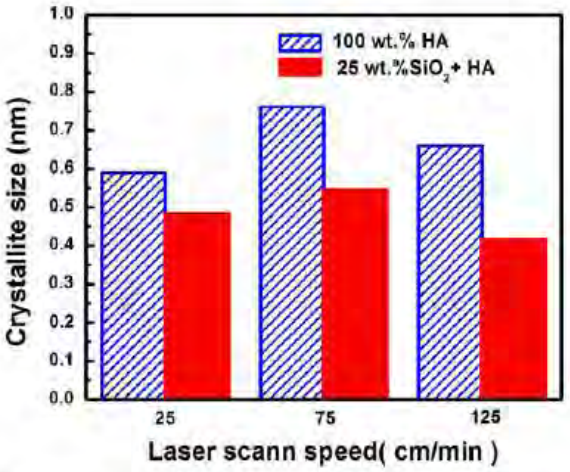


Fig. 3 Crystallite size of different samples processed with different laser scan speed

growth of TiO_2 crystal is suppressed by the addition of SiO_2 which in turn led the particle size of TiO_2 to become smaller and thereby its improved hydrophilic behavior. In the work by Takeli et al. [34, 35], it was reported that grain-growth rate could be controlled by the addition of SiO_2 and the grain size decreased with increasing SiO_2. The grain growth kinetics of both 100 wt% HA samples and 25 wt% SiO_2-HA samples can be semi quantitatively described by the grain growth model as described below [36]:

$$G^n - G_0^n = kt \tag{11}$$

Here G is the average grain size, G_0 is the initial grain size, k is a rate constant, n is a constant for a given grain-growth mechanism, and t is the crystallization time. From Eq. 11 it is clear that for a given initial grain of size G_0 the average grain size G depends on the crystallization time t. A lower crystallization time t corresponds to a smaller average grain size G. It was reported that the addition of SiO_2 can accelerate the material transfer and results in a fast microstructural evolution [37], and also control microstructure by suppressing abnormal grain growth [38]. Hence, it is clear from the above results that SiO_2 addition can reduce the crystallization time, which in turn attributes to a smaller crystallite size. In the present work, laser-based processing is inherently associated with the rapid cooling rates [39], thus further expected to contribute substantially reduced crystallization time and crystallite size.

3.2 Surface energy and surface roughness

The variation of surface energy components (γ^+, γ^-, γ^{LW}, and γ_s) as a function of laser scan speed for the 100 wt% HA and 25 wt% SiO_2-HA samples are illustrated in Fig. 4.

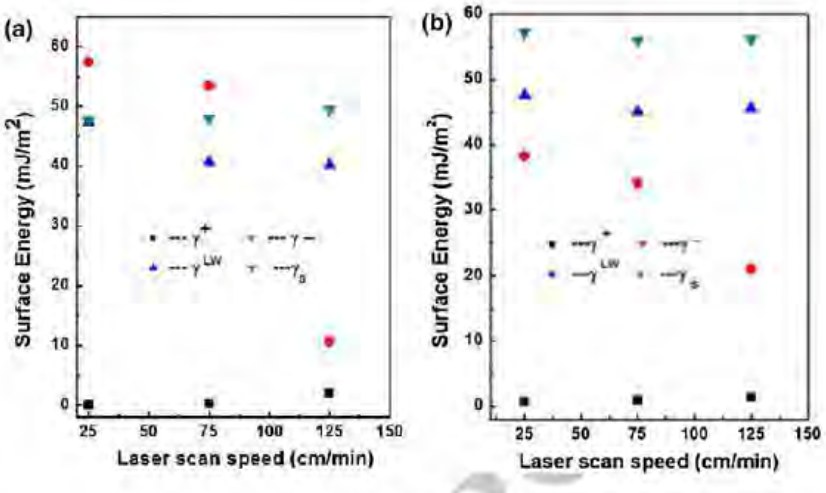


Fig. 4 Surface energy components for **a** 100 wt% HA and **b** 25 wt% SiO_2-HA coatings

For 100 wt% HA samples, the dispersive component (γ^{LW}) decreases with increasing laser scan speed and remains in the range of 40–47 mJ m^{-2}. The basic polar component (γ^-) also follows a decreasing trend with increasing laser scan speed from 25 to 125 cm/min. The acidic polar component (γ^+) has values less than 2.0 mJ m^{-2} and follows a slightly increasing trend with increasing laser scan speed. The surface free energy of the 100 wt% HA samples is around 48 mJ m^{-2} (Table 3). For 25 wt% SiO_2-HA samples, the dispersive component floats between 45 and 47 mJ m^{-2}. The basic polar component follows the same trend as with the 100 wt% HA samples. Compared to 100 wt% HA samples, 25 wt% SiO_2-HA samples present lower acidic polar component (its acidic polar component is less than 1.4 mJ m^{-2}) and higher surface free energy (around 56 mJ m^{-2}). It can be seen from Table 3 that for both 25 wt% SiO_2-HA and 100 wt% HA precursor, the surface free energy varied slightly at different laser scan speeds. This can be attributed to the minor variation in phase constituents with the varying laser scan speed. As described earlier from the XRD studies (Fig. 2), the addition of SiO_2 in the precursor leads to the formation of dicalcium silicate (Ca_2SiO_4) in the matrix of various other phases. The formation of such a wetting silicate based phase at the grain boundaries owing to the addition of SiO_2 has already been reported [32]. This further might have contributed to the increase in surface free energy for 25 wt% SiO_2-HA samples as compared to 100 wt% HA samples (Table 3). Another possible reason for the variation in surface energy for these samples may also be due to the grain size. As described above (Fig. 3), the average grain size of 25 wt% SiO_2-HA samples is smaller than that of the 100 wt% HA samples. Therefore, more grain boundary grooves were formed with SiO_2 addition leading to formation of more pinning of tripple lines. These pinned tripple lines act as open capillaries to reinforce wetting [40]. The work by Ishida [41] also stated that grain size strongly influences the grain boundary segregation. In the work by Tekeli et al. [34], it was also stated that SiO_2 addition results in a lower grain boundary cohesive strength and a higher grain boundary mobility and energy. Hence, 25 wt% SiO_2-HA possessed a higher surface energy value (55.94–57.21 mJ/m^2) compared to 100 wt% HA samples (47.71–49.47 mJ/m^2) and the Ti-6Al-4V control (34.19 mJ/m^2). Also, as described earlier from the XRD results (Figs. 1, 2), it can be realized that following laser processing the coating is not phase pure and is composed of various phases. Hence, each of these phases is expected to contribute to the wetting behavior and thereby its surface energy. However, in the present work following laser processing of both the precursor materials, most of the phases such as $CaTiO_3$, $Ca_3(PO_4)_2$, and TiO_2 except Ca_2SiO_4 are found common. Hence, the improved wetting behavior for the 25 wt% SiO_2-HA precursor as compared to 100 wt% HA can only be attributed to the presence of Ca_2SiO_4 following laser processing.

The surface microstructure and the cross-sectional microstructure of 100 wt% HA and 25 wt% SiO_2-HA samples processed at laser scan speed of 125 cm/min are presented in Fig. 5. The surface roughness values, R_a, and RMS are listed in Table 3. It can be seen that the surface roughness values of both 100 wt% HA samples and 25 wt% SiO_2-HA samples are larger than that of the Ti-6Al-4V control. In addition, from the SEM cross-sectional views (Fig. 5c, d), less number of cracks were observed in 25 wt% SiO_2-HA sample compared to 100 wt% HA sample. It indicates that SiO_2 addition cannot only refine the grain size, but also can suppress the cracks formation. This is in compliance with the work by Izquierdo-Barba [42], where the authors reported that more amount of Si in the coating

Table 3 Surface roughness, contact angle with SBF, and surface energy of the samples

Precursor	Laser speed (cm/min)	R_a (μm)	RMS (μm)	Contact angle in different fluid				Surface energy (mJ/m^2)
				Distilled water	Formamide	Dioiodomethane	Simulate body fluid (SBF)	
25 wt% SiO_2-HA	125	2.0 ± 1.1	12.4 ± 4.0	48.5 ± 0.6	18.5 ± 0.6	26.9 ± 0.8	21.2 ± 1.4	56.20 ± 0.97
								
	75	1.8 ± 0.8	12.1 ± 3.2	36.6 ± 0.4	17.2 ± 0.8	28.3 ± 1.0	26.4 ± 1.3	55.94 ± 0.87
								
	25	3.7 ± 1.8	18.0 ± 3.5	35.0 ± 0.7	14.6 ± 0.9	21.2 ± 0.5	19.2 ± 1.8	57.21 ± 0.74
								
100 wt% HA	125	1.4 ± 0.2	11.6 ± 1.0	62.4 ± 0.5	32.4 ± 0.7	39.2 ± 1.3	40.8 ± 1.0	49.47 ± 0.18
								
	75	4.1 ± 0.7	16.8 ± 1.2	26.8 ± 1.8	30.6 ± 1.2	38.2 ± 0.6	32.8 ± 1.9	48.01 ± 0.92
								
	25	3.3 ± 1.9	13.6 ± 1.0	20.6 ± 0.9	28.3 ± 0.5	22.3 ± 0.8	31.0 ± 1.8	47.71 ± 0.21
								
Ti-6Al-4V control		0.3 ± 0.07	9.47 ± 0.2	82.6 ± 0.1	57.4 ± 0.1	53 + 0.04	55.7 ± ±1.6	34.19 ± 0.05
								

UNCORRECTED PROOF

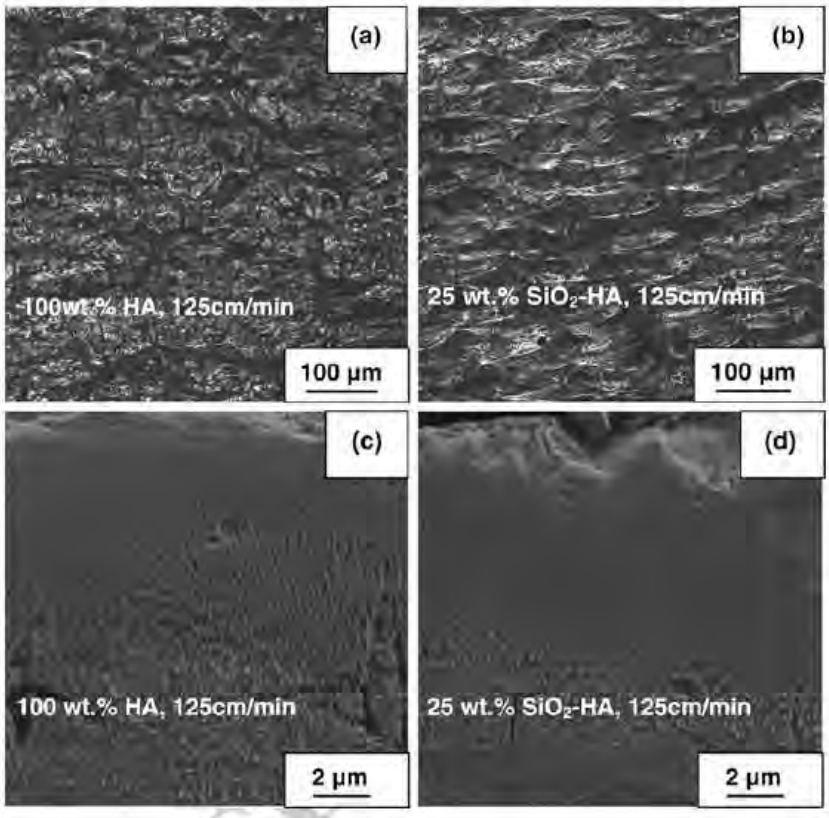


Fig. 5 Surface texture images and SEM micrographs of 100 wt% HA samples and 25 wt% SiO_2-HA samples processed with laser scan speed of 125 cm/min

can reduce the porosity of the surface leading to reduced presence of cracks across the cross-section.

3.3 Wettability and in vitro bioactivity

When a biomaterial is implanted into a biological system, among the plethora of events that takes place, the first and the foremost one is the wetting of the implant material by the physiological fluids. This further determines the degree and confirmation of specific proteins which in turn influence recruitment and activation of cells and stimulation of new tissue development [43, 44]. Hence, besides analyzing the phase constituents, surface roughness, and surface free energies, understanding the wettability of the coatings with SBF were also the important aspects of this work. Further, the contact angle measurements obtained from SBF liquid can also provide an understanding of the effect of SiO_2 addition on the wetting behavior. Table 3 represents the contact angle measurements and corresponding light optical images of the liquid droplet shadow on 100 wt% HA samples, 25 wt% SiO_2-HA samples, and the control (untreated Ti-6Al-4V). The results (Table 3) demonstrated improved wettability for the laser processed samples (100 wt% HA and 25 wt% SiO_2-HA samples) as compared to the control (untreated Ti-6Al-4V). Furthermore, compared to 100 wt% HA samples, 25 wt% SiO_2-HA samples indicated a more hydrophilic behavior (better improved wettability). As discussed earlier, the addition of SiO_2 not only influenced the phase constituents and the surface roughness, but also contributed to increase in the surface energy. This increase in surface free energy of 25 wt% SiO_2-HA samples was responsible for improved wettability of the coatings in SBF.

The wettability of the coatings was finally correlated to its mineralization or in vitro bioactivity by immersing the samples in SBF and analyzing for the precipitation of an apatite like phase. The mineralized layer or the precipitate on the 100 wt% HA sample and 25 wt% SiO_2-HA sample after 7 day immersion in SBF is shown in Fig. 6. The presence of a cuboidal like apatite crystallites can be clearly seen on the surfaces of 100 wt% HA and 25 wt% SiO_2-HA samples (Fig. 6a, b, respectively). The EDS spectra from a selected region indicates the presence of various elemental species such as Ca, P, Na, Cl, Al, O, Ti and V in the precipitated layer. In the current work,

UNCORRECTED

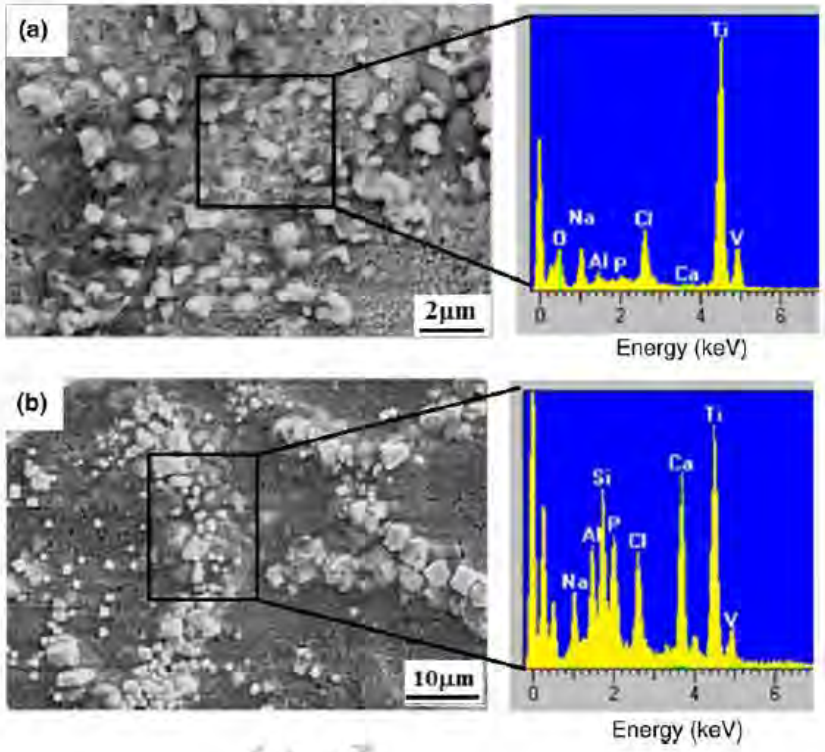


Fig. 6 SEM morphological analysis and corresponding EDS results on **a** 100 wt% HA sample and **b** 25 wt% SiO_2-HA sample after 7 days immersion in SBF

as the EDS analysis are carried out using an electron beam energy of 20 keV, a significant amount of material underneath the coating is sputtered resulting in detection of the sub-surface elemental species such as Ti and V in the spectrum. The EDS spectra from the mineralized surface of 100 wt% HA demonstrated for a small amount of Ca and P with a Ca/P atomic ratio of 0.62. In contrast, the selected region EDS spectra of the mineralized layer on 25 wt% SiO_2-HA demonstrated strong presence of Ca and P with a Ca/P atomic ratio of 1.68. As, the Ca/P atomic ratio of the mineralized layer on 25 wt% SiO_2-HA is close to that of the Ca/P atomic ratio of stoichiometric HA (1.67), it was therefore confirmed that the cuboid like precipitates were an apatite like phase and hence the sample is more bioactive as compared to the 100 wt% HA sample. Thus, the effects of SiO_2 addition on the phase constituents, grain size, and surface free energy can be systematically correlated to their consequential effects on wettability and in vitro bioactivity of HA coated Ti-6Al-4V alloy samples. Further analysis for mineralization kinetics and in vitro biocompatibility of the laser processed samples are being studied by exposing the samples to SBF for different time periods and culturing of mouse MC3T3-E1 pre-osteoblast cells, respectively. The results pertaining to the above efforts are being simultaneously prepared in a separate paper for publication in a referred journal.

4 Conclusions

The process of laser direct melting of Ca-P and SiO_2/Ca-P precursors on Ti-6Al-4V substrate resulted in the formation of various phases, such as $CaTiO_3$, $Ca_3(PO_4)_2$, TiO_2 (Rutile and Anatase), Al_2O_3, and Ca_2SiO_4 within the coatings. With SiO_2 addition in the precursor, a new phase (Ca_2SiO_4) was formed. No significant variation of the phase type with the laser speed variation was observed. Addition of SiO_2 in the precursor also produced more grain boundary grooves, resulting in a rough surface (higher RMS value) compared to the titanium control. Furthermore, the presence of SiO_2 in the precursor led to formation of the smaller average crystallite size and reduced cracking in the coating. The samples coated with SiO_2-HA precursor demonstrated a higher surface free energy and hence better wettability compared to the samples coated with pure HA precursor and the Ti-6Al-4V control. Additionally, the improved wettability and in vitro bioactivity of the samples with SiO_2 addition is also clearly due to the formation of Ca_2SiO_4 at the grain boundaries, the finer grain size and the higher surface roughness.

Acknowledgments A support to Yuling Yang during this work at the University of Tennessee by National Science Foundation of China for Young Scholars (Grant # 50801012) is highly acknowledged. Yuling Yang also thanks China Scholarship Council (CSC) and Northeastern University (NEU) for providing a financial support as visiting scholar at the University of Tennessee.

References

1. Driessens FCM, Verbeeck RMH. Biomaterials. Boca Raton: CRC Press; 1990. p. 5.
2. Foppiano S, Marshall SJ, Marshall GW, Saiz E, Tomsia AP. The influence of novel bioactive glasses on in vitro osteoblast behavior. J Biomed Mater Res. 2004;71:242–9.
3. Bosetti M, Cannas M. The effect of bioactive glasses on bone marrow stromal cells differentiation. Biomaterials. 2005;26: 3873–9.
4. Hattar S, Asselin A, Greenspan D, Oboeuf M, Berdal A, Sautier JM. Potential of biomimetic surfaces to promote in vitro osteoblast-like cell differentiation. Biomaterials. 2005;26:839–48.
5. Lopez-Heredia MA, Legeay G, Gaillard C, Layrolle P. Radio frequency plasma treatments on titanium for enhancement of bioactivity. Acta Biomater. 2008;4:1953–62.
6. Pecheva Emilia V, Pramatarova Liliana D, Maitz Manfrfed F, Pham Mihn T, Kondyurin Aleye V. Kinetics of hydroxyapatite deposition on solid substrates modified by sequential implantation of Ca and P ions: Part I. FTIR and Raman spectroscopy study. Appl Surf Sci. 2004;235:176–81.
7. Weng J, Liu Q, Wolke JGC, Zhang XD, de Groot K. Formation and characteristics of the apatite layer on plama-sprayed hydroxyapatite coatings in simulated body fluid. Biomaterials. 1997;18:1027–35.
8. Bang HG, Kim SJ, Park SY. Biocompatibility and the physical properties of bio-glass ceramics in the Na_2O-CaO-SiO_2-P_2O_5 system with CaF_2 and MgF_2 additives. J Ceram Process Res. 2008;9:588–90.
9. Hristov JH, Bogdanov BI, Chomakov IG, Markov IG, Markovska IG. Drawing standard curve for quantitative determination of the crystalline phase in wollastonite glass ceramics. J Balkan Tribolog Assoc. 2009;15:347–54.
10. Choi SW, Hong SH, Kim YJ. Characterization of Ca_2SiO_4: Eu^{2+} phosphors synthesized by polymeric precursor process. J Am Ceram Soc. 2009;92:2025–8.
11. Carlise E. Si: an essential element for the chick. Science. 1972;178:619–21.
12. Schwarz K, Milne D. Growth promoting effects of Si in rats. Nature. 1972;239:333–4.
13. Seaborn C, Nielson F. Si depravation decreases collagen formation in wounds, bone and ornithine transaminase enzyme activity in liver. Biol Trace Elem Res. 2002;89:251–61.
14. Schwarz K. A bound form of Si in glycosaminoglycans and polyuronides. Proc Nat Acad Sci USA. 1973;70:1608–12.
15. Pietak AM, Reid JW, Stott MJ, Sayer M. Silicon substitution in the calcium phosphate bioceramics. Biomaterials. 2007;28:4023–32.
16. Tanizawa Y, Suzuki T. Effects of silicate ions on the formation and transformation of calcium phosphates in neutral aqueous solutions. J Chem Soc Faraday Trans. 1995;91:3499–503.
17. Damen J, Ten Cate J. Silica-induced precipitation of calcium phosphate in the presence of inhibitors of hydroxyapatite formation. J Dent Res. 1992;71:453–7.
18. Sayer M, Stratilatov A, Reid J, Calderin L, Stott M, Yin X, et al. Structure and composition of silicon stabilized tricalcium phosphate. Biomaterials. 2002;24:369–82.
19. Gibson I, Best S, Bonfield W. Effect of silicon substitution on the sintering and microstructure of hydroxyapatite. J Am Ceram Soc. 2002;85:2771–7.
20. Tang X, Xiao X, Liu R. Structural characterization of silicon substituted hydroxyapatite synthesized by hydrothermal method. Mater Lett. 2005;59:3841–6.
21. Reid J, Tuck L, Sayer M, Fargo K, Hendry J. Synthesis and characterization of single-phase silicon-substituted alpha-tricalcium phosphate. Biomaterials. 2006;27:2915–6.
22. Cheng XM, Nie BM, Kumar S. Preparation and bioactivity of SiO_2 functional films on titanium by PACVD. Trans Nonferrous Met Soc China. 2008;18:627–30.
23. Acros D, Rodriguez-Carvajal J, Vallet-Regi M. Silicon incorporation in hydroxyapatite obtained by controlled crystallization. Chem Mater. 2004;16:2300–8.
24. Pietak A, Sayer M. Crystallization kinetics of Si-TCP bioceramic. J Mater Sci. 2004;39:2443–9.
25. Patel N, Best S, Bonfield W, Gibson I, Hing K, Damien E, et al. A comparative study on the in vivo behavior of hydroxyapatite and silicon substituted hydroxyapatite granules. J Mater Sci Mater Med. 2002;13:1199–206.
26. Thian ES, Ahmad Z, Huang J, Edirisinghe MJ, Jayasinghe SN, Ireland DC, Brooks RA, Rushton N, Bonfield W, Best SM. The role of surface wettability and surface charge of electrosprayed nanoapatites on the behavior of osteoblasts. Acta Biomater. 2010;6:750–5.
27. Cullity BD. Elements of X-ray diffraction. 2nd ed. Reading: Addison-Wesley Publishing Company, Inc; 1978. p. 284.
28. Van Oss CJ, Good RJ, Chaudhury MK. Additive and non additive surface tension components and the interpretation of contact angles. Langmuir. 1988;4:884–91.
29. Randeniya LK, Bendavid A, Martin PJ, Amin MS, Preston EW, Ismail FSM, Coe S. Incorporation of Si and SiO_x into diamond-like carbon films: impact on surface properties and osteoblast adhesion. Acta Biomater. 2009;5:1791–7.
30. Van Oss CJ, Giese RF Jr, Good RJ. Reevaluation of the surface tension components and parameters of polyacetylene from contact angle of liquids. Langmuir. 1990;6:1711–3.
31. Roseman RD, Mukherjee N. PTCR effect in $BaTiO_3$: structural aspects and grain boundary potentials. J Electroceram. 2003;10: 117–35.
32. Zubair MA, Leach C. The effect of SiO_2 addition on the development of low-$\sum$ grain boundaries in PTC thermistors. J Eur Ceram Soc (in press, available on line).
33. Guan K, Lu B, Yin Y. Enhanced effect and mechanism of SiO_2 addition in super-hydrophilic property of TiO_2 films. Surf Coat Technol. 2003;173:219–23.
34. Tekeli S, Erdogan M, Aktas B. Structural evolution in 8 mol% Y_2O_3-stabilized cubic zirconia (8YSCZ) with SiO_2 addition. Mater Sci Eng A. 2004;386:1–9.
35. Tekeli S, Boyacioğlu T, Gűral A. The effect of silica doping on the microstructure and mechanical properties of c-ZrO_2/SiO_2 composites. Ceram Int. 2008;34:1959–64.
36. Brook RJ. Treatise on materials science and technology. New York: Academic Press; 1976.
37. Yoo Y-S, Kim H, Kim D-Y. Effect of SiO_2 and TiO_2 addition on the exaggerated grain growth of $BaTiO_3$. J Eur Ceram Soc. 1997;17:805–11.
38. Hussaina S, Anis-ur-Rehmanb M, Maqsooda A, Awan MS. The effect of SiO_2 addition on structural, magnetic and electrical properties of strontium hexa-ferrites. J Cryst Growth. 2006;297: 403–10.
39. Paital SR, Dahotre NB. A thermal model for laser interaction with thick dielectric film on metallic substrate: application to Ca-P layer on Ti alloy. J Alloys Compd. 2009;487:499–503.

UNCORRECTED PROOF

40. Eustathopoulos N, Nicholas MG, Drevet B. Wettability at high temperatures. 2nd ed. New York: Pergamon; 1999. p. 108.
41. Ishida K. Effect of grain size on grain boundary segregation. J Alloys Compd. 1996;235:244–9.
42. Izquierdo-Barba I, Conde F, Olmo N, Lizarbe MA. Vitreous SiO_2-CaO coatings on Ti6Al4V alloys: reactivity in simulated body fluid versus osteoblast cell culture. Acta Biomater. 2006;2: 445–55.
43. Ducheyne P, Qui Q. Bioactive ceramics: the effect of surface reactivity on bone formation and function. Biomaterials. 1999;20: 2287–303.
44. Hench L. Surface reaction kinetics and adsorption of biological moieties: a mechanistic approach to tissue attachment. In: Davies JE, editor. The bone biomaterial interface. Toronto: University of Toronto Press; 1991. p. 33–42.

UNCORRECTED PROOF

Journal of Alloys and Compounds 487 (2009) 499–503

Contents lists available at ScienceDirect

Journal of Alloys and Compounds

journal homepage: www.elsevier.com/locate/jallcom

A thermal model for laser interaction with thick dielectric film on metallic substrate: Application to Ca–P layer on Ti alloy

Sameer R. Paital, Narendra B. Dahotre*

Laboratory for Laser Materials Synthesis and Fabrication, Department of Materials Science and Engineering, The University of Tennessee, Knoxville, TN 37996, USA

ARTICLE INFO

Article history:
Received 11 July 2009
Received in revised form 21 July 2009
Accepted 25 July 2009
Available online 5 August 2009

Keywords:
Laser
Thermal model
Calcium phosphate tribasic
Bioceramics
Phase transformations

ABSTRACT

Ca–P coatings on Ti–6Al–4V substrates were synthesized using a direct pulsed Nd:YAG laser writing technique. The phase and morphological evolutions within the coatings as a function of laser processing parameters were evaluated using X-ray diffraction and scanning electron microscopy techniques. A three dimensional modeling based on COMSOL's™ Multiphysics was adopted to understand the temperature evolution and corresponding cooling rate as a function of laser processing parameters. The temperature evolutions and cooling rate estimated from the model, satisfactorily explained the variation in phases and melt depth with varying pulse frequency of the laser beam.

© 2009 Elsevier B.V. All rights reserved.

1. Introduction

Titanium-based alloys owing to their excellent mechanical properties, corrosion resistance and biocompatibility are most commonly used for load bearing implant applications, such as hip joint prosthesis, knee joint prosthesis and dental implants. However, these bioinert materials when placed inside a human body elicit minimal interaction with the surrounding tissues and thereby induce the formation of a fibrous capsule at the interface [1,2]. Hence, to improve the reaction between the implant and surrounding tissue, bioresorbable materials such as tricalcium phosphate (α-TCP, $Ca_3(PO_4)_2$) [2] and bioactive materials such as hydroxyapatite [$Ca_{10}(OH)_2(PO_4)_6$] (HA) [3], calcium phosphate tribasic [$Ca_5(OH)(PO_4)_3$] [4], and bioglass [5] are most commonly used as coatings on Ti-based alloys. These bioceramics react with the surrounding tissue and thereby provide a strong chemical bonding between the implant and the remodeling bone. Further, coatings of these bioceramics on Ti-based alloys provide the appropriate surface chemistry for tissue compatibility without altering the bulk mechanical properties of the material.

The several coating techniques that can be used to achieve Ca–P coatings on Ti-based alloys are plasma spray deposition [6], pulsed laser physical vapor deposition [7], ion beam assisted deposition [8], magnetron sputtering [9], sol–gel-based coatings [10] and electrodeposition [11]. Most of the above coatings however suffer from certain drawbacks such as poor adherence of the coating to the substrate material, lack of uniformity in the coating and absence of textures or topographical cues [12,13]. Hence, in the present work, a laser-based direct writing technique to synthesize Ca–P coatings on titanium alloys is introduced. In this approach, by proper selection of laser processing parameters both the precursor (calcium phosphate tribasic) and a part of the substrate material (Ti–6Al–4V) can undergo rapid melting and thereby a chemical and microstructural bonding can be achieved at the interface. Further, by controlling the pulse frequency, the input laser energy and thereby the phase and morphological evolutions within the coatings can also be modulated. Finally, a three dimensional thermal model based on COMSOL's™ Multiphysics is adopted to understand the phase transformations with varying laser processing parameters.

2. Materials and methods

Ti–6Al–4V substrate coupons (100 mm × 50 mm × 3 mm) cut from the rolled sheets were polished using 30 μm grit SiC emery paper followed by rinsing with acetone. Calcium phosphate tribasic ($Ca_5(OH)(PO_4)_3$) powder (Fisher Scientific, USA) was used as the precursor material. This precursor powder had a spherical morphology with a unimodal distribution in the range of 10–30 μm. The precursor was mixed in a water-based organic solvent LISI W 15853 (Warren Paint and Color Company, Nashville, TN, USA) and sprayed onto the substrate coupons using an air pressurized spray gun. This green body was air dried to remove the moisture and a uniform thickness of 40 μm was maintained for all precoating precursor deposits. The samples were then scanned using a 400 W average power, JK701 model pulsed Nd:YAG laser to obtain the coating. The additional details related to the laser processing technique are available in the previously published article [4]. The processing parameters used for the above process are listed in Table 1.

Phase evolutions within the coatings were studied using a Philips Norelco X-ray diffractometer (XRD) with Cu-Kα radiation of wavelength 1.5418 Å. The system was

* Corresponding author. Tel.: +1 865 974 3609; fax: +1 865 974 4115.
E-mail address: ndahotre@utk.edu (N.B. Dahotre).

0925-8388/$ – see front matter © 2009 Elsevier B.V. All rights reserved.
doi:10.1016/j.jallcom.2009.07.162

Table 1
Laser parameters used for the experiment.

Pulse duration	0.5 ms
Energy of a single pulse (e)	4 J
Pulse frequency	10, 20, 30, 40 Hz
Input laser energy (E)	4, 7.92, 10.48, 13.8 J
Laser scan speed	36 cm/min
Focus position	0.8 mm above the surface of the sample
Laser spot diameter on the surface	900 μm
Pulse shape	Rectangular

operated at 20 kV and 10 mA in a 2θ range of 20–100° using a step size of 0.02° and count time of 1 s. The observations for microstructure evolution and depth of heat-affected zone due to laser direct writing were conducted across the cross-section of samples. The samples were chosen from the center of the coated plate and were sectioned using a low speed diamond cutter (Buehler) so as to have at least three overlapping laser tracks. The samples in cross-section were then prepared by polishing with emery papers of grit sizes ranging from 200 to 1000 μm in succession followed by disc polishing with colloidal silica of 0.3 and 0.05 μm to get a mirror finished surface. The polished samples were then cleaned with acetone and etched with 5 vol% HF, 3 vol% HNO_3, and 92 vol% H_2O for 10–20 s by immersion etching to reveal the microstructural features. A Jeol scanning electron microscope (SEM) coupled with EDS (energy dispersive spectrometer) was used to characterize for the microstructural and elemental analysis at different locations of the coatings.

A three dimensional thermal model based on COMSOL's™ Multiphysics was adopted in the present work to predict thermal parameters (temperature evolution and cooling rate) which in turn influence the phase evolutions within the coatings. The composite nature of the material system (coating + substrate), temperature dependent thermophysical properties, conduction, convection and radiation dependent heat transfer during laser processing were taken into account. Apart from this, various other assumptions and dimensions of the geometry considered in the present work are based on the earlier work by the group [14]. The residence time (time required to travel the diameter of the beam), the on and off period during each residence time and the peak power (input power density in W/m²) during the laser on periods were employed for thermal analysis. The residence time (t) of the laser beam for a pulsed Nd:YAG laser can be calculated as per the following equation:

$$t = \frac{D}{V} \tag{1}$$

Here, D is the laser beam diameter on the surface and V is the laser scan speed. The total on time (t_{on}) and off time (t_{off}) of the laser beam within the residence time is therefore given as:

$$t_{on} = \frac{f \times w \times D}{V} \tag{2}$$

$$t_{off} = t - t_{on} \tag{3}$$

Here, f is the laser frequency and w is the pulse duration of laser beam. The input power density or the intensity (I) of the laser beam used in the model was calculated as per the following equation:

$$I = \frac{D \times E \times f}{V \times \Phi \times w} \tag{4}$$

Here, E is the input energy and Φ the cross-sectional area of the laser beam. As, with increasing pulse frequency, the number of pulses within the residence time of the laser beam increases, the input energy E of the laser beam contributed by these pulses is given by the following equation [15]:

$$E = \left[\sum_{n}^{N_d} \frac{D-(n-1)b}{D}\right] e \tag{5}$$

Here, N_d is the total number of pulses that can be obtained dividing the total on time of the laser beam (Table 2) by the pulse duration of laser beam, n corresponds to each of these pulses and is taken as $n = 1, 2, 3, \ldots, N_d$ and e is the energy from a single pulse. The distance traveled by the laser between two successive pulses is b and calculated as follows:

$$b = (1 - X) \times D \tag{6}$$

Here, X is the spot overlap of the laser beam and can be calculated from the following equation:

$$X = 1 - \frac{V}{fD} \tag{7}$$

The Fourier's second law of heat transfer (Eq. (8)) in COMSOL's™ heat transfer mode was used to model the energy transfer from the laser beam to the precursor during coating:

$$\frac{\partial T(x,y,z,t)}{\partial t} = \alpha\left[\frac{\partial^2 T(x,t)}{\partial x^2} + \frac{\partial^2 T(y,t)}{\partial y^2} + \frac{\partial^2 T(z,t)}{\partial z^2}\right] \tag{8}$$

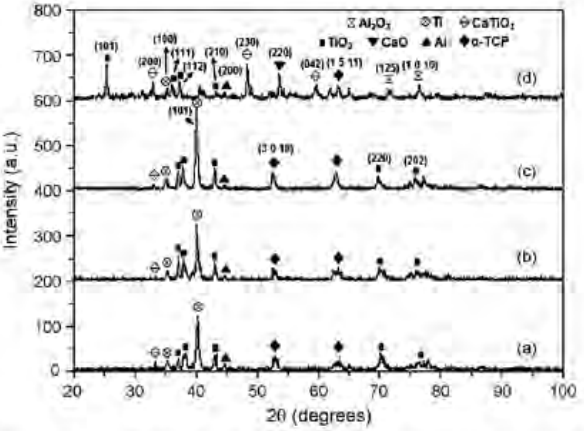


Fig. 1. XRD patterns of the samples processed at varying laser pulse frequency of (a) 10 Hz, (b) 20 Hz, (c) 30 Hz and (d) 40 Hz.

Here, α is the thermal diffusivity and is equal to $K/\rho C_p$, K is the thermal conductivity, C_p is the specific heat, and ρ is the density (precursor = 3156 kg/m³ [16] and substrate = 4420 kg/m³ [17]) of the material. At time $t = 0$ the initial temperature $T = T_0 = 298$ K was used in the model. For improved accuracy of temperature and cooling rate evolution, variations in specific heat and thermal conductivity of the material as a function of temperature were incorporated into the model [16,18].

The equation used to model the balance between the absorbed laser energy and radiation loss at the surface is given as:

$$-K\left[\frac{\partial T(x,t)}{\partial x} + \frac{\partial T(y,t)}{\partial y} + \frac{\partial T(0,t)}{\partial z}\right] = \delta A I - \varepsilon\sigma[T(x,y,0,t)^4 - T_0^4] \tag{9}$$

$\delta = 1$ for $0 \le t \le t_{on}$
$\delta = 0$ for $t > t_{on}$

Here, A is the absorptivity of the material and is taken as 0.1 [14,19], ε is the emmisivity of the material, and σ is the Stefan–Boltzmann constant. The emmisivity of calcium phosphate tribasic when exposed to 1064 nm wavelength laser beam is not available in the open literature. Hence, in the present model only the absorptivity was considered and attempts are being made for *in situ* emmisivity measurements under laser processing conditions similar to the ones employed in the present study and they will be incorporated in future calculations.

The convection at the bottom surface of the sample during laser processing was also incorporated into the model and is given by the following equation:

$$-K\left[\frac{\partial T(x,t)}{\partial x} + \frac{\partial T(y,t)}{\partial y} + \frac{\partial T(L,t)}{\partial z}\right] = h[T(x,y,L,t) - T_0] \tag{10}$$

Here, h is the convective heat transfer coefficient (W/m² K), incorporated as function of temperature [20], and L the thickness of sample (0.04 mm for the precursor, Ca–P + 3 mm for the substrate, Ti–6Al–4V). The solutions of the above three equations were obtained by using the heat transfer module of COMSOL's™ Multiphysics package, and the results were discussed in later part of the paper.

3. Results and discussions

As the interaction of the laser beam with the precursor and substrate material is an energy intensive process the precursor $Ca_5(OH)(PO_4)_3$ is not expected to be retained and hence X-ray diffraction studies were carried out to observe the change in phases. The overlap of XRD patterns of the coatings processed at varying laser frequencies are represented in Fig. 1. It can be observed (Fig. 1a–c) that there is no change in the types of phases evolved when the pulse frequency is varied from 10 to 30 Hz and α-TCP, TiO_2, Ti, $CaTiO_3$, and Al are the major phases within the coatings. Nevertheless, additional phases such as CaO and Al_2O_3 along with the above phases are observed (Fig. 1d) as the laser pulse frequency is increased to 40 Hz. From the peak intensities it can be realized that, although the phase constituents within the coatings are same for 10, 20 and 30 Hz there is a variation in the amounts of these phases with varying pulse frequency. The relative amounts of

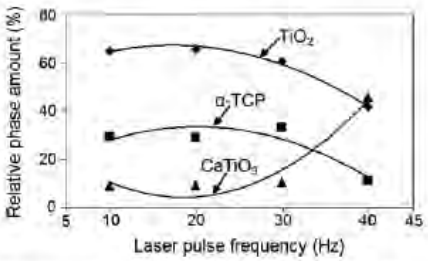


Fig. 2. Relative phase fractions as a function of laser pulse frequency.

phases of interest with regard to bio-application (α-TCP, TiO_2, and, $CaTiO_3$) were semi-quantitatively calculated as per the following equation [21]:

$$\%I = \frac{I_i}{\sum_1^3 I_i} \times 100 \quad (11)$$

Here, I_i is the integrated intensity of the phase in concern normalized to the integrated intensity of the Ti peaks and $\sum_1^3 I_i$ is the sum of these integrated intensities for the three phases. The results as illustrated in Fig. 2 show a decrease in the relative amounts of TiO_2 and α-TCP phase and an increase in the relative amount of $CaTiO_3$ phase with increasing pulse frequency. The kinetics and stability of these phase transformations and the relative amounts of these phases was understood from the temperature evolutions and cooling rate estimations during processing of the composite system (coating + substrate) made by using the thermal model as explained in the earlier section.

The temperature evolutions as a function of depth for all laser frequencies employed in the present work and corresponding cooling rates during processing of the composite system are represented in Fig. 3. It can be observed (Fig. 3) that within the frequency range of 10–30 Hz the temperatures at the surface (2100, 2680, 3688 K) and corresponding substrate-coating interface (1850, 2400, 3200 K) were high enough to melt the precursor calcium phosphate tribasic (melting point of 1843 K [16]) and substrate Ti–6Al–4V (melting point of 1800 K [18]) respectively. Hence, the dissociation products (α-TCP, TiO_2, and $CaTiO_3$,) are a result of direct interaction between the calcium phosphate tribasic and the substrate and their oxidation in the melt pool as per the following possible equations [4,22,23]:

$$2[Ca_5(OH)(PO_4)_3] + TiO_2 \rightarrow CaTiO_3 + 3\alpha\text{-}TCP + H_2O(g)\uparrow \quad (1)$$

$$\alpha\text{-}TCP + TiO_2 \rightarrow CaTiO_3 + \alpha\text{-}Ca_2P_2O_7 \quad (2)$$

$$\alpha\text{-}Ca_2P_2O_7 + Ti \rightarrow CaTiO_3 + CaO + P_2O_3(g)\uparrow \quad (3)$$

Once CaO is formed, it can easily react with TiO_2 to form $CaTiO_3$ as per the following equation:

$$CaO + TiO_2 \rightarrow CaTiO_3 \quad (4)$$

Further, as the laser pulse frequency is increased to 40 Hz the temperature at the surface (4800 K) and at substrate coating interface (4150 K) was sufficient enough to evaporate a major portion

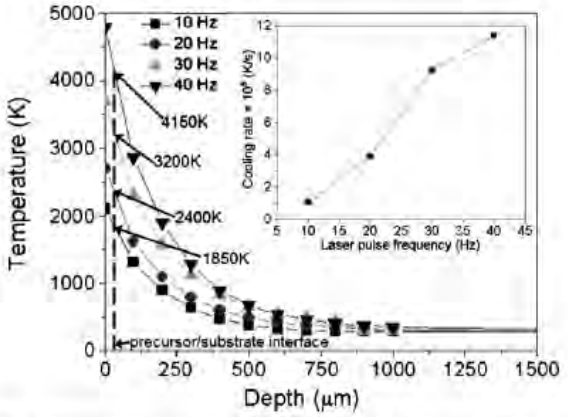


Fig. 3. Temperature evolution as a function of depth for samples processed at varying laser pulse frequency and the inset showing the cooling rate for all laser pulse frequencies.

of the precursor (boiling point of 3500 K [16]) and substrate (boiling point of 3315 K [18]) material. Hence a severe oxidation of the substrate material has taken place resulting in the presence of additional oxidation products such as Al_2O_3 as observed in the XRD (Fig. 1). Although the temperature at surface reaches as high as 3688 K for 30 Hz there is no presence of CaO (melting point of 2843 K and boiling point of 3171 K) [14] in the XRD (Fig. 1) unlike its presence in 40 Hz pulsing. This is attributed to the fact that as the cooling rates (inset in Fig. 3) for lower frequencies were relatively lower ($<9.25 \times 10^6$ K/s) compared to the cooling rate of 40 Hz (11.4×10^6 K/s), there was enough time for most of CaO formed in the melt pool to evaporate and remaining to involve in formation of $CaTiO_3$ as per reaction (4). On the contrary, the associated very high cooling rate for 40 Hz pulsing resulted in solidifying some of the CaO in the matrix along with formation of $CaTiO_3$ through reaction with CaO. Hence, there was an increase in the relative amount of $CaTiO_3$ phase and decrease in the TiO_2 phase with increasing laser pulse frequency (Fig. 2).

Microstructure and depth of melt zone across the cross-section for the coated surfaces were observed using a SEM. Since, there was no change in phase evolution for the samples processed at 10, 20, and 30 Hz, for comparison purpose, microstructural evolution and depth of melt zone across the cross-section were presented for only the samples processed at 20 and 40 Hz (Fig. 4). For the sample processed at 20 Hz the geometry of the textured topography is clearly visible and the depth of melt is approximately 220 μm (Fig. 4a). A higher magnification SEM image of the coating area, presented as an inset in Fig. 4a clearly demonstrated the rapid solidification of the precursor material to form dendrite like structures. The EDS spectra obtained from a random location in this area indicated the strong presence of Ca, P, Ti, Al, V and O peaks (inset in Fig. 4a). The presence of Ti, Al and V atoms within the coating was due to the fact that a certain amount of dilution has taken place as a part of the substrate material was also melted during this process. Further, as

Table 2
Variations in total on time, total off time, melt depth and experimental laser fluence with varying pulse frequency and the theoretical fluence for evaporation of calcium phosphate tribasic.

Laser pulse frequency (Hz)	Total on time (μs)	Total off time (ms)	Melt depth (μm)	Experimental laser fluence × 10^6 (J/kg)	Theoretical fluence for evaporation × 10^6 (J/kg)
10	750	149,250	300	6.6	
20	1500	148,500	220	17.7	
30	2250	147,750	140	37.0	4.5
40	3000	147,000	80	85.1	

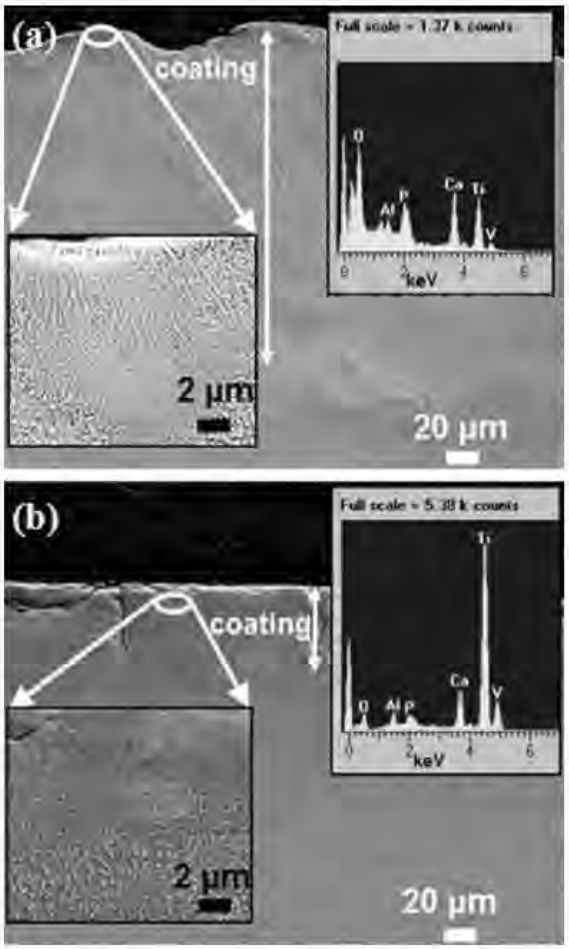


Fig. 4. SEM image and the corresponding EDS spectra for the sample processed at (a) 20 Hz and (b) 40 Hz.

the processing was carried out in an ambient atmosphere and temperature developed at the surface was very high (>2500 K, Fig. 3), a part of the precursor and substrate material may have oxidized for the presence of O peak. For samples processed at 40 Hz, the surface is less rough (Fig. 4b) compared to the sample processed at 20 Hz (Fig. 4a) and the depth of melt zone is approximately 80 μm (Fig. 4b). The less surface roughness in 40 Hz sample is attributed to the increased pulse overlap with increasing pulse frequency [24]. In addition EDS (inset in Fig. 4b) indicate that 40 Hz sample has very weak peak of Ca and P from coated region. Such weak peaks of Ca and P along with lower melt depth in 40 Hz sample compared to 20 Hz sample even with higher input laser energy (Table 1) is explained in the following section.

The correlation between melt depth and pulse frequency strongly depends upon the input energy and corresponding thermal parameters (temperature and cooling rate) and physical conditions generated and prevailed during processing. Depending upon the input energy, the temperature will rise to melt or vaporize the material. Especially, during laser material processing, presence of vapor over the surface of sample strongly influences the transfer (coupling) of the incoming laser beam energy and accordingly affects the chemical and physical nature of modified surface region. The theoretical energy $Q_{theoretical}$ required to vaporize a unit mass of material can be calculated by the following equation:

$$Q_{theoretical} = \int_{298}^{T_m} (C_p\,dT) + \Delta H_m + \int_{T_m}^{T_v} (C_p\,dT) + \Delta H_v \quad (12)$$

Here, C_p is the specific heat of calcium phosphate tribasic and its variation with temperature is taken as $C_p = 201.68T^{0.245}$ J/kg K[10]. ΔH_m and ΔH_v are the latent heat of melting and latent heat of vaporization for calcium phosphate tribasic and are taken as 15.5 kJ/mol [16], and 458.24 kJ/mol [16] respectively. With increase in pulse frequency, the number of pulses within a single beam area is increased and therefore the experimental energy $Q_{experimental}$ delivered per unit mass can be calculated as per the following equation:

$$Q_{experimental} = \frac{4E}{\rho_{Ca-P}\pi D^2 l} \quad (13)$$

Here, ρ_{Ca-P} is the density of calcium phosphate tribasic (3156 kg/m^3 [16]) and l the melt depth. The theoretical and experimental energy obtained from these calculations and melt depths measured in the cross-section are listed in Table 2. While the experimental laser energies for the samples processed at 10, 20 and 30 Hz are higher but less than an order of magnitude to that of the theoretical energy, the experimental energy for the sample processed at 40 Hz is approximately 2 orders of magnitude higher than the theoretical energy. Hence, a predominant amount of precursor material likely to have evaporated while processing at 40 Hz thereby resulting in a reduced melt depth as stated earlier. Further, for the sample processed at 40 Hz the total on time of the laser beam (Table 2) was sufficiently long (3000 μs) as compared to the samples processed at 10, 20 and 30 Hz, for formation of a stable plasma on the surface. Such plasma is likely to block the incoming laser beam and further reduce the melt depth. The presence of cracks (Fig. 4b) for the sample processed at 40 Hz might be due to the shock waves generated at the interface as a result of the stable plasma plume.

4. Conclusions

From the model calculations it was observed that as the laser pulse frequency is increased, the surface temperature and the cooling rate increased. This in turn resulted in a reduction of the relative phase amounts of α-TCP and TiO_2 and an increase in $CaTiO_3$ phase. Further, with increasing pulse frequency the input energy needed to vaporize a unit mass of material increases beyond the theoretical energy. This in turn resulted in evaporation of precursor material at higher laser frequencies (40 Hz). The stable plasma plume formed on the surface at such higher laser frequencies is likely to decouple the incoming laser beam and further reduce the melt depth.

References

[1] L.L. Hench, J.M. Polak, Science 295 (2002) 1014–1017.
[2] L.L. Hench, R.E. Newnham, Journal of American Ceramic Society 74 (1991) 1487–1510.
[3] H.W. Kim, Y.H. Koh, L.H. Li, S. Lee, H.E. Kim, Biomaterials 25 (2004) 2533–2538.
[4] S.R. Paital, K. Balani, A. Agarwal, N.B. Dahotre, Biomedical Materials 4 (2009) 1–10.
[5] K. Takatsuka, T. Yamamuro, T. Kitsugi, T. Nakamura, T. Shibuya, T. Goto, Journal of Applied Biomaterials 4 (2004) 317–329.
[6] Y.C. Tsui, C. Doyle, T.W. Clyne, Biomaterials 19 (1998) 2015–2029.
[7] C.K. Wang, J.H. Chern Lin, C.P. Ju, H.C. Ong, R.P.H. Chang, Biomaterials 18 (1997) 1331–1338.
[8] T. Blalock, X. Bai, A. Rabiei, Surface and Coatings Technology 201 (2007) 5850–5858.
[9] A.R. Boyd, B.J. Meenan, N.S. Leyland, Surface and Coatings Technology 200 (2006) 6002–6013.
[10] D.B. Haddow, P.F. James, R. Van Noort, Journal of Materials Science: Materials in Medicine 7 (1996) 255–260.
[11] M. Shirkhanzadeh, Journal of Materials Science Letters 10 (1991) 1415–1417.
[12] A.A. Campbell, G.E. Fryxell, J.C. Linehan, G.L. Graff, Journal of Biomedical Materials Research 32 (1996) 111–118.

[13] F.J. Gracia-Sanz, M.B. Mayor, J.L. Arias, J. Pou, B. Leon, M. Perez-Amor, Journal of Materials Science: Materials in Medicine 8 (1997) 861–865.
[14] A.K. Kurella, A.N. Samant, N.B. Dahotre, Journal of Applied Physics 105 (2009) 149131–149138.
[15] A.N. Samant, Laser Machining of Structural Ceramics: Computational and Experimental Analysis, Doctoral Dissertation, The University of Tennessee, Knoxville, 2009, p. 131.
[16] S. Dyshlovenko, B. Pateyron, L. Pawlowski, D. Murano, Surface and Coatings Technology 179 (2004) 110–117.
[17] R. Singh, A. Kurella, N.B. Dahotre, Journal of Biomaterials Applications 21 (2006) 49.
[18] M. Boivineau, C. Cagran, D. Doytier, V. Eyraud, M.-H. Nadal, B. Wilthan, G. Pottlacher, International Journal of Thermophysics 27 (2006) 507–529.
[19] O. Guillot-Noël, R. Gomez-San Roman, J. Perrière, Jörg Hermann, V. Craciun, C. Boulmer-Leborgne, P. Barboux, Journal of Applied Physics 80 (1996) 1803.
[20] F.P. Incropera, D.P. Dewitt, Fundamentals of Heat and Mass Transfer, 6th ed., John Wiley and Sons, New York, 2002, p. 543.
[21] B. Du, S.R. Paital, N.B. Dahotre, Scripta Materialia 59 (2008) 1147–1150.
[22] A. Kurella, N.B. Dahotre, Acta Biomaterialia 2 (2006) 677–683.
[23] F. Lusquiños, A. De Carlos, J. Pou, J.L. Arias, M. Boutinguiza, B. León, M. Pérez-Amor, F.C.M. Driessens, K. Hing, I. Gibson, S. Best, W. Bonfield, Journal of Biomedical Materials Research 64A (2003) 630–637.
[24] S.R. Paital, N.B. Dahotre, Wettability and kinetics of hydroxyapatite precipitation on a laser-textured Ca-P bioceramic coating, Acta Biomaterialia, (2009), doi:10.1016/j.actabio.2009.03.004.

Available online at www.sciencedirect.com
ScienceDirect
Acta Biomaterialia 5 (2009) 2763–2772
Acta BIOMATERIALIA
www.elsevier.com/locate/actabiomat

Wettability and kinetics of hydroxyapatite precipitation on a laser-textured Ca–P bioceramic coating

Sameer R. Paital, Narendra B. Dahotre *

Laboratory for Laser Materials Synthesis and Fabrication, Department of Materials Science and Engineering, The University of Tennessee, Knoxville, TN 37996, USA

Received 23 January 2009; received in revised form 26 February 2009; accepted 5 March 2009
Available online 11 March 2009

Abstract

Surface-textured calcium phosphate coatings at four different length scales were synthesized on titanium-based alloys using a pulsed Nd:YAG laser system by a direct melting technique. The textures were obtained by varying the laser spot overlap with a change in laser traverse speed. Surface roughness measurements of the textured coatings carried out using a white light interferometer indicated a decrease in roughness with increasing laser scan speed. Wettability of the coated samples measured using a static sessile drop technique demonstrated an increased hydrophilicity with increasing laser scan speed. The influence of such textures and the associated surface roughness on the precipitation kinetics of hydroxyapatite (HA) during immersion in simulated body fluid (SBF) was the prime focus of the present paper. The mineralized samples obtained after immersion in SBF were characterized using X-ray diffraction, energy-dispersive spectroscopy and scanning electron microscopy to understand the kinetics of HA precipitation. The results thereafter confirmed that the precipitation kinetics of HA was strongly modulated by the varying surface roughness.
© 2009 Acta Materialia Inc. Published by Elsevier Ltd. All rights reserved.

Keywords: Wettability; Kinetics; Hydroxyapatite; Laser; Ca–P

1. Introduction

Bone is a specialized hard connective tissue composed of an extracellular matrix (ECM), which is approximately two-thirds inorganic. This inorganic mineral phase consists primarily of calcium and phosphate ions, with traces of magnesium, carbonate, hydroxyl, chloride, fluoride and citrate ions [1]. Synthetic calcium phosphate (Ca–P)-based bioceramics possess bioactivity, biocompatibility, osteoconductive, nontoxic, noninflammatory and nonimmunogenic characteristics, and thus have received much attention as an artificial bone graft substitute material. However, due to their poor mechanical properties, such as lower fatigue strength and higher elastic modulus, in comparison with the human bone, these bioceramics cannot be used as bulk in the manufacture of load-bearing implants [2]. Synthesizing Ca–P based coatings on Ti-based alloys, however, is an area of active research as both the beneficial mechanical properties owing to the underlying titanium alloy substrate and the improved bioactivity due to the altered surface chemistry (presence of Ca–P) can be achieved by this process. Several coating methodologies have been studied by various researchers to date, including plasma spray [3], ion beam-assisted deposition [4], sol–gel-based coatings [5], pulsed laser deposition [6] and electrophoretic deposition [7].

The in vitro bioactivity of these ceramic coatings, assessed by the precipitation of a hydroxyapatite (HA, $[Ca_{10}(PO_4)_6(OH)_2]$; an apatite-like mineral) layer on their surface during immersion in simulated body fluid (SBF) has also been studied by several researchers [8–10]. Such precipitation of HA on the sample surface is beneficial as HA is a naturally occurring mineral component of the human bone lying alongside the collagen fibrils. Hence, this layer provides the appropriate surface chemistry and

* Corresponding author. Tel.: +1 865 974 3609; fax: +1 865 974 4451.
E-mail address: ndahotre@utk.edu (N.B. Dahotre).

1742-7061/$ - see front matter © 2009 Acta Materialia Inc. Published by Elsevier Ltd. All rights reserved.
doi:10.1016/j.actbio.2009.03.004

thereby acts as a bone bonding interface, where the cells can preferentially proliferate and differentiate into complex tissues such as bone. The kinetics of such precipitation from the SBF, a solution with ion concentrations and pH value similar to those of human blood plasma, has attracted the attention of a number of researchers as it is a process similar to biological mineralization [11,12]. The above technique also provides an alternate method for developing HA coatings on Ti-based alloys [2,13–15].

The various factors that might affect the kinetics of HA precipitation on a substrate material include, but are not limited to, (i) the pH of the supersaturated SBF solution; (ii) ionic concentrations of the SBF solution; (iii) the ambient temperature in which the nucleation is allowed to take place; (iv) the substrate surface chemistry and (v) the surface roughness of the substrate. Theoretical calculations of HA precipitation by Lu and Leng [12] demonstrated that a higher thermodynamic driving force is needed for the precipitation of HA than for the other metastable phases, such as octacalcium phosphate (OCP, [$Ca_8(HPO_4)_2(PO_4)_4{\cdot}5H_2O$]) and dicalcium phosphate (DCP, [$CaHPO_4{\cdot}2H_2O$]), that are usually present in supersaturated SBF. Their modeling results showed that the HA nucleation rate is significantly enhanced at higher pH and approaches the nucleation rate of OCP at a pH of 10. Their calculations also indicated that DCP does not nucleate in normal SBF although it is kinetically favorable, and only precipitates when the calcium and phosphate ion concentrations increase to higher than normal levels in SBF. Based on their models, the authors reported that the presence of carbonate or a deficiency of calcium in SBF can also affect the kinetics of HA precipitation considerably. Their results showed that a carbonate-containing and calcium-deficient HA is more thermodynamically favored than stoichiometric HA. The experiments by Valero and co-workers [16] proved that DCPs nucleate more easily at lower pH (5–6.5) than HA and OCP, while OCP nucleates more easily than HA at mean to high pH (7–8). Such a discrepancy in nucleation rate was attributed to the variation in kinetic coefficients of OCP and HA, which are smaller than that of DCP by 10 and 18 orders of magnitude, respectively, at pH 6.5.

The effect of reaction temperature (15–60 °C) on the kinetics of HA precipitation was studied by Cui and co-authors [17]. They reported that the HA precipitation is highly temperature dependent and the nucleation rate is faster at higher temperatures. Further, they also demonstrated that the temperature has a great influence on both the particle size and the morphology of the precipitated hydroxyapatite. Kondyurin and co-workers [9] studied the kinetics of HA deposition on three solid substrates (stainless steel, silicon and silica glass) modified by sequential implantation of Ca and P ions. Following the kinetic studies using Fourier transform infrared (FTIR) and Raman spectroscopy, they concluded that the speed of deposition was different on the three substrate materials. Ducheyne et al. [18] used a self-assembled monolayer technique to create amine, carboxyl and hydroxyl functional groups on oxidized silicon wafers, and then studied its bioactivity by immersing in a supersaturated SBF. From their studies they concluded that a hydroxylated surface provides appropriate surface chemistry and thereby enhances biomineralization compared to other surfaces. Two different treatment techniques (alkali treatment and radiofrequency plasma treatment) on titanium alloys were carried out by Layrolle et al. [8] to alter the surface chemistry and the surface roughness simultaneously, and thereby study its influence on biomineralization. From their results they concluded that the radiofrequency plasma-treated surface showed pronounced biomineralization compared to the alkali treated surface.

In all of the above studies, the kinetics of HA precipitation was understood based on the theoretical models or by experiments with two or more controlling factors. In the present case, however, we only studied the effects of surface roughness on wettability and the precipitation kinetics of HA. A direct laser-based melting technique was employed to achieve Ca–P coatings with controlled texture and surface roughness on the Ti–6Al–4V substrate. Here the intermittent delivery of pulses from a pulsed Nd:YAG laser was used to control texture by varying the spot overlap with change in laser traverse speed. The textured samples were then immersed in a supersaturated SBF solution and the precipitation kinetics of HA was studied using X-ray diffraction (XRD) and energy-dispersive spectroscopy (EDS).

2. Materials and methods

Substrate coupons of Ti–6Al–4V ($100 \times 50 \times 3$ mm) were cut from rolled sheets using an abrasive cutter. The cut coupons were then prepared for coating by initially polishing using a 30 μm grit silicon carbide emery paper followed by rinsing with acetone. Calcium phosphate tribasic ($Ca_5(OH)(PO_4)_3$) powder obtained from Fischer Scientific was taken as the precursor material. This precursor powder had a spherical morphology with a unimodal distribution in the range of 10–30 μm. The precursor was mixed in a water-based organic solvent LISI W 15853 obtained from Warren Paint and Color Company (Nashville, TN, USA). The mixed slurry was then sprayed onto the preheated (~50 °C) substrate coupons using an air-pressurized spray gun. The sprayed coupons were air dried to remove the moisture and a uniform thickness of 40 μm was maintained for all precoating deposits. Finally, the samples were scanned using a 400 W average power, JK701 model pulsed Nd:YAG laser to obtain a metallurgical bonding between the precursor and the substrate material. The laser was equipped with a fiberoptic beam delivery system to transfer the laser beam from the laser head to the material. The control panel for laser allows the control of pulse height, pulse width, pulse repetition rate and pulse shape. The lens assembly is equipped with a 120 mm focal length convex lens, which gives a spot diameter of approximately 240 μm at focus. The focused spot is kept at

approximately 0.8 mm above the surface of the sample so as to have a spot size of approximately 900 μm on the surface. The processing parameters used for the above process are listed in Table 1. From the table it can be observed that only the linear scan speed was varied (36, 48, 78 and 102 cm min^{-1}), the rest of the parameters being kept constant. This linear scan speed can be related to the spot overlap by the following equation [19]:

$$(\text{spot diameter}) \times (1 - \text{spot overlap}) \times (\text{pulse frequency}) = \text{linear scan speed} \quad (1)$$

Hence, four different samples, with spot overlaps of 65, 55, 28 and 5.5%, were obtained.

The surface roughness of the coated samples was measured using a white light interferometer. As proposed by Zhou and De Hosson [20] the rough grooves are assumed to hold Gaussian profile with a cosine distribution. Based on a combination of the magnitudes of amplitude and wavelength of such distribution, these grooves are characterized as radial grooves and circular grooves. Hence, in the present work, the surface structure was characterized in terms of the roughness parameters σ_A (the standard deviation of amplitude of random points on the surface from a line drawn through the trace such that cross-sectional areas of the asperities above and below the grooves are equal) and λ (the wavelength of the profile or the distance between any two successive crests or troughs), and their ratio (σ_A/λ) was used as a unique measure of surface texture. A total of five readings were taken from different locations in each sample and the sampling showed that both parameters (σ_A and λ) could be defined with an accuracy of 2–4%.

The wettability of the coated samples with SBF was measured by a static sessile drop technique using a Tantec contact angle goniometer. The SBF solution was prepared by mixing reagent-grade chemicals in the following order: NaCl (8.026 g), $NaHCO_3$ (0.352 g), KCl (0.225 g), $K_2HPO_4{\cdot}3H_2O$ (0.230 g), $MgCl_2{\cdot}6H_2O$ (0.311 g), $CaCl_2$ (0.293 g) and Na_2SO_4 (0.072 g) in distilled water (700 ml). The fluid was then buffered to pH 7.4 at 37 °C with trihydroxymethyl aminomethane (6.063 g) and hydrochloric acid (40 ml). SBF drops of approximately 8 mm diameter were placed on the thoroughly cleaned sample by a hypodermic syringe and the advancing contact angle was taken as a measure of wettability. The test was conducted at room temperature and a minimum of 10 contact angle readings were taken on each sample to minimize errors in the measurement. Further, the measurement was based on the patented half angle method (US Patent 5268733), which eliminates the errors associated with the arbitrary tangential alignment.

Table 1
The laser parameters used for the study.

Pulse width	0.5 ms
Pulse energy	4 J
Pulse repetition rate	20 Hz
Average power	80 W
Laser Scan speed	36, 48, 78, 102 cm min^{-1}
Input energy density	1887, 1415, 871, 666 J cm^{-2}
Focus position	0.8 mm above the surface of the sample
Spot diameter on the surface	900 μm
Pulse height	94% of the maximum lamp current
Pulse shape	Rectangular

Nondestructive phase evaluation of the samples prior to and after immersion in SBF was conducted using a Philips Norelco X-ray diffractometer, with Cu K_α radiation of wavelength 1.5418 Å. The system was operated at 20 kV and 10 mA in a 2θ range of 20–100° using a step size of 0.02° and a count time of 1 s. Microstructure and morphological evolutions of the coated samples prior to and after immersion in SBF were characterized using low-magnification Leica optical microscopes and an LEO 1525 scanning electron microscope. An energy-dispersive spectrometer with the scanning electron microscope was used to study the elemental analysis of the mineralized samples.

To study the kinetics of HA precipitation on the coated samples, a set of four samples from each processing condition was immersed in the SBF solution. Plastic containers were used to soak the samples in SBF for different time periods (24, 48, 72 and 96 h). The solution was refreshed every 24 h to maintain a pH of 7.4, and the temperature was maintained at 37 °C during the course of the test. The samples were removed at regular intervals from the SBF solution and an increase in weight owing to the precipitation of HA was measured using a microbalance.

3. Results and discussion

3.1. Effects of phase and morphology on wettability

Low-magnification optical microscopic images (Fig. 1) of the surfaces of the coated samples clearly demonstrate the effect of varying the laser scan speed on the texture evolution. The laser scan speed influences the input energy density [19] and the laser spot overlap. These two parameters, in turn, greatly influence the surface morphology and texture evolution of the coating. As seen in Fig. 1, each pulse of a laser produces a solidified crater with a defined boundary and a flat region at the center. Hence, as the laser scan speed is increased the laser spot (crater) overlap is decreased as per Eq. (1), which in turn modifies the crater area as well as the surface texture. Also with increasing laser scan speed the input energy density (fluence) decreased, and resulted in reduced surface melting or less thermal effect at the surface. Thus, variation of the laser processing parameters produced variable thermodynamic conditions, resulting in the creation of different physical surface textures (Fig. 1). However, variation in the thermodynamic conditions under the range of laser scanning speeds (fluences: 1887, 1415, 871, 666 J cm^{-2}) employed in the present work appeared to have no detectable influence on the type or amount of phase evolution in the modified surface region. All samples processed using these laser

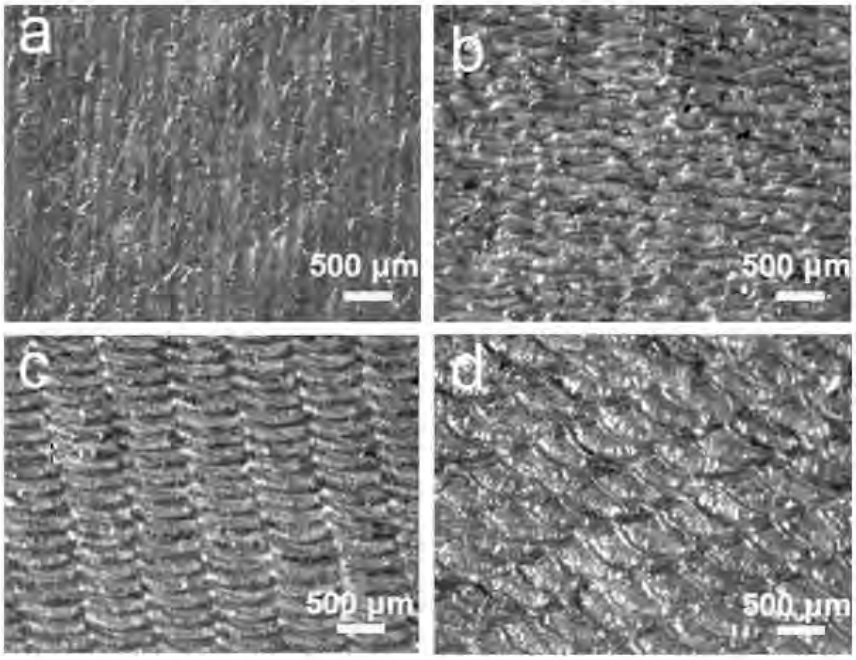


Fig. 1. Low-magnification optical microscopic images of the surfaces of the coatings obtained at laser scan speeds of (a) 36 cm min^{-1}, (b) 48 cm min^{-1}, (c) 78 cm min^{-1} and (d)102 cm min^{-1}.

speeds (fluences) demonstrated the evolution of the same phases (Fig. 2). The major phases identified within the detectable limits of the instrument were α-tricalcium phosphate (TCP), TiO_2 (rutile and anatase), Ti and Al. The presence of identical phases in the coatings of all laser-processed samples is expected to provide minimal or no variation on the wetting characteristics during SBF immersion. However, as stated in the following section, all the coatings in the presence of these phases and with the varying surface topographic cues demonstrated a significant increase in wetting compared to uncoated Ti–6Al–4V alloy.

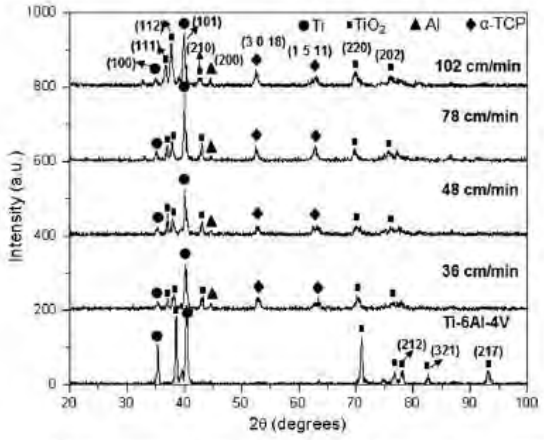


Fig. 2. XRD patterns of the uncoated Ti–6Al–4V and the samples processed at various laser scan speeds.

The variation in surface roughness (texture) of the coated samples with varying laser scan speed was evaluated using a white light interferometer. As defined earlier, the roughness parameters, such as standard deviation in amplitude σ_A and wavelength λ, were obtained from five random locations on each sample and are presented as mean values with related scatter in Table 2. The corresponding mean values of σ_A/λ and related scatter as a measure of surface texture are also included in Table 2. The correlation between the experimental observations (Fig. 1) and the measurement of roughness parameters (Table 2) indicate that the decreasing values of σ_A/λ ratio corresponded with increasing values of laser scan speed. In other words, the surface roughness transitioned from circular grooves to radial grooves as the laser scan speed increased. A schematic of this process is illustrated in Fig. 3. The above transition or smoothening effect can be attributed to the fact that as the linear scan speed is increased the number of pulses per unit area (pulse overlap), and thereby the input energy density, is reduced. As stated earlier, this in turn resulted in less thermal effect and reduced melting on the surface, and therefore a low σ_A/λ value.

It is also well understood that wetting of a surface by a liquid is significantly affected by its surface roughness [20–24]. Table 2 lists the experimental contact angles (θ) subtended by an SBF drop and corresponding texture parameter (σ_A/λ) for uncoated and coated Ti–6Al–4V samples.

Table 2
Experimental results of the contact angle of SBF and the texture parameter (σ_A/λ) on the Ca–P coated sample obtained at various laser scan speeds.

Sample	Standard deviation of amplitude, σ_A (μm)	Wavelength, λ (μm)	Texture parameter, σ_A/λ	Contact angle θ (°)
Bare Ti–6Al–4V	12.56 ± 0.37	2.79 ± 0.08	4.38 ± 0.04	60.5 ± 0.85
Ti–6Al–4V/Ca–P 36 cm min^{-1}	5.384 ± 0.053	2.6 ± 0.026	2.28 ± 0.06	22 ± 0.44
Ti–6Al–4V/Ca–P 48 cm min^{-1}	16.2 ± 0.024	9.46 ± 0.14	1.80 ± 0.036	19.5 ± 0.48
Ti–6Al–4V/Ca–P 78 cm min^{-1}	12.93 ± 0.3235	7.98 ± 0.1995	1.14 ± 0.0171	18 ± 0.21
Ti–6Al–4V/Ca–P 102 cm min^{-1}	14.033 ± 0.18	12.52 ± 0.25	0.78 ± 0.0195	15 ± 0.45

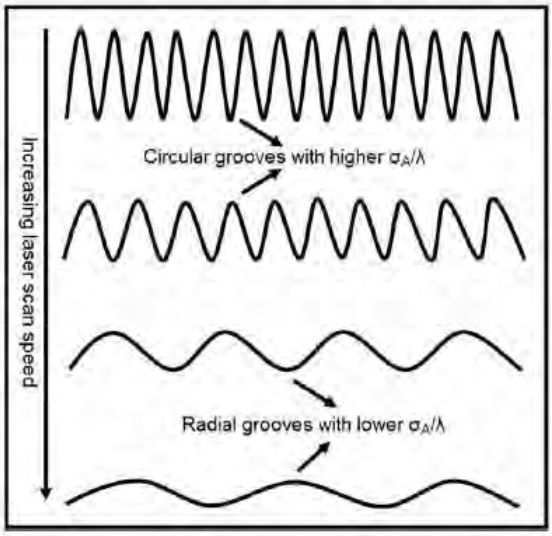


Fig. 3. Schematic showing the variation in surface profiles with varying laser scan speed.

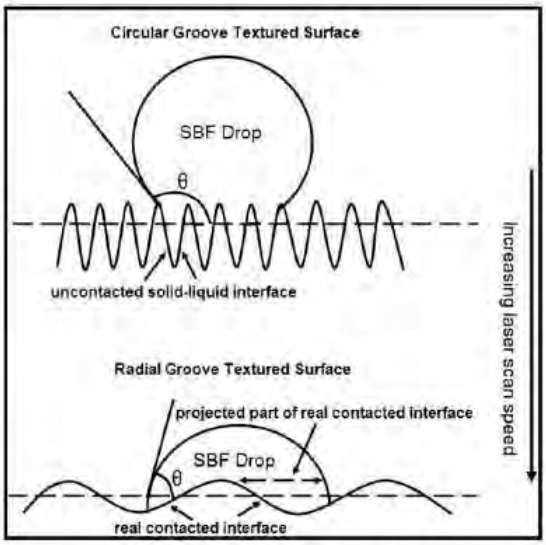


Fig. 4. Schematic showing the wetting behavior of a liquid drop on a rough surface having (a) circular grooves and (b) radial grooves.

The texture parameter (σ_A/λ) and the experimental contact angle (θ) for coated samples can be seen to have significantly lower values compared to that of the uncoated sample, indicating the influence of various phases evolved during laser processing. In contrast, within the set of laser-coated samples it can be noticed that with increasing laser scan speed the texture parameter (σ_A/λ) and the experimental contact angle (θ) both decrease, indicating the influence of various surface textures, and the same phases (α-TCP, TiO_2 (rutile and anatase), Ti and Al) evolved during laser processing. Therefore, the surface undergoes more wetting with increasing laser scan speed and decreasing σ_A/λ value, as schematically illustrated in Fig. 4. When a liquid drop is placed on a surface with radial grooves (smaller σ_A/λ value), it can easily overcome the energy barriers associated with such a surface to completely wet it. Thus, an equilibrium state of wetting is achieved when the grooves are radial. Hence, applying an energy-minimum condition, a relationship between the experimental contact angle affected by the radial grooves (θ_{rad}) and the theoretical contact angle (θ_{th}) can be obtained as follows [20]:

$$\cos\ \theta_{rad} = D(1-F)\cos\ \theta_{th} - F \quad (2)$$

where D is defined as the average area ratio of real contacted interface to its projected part and F is the area fraction of an uncontacted solid–liquid interface on a solid (Fig. 4). The theoretical contact angle θ_{th} is defined as: $\cos\ \theta_{th} = (\gamma_s - \gamma_{ls})/\gamma_l$, where γ_s, γ_{ls} and γ_l are the interface energies between solid–vapor, liquid–solid and liquid–vapor interfaces, respectively. For a radial groove both D and F are constant and, since the rough surface is assumed to distribute as a cosine profile with a Gaussian distribution, they are both a function of σ_A/λ [20]. Hence, through this energy-minimum route it can be clearly understood that the decrease in contact angle is due to the formation of radial grooves (smaller σ_A/λ value) on a surface.

In contrast, when the surface features are sharp (higher σ_A/λ value) at lower laser scan speed, the intrinsic energy associated with the liquid drop may not be sufficient enough to overcome the energy associated with the sharp features or circular grooves. Hence, when a liquid drop is placed on such a surface an equilibrium state of wetting could never be achieved. In such a case, the contact angles

affected by the circular grooves can be related to the theoretical contact angle as per the following equation [20]:

$$\theta_{cir} = \theta_{th} + \left(\frac{\sqrt{8\pi}}{\lambda}\sigma_A\right) \quad (3)$$

Therefore, from the above equation it can be clearly explained that a circular or sharp groove with a higher σ_A/λ value always results in an increase in contact angle and thereby a decrease in wettability (Fig. 4).

3.2. Mechanism and kinetics of HA precipitation

Figs. 5–8 represent the XRD studies prior to and after immersion in SBF (for different time periods) for samples processed at laser scan speeds of 36, 48, 78 and 102 cm min^{-1}, respectively. In each of these, the base spectrum (prior to immersion in SBF) is included for comparison. As discussed earlier, since there was no detectable change in the surface phase composition (Fig. 2) in all samples processed using the set of laser parameters employed in the present work, it was inferred that surface roughness (textures) was the only controlling factor that influenced the precipitation kinetics of HA on the sample surfaces during immersion in supersaturated SBF. However, as explained later, in comparison, the precipitation kinetics is expected to be significantly different in uncoated and coated samples due to the influence of both surface phase composition and surface texture.

For the samples processed at laser scan speeds of 36 and 48 cm min^{-1} (Figs. 5 and 6), a maximum attributed to the apatite phase at $2\theta = 31.75°$ corresponding to the plane (211) was detected only after 48 h of immersion of the samples in SBF. In contrast, for the sample processed at a laser scan speed of 78 cm min^{-1} (Fig. 7), the same peak was observed soon after 24 h of immersion in SBF. In addition to the above peak ($2\theta = 31.75°$), two more apatite peaks appeared at $2\theta = 22.0$ and 22.9°, corresponding to planes (200) and (111), respectively, for the sample processed at a laser scan speed of 102 cm min^{-1} (Fig. 8). This clearly indicates that the sample processed at a laser scan speed of 102 cm min^{-1} has a pronounced biomineralization compared to all the other samples. It can also be observed that there is an increased crystallographic texturing along the planes (200) and (211) with increasing immersion time. Such a phenomenon may be attributed to both the increase in volume fraction of the apatite-like phase and crystal growth along the c-axis.

Scanning electron microscopy (SEM) observations for the sample processed at a laser scan speed of 102 cm min^{-1} demonstrated (Fig. 9) the formation of a globular apatite-

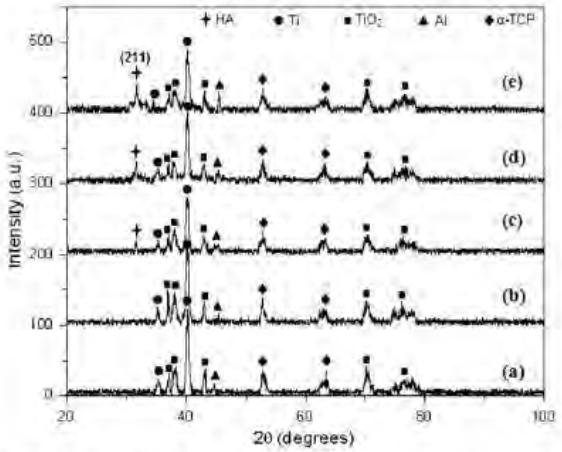


Fig. 5. XRD studies of the sample (processed at a laser scan speed of 36 cm min^{-1}) (a) prior to immersion in SBF and after immersion in SBF for (b) 24 h, (c) 48 h, (d) 72 h and (e) 96 h.

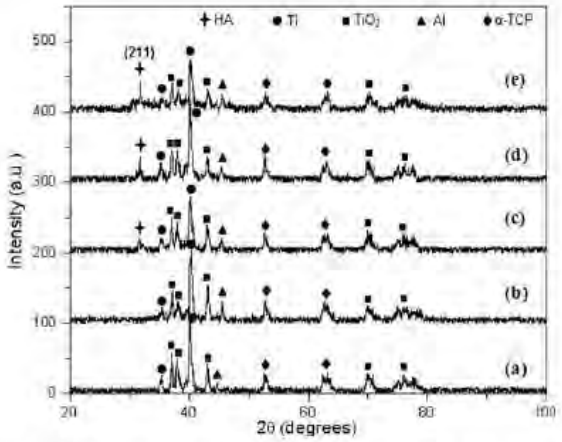


Fig. 6. XRD studies of the sample (processed at a laser scan speed of 48 cm min^{-1}) (a) prior to immersion in SBF and after immersion in SBF for (b) 24 h, (c) 48 h, (d) 72 h and (e) 96 h.

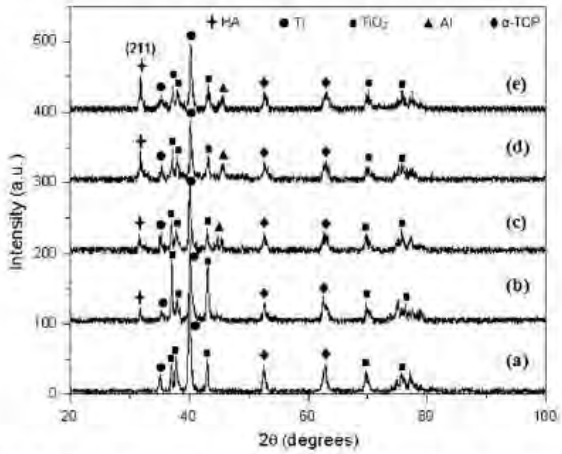


Fig. 7. XRD studies of the sample (processed at a laser scan speed of 78 cm min^{-1}) (a) prior to immersion in SBF and after immersion in SBF for (b) 24 h, (c) 48 h, (d) 72 h and (e) 96 h.

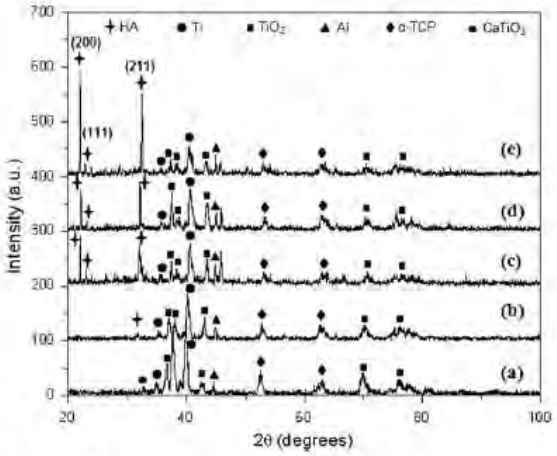


Fig. 8. XRD studies of the sample (processed at a laser scan speed of 102 cm min^{-1}) (a) prior to immersion in SBF and after immersion in SBF for (b) 24 h, (c) 48 h, (d) 72 h and (e) 96 h.

like layer, following immersion in SBF for different time periods. The formation of cracks within the thin apatite-like layer was attributed to the removal of moisture during drying [25]. Further, it can be concluded from the reduced dimensions of the islands between cracks that, with increasing immersion time, there is an increased accumulation of an apatite-like layer or enhancement in biomineralization. The thickness of this apatite layer varied from 8 to 15 μm with increasing immersion time. It can also be observed from the EDS spectra (presented as an inset within the SEM images) that there is a strong presence of Ca and P atoms following immersion in SBF, and also an increased intensity of both Ca and P with increasing immersion time. These studies therefore further complement the earlier findings from the XRD studies (Figs. 5–8). As well as Ca and P, a small amount of Na and Cl precipitated from the SBF solution can also be observed in the EDS spectra. This enhancement in mineralization or bioactivity for the sample processed at a laser scan speed of 120 cm min^{-1} is, as explained in earlier sections, a result of its improved wettability with SBF solution due to the textured surface produced during laser processing.

The mechanism for improvement in mineralization can also be explained as per the schematic illustrations presented in Fig. 10. As explained earlier, when the laser scan speed is increased, the coated surface undergoes a transition from surface features with circular grooves (high σ_A/λ value) to surface features with radial grooves (low σ_A/λ value), thereby improving its wettability in SBF. This improvement in wetttability enhances the reaction of water molecules present in the SBF with the TiO_2 and α-TCP phases present on the surface of the sample as per the following equations [26–28]:

$$TiO_2 + 2H_2O \rightarrow Ti(OH)_4 \quad (4)$$

$$3\alpha\text{-}Ca_3(PO_4)_2 + H_2O \rightarrow Ca_9HPO_4(PO_4)_5OH \quad (5)$$

Such a vigorous reaction at the higher laser scan speed (low σ_A/λ value) leads to the precipitation of more OH^- ions in stage 1, thereby increasing the negative charge density on the surface of the sample (Fig. 10a). It has been widely reported that the presence of a negatively charged surface enhances the formation of apatite on the substrate [29,30]. Following the precipitation of OH^- ions in stage 1 (Fig. 10a), in stage 2 of this mechanism calcium ions (Ca^{2+}) from the SBF are attracted towards the negatively

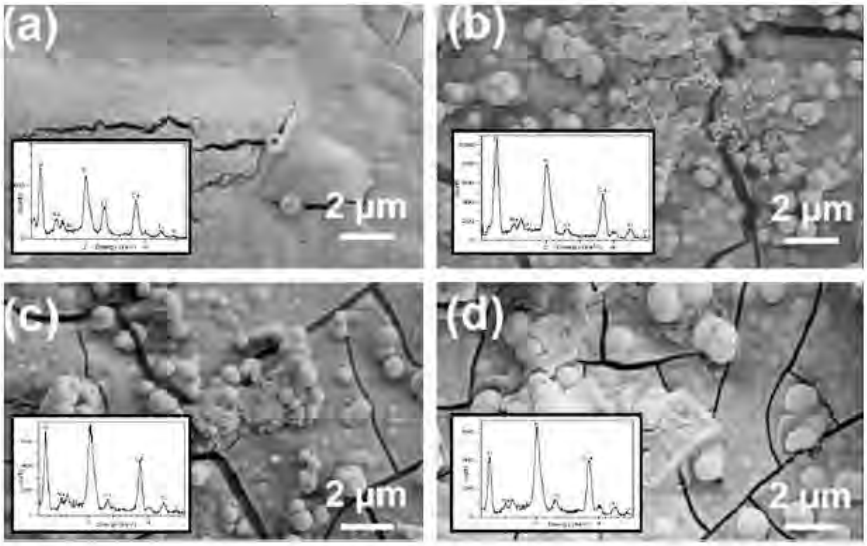


Fig. 9. SEM micrographs of the samples processed at a laser scan speed of 102 cm min^{-1} revealing the formation of a globular apatite-like layer following immersion in SBF for different time periods, with the inset showing the corresponding EDS spectra: (a) 24 h, (b) 48 h, (c) 72 h and (d) 96 h.

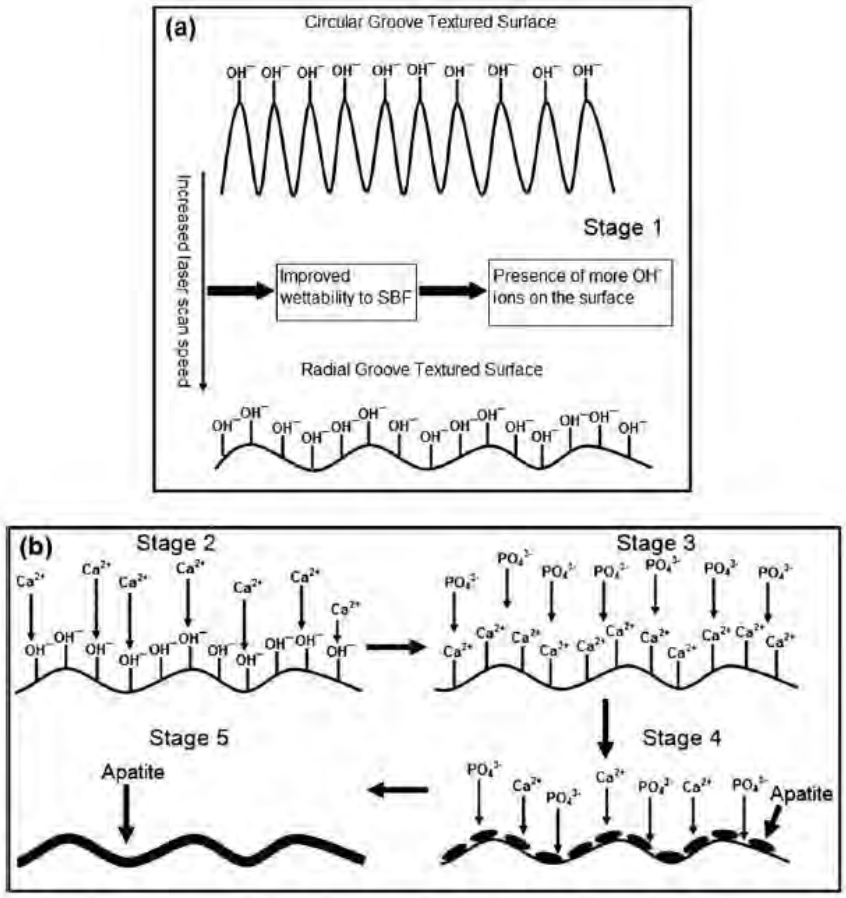


Fig. 10. Schematic illustrations demonstrating (a) the favored mechanism for the formation of more OH^- ion groups on the surface of the sample processed at a higher laser scan speed and (b) the mechanism of apatite formation on such a surface.

charged (OH^-) surface (Fig. 10b). In stage 3, the calcium hydroxide formed reacts with the phosphate ions (PO_4^{3-}) present in the SBF and consequently in stage 4 apatite nuclei are formed on the surface as per the following equation (Fig. 10b) [31]:

$$10Ca(OH)_2 + 6H_3PO_4 \rightarrow Ca_{10}(PO_4)_6(OH)_2 + 18H_2O \quad (6)$$

As the immersion time is increased, a large amount of a calcium and phosphate ions are attracted towards the surface (stage 4) and a thick layer of apatite is finally formed on the surface (stage 5, Fig. 10b).

Further, the nature of precipitation kinetics was evaluated for HA stoichiometry through EDS analysis of all the samples for each immersion period. A total of five readings were taken from different locations on each sample. It can be observed (Fig. 11) that there is an increase in Ca and P atomic concentration with increasing immersion time for all the samples. This can be attributed to the presence of already formed apatite nuclei (stage 4, Fig. 10b), which act as nucleating sites for the deposition of more Ca and P ions from the SBF. From Fig. 11a and b, for the samples processed at laser scan speeds of 36 and 48 cm min^{-1}, respectively, the Ca/P atomic ratio following 24 h of SBF immersion was more than 2 and dropped to ~1.67 (the Ca/P atomic ratio for HA) after 48 h of immersion, then remained the same during 72 and 96 h of immersion time. In contrast, for the samples processed at laser scan speeds of 78 and 102 cm min^{-1} (Fig. 11c and d), the Ca/P atomic ratio immediately reached ~1.67 during the first 24 h of SBF immersion and remained the same with increasing immersion time (48, 72 and 96 h). Such rapid saturation of Ca/P atomic ratio to the value of the atomic ratio for HA (~1.67) at higher processing speeds (78 and 102 cm min^{-1}) compared to at lower speeds (36 and 48 cm min^{-1}) further indicates the transition of the surface texture from circular grooves to radial grooves and the associated increased wettability.

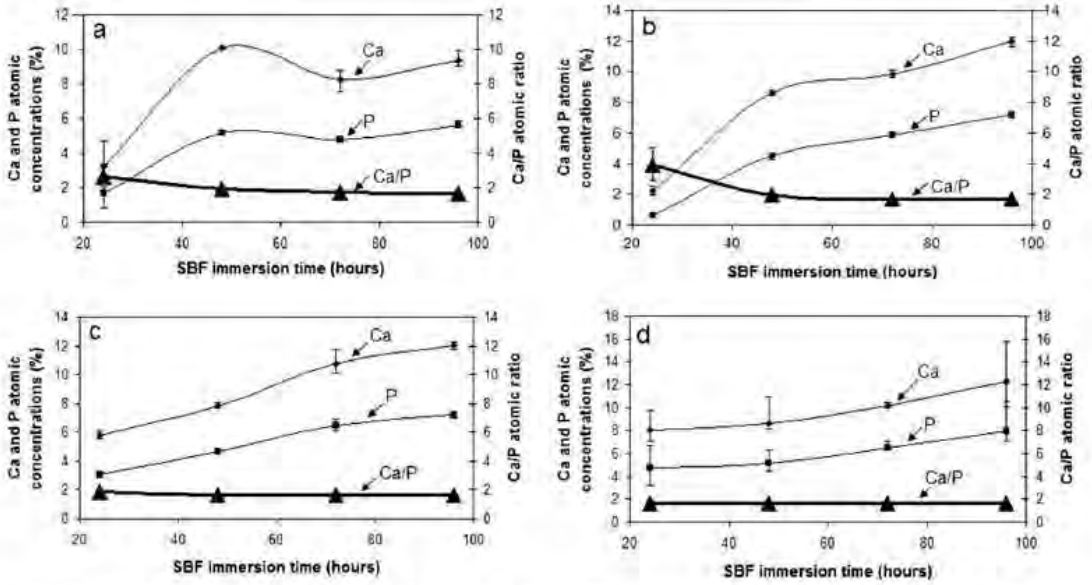


Fig. 11. Dependence of Ca and P atomic concentration and Ca/P atomic ratio to SBF immersion time for the samples processed at laser scan speeds of (a) 36 cm min^{-1}, (b) 48 cm min^{-1}, (c) 78 cm min^{-1} and (d) 102 cm min^{-1}.

Finally, the effects of surface phase and surface texture (roughness) on the growth kinetics of HA on the bare Ti–6Al–4V and the samples processed at different laser scan speeds was studied by measuring the increase in weight following immersion in SBF for different time periods. The Ca–P coated samples processed at higher laser scan speeds (78 and 102 cm min^{-1}) have pronounced biomineralization compared to the samples processed at lower laser scan speeds (36 and 48 cm min^{-1}) and uncoated Ti–6Al–4V (Fig. 12). The growth kinetics of HA on the substrate material was studied by curve fitting and determining the kinetic constants. The weight increase for bare Ti–6Al–4V and the samples processed at laser scan speeds of 36 and 48 cm min^{-1} followed a linear relationship with immersion time as per the following equation:

$$W = K(t) + A \tag{7}$$

In contrast, the weight increase for samples processed at laser scan speeds of 78 and 102 cm min^{-1} followed a power relationship with immersion time as per the following equation:

$$W = A(t)^K$$

Here, W is the growth rate, A and K are the kinetic constants and t is the immersion time. The kinetic constants A and K obtained from the curve fits are listed as an inset in Fig. 12. These constitutive relationships and corresponding kinetic constants clearly define the nature of biomineralization and the effects of surface phase and surface texture on wettability as a function of laser processing parameter (scan speed).

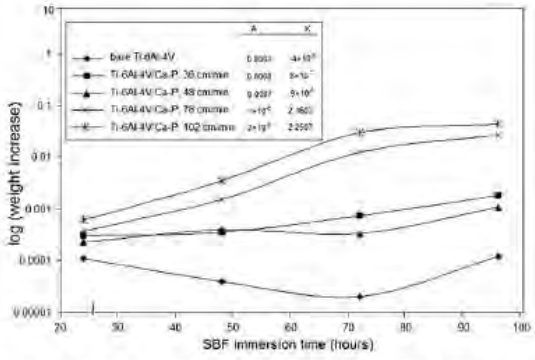


Fig. 12. Deposition of HA in grams on Ca–P coated samples (laser textured at various laser scan speeds) and bare Ti–6Al–4V substrate from the SBF solution as a function of immersion time.

4. Conclusion

The process of directly melting Ca–P precursor on Ti–6Al–4Vsubstrate resulted in the formation of various phases, such as α-TCP, TiO_2 (rutile and anatase), Ti and Al, within the coated samples. There was no significant variation in the types and amount of these phases within the coated samples. The surface textures or topographic cues were controlled by varying the spot overlap by varying laser scan speed. Within the set of laser parameters employed for the coating process, there was a transition from surface textures with circular grooves (high σ_A/λ

value) to surface textures with radial grooves (low σ_A/λ value) with increasing laser scan speed. Textured coatings with radial grooves (low σ_A/λ) obtained at higher laser scan speed (78 and 102 cm min^{-1}) demonstrated better wettability compared to sharp or circular grooves (high σ_A/λ value) obtained at lower laser scan speed (36 and 48 cm min^{-1}) and uncoated Ti–6Al–4V. However, the reduced wettability of uncoated Ti–6Al–4V compared to all the coated samples is clearly due to the surface chemistry along with the surface texture. Hence, the samples processed at these higher laser scan speeds demonstrated improved biomineralization compared to the uncoated Ti–6Al–4V and the samples processed at lower laser scan speeds. There was also a rapid saturation of the Ca/P atomic ratio to the atomic ratio of HA (1.67) at higher laser scan speeds. The growth kinetics (weight increase) of HA on the uncoated Ti–6Al–4V and the samples processed at lower laser scan speeds followed a linear relationship with SBF immersion time. In contrast, for the samples processed at higher laser scan speeds the growth kinetics followed a power relationship with immersion time. The kinetic constants determined by curve fit on the weight increase vs. SBF immersion time graph further supported the above results.

References

[1] Ratner Buddy D, Hoffman Allan S, Schoen Fredrick J, Lemons Jack E. Biomaterials Science. 2nd ed. San Diego, CA: Elsevier Academic Press; 2004.

[2] Guo Yaping, Zhou Yu, Jia Dechang. Fabrication of hydroxycarbonate apatite coatings with hierarchically porous structures. Acta Biomater 2008;4:334–42.

[3] Ji Huaxia, Ponton CB, Marquis PM. Microstructural characterization of HA coating on titanium. J Mater Sci Mater Med 1992;3:283–7.

[4] Rabiei A, Thomas B, Jin C, Narayan R, Cuomo J, Yang Y, et al. A study of functional graded HA coatings processed using ion beam assisted deposition with in situ heat treatment. Surf Coat Technol 2006;200:6111–6.

[5] Nguyen HQ, Deporter DA, Pilliar RM, Valiquette N, Yakubovich R. The effect of sol–gel-formed calcium phosphate coatings on bone ingrowth and osteoconductivity of porous-surfaced Ti alloy implants. Biomaterials 2004;25:865–76.

[6] Bigi A, Bracci B, Cuisinier F, Elkaim R, Fini M, Mayer I, et al. Human osteoblast response to pulsed laser deposited calcium phosphate coatings. Biomaterials 2005;26:2381–9.

[7] Wang Cong, Ma J, Cheng Wen, Zhang Ruifang. Thick hydroxyapatite coatings by electrophoretic deposition. Mater Lett 2002;57:99–105.

[8] Lopez-Heredia MA, Legeay G, Gaillard C, Layrolle P. Radio frequency plasma treatments on titanium for enhancement of bioactivity. Acta Biomater 2008;4:1953–62.

[9] Pecheva Emilia V, Pramatarova Liliana D, Maitz Manfrfed F, Pham Mihn T, Kondyurin Alexey V. Kinetics of hydroxyapatite deposition on solid substrates modified by sequential implantation of Ca and P ions Part I. FTIR and Raman spectroscopy study. Appl Surf Sci 2004;235:176–81.

[10] Weng Jie, Liu Qing, Wolke JGC, Zhang Xingdong, de Groot K. Formation and characteristics of the apatite layer on plasma-sprayed hydroxyapatite coatings in simulated body fluid. Biomaterials 1997; 18:1027–35.

[11] Mann Stephen. Biomineralization: principles and concepts in bioinorganic materials chemistry. 1st ed. New York: Oxford University Press; 2001.

[12] Lu Xiong, Leng Yang. Theoretical analysis of calcium phosphate precipitation in simulated body fluid. Biomaterials 2005;26: 1097–108.

[13] Guo Yaping, Zhou Yu, Jia Dechang, Meng Qingchang. Fabrication and in vitro characterization of magnetic hydroxycarbonate apatite coatings with hierarchically porous structures. Acta Biomater 2008;4: 923–31.

[14] Yang Zhengpeng, Si Shihui, Zeng Xiaoming, Zhang Chunjing, Dai Hongjuan. Mechanism and kinetics of apatite formation on nanocrystalline TiO_2 coatings: a quartz crystal microbalance study. Acta Biomater 2008;4:560–8.

[15] Ma J, Wong Huifen, Kong LB, Peng KW. Biomimetic processing of nanocrystallite bioactive apatite coating on titanium. Nanotechnology 2003;14:619–23.

[16] Boistelle Roland, Lopez-Valero Isabel. Growth units and nucleation: the case of calcium phosphates. J Cryst Growth 1990;102:609–17.

[17] Liu Changsheng, Huang Yue, Shen Wei, Cui Jinghua. Kinetics of hydroxyapatite precipitation at pH 10 to 11. Biomaterials 2001;22: 301–6.

[18] Toworfe GK, Composto RJ, Shapiro IM, Ducheyne P. Nucleation and growth of calcium phosphate on amine-, carboxyl- and hydroxyl-silane self-assembled monolayers. Biomaterials 2006;27: 631–42.

[19] Paital Sameer R, Balani Kantesh, Agarwal Arvind, Dahotre Narendra B. Fabrication and evaluation of pulse laser-induced Ca–P coating on a Ti alloy for bioapplication. Biomed Mater 2009:4.

[20] Zhou XB, De Hosson JThM. Influence of surface roughness on the wetting angle. J Mater Res 1995;10:1984–92.

[21] Baker KC, Drelich J, Miskioglu I, Israel R, Herkowitz HN. Effect of polyethylene pretreatments on the biomimetic deposition and adhesion of calcium phosphate films. Acta Biomater 2007;3:391–401.

[22] Hitchcock SJ, Carroll NT, Nicholas MG. Some effects of substrate roughness on wettability. J Mater Sci 1981;16:714–32.

[23] Oliver JF, Mason SG. Liquid spreading on rough metal surfaces. J Mater Sci 1980;15:431–7.

[24] Miller JD, Veeramasuneni S, Drelich J, Yalamanchili MR, Yamauchi G. Effect of roughness as determined by atomic force microscopy on the wetting properties of PTFE thin films. Polym Eng Sci 1996;36:1849–55.

[25] Habibovic Pamela, Barrere Florence, van Blitterswijk Clemens A, Groot Klaas de, Layrolle Pierre. Biomimetic hydroxyapatite coating on metal implant. J Am Ceramic Soc 2002;85:517–22.

[26] Ellingsen Jan Erik. A study on the mechanism of protein adsorption to TiO_2. Biomaterials 1991;12:593–6.

[27] Paital Sameer R, Dahotre Narendra B. Laser surface treatment for porous and textured Ca–P bio-ceramic coating on Ti–6Al–4V. Biomed Mater 2007;2:274–81.

[28] Greish Yaser E, Brown Paul W. Phase evolution during the formation of stoichiometric hydroxyapatite at 37.4 °C. J Biomed Mater Res B Appl Biomater 2003;67B:632–7.

[29] Liu Xuanyong, Ding Chuanxian, Chu Paul K. Mechanism of apatite formation on wollastonite coatings in simulated body fluids. Biomaterials 2004;25:1755–61.

[30] Yamashita Kimihiro, Oikawa Noriyuki, Umegaki Takao. Acceleration and deceleration of bone-like crystal growth on ceramic hydroxyapatite by electric poling. Chem Mater 1996;8:2697–700.

[31] Karanjai Malobika, Sundaresan Ranganathan, Mohan Tallapragada Raja Rama, Kashyap Bhagwati Prasad. Evaluation of growth of Ca–P ceramics on sintered Ti–Ca–P composites. Mater Sci Eng C 2008; 28:1401–7.

IOP Publishing Biomedical Materials

Biomed. Mater. 4 (2009) 015009 (10pp) doi:10.1088/1748-6041/4/1/015009

Fabrication and evaluation of a pulse laser-induced Ca–P coating on a Ti alloy for bioapplication

Sameer R Paital[1], Kantesh Balani[2], Arvind Agarwal[2] and Narendra B Dahotre[1]

[1] Department of Materials Science and Engineering, The University of Tennessee, Knoxville, TN 37996, USA

[2] Department of Mechanical and Materials Engineering, Florida International University, EAS 3400, Miami, FL 33174, USA

E-mail: ndahotre@utk.edu

Received 13 August 2008
Accepted for publication 8 October 2008
Published 19 November 2008
Online at stacks.iop.org/BMM/4/015009

Abstract

In the present paper, we demonstrate the feasibility of depositing a tailored calcium phosphate (Ca–P) coating on a Ti–6Al–4V substrate by using a pulsed Nd:YAG laser system. Different textures were obtained by varying the laser spot overlap with change in laser traverse speed. Surface roughness measurements using laser confocal microscopy indicated a decrease in roughness with increasing laser scan speed. X-ray diffraction studies revealed the formation of α-TCP, TiO_2, Ti and Al as the major phases. An instrumented nanoindenation technique used to study the mechanical properties of the coatings, revealed a very high hardness and Young's modulus of the coating surface as compared to the substrate. This further proved the retainment of the ceramic phase on the surface. Wear studies in a simulated biofluid (SBF) environment demonstrated an increased wear resistance of the coated samples as compared to the bare Ti–6Al–4V. Formation of an apatite-like layer after immersion in SBF for different time periods further demonstrated the bioactivity of the coated samples.

Introduction

Titanium and its alloys are widely used metallic materials for implant fabrication owing to their suitable mechanical properties, corrosion resistance and biocompatibility in the body environment [1–3]. These materials without any surface treatments are considered as bioinert materials [3]. Such inert implant materials do not provide a chemical or a biological bonding at the interface and as a result implant failure may take place due to relative motion and the progressive development of a fibrous capsule at the interface [4, 5]. Hence, Ca–P based nontoxic and bioactive coatings on Ti alloys are being extensively studied to improve the bone bonding and fasten the new bone regeneration at the interface. Further, such a ceramic layer may also act as a biological barrier to some of the toxic elements like vanadium and aluminum present in the frequently used implant grade Ti alloy Ti–6Al–4V [6, 7]. The various coating methodologies that are being studied at the lab scale are (1) plasma spray deposition [8–10], (2) pulsed laser physical vapor deposition [11, 12], (3) magnetron sputtering [13], (4) sol–gel based coatings [14], (5) electrodeposition [15] and (6) laser-induced coatings [16]. Plasma spray coating is the most commercially used method for orthopedics and dental applications, but it suffers from certain drawbacks such as poor adherence of the coating to the substrate and nonuniformity in morphology and crystallinity [17]. Further, most of these coating techniques also lack the ability to generate a textured surface simultaneously. It is well established that the surface textures can affect the cell morphology and cell behavior. A surface with a greater texture exposes more surface area for the interaction with proteins, which further modulates the cell interaction and thereby the organization of complex tissues such as bone [18]. Therefore, creating three-dimensional features or textures on the surface

 © 2009 IOP Publishing Ltd Printed in the UK

of a biomaterial to support cells and tissue growth is becoming a reality.

In a previous work done by Kurella *et al* [16] laser-induced direct melting of a Ca–P precursor on a Ti–6Al–4V substrate was carried out using a continuous wave Nd:YAG laser system. In a continuous wave Nd:YAG laser system, the output energy of the laser beam is constant with time. Here a systematic organization of calcium phosphate coating on the Ti-alloy substrate was obtained by effectively controlling the thermo-physical interactions during laser processing. In contrast, in a pulsed Nd:YAG laser system the laser energy is provided through intermittent delivery of pulses. These individual pulses were controlled for duty cycle (on–off time), frequency (number of pulsed delivered) and energy. Such control over selection of pulse parameters can provide more precise control over spatial and temporal modes of delivery of laser energy, which in turn can create far more different thermal conditions, microstructual and phase features within the laser–substrate interaction region than are obtained in the samples processed using a CW laser.

In the present work, such feasibility of simultaneous synthesis of a textured and bioactive Ca–P coating on the Ti–6Al–4V substrate using a pulsed Nd:YAG system has been demonstrated. In the first step using an air spray gun, only a green body of a uniform calcium phosphate tribasic precursor layer on the Ti–6Al–4V substrate is obtained. This precursor layer is neither well bonded nor has the kind of surface features desired for the final intended bioapplication. The actual metallurgical bonded coating and surface topography are obtained in one step by scanning this green body under the high intensity of a pulsed laser beam. Proper adjustments of the pulsed Nd:YAG laser parameters and operation mode are carried out for the first time by this group to achieve surface coatings by direct melting without any major ablation or material vaporization. Both macro- and micro/nano-scale features are obtained by such laser-induced direct melting. The micro/nano-scale features produced due to temporal and spatial variation of energy distribution within the beam can induce protein interaction, attachment and alignment with the substrate whereas the macro-scale features such as troughs, valleys and pores obtained by the laser spot overlap may aid cell attachment and bone ingrowth [16, 19–22]. Due to the shorter pulse widths, the associated cooling rate is extremely high as compared to a continuous wave operation. This may be helpful in retaining some metastable or amorphous phases of Ca–P beneficial for bioapplications. Further, such a high cooling rate during the laser–material interaction and the thermal expansion mismatch between the coating and/or modified surface region and the substrate may also result in a certain amount of trapped residual stresses in the material [23]. Although the study of residual stress was not the prime focus of the present work, the study of the influence of laser parameters on the residual stresses in a laser-coated Ca–P coating on the Ti alloy is an on-going parallel effort of the present group. The observations/results of these efforts will be presented in a separate paper in due course of time.

Table 1. Laser parameters used for the study.

Pulse width	0.5 ms
Pulse energy	4 J
Pulse repetition rate	20 Hz
Average power	80 W
Laser scan speed	36, 48, 66, 78, 102 cm min^{-1}
Focus position	0.8 mm above the surface of the sample
Spot diameter on the surface	900 μm
Input energy density	1887, 1415, 1029, 871, 666 J cm^{-2}
Pulse height	94% of the maximum lamp current
Pulse shape	Rectangular

Experimental details

Ti-alloy (Ti–6Al–4V) substrate coupons of dimensions 100 mm × 50 mm × 3 mm were cut from the rolled sheets using an abrasive cutter. The samples were then lightly polished using a 30 μm grit silicon carbide emery paper to remove dust and grease from the surface. The coupons were further washed and cleaned with acetone. Calcium phosphate tribasic ($Ca_5(OH)(PO_4)_3$) powder obtained from Fischer Scientific was taken as the precursor. The powder morphology was spherical with a unimodal distribution in the range of 10–30 μm. The powder was initially mixed in a proprietary water-based organic solvent LISI W15853 obtained from the Warren Paint and Color Company, Nashville, TN 37209, USA. This mixed slurry was then sprayed on the preheated coupons (~50 °C) using an air spray gun. The sprayed coupons were then air dried to remove the moisture. A uniform thickness of approximately 40 μm was maintained for all precoating deposits. The samples were then processed using a 400 W average power JK701 model pulsed Nd:YAG laser. A schematic of the laser system is shown in figure 1. The laser is equipped with a fiber optic beam delivery system to transfer the laser beam from the laser head to the material. The control panel for the laser allows the control of pulse height, pulse width, pulse repetition rate and pulse shape. The lens assembly is equipped with a 120 mm focal length convex lens, which gives a spot diameter of approximately 240 μm at the focus. The focused spot is kept at approximately 0.8 mm above the surface of the sample so as to have a spot size of approximately 900 μm on the surface. The processing parameters used for the above process are tabulated in table 1. The pulse width (0.5 ms), pulse energy (4 J), pulse repetition rate (20 Hz) and focal point (0.8 mm above the surface of the sample) are kept constant, and the laser scan speed was varied at 36, 48, 66, 78 and 102 cm min^{-1}. This linear scan speed is related to the spot overlap by the following equation:

$$(\text{spot diameter}) \times (1 - \text{spot overlap}) \times (\text{pulse frequency}) = \text{linear speed}.$$

Consequently, five different samples with spot overlap varying as 65%, 55%, 38%, 28% and 5.5% were obtained. A variation in the laser scan speed also varies as the residence time (the time taken by the laser to traverse a distance equivalent to the beam diameter) and thereby changes the input energy density.

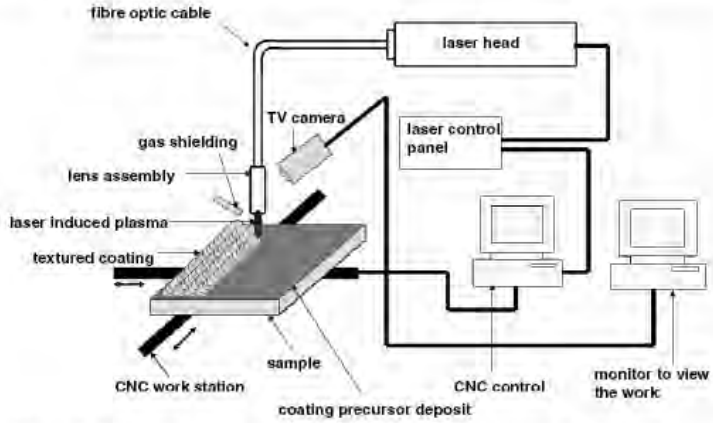


Figure 1. Schematic of the pulsed Nd:YAG laser system used for the coating process.

This input energy density, E (J cm^{-2}) for a pulsed laser can be calculated as per the following equation:

$$E = \frac{D \times P}{V \times A}, \tag{1}$$

where D is the laser spot diameter (cm), P is the laser average power (W), V is the laser traverse speed (cm s^{-1}) and A is the beam area (cm^2). Thus, the input energy density varied as 1887, 1415, 1029, 871 and 666 J cm^{-2} with increasing laser scan speed.

A Philips Norelco x-ray diffractometer (XRD) with CuKα radiation of wavelength 1.5418 Å was used to study the phases evolved in the coated region under various processing conditions. The XRD system was operated at 20 kV and 10 mA in a 2θ range of 20°–100° using a step size of 0.02° and count time of 1 s. Samples being processed at varying laser scan speeds, the effective heating rate and cooling rate will vary accordingly, and as a result there may be a variation in relative amount of phases. Based on XRD analysis, the weight fraction or volume fraction of these phases in a multiphase sample is given by the following equation [24]:

$$E_{\alpha,i} = K_m K_{p,\alpha,i} \frac{V_\alpha}{\mu_{l,s}} = K_m K_{p,\alpha,i} \frac{W_\alpha}{\rho_\alpha \mu_{m,s}}, \tag{2}$$

where $E_{\alpha,i}$ is the integrated intensity of the ith peak of the α phase which is given as

$$E_{\alpha,i} = \int_{\theta_i}^{\theta_n} I \, \mathrm{d}\theta, \tag{3}$$

where θ_i and θ_n are the diffraction angles at the starting and end point of the peak widths, V_α and W_α are the volume fraction and weight fraction of the α phase, respectively, ρ_α is the density of the α phase, $\mu_{l,s}$ and $\mu_{m,s}$ are the linear absorption and mass absorption coefficients of the multiphase mixture respectively, and K_m and $K_{p,\alpha,i}$ are the physical constant and the phase related factor. For a particular phase $\mu_{l,s}$, $\mu_{m,s}$, K_m and $K_{p,\alpha,I}$ can be taken as constants and presented together as another constant C. Therefore, a variation in integrated intensities can be taken as a measure of the variation in volume fraction of the phases as per the following equation:

$$V_\alpha = C \times E_{\alpha,i}. \tag{4}$$

Roughness measurements of the coated samples were carried out using Leica laser confocal microscopy. The roughness values are recorded in the form of *Ra* (defined as the arithmetic average of all points of the profile also called the center line average height) and *Rmax* (maximum individual roughness depth). The dimensional construction of the textured surface was also studied using Leica confocal laser microscopy. Microstructure and morphological evolutions of the coated samples were conducted using a LEO 1525 scanning electron microscope (SEM) and optical microscopy.

The mechanical integrity of the coated samples was evaluated using nanoindentation and wear performance in a simulated bioenvironment. A Hysitron® Triboindenter (Minneapolis, MN, USA) with a 100 nm radius Berkovich pyramidal tip was used for nanoindentation studies. The load cycle involved a peak load of 2000 μN ramped at 10 s, followed by a 3 s hold at the peak load, and consequent unloading in 10 s. The peak load was automatically adjusted by a nanoindenter to keep the segment times constant for loading, dwell and unloading. A minimum of ten indentations were performed across the polished cross section for each sample, thereby extracting data from three different locations with a test area of 20 μm × 10 μm. Young's modulus and hardness were calculated from the load–displacement curve using Oliver–Pharr analysis [25–27].

The wear performance of the coated samples in a simulated body environment was studied using a pin-on-disc wear tester with an arrangement for immersion of the pin and sample in SBF contained in a test cell attached to the tester. The SBF solution for wear studies was prepared by dissolving reagent grade chemicals in the following order: NaCl (8.026 g), $NaHCO_3$ (0.352 g), KCl (0.225 g), $K_2HPO_4.3H_2O$ (0.230 g), $MgCl_2.6H_2O$ (0.311 g), $CaCl_2$ (0.293 g) and Na_2SO_4 (0.072 g) into distilled water (700 ml). The fluid was then buffered at pH = 7.4 at 37 °C with tri-hydroxymethyl-aminomethane (6.063 g) and hydrochloric acid (40 ml). Since alumina (Al_2O_3) is used as a ceramic acetabular component which comes in contact with the femoral head, a 50 mm long and 3 mm diameter alumina pin was used to slide against the Ca–P coated specimens. The tip of the pin was polished flat

to have a close contact with the sample, and the SBF solution was maintained the whole time in the cell so that the specimen remains immersed throughout the test. The test was conducted at a normal load of 8.8 N and the wear cell rotating at a speed of 100 rpm or equivalent linear speed of 32 m min^{-1}. The total duration of the test was 100 min, and the weight loss for the sample was noted down for every 10 min.

The bone bonding ability or bioactivity of the coated samples was studied by examining the presence of apatite following immersion in SBF. Plastic containers were used to soak the samples in SBF for different time periods. The solution was refreshed every 24 h to maintain a pH of 7.4, and the temperature was maintained at 37 °C during the course of the test. The rate of apatite formation or the biomineralization rate as a dimensionless quantity can be calculated as per the following equation:

$$\text{Biomineralization rate} = \frac{W_f - W_i}{W_i}, \tag{5}$$

where W_f is the final weight after immersion and W_i is the initial weight before immersion in SBF.

Results and discussions

Surface morphology

An optical microscope image (figure 2(*a*)) of the cross section of the sample processed at a laser scan speed of 36 cm min^{-1} indicates a sound interface between the coating and substrate material. The surface of the coating demonstrated a porous morphology with wide pore size distribution (figure 2(*b*)). The variation in surface roughness with varying laser scan speed was evaluated using confocal laser microscopy. A two-dimensional overview of the coating (figure 3(*a*)) processed at a scan speed of 36 cm min^{-1} and the corresponding roughness profile along the randomly selected straight line (an inset, figure 3(*b*)) demonstrate the variation in roughness at various length scales. A three-dimensional image of the surface (an inset, figure 3(*c*)) represents the pits or the geometrically textured coating that is achieved by this process. A total of five random lines are selected to evaluate the variation in *Ra* and *Rmax* with the variation in laser scan speed. It can be observed that both *Ra* and *Rmax* followed a decreasing trend with increasing laser scan speed (figure 4). This is because with increasing laser scan speed the spot overlap decreases, which in turn results in reduced surface melting or less thermal effect at the surface, thereby producing a smoother surface finish. The formation of such geometrical textures may enhance biomineralization and induce cell proliferation and bone ingrowth under *in vivo* conditions.

Phase evolution

XRD analysis of phase evolution within the processed samples clearly indicated the presence of α-TCP, TiO_2, Ti and Al as the major phases for all laser scan speeds (figure 5). The formation of α-TCP is mostly due to the dehydration of the $Ca_5(OH)(PO_4)_3$ precursor during laser processing. This is a biocompatible phase as it can hydrolyze under physiological

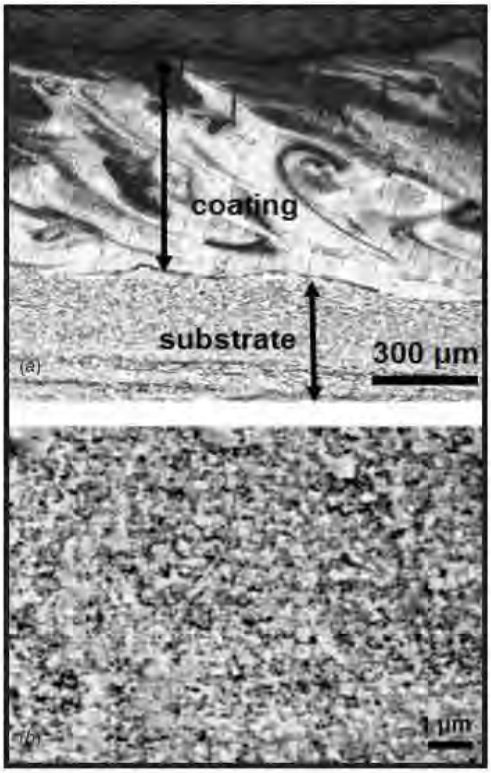


Figure 2. Sample processed at a laser scan speed of 36 cm min^{-1}: (*a*) optical cross sectional view and (*b*) SEM of the coating surface revealing a porous morphology with wide pore size distribution.

conditions to form a calcium-deficient hydroxyapatite [16, 28]. The formation of TiO_2 is attributed to the oxidation of the underlying substrate as the samples were processed under ambient conditions at extreme laser fluence of the order of 10^5–10^6 W cm^{-2}. TiO_2, being a hard and chemically stable ceramic phase, is expected to enhance beneficial corrosion and wear resistance under *in vivo* conditions. The existence of the $CaTiO_3$ phase is detected only at the higher laser scan speed (102 cm min^{-1}) within the range of speeds employed in the present work. This may be attributed to the interaction between the Ca-rich phases such as calcium phosphate tribasic and TiO_2 as per the following reaction [16]:

$$2[Ca_5(OH)(PO_4)_3]_{(l)} \pm TiO_2 \rightarrow CaTiO_3 \pm 3\alpha\text{-TCP} \pm H_2O(g)\uparrow.$$

The formation of $CaTiO_3$ during laser cladding of HA on Ti–6Al–4V is also previously reported [29]. Furthermore, the evolution of CaO may also take place through the partial decomposition of α-TCP as per the following intermediate reactions [29]:

$$\alpha\text{-TCP} \pm TiO_2 \rightarrow CaTiO_3 \pm \alpha\text{-}Ca_2P_2O_7$$

$$\alpha\text{-}Ca_2P_2O_7 \pm Ti \rightarrow CaTiO_3 \pm CaO \pm P_2O_{3(g)}\uparrow.$$

Although the formation of CaO was highly anticipated during laser direct melting of the calcium phosphate tribasic powder,

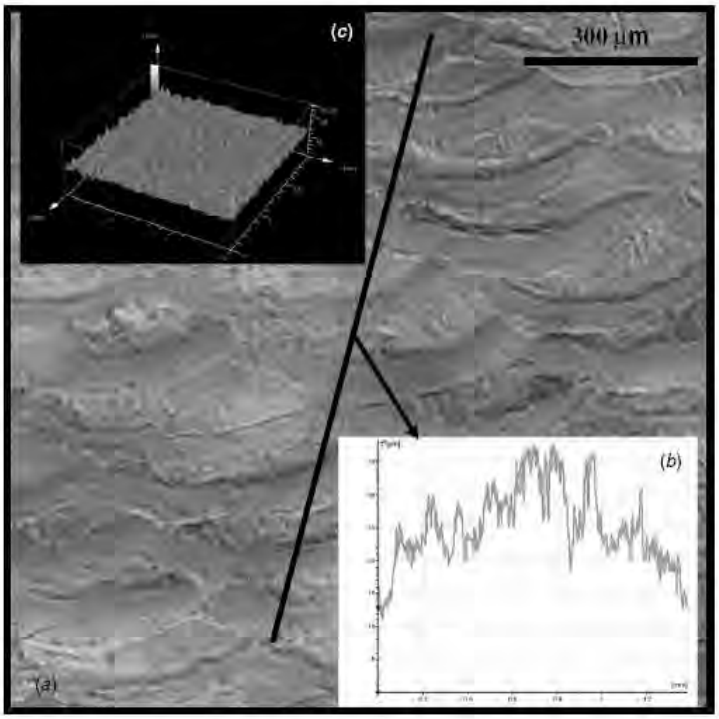


Figure 3. Sample processed at a laser scan speed of 36 cm min^{-1}: (*a*) two-dimensional image, (*b*) corresponding roughness profile along the straight line picked at random location, and (*c*) the three-dimensional image of the coating surface.

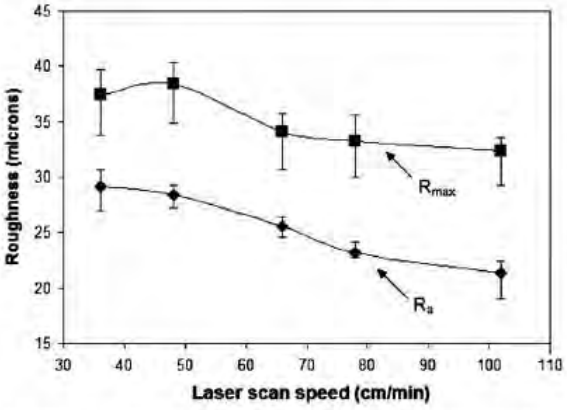


Figure 4. Variation in surface roughness parameters (with standard deviations) as a function of laser scan speed.

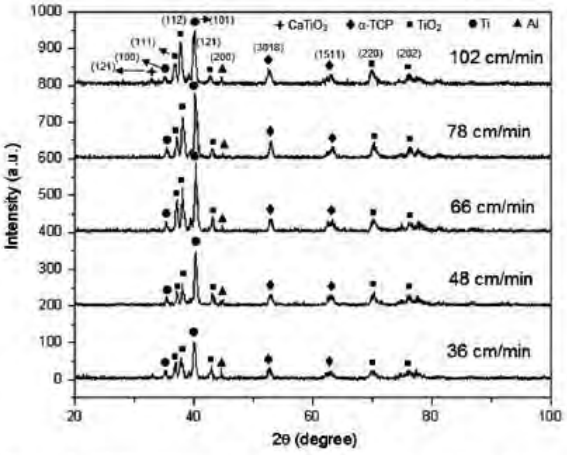


Figure 5. XRD patterns of the samples processed at varying laser scan speeds.

in the present case the presence of such a phase was not observed from the XRD peaks (figure 5). Since CaO is water soluble through the formation of hydroxide ($Ca(OH)_2$) [30], and the samples were thoroughly cleaned prior to XRD studies, the absence of such a phase was greatly justified. The removal of CaO from the coating by water rinsing is desired to avoid its entering into the body fluid. Similar dissolution nature of the CaO phase was also previously reported in the work done by Kurella *et al* [16] and Gu *et al* [31] during the studies related to Ca–P coatings on the Ti-alloy substrate for bioapplication.

The variation in volume fraction of each of the phases with varying laser input energy density was calculated as per equations (2), (3) and (4) discussed in the experimental section. The highly resolved TiO_2 (1 1 2) and (2 2 0), α-TCP (3 0 1 8) and (1 5 1 1), and $CaTiO_3$ (1 2 1) peaks are taken

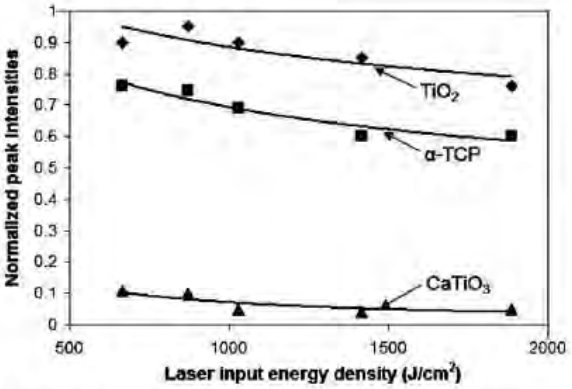


Figure 6. Variation in volume fraction of the phases with varying laser input energy density.

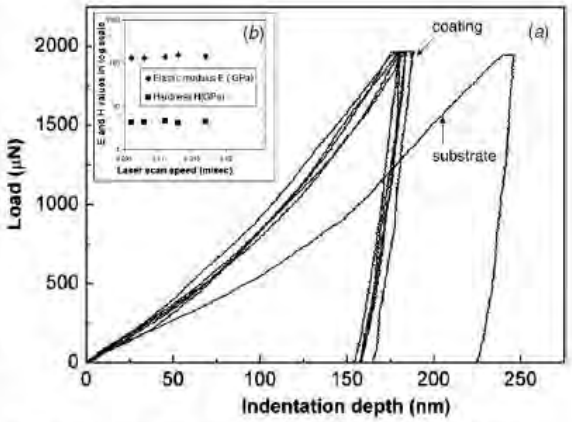


Figure 7. Nanoindentation data: (*a*) characteristic loading and unloading curves for the coating and the substrate, and (*b*) variation in E and H of the coatings as a function of laser scan speed.

for measurement. The integrated intensity of each peak is normalized by dividing by the integrated intensity of the Ti (1 0 1) peak. An increase in the volume fraction of TiO_2, α-TCP and $CaTiO_3$ phase with increasing laser scan speed is realized (figure 6). As the energy density decreased from 1887 J cm^{-2} to 666 J cm^{-2} with increasing laser scan speed, the surface experienced a lower temperature rise due to a shorter residence time. In contrast, during exposure to the higher temperature corresponding to the longer residence time (slow processing speeds) dehydroxylation of the precoat Ca–P material may have taken place [32]. Such dehydroxylation would create a barrier for the nucleation of crystalline phases, and as a result, a reduction in the amount of various phases at lower scan speeds (higher energy densities) is observed.

Mechanical characterization

Physical stability of the coating when it comes in contact with the body plasma was important. Nanoindentaton and wear in a SBF environment were carried out to assess the mechanical behavior of the coatings. The characteristic nanoindentation loading and unloading curves for different scan speeds and the variation in E and H with varying laser scan speed for the coatings are presented in figure 7 and in its inset, respectively. In general, all coatings possessed higher elastic modulus (~145 GPa) and hardness (~4.4 GPa) than the substrate material ($E \sim 120$ GPa and $H \sim 2.20$ GPa), and they do not differ substantially from each other (elastic modulus: ±20 GPa and hardness: ±0.59 GPa). Such minor variation in these mechanical properties can be attributed to similar types and amounts of phases evolved in the coating under the processing parameters employed in the present work (figure 5).

A good bioceramic coating is expected to exhibit resistance to attack by the body fluids and low metal ion release. The metal ions released through the chemical interactions and the metal particles separated through the wear mechanism are perceived as foreign elements in the body environment and may lead to osteolysis. Osteolysis results in loosening of the implant and creation of a fibrous capsule

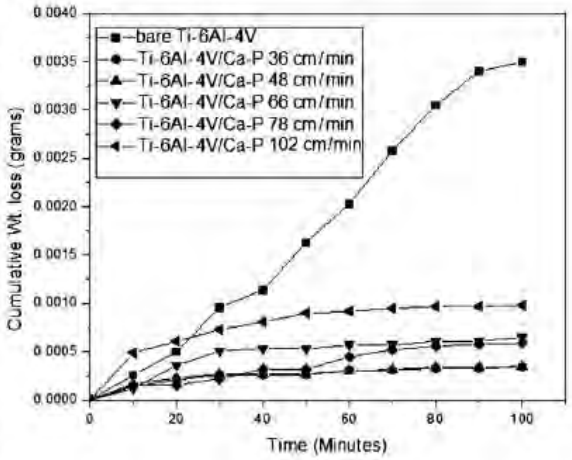


Figure 8. Cumulative weight loss for the sample processed at varying laser scan speed and bare Ti–6Al–4V in a SBF environment.

at the interface. Hence, evaluating a wear performance of the coatings in a SBF condition was vital. It is observed (figure 8) that the cumulative weight loss of the bare Ti–6Al–4V after 100 min of wear test is 3–10 fold (0.0035 g) higher compared to the Ca–P coatings (ranging from 0.000 34 g to 0.000 98 g for laser scan speeds varying from 36 cm min^{-1} to 102 cm min^{-1}, respectively) whereas the cumulative weight loss among various laser treated coatings varies between ±4 times (figure 8). Such a large variation may be due to the variation in the nature of the interfacial bond between the coating and substrate.

The effect of laser surface melting of Ti–6Al–4V on corrosion and wear performance was also previously reported by this group [33, 34]. The laser surface treatment of the alloy indicated significantly improved corrosion resistance in a biosimulated fluid compared to an untreated alloy. Although the treatment provided improved sliding wear resistance in the physiological solution for the laser surface treated

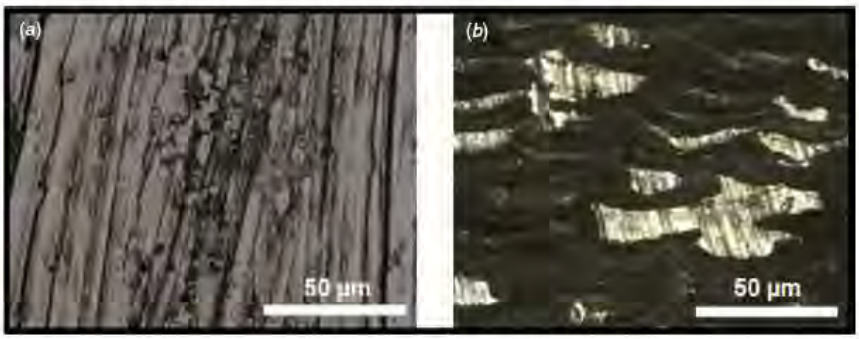


Figure 9. Optical microscopic image of the wear tracks on (*a*) bare Ti-6Al-4V and (*b*) Ca–P coatings processed at a laser scan speed of 102 cm min^{-1}.

alloy compared to the untreated alloy, the improvement was significantly less compared to the wear resistance of the Ti alloy coated with Ca–P using a laser-based technique. Optical microscopy images (figure 9) of the wear tracks on bare Ti–6Al–4V and Ca–P coated Ti–6Al–4V illustrate the severity of damage on both surfaces. The typical appearance of surface damage in bare Ti–6Al–4V can be attributed to a mixed effect of adhesion and abrasion wear mechanisms. The flat mating surfaces of the pin and bare Ti–6Al–4V would have resulted in adhesion and cohesion at the interface due to sliding and/or vibratory motions. As a result, the damage due to adhesive wear would result in the transfer of adhesively bound particles from one surface to the other. Progressive accumulation and strong adhesion of more material finally lead to increased abrasive wear and more material removal by ploughing. Thus, the significant cumulative weight loss or low sliding wear resistance of bare Ti–6Al–4V can be associated with this mutual effect of the wear mechanism. On the other hand, the appearance of surface damage in the Ca–P coating is characteristic of an abrasion wear mechanism. In addition to the presence of hard ceramic phase on the surface, the physical texture also contributed to high sliding wear resistance of the Ca–P coating. It is known that introduction of surface textures in the form of depressions and undulations can improve the tribological properties [35]. In that case, the textured Ca–P coating acts as a reservoir for the SBF and reduces the contact between the two surfaces. Thus the only wear mechanism associated with the textured coating is slight ploughing of the material when the pin comes in contact with the undulations. For all these reasons, the textured Ca–P coatings exhibited very low cumulative weight loss or high sliding wear resistance.

Test for bioactivity

The bone bonding ability of an artificial material can be evaluated by its ability to form an apatite-like phase following immersion in SBF having ionic concentrations equal to those of human blood plasma [36, 37]. In the present case, an *in vitro* bioactivity test was carried out by soaking the sample processed at a laser scan speed of 102 cm min^{-1} in SBF, for time periods of 24, 48, 72 and 96 h. This particular sample was chosen for the bioactivity test for the reason that it contains all the biocompatible phases ($CaTiO_3$, α-TCP and TiO_2) in relatively greater amounts than the other samples. The formation of a globular apatite-like layer following immersion in SBF for different time periods can be realized from the SEM micrographs (figure 10). This thin apatite-like layer exhibits some cracks which may be due to the removal of moisture during drying [38]. Another important phenomenon that can be observed is the reduced dimensions of the islands between cracks on the samples immersed in SBF from 48 to 96 h. This is either due to the increased accumulation of an apatite-like layer or enhancement in biomineralization with increased immersion time. The biomineralization rate as a dimensionless quantity was computed as per equation (5) and presented in figure 11 as a function of immersion time for both bare Ti–6Al–4V and the sample processed at a laser scan speed of 102 cm min^{-1}. The bare Ti–6Al–4V sample was polished using a 800 grit emery paper to achieve a surface roughness ($Ra \sim 23$ μm) equivalent to that of the laser-processed sample. The biomineralization rate of laser-coated Ca–P followed an exponential relation ($y = 10^{-4}\, e^{0.04x}$) with immersion time. In contrast, the biomineralization rate of bare Ti–6Al–4V followed a nearly linear fit ($y = 6 \times 10^{-6}\, x - 10^{-4}$) with immersion time. This 2–8 fold increase in bioactivity of the laser-coated sample for the immersion time ranging from 24 h to 96 h can be attributed to an alteration in surface chemistry. This can possibly be explained as per the following reactions.

The anatase TiO_2 phase present can easily form an O–H bond under wet conditions [39]. Due to the presence of these negatively charged OH^- ions, it reacts easily with the Ca^{2+} ions present in SBF and forms calcium titanate. As the surface gets accumulated with the positively charged Ca^{2+} ions, it reacts with the phosphate anions HPO_4^{2-} in SBF to form an amorphous calcium phosphate. This, being a metastable phase, eventually transforms to crystalline hydroxyapatite [40]. In contrast, the α-TCP phase present can easily hydrolyze under physiological conditions and form a calcium-deficient HA as per the following equation [41]:

$$3\alpha\text{-}Ca_3(PO_4)_2 \xrightarrow{H_2O} Ca_9HPO_4(PO_4)_5OH.$$

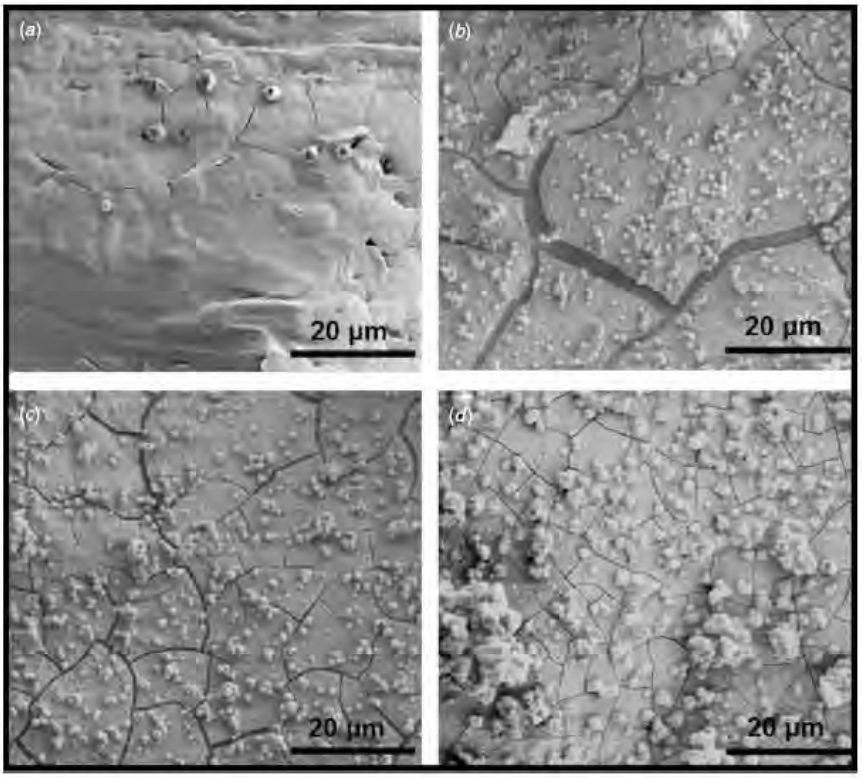


Figure 10. SEM micrographs revealing the formation of a globular apatite-like layer following immersion in SBF for different time periods: (*a*) 24 h, (*b*) 48 h, (*c*) 72 h and (*d*) 96 h (for samples processed at a laser scan speed of 102 cm min^{-1}).

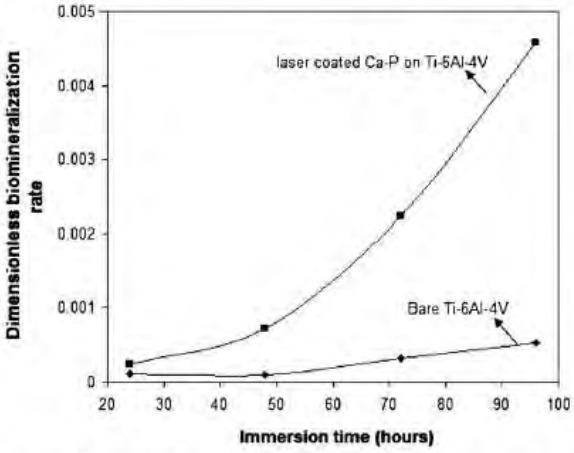


Figure 11. Variation in the biomineralization rate as a function of immersion time in SBF (for samples processed at a laser scan speed of 102 cm min^{-1}).

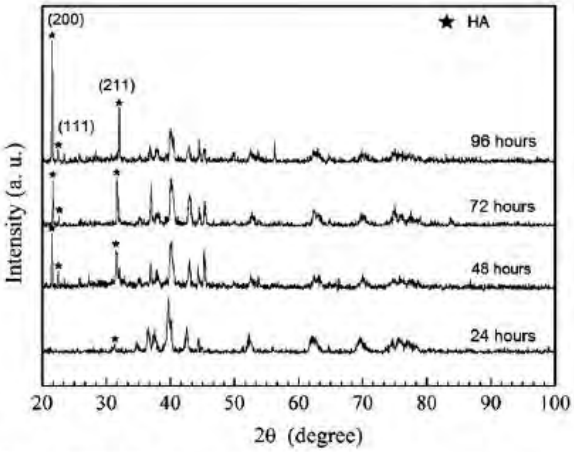


Figure 12. XRD patterns of the samples following immersion in SBF for different time periods (for samples processed at a laser scan speed of 102 cm min^{-1}).

As discussed above the $CaTiO_3$ phase detected from XRD studies for this sample (figure 5) also can react with the phosphate ions to form a metastable amorphous Ca–P and finally transforms to a stable crystalline HA [42, 43].

XRD studies of the laser-coated sample (figure 12) following immersion in SBF for different time periods also revealed the formation of a crystalline apatite-like phase. Maxima attributable to this phase at $2\theta \sim 22.0°$, 22.9° and

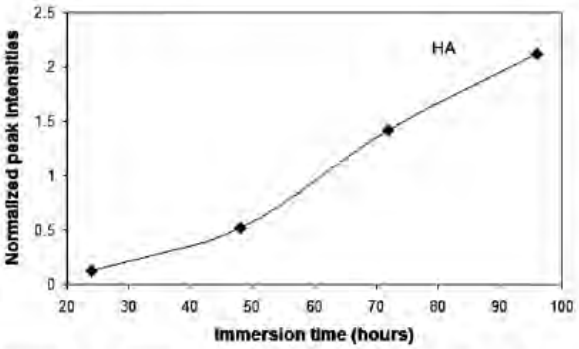


Figure 13. Variation in volume fraction of HA with varying laser scan speeds as a function of immersion time in SBF for the sample processed at a laser scan speed of 102 cm min^{-1}.

31.75°, and corresponding to planes (2 0 0), (1 1 1) and (2 1 1), respectively, are confirmed from the JCPDS 09-0432. It can be observed that there is an increased crystallographic texturing along the (2 0 0) and (2 1 1) planes with increasing immersion time. This is possibly due to both the increase in volume fraction of the apatite-like phase and crystal growth along the *c*-axis. The variation in normalized peak intensities of the HA peaks is calculated by dividing the integrated intensities of the HA peaks by the integrated intensity of the Ti (1 0 1) peak. An increase in normalized peak intensity (figure 13) also suggests an increase in volume fraction with increasing immersion time.

Conclusions

In the present work, a novel pulsed Nd:YAG laser-induced direct melting technique is established to synthesize physically textured Ca–P coatings on Ti–6Al–4V. It is further demonstrated that the surface roughness or topographic cues can be controlled by varying the spot overlap with varying laser scan speed. XRD studies of the laser-processed samples showed an increase in volume fraction of TiO_2, Ti and α-TCP phases with increasing laser scan speed. The higher elastic modulus ($E \sim 145$ GPa) and hardness ($H \sim 4.5$ GPa) of the coating assessed using the instrumented nanoindentation technique confirmed the retention of a hard ceramic phase. Wear studies in a SBF environment indicated a 4–10 fold increase in sliding wear resistance of the Ca–P coated samples compared to bare Ti–6Al–4V. *In vitro* bioactivity of the coated samples was demonstrated by the formation of an apatite-like phase following immersion in SBF. The biomineralization rate as a dimensionless quantity showed an exponential increase in biomineralization with increasing immersion time for the laser coated Ca–P samples compared to bare Ti–6Al–4V of equal average roughness which followed a linear relation. There is a 2–8 fold increase in biomineralizaton for the laser-coated Ca–P samples compared to bare Ti–6Al–4V. This enhancement in biomineralization for laser-coated Ca–P samples can therefore be attributed to the alteration in surface chemistry following laser processing.

References

[1] Liu X, Chu P K and Ding C 2004 Surface modification of titanium, titanium alloys, and related materials for biomedical applications *Mater. Sci. Eng.* R **47** 49–121
[2] Metikoš-Huković M, Tkalčec E, Kwokal A and Piljac J 2003 An *in vitro* study of Ti and Ti-alloys coated with sol–gel derived hydroxyapatite coatings *Surf. Coat. Technol.* **165** 40–50
[3] Lu X, Zhao Z and Leng Y 2007 Biomimetic calcium phosphate coatings on nitric-acid-treated titanium surfaces *Mater. Sci. Eng.* C **27** 700–8
[4] Hench L L and Polak J M 2002 Third-generation biomedical materials *Science* **295** 1016–7
[5] Hench L L and Newnham R E 1991 Bioceramics: from concept to clinic *J. Am. Ceramic. Soc.* **74** 1487–510
[6] Choubey A, Balasubramaniam R and Basu B 2004 Effect of replacement of V by Nb and Fe on the electrochemical and corrosion behavior of Ti-6Al-4V in simulated physiological environment *J. Alloys Compounds* **381** 288–94
[7] Khan M A, Williams R L and Williams D F 1999 The corrosion behavior of Ti-6Al-4V, Ti-6Al-7Nb and Ti-13Nb-13Zr in protein solutions *Biomaterials* **20** 631–7
[8] Ji H, Ponton C B and Marquis P M 1992 Microstructural characterization of hydroxyapatite coating on titanium *J. Mater. Sci. Mater. Med.* **3** 283–7
[9] Tsui Y C, Doyle C and Clyne T W 1998 Plasma sprayed hydroxyapatite coatings on titanium substrates: part 2. Optimization of coating properties *Biomaterials* **19** 2031–43
[10] Inagaki M and Kameyama T 2007 Phase transformation of plasma-sprayed hydroxyapatite coating with preferred crystalline orientation *Biomaterials* **28** 2923–31
[11] Nelea V, Ristoscu C, Chiritescu C, Ghica C, Mihailescu I N, Pelletier H, Mille P and Cornet A 2000 Pulsed laser deposition of hydroxyapatite thin films on Ti-5Al-2.5Fe substrates with and without buffer layers *Appl. Surf. Sci.* **168** 127–31
[12] Wang C K, Chern Lin J H, Ju C P, Ong H C and Chang R P H 1997 Structural characterization of pulsed laser-deposited hydroxyapatite fim on titanium substrate *Biomaterials* **18** 1331–8
[13] Boyd A R, Meenan B J and Leyland N S 2006 Surface characterization of the evolving nature of radio frequency magnetron sputter deposited calcium phosphate thin films after exposure to physiological solution *Surf. Coat. Technol.* **200** 6002–13
[14] Haddow D B, James P F and Vannoort R 1998 Sol–gel derived calcium phosphate coatings for biomedical applications *J. Sol-gel Sci. Technol.* **13** 261–5
[15] Shirkhanzadeh M 1991 Bioactive calcium phosphate coatings prepared by electrodeposition *J. Mater. Sci. Lett.* **10** 1415–7
[16] Kurella A and Dahotre N B 2006 Laser induced hierarchical calcium phosphate structures *Acta Biomater.* **2** 677–83
[17] Gracia-Sanz F J, Mayor M B, Arias J L, Pou J, Leon B and Perez-Amor M 1997 Hydroxyapatite coatings: a comparative study between plasma-spray and pulsed laser deposition techniques *J. Mater. Sci. Mater. Med.* **8** 861–5
[18] Dee K C, Puleo D A and Bizios R 2008 *Tissue Biomaterial Interactions* 2nd edn (NewYork: Wiley-Liss) chapter 3
[19] Stevens M M and George J H 2005 Exploring and engineering the cell surface interface *Science* **310** 1135–8
[20] Kasemo B 2002 Biological surface science *Surf. Sci.* **500** 656–77
[21] Assender H, Bliznyuk V and Porfyrakis K 2002 How surface topography relates to materials properties *Science* **297** 973–6

[22] Lutolf M P and Hubbell J A 2005 Synthetic biomaterials as instructive extracellular microenvironments for morphogenesis in tissue engineering *Nat. Biotechnol.* **23** 47–55

[23] Kadolkar P B, Watkins T R, De Hosson J Th M, Kooi B J and Dahotre N B 2007 State of residual stress in laser-deposited ceramic composite coatings on alluminium alloys *Acta Mater.* **55** 1203–14

[24] Krawitz A D 2001 *Introduction to Diffraction in Materials Science and Engineering* (New York: Wiley) 1st edn

[25] Pharr G M 1998 Measurement of mechanical properties by ultra low indentation *Mater. Sci. Eng.* A **253** 151–9

[26] Li X and Bhusan B 2002 A review of nanoindentation continuous stiffness measurement technique and its applications *Mater. Charact.* **48** 11–36

[27] Chen X, Yan J and Karlsson A M 2006 On the determination of residual stress and mechanical properties by indentation *Mater. Sci. Eng.* A **416** 139–49

[28] Paital S R and Dahotre N B 2007 Laser surface treatment for porous and textured Ca-P bio-ceramic coating on Ti-6Al-4V *Biomed. Mater.* **2** 274–81

[29] Lusquiños F *et al* 2003 Calcium phosphate coatings obtained by Nd:YAG laser cladding: physicochemical and biological properties *J. Biomed. Mater. Res.* **64A** 630–7

[30] Bang S W, Lec R M, Genco J M and Ransdell J C 1993 Acoustic emission chemical sensor *IEEE Ultrasonics Symp. Proc.* 439–43

[31] Gu Y W, Khor K A and Cheang P 2003 *In vitro* studies of plasma sprayed hydroxyapatite/Ti-6Al-4V composite coating in simulated body fluid (SBF) *Biomaterials* **24** 1603–11

[32] Sun L, Berndt C C and Grey C P 2003 Phase, structural and microstructural investigations of plasma sprayed hydroxyapatite coatings *Mater. Sci. Eng.* A **360** 70–84

[33] Singh R, Kurella A and Dahotre N B 2006 Laser surface modification of Ti-6Al-4V: wear and corrosion characterization in simulated biofluid *J. Biomater. Appl.* **21** 49–73

[34] Singh R, Chowdhury S G, Tiwari S K and Dahotre N B 2008 Laser surface processing of Ti-6Al-4V in gaseous nitrogen: corrosion performance in physiological solution *J. Mater. Sci: Mater. Med.* **19** 1363–9

[35] Pettersson U and Jacobson S 2003 Influence of surface texture on boundary lubricated sliding contacts *Tribol. Int.* **36** 857–64

[36] Lu X and Leng Y 2005 Theoretical analysis of calcium phosphate precipitation in simulated body fluid *Biomaterials* **26** 1097–108

[37] Pecheva E V, Pramatarova L D, Maitz M F, Pham M T and Kondyuirin A V 2004 Kinetics of hydroxyapatite deposition on solid substrates modified by sequential implantation of Ca and P ions: part I. FTIR and Raman spectroscopy study *Appl. Surf. Sci.* **235** 176–81

[38] Habibovic P, Barrere F, van Blitterswijk C A, Groot K and Layrolle P 2002 Biomimetic hydroxyapatite coating on metal implant *J. Am. Ceram. Soc.* **85** 517–22

[39] Ellingsen J E 1991 A study on the mechanism of protein adsorption to TiO_2 *Biomaterials* **12** 593–6

[40] Kokubo T, Matsushita T and Takadama H 2007 Titania-based bioactive materials *J. Eur. Ceram. Soc.* **27** 1553–8

[41] Grish Y E and Brown P W 2003 Phase evolution during the formation of stoichiometric hydroxyapatite *J. Biomed. Mater. Res. Part B, Appl. Biomater.* **67B** 632–7

[42] Wiff J P, Fuenzalida V M, Arias J L and Fernandez M S 2007 Hydrothermal-electrochemical $CaTiO_3$ coatings as precursor of biomimetic calcium phosphate layer *Mater. Lett.* **61** 2739–43

[43] Takadama H, Kim H-M, Kokubo T and Nakamura T 2001 XPS study of the process of apatite formation on bioactive Ti-6Al-4V alloy in simulated body fluid *Sci. Technol. Adv. Mater.* **2** 389–96

IOP PUBLISHING BIOMEDICAL MATERIALS
Biomed. Mater. 2 (2007) 274–281 doi:10.1088/1748-6041/2/4/011

Laser surface treatment for porous and textured Ca–P bio-ceramic coating on Ti–6Al–4V

Sameer R Paital and Narendra B Dahotre

Department of Materials Science and Engineering, University of Tennessee, Knoxville, TN 37996, USA

E-mail: ndahotre@utk.edu

Received 2 August 2007
Accepted for publication 24 October 2007
Published 13 November 2007
Online at stacks.iop.org/BMM/2/274

Abstract

In the present paper the feasibility of depositing a porous calcium phosphate (CaP) bio-ceramic coating using a continuous wave Nd:YAG laser on a Ti–6Al–4V substrate has been demonstrated. The advantages offered by such porous bio-ceramic coating are its inertness combined with the mechanical stability of the highly convoluted interface that develops when bone grows into the pores of ceramic. The formation of different phases with varying laser fluences is studied using x-ray diffraction (XRD). A quantitative estimation of the crystallite size and relative amounts of Ti and other predominant phases such as TiO_2 and α-tricalcium phosphate (α-TCP) were obtained. An increase in the crystallite size with increasing laser fluence is observed for all the above three phases. It is observed that TiO_2 is the predominant phase for all laser fluences and there is an increase in the α-TCP phase with increasing laser fluence. Surface porosity measurements indicated a decreasing trend with increasing laser fluence. Microhardness measurements in the cross section of samples showed a maximum hardness within the coating. The bioactivity of the coatings was further demonstrated by the formation of an apatite-like layer on the surface of the sample after being immersed in a simulated biofluid.

1. Introduction

Human bone typically consists of 60% mineral phases, 25% water, and the rest as organic material. These mineral phases essentially consist of calcium, phosphate, magnesium, carbonate, hydroxyl, chloride, fluoride and citrate ions [1]. Hence calcium phosphate is regarded as an essential mineral in the human body [1, 2]. This gives an indication why there is intensified research in producing calcium phosphate coatings for bio-implant applications. Calcium phosphate being a ceramic material it has inferior mechanical properties such as low plasticity, fatigue and creep resistance. Therefore it cannot be used as sintered products for load-bearing applications such as hip-joint prosthesis. Hence people have tried to explore the coatings of calcium phosphate on various metallic and non-metallic substrates. Work done by Kim *et al* developed calcium phosphate coatings on a zirconia scaffold [3]. Shih and co-workers deposited calcium phosphate coatings by an electrolytic method on Ti–6Al–4V [4]. Blalock and co-workers deposited calcium phosphate coatings using an ion-beam-assisted deposition system on a titanium substrate [5]. Thin films of calcium phosphate coatings can also be deposited using a KrF excimer-pulsed laser deposition system on a Ti–6Al–4V substrate [6]. Ti–6Al–4V is chosen as the most commonly used substrate as it has an excellent fatigue strength (~550 MPa), tensile strength (~860 MPa), yield strength (~790 MPa at 0.2% offset), corrosion resistance and biocompatibility. Even though the plasma spray coating is the most commercially used technique, it suffers from certain demerits such as lower adhesion strength at the coating and substrate interface and lack of uniformity of the coating [7, 8]. Therefore various other techniques such as ion-beam-assisted deposition [5], pulsed laser deposition [6], electrolytic deposition [4], magnetron sputtering [9], etc have been employed for these kinds of coatings. In the present work, attempts were made to demonstrate the formation of a surface porous and textured calcium phosphate coating on a

Ti–6Al–4V substrate by laser-assisted melting of the precursor using a continuous wave Nd:YAG system.

An essential requirement for cement-less implants is to osseointegrate rapidly, so as to avoid the risks of accidental early load which may act on the implant and cause excessive relative displacement at the host bone interface. This in turn inhibits the formation of bone and osseointegration. Several factors which affect the strength of fixation and osseointegration include (1) implant topography, (2) surface chemistry, (3) nature of the host site and (4) the stress/strain field acting on early repair tissues [10]. The implant topography needs to be engineered in a way to induce minimum stress and create a certain amount of mechanical stimulation on the surrounding bone so that there is no bone loss during the early days of implantation and osseointegration takes place rapidly. This can be achieved by creating pits on the coated surface. According to Hansson and Norton the interfacial shear strength at the interface depends on the packing density and size and shape of the pits [10]. They proposed a very high packing density of pits of favorable size and shape so as to have the maximum shear strength at the interface and a minimum peak stress on the surrounding bone. Of the different shapes investigated, they proposed a half spherical and square shape of a particular size to have the highest retention capacity. The surface chemistry is brought to change by producing coatings of biocompatible materials such as zirconia, calcium phosphates, hydroxyapatite (HA), glass ceramics, etc. As far as the nature of the host site is concerned porous and inert bio-ceramic implants are considered to be critical for tissue integration. These interconnecting pores facilitate rapid bone ingrowth by providing appropriate conditions during tissue healing such as adequate blood supply, osteogenic potential of host tissues and limited movement of the implant [10].

Shimko *et al* [11] showed that tantalum scaffolds with a large range of porosities were found to have fluid flow and mechanical characteristics similar to that of human, bovine and porcine trabecular bone from a variety of anatomical locations. Further work done by Shimko and Nauman [12] developed a porous scaffold from poly(methyl methacrylate) (PMMA), and showed no cytotoxic effect by *in vitro* culture with marrow-derived bone cells. Wen *et al* [13, 14] fabricated porous Ti and Mg foams by powder metallurgical process for bone substitute applications. They attributed the formation of these micropores to volume shrinkage during sintering. Charriere and co-workers fabricated HA cement scaffolds with micro porosity of a controlled size and shape using a solid freeform fabrication process (SFF) by an inkjet system [15]. In all the above cases, the scaffolds are made of either a completely ceramic material, metallic materials or polymeric materials. As discussed earlier for extreme load-bearing conditions scaffolds made from ceramic materials and polymeric materials cannot be the final choice as they possess inferior mechanical properties as compared to metallic materials. But metallic scaffolds may be comparatively less biocompatible than calcium-phosphate-based ceramic material. Therefore, in the present work, a laser-based coating technology is introduced by which a geometrically textured and surface porous calcium phosphate coat on the Ti–6Al–4V substrate is made. Laser is the preferred choice as it has several advantages associated with it: (1) it is a non-contact process; (2) the high intensity and directionality of a laser beam allows a completely localized treatment without affecting the bulk of the properties; (3) the monochromaticity of the laser also allows control of the heat-affected zone; (4) laser beams can also be allowed to travel at great speeds which cannot be achieved by any mechanical tools or conventional heat sources [16].

2. Experimental details

Ti–6Al–4V substrate coupons of dimensions 100 mm × 50 mm × 3 mm were cut from the rolled sheets using an abrasive cutter. They were then polished using a 600 grit silicon carbide emery paper to produce a rough surface having R_a of approximately 0.5 μm. The coupons were then washed with water followed by acetone. Commercially available calcium phosphate tribasic, $Ca_5(OH)(PO_4)_3$ powder obtained from Fisher Scientific was taken as the precursor. The powder morphology was spherical with unimodal distribution in the range of 10–30 μm for diameter. The powder was mixed with a proprietory water-based organic solvent and sprayed using an air spray gun on the preheated (∼50 °C) Ti–6Al–4V coupons. The sprayed coupons were heated at 100 °C for approximately 2–3 min to remove the moisture from the predeposit. A uniform thickness of 40 μm was maintained for all predeposit coatings. The predeposited sample surfaces were processed using a 2.5 kW Hobart continuous wave Nd:YAG laser equipped with a fiber optic beam delivery system. The laser operates in the infrared region with a wavelength of 1064 nm. Parallel tracks with an overlap of 15% were laid by the laser beam focused 0.5 mm above the surface of the sample. The fiber equipped with the laser system is interfaced with an end effector that houses a set of spherical and cylindrical lenses. A combination of spherical and cylindrical lenses is put together to shape the laser beam output into a spot size of approximately 3.5 mm at focus. As the beam size at focus was 3.5 mm, defocusing it by 0.5 mm will have a spot size of approximately 3.8 mm on the surface of the sample. The samples were then processed with argon as cover gas at a fixed laser traverse speed of 200 cm min^{-1} and varying powers of 500, 600, 700, 800, 900 and 1000 watts corresponding to laser fluences of 503, 603, 704, 805, 905 and 1006 J cm^{-2}, respectively.

The phase evolution studies in processed sample were conducted using an x-ray diffraction (XRD) technique. A Philips Norelco X-ray Diffractometer with Cu-Kα radiation of a wavelength of 1.5418 Å was used for XRD study. The XRD system was operated at 20 kV and 10 mA in a 2θ range of 20°–100° using a step size of 0.02° and a count time of 1 s. The observations of microstructure variation and depth of the heat-affected zone due to the laser surface treatment were done in the cross section of the samples. The samples in cross section were prepared by polishing with emery papers of different grits ranging from 200 μm to 1000 μm in succession followed by disc polishing with

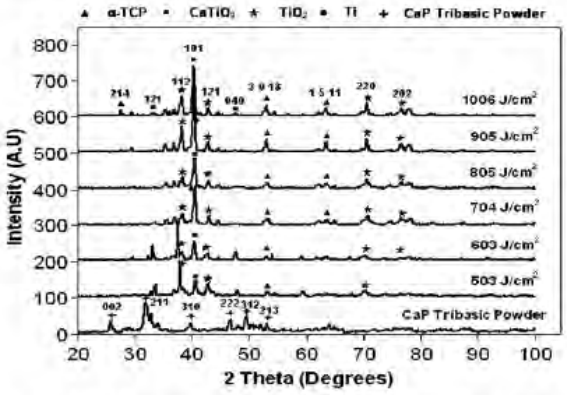


Figure 1. XRD patterns of the samples processed at different laser powers.

colloidal silica of 0.3 μm and 0.05 μm to get a mirror-finished surface. The polished samples were cleaned with acetone and etched with 5 vol% HF, 3 vol% HNO_3 and 92 vol% H_2O for 10–20 s by immersion etching to reveal the microstructural features. Microstructure and morphological observations were conducted using a LEO 1525 scanning electron microscope (SEM). The surface porosity measurements were carried out using the ImageJ software. As the porosity has to be calculated at the surface of the samples, the samples were cleaned thoroughly using acetone in an ultrasonic cleaner so as to remove all kinds of trapped impurities. Further, all the SEM images were initially converted into binary, and based on visual observations the threshold was kept at 190 for a scale of 0–256 where 0 indicates complete white and 256 indicates complete black. Over that a total of five measurements each were taken from different areas for a particular processing condition so as to arrive at a statistical result. There may be some errors but variation in measurements from one sample to another remains the same or is minimal. Vickers microhardness measurements across the depth of the melted region were carried out using a Buehler microhardness tester with the normal load of 300 gram-force or an axial force of 2.94 N and an indentation time of 12 s.

A static bioactivity test of the coated samples was carried out by soaking the samples in a simulated biofluid (SBF) at 37 °C for several days ranging from 1–10 days. The pH of the SBF solution was maintained at 7.4 during the course of the test. The composition of SBF was in accordance with reference [17].

3. Results and discussions

Non-destructive phase analysis of the laser-processed samples was carried out using XRD. Samples being processed at laser fluences ranging from 503 J cm^{-2} to 1006 J cm^{-2}, the formation of different phases was expected as the maximum temperature rise and the associated cooling rate vary accordingly [18, 19]. XRD spectra of the processed samples at varying laser fluences along with the calcium phosphate tribasic powder used as the precursor are illustrated in figure 1. The processed samples showed the existence of TiO_2, Ti, α-TCP and $CaTiO_3$ phases. All these phases in laser-processed Ti–6Al–4V for the calcium phosphate coating were also previously reported in the work done by Kurella *et al* [20] where the processing was carried out with varying speeds at constant power. As laser processing in air would be most feasible and desirable for the intended application of fabrication of bioimplant, the processing in air was pursued. Although formation of TiO_2 is not intended, it formed as a byproduct of the process. In addition to the strong affinity toward oxygen the oxidation of Ti–6Al–4V was further enhanced due to the development of very high processing temperatures sufficient for melting both the coating and the substrate. It is observed that the TiO_2 phase exists under all laser-processing fluences with increased crystallographic texture along (1 1 2) and (2 2 0) planes (figure 1). The formation of the TiO_2 phase is considered very beneficial because of its good corrosion and wear resistance [21–25]. It is also biocompatible as it forms an O–H bond on TiO_2 under wet conditions [26, 27].

In contrast, the formation of α-TCP is attributed to the dehydration of the calcium phosphate precursor during laser processing [20]. The formation of the α-TCP phase is considered desirable as it hydrolyzes under physiological conditions to form hydroxyapatite according to the following reaction [28]:

$$3\alpha\text{-}Ca_3(PO_4)_2 \xrightarrow{H_2O} Ca_9HPO_4(PO_4)_5OH.$$

The crystallographic texturing of the Ti phase along the (1 0 1) plane at 2θ of 40.6° has shown an increased trend with increasing fluence. This is mostly due to the decreased cooling rate associated with increasing laser fluence, which slows down the kinetics of atomic motion and allows sufficient time for them to arrange in regular lattice sites and thereby increases its crystallinity. Evolution of the crystallographic texture depends upon the development of morphological (growth of atomic planes) features within a grain. An atomic plane grows with a specific growth velocity, which is different for each plane. Depending upon the growth velocity and the cooling rate of the medium within which the planes are growing, only the fastest growing planes prevail (at the expense of slow growing planes) and impinge on each other at the boundary, thereby forming a morphological/crystallographic texture [18]. If the cooling rate of the medium is extremely rapid, only one or a few types of the fastest growing planes grow to provide single or multi-textured crystal development. Therefore, the cooling rate of the medium has tremendous bearing on the development of the crystallographic texture. The formation of the $CaTiO_3$ phase is mostly due to reaction between the calcium phosphate precursor and titania as proposed by Kurella *et al* [20]. As the samples were cleaned and washed with acetone followed by water prior to XRD studies no peaks of CaO, a water soluble phase, were detected in our case. This dissolution nature of CaO was proposed by Kurella *et al* [20].

The thermodynamic and kinetic effects of processing conditions can be realized through the evolution of the crystallite size within the processed region. For biomaterials crystallinity and amorphism are two competing issues.

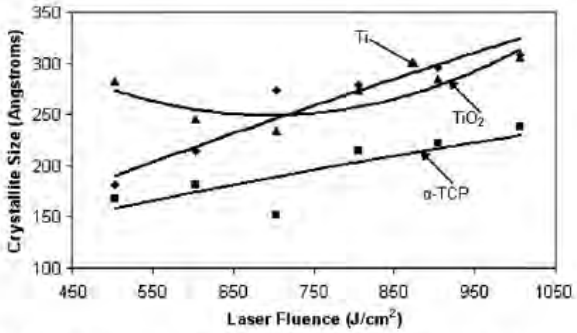


Figure 2. Variation in the crystallite size with increasing laser power.

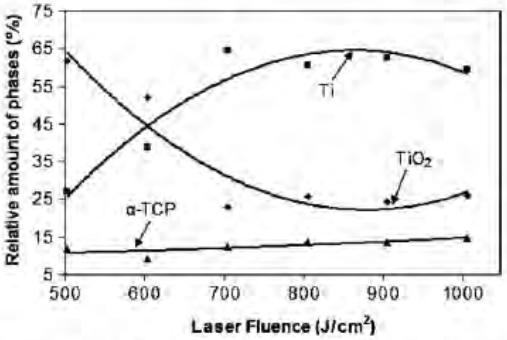


Figure 3. Relative amounts of various phases with increasing laser power.

Crystalline phases show improved mechanical properties and amorphous phases are good for biocompatibility and bioactivity. Hence the transition from crystalline to amorphous or vice versa with varying laser fluences for these phases can be understood by measuring the crystallite size. The crystallite size determination was performed through the measurement of XRD peak broadening using the peak paint method in Jade software. The peak centroid is based on all data points in the painted area, and the crystallite size, from a well-resolved single peak is estimated using the following Scherrer equation:

$$S = 0.9\lambda(\mathrm{FWHM}^2 - \mathrm{GW}^2)^{-1/2} \cdot \cos\theta^{-1},$$

where λ is the wavelength of the x-ray source (1.54 Å), θ is half of the reported peak centroid, FWHM is the reported peak width at half maximum in radians, and GW is the instrumental broadening. Jade obtains the instrumental broadening from the WINJADE.WHM file, which contains the GW curves as a function of 2θ by instrument types. The highly resolved and strongly textured TiO_2 (1 1 2), Ti (1 0 1) and α-TCP (3 0 18) peaks were used for the study. From figure 2 it can be explained that both Ti and α-TCP phases show an increase in crystallite size with increasing fluence while TiO_2 follows a marginally decreased trend in the lower fluence range (<704 J cm^{-2}) and an increasing trend at higher laser fluences (>704 J cm^{-2}). This may be mostly due to the decrease in cooling rate with increasing laser power, which facilitates the grain growth. The relative amounts of the three phases were semi-quantitatively obtained by the following equation [28]:

$$\%I1 = \frac{[I1]}{[I1 + I2 + I3]} \times 100,$$

where $I1$, $I2$ and $I3$ are integrated intensities under the peaks of TiO_2 (1 1 2), Ti (1 0 1) and α-TCP (3 0 18), respectively. From figure 3 it can be observed that the relative amount of TiO_2 phase is comparatively higher for lower laser-processed fluences, indicating that a considerable amount of the substrate material underwent oxidation. With increasing laser fluence an increase in the relative amounts of both Ti and α-TCP phases but decrease in TiO_2 phase are realized. This behavior can be explained based on the following equation [20].

$$\text{Calcium Phosphate}_{(l)} + TiO_2 \rightarrow CaTiO_3 + \alpha\text{-TCP} + H_2O_{(g)}\uparrow$$

With increase in fluence at a constant traverse speed the heat input (laser fluence) also increases and as a result TiO_2 reacts with the already existing calcium phosphate, leading to the formation of $CaTiO_3$, α-TCP and H_2O. Therefore, there is depletion in the relative amount of the TiO_2 phase at higher laser processing fluences.

The schematic representation of a porous and geometrically textured calcium phosphate coating versus a non-porous and flat coating is presented in figure 4. A porous coating helps in supplying an adequate amount of blood and oxygen to the implant surface, which further helps in the regeneration of a new tissue and rapid bone ingrowth [12, 15]. The geometrically textured topography helps in inducing a mechanical stimulation with the surrounding bone and also provides high interfacial shear strength. Therefore osseointegration takes place rapidly with these kinds of coatings as compared to a flat and non-porous coating where there exists a thick connective tissue in between the bone and implant coating. In light of this requirement, as described below in the present study attempts were made to produce physically textured and surface porous coatings.

A SEM micrograph of a cross-sectional view of a laser-coated sample (1006 J cm^{-2}) is presented in figure 5(*a*). The geometrically textured topography is clearly visible with a pit depth of ~150 μm and a width of ~600 μm. The formation of the porous coating at the surface is presented as inset in figure 5(*b*). This is an indication of the formation of multi-scale features at the surface of the coating. These microscale features in the form of pits create surface roughness, which may help toward numerous protein interactions and thereby aid cell orientation, alignment and finally tissue integration [20, 29–32]. Further, these microscale features also mimic the ECM (extra cellular matrix) present in the body to support cells [29]. These topographies in the form of pits also induce a mechanical stimulation on the surrounding bone during the early days of implantation and help in quick fixation. The mechanical stimulation is provided by the improved shear strength at the interface and mechanical interlocking when the bone grows into these pits [10]. Thus the textured coating provides physical and chemical biocompatibility. The physical compatibility is provided through the textured surface that aids alignment and mechanical attachment of the cells, and various Ca- and Ti-based phases within the coating on the surface are likely to provide the chemical biocompatibility.

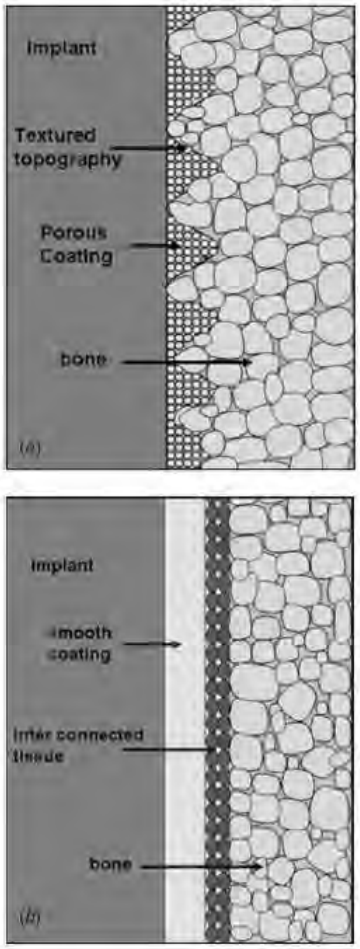


Figure 4. Schematic representation of (*a*) geometrically textured and porous coating and (*b*) flat and non-porous coating with interconnected tissue.

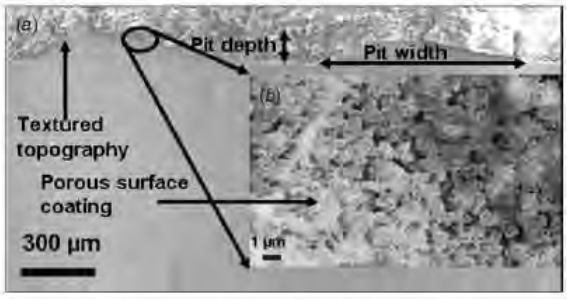


Figure 5. SEM micrographs of the sample processed at 1006 J cm^{-2}: (*a*) with textured topography in a cross-sectioned sample and (*b*) the inset with multi-scale features at the coating surface (1006 J cm^{-2}).

Porosities in the range of 1 μm or less may support cells and thereby provide an instructive background to guide their

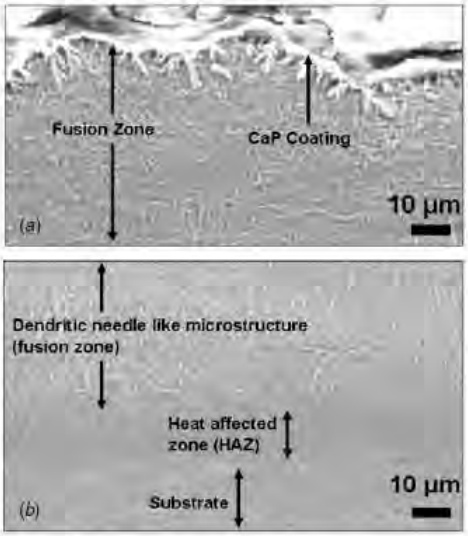


Figure 6. SEM micrographs (*a*) revealing the adhesion of coating to the substrate material and (*b*) the microstructural features across various zones of a sample processed at 1006 J cm^{-2}.

behavior toward tissue growth [29]. Additional features such as melt zone grain/phase structure are also visible in figures 6(*a*) and (*b*). Due to inherent rapid cooling rates ($> 10^3$ °C s^{-1}), the laser treatment has produced acicular α-Ti (transformed β-Ti) in the melt region and martensitic structure in the heat-affected zone (HAZ), indicating variable rates of cooling in these regions. Apart from phase transformations figure 6(*a*) also clearly reveals the geometrically textured CaP coating and the infiltration of the coating into the substrate due to a high laser fluence. Under the set of laser parameters employed in the present study, the Ca–P-based precursor and part of the substrate melt, thereby forcing infiltration of Ca–P into the molten volume of the substrate. With increase in laser fluence, more volume of the substrate is melted. The higher volume of the substrate melt and higher temperature associated with higher fluences are likely to increase the infiltration of the Ca–P coating precursor into the substrate. The thickness of the coating varied from 2 to 3 μm for all laser fluences employed. The melt depth measurements conducted in the cross sections are presented in figure 7. In general, the melt depth increased with increasing laser fluence, which can be directly related to the increase in surface temperature with increase in laser fluence. Based on post-process microstructural observations, it appeared that under all processing conditions employed in the present work, the maximum temperatures were well within the melt regime, leading to increased thermal conductivity and thermal diffusivity of the surface-treated region and deeper melting zones into the substrate.

Hardness measurements are carried out to ensure that the top surface is enriched with a ceramic-based composition. Vickers hardness measurements along the cross section in the melted region are presented in figure 8. A maximum hardness of 680–760 HV was measured at the coating surface and there is a gradual drop in hardness as we move toward

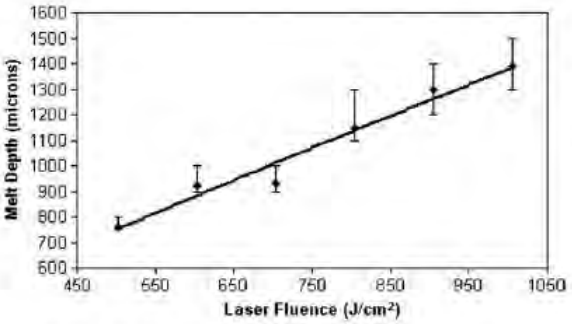


Figure 7. Variation in the melt depth with laser power.

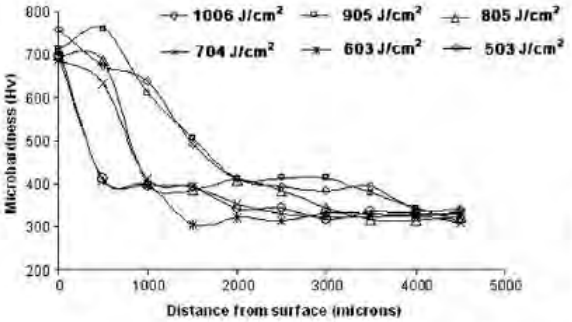


Figure 8. Variation in microhardness from the coating to the substrate with different laser processing powers.

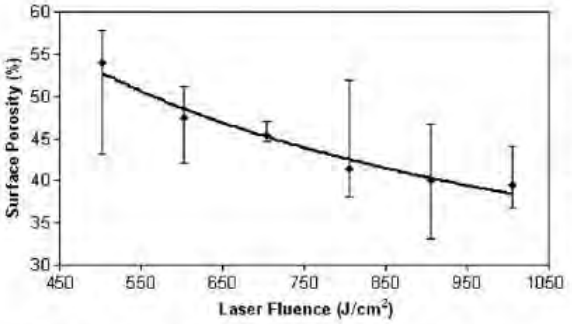


Figure 9. Effect of surface porosity with increasing laser power.

the substrate. This is an indication of the existence of the ceramic-based composition such as TiO_2 and α-TCP at the top surface which is in accordance with the XRD studies in figure 1. Approximately beyond the depth of 2500 μm away from the coating surface there was no change in hardness as there was no effect from the laser fluence. A decrease in surface porosity with increasing laser fluence (figure 9) may be attributed to the increased volume of the molten metal pool. This in turn can significantly vary the hydrodynamic conditions such as the molten metal flow and cooling rate affecting the surface porosity. Pores are considered to be formed due to the trapped cover gas bubbles in the coating.

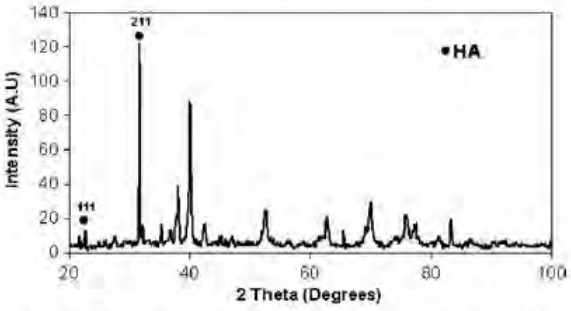


Figure 10. XRD pattern of the sample processed at 1006 J cm^{-2} after immersion in simulated biofluid for five days.

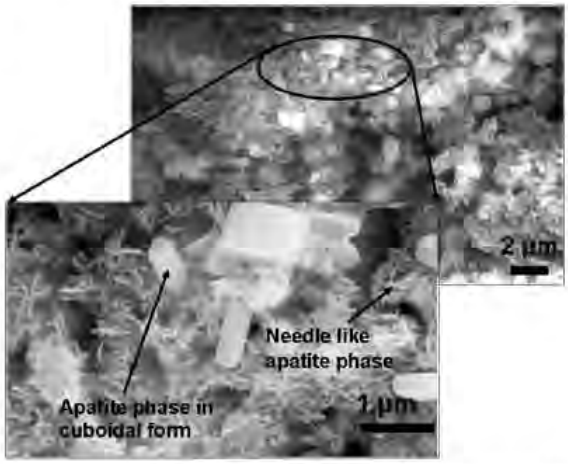


Figure 11. Scanning electron micrograph of laser-processed coating at 1006 J cm^{-2} after immersion in SBF for one day.

According to Triantafyllidis *et al* [33] two basic mechanisms led to pore formation during laser processing of ceramic materials: the bubble motion in the molten pool due to thermocapillary forces in the direction of temperature gradient and pore coalescence due to this bubble motion.

In vitro bioactivity test was carried out by soaking the sample processed at 1006 J cm^{-2} in a SBF. This particular sample was chosen for bioactivity assay as it has the minimum surface porosity (~40 vol%) among all samples processed under the set of parameters employed in the present study and it is expected to keep up with the strength of the coating. Furthermore, this sample also has all the beneficial phases in relatively greater amounts, which can enhance its biocompatibility. The formation of an apatite-like phase and a maximum attributable to this phase at $2\theta \approx 37.713^\circ$ corresponding to the plane (2 1 1) (JCPDS 09-0432) is confirmed from the XRD pattern (figure 10). The SEM micrographs (figure 11) revealed the needle- and cuboid-like morphologies of apatite phases just after one-day exposure to SBF. The formation of the needle-like apatite layer is very much in accordance with the observation by various other authors [34, 35]. In contrast, the formation of a cuboidal morphology within these needle-like features (the inset of

figure 11) was something new for these kinds of coatings. These cuboids were confirmed as apatite phase from the energy dispersive spectroscopy (EDS) and have the same spectra as obtained from the needle-like phases. Due to the hexagonal crystal structure of the apatite phase, formation of these cuboids may be due to the clustering and grain growth along the *c* axis from these primary needles.

The long time immersion of the CaP-coated samples in SBF is ongoing. The detailed observation of precipitation of various types (morphology) and amount (vol%) of phases will be reported in future subsequent publications. These publications will also attempt to report the kinetics of growth of such phases. Attempts will also be made to study the biocompatibility of these coatings by cell spread, and proliferation with human osteoblast-like cells.

4. Conclusions

In the present work the formation of a geometrically textured and surface porous calcium phosphate bio-ceramic coating by laser processing is demonstrated. Surface coatings are performed with increasing power using a continuous wave Nd:YAG laser and the parameters are kept within the melting regime. It has been observed that with increasing power the relative amounts of Ti and α-TCP increase and the relative amounts of TiO_2 decrease. The crystallite size of the above phases also follows an increasing trend with increasing power. The fusion zone shows a dendritic microstructure indicating the faster rate of cooling associated with the laser materials processing. The melt depth follows a linear increase with laser power. Vickers hardness was maximum at the coating surface and varied between 680 and 760 HV. The surface porosity also decreased with increasing laser power, because of more molten metal formation and melt infiltration. Further the formation of an apatite-like layer on the surface of these coatings immersed in a SBF proved the integrity and the bioactivity of these coatings.

References

[1] Ratner B D, Hoffman A S, Schoen F J and Lemos J E 2004 *Biomaterials Science* 2nd edn (San Diego, CA: Elsevier)

[2] Compton R G, Davies S G and Evans J 2001 *Biomineralization: Principles and Concepts in Bioinorganic Materials Chemistry* 1st edn (New York: Oxford University Press)

[3] Kim H-W, Kim H-E, Salih V and Knowles J C 2004 Dissolution control and cellular responses of calcium phosphate coatings on zirconia porous scaffold *J. Biomed. Mater. Res.* A **68** 522–30

[4] Shih W-J, Wang S-H, Li W-L, Hon M-H and Wang M-C 2007 The phase transition of calcium phosphate coatings deposited on a Ti-6Al-4V substrate by an electrolytic method *J. Alloys Comp.* **434** 693–6

[5] Blalock T, Bai X and Rabiei A 2007 A study on microstructure and properties of calcium phosphate coatings processed using ion beam assisted deposition system on heated substrates *Surf. Coat. Technol.* **201** 5850–8

[6] Cleries L, Fernandez-Pradas J M and Morenza J L 2000 Bone growth on and resorption of calcium phosphate coatings obtained by pulsed laser deposition *J. Biomed. Mater. Res.* **49** 43–52

[7] Campbell A A, Fryxell G E, Linehan J C and Graff G L 1996 Surface induced mineralization: a new method for producing calcium phosphate coatings *J. Biomed. Mater. Res.* **32** 111–8

[8] Gracia-Sanz F J, Mayor M B, Arias J L, Pou J, Leon B and Perez-Amor M 1997 Hydroxyapatite coatings: a comparative study between plasma-spray and pulsed laser deposition techniques *J. Mater. Sci.: Mater. Med.* **8** 861–5

[9] Boyd A R, Meenan B J and Leyland N S 2006 Surface characterization of the evolving nature of radio-frequency magnetron sputter deposited calcium phosphate thin films after exposure to physiological solution *Surf. Coat. Technol.* **200** 6002–13

[10] Hansson S and Norton M 1999 The relation between surface roughness and interfacial shear strength for bone anchored implants: a mathematical model *J. Biomech.* **32** 829–36

[11] Shimko D A, Shimko V F, Sander E A, Dickson K F and Nauman E A 2005 Effect of porosity on the fluid flow characteristics and mechanical properties of tantalum scaffolds *J. Biomed. Mater. Res.* B **73** 315–24

[12] Shimko D A and Nauman E A 2007 Development and characterization of a porous poly(methyl methacrylate) scaffold with controllable modulus and permeability *Biomed. Mater. Res.* B **80** 360–9

[13] Wen C E, Mabuchi M, Yamada Y, Shimojima K, Chino Y and Asahina T 2001 Processing of biocompatible porous Ti and Mg *Scr. Mater.* **45** 1147–53

[14] Wen C E, Yamada Y, Shimojima K, Chino Y, Hosokawa H and Mabuchi M 2004 Compressibility of porous magnesium foam: dependency on porosity and pore size *Mater. Lett.* **58** 357–60

[15] Charriere E, Lemaitre J and Zysset Ph 2003 Hydroxyapatite cement scaffolds with controlled macroporosity: fabrication protocol and mechanical properties *Biomaterials* **24** 809–17

[16] Bauerle D 2000 *Laser Processing Chemistry* 3rd edn (New York: Springer)

[17] Oyane A, Kim H-M, Furuya T, Kokubo T, Miyazaki T and Nakamura T 2003 Preparation and assessment of revised simulated body fluids. *J. Biomed. Mater. Res.* A **65** 188–95

[18] Harimkar S P and Dahotre N B 2006 Crystallographic and morphological textures in laser surface modified alumina ceramic *J. Appl. Phys.* **100** 024901

[19] Harimkar S P, Samant A N and Dahotre N B 2007 Temporally evolved recoil pressure-driven melt infiltration during laser surface modification of porous alumina ceramic *J. Appl. Phys.* **101** 054911

[20] Kurella A and Dahotre N B 2006 Laser induced hierarchical calcium phosphate structures *Acta Biomater.* **2** 677–83

[21] Liu J-X, Yang D-Z, Shi F and Cai Y-J 2003 Sol-gel deposited TiO_2 film on NiTi surgical alloy for biocompatibility improvement *Thin Solid Films* **429** 225–30

[22] Gurrappa I 2002 Characterization of different materials for corrosion resistance under simulated body fluid conditions *Mater. Charact.* **49** 73–9

[23] Nie X, Leyland A and Matthews A 2000 Deposition of layered bioceramic hydroxyapatite/TiO_2 coatings on titanium alloys using a hybrid technique of micro-arc oxidation and electrophoresis *Surf. Coat. Technol.* **125** 407–14

[24] Shukla A K, Balasubramanium R and Bhargava S 2005 Properties of passive film formed on CP titanium, Ti-6Al-4V and Ti-13.4Al-29Nb alloys in simulated human body conditions *Intermetallics* **13** 631–7

[25] Huang H-H 2002 Effects of fluoride concentration and elastic tensile strain on the corrosion resistance of commercially pure titanium *Biomaterials* **23** 59–63

[26] Ramires P A, Romito A, Cosentino F and Millela E 2001 The influence of titania/hydroxyapatite composite coatings

on *in vitro* osteoblasts behavior *Biomaterials* **22** 1467–74
[27] Ellingsen J E 1991 A study on the mechanism of protein adsorption to TiO_2 *Biomaterials* **12** 593–6
[28] Grish Y E and Brown P W 2003 Phase evolution during the formation of stoichiometric hydroxyapatite *J. Biomed. Mater. Res.* B **67** 632–7
[29] Stevens M M and George J H 2005 Exploring and engineering the cell surface interface *Science* **310** 1135–8
[30] Kasemo B 2002 Biological surface science *Surf. Sci.* **500** 656–77
[31] Assender H, Bliznyuk V and Porfyrakis K 2002 How surface topography relates to materials properties *Science* **297** 973–6
[32] Lutolf M P and Hubbell J A 2005 Synthetic biomaterials as instructive extracellular microenvironments for morphogenesis in tissue engineering *Nat. Biotechnol.* **23** 47–55
[33] Triantafyllidis D, Li L and Stott F H 2003 Mechanisms of porosity formation along the solid/liquid interface during laser melting of ceramics *Appl. Surf. Sci.* **208** 458–62
[34] Hijon N, Cabanas M V, Pena J and Regi M V 2006 Dip coated silicon substituted hydroxyapatite films *Acta Biomater.* **2** 567–74
[35] Padilla S, Roman J, Sanchez Salcedo S and Vallet Regi M 2006 Hydroxyapatite/SiO_2–CaO–P_2O_5 glass materials: *In vitro* bioactivity and biocompatibility *Acta Biomater.* **2** 331–42

Materials Science and Engineering R 66 (2009) 1–70

Contents lists available at ScienceDirect

Materials Science and Engineering R

journal homepage: www.elsevier.com/locate/mser

Calcium phosphate coatings for bio-implant applications: Materials, performance factors, and methodologies

Sameer R. Paital, Narendra B. Dahotre *

Department of Materials Science and Engineering, The University of Tennessee, Knoxville, TN 37996, USA

ARTICLE INFO

Article history:
Received 30 September 2008
Received in revised form 20 May 2009
Accepted 21 May 2009
Available online 22 July 2009

Keywords:
Calcium phosphate
Bio-implant
Coatings
Titanium alloys

ABSTRACT

With an ageing population, war, and sports related injuries there is an ever-expanding requirement for hard tissue replacement such as bone. Engineered artificial scaffold biomaterials with appropriate mechanical properties, surface chemistry and surface topography are in a great demand for enhancing cell attachment, cell growth and tissue formation at such defect sites. Most of these engineering techniques are aimed at mimicking the natural organization of the bone tissues and thereby create a conducive environment for bone regeneration. As the interaction between the cells and tissues with biomaterials at the tissue–implant interface is a surface phenomenon, surface properties play a major role in determining both the biological response to implants and the material response to the physiological condition. Hence surface engineering of biomaterials is aimed at modifying the material and biological responses through changes in surface properties while still maintaining the bulk mechanical properties of the implant. Therefore, there has been a great thrust towards development of Ca–P-based surface coatings on various metallic and nonmetallic substrates for load bearing implant applications such as hip joint prosthesis, knee joint prosthesis and dental implants.

Typical coating methodologies like ion beam assisted deposition, plasma spray deposition, pulsed laser physical vapor deposition, magnetron sputtering, sol–gel derived coatings, electrodeposition, micro-arc oxidation and laser deposition are extensively studied at laboratory scale. In the present article, attempts are made to give an overview of the basic principles behind the coating techniques as well as advantageous features such as bioactivity and biocompatibility associated with these coatings. A strong emphasis will be given on laser-induced textured and bioactive coatings obtained by the author's research group [A. Kurella, N.B. Dahotre, Journal of Biomedical Applications 20 (2005) 5–50; A. Kurella, N.B. Dahotre, Acta Biomaterialia 2 (2006) 677–688; A. Kurella, N.B. Dahotre, Journal of Minerals, Metals and Materials Society (JOM) 58 (2006) 64–66; A. Kurella, N.B. Dahotre, Journal of Materials Science: Materials in Medicine 17 (2006) 565–572; P.G. Engleman, A. Kurella, A. Samant, C.A. Blue, N.B. Dahotre, Journal of Minerals, Metals and Materials Society (JOM) 57 (2005) 46–50; R. Singh, A. Kurella, N.B. Dahotre, Journal of Biomaterials Applications 21 (2006) 46–72; S.R. Paital, N.B. Dahotre, Biomedical Materials 2 (2007) 274–281; S.R. Paital, N.B. Dahotre, 2009, Acta Biomaterialia, doi:10.1016/j.actbio.2009.03.004; R. Singh, N.B. Dahotre, Journal of Materials Science: Materials in Medicine 18 (2007) 725–751.]. Since cells are sensitive to topographical features ranging from mesoscale to nanoscale, formation of these features by both pulsed and continuous wave Nd:YAG laser system will be highlighted. This can also be regarded as advancement towards third generation biomaterials which are bioinert, bioactive and which once implanted will stimulate cell adhesion, proliferation and growth at the interface. Further, an overview of various bio-implants and bio-devices and materials used for these kinds of devices, performance factors such as mechanical and corrosion behavior and surface science associated with these materials are also explained. As the present article is aimed at describing the multidisciplinary nature of this exciting field it also provides a common platform to understand this subject in a simple way for students, researchers, teachers and engineers in the fields ranging from medicine, dentistry, biology, materials science, biomedicine, biomechanics to physics.

© 2009 Elsevier B.V. All rights reserved.

* Corresponding author. Tel.: +1 865 974 3609; fax: +1 865 974 4115.
E-mail address: ndahotre@utk.edu (N.B. Dahotre).

0927-796X/$ – see front matter © 2009 Elsevier B.V. All rights reserved.
doi:10.1016/j.mser.2009.05.001

Contents

1. Introduction . . . 2
   1.1. Bio-implants and bio-devices . . . 2
   1.2. Materials for bio-implants and bio-devices . . . 4
      1.2.1. Metallic materials . . . 4
      1.2.2. Ceramics . . . 6
      1.2.3. Polymers . . . 8
      1.2.4. Composites . . . 10
      1.2.5. Natural materials . . . 10
   1.3. Performance factors of bio-implants and bio-devices . . . 10
      1.3.1. Mechanical behavior . . . 11
      1.3.2. Corrosion . . . 15
      1.3.3. Surface properties . . . 15
   1.4. Surface science and engineering for performance enhancement . . . 22
      1.4.1. Morphological modifications . . . 23
      1.4.2. Physiochemical modifications . . . 24
      1.4.3. Biological modification . . . 26
2. Methodologies for coating Ca–P ceramics on Ti-alloys . . . 28
   2.1. Ion beam assisted deposition . . . 30
   2.2. Plasma spray deposition . . . 32
   2.3. Electrophoretic deposition . . . 37
   2.4. Pulsed laser physical vapor deposition . . . 40
   2.5. Micro-arc oxidation . . . 44
   2.6. Magnetron sputtering deposition . . . 50
   2.7. Sol–gel derived coatings . . . 51
   2.8. Direct laser melting . . . 55
      2.8.1. Continuous wave (CW) and pulsed laser melting . . . 55
3. Performance of Ca–P coatings in body (in vivo) environment . . . 59
4. Future work . . . 60
   References . . . 67

1. Introduction

Biomaterials are synthetic or natural materials intended to function appropriately in a bio-environment. After the invention of first generation of materials during 1960–1970 for use inside a human body, synthetic biomaterials became a subject of interest [10]. In fabricating a biomedical implant aimed at restoring the function of a body tissue, one is concerned about the mechanical properties of the material, design, and its biocompatibility [11]. The material or system of materials chosen should have the appropriate mechanical properties such as elasticity, yield stress, ductility, toughness, wear resistance, etc. to name a few. Further it should be amenable to being formed or machined into different shapes, at relatively low cost and be readily available. A proper design of an implant material is aimed to provide the requisite durability, functionality and biological response. Durability and functionality are governed by the bulk properties of the material, whereas biological response depends on the surface chemistry, surface topography, surface roughness, wettability, surface charge, and surface energy [12–14]. Biocompatibility may be defined as the acceptance of the implant material by the surrounding tissues without any adverse response from the body and vice versa. [11,15]. Therefore, a biocompatible implant material should be nontoxic, noncarcinogenic, with little or no foreign body reaction and be chemically stable or corrosion resistant. In light of this, some important applications of biomaterials include (1) orthopedics, (2) cardiovascular systems, (3) ophthalmics, (4) dental applications, (5) wound healing and (6) drug delivery systems [11].

1.1. Bio-implants and bio-devices

Orthopedic implant devices are intended to restore the function of load-bearing joints which are subjected to high level of mechanical stresses, wear, and fatigue in the course of normal activity. These devices include prostheses for hip (Fig. 1(a)) [16], knee (Fig. 1(b)) [17], ankle, shoulder (Fig. 1(c)) [18], and elbow joints (Fig. 1(d)) [16]. They also include the fracture fixation devices such as wires, pins, plates, screws, etc. Metals (Ti–6Al–4V, Co–Cr–Mo, stainless steel), polymers (poly(methyl methacrylate) (PMMA), ultrahigh-molecular-weight polyethylene (UHMWPE), and ceramics (alumina, zirconia, hydroxyapatite) are the three classes of materials that are most commonly used for fabricating orthopedic implants.

Cardiovascular devices are desired to treat problems related to the heart and arteries. The heart undergoes rhythmic expansion and contraction so as to supply blood to different organs of the body. After several years of its function, this may result in a structural change in the valve and thereby it may not open and close fully. This rhythmic function of the heart can be restored using a heart valve prosthesis (Fig. 2) [19]. Apart from just heart valve prostheses several other cardiovascular devices include stents and grafts for atherosclerotic vascular disease, pacemakers and ICDS for cardiac arrhythmias, and cardiac assist and replacement devices for heart failure.

Ophthalmic devices such as intraocular lenses (IOL) (Fig. 3) [20] are used to restore the vision for patients suffering visual disability (blindness) and clouding of the lens (cataract). Intraocular lens was first invented by Sir Harold Ridley [21]. Since they are used in contact with the tissues of the eye, they are regarded as biomaterials. An implant material for IOL should maintain a stable, clear path for optical imaging and be biocompatible to the biology of eye. Poly(methyl methacrylate) is the most frequently used implant material for IOL.

Dental implants are used to restore lost tooth by replacing both the tooth and its root (Fig. 4) [22]. Here a metallic implant (titanium) is first inserted into the gum (gingival) so that the bone cells grow tightly around it and anchors it firmly. Then an abutment is placed over the anchor followed by an artificial tooth (crown) attached to the abutment. Titanium is most commonly used as an implant material as it osseointegrates rapidly to the

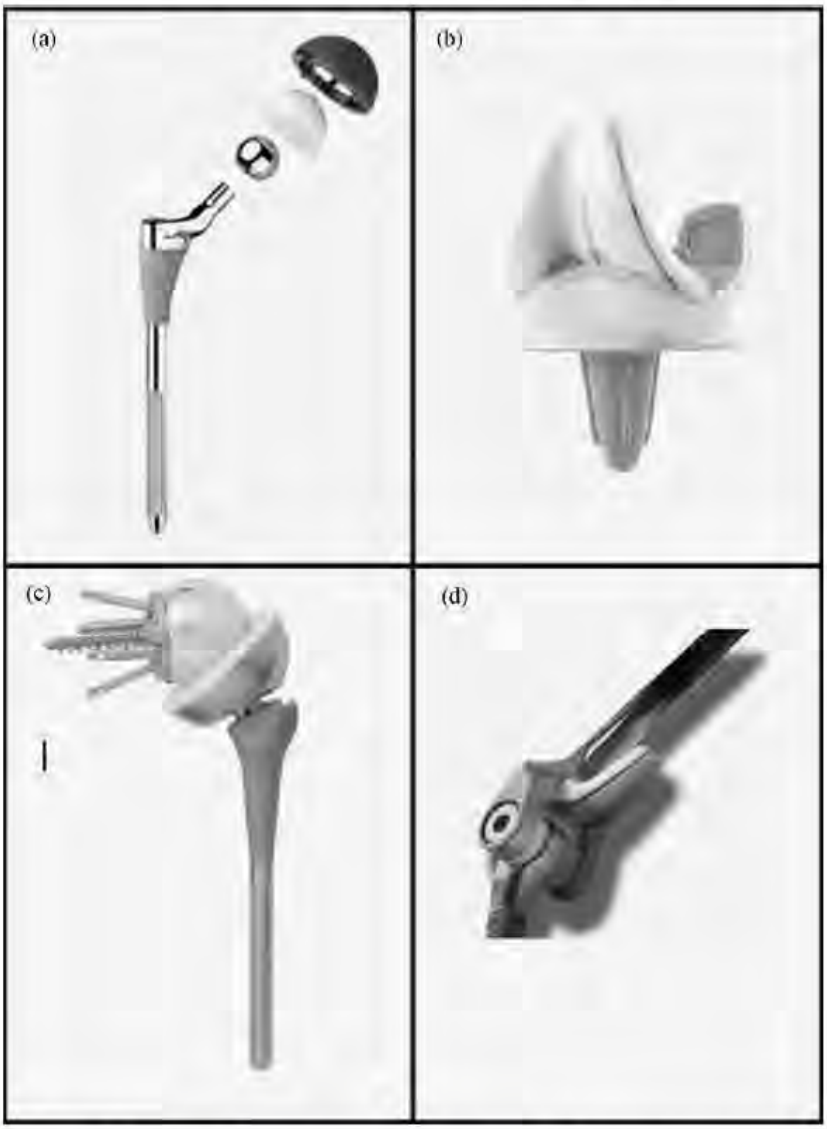


Fig. 1. Orthopedic implant devices used for load bearing applications: (a) hip implant (reprinted from [16] with permission from source: www.zimmer.com), (b) knee implant (reprinted from [17] with permission from source: http://thehipkneesurgeon.com/jointKnee.php), (c) shoulder implant (reprinted from [18] with permission from source: http://www.djosurgical.com/products/shoulder/rsp/index.htm) and (d) elbow implant (reprinted from [16] with permission from source: www.zimmer.com).

surrounding tissues and thereby forms a tight seal against any kind of bacterial invasion.

Wound healing involves the use of alternate skin substitutes to treat patients suffering from severe burns, injuries, chronic nonhealing ulcers, etc. [23]. Wound healing is a complicated process separated into a series of phases, each characterized by the integrated action of different cells. These phases in order are the inflammatory response, migration and proliferation of cells, collagen synthesis, collagen remodeling and collagen maturation. The most frequently used skin substitute materials for wound healing includes allografts of cultured cells and collagen, xenografts, and autografts of sheets of cultured keratinocytes.

Drug delivery systems are used for controlled and targeted delivery of drugs to the body. Some potential advantages of such systems include [24]:

- Maintenance of drug levels in a therapeutically desirable range at the repair site.
- Minimization in side effects owing to the targeted delivery of the drug to a particular cell type or tissue.
- Potentially reduced or an optimum usage of the drug.

Among the different classes of materials, polymeric materials are the most common in drug delivery devices. The four basic mechanisms by which a drug can be delivered from a polymer system are (a) diffusion of the drug species from or through the system, (b) degradation or cleavage of the drug from the system through a chemical or enzymatic reaction, (c) solvent activation, either through osmosis or swelling of the system and (d) a combination of any of the above systems. The various polymeric materials used in drug delivery systems include silicone rubber,



Fig. 2. A replacement heart valve. (Reprinted from [19] with permission from source [19]: www.ascensionortho.com.)



Fig. 3. An intraocular lens. (Reprinted from [20] with permission from Elsevier.)

ethylene–vinyl acetate copolymer, various hydrogels, lactic/glycolic acid copolymers, etc.

1.2. Materials for bio-implants and bio-devices

The different classes of materials used for the fabrication of bio-implants and bio-devices can be broadly classified as (1) metallic materials, (2) polymers, (3) ceramics, (4) composites and (5) natural materials.

1.2.1. Metallic materials

Metallic materials are most commonly used for load bearing implants and internal fixation devices. Processing method and purity of the metal determines its properties. Some featured properties of a metallic material are its high tensile strength, high yield strength, resistance to cyclic loading (fatigue), resistance to time dependent deformation (creep) and its corrosion resistance. They generally find applications in the fabrication of implant devices such as hip joint prosthesis, knee joint prosthesis, dental implants, cardiovascular devices, surgical instruments, etc. The most commonly used metals and alloys for medical device applications include stainless steels, commercially pure titanium and its alloys, and cobalt-based alloys.

1.2.1.1. Stainless steels. Stainless steels are iron-base alloys with a minimum of 10.5% Cr as an alloying element, needed to prevent the formation of rust. Stainless steel (18Cr–8Ni) was first used in orthopedic surgery in 1926 [25]. For implant applications they must have the resistance to pitting and crevice corrosion from the body plasma. Special production techniques such as vacuum melting, vacuum arc melting, and electro slag refining are required to produce high-quality stainless steels with minimum nonmetal inclusions for implant applications [11]. Apart from implant applications commercial-grade stainless steels are also widely used for the manufacture of surgical and dental instruments. Although there are several types of stainless steels (Table 1) in use for medical applications, 316L (18Cr–14Ni–2.5Mo) single phase austenitic (FCC) stainless steel is the most popular one for implant applications [11,15–23,25–33]. The "L" in the designation denotes its low carbon content and as a result it has high corrosion resistance in in vivo conditions. Shih and coworkers studied the effect of surface treatment on the in vitro corrosion resistance and in vivo biocompatibility of 316L stainless steel [26,34]. They demonstrated that passivation with an amorphous oxide layer has excellent corrosion resistance and low degree of thrombosis (Fig. 5) than the as-received sample.

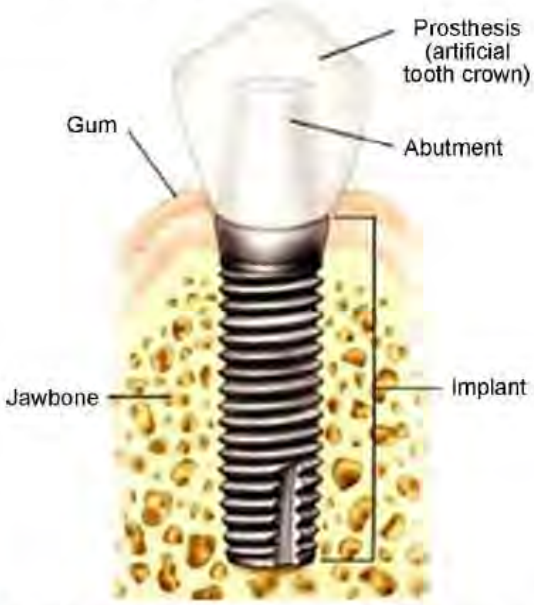


Fig. 4. A dental implant. (Reprinted from [22] with permission from source: http://www.lymebaydentistry.co.uk/lbd/jsp/dental_implants.jsp.)

1.2.1.2. Cobalt alloys. Co–Cr-based alloys are the most commonly used representative Co alloys for biomedical applications. The presence of Cr imparts the corrosion resistance and the addition of small amounts of other elements such as iron, molybdenum, or tungsten can give very good high temperature properties and abrasion resistance [25]. The various types of Co–Cr alloys used for implant applications include Co–Cr–Mo (ASTM F75), Co–Cr–Mo (ASTM F799), Co–Cr–W–Ni (ASTM F90) and Co–Ni–Cr–Mo–Ti (ASTM F562) [15]. Clinical applications of such alloys include its use in dentistry and maxillofacial surgery as (a) partial denture, (b) dental implants, and (c) maxillofacial implants and in orthopedics as (a) fracture fixation plates and screws and (b) hip and knee prosthesis [25]. Casting Co–Cr-based alloys for the fabrication of implants is not a preferred technique as solidification during casting may result in large dendritic grains (Fig. 6) [35] and thereby decrease its yield strength. Also casting defects such as inclusions

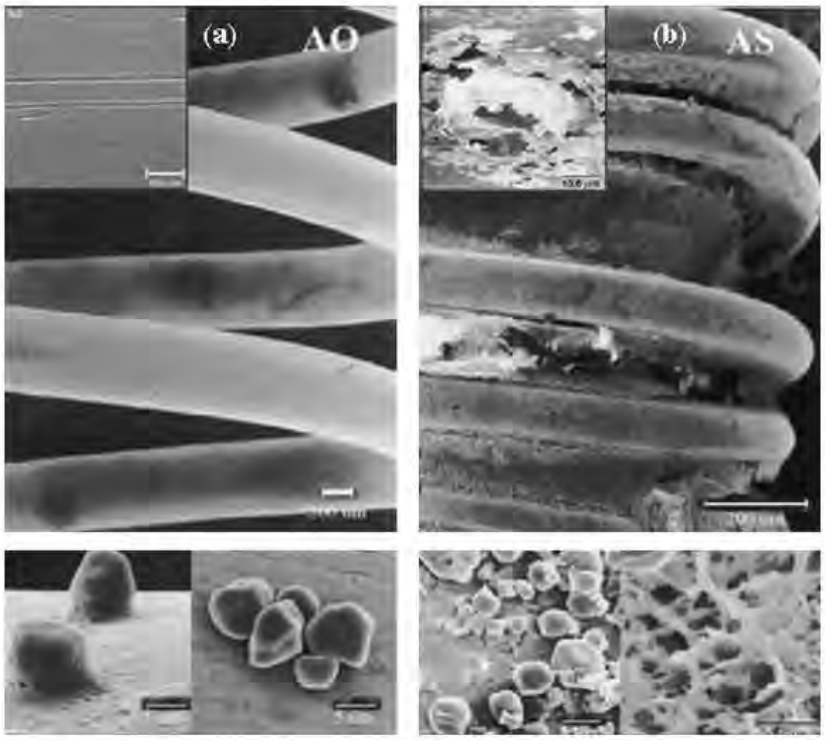


Fig. 5. SEM micrograph of 316L stainless steel wire surface with two different surface chemistries under both in vivo and in vitro conditions (a) 316L wire surface coated with an amorphous oxide layer (AO), and (b) as received 316L stainless steel wire surface (AS). The inset in the upper left hand side in figure (a) reveals a clean and free of pitting damage after anodic polarization test for the (AO) sample, whereas the inset in upper left hand side figure (b) reveals severe pitting degradation for the (AS) sample. Further the inset at the bottom in figure (a) reveals absence of proteins, fibrins and a clean surface for the coils passivated with amorphous oxide film, and the inset in bottom of figure (b) clumps of platelets, red cells, and fibrin under in vivo conditions. (Reprinted from [26] and [34] with permission from Elsevier.)

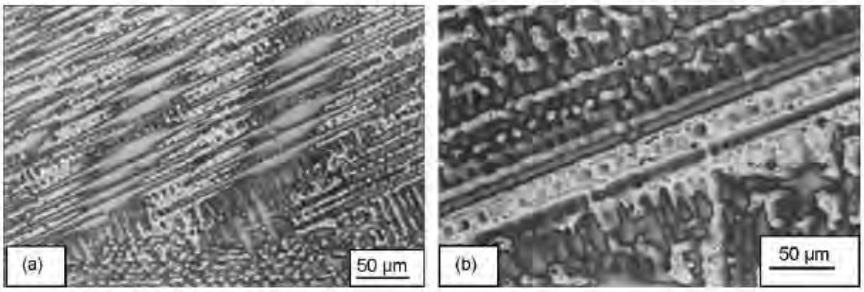


Fig. 6. As cast Co–Cr–Mo alloys revealing (a) carbide separation in interdendrites and (b) abnormally long bands of interdendritic carbides near grain boundary. (Reprinted from [35] with permissions from Springer.)

and micropores cannot be avoided and may act as stress risers and thereby result in the overall decrease of fatigue strength of the material [35–39]. Therefore, powder metallurgical techniques such as hot isostatic pressing (HIP) followed by forging [40] have been used for such applications (Fig. 7) [16]. This results in improved mechanical properties and corrosion resistance pertaining to the finer grain size (Fig. 8) [38] and reduction in segregation of the alloying elements obtained by this technique.

Table 1
Types of stainless steels in use for medical applications.

Types of stainless steel	Variation in Cr content (%)	Medical applications
Martensitic stainless steel	10.5–18	Bone curettes, chisels and gouges, dental burs, dental chisels, curettes, explorers, root elevators and scalers, forceps, hemostats, reactors, orthodontic pliers and scalpels
Ferritic stainless steel	11–30	Solid handles for instruments, guide pins and fasteners
Austenitic stainless steel	16–26	Cannulae, dental impression trays, guide pins, hollowware, hypodermic needles, steam sterilizers, storage cabinets, hip implants and knee implants



Fig. 7. Hot isostaic pressed (HIP) and forged Co–Cr based articulating components for hip implants. (Reprinted from [16] with permission from source: www.zimmer.com.)

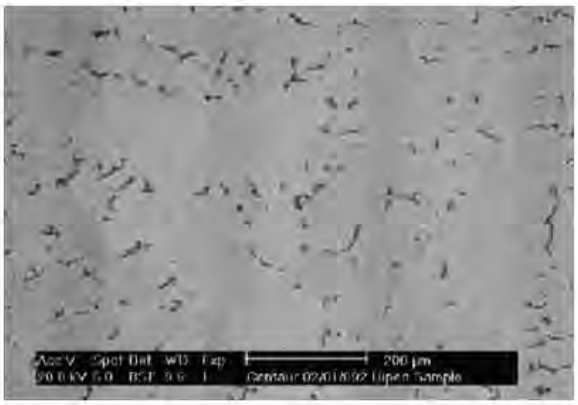


Fig. 8. Microstructure of a hot isostatic pressed (HIP) Co–Cr–Mo alloy. (Reprinted from [38] with permission from Elsevier.)

1.2.1.3. Titanium and titanium alloys. Titanium as a pure metal was implanted for the first time into laboratory animals in 1940 by Bothe, Beaton, and Davenport [25]. They concluded titanium as a well-tolerated material as compared to stainless steel and Co–Cr-based alloys under in vivo conditions. The two most commercially used specifications for implants are Pure Ti (ASTM F67) and Ti–6Al–4V (ASTM F136) [15]. These alloys have driven a lot of interest for load bearing implants due to its superior mechanical properties (tensile strength and fatigue strength), chemical stability (corrosion resistance), and biocompatibility under in vivo conditions [41–54]. Commercially pure Ti is selected for applications where corrosion resistance is of prime importance than its mechanical properties. Ti–6Al–4V (ASTM F136) is an alpha–beta alloy, the microstructure (Fig. 9) [55–57], mechanical behavior and chemical stability of which depend upon the type of heat treatment and mechanical working. In the recent past, however there has been a great concern on the dissolution of aluminum and vanadium ions into the body fluid and the possibility of any toxic effect, as a result of the passivation layer break down during wear in Ti–6Al–4V [58]. Consequently, other titanium alloys such as Ti–6Al–7Nb and Ti–13Nb–13Zr are under study in terms of their corrosion rate, mechanical properties, and biocompatibility as compared to Ti–6Al–4V [59–61]. Table 2 lists the mechanical properties and the clinical applications of these compositions. Fig. 10 [62] shows the components of Ti-based hip implant.

1.2.2. Ceramics

Ceramics are inorganic compounds of metallic or nonmetallic materials, with interatomic bonding as ionic or covalent and which are generally formed at elevated temperatures. A class of such materials used for skeletal or hard tissue repair are commonly referred to bioceramics. These bioceramics may be bioinert (alumina, zirconia), bioresorbable (tricalcium phosphate), bioactive (hydroxyapatite, bioactive glasses, and glass ceramics), or porous for tissue in growth (hydroxyapatite coating, and bioglass coating on metallic materials) [63–65]. Their success depends on their ability to induce bone regeneration and bone in growth at the tissue–implant interface without the intermediate fibrous tissue layer. The featured clinical applications include their use in orthopedics as (a) bone plates and screws, (b) total and partial hip

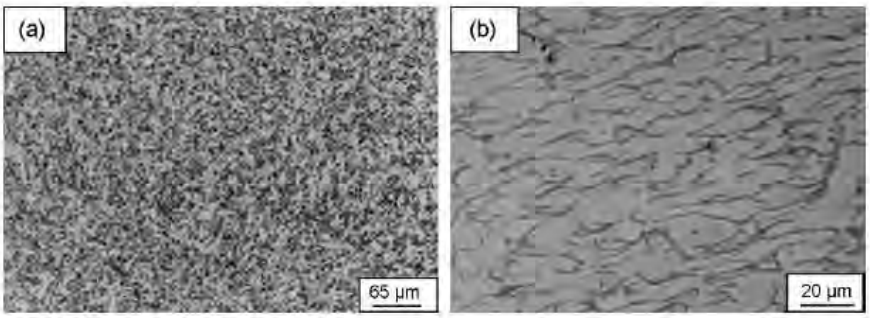


Fig. 9. Microstructure of Ti–6Al–4V (a) under as received and annealed condition and (b) after cold working by equal channel angular pressing (ECA) technique. (Reprinted from [55] and [56] with permission from Elsevier.)

Table 2
Mechanical properties and clinical applications of Ti-based metallic materials.

Alloy designation	Elastic modulus (GPa)	0.2% offset yield strength (MPa)	Ultimate tensile strength (MPa)	Elongation (%)	Clinical applications
Pure Ti	102–110	170–480	240–550	15–24	Pace maker cases, housings for ventricular-assist devices, implantable infusion drug pumps, dental implants, maxillofacial and craniofacial implants, screws and staples for spinal surgery
Ti–6Al–4V	110	860	930	10–15	Total joint replacement arthroplasty primarily for hips and knees
Ti–6Al–7Nb	105	795	860	10	Femoral hip stems, fracture fixation plates, spinal components, fasteners, nails, rods, screws and wire
Ti–13Nb–13Zr	79–84	836–908	973–1037	10–16	Orthopedic implants



Fig. 10. Components of Ti based hip implant. (Reprinted from [62] with permission from source: http://www.disanto.com/Product%20Pics.htm.)

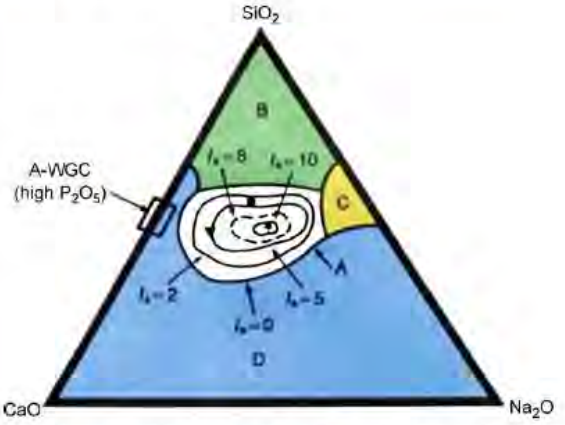


Fig. 11. Compositional dependence (in wt%) of bone bonding and soft tissue bonding of bioactive glasses and glass–ceramics. (Reprinted from [63] with permissions from Blackwell Publishing.)

components, (c) coatings on metal prosthesis for controlled implant or tissue interfacial response, (d) space fillings of diseased bone, and (e) vertebra prostheses, vertebra spacers, iliac crest prostheses, etc. They are also widely used in drug delivery devices, heart valves, cochlear implants, ocular implants and in dentistry as (a) dental restorations, (b) implants, (c) orthodontics, and (d) glass ionomer cements and adhesives [11,15].

Among the various types of bioceramics, bioactive ceramics such as hydroxyapatite ($Ca_{10}(PO4)_6(OH)_2$), and bioglass ($CaO–SiO_2–P_2O_5–Na_2O$) are materials of major interest for load bearing implant applications. Bioglass, once implanted into the body can easily react with the physiological fluids and form a tenacious bond to hard and soft tissues through cellular activity [66–73]. Regeneration and bonding of the hard and soft tissues depend on the compositional variation of Na_2O, CaO, and SiO_2 as illustrated in Fig. 11 [63]. Composition of P_2O_5 is kept constant at 6 wt% for all glasses. Glasses within region A (middle of the tertiary phase diagram) can easily form a bond with the bone and therefore region A can be termed as the bone-bonding boundary. Glasses within region B behave as inert materials and therefore form a fibrous capsule at the tissue–implant interface. Glasses within region C are resorbable or biodegradable and may disappear within 10–30 days of implantation. Glasses within region D are not technically practical to be synthesized and therefore never been tested for implant applications [15,63]. Chen et al. developed a bioglass derived sintered foam scaffold using the replication technique and proved its bioactivity by the formation of an apatite-like phase following immersion in a simulated bio-fluid (Fig. 12)

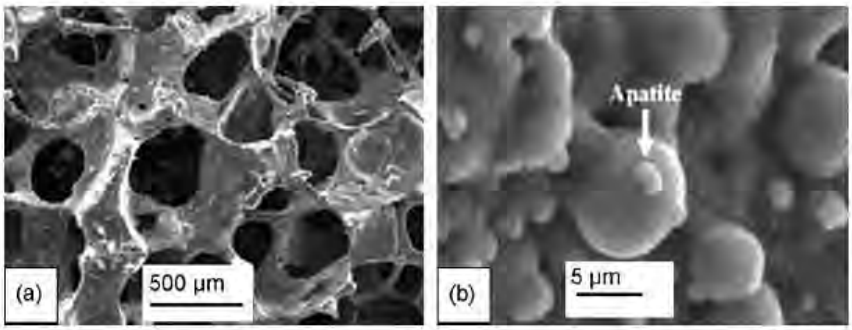


Fig. 12. Scanning electron micrograph revealing the (a) pore structure of a 45S5 Bioglass-derived foam sintered at 1000°C for 1 h, and (b) precipitation of an apatite-like phase on the foam structure following immersion in a simulated bio-fluid for 3 days. (Reprinted from [74] with permissions from Elsevier.)

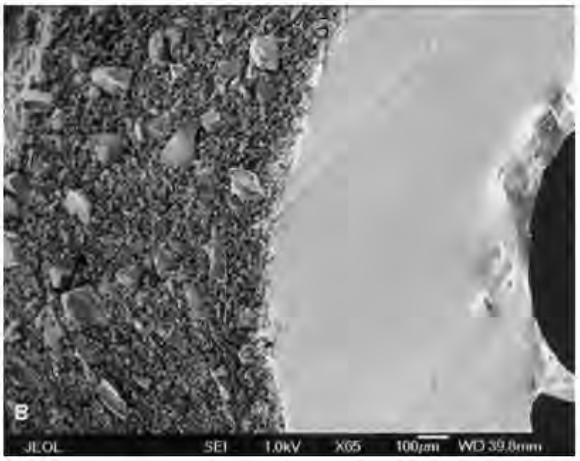


Fig. 13. Scanning electron micrograph of the bioactive glass-coated silicone tubing segment in cross section, magnification 65×. (Reprinted from [75] with permissions from Nature Publishing Group.)

[74]. Ross and coauthors developed bioglass coating on silicone tube using a solvent-based method for use as a peritoneal dialysis catherter. The cross-sectional image of the tube (Fig. 13) [75] reveals the embedded glass particles and a rough feature on the outer surface of the tube suitable for reactions with the adjacent tissue. The biocompatibility of the coated and uncoated tubes were studied by subcutaneous implantation into rats. It was observed (Fig. 14(a)) [75] that the uncoated specimens had no adherence to surrounding tissues and was separated by a thin fibrous capsule at the interface. In contrast, the coated tubes (Fig. 14(b)) [75] were fixed to the soft tissues, by promoting adhesion by collagen and cell proliferation.

Brushite ($CaHPO_4{\cdot}2H_2O$), octacalcium phosphate ($Ca_8H_2[PO_4]_6{\cdot}5H_2O$), and calcium hydroxyapatite ($Ca_{10}[PO4]6{\cdot}5H_2O$) are some prominent calcium phosphate salts found in bone [25]. But crystallographically hydroxyapatite (HA) is the dominant lattice structure of hard tissue. Therefore, there has been a tremendous interest in using synthetically derived HA for regenerating bone at the defect sites. HA can be synthesized from biological skeletal carbonate by hydrothermal exchange as per the following reaction [25]:

$$10CaCO_3 + 6(NH_4)_2 + 2H_2O \rightarrow Ca_{10}(PO_4)_6(OH)_2 + 6(NH_4)_2CO_3 + 4H_2CO_3$$

Table 3
Chemical name, mineral name, and composition of various Ca–P based ceramics. (Reprinted from [76] with permission from Institute of Mechanical Engineers (I.MechE).).

Ca–P	Formula	Name/mineral	Abbreviation
1.0	$CaHPO_4{\cdot}2H_2O$	Hydrated calcium phosphate/Brushite	DCP
1.0	$CaHPO_4$	Anhydrous calcium phosphate/Monetite	ADCP
1.33	$Ca_8H_2(PO_4)_6{\cdot}5H_2O$	Octacalcium phosphate	OCP
1.5	$Ca_3(PO_4)_2$	Tricalcium phosphate/ Whitlockite	TCP
1.67	$Ca_{10}(PO_4)_6{\cdot}F2$	Flourapatite	FA
1.67	$Ca_{10}(PO4)_6(OH)_2$	Hydroxyapatite	HA
2.0	$CaO{\cdot}Ca_3(PO4)_2$	Tetracalcium phosphate/ Hilgenstockite	TTCP

It also gets mineralized in situ on implants made of tricalcium phosphate and tetra calcium phosphate, due to interactions with the serum as per the following equations [25]:

$$H_2O + 4Ca_3(PO_4)_2 \rightarrow Ca_{10} + (PO_4)_6(OH)_2 + 2Ca^{2+} + 2HPO_4$$

$$3H_2O + 3Ca_4P_2O_9 \rightarrow Ca_{10}(PO_4)_6(OH)_2 + 2Ca^{2+} + 4OH^-$$

It is however realized that scaffolds fabricated using calcium phosphate salts (Table 3) [76], with $1 \leq Ca/P \leq 2$ are not encapsulated by a fibrous tissue and allows for bone in growth to the implant surface [25].

Several authors have studied the bioactivity and biocompatibility of such salts [77–87]. Detsch et al. [77] studied the response of osteoclast-like cells derived from human leukoma monocytic lineage on sintered tricalciumphosphate (TCP) and hydroxyapatite (HA). Their studies showed that the osteoclast-like U-937 cells responded in a different manner to HA and TCP (Fig. 15) [77]. Sintered HA plates favored giant cell formation with pronounced actin rings (Fig. 15(a) and (b)) and therefore larger lacunas as compared to TCP (Fig. 15(c) and (d)). The authors, therefore, proposed that calcium phosphate-based ceramics as a bone substitute material must be chosen either for their fast degradation (TCP) or for the slow remodeling of the biomaterial (HA). The choice of ceramic depends on the location and size of the bone defect and the patient's personal characteristics.

1.2.3. Polymers

Polymers are long chain molecules consisting of large number of small repeating units known as monomers. They belong to the family of macromolecules and represent the largest class of biomaterials. Polymers can be derived either from natural sources or from synthetic organic sources. The different types of polymers

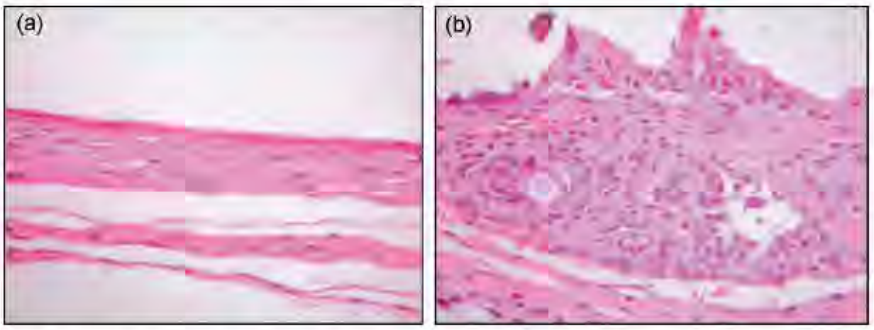


Fig. 14. Histology of capsules surrounding the (a) uncoated and (b) bioglass coated, catherter segments. (Reprinted from [75] with permissions from Nature Publishing Group.)

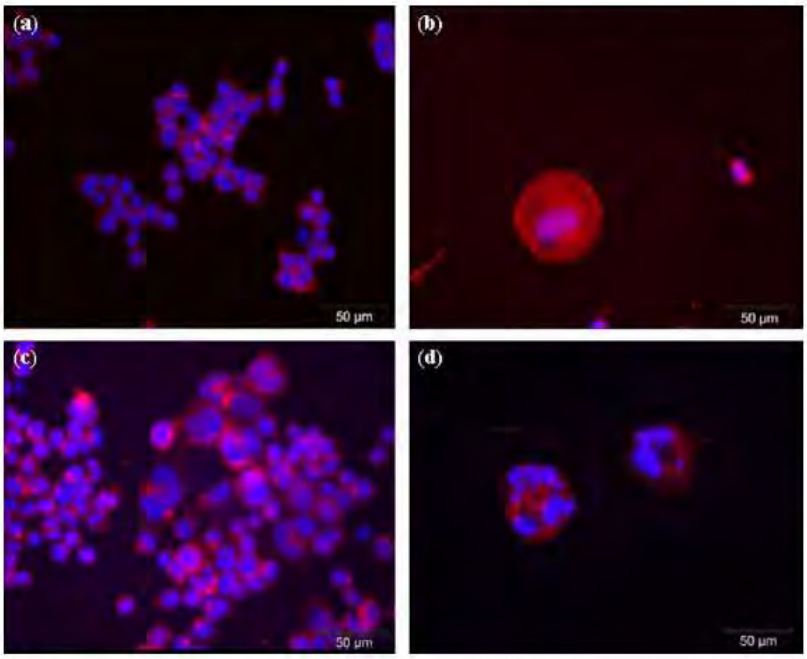


Fig. 15. Fluorescence microscopy images of U-937 cells cultured on (a and b) TCP, and (c and d) HA, with VD_3 and PDBu for 21 days. (Reprinted from [77] with permission from Elsevier.)

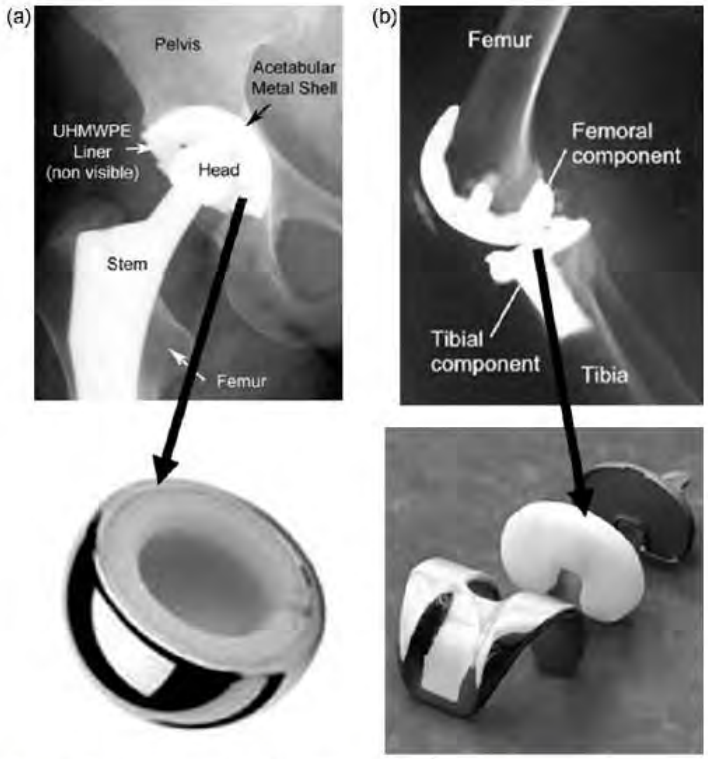


Fig. 16. Figure illustrating the use of UHMWPE as a bearing metal for (a) hip joint (reprinted from [89] and [90] with permission from sources: www.devicelink.com and http://www.genesis-tech.ch/company/ respectively) and (b) knee joint prosthesis (reprinted from [91] and [92] with permission from sources: http://tc.engr.wisc.edu/UER/uer01/author1/content.html and http://www.jri-ltd.co.uk/total_knee_replacement.asp respectively).

Table 4
Examples of polymers used as biomaterials. (Reprinted from [88] with permission from Springer.).

Applications	Polymer
Knee, hip, shoulder joints	Ultrahigh-molecular-weight polyethylene
Finger joints	Silicone
Sutures	Polylactic and polyglycolic acid
Tracheal tubes	Silicone, acrylic, nylon
Heart pacemaker	Acetal, polyethylene, polyurethane
Blood vessels	Polyester, polytetrafluroethylene, PVC
Gastrointestinal segments	Nylon, PVC, silicones
Facial prostheses	Polydimethyl siloxane, polyurethane, PVC
Bone cement	Polymethylmethacrylate

and their corresponding medical applications are listed in Table 4 [88]. Fig. 16 [89–92] shows the use of UHMWPE as a bearing material for hip joint and knee joint prostheses. Some advantages associated with polymers, for use as biomaterials can be listed as follows:

- Polymers can be easily fabricated to various complex shapes and structures.
- Provide wide range of bulk compositions and physical properties.
- Surface properties can be easily tuned.
- On the other hand their disadvantages include:
- Difficulty in sterilization.
- Easily absorb water and biomolecule from the surroundings and thereby alter the surface chemistry.
- Being soft materials may undergo mechanical wear and breakdown.
- May leach some harmful compounds to the body under in vivo conditions.

1.2.4. Composites

A composite consists of two or more materials each with distinct physical or chemical properties. It is designed to have a combination of best characteristic of each component materials. Biomedical composites are often designed to provide superior mechanical and biological compatibility. They can be classified based on the matrix material or on the bioactivity of the composites. Considering matrix material as the basis for classification, there are three different types of biomedical composites [93]:

- Polymer matrix composites, e.g., carbon/PEEK (polyetheretherketone), HA/HDPE.
- Metal matrix composites, e.g., HA/Ti, HA/Ti–6Al–4V.
- Ceramic matrix composites, e.g., stainless steel/HA, glass/HA.

Considering bioactivity of the composite as the basis for classification, there are three different types of biomedical composites [93]:

- Bioinert composites, e.g., carbon/carbon, carbon/PEEK.
- Bioactive composites, e.g., stainless steel/bioglass, HA/HDPE, HA/Ti–6Al–4V.
- Bioresorbable composites, e.g., tricalcium phosphate (TCP)/poly lactic acid (PLA), TCP/polyhydroxybutyrate (PHB).

The various factors that affect the performance of a biomedical composite material can be listed as follows [93]:

- shape, size and distribution of reinforcement;
- reinforcement properties and volume percentage;
- bioactivity of the reinforcement;
- matrix properties such as molecular weight and grain size;
- reinforcement-matrix interfacial state.

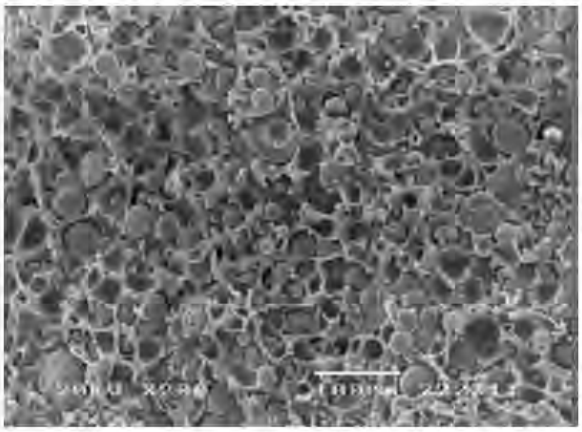


Fig. 17. Fracture surface of a polyetheretherketone (PEEK) composite with 20 vol% HA, suggesting good dispersion and distribution of HA in the PEEK matrix. It can also be seen that the main fracture mechanism is through-debending of HA from PEEK polymer matrix. (Reprinted from [96] with permission from Elsevier.)

Some promising medical applications of biomedical composites include their use in total joint replacements, spine rods, discs, plates, dental posts, screws, ligaments, and catherters [94,95]. Bakar et al. developed a polyetheretherketone–hydroxyapatite composite (Fig. 17) [96] by injection molding technique for load-bearing orthopedic implants. In vivo studies (Fig. 18) [96] of the composite material following implantation in pig suggested its favorable bioactivity and biocompatibility. Following 6 weeks of implantation it was observed that normal bone is abutting on the implant with no indication of bone growing into the pores of the implant. After 16 weeks of implantation mature bone were formed within the pores of the implant.

1.2.5. Natural materials

Natural polymers such as collagen and glycosaminoglycans are the most commonly used natural materials for clinical applications [97]. Collagen is a fibrous protein that connects and supports other bodily tissues such as skin, bone, tendons, muscles, and cartilage. It is the most plentiful available protein present in the bodies of mammals, including humans. Glycosaminoglycan is the most abundant heteropolysaccharide present in the body. Glycosaminoglycans occur primarily on the surface of the cells or in the extracellular matrix (ECM). The advantages associated with these natural biomaterials can be listed as follows [15]:

- These materials being similar to the macromolecular substances, get easily recognized by the biological environment and therefore deal metabolically.
- Problems of toxicity, chronic inflammation, and lack of recognition by cells which occurs mostly with synthetic materials can be avoided.
- These materials are biodegradable, and therefore it can be used for applications where it is desired to deliver a specific function for a temporary period of time.

1.3. Performance factors of bio-implants and bio-devices

It is well established that the bulk and surface properties of synthetic biomaterials, determine their long-term performance and stability under in vivo conditions. The bulk properties of an implant material can be characterized by its mechanical behavior and chemical stability under in vivo conditions. Based on the intended application and normal activity of the patient, an implant

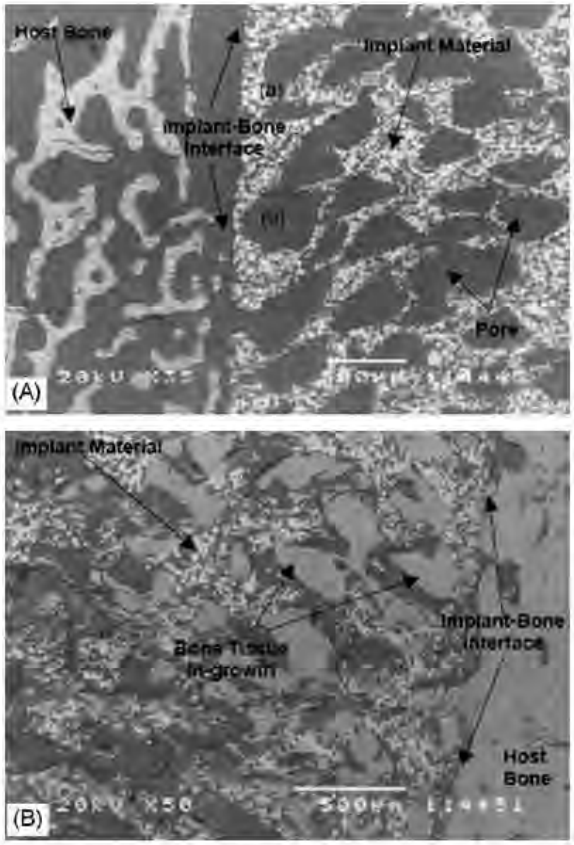


Fig. 18. Scanning electron micrographs of porous polyetheretherketone-hydroxyapatite (PEEK-HA) composite after implantation for 6 weeks (labeled A) and 16 weeks (labeled B). (Reprinted from [96] with permission from Elsevier.).

material may fail due to yielding, plastic deformation, rupture, fatigue, creep, corrosion, wear, and impact fracture. Further, since the atoms at the surface are highly unstable and drive most of the biological reactions at the tissue–implant interface, characterization and evaluation of surface properties plays an important role in determining its biocompatibility to the surrounding environment. The various surface parameters that dictate the biological response to surfaces include surface roughness, surface morphology, wettability, chemical composition, electrical charge, crystallinity, and heterogeneity to biological reactions. In the present context, however, we are going to discuss only the first four important surface parameters, their interpretation techniques, and their importance to biomaterials.

1.3.1. Mechanical behavior

The yield strength, elastic modulus, tensile strength, ductility, fracture strength and toughness of a material can be determined by a simple tensile test. In a tensile test a specimen is subjected to a continually increasing uniaxial tensile force and the applied load is plotted against the elongation or the extension of the specimen (Fig. 19). All of these parameters not only give valuable information to a design engineer, but also play an important role in deciding the long-term stability and biocompatibility of an implant material. For example a material with high elastic modulus may not be ideal for load bearing implants. This is because insufficient load transfer from an artificial implant to the

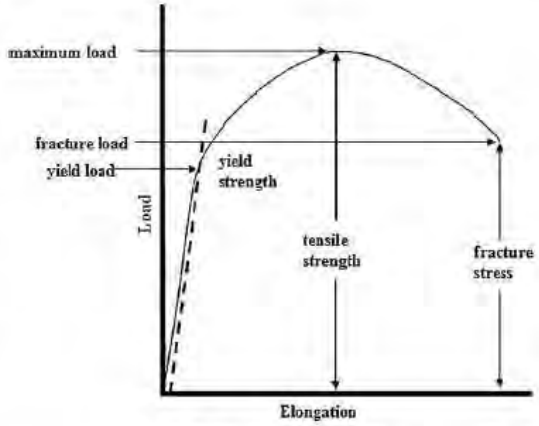


Fig. 19. A load-elongation curve.

adjacent remodeling bone may result in bone resorption and eventual loosening of the prosthetic device [11]. Modulus of elasticity is the slope of the initial linear portion of the stress–strain curve that can be constructed from the load-elongation measurements. Since the extension for a given load varies with the geometry of the specimen both the load and elongation has to be normalized to get this constant. The normalized load is called the stress and is obtained by dividing the load to the initial cross-sectional area of the specimen. The normalized elongation is called the strain and is obtained by dividing the elongation to the initial length of the specimen. Modulus of elasticity determines the stiffness of the material. Yield strength of a material determines the minimum stress necessary to produce plastic deformation. Hence, yield strength determines the ease at which a material can be deformed plastically into different shapes. Yield strength of a material can be calculated as the load at 0.2% offset strain divided by the initial cross-sectional area of the specimen. Tensile strength gives an idea of the maximum load a material can withstand before failure. Tensile strength is obtained by dividing the maximum load to the initial cross-sectional area of the specimen. Ductility of a material indicates the extent to which a material can be deformed without fracture. Fracture strength determines the stress at which a material fails following necking after reaching the peak stress or the ultimate tensile strength. It occurs when the cohesive strength of a material is exceeded. This is an important parameter for designing hip implants as they are expected to withstand the loads during service without fracture. Toughness of a material may be defined as the area under the stress–strain curve. It determines the amount of work per unit volume that can be done on the material without rupture. Alternatively, toughness of a material may also be defined as the ability of a material to deform plastically under the influence of a complex stress field existing at a sharp crack tip. Such plastic deformation at a sharp crack tip serves to blunt the crack and lower the locally enhanced stresses, thus hindering crack propagation. Hence, toughness is considered as an important parameter to design "failsafe" structures from brittle materials such as ceramics most commonly used as biocoatings.

Failures occurring due to repetitive or fluctuating stress cycles are called fatigue failures. The three basic factors necessary to cause fatigue failures are (1) maximum tensile stress of sufficiently high value, (2) large enough variation or fluctuation in applied stress, and (3) large number of cycles of applied stress. The three different approaches of fatigue tests used to evaluate biomaterials can be categorized as follows [98]:

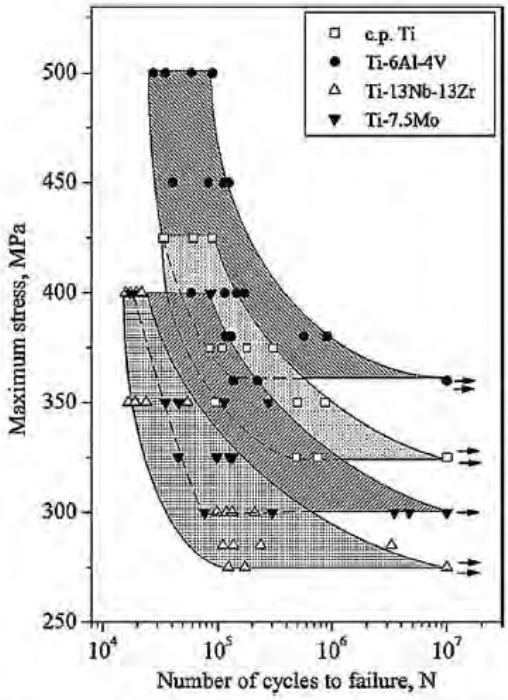


Fig. 20. *S–N* curve for four medical grade Ti based alloys. (Reprinted from [102] with permission from Elsevier.)

- stress/life (S/N) approach,
- fracture mechanics approach, and
- fatigue wear approach using simulated physiologic multi-axial loading.

The first two methods are basically used to screen various materials under high cyclic loading conditions and select materials suitable for implant applications. The third method is used to determine the fatigue behavior in a physiological environment and is generally a precursor to animal experiments. Resistance to fatigue is an important requirement for both load bearing orthopedic biomaterials as well as heart valves [99–104]. Owing to the brittle nature of ceramics, fatigue may be a major area of concern for implants coated with bioactive and biocompatible ceramics as it may result in wear debris generated due to the fatigue process. This in turn may invoke adverse host–tissue response at the interface. Fatigue failure is also a common phenomenon in medical grade UHWMPE used as a bearing surface in total joint replacement [104]. Cyclic loading on polymeric materials such as UHWMPE may lead to softening accompanied by reduction in elastic modulus and yield stress. Fatigue is also often considered as a prime cause of failure for titanium base load bearing implant materials. Cyclic loading on Ti base metallic materials may result in alternating plastic deformation of microscopically small zones of stress concentrations produced by notches or microstructural inhomogenities [100]. These small zones of stress concentrations are the regions where the crack initiates, propagates, and finally fractures due to prolonged cyclic loading. Fig. 20 [102] represents the S/N curves of four medical grade Ti base alloys. It is observed that Ti–6Al–4V has higher high-cycle stress-controlled fatigue resistance as compared to other alloys. Fatigue fracture surface morphology (Fig. 21) [102] represents the crack initiation, propagation and overload site due to cyclic loading on Ti–6Al–4V.

Wear may be defined as a surface damage or material removal process resulting from two surfaces in contact and in motion with each other. The rate of wear depends both on the applied load P and hardness H of the surface that is worn. Wear volume V of the wear debris as a function of the distance x moved by the sliding surface can be calculated as follows [105]:

$$V = k\left(\frac{Px}{H}\right)$$

Here k is a dimensionless wear coefficient or constant that depends both on the materials in contact and the presence or absence of lubrication, and hardness H is considered as the yield strength of the material being worn. Higher the mutual solid solubility between two materials in contact, higher is the wear. Hence wear is generally higher for similar materials in contact than for dissimilar materials. In contrast, for biomaterials used inside a

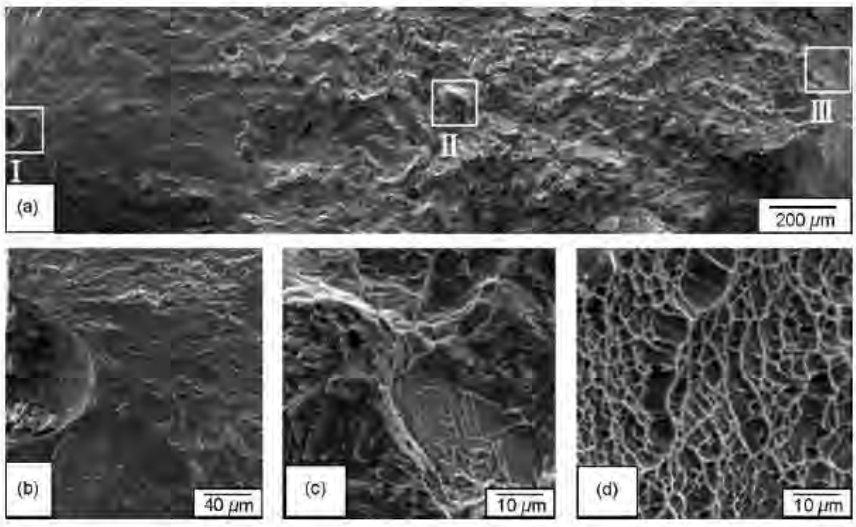


Fig. 21. Fatigue fracture surface morphology of Ti–6Al–4V. ((a) overall fracture surface; (b) crack initiation site taken from area "I"; (c) crack propagation site taken from area "II"; (d) overload site taken from area "III"). (Reprinted from [102] with permission from Elsevier.)

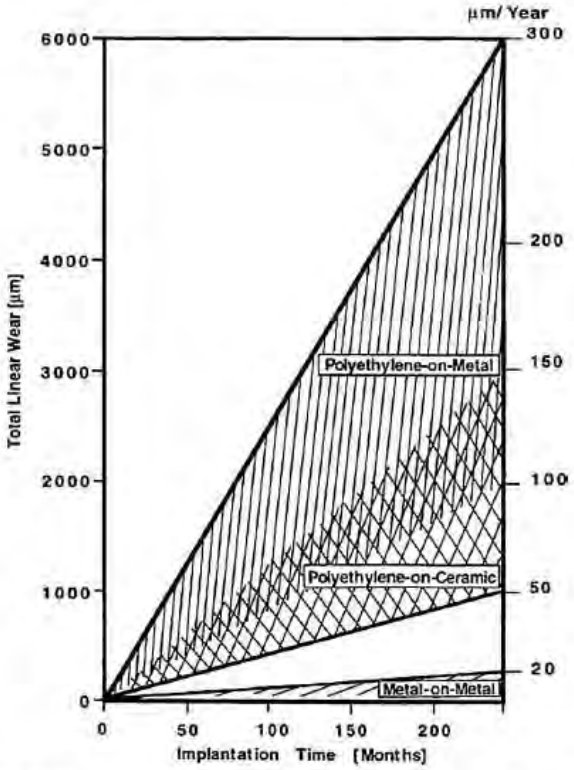


Fig. 22. Wear areas of implanted polyethylene cups paired with metal and with ceramic balls respectively and of CoCrMoC metal cups paired with metal balls. (Reprinted from [107] with permissions from Institute of Mechanical Engineers.)

human body wear may be extremely high for dissimilar materials. This is due to the fact that dissimilar materials in contact in saline or aqueous environment form a galvanic cell and result in corrosion, which may further exacerbate the wear phenomena. This is a very common experience in hip implant prostheses where a metal or ceramic femoral head articulates with an UHMWPE acetabular cup [106–110]. Wear debris generated from such joint replacements enters the periprosthetic tissue and is phagocytosed by macrophages. These macrophages then release pro-inflammatory cytokines and other mediators of inflammation that stimulates osteoclastic bone resorption, leading to osteolysis and eventual loosening of the device [110]. Therefore, there has been a significant interest in developing metal-on-metal and ceramic-on-ceramic bearing surfaces for hip joint prostheses [111–113]. Semlitsch et al. [107] studied the linear wear behavior of various material pairing for the cup and the ball and concluded that metal–metal pairing has the minimum wear loss as compared to both polyethylene-on-metal and polyethylene-on-ceramic (Fig. 22) [107].



Fig. 23. Detail of a hip joint simulator station, illustrating the holders of the femoral head and the acetabular cup. (Reprinted from [114] with permission from Elsevier.)

Although there are several lab test methods such as pin-on-disc, block-on-ring, ball-on-disc, etc. to evaluate the wear performance, none of these techniques closely simulate to the wear that takes place at the joints in the body. A hip joint simulator as shown in Fig. 23 [114] provides dynamic loading close to the body during walking and running and may be considered as a preferred technique to evaluate the wear performance of materials intended for hip joint prostheses. Scanning electron microscopy (SEM) micrographs (Fig. 24) [112] reveal the damaged surfaces of Co–Cr–Mo femoral heads worn against a similar alloy acetabular cup at different stages by a hip joint simulator.

Further from the basic principles of metallurgy it is known that the mechanical properties of a material depend on its microstructural features such as grain size, grain orientation, etc. which in turn depends on its manufacturing history such as solidification

Table 5
Representative mechanical properties of three implant grade metallic materials based on its processing conditions. (Reprinted from [15] with permission from Elsevier.).

Material	ASTM designation	Condition	Young's modulus (GPa)	Yield strength (Mpa	Tensile strength (MPa)	Fatigue endurance limit (at 107 cycles, R = −1c) (MPa)
Stainless steel	F745	Annealed	190	221	483	221–280
	F55, F56, F138, F139	Annealed	190	331	586	241–276
		30% cold worked	190	792	930	310–448
		Cold forged	190	1213	1351	820
Co–Cr alloys	F75	As-cast/annealed	210	448–517	655–889	207–310
	F799	Hot forged	210	896–1200	1399–1586	600–896
	F90	Annealed	210	448–648	951–1220	Not available
		44% cold worked	210	1606	1896	586
	F562	Hot forged	232	965–1000	1206	500
		Cold worked and aged	232	1500	1795	689–793
Ti alloys	F67	30% cold worked Grade 4	110	485	760	300
	F136	Forged annealed	116	896	965	620
		Forged, heat treated	116	1034	1103	620–689

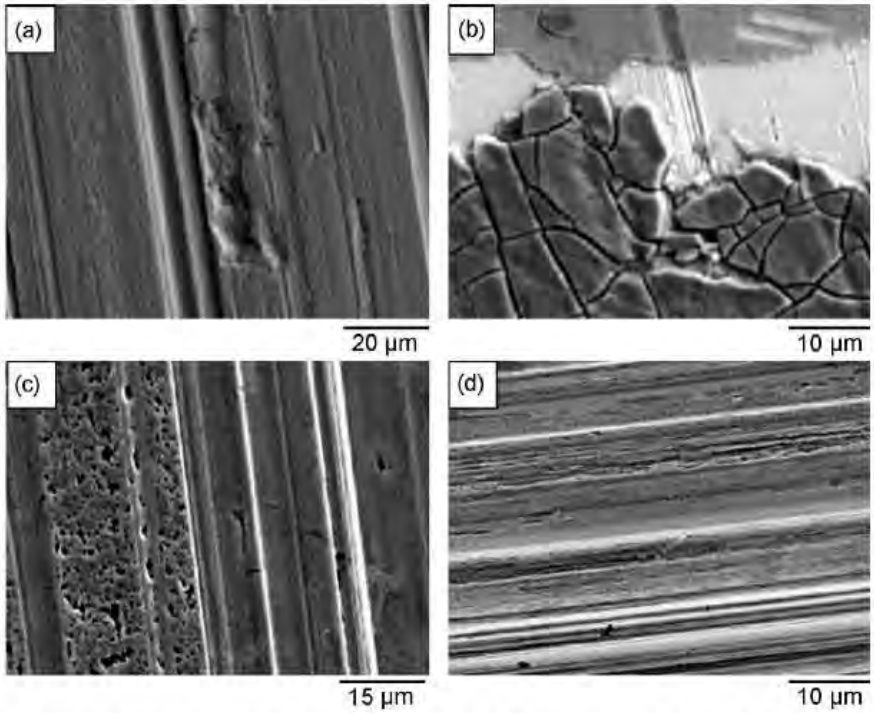


Fig. 24. SEM micrographs of femoral heads worn surfaces, (a) after 100 thousand cycles showing abrasive wear grooves, (b) after 300 thousand cycles showing breakdowns of adhered lubricant film, (c) after 500 thousand cycles showing surface micro pits and (d) surface delaminations. (Reprinted from [112] with permission from Elsevier.)

conditions, cold working, annealing cycles, etc. A summary of the representative mechanical properties of three implant grade metallic materials based on its processing conditions is listed in Table 5 [15]. Unfortunately, all of these values are obtained from standard samples with simple and regular geometries and may not represent the actual stress or loading conditions occurring on a complex shaped implant under in vivo conditions. Hence, a computational-based finite element analysis (FEA) is mostly followed to solve this problem [15,115–119]. Using a finite element approach the distribution of stresses at various locations of a complex shape implant under in vivo conditions can be easily calculated. Fig. 25 shows the stress distribution across a ceramic head and a hip stem used for hip implant prosthesis obtained by FEA technique [119]. Apart from its use for proper design of a prosthetic device, FEA may also be used to evaluate the stresses occurring across the surrounding tissues upon the insertion of an implant material and thereby its effect on tissue growth, remodeling and degeneration [118].

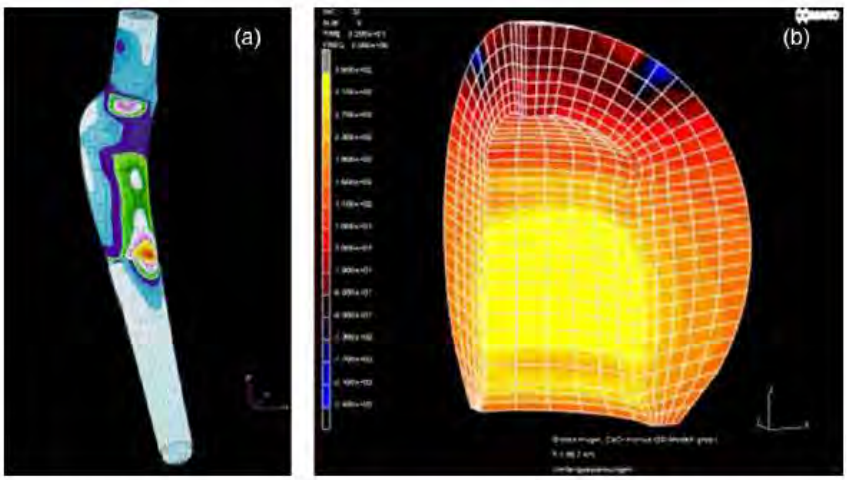


Fig. 25. A three-dimensional finite element model for the stress distribution under in vivo conditions across (a) a metallic hip endoprosthesis, and (b) a ceramic ball, used in a hip implant. (Reprinted from [119] with permission from source: http://www.endolab.de/computer/computersimulation_e.htm.)

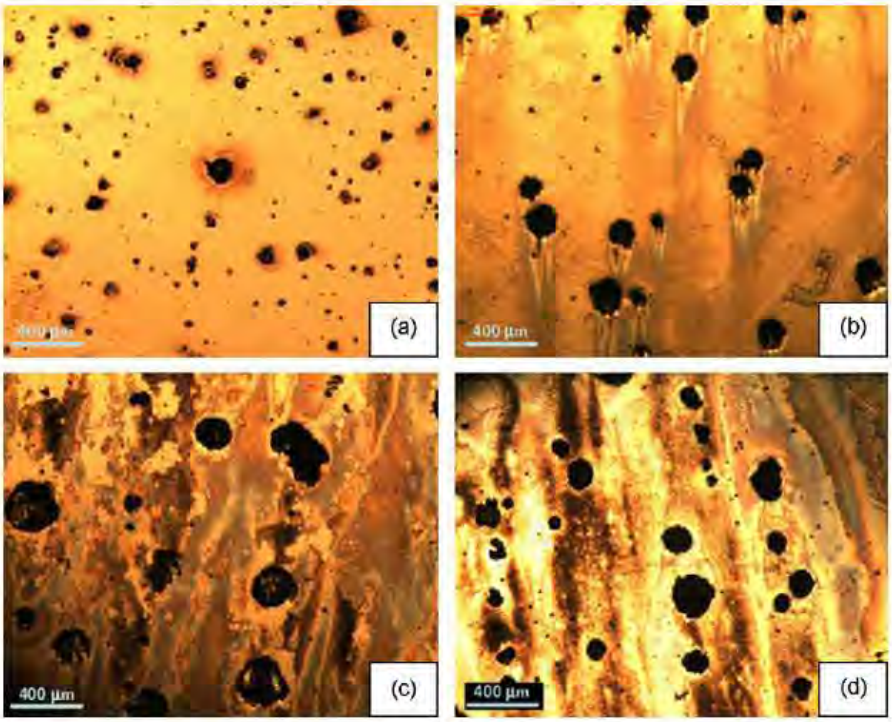


Fig. 26. Optical micrographs illustrating the formation of pitting corrosion in medical grade AISI 316L stainless steel following immersion in (a) NaCl, (b) NaCl + albumin, (c) phosphate buffered solution (PBS) and (d) PBS + albumin. (Reprinted from [122] with permission from Elsevier.)

1.3.2. Corrosion

Corrosion is the deterioration of a material as a result of chemical and electrochemical reactions with its surrounding environment. Implant materials used inside a human body are generally exposed to a harsh aqueous environment containing various anions (Cl^-, HCO_3^-, HPO_4^{2-}), cations (Na^+, K^+, Ca^{2+}, Mg^{2+}), organic substances, and dissolved oxygen [15,120–121]. Hence metallic implant materials are prone towards aqueous corrosion. The mechanism of corrosion for metallic implant materials is based on the following fundamental equations [15]:

Anodic dissolution:

$$M \rightarrow M^{n+} + n(\text{electrons})$$

Cathodic reduction:

$$O_2 + 2H_2O + 4e \rightarrow 4OH^-$$

Corrosion product:

$$M^+ + OH^- \rightarrow N(OH)$$

The metallic components of the alloy are initially oxidized to their ionic forms and release a free electron. The dissolved oxygen present in the aqueous environment then react with the water molecules and free electron to form hydroxyl ions. These hydroxyl anions then react with the metallic cations to form a corrosion product.

In the absence of oxygen the usual cathodic reactions are the reduction of hydrogen ions or water:

$$2H^+ + 2e^- \rightarrow H_2$$

$$2H_2O + 2e^- \rightarrow H_2 + 2OH^-$$

During the corrosion process, both the anodic and cathodic reactions must proceed in balance to maintain the overall electrical neutrality. The different types of corrosion that may take place on implant metallic materials are pitting, crevice, galvanic, intergranular, stress-corrosion cracking, corrosion fatigue, and fretting corrosion. Optical micrographs (Fig. 26) [122] illustrate the formation of pitting corrosion in medical grade AISI 316L stainless steel following immersion in four different simulating body fluids. The general principles and types of corrosion and their implications in bio-environment are extensively reviewed in several earlier publications [9,123,124].

1.3.3. Surface properties

When an implant material is inserted into the living tissue, an interface is created between the surface of the foreign implant material and the surrounding tissues. The surrounding tissue consists of water molecules, oxygen, negative and positive ions, proteins, and other biomolecules which may further built into larger structures such as cells and cell membranes. On the other hand, the surfaces of a foreign material may consist of individual atoms, molecules or large polymeric structures. Hence the surface of an implant is a termination of an extended, three-dimensional structure and thus generally represents broken bonds with higher surface energy. For thermodynamic and kinetic reasons when such a surface comes in contact with the biological environment it reacts immediately to form new bonds and compounds, thus lowering the surface energy. Therefore, biomaterial surfaces with different surface morphology, surface chemistry, and surface wettability may strongly influence the cell interaction and thereby tissue integration at the defect sites.

1.3.3.1. Surface morphology. It is well established that morphological features such as surface roughness and its topography can

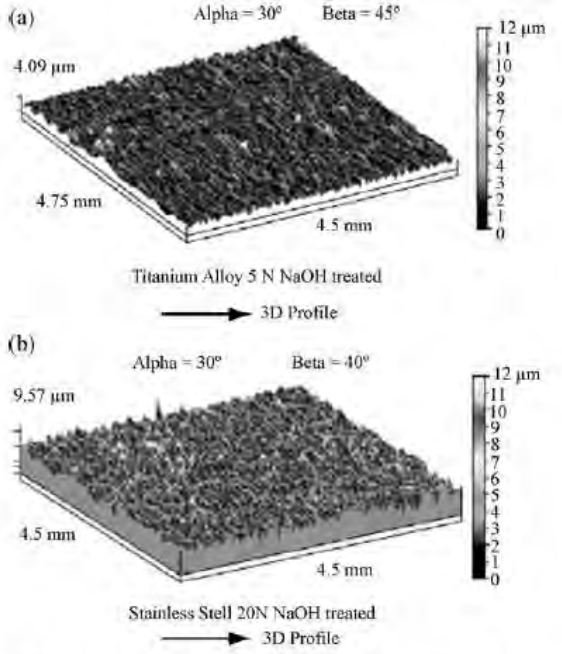


Fig. 27. 3D-profiles of (a) titanium alloy surface treated in NaOH 5N and (b) stainless steel surface treated in NaOH 20N, using a mechanical stylus profilometer. (Reprinted from [128] with permissions from Materials Research.)

strongly influence the protein adsorption, cell attachment, cell proliferation, contact guidance, and differentiation [125–127]. Hence, it controls the rate and quality of new tissue formation at the interface. The surface roughness or its topography can be characterized by atomic force microscopy (AFM), mechanical stylus profilometry, SEM, laser profilometry, and confocal laser scanning microscopy.

Mechanical stylus profilometry consist of a sharp stylus tip which directly traces across the surface and measures the surface roughness by measuring the tip displacement from the surface. The major advantage of this technique is the generation of direct, reproducible, quantitative data. The stylus is normally made of diamond with a tip radius of approximately 2 μm, and a static load of approximately 7×10^{-4} N is applied while it traces the surface. Therefore if the size of the stylus tip is larger than the surface asperities, this technique may not be suitable for a true representation of the surface roughness. Another major disadvantage may be scratching of the test specimen surface by the stylus tip.

Teixeira et al. [128] used a mechanical stylus profilometer to study the effect of alkaline treatments on the surface morphology of two substrates, i.e. stainless steel and titanium alloy, usually used for implants and orthopedic prosthesis. 3D profiles of the titanium alloy and stainless steel substrate after treatment with NaOH 5N at 60 °C for 24 h and NaOH 20N at 90 °C for 30 min, respectively is illustrated in Fig. 27. A higher surface roughness on the stainless steel substrate as compared to the titanium alloy was observed. Such a high surface roughness on the stainless steel substrate may be attributed to the high concentration of NaOH and lower corrosion resistance of stainless steel substrate as compared to titanium alloys.

AFM consists of a sharp cantilever tip (aspect ratio ≥5:1) made from Si_3N_4 or Si with a feed back mechanism that enables a piezoelectric device to maintain the tip at a constant force, or height above the surface of the sample (Fig. 28). As the tip is scanned over the surface, a laser beam focused onto the back of the reflective AFM cantilever, gets deflected onto a photodetector. The photodetector then measures the variation in light intensities due to the up and down movement of the tip and converts it to a three-dimensional topographical image of the surface. The force between the tip and sample surface is usually in the order of 10^{-9} N. Apart

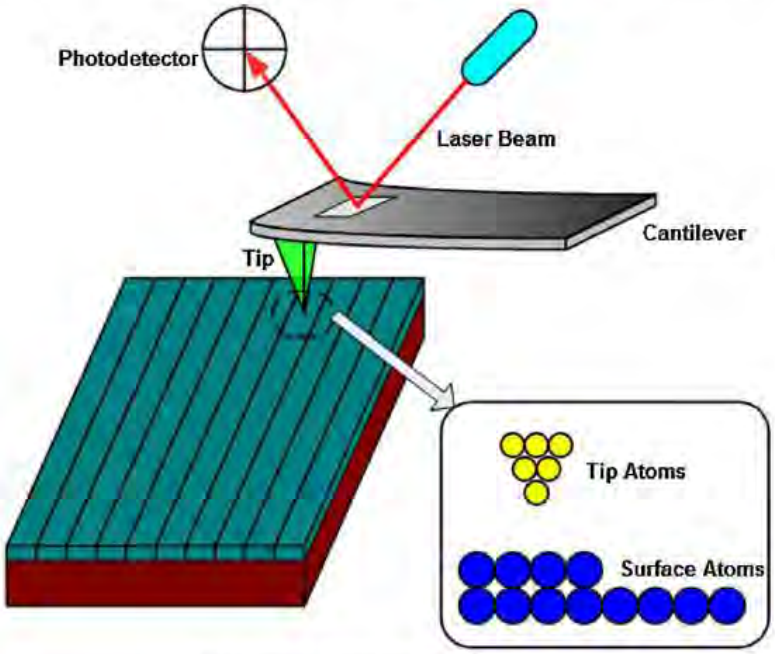


Fig. 28. Schematic illustration of the working of an AFM.

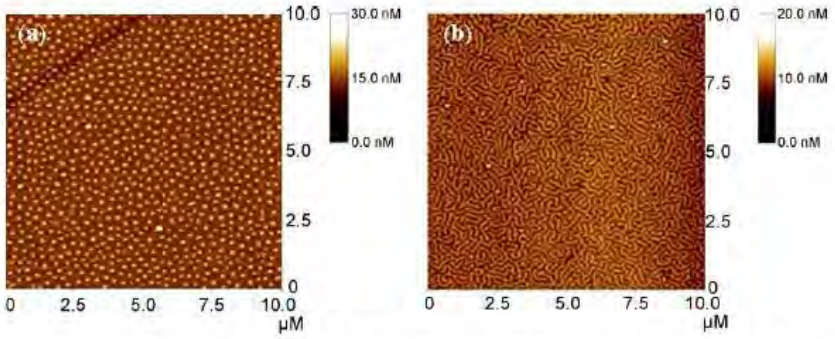


Fig. 29. AFM images of (a) a poly (styrene)-block-poly (2-vinylpyrindine) diblock copolymer (PS-b-P2VP) with a dot like nano-pattern, and (b) poly (styrene)-block-poly (4-vinylpyrindine) diblock copolymer (PS-b-P4VP) with a worm like nano-pattern. (Reprinted from [129] with permissions from American Chemical Society (ACS).)

from atomic scale resolution a major advantage of AFM is its ability to image any kind of surfaces such as polymers, ceramics, composites, metals, glass and biological samples. Various phenomena such as abrasion, adhesion, cleaning, corrosion, etching, friction, lubrication, plating and polishing can also be studied using AFM.

Khor et al. [129] used poly(styrene)-block-poly(2-vinylpyrindine) diblock copolymer (PS-b-P2VP) and poly(styrene)-block-poly(4-vinylpyrindine) diblock copolymer (PS-b-P4VP) to form surface-induced nanopatterns on mica substrate. Such surfaces were expected to attach mesenchymal stem cells and thereby induce a hierarchy of bone cell population. Diblock copolymers were dissolved in nonselective solvent, chloroform and then freshly cleaved mica substrates were dip-coated with the dilute polymer solution for 30 s and pulled out at a constant velocity of 10 mm/min. The polymer films were then annealed at 1400 C for 2–3 h under vacuum in a vacuum oven. It was believed that surface interaction controlled micro phase separation led to the formation of chemically heterogeneous surface and nanopatterns on dry ultra thin film. A dot-like and worm-like nanopattern of the polymer surfaces were observed (Fig. 29) [129] by scanning the coated samples under AFM in tapping mode.

Wilson et al. [130] used a low-powered gas plasma with O_2, Ar, and N_2 as the treatment gasses to modify the surface of a medical

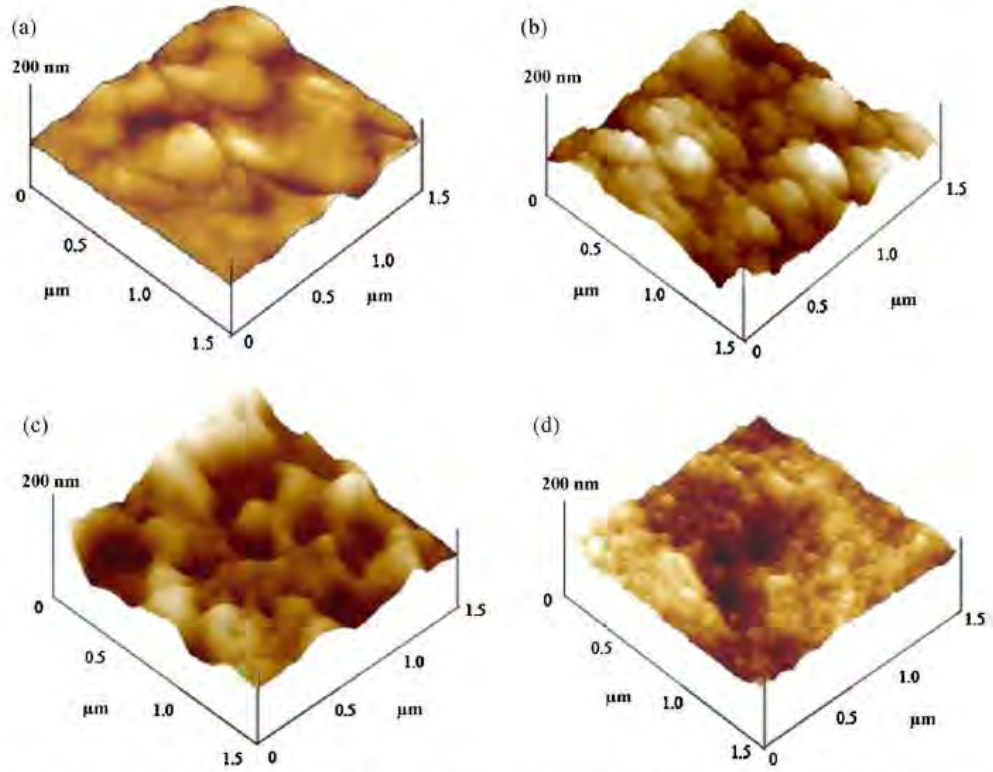


Fig. 30. AFM micrographs of an (a) untreated polyetherurethane surface, (b) O_2 treated polyetherurethane surface, (c) Ar treated polyetherurethane surface and (d) N_2 treated polyetherurethane surface. (Reprinted from [130] with permission from Elsevier.)

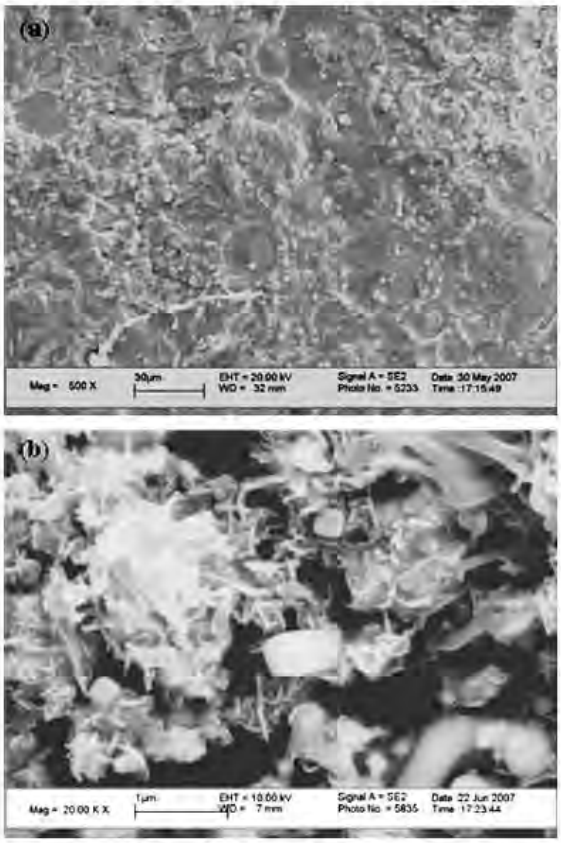


Fig. 31. SEM images of (a) the rough surface of a Ca–P coating on Ti–6Al–4V substrate obtained by direct laser melting technique, and (b) both cuboid and needle-like apatite phase on such coating following immersion in simulated bio fluid for 1 day.

grade segmented polyetherurethane (PEU). The variation in surface morphology due to such a treatment was studied using AFM and is illustrated in Fig. 30. It was observed that all the plasma treated surface demonstrated a modification in surface morphology (Fig. 30(b)–(d)) as compared to the untreated surface (Fig. 30(a)). O_2 plasma treatment demonstrated the mildest modification of the surface with a fine globular texture as compared to both Ar and N_2 plasma treatment.

In a scanning electron microscope a high energy (typically, 5–100 keV) electron beam is scanned across the surface of the sample, to generate low-energy secondary electrons. These secondary electrons are then captured by a Everhart-Thornley electron detector to form a SEM image. Apart from just a 3D topographic image of a biomaterial surface, a SEM can also be used for observing the microstructural or various phase evolutions at the surface. Fig. 31(a) shows the rough surface of a Ca–P coating on Ti–6Al–4V substrate obtained by direct laser melting technique. Following immersion in a simulated bio-fluid (SBF) for 1 day the sample demonstrated the formation of both cuboid and needle-like apatite phase (Fig. 31(b)) on the surface.

Richards et al. [131] demonstrated suitability of a field emission scanning electron microscope, using low voltage, high current backscattered electron detection for producing stereo images with great detail and resolution. Fig. 32(a) shows the SEM image of an etched titanium surface revealing the fine surface structure as well as the grain boundary. The protrusions in each grain are oriented differently and are believed to be formed due to the etching process. Also the technique was effectively used to analyse biological samples. Fig. 32(b) shows the L929 fibroblast cell cultured on a plastic coated with 8 nm gold/palladium. The fine fillopodia emerging from the cell for anchorage to the substrate as well as the detail and the spatial orientation of the surface belbs on the main cell body can be clearly seen.

1.3.3.2. Surface wettability. When an implant material is placed inside a human body, among the plethora of events that take place the first and the foremost one is the wetting of the implant material by the physiological fluids. This further controls the adsorption of proteins followed by attachment of cells to the implant surface. Hence surface wettability is considered as an important criterion that can dictate the biocompatibility of the implant material. The three most important factors that affect the wettability of a surface are its chemical composition, microstructural topography, and surface charge. Contact angle measurements are probably the most adopted technique to measure the average wettability of a surface [132–138]. Contact angle measurements can be carried out by five different techniques known as the (1) static or sessile drop method, (2) Wilhelmy plate method, (3) captive air bubble method, (4) capillary rise method, and (5) tilted drop method. Among the above techniques, static or sessile drop is the most commonly used method. In this case, a droplet of properly purified liquid is put on the solid surface using a contact angle goniometer as shown in Fig. 33(a) [139], (b), and (c). The angle formed between the solid–liquid interface and liquid–vapor interface and which has a vertex where the three interfaces meet is called the contact angle (Fig. 34). The interfacial tensions of the solid–vapor (γ_{sv}), liquid–vapor (γ_{lv}) and solid–liquid (γ_{sl}) interface, and the contact angle (θ), are related by an equation known as the Young's equation:

$$\gamma_{lv}\cos\theta = \gamma_{sv} - \gamma_{sl}$$

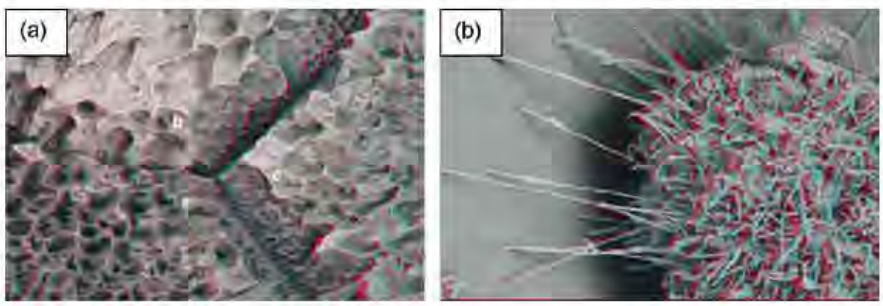


Fig. 32. Stereo images of (a) an etched titanium surface, and (b) L929 fibroblast cell cultured on a plastic coated with 8 nm gold/palladium, obtained by a field emission scanning electron microscope, using a low voltage, high current backscattered electron detector. (Reprinted from [131] with permission from Elsevier.)



Fig. 33. Picture of a contact angle goniometer used to measure the measure the contact angle by the static or sessile drop technique (a) (reprinted from [139] with permission from source: http://www.labkorea.com/products/cam/tantec/cammicro.html#specs), digital images of (b) a liquid drop formed on the surface of a sample and, (c) the corresponding contact angle formed by such a drop as measured by the goniometer.

If the contact angle is high (>90°) (Fig. 35(a)) then the surface is considered as a nonwetting or a hydrophobic surface. If the contact angle is small (Fig. 35(b)), then the surface is considered as a wetting or a hydrophilic surface. The energy of the surface (γ_{sv}) which is directly related to the wettability is also a very useful parameter that can strongly affect the biological interaction. But γ_{sv} cannot be directly obtained from the above equation as we have two unknowns γ_{lv} and γ_{sl} γ_{sv} can only be calculated by solving simultaneous equations with data collected from liquids of different surface tension.

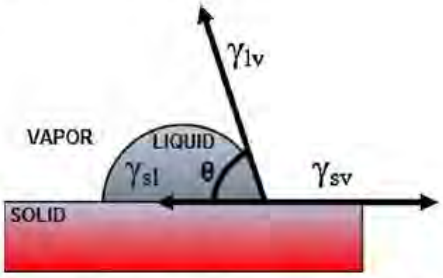


Fig. 34. Schematic illustration of a contact angle formed by a liquid drop at the solid/liquid interface and the liquid/vapor interface.

Several researchers have studied the interaction of different types of cultured cells or blood proteins with various solid substrates having different wettabilities to correlate the relationship between surface wettability and cell or blood compatibility [140–142]. Wei et al. [140] modeled the surfaces of hexamethyldisiloxane to different degrees of wettability and thereby studied its effect on cell attachment, cell proliferation, and cell morphology. Plasma polymerization followed by O_2 plasma treatment was used to modify the surface of hexamethyldisiloxane. It was observed (Fig. 36) that with an increase in O_2 plasma treatment duration there was a decrease in contact angle of distilled water on these surfaces. Such a decrease was attributed to the introduction of more hydrophilic –COOH groups and a decrease of hydrophobic groups such as $-CH_3$ on the surface. SEM images in Fig. 37 demonstrate the number variation in L929 cell attachment with varying surface wettability. After 6 and 24 h of incubation it can be observed that the hydrophilic surface has more cells attached as compared to the hydrophobic surface. Further cell spreading also was farther at lower contact angles as compared to higher contact angles.

1.3.3.3. Surface chemistry. Chemical composition of a biomaterial surface can be characterized using X-ray photo electron spectroscopy (XPS), auger electron spectroscopy (AES), Fourier transformation infrared (FTIR) spectroscopy, X-ray diffraction (XRD), and secondary ion mass spectroscopy (SIMS).

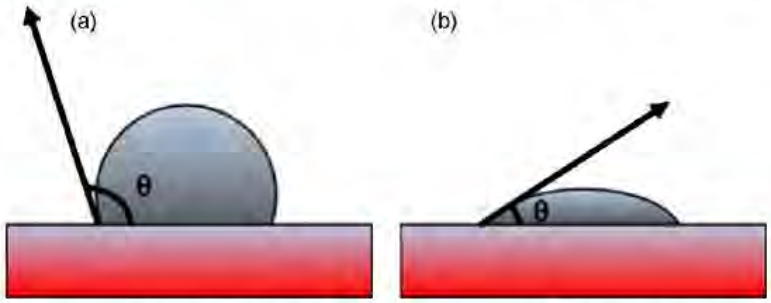


Fig. 35. Schematic illustration of (a) a hydrophobic or non-wetting surface and (b) hydrophilic or wetting surface.

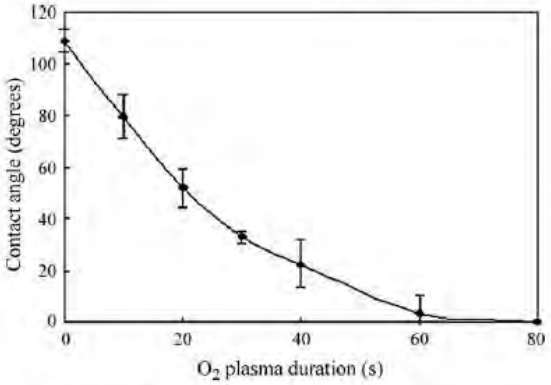


Fig. 36. Surface contact angle of hexamethyldisiloxane surface with different O_2-plasma treatment duration. (Reprinted from [140] with permissions from Wiley Inter Science.)

XPS is widely used to determine the elemental composition of solid surfaces (except H and He). It is capable of providing elemental depth profiles up to 10 nm into the sample. AES can be used for determining both the chemical composition of a solid surface and mapping the spatial distribution of the surface constituents and obtain a depth profile of these constituents into the bulk of the material. FTIR holds the capability for chemical analysis of solids, liquids and gasses. Its other advantages include multicomponent analysis capability, good sensitivity, excellent specificity, speed and simplicity of calibration. It is based on the fact that every molecule has a vibrational spectrum, which is a unique physical property and is a characteristic of the molecule. SIMS is used to determine the surface and near-surface composition in a wide range of solid materials. It is based on the principle that bombardment of a material with a high-energy (1-30 keV) ion beam results in the ejection or sputtering of atoms from the material. Some of these ejected atoms leave as either positively or negatively charged ions and are referred as secondary ions. Collection of these sputtered secondary ions and their analysis by

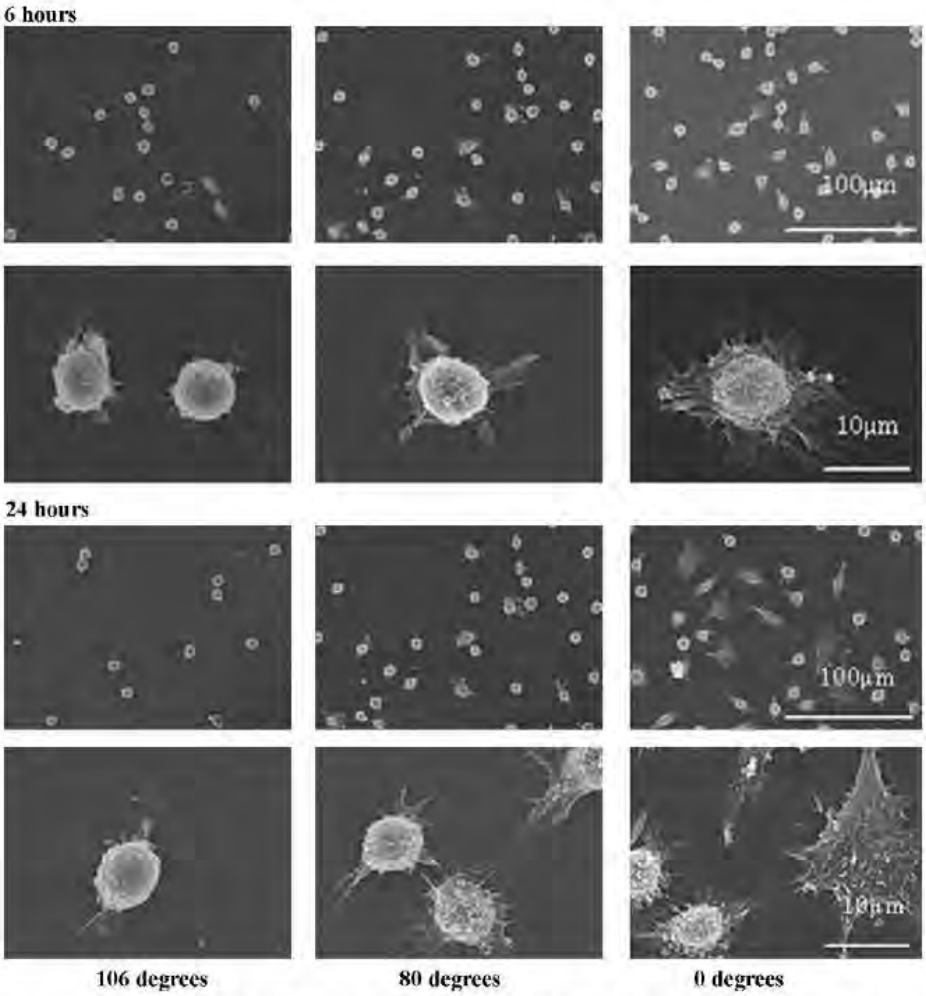


Fig. 37. SEM of L929 attached to surfaces with different wettability in 6 and 24 h in low magnification (original: 500×) and high magnification (original: 3000×). (Reprinted from [140] with permissions from Wiley Inter Science.)

mass-to-charge spectrometry gives information on the composition of the sample. Since sputtering of atoms from the surface of a material is a surface erosion process, it is a destructive technique. XRD is a nondestructive technique that provides detailed information about the chemical composition and crystallographic structure of natural and manufactured materials.

Surface chemical composition and its analysis by the above techniques are important criteria in the design of biomaterials as it determines which functional groups are available for interaction with the biomolecules. Depending on the type of species available and its exposure, the biomolecules may have different affinities for various surfaces [15]. Further at a microscopic level, a biomaterial surface may have patches, or domains, of different functionality and these patches or domains can interact differently with the biomolecules. For example metallic materials mostly exist in more than one phase. Ti–6Al–4V a commonly used orthopedic implant material consists of two different phases, i.e. the α- and β-phase. Not only these different phases but also the grain boundaries may have a different chemical composition and thereby a different interaction with biomolecules. In polymers, segregation resulting

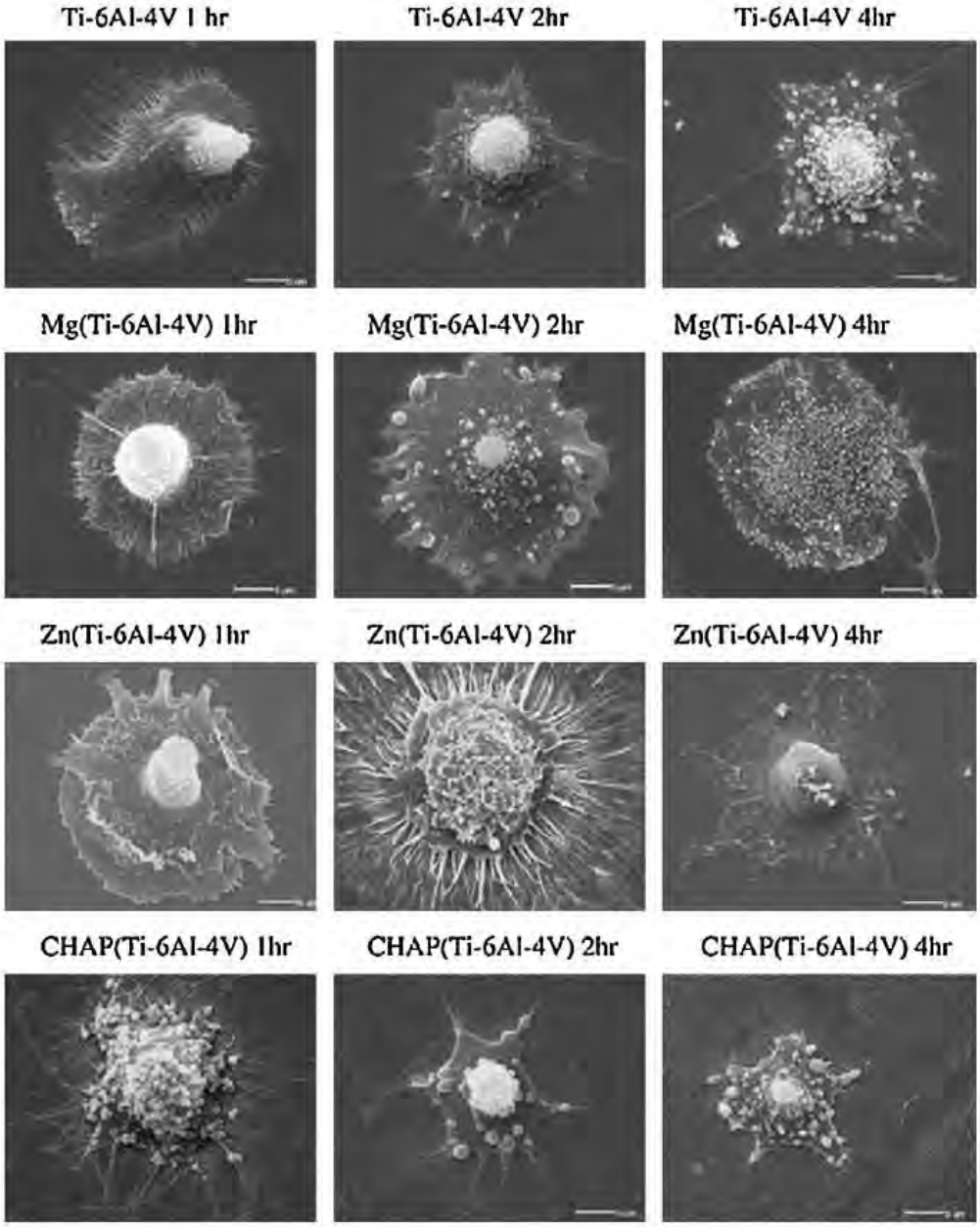


Fig. 38. Scanning electron micrographs of human bone-derived cells cultured on Ti–6Al–4V, Zn–Ti–6Al–4V, Mg–Ti–6Al–4V, and CHAP–Ti–6Al–4V for 1, 2, and 4 h. The cells demonstrated normal morphology on all surfaces. Images at 2000× magnification. (Reprinted from [143] with permission from Elsevier.)

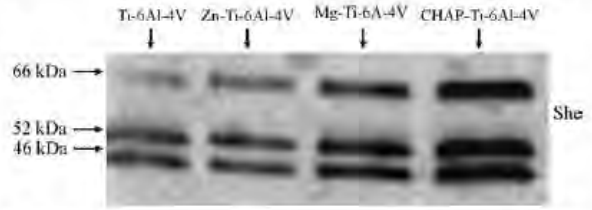


Fig. 39. Shc expressed by serum-starved primary human bone-derived cells (HBDC) cultured for 2 h on titanium alloy (Ti–6Al–4V), titanium alloy modified with zinc (Zn–Ti–6Al–4V), magnesium (Mg–Ti–6Al–4V) or alkoxide-derived hydroxy carbonate apatite (CHAP–Ti–6Al–4V). Equal amounts of total proteins were resolved by 10% Tris–HCl polyacrylamide gel electrophoresis and analysed by immunoblotting with anti Shc. Maximum levels of the three isoforms (66, 52, and 46) of Shc expression were found when HBDC were cultured on CHAP–Ti–6Al–4V. (Reprinted from [143] with permission from Elsevier.)

from folding of macromolecular chains can provide various microstructural domains. Depending on the chemical species present within these domains, proteins may have different interaction with each phase. An extensive amount of research involving the modulation of surface chemistry and there by its effect on in vitro and in vivo cellular responses, including adhesion, survival, cell cycle progression, and expression of different phenotypes have already been studied [143–148].

Zreiqat et al. [143] investigated the effect of surface chemistry modification of Ti–6Al–4V alloy with zinc, magnesium, and alkoxide-derived hydroxy carbonate apatite (CHAP) on the regulation of key intracellular signaling proteins in human bone-derived cells (HBDC) cultured on these modified surfaces. An ion beam implantation technique was used to modify the surface of Ti–6Al–4V with Zn and Mg and a sol gel coating technique was used to deposit alkoxide-derived hydroxy carbonate apatite on the surface of Ti–6Al–4V. SEM images (Fig. 38) [143] of HBDC cultured on the three different surfaces for 1, 2, and 4 h demonstrated the attachment, spreading and normal, healthy morphological features of the cell at all time. Western blotting analysis (Fig. 39) [143] demonstrated an enhanced activation of key intracellular signaling proteins such as Shc on surfaces of Ti–6Al–4V modified with CHAP and Mg. The authors therefore concluded that Ti–6Al–4V surfaces modified with CHAP and Mg may contribute to successful osteoblastic function and differentiation at the skeletal tissue–device interface.

Scotchford et al. [144] cultured human osteoblast cells on self-assembled monolayers (SAMs) of alkylthiols on gold with carboxylic and methyl termini. They studied the kinetics and proliferation of cell attachment in response to the two different surface chemistries. Here the single-component SAMs were produced by the adsorption of 3-mercaptopropanoic acid [MPA, $HS(CH_2)_2COOH$] and octanethiol [OT, $HS(CH_2)_7CH_3$] onto gold-coated glass coverslips to produce carboxylic-acid-terminated hydrophilic monolayers or methyl-terminated hydrophobic monolayers, respectively. Osteoblasts in response to the two contrasting chemistries showed a significant difference in the extent of cell attachment and spreading (Fig. 40) [144]. Osteoblast seeded on MPA SAMs showed a greater extent of spreading, with polyhedral morphologies while the cells on OT SAMs remained rounded or assumed more restricted bipolar morphologies. Also the number of cells on MPA SAMs after 90 min of incubation were approximately twice, and after 18 h were approximately 10 times the number of cells on OT SAMs. Such an improvement on MPA SAMs might be attributed to the hydrophilic nature of the carboxylic-acid terminated monolayers.

1.4. Surface science and engineering for performance enhancement

The various phenomena that may occur at the interface after implantation of a biomaterial into a living system are sequential and is schematically shown in Fig. 41. Initially the proteins respond to the implant surface and form a thin layer of protein film on the

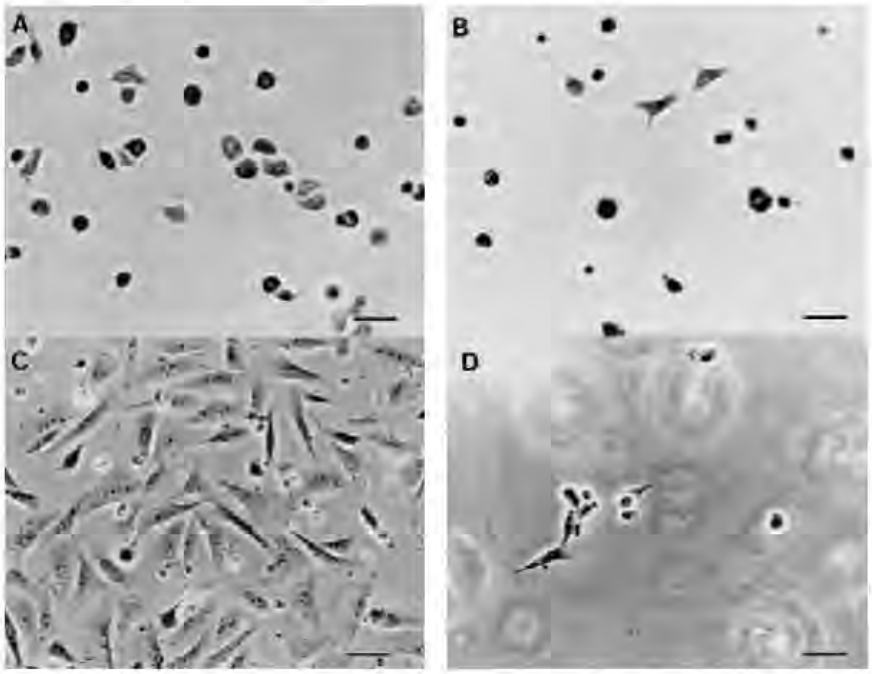


Fig. 40. Osteoblast attachment to PMA and OT SAMs at 90 min (A: MPA, B: OT) and 18 h (C: MPA, D: OT). Bar = 50 μm. Original magnification 180×. (Reprinted from [144] with permissions from Wiley Inter Science.)

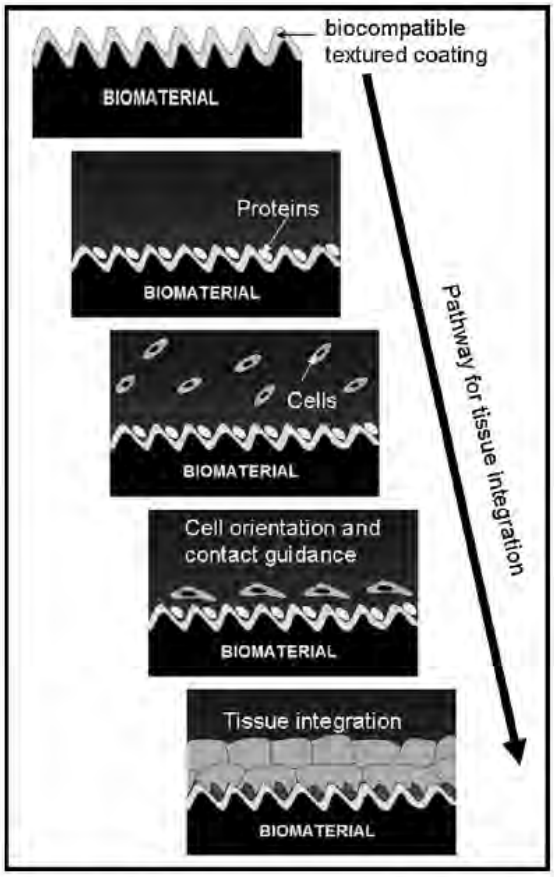


Fig. 41. Schematic illustration of the sequential reactions that take place after the implantation of an biomaterial into a living system.

surface within few seconds. Since cells respond to the proteins, this protein film then controls the subsequent bioreaction. The cells then multiply and organize into various types of complex tissues. Therefore, the adsorption of proteins plays a vital role in determining the nature of the tissue–implant interface. Protein adsorption to the surface of a biomaterial depends both on the type of protein and nature of the surface. The properties of protein that affect their interaction with surfaces are [149]:

- *Size*: Larger protein molecules are expected to have more sites of contact with the surface than a smaller one.
- *Charge*: Distribution of charge on the protein surface can greatly influence the protein adsorption. Molecules near the isoelectric point generally adsorb more readily to the surfaces.
- *Structure stability*: Molecules with less intramolecular cross-linking are considered as less stable molecules. These molecules can unfold to a greater extent and form more contact points with the surfaces.
- *Unfolding rate*: Molecules that rapidly unfold can form contact points with the surfaces quickly.

The properties of a biomaterial surface that affect their interaction with proteins are as follows [149]:

- *Topography*: Greater textures or three-dimensional topographic cues expose more surface area for interaction with biomaterials. Surfaces with grooves and pores have greater surface area as compared to a smooth surface.
- *Chemical composition*: The chemical composition that makes up the surface, determine the type of intermolecular forces governing the interaction with proteins.
- *Heterogeneity*: Nonuniformity of surfaces provides multiple domains for the interaction with proteins. For example a metallic material may have grains with different phases which may interact with the proteins differently. Not only the grains, also the grain boundaries interact in a different manner.
- *Potential*: Surface potential influences the structure and chemical composition of the environment surrounding the biomaterial. It influences the distributions of ions in the solution and thereby its interaction with proteins.

In addition to protein and surface properties, adsorption also depends on the availability of molecules for interaction with the surface. Protein molecules can be brought to the surface by one or more of the following four transport mechanisms: (1) diffusion, (2) thermal convection, (3) flow, and (4) coupled transport, such as combination of convection and diffusion.

Hence, adsorption of proteins to the surface of a biomaterial is an important issue in its design. This leads to the exciting field of surface science and engineering. Surface engineering for biomaterials offers the ability to modify material and biological responses through changes in surface properties while still maintaining the bulk properties of the implant. Surface modifications for biomaterials can be classified according to the surface properties being altered, e.g., morphological, and physiochemical or biological modifications.

1.4.1. Morphological modifications

Morphological modification of biomaterial surfaces are aimed at creating three-dimensional features in the form of pores, gratings, columns, dots, pits and random surface roughness [130–171]. These three-dimensional features mimic the extra-cellular matrix (ECM), a natural cell environment which possesses complicated nano- and macro-architecture. This can be achieved by various techniques such as ion beam etching, chemical etching, plasma etching, electron beam lithography, photolithography, surface coatings, freeze casting, sintering, UV-irradiation, mechanical roughening, etc.

Kim and coworkers studied a sand blasted and acid etched titanium surface (Fig. 42) [160] for its biocompatibility and osseointegration. This technique has the advantage of both sand blasting and acid-etching and thereby creating both macroroughness and micro pits on the surface. Human osteoblast cells grown on the sand blasted and acid etched titanium surface shows very good adherence and spread over the surface after 7 days of incubation (Fig. 43) [160]. In vivo evaluations of the samples were carried out using a screw shaped sand blasted and acid etched titanium implants. The implants were placed in New Zealand white rabbits in each proximal tibial metaphysic after giving them a general anesthesia. After 4 weeks of healing period the rabbits were sacrificed and bone blocks were removed to measure the percentage of bone-to-implant contact. Histological image (Fig. 44) [160] shows very good bone bonding and bone formation at the interface.

Since naturally occurring bone is a porous material, there is a physiological rationale for the use of porous scaffolds for its replacement at defect sites. Apart from just mimicking the natural organization of bone a porous structure also helps in the supply of blood and oxygen to the implant interface and facilitates bone ingrowth and anchoring at the interface. Fig. 45(a) [171] shows a nanohydroxyapatite and poly(L-lactic acid) porous composite scaffold fabricated using a phase separation technique. Porous

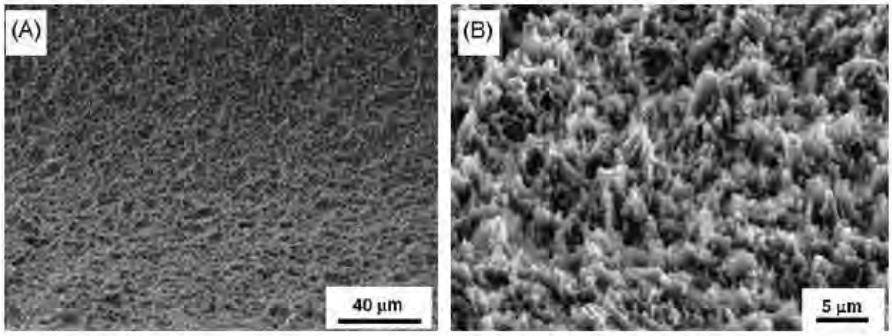


Fig. 42. (A and B) SEM image of a sand blasted and acid etched titanium surface. (Reprinted from [160] with permissions from Institute of Physics Publishing (IOP).)

coatings (Fig. 45(b)) [163] are also being widely used for load bearing hip and knee implants.

Lu et al. patterned Ti surfaces with micrometer to nanometer features (Fig. 46) [164] utilizing a novel plasma-based dry etching technique. In vitro studies using rat aortic endothelial cell demonstrated enhanced endothelial cell coverage and alignment on nanometer-scale Ti patterns as compared to micrometer-scale Ti patterns and random nanostructured surfaces (Fig. 47) [164]. Choi et al. [169] developed two distinct nanopatterns (posts and grates) (Fig. 48) with varying three-dimensionalities on silicon substrate using a combination of interference lithography and deep reactive ion etching technique. Culture of human foreskin fibroblast (Fig. 49) on these surfaces exhibited smaller cell size and lower proliferation on needle-like nanoposts, and enhanced elongation and alignment on blade-like nanogrates. This phenomenon is attributed to the distinct contact guidance provided by the two surfaces.

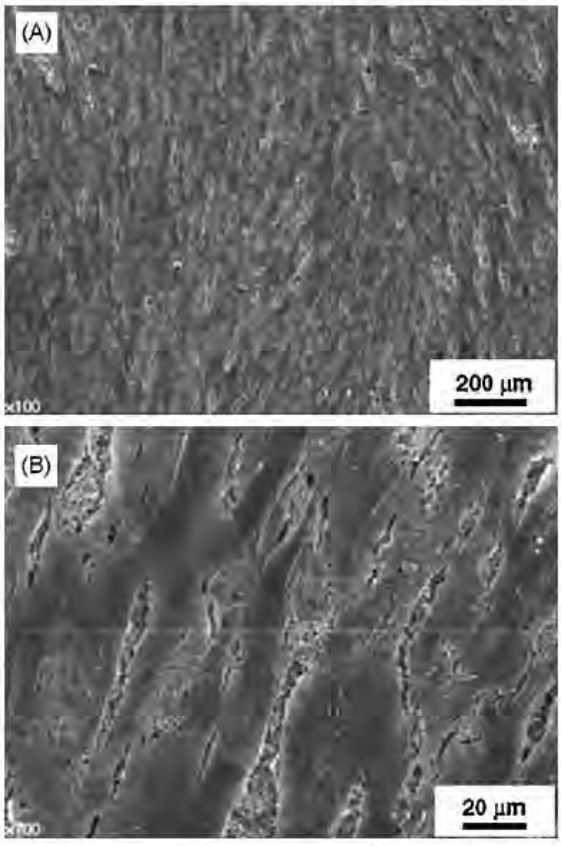


Fig. 43. SEM image of human osteoblast on the SLA surface after seven days of incubation at different magnification. (A) 100× and (B) 700×. (Reprinted from [160] with permissions from Institute of Physics Publishing (IOP).)

1.4.2. Physiochemical modifications

Material and biological responses can be altered by changing physiochemical characteristics such as surface energy, surface charge and surface composition. This can be achieved by various techniques such as glow discharge, ion implantation, grafting and surface coatings.

Glow discharge involves the exposure of surface to a highly energized inert gas such as plasma [172]. Plasma glow discharge is most commonly used to sterilize the surface of biomedical devices and surgical instruments used for clinical applications. The energetic species in the plasma can easily kill a broad range of bacteria by generating oxygen, hydroxyl free radicals and other active species. This further improves the wettability of the implant material or its hydrophilicity. It has got several advantages compared to other sterilization techniques and can be listed as follows [172]:

- It is a nontoxic and fast procedure.
- Since plasma sterilization is similar to plasma etching it not only kills the bacteria, but also removes them from the surface.
- It is inexpensive and relatively a safe technique.

Ion implantation involves the bombardment of highly energetic ionic species to the surface of a material. The ions penetrate the surface and thereby bring significant changes in chemical composition and structure at the near surface region. This further improves the wear resistance, corrosion resistance and biocompatibility of implant materials. For example calcium ions implanted into the surface of titanium can improve its bone conductivity. Penetration and phase changes at the surface of Titanium following varying dosages of Ca ion implantation are schematically illustrated in Fig. 50 [173]. Calcium titanate is formed at the surface when Ca ions are implanted at the rate of 10^{16} and 10^{17} ions/cm^2 and both calcium oxide and calcium titanate are formed when ions are implanted at 10^{18} ions/cm^2. Fig. 51 [173] shows the scanning electron micrographs of unimplanted titanium (a) and calcium-ion-implanted titanium (b) after immersion in a simulated body fluid for 30 days. It is observed that calcium ions implanted titanium accelerated calcium phosphate precipitation following immersion. Zhao et al. [174] implanted NH^{2+} ions by ion implantation technique

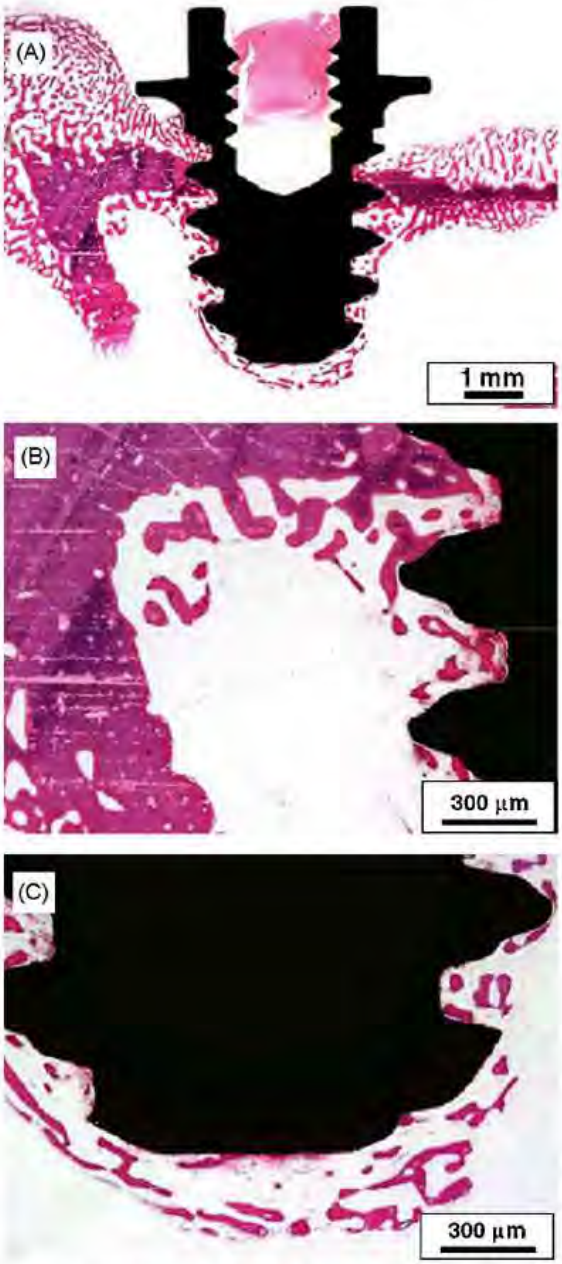


Fig. 44. Bone formation along the SLA surface from the cortical bone to the apex. (Reprinted from [160] with permissions from Institute of Physics Publishing (IOP).)

into the surface of Al_2O_3 ceramics to improve its biocompatibility. The implanted samples kept in the jaw bone of dogs and removed after 8 months by surgery clearly demonstrated the formation of new Haversian system of bone formation across the interface.

Grafting involves the attachment of specific functional groups (mostly polymeric chains) onto the surface of a biomaterial [175–177]. This can be achieved by graft polymerization technique provided that the surface active sites or free radicals are available to react with a monomer. If reactive groups are available on the surface, the desired polymer can be attached through free radical graft polymerization of a monomer or through chemical reaction of a polymer with functional end groups. If there are no reactive groups available on the surface then plasma, γ-ray and UV light-induced graft polymerization is a useful technique.

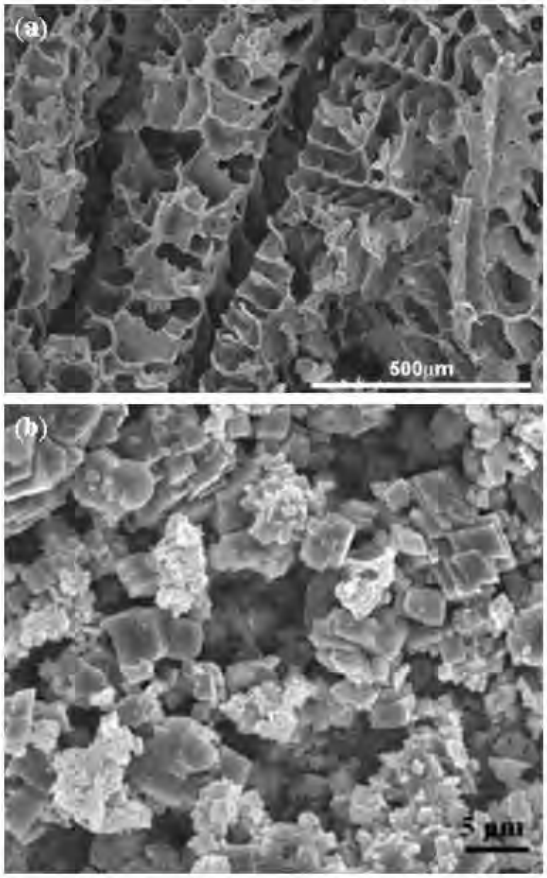


Fig. 45. Figure illustrating (a) a nanohydroxyapatite and poly (L-lactic acid) porous composite scaffold fabricated using a phase separation technique and (b) a porous calcium carbonate coating on Ti–6Al–4V obtained by electrophoresis deposition. (Reprinted from [171] and [163] with permission from Elsevier.)

A hydrophilic polymer, poly(N-vinyl-2-pyrrolidone) attached on to the surface of a polypropylene microfiltration membrane by UV photo-assisted and γ-ray pre-irradiated induced graft polymerization technique is schematically illustrated in Fig. 52 [175]. For UV assisted graft polymerization technique the membrane was first dipped in an acetone solution of benzophenone for 20 min. After thorough washing and drying, it was put into a solution containing N-vinyl-2-pyrrolidone and deionized water followed by irradiation under a UV lamp to achieve the attachment of the polymer chain to the membrane substrate. For γ-ray-induced graft polymerization the membrane was initially irradiated with a series of γ-ray dosages inside a reaction flask under nitrogen atmosphere at room temperature. After irradiation, a mixture of N-vinyl-2-pyrrolidone solution and deionized water is injected into the flask and the whole unit is immersed in a water bath maintained at 75 °C. The reaction is continued for 10 h for the attachment.

Grafting of poly(ethylene glycol) methacrylate on the surface of stainless steel for reduction in protein adsorption and thereby thrombosis is schematically illustrated (Fig. 53) [176] in a three

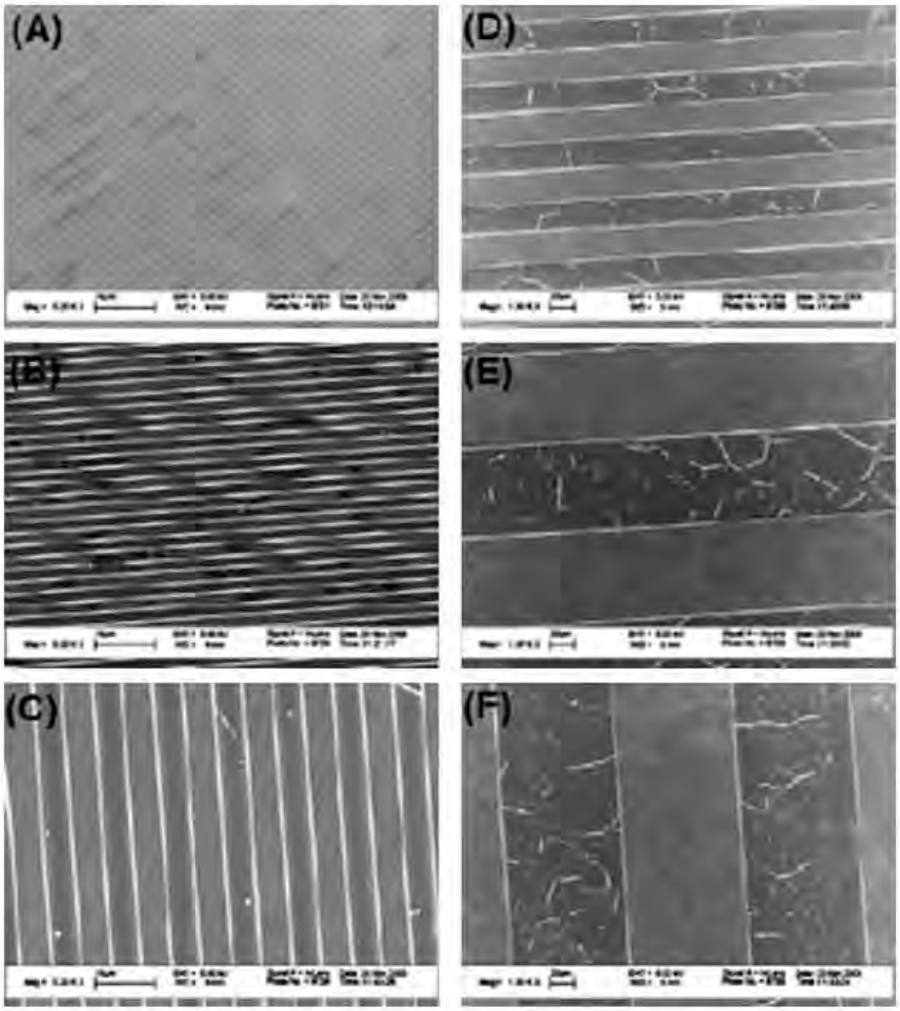


Fig. 46. Scanning electron microscope (SEM) images of Ti patterned surface features of (A) 750 nm, bar = 1 μm; (B) 2 μm, bar = 1 μm; (C) 5 μm, bar = 1 μm; (D) 25 μm, bar = 20 μm; (E) 75 μm, bar = 20 μm; and (F) 100 μm, bar = 20 μm. The thin nonuniform bright lines and spots observed in the etched grooves (darker stripes) are artifacts of dry etching process. (Reprinted from [164] with permission from Elsevier.)

step process. Here the stainless steel surface was first modified by a silane coupling agent (SCA), (3-mercatopropyl)trimethoxysilane. The silanized surface was then activated by argon plasma and subsequently subjected to UV-induced graft polymerization of poly(ethylene glycol)methacrylate. As electrostatic interactions play an important role in many biological events, charged surfaces can also modify the protein and cell behavior at the interface [149]. Negatively charged surface can be created by grafting acidic or sulfonate containing functional groups and positively charged surface by grafting amino-containing functional groups. Negatively charged surface delay thrombosis, and those with positively charged surface accelerate it [149].

Surface coatings can also be used to provide surface composition chemically different from the substrate. For orthopedics engineered bio coatings of alumina, zirconia, bioactive glasses (glass ceramics) and calcium phosphate-based (Ca–P) ceramics on Ti base alloys is a common practice. Alumina and zirconia are considered as bioinert as they do not induce the formation of a fibrous tissue at the interface and direct bonding with the surrounding tissues. Bioactive glasses and Ca–P-based ceramics are considered as bioactive as they form a direct chemical bonding with the bone. Ca–P-based ceramics are widely used as bioactive coatings as it possess similarity with the mineral phase hydroxyapatite present in the human bone and teeth. Ion beam assisted deposition, plasma spray coating, pulsed laser physical vapor deposition, magnetron sputtering, etc. are among the several types of coating methodologies that are being employed to achieve such a surface. Microstructure, bioactivity and biocompatibility of Ca–P-based surface coatings using all of these techniques is the central theme of this review article and is going to be covered in the later part.

1.4.3. Biological modification

In the last few years there has been a major shift in the design criteria for modern synthetic biomaterials. An understanding of cell and molecular biology had led biologists, chemists and material scientists to design biomaterials equipped with molecular cues mimicking certain aspects of structure or function of natural extra-cellular microenvironments [149,178–185]. Hence biological surface modification is aimed at controlling cell and tissue

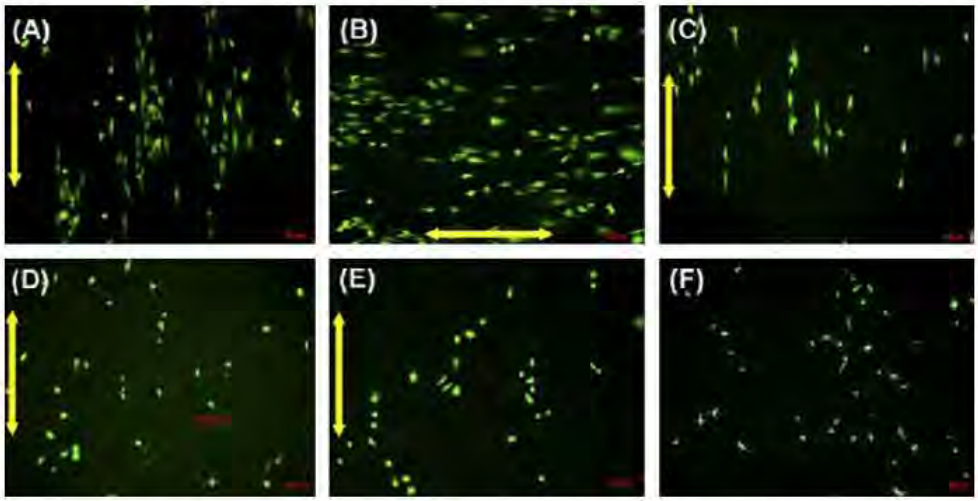


Fig. 47. Rat aortic endothelial cell (RAEC) cell density after the first day of culture on Ti patterns of (A) 750 nm; (B) 2 μm; (C) 5 μm; (D) 75 μm; (E) 100 μm and (F) random nanostructured Ti surfaces. (A–F) bars = 50 μm. Arrows indicate groove alignment direction on patterned samples. (Reprinted from [164] with permission from Elsevier.)

response to an implant by immobilizing biomolecules representing such molecular cues on the surface of biomaterials. Adsorption, entrapment, and covalent attachment are the three mechanisms by which biomolecules are immobilized on the surface of a biomaterial. The most frequently used biomolecules for immobilization include, RGD peptides, heparin and heparin sulfate binding peptides, and purified protein components such as fibronectin, laminin, and collagen. Purified protein components such as collagens from animal tissues are advantageous because of their inherent properties of biological recognition, presentation of receptor binding ligands and susceptibility to cell triggered degradation and remodeling [178]. RGD peptide sequence on the surface of a biomaterial can promote the adhesion of cells through integrin receptors and, therefore, stimulate cell spreading and growth [179–180]. Heparan sulfate proteoglycans present on cell surfaces can mediate cell attachment through interaction between the negatively charged proteoglycans and positively charged peptides [149].

A novel mechanism where the molecular recognition between avidin and biotin is used as a foundation for the immobilization of RGD peptides to a polymer surface is schematically illustrated in Fig. 54 [181]. Here a biotinylated biodegradable polymer, PLA-PEG-biotin is initially synthesized as the first step in the process. The structure of such a polymer is shown in Fig. 54(a). The three components in this polymer have their own advantages. PLA is a biodegradable polymer which ensures that the material is eliminated by the body once its function is accomplished. PEG is a hydrophilic, protein-resistive component included to reduce

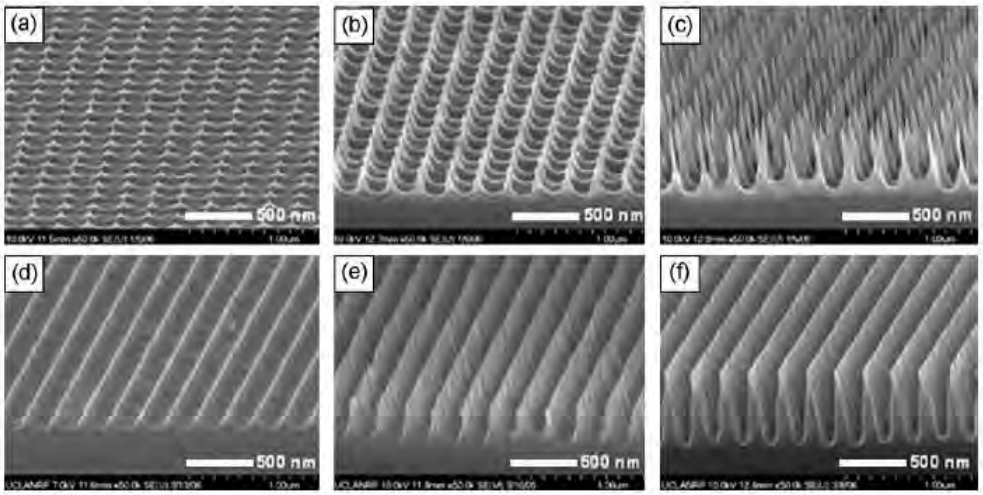


Fig. 48. SEM images of 3D sharp-tip nanotopography samples of silicon. The well-regulated 'nanopost' (a–c) and 'nanograte' (d-f) structures were formed by interference lithography and DRIE uniformly on 2 cm × 2 cm silicon substrate, which was then cut into 1 cm × 1 cm samples for the study. While the nanostructure pitch was all kept constant to be 230 nm and tips were all sharpened to be needle- or blade-like, structure heights were varied from 'low' (a and d: 50–100 nm high), 'mid' (b and e: 200–300 nm high) to 'high' (c and f: 500–600 nm high) to investigate he exclusive effect of the nanotopographical three-dimensionality to cell behaviors. (Reprinted from [169] with permission from Elsevier.)

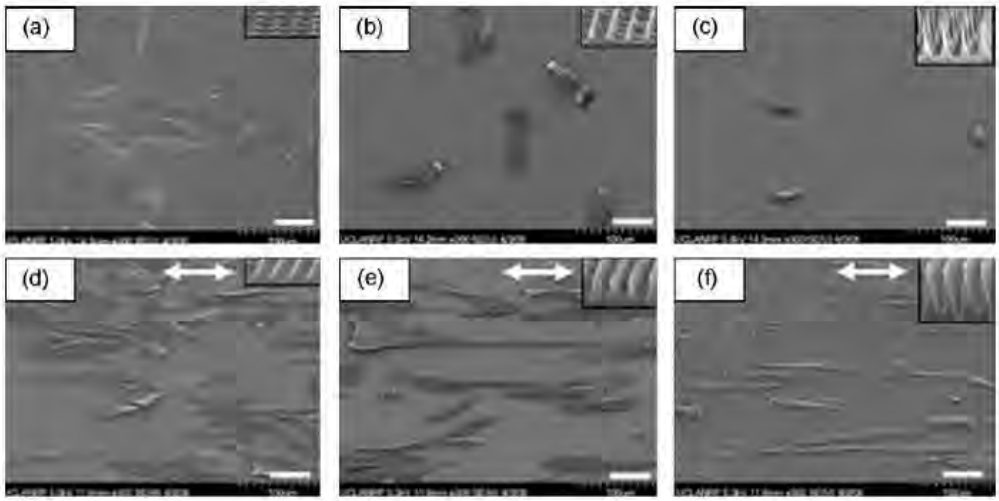


Fig. 49. Cell morphology on 3D sharp-tip nanotopography. To examine fibroblast cells' morphology, the SEM images were taken at the culture periods of 3 days on nanopost (a: low, b: mid, c: high), and nanograte (d: low, e: mid, f: high) samples. The scale bar in each image indicates 50 μm. Each inset in (a–c) and (d–f) represents the sample's nanotopography, shown in higher magnification. Each arrow (⟷) in (d–f) represents the direction of nanograte patterns on the sample. (Reprinted from [169] with permission from Elsevier.)

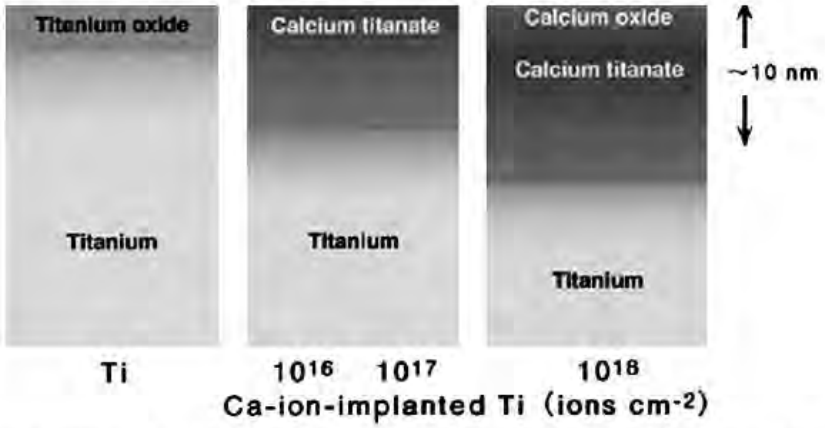


Fig. 50. Schematic illustration of cross-sections of surface-modified layers of titanium specimens with and without calcium-ion-implantation. (Reprinted from [173] with permission from Elsevier.)

nonspecific interactions between the biomaterial and the living environment. Finally, the biotin allows for surface engineering using avidin (Fig. 54(b)). Since avidin has a tetrameric structure with four available sites, it binds the biotin using one of these sites. The free available sites are, therefore, available for the attachment of biotinylated ligand motifs.

Biological surface modifications can also be aimed at producing surfaces resistant to biofouling, protein and cell adhesion and thereby improve its blood compatibility. The outer membrane of intact blood cells consists mainly of phosphorycholine containing phospholipids that provide a nonthrombogenic surface. Hence phosphorycholine polymers can, therefore, be grafted on to biomaterial surfaces to mimic the phospholipid head groups of the cell surface and thereby improve its biocompatibility. Fig. 55 [182] shows the immobilization of phosphorycholine polymers on a titanium surface controlled by a vinyldimethylsilane (VDMS) monolayer.

2. Methodologies for coating Ca–P ceramics on Ti-alloys

In the past few decades extensive research on Ca–P-based coated implants have not only focused on the tissue–implant interface, but also on the problems associated with the coating process and optimization of coating parameters to enhance tissue response. The minimal requirements of Ca–P coating as described by the Food and Drug Administration USA (FDA) and International Standard Organization (ISO) is listed in Table 6 [186,187]. A variety of surface coating methodologies such as ion beam assisted deposition, plasma spray deposition, electrophoretic deposition, pulsed laser physical vapor deposition, micro-arc oxidation, magnetron sputtering, sol–gel derived coatings, etc. are being currently employed to deposit Ca–P on Ti-based alloys and thereby meet the standards and guidelines set by FDA and ISO. Most of these techniques are aimed to enhance short- and long-term performance of implants by encouraging bone ingrowth and

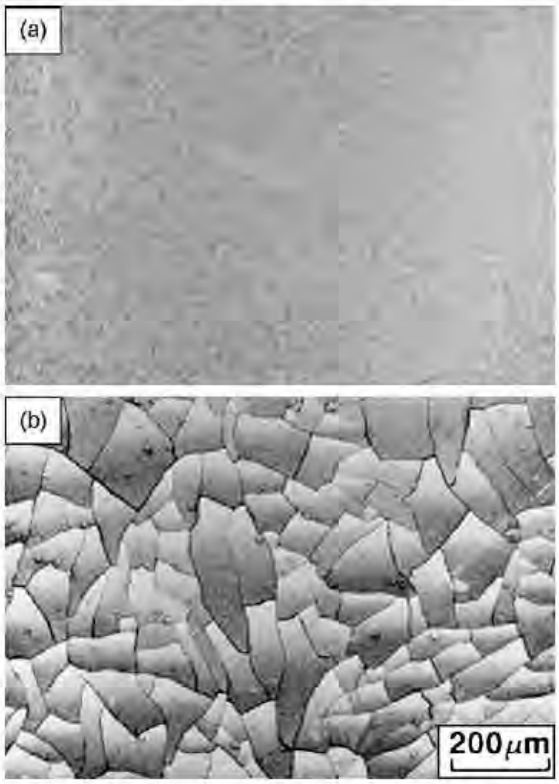


Fig. 51. Scanning electron micrographs of unimplanted titanium (a) and calcium-ion-implanted titanium (b) immersed in Hank's solution for 30 days. (Reprinted from [173] with permission from Elsevier.)

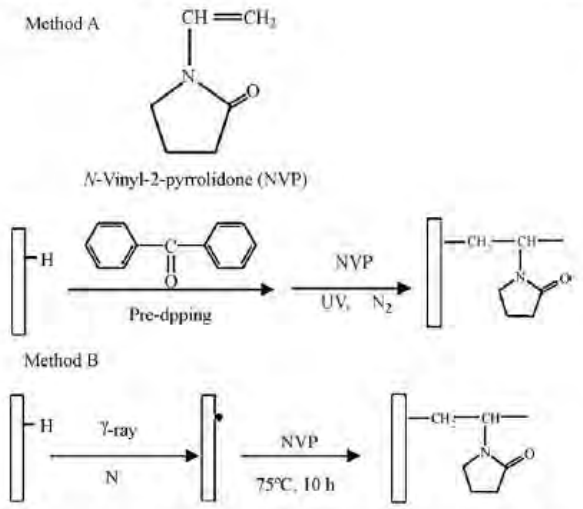


Fig. 52. Molecular structure of N-vinyl-2-pyrrolidone and schematic representation of the grafting process. Method A: UV-assisted grafting and Method B: γ-ray pre-irradiation grafting. (Reprinted from [175] with permission from Elsevier.)

Table 6
FDA requirements for HA coating.

Properties	Specification
Thickness	Not specific
Crystallinity	62% minimum
Phase purity	95% minimum
Ca/P atomic ratio	1.67–1.76
Density	2.98 g/cm^3
Heavy metals	<50 ppm
Tensile strength	>50.8 MPa
Shear strength	>22 MPa
Abrasion	Not specific

providing enhanced fixation. Further, coatings of these bioceramics on Ti-based alloys also provide the appropriate surface chemistry for tissue compatibility without altering the bulk mechanical properties of the material. Among the above coating methodologies plasma spray deposition is the most commercially used technique for orthopedics and dental implants, but it suffers from certain draw backs such as poor adherence of the coating to the substrate, low fracture toughness of the ceramic coating, lack of uniformity of the coating, thickness, biodegradation, fatigue and third body wear of the coating [7,188]. The higher coating thickness (>100 μm) associated with plasma spraying technique poses a major problem as it can cause failure due to fatigue under tensile loading conditions [188]. Also with increasing thickness the

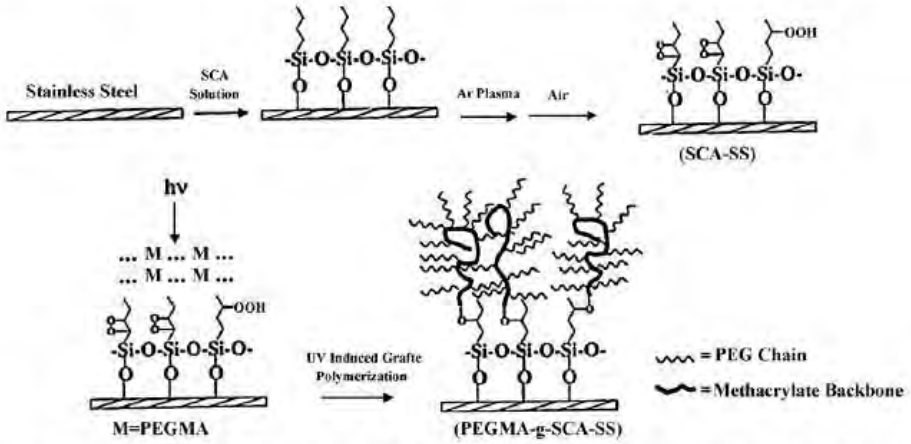


Fig. 53. Schematic illustration of the process of surface modification of stainless steel by silane treatment, Ar plasma treatment and UV-induced surface graft polymerization. (Reprinted from [176] with permission from Elsevier.)

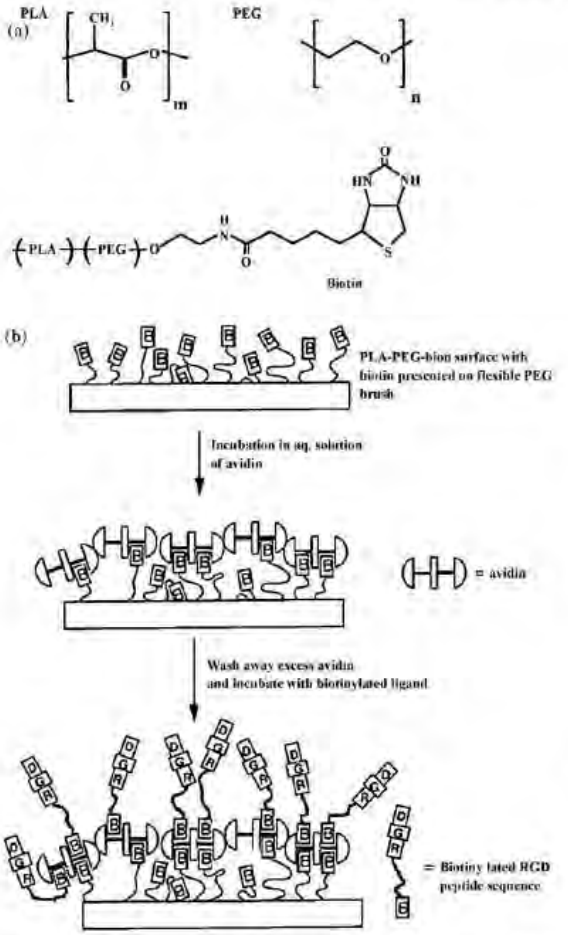


Fig. 54. (a) Molecular structure of a PLA-PEG-biotin and (b) Schematic diagram showing the surface engineering of a PLA–PEG–biotin to produce a cell-adhesive surface. (Reprinted from [181] with permissions from American Chemical Society.)

residual stresses within the coatings increases and its energy release may promote cracking at the substrate/coating interface [188]. Hence, to address these issues a variety of thin film-based coating techniques such as pulsed laser physical vapor deposition, magnetron sputtering, ion beam assisted deposition, etc. are being employed to deposit Ca–P coatings on metallic substrates [188]. Nonetheless, this and all other techniques listed above and the

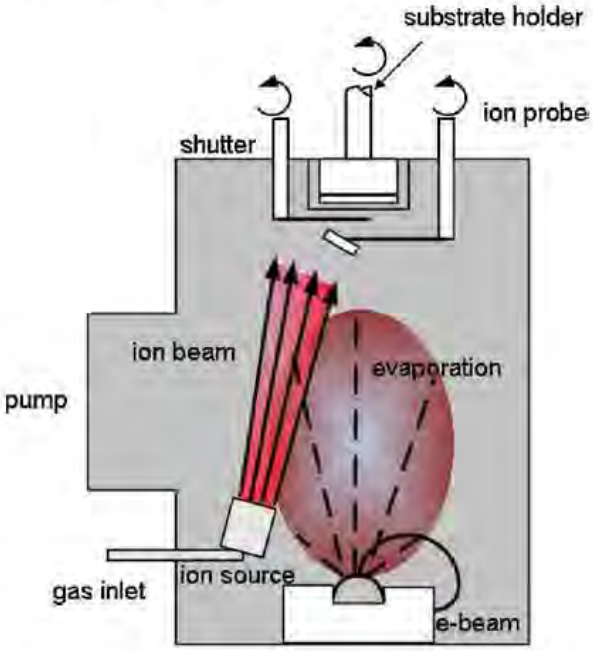


Fig. 56. Experimental set up for ion beam assisted deposition using a single ion source.

performance of Ca–P coatings in bio-environment produced using these techniques are reviewed in the following sections.

2.1. Ion beam assisted deposition

Ion sources for material modification first started with the ion implantation technique in the semiconductor industry in 1970 [189]. In this case, materials were doped in the neat surface region by implantation of highly energetic ion beams. Several years later another branch of ion beam technology evolved, where the ion beam is used to coat the surface of a material with thin films. This is referred to as the ion beam assisted deposition process (IBAD) and is useful for depositing films with variety of film properties with respect to their applications. Some featured applications include thin films for optical and electronic devices and corrosion and wear resistant films. IBAD system consists of two main parts: sources for low energy particles which constitute the film to be deposited and sources for simultaneous irradiation with highly energetic ion source. Low energy species are mostly vapor sources where the vapor is generated either by resistive heating or electron beam

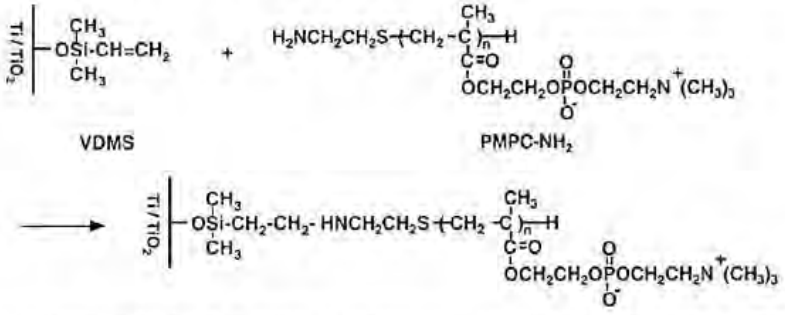


Fig. 55. Figure illustrating the immobilization of phosphorycholine polymers on to titanium surface controlled by a vinyldimethylsilane (VDMS) monolayer. (Reprinted from [182] with permission from Elsevier.)

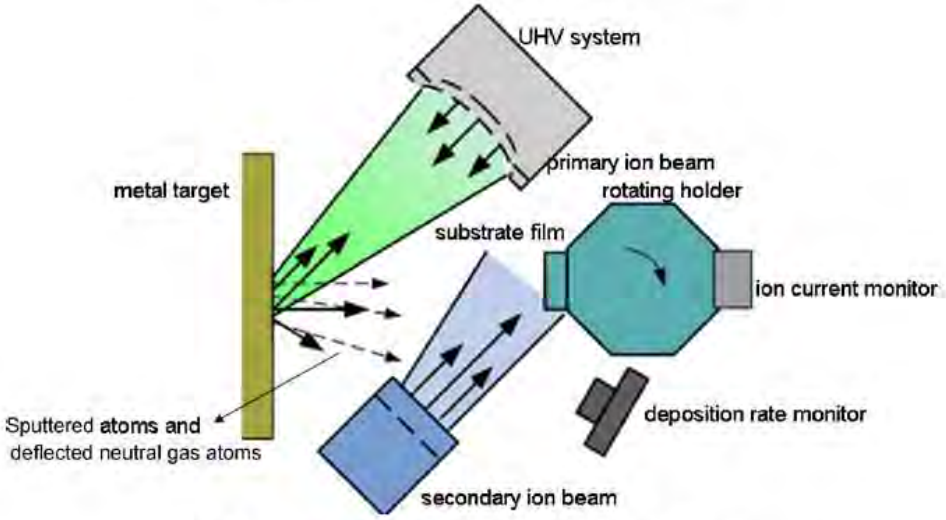


Fig. 57. Experimental set up for a dual ion beam assisted deposition system.

heating of the material. Electron beam evaporation is a suitable technique owing to the good controllability of the electron beam, versatility and high deposition rates even for materials with low vapor pressure. A second ion beam can also be used for evaporation of the target material. Here an inert ion beam sputters the target material and deposits it on the substrate and simultaneously a reactive ion beam hits the growing film to form a compound. This technique is often called as the dual ion beam deposition (DIBD). Figs. 56 and 57 show the typical setups for IBAD with a single ion source and dual ion source, respectively.

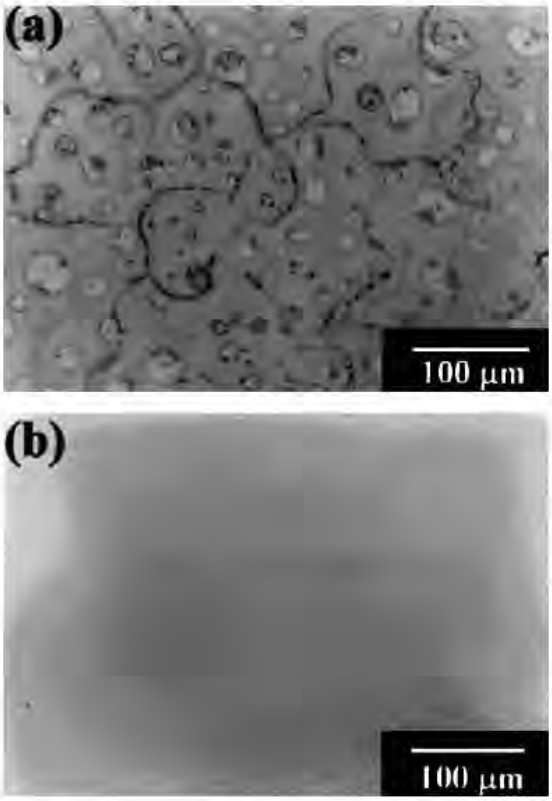


Fig. 58. Optical micrographs of coating layer deposited on Si wafer (a) without ion beam bombardments and (b) with Ar ion beam bombardments (120 V, 0.8 A). (Reprinted from [190] with permission from Elsevier.)

Lee et al. [190] synthesized Ca–P-based films on silicon wafers by electron beam evaporation of β-TCP with and without simultaneous Ar ion beam bombardments. Fig. 58 shows the optical micrographs of such films. It was observed that a simultaneous bombardment with Ar ion beam had a significant effect on the composition and morphology of the coating layer. The film formed without Ar ion beam bombardment had a Ca/P ratio of 0.76 and reacted immediately with the moisture in the air as soon as it is removed from the chamber. In contrast, the film formed with Ar ion beam bombardment had a Ca/P ratio of 0.80 with smooth and featureless surface morphology.

Hamdi and Ide-Ektessabi [191] synthesized hydroxyapatite (HA) films on silicon substrate by vaporizing both CaO and P_2O_5 targets using electron beam heater and resistance heater, respectively and by simultaneous bombardment with Ar ion beams. The effects of ion beam current density on the phase evolution during the deposition process were investigated. From the XRD spectra (Fig. 59) [191] a strong tricalcium phosphate (TCP) phase together with the HA phase was observed when the ion beam is not used to assist the deposition. At ion beam current density of 180 $\mu A/cm^2$ a small TCP peak was observed, and at ion beam current density of 260 $\mu A/cm^2$ only the HA peaks were observed. The increase in Ca/P ratio with increasing ion beam current density is mostly due to the high sputtering of P compared to that of Ca from the layer being coated.

Rabiei et al. [192] deposited functionally graded HA films on silicon substrate using a dual ion beam assisted deposition and simultaneous heat treatment process. Fig. 60 [192] shows the TEM cross-sectional view of the graded film. It was observed that grain size and crystallinity gradually decreased from the film/substrate interface to the film surface. The microstructure at the interface reveals very fine nanoscale crystalline columnar grains and at the top surface it is mostly amorphous. Microscratch adhesion test and nanoindentation test on the deposited films were carried out to study the mechanical behavior of the coatings. The functionally graded HA film has a higher average hardness (6.4 GPa) and

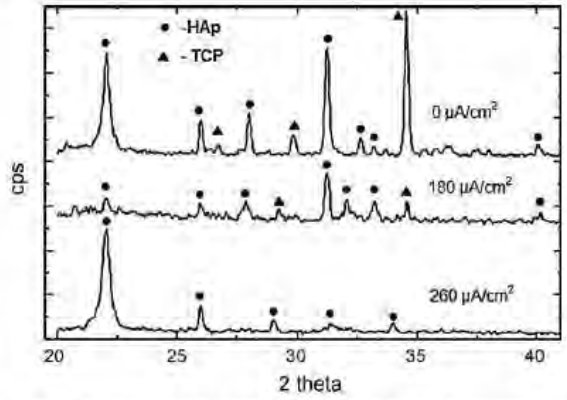


Fig. 59. XRD patterns of fully crystallized samples following heat-treatment at 1200 °C. (Reprinted from [191] with permission from Elsevier.)

Young's modulus (132 GPa) as compared to both sputter-deposited and sintered HA. Microscratch adhesion test (Fig. 61) illustrated a better integrity of the graded film with no transverse cracking and delamination from the substrate.

Several authors also studied the microstructure and morphological evolutions of the Ca–P coatings on Ti base alloys synthesized using IBAD process [193–196]. Choi et al. [193] deposited HA films on Ti–6Al–4V by electron beam vaporization of pure HA target and simultaneous bombardment using a focused Ar ion beam on the metal substrate to assist deposition. SEM micrograph of the deposited film is shown in Fig. 62 [193]. The effect of Ar ion beam current on the bond strength and dissolution of the coating in a physiological solution is studied. The bond strength between the coating and the substrate increased with increasing current, whereas the dissolution rate in physiological solution decreased remarkably.

Luo et al. [194] studied the morphological and structural evolution of HA crystals in the coating during post-heat-treatment. In this study, they hypothesized that the crystallization temperature of IBAD Ca–P coating on Ti–6Al–4V decreased from 500 to 400 °C through the introduction of water vapor in an ion beam assisted deposition and post-heat-treatment process. This decrease in crystallization temperature is attributed to the fact that the crystallization of amorphous calcium phosphate phase into HA is a hydroxyl-diffusion-controlled process. Further recrystallization phenomena also occurred in the coating during heat treatment at 400 °C for different time periods. The driving force for the process was mainly contributed by the high stress field caused by the difference in density between the amorphous calcium phosphate and HA. Hence the results confirmed that both the crystallinity and morphology of the Ca–P coating can be tailored by appropriate post-heat-treatment process.

Zhao et al. [196] deposited two types of Ca–P coatings, i.e. HA and porous tricalcium phosphate/hydroxyapatite (TCP/HA) on cpTi by IBAD. The biocompatibility of commercially pure titanium (cpTi), HA-coated cpTi, and porous TCP/HA-coated cpTi were investigated by culture of human gingival fibroblasts for different time periods. Cell attachment, cell spreading, collagen formation and the number of focal adhesion plaque was predominant with TCP/HA coated substrate as compared to Ti and HA coated substrate. Fluorescence staining (Fig. 63) [196] of vinculin on the three samples represents an increase in focal adhesion plaque with increased time periods of seeding and the TCP/HA coated substrate showing the maximum number of plaques as compared to HA-coated and Ti substrates. This improved biocompatibility of TCP/HA coated substrate is attributed to the lower Ca/P ratio.

2.2. Plasma spray deposition

Plasma spray involves the spraying of molten or heat-softened material onto a surface to provide coating. Material in the form of powder is injected into a high-temperature plasma flame, where it is rapidly heated and accelerated at a high velocity towards a substrate for coating. It uses an electric arc to ionize the gas and create high-pressure plasma. The temperature at the core region of plasma exceeds 30,000 K. Plasma arcs are of two types, the transferred and the non-transferred arc. In transferred arc the workpiece acts as the anode and the arc is struck between the cooled cathode and the anode. This is mostly employed for welding. For coating applications the non-transferred arc of a plasma gun is most suitable, as it does not create a predominant thermal effect on the substrate [197,198]. Fig. 64 illustrates a schematic setup of a non-transferred arc plasma system. Typically used plasma gasses are He, Ar, N_2, H_2 and mixture of these gasses. Argon is usually chosen as the base gas as it ionizes easily and also provides a stable arc at very low operating voltage [197,198]. The most essential parameters that may affect the coating microstructure and morphology are tabulated in Table 7 [199]. Some of the key applications that can be addressed by plasma spray technique include (1) in-flight melting, (2) densification and spheroidization of powders, (3) atmospheric and vacuum plasma spraying of protective coatings, (4) plasma deposition of near net shape bodies, (5) dc and rf induction plasma deposition of metal matrix composites, and (6) plasma reactive deposition [200]. Among the different coating methodologies applied to obtain hydroxyapatite coatings on various substrates, plasma spray coating is regarded as the most efficient and economical technique [201–205]. As these coatings enter into a human body, proper

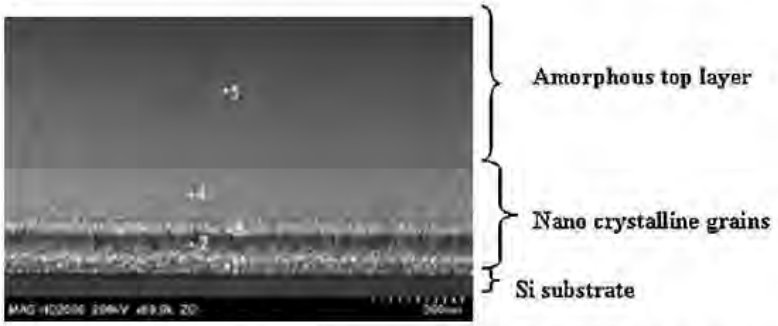


Fig. 60. TEM image showing the cross-section of HA film with graded crystallinity on Si substrate. (Reprinted from [192] with permission from Elsevier.)

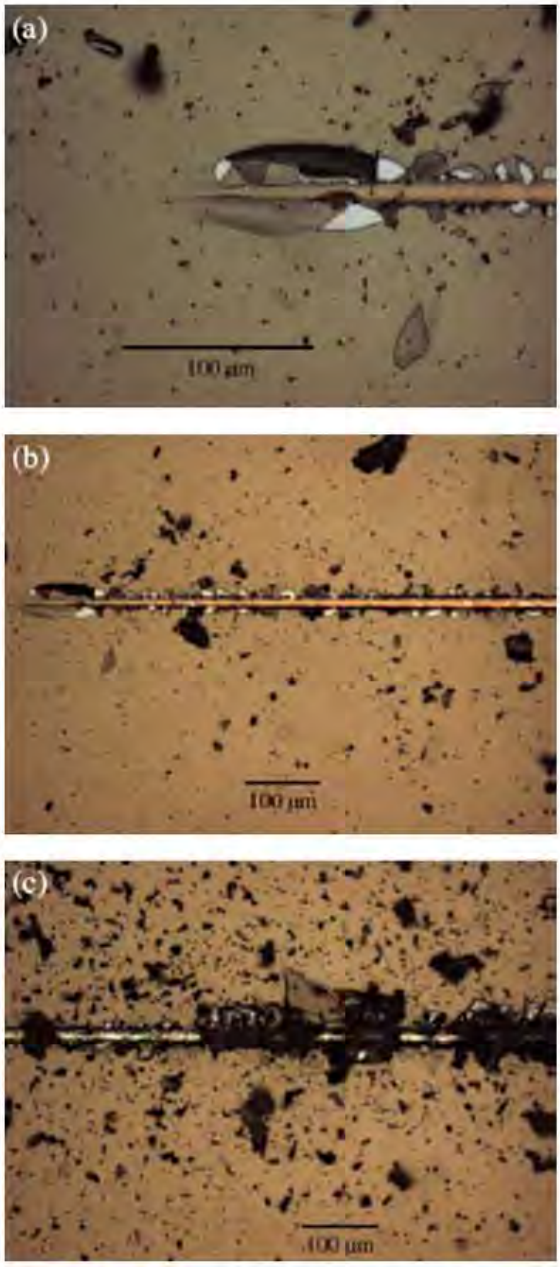


Fig. 61. Microscratch adhesion result for functionally graded hydroxyapatite composite film on silicon. (a) Film delamination occurs at 0.30N; (b) continuous film delamination occurs between 0.30 and 1N; (c) complete film penetration and plastic deformation of substrate occurs at 1N, showing very good integrity of the film. (Reprinted from [192] with permission from Elsevier.)

control and optimization of their quality and phases has to be done. Dyshlovenko et al. suggested a numerical simulation model of hydroxyapatite powder behavior in plasma jet [205]. Fig. 65 [205] shows the temperature fields inside the powder particle before impact and their transformation into crystal phases after rapid solidification and cooling. The temperature fields of the hydroxyapatite powders across the $Ar + N_2$ plasma jet at atmospheric

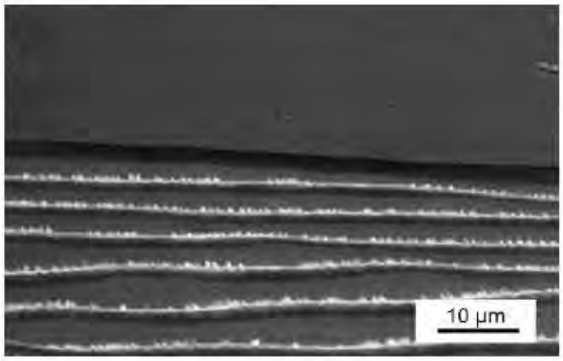


Fig. 62. SEM micrograph of the deposited HA film on Ti–6Al–4V substrate. (Reprinted from [193] with permission from Elsevier.)

pressure were calculated with the use of GENMIX numerical code. The particle temperature at the surface was calculated by assuming a convective heat transfer from the plasma to the particles described by the Nusselt number (Nu). This is related to the Reynolds number (Re) and the Prandtl Number (Pr) in the following way:

$$Nu = 2 + 0.6\,Re^{0.5}\,Pr^{0.33}\quad Re < 2.$$

The powder particle dimensions for the present simulation were taken in the range of 30–160 μm. Fig. 66 [205] shows that the surface temperature of a particle of this size is approximately close to the boiling point at a spray distance greater than 30 mm.

Chou and Chang [206] studied the microstructural characterization of plasma-sprayed hydroxyapatite–10 wt% ZrO_2 composite coating on Ti–6Al–4V substrates. ZrO_2 was used as the second phase to improve the fracture toughness of the coating owing to the high strength and stress-induced phase transformation toughening of these ceramics [207]. Fig. 67(a) and (b) [206] shows the bright field and dark field TEM images from the coating region. The corresponding selected area diffraction pattern is shown in Fig. 67(c) and (d). The selected area diffraction pattern in Fig. 67(c) is closely indexed to hydroxyapatite with a hexagonal crystal

Table 7
Essential parameters in plasma spraying. (Reprinted from [199] with permission from Elsevier.).

Burner chamber and nozzle
1) Power supply
2) Plasma gas
3) Mass flow rate of plasma gas
4) Mass flow rate of cooling fluid
5) Nozzle geometry
Powder feed
1) Powder fraction and shape
2) Thermal properties of powder material
3) Carrier gas
4) Mass flow rate of carrier gas
5) Injection geometry
Plasma jet
1) Jet velocity and temperature
2) Particle velocity and temperature
3) Particle trajectories
Particle impact
1) Particle impact distribution
2) Particle velocity at impact
3) Particle impact angle
4) Molten state of particle at impact
5) Substrate type
6) Substrate temperature

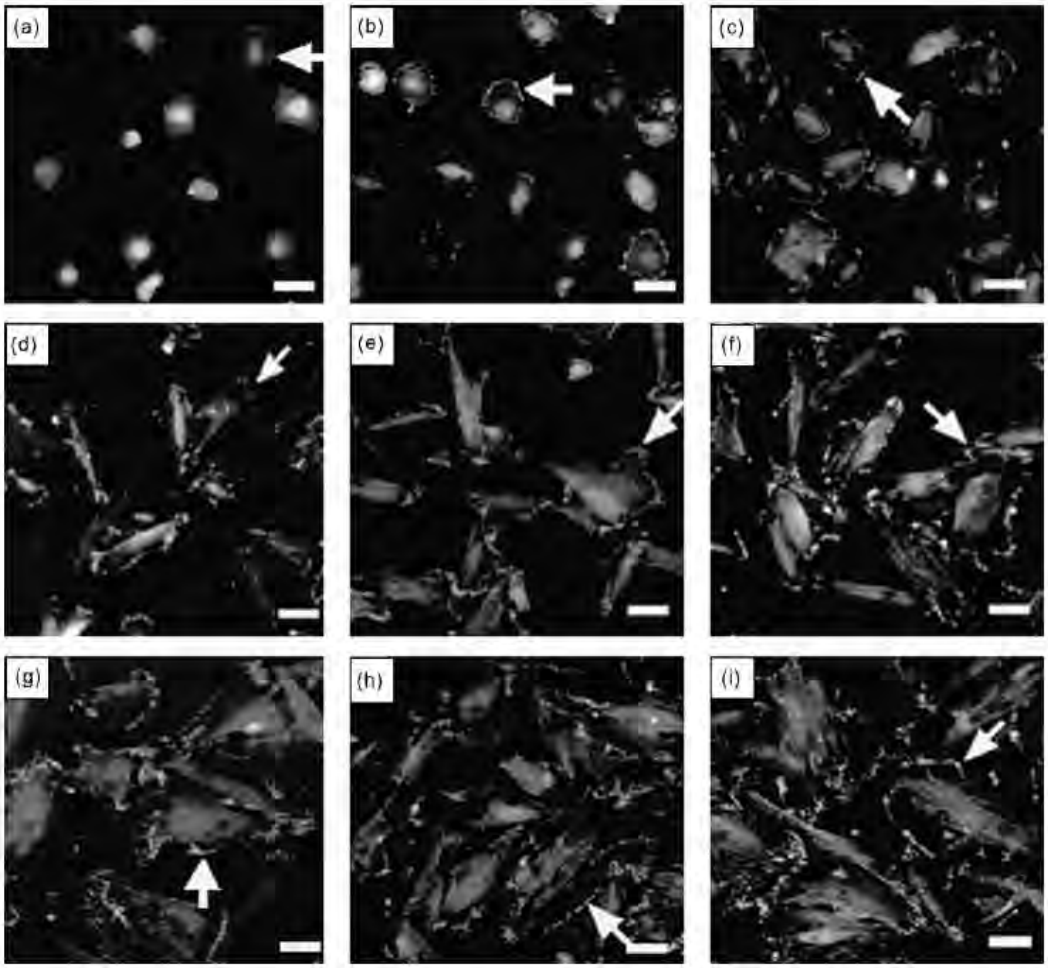


Fig. 63. Immunofluorescent staining image of vinculin. Immunofluorescent staining image of vinculin on titanium (a, d, g), HA (b, e, h), and TCP/HA (c, f, i) at 3 h (a–c), 12 h (d–f), and 24 h (g–i). The number of vinculin-positive adhesions (arrows) on HA and TCP/HA is more than that on titanium at 3 and 12 h ($p < 0.05$), but there is no significant difference at 24 h ($p > 0.05$). The number of stained vinculin on TCP/HA is more than that on HA ($p < 0.05$) at 3 h, but no difference at 12 and 24 h ($p > 0.05$) (bar = 20 μm). (Reprinted from [196] with permission from Elsevier.)

structure, in which the direction of the zone axis is $[2\bar{2}0\bar{1}]$ and the hydroxyapatite grain size is 0.5 μm. Fig. 68(a) [206] shows a lattice image of the HA crystal in the $(10\bar{1}0)$ plane and surrounding amorphous calcium phosphate region. The microdiffraction pattern taken from this amorphous region shows the characteristics of an amorphous state in Fig. 68(b). The formation of amorphous calcium phosphate is attributed to the rapid cooling rate associated when the molten HA impinges on a relatively cooler substrate and as a result of which the kinetics of crystallization is slowed down. The good bonding between the ZrO_2 aggregate and the calcium phosphate matrix is attributed to the melting of HA and welding to the ZrO_2 particle during the short period of plasma spraying. The initial ZrO_2 cubic phase is also retained after plasma spraying. This indicates that the toughening mechanism is mostly due to composite formation rather than transformation toughening mechanism of ZrO_2.

Khor et al. [201] performed a bifunctional composite coating of HA/Ti–6Al–4V powders on Ti–6Al–4V substrates. This approach was aimed to overcome the poor mechanical properties of pure HA and the poor bond strength between HA coating and metallic prosthesis. Fig. 69(a) shows the SEM image of a cross-sectioned as sprayed composite coating. A TEM bright field image of the composite coating in Fig. 69(b) shows the Ti–6Al–4V fine grains (Ti), amorphous phase (A) and HA crystals (HA). The good adherence of the composite coating and substrate was believed to be due to the good wetting characteristics of the ceramic and the metallic phases in the plasma stream. The coatings were then heat treated at 600 °C for 6 h to promote crystallization and relieve the residual stresses. TEM images of the heat-treated samples revealed the nucleation of HA crystals within the amorphous (Fig. 70(a)) and at the interface of the amorphous and crystalline regions (Fig. 70(b)) due to rapid solidification. The authors also concluded that the HA/Ti–6Al–4V composite has demonstrated a higher bond strength value than that of as sprayed composite coating.

Huaxia et al. [208] studied the microstructural evolution that takes place in HA during plasma spraying of HA on titanium substrate. The SEM image (Fig. 71(a)) of a cross-sectioned sample and the XRD pattern taken from the surface of the coating ((Fig. 71(b)) shows the formation of pure HA. The TEM micrograph in Fig. 72(a) shows the formation of crystalline phase in

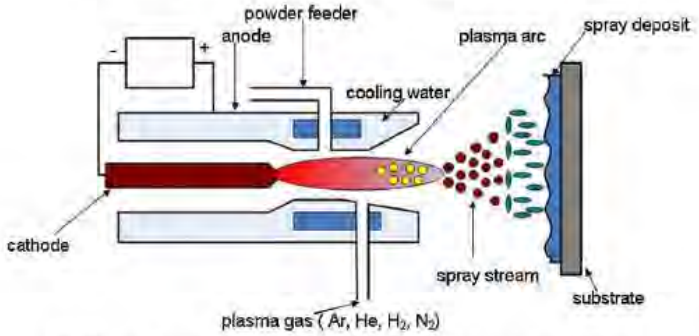


Fig. 64. Figure illustrates a schematic setup of a non-transferred arc plasma system.

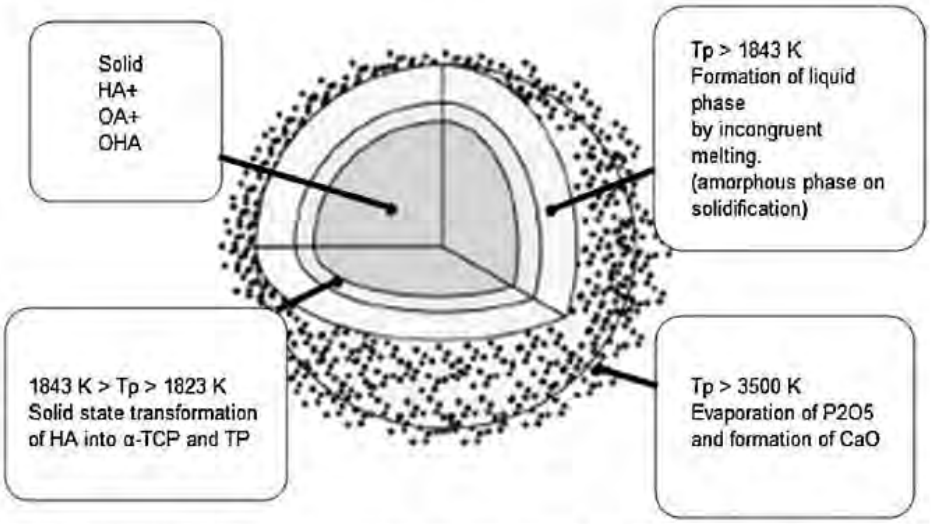


Fig. 65. Temperature fields inside powder particle before impact and their transformations into crystal phases after rapid solidification and cooling. Oxyhydroxyapatite (OHA) and oxyapatite (OA) are the products of the solid-state decomposition of HA (dehydration). (Reprinted from [205] with permission from Elsevier.)

amorphous matrix. Selected area diffraction patterns from the crystalline phase in Fig. 72(b) shows the formation of series of rings associated with the size and magnitude of the crystalline grains. In contrast the pattern from the amorphous phase shows a diffused pattern in Fig. 72(c). The formation of a good bonding between the coating and the substrate is revealed in the TEM micrograph in Fig. 73. This may be attributed to the chemical bonding between the substrate and interface and mechanical interlocking due to plasma spraying. Further, Tsui et al. [209] studied for the optimization of coating properties and recommended the following steps in order to produce stable and adherent coating. (1) Spraying with high plasma power and suitable plasma gas mixture so as to sufficiently heat the HA particles and ensure low porosity and good cohesive and adhesive strength, (2) improving interfacial adhesion by adding titanium precoat prior to the deposition of HA, and (3) heat treatment at 700 °C for 1 h to improve its crystallinity and OH^- content without significantly affecting its mechanical degradation. Inagaki et al. [210] obtained highly crystallized and highly (0 0 1)—oriented HA coatings by thermal plasma spraying technique on titanium substrates. The formation of a prismatic HA grains with c axis

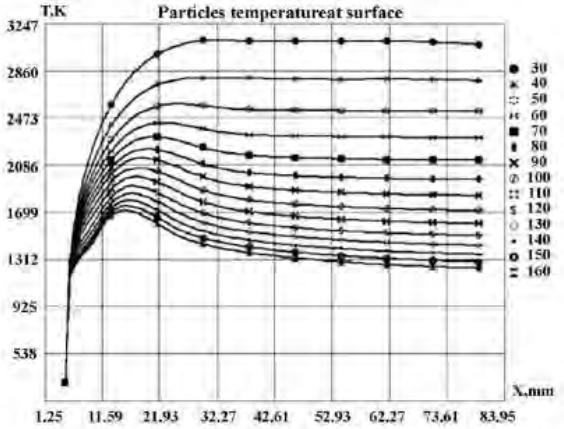


Fig. 66. Graphs illustrating the surface temperatures of HA powder particles. (Reprinted from [205] with permission from Elsevier.)

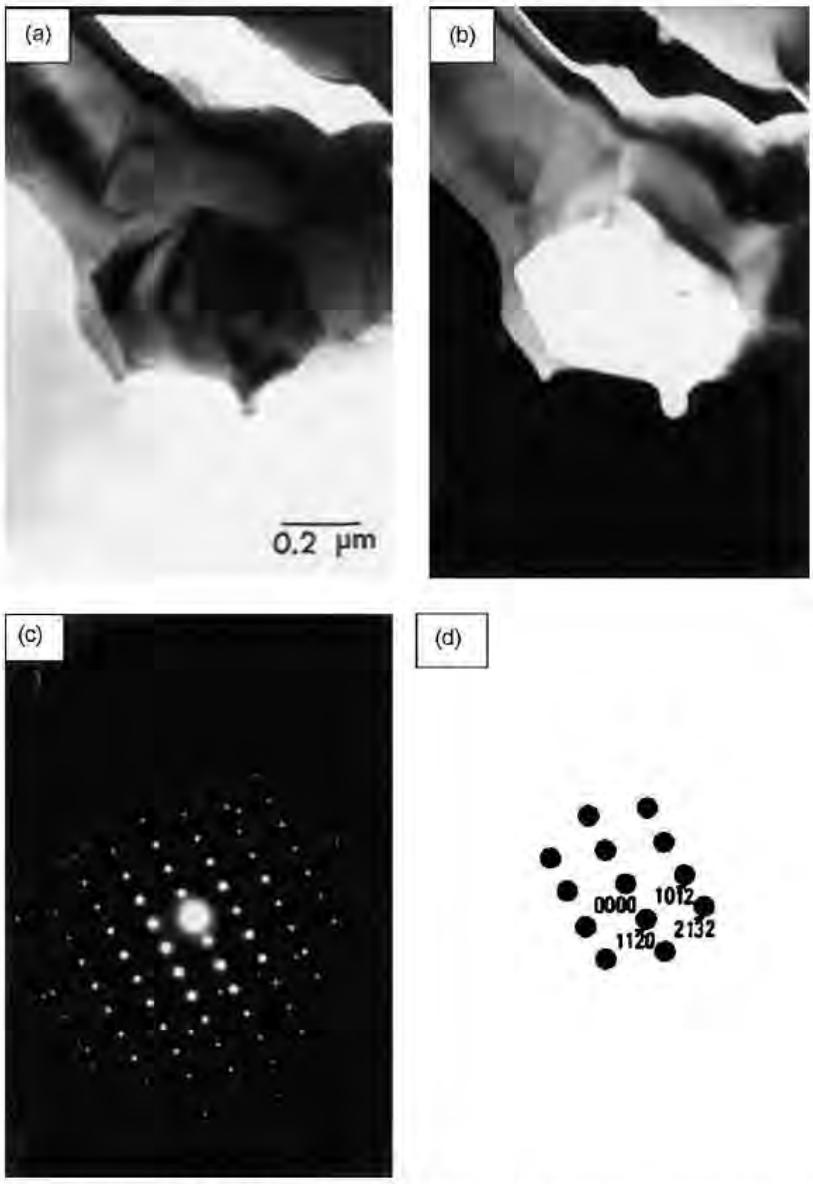


Fig. 67. TEM micrographs of HA crystal: (a) bright field, (b) dark field, (c) $[2\bar{2}01]$ zone selected area diffraction pattern, and (d) indexing of (c). (Reprinted from [206] with permission from Elsevier.)

orientation was observed by heat treatment at 600 °C for 2 h and then hydrothermally treated at 120 °C for 2 h in Milli-Q water. The TEM image in Fig. 74(a) reveals uniaxially oriented 200–800 nm HA splats. The SAD pattern from this region in Fig. 74(b) reveals the crystallinity of the layer. Such preferentially oriented microstructure of HA is supposed to improve the wear properties and may possess strong anisotropic material properties such as proton conductivity, polarizability and magnetic susceptibility.

Several researchers also studied the in vitro and in vivo biocompatibility of plasma sprayed Ca–P coatings on Ti base alloys [211,212]. Lavos-Vaalereto et al. studied the in vitro and in vivo biocompatibility of plasma sprayed hydroxyapatite coating on Ti–6Al–7Nb alloy. In vitro evaluation with osteoblast-like cells cultured for 15 days on these samples demonstrate the formation of large amount of extra-cellular matrix as observed in Fig. 75 [211]. Bundle of collagen fibrils, covered with globular deposits and calcified globules are found in intimate contact with the coating material. This, therefore, proved the biomineralization ability of the coated specimen. In vivo tests were carried out by inserting the coated implants into mandibular bone of mongrel dogs, and then removing it after a healing period of 16 weeks for evaluation. SEM micrographs (Fig. 76) reveal bone regeneration and integration into the implant material. This, therefore, proved both the osseoconduction and osseointegration ability of the coatings.

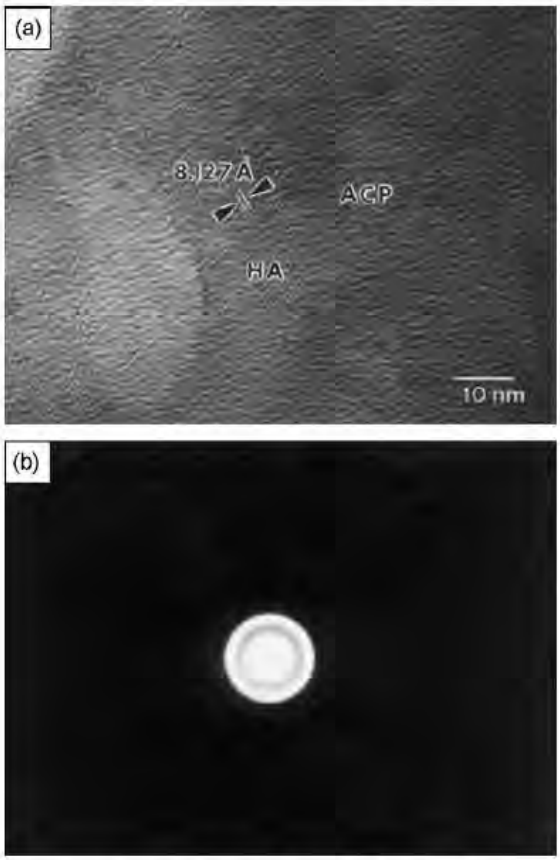


Fig. 68. (a) Lattice images of HA crystal showing $(10\bar{1}0)$ plane and surrounding amorphous calcium phosphate, and (b) microdiffraction pattern taken from amorphous calcium phosphate (ACP). (Reprinted from [206] with permission from Elsevier.)

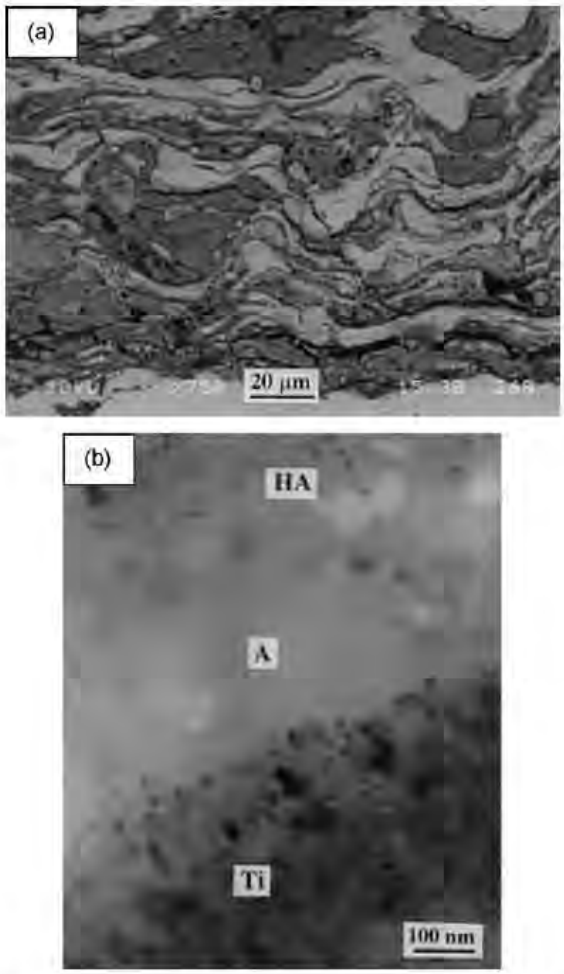


Fig. 69. Figure illustrating the (a) SEM image and (b) TEM bright field image of the cross-sectioned as sprayed composite coating. (Reprinted from [201] with permission from Elsevier.)

2.3. Electrophoretic deposition

Electrophoretic deposition (EPD) involves the deposition of charged powder particles suspended in a liquid medium onto a conductive substrate of opposite charge by the application of a dc electric filed [213,214]. Most often the term 'electrodeposition' is used to refer either electroplating or electrophoretic deposition, although it more usually refers to the former. Electrophoretic deposition is based on the suspension of particles in a solvent whereas the former is based on the solution of salts, i.e. ionic species. Electrophoretic deposition can be broadly classified into two types based on which electrode the deposition occurs. When the particles in suspension are positively charged, the deposition takes place on the cathode and the process is called cathodic electrophoretic deposition. If the particles in suspension are negatively charged the deposition takes place on the anode and the process is called anodic electrophoretic deposition. Hence by suitable modification of the surface charge of the particles, any of the two modes of deposition can be achieved. A schematic of the two modes of deposition process is illustrated in Fig. 77 [213]. Its technological applications include wear resistant coatings, anti-oxidant ceramic coatings, fabrication of functional films for advanced microelectronic devices and solid oxide fuel cells, and development of novel composites or bioactive coatings for medical implants. Some advantages associated with EPD can be listed as follows:

- EPD can be carried out on any kind of surfaces such as flat, cylindrical or any other shaped substrate with minor changes in electrode design and positioning.
- It is a quick process, needs simple apparatus, and no requirement for binder burnout as the green coating contains few or no organics.
- EPD also enables deposition of complex compounds and ceramic laminates.
- It also provides strongly adhered and homogeneous coatings than any other dip and spray coating technologies.

The only disadvantage associated with EPD, compared to other colloidal processes, is that it cannot use water as the liquid medium, because the application of voltage to water causes the evolution of hydrogen and oxygen gases at the electrodes which could adversely affect the quality of deposits formed.

Due to simplicity of the process, low equipment cost and the possibility of forming coatings with complex shapes or patterns, EPD has been widely used to synthesize Ca–P coatings on various

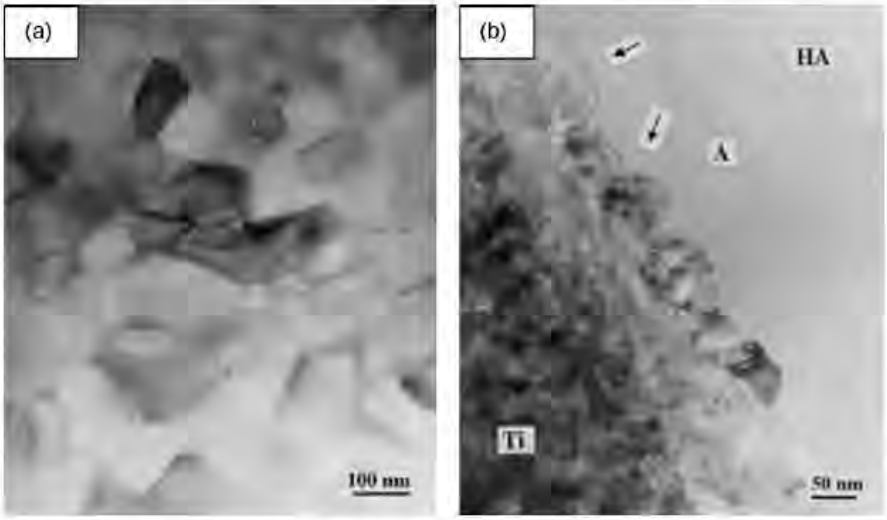


Fig. 70. TEM micrographs revealing the nucleation of crystalline HA grains (a) from the amorphous calcium phosphate phase and (b) at the interface of the amorphous and crystalline regions. (Reprinted from [201] with permission from Elsevier.)

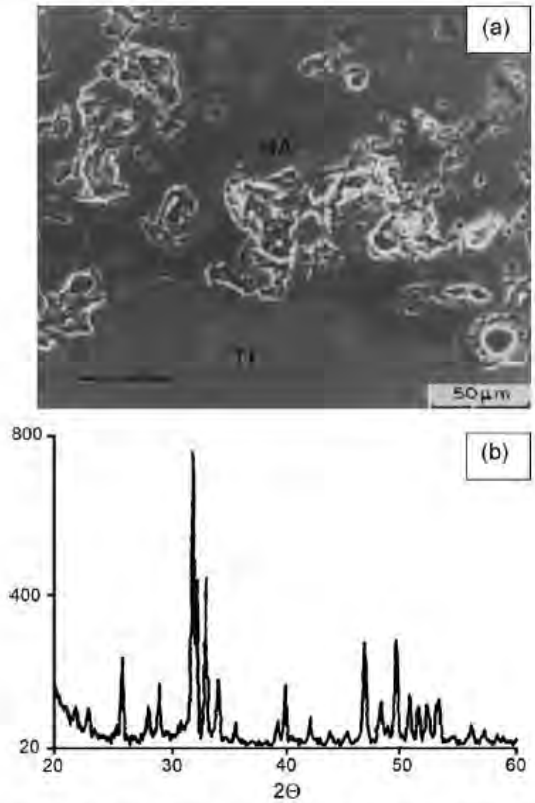


Fig. 71. (a) SEM micrograph of a cross-sectioned sample of plasma-sprayed hydroxyapatite coating on the titanium: (HA) hydroxyapatite, (Ti) titanium and (b) an X-ray diffraction pattern taken from the surface of a plasma sprayed hydroxyapatite coating on titanium. (Reprinted from [208] with permissions from Springer.)

substrate materials for implant applications [215–227]. Further, owing to its uniformity and good sinterability of the deposits, possibility of impregnation of porous substrates, and composite consolidation there is tremendous potential for a growth in this area.

Wang et al. [215] electrophoretically deposited HA powders prepared by thermal spray method on carbon rod by repeated depositions at room temperature. The repeated deposition process is useful in producing thicker coatings with no surface cracks. This avoidance of spalling or cracking is attributed to its layer structure, which fills up cracks and hinders crack propagation. The green body was then sintered under a range of temperatures varying from 1150 to 1300 °C to obtain a uniform HA ceramic tube. SEM micrographs of the cross-section of the coated tubes thermally treated at 1150, 1200, 1250, and 1300 °C are shown in Fig. 78 [215]. It can be observed that with increasing sintering temperature the interconnected microporosity decreases, resulting in a denser structure. This may, therefore, be considered beneficial for the enhancement of mechanical strength of the material. Fourier transform-infrared spectroscopy analyses (Fig. 79) [215] demonstrate that the intensity band at ~3572 cm^{-1}, corresponding to O–H stretching, decreases with the increase in sintering temperature. This decrease in hydroxyl groups with increasing temperature correlates well with the microstructure evolution observed by SEM.

Zhitomirsky [216] fabricated hollow HA fibers of various diameters by a novel electrophoretic deposition technique. In the first step, submicron hydroxyapatite (HA) powders prepared by chemical precipitation method were electrophoretically deposited on individual carbon fibers, carbon fibers bundles and felts (Fig. 80(a)) [216]. They were then burned out and sintered to evaporate the fibrous carbon substrate and leave behind the corresponding ceramic replicas (Fig. 80(b)) [216]. The inner diameter of the hollow HA fiber is controlled by the variation of the number of carbon fibers in the bundles, used as working electrodes. This research paved the way for the formation of various carbon fiber reinforced HA matrix composites, and other ceramic composites with HA-lined open porosity.

Ma et al. [217] synthesized hydroxyapatite (HA) powders by a modified chemical co-precipitation method and electrophoretically deposited it onto a titanium substrate. Zeta potential,

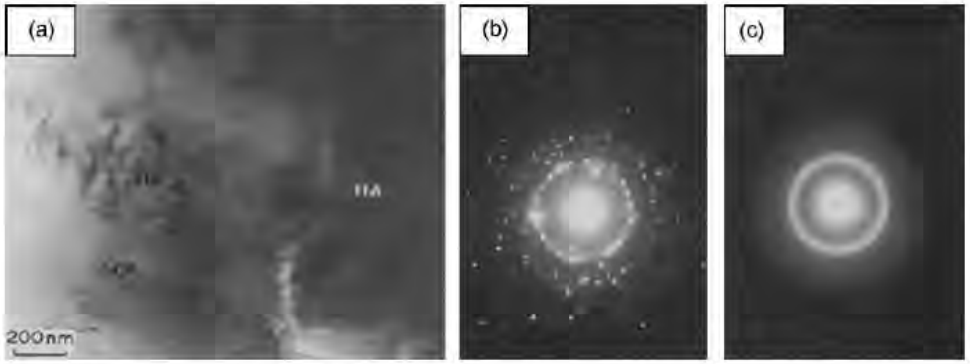


Fig. 72. (a)TEM micrograph taken from hydroxyapatite coatings show crystalline phases within amorphous phase. (b) A selected area diffraction pattern from the crystalline phase showing a ring pattern consistent with a polycrystalline structure. (c) A selected area diffraction pattern taken showing diffuse rings from the amorphous phase. (HA) crystalline hydroxyapatite, (ACP) amorphous calcium phosphate. (Reprinted from [208] with permissions from Springer.)

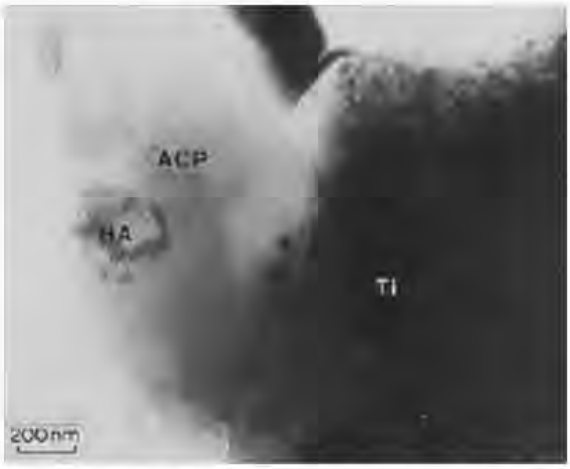


Fig. 73. TEM micrograph showing the interface between amorphous calcium phosphate and the titanium substrate: (HA) crystalline hydroxyapatite, (ACP) amorphous calcium phosphate, (Ti) titanium. (Reprinted from [208] with permissions from Springer.)

electromobility, and the particle size of HA suspension was initially characterized at various pH values to obtain a stable and dispersed suspension. The optimum suspension conditions were then utilized for EPD of HA particles on the Ti tubular substrate. The HA deposited Ti tubes were then sintered at 1000, 1150, and 1300 °C for 2 h. SEM micrographs (Fig. 81) [217] represent the cross-section of the deposits obtained at these sintering temperatures. It can be observed (Fig. 82) [217] that as the sintering temperature increases the inter-connected porosity decreases and the structure becomes denser. Since inter-connected porosity is advantageous for bone integration and mechanical stability of the implant, only the deposits obtained at a sintering temperature of 1000 °C may be considered beneficial for such applications.

Sintering conditions (such as sintering in air or vacuum) and sintering temperature can strongly affect the stability of electrophoretically deposited hydroxyapatite coatings in body environment. Sridhar et al. [218] performed potentiodynamic cyclic polarization experiments in Ringer's solution on two different sets of samples. Fig. 83 [218] represents the polarization curves in Ringer's solution of uncoated and HA coated 316L stainless steel sintered at various temperatures in air. The E_b and E_p values of the coated samples decrease with increasing sintering temperature in air. Hence, the corrosion resistance decreases or the corrosion rate increases with increasing sintering temperature. This is attributed

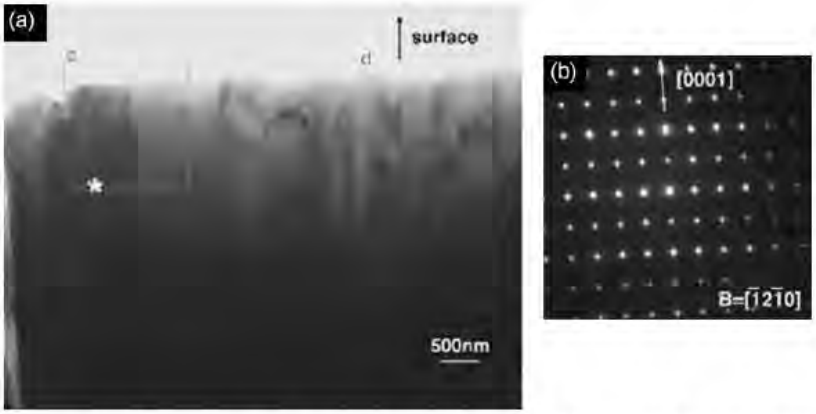


Fig. 74. A cross-sectional TEM image of a well-oriented HA splat in a heat-treated HAC (HHT–HAC) (a); (b) shows a typical SAD pattern from the location marked in (a). (Reprinted from [210] with permission from Elsevier.)

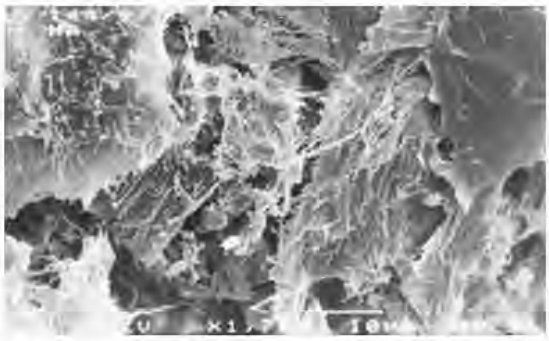


Fig. 75. Scanning electron micrograph of osteoblasts cultured on hydroxyapatite-coated Ti–6Al–7Nb alloy after 15 days in vitro. The surface of the cell layer is complete, and osteoblasts (arrowhead) and collagen fibers can be identified: 1700×. (Reprinted from [211] with permissions from Wiley Inter Science.)



Fig. 76. Scanning electron micrograph of an intraosseous hydroxyapatite-coated Ti–6Al–7Nb alloy implant after a healing period of 16 weeks in the mandibular bone of a mongrel dog. The bone is originated in the compact and grows in the implant direction (arrow). Original magnification: 17×. (Reprinted from [211] with permissions from Wiley Inter Science.)

to the formation of oxides on the base which induces the early initiation of pits and further reduces the adhesion of the coating to the base metal. Fig. 84 [218] represents the polarization curves in Ringer's solution of uncoated and HA coated 316L stainless steel sintered at various temperatures in vacuum. The E_b values of the coated samples were found to be +0.398, +0.508, and +0.490 V (vs. SCE) and E_p values were −0.081, +0.033, and +0.022 V (vs. SCE) at sintering temperatures of 600, 800 and 900 °C, respectively. The corrosion resistance of the samples sintered 600 °C was found to be lower as compared to the samples sintered at the other two temperatures. This might be due to insufficient sintering leading to the penetration of chloride ions through the coating and susceptibility of the base to chloride attack.

2.4. Pulsed laser physical vapor deposition

Lasers can be used to ablate a target material and condense it on the surface of a substrate material to form a thin film. Depending on the type of laser and material thermo-physical properties, ablation can take place under quasi-equilibrium conditions, as in laser-induced thermal vaporization, or far from equilibrium, as in pulsed laser ablation [228]. Thin film formation due to pulsed laser ablation of a target material is termed as pulsed laser deposition (PLD). PLD technique for producing thin films became increasingly popular in 1970s due to the advent of lasers delivering nanosecond pulses [229]. A typical setup for thin film deposition by PLD technique is schematically shown in Fig. 85. It essentially consists of a laser source, reaction chamber, a target, and substrate. Initially an intense laser pulse passes through an optical window of the vacuum chamber and allowed to focus on the bulk target. Above certain power density, significant material removal occurs from the target and a plasma plume is formed. The threshold power density required to produce a plasma plume depends on the thermo-physical properties of the target material, its morphology, laser pulse wavelength, and pulse duration [229–232]. In general, for ablation using an ultraviolet (UV) excimer laser with pulses of 10 ns duration and power densities in the order of 10–500 MW/cm^2 is required [232]. Material from the plume is then allowed to condense on the surface of a substrate to form a thin film. The distance between the target and the substrate is adjusted to match the length of the plasma plume. The substrate is rotated or moved with respect to the plasma plume to form a film of uniform thickness. Assuming an adiabatic expansion of the plasma plume in vacuum the thickness of the film profile obtained by PLD can be calculated as per the following [233]:

$$h(\theta) = \frac{Mk^2}{2\pi\rho_s z_s^2}(1 + k^2\tan^2\theta)^{-3/2}$$

where k is a constant which varies with the pulse width of the laser beam, M is the mass of the plasma plume, z_s is the distance at which the substrate is placed with respect to the target and θ is the radial angle and ρ_s is the density of the substrate. The variation in film

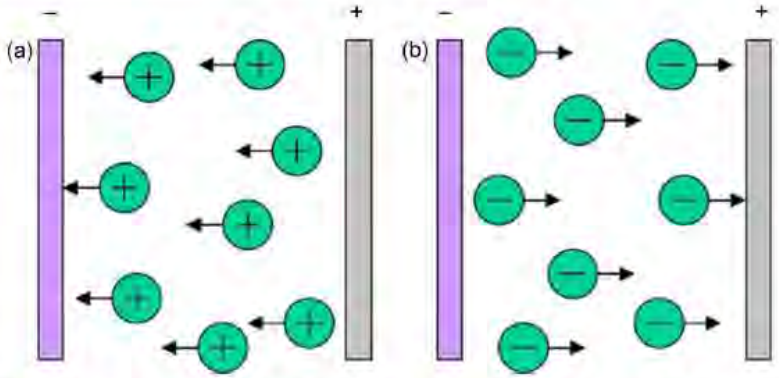


Fig. 77. Schematic illustration of electrophoretic deposition process. (a) Cathodic EPD and (b) anodic EPD. (Reprinted from [213] with permission from Elsevier.)

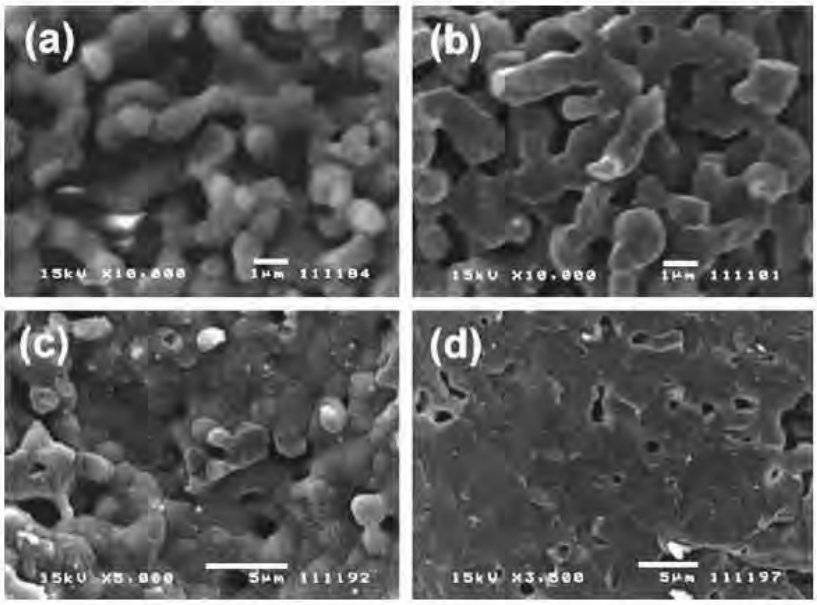


Fig. 78. SEM micrographs of sintered HA coatings: (a) 1150 °C, 2 h; (b) 1200 °C, 2 h; (c) 1250 °C, 2 h and (d) 1300 °C, 2 h. (Reprinted from [215] with permission from Elsevier.)

thickness profiles at varying θ is illustrated in Fig. 86 [233]. For a spherical expansion of the plasma $h(\theta)$ can be expressed as [230]

$$h(\theta) = \frac{M}{2\pi\rho_s z_s^2}\cos^3\theta$$

A knowledge of the film thickness profile can be used to estimate the kinetic energy of the moving species and thereby the temperature of the expanding plasma plume. This in turn may help us in predicting the phase transformations that take place for a particular set of laser parameters employed for the deposition process. Also as the high energetic species bombard the surface of the substrate, it may either improve or deteriorate the overall morphology, stoichiometry, and microstructure of the film. Knowledge of the film thickness profile can be used to predict the distance between the target and substrate and thereby the energy of the impinging species.

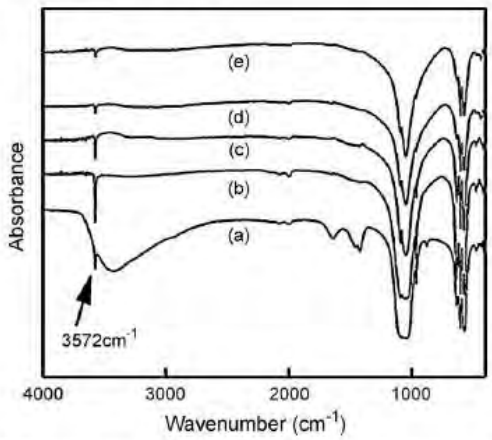


Fig. 79. FT-IR spectra for HA coatings heat-treated at (a) room temperature; (b) 1150 °C, 2 h; (c) 1200 °C, 2 h; (d) 1250 °C, 2 h and (e) 1300 °C, 2 h. (Reprinted from [215] with permission from Elsevier.)

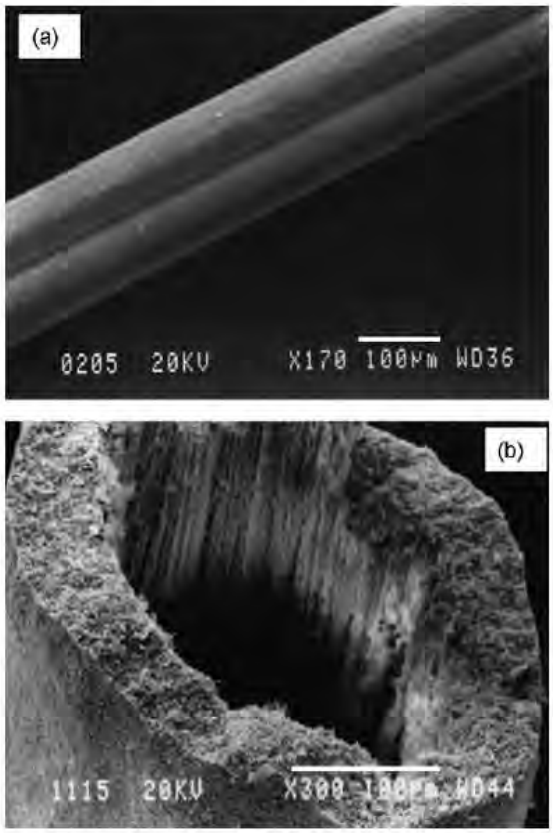


Fig. 80. SEM micrograph of (a) green hydroxyapatite deposits on carbon fibers and (b) cross-section of hollow fibers sintered at 1200 °C for 1 h. (Reprinted from [216] with permission from Elsevier.)

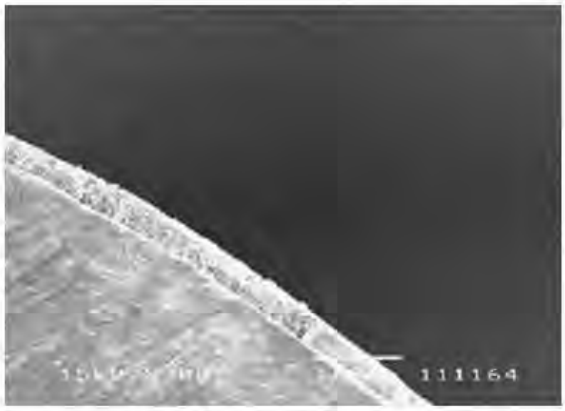


Fig. 81. Cross-section SEM micrograph of the electrophoretically deposited HA under the identified optimum suspension condition. (Reprinted from [217] with permissions from Springer.)

Some advantages associated with PLD process can be listed as follows [228,230,232]:

- The shorter duration of the pulses enables the synthesis of metastable materials which is difficult to be obtained by any other standard technique.
- High intensity of the laser pulse associated with this process allows the possibility to ablate any kind of material for its condensation on a substrate.
- Due to the pulsed nature of the PLD process film growth rate can be controlled to any desired amount.
- Fabrication of composite films consisting of different materials can also be obtained.
- Nanocrystalline films can also be fabricated.

Due to its capability to produce highly adherent thin films with controlled phases and Ca/P ratios, PLD technique has also been widely explored to deposit calcium phosphate coatings for bioimplant applications [234–248]. The various Ca–P phases synthesized using PLD techniques includes α-TCP, β-TCP, tetra calcium phosphate, octacalcium phosphate, amorphous HA, and crystalline HA.

As PLD is carried out at high substrate temperatures, it has been observed that a thin oxide layer forms on Ti prior to the deposition of HA and thereby reduces its adherence to the substrate [234]. Nelea et al. [234] proposed the introduction of a ceramic layer between HA coating and Ti-based substrate which will passivate the metallic surface and thereby improve its mechanical and chemical properties. Therefore, thin films of HA were grown on Ti–5Al–2.5Fe substrate precoated with a buffer layer of TiN by PLD technique using a KrF pulsed laser system. Grazing angle incidence X-ray diffraction (GIXRD) patterns in Fig. 87 represent the spectra of annealed HA films grown without buffer (a), with buffer interface of TiN (b), ZrO_2 (c), and Al_2O_3 (d) prior to deposition of HA. The film grown without buffer (Fig. 87(a)) contains two calcium phosphate phases, $Ca_4P_2O_9$ (tetra calcium phosphate, TTCP) and $Ca_2P_2O_7$ mixed with the pure HA phase. The films obtained with previously coated ceramic interlayer showed primarily the HA peaks (Fig. 87(b–d)). They also concluded that the films with the buffer interlayer showed a higher micro-hardness as compared to a film grown directly on the Ti–5Al–2.5Fe substrate. In order to study the growth morphology of the HA layer deposited on a TiN buffer, the authors carried out the deposition process on a Si substrate. Fig. 88 [234] illustrates the TEM image and selected area diffraction pattern of the HA film grown on TiN buffer and Si substrate by PLD technique. The HA layer represents a spongy morphology with isolated crystal grains, 20 nm large and scattered in the porous mass of the film (Fig. 88(a)). The selected area diffraction pattern (Fig. 88(b)) from the HA film represents the crystalline nature of the film.

Ball et al. [235] cultured human osteoblast cells, on pulsed laser deposited HA thin films on Ti substrates. The effect of crystallinity and laser fluence on cell attachment was studied. Confocal laser scanning microscopic images (Fig. 89) [235] of the cell-cultured

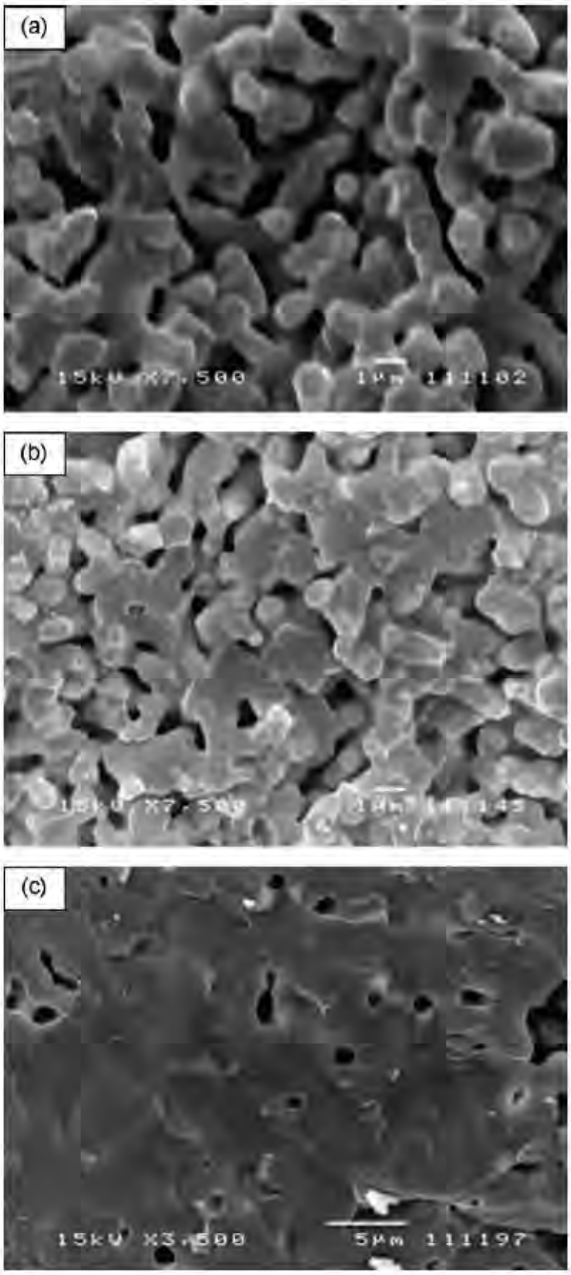


Fig. 82. The microstructure of the HA deposits at various sintering temperatures: (a) 1000 °C, (b) 1150 °C and (c) 1300 °C. (Reprinted from [217] with permissions from Springer.)

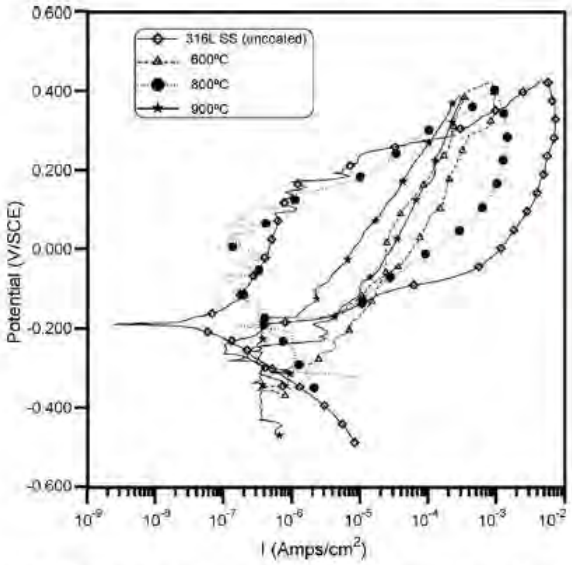


Fig. 83. Cyclic polarization curves in Ringer's solution of uncoated and HAP-coated type 316LSS at the optimum coating parameters of 60 V and 3 min after sintering at various temperatures in air. (Reprinted from [218] with permission from Elsevier.)

samples indicates enhanced cell attachment and proliferation with increasing laser fluence and crystallinity. The enhanced cell activity with a crystalline HA film is attributed to the less dissolution of the crystalline phase and thereby less release of Ca and P ions into the solution. With increase in laser fluence the surface roughness and the distribution of particles on the surface must have varied and which in turn also would have influenced the cell response.

Bigi and coauthors [236] synthesized octacalcium phosphate (OCP) and Mn^{2+} doped carbonate hydroxyapatite (Mn-CHA) thin films on Ti substrates by PLD process. The PLD was performed

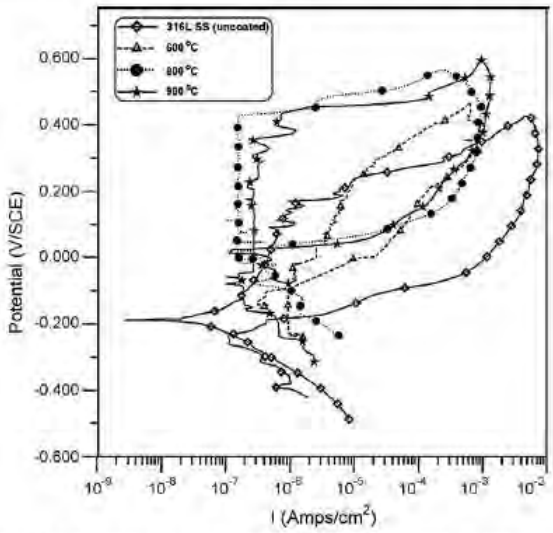


Fig. 84. Cyclic polarization curves in Ringer's solution of uncoated and HAP-coated type 316LSS at the optimum coating parameters of 60 V and 3 min after sintering at various temperatures in vacuum. (Reprinted from [218] with permission from Elsevier.)

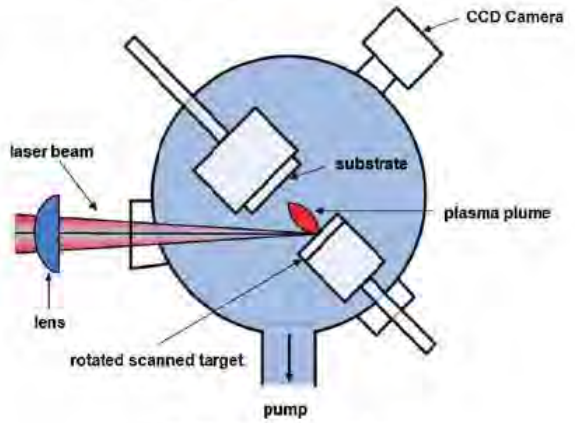


Fig. 85. Schematic of a PLD setup.

using a UV KrF Excimer laser source generating pulses ≤30 ns and operating at a wavelength of 248 nm. SEM micrographs (Fig. 90) [236] represent the surface morphology of the OCP and Mn-CHA films. Mn-CHA films exhibited more granular structure with mean dimensions of the grains smaller than those of OCP and apparently a compact structure as compared to OCP. In vitro biocompatibility of the coated samples was tested by culture of human osteoblast cells, and cell attachment, proliferation, and differentiation were evaluated up to 21 days. SEM micrographs in Fig. 91 [236] represent the osteoblast cell morphologies on the pure Ti, and on the Ca–P coatings. Although osetoblast cells were appeared to attach on all surfaces they were more spreading and flattening on the Ca–P coatings as compared to bare Ti.

Socol et al. [237] synthesized nanocrystalline octacalcium phosphate OCP thin films on Ti substrate by PLD technique using a UV KrF Excimer laser source operating at a wavelength of 248 nm. Both deposition and subsequent annealing of the deposited films were carried out in an intense flux of hot water vapors maintained at a constant temperature within the range 2–200 °C. The best results were obtained for a substrate temperature of 150 °C during both deposition and post-deposition treatment. SEM micrographs [237] (Fig. 92) of films deposited by this technique on a Ti substrate heated at 150 °C and post-deposition treatment at 150 °C reveal a droplet-like feature at the surface of the coating (Fig. 92(a)) and a morphologically homogeneous and brush-like layer at the inner structure (Fig. 92(b)). The biocompatibility of the deposited films was carried out by culture of human fetal osteoblast-like cell line hFOB 1.19. Fig. 93 compares the SEM micrographs of hFOB 1.19 cells on control Ti (a) and OCP coating (c). The coatings exhibited strong attachment and proliferation of cells, supporting its good biocompatibility and absence of toxicity. At higher magnification

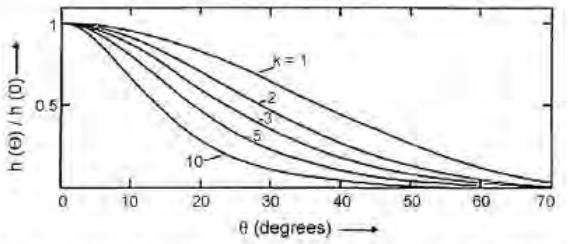


Fig. 86. Variation in film thickness profiles at varying radial angles. (Reprinted from [233] with permissions from American Physical Society (APS).)

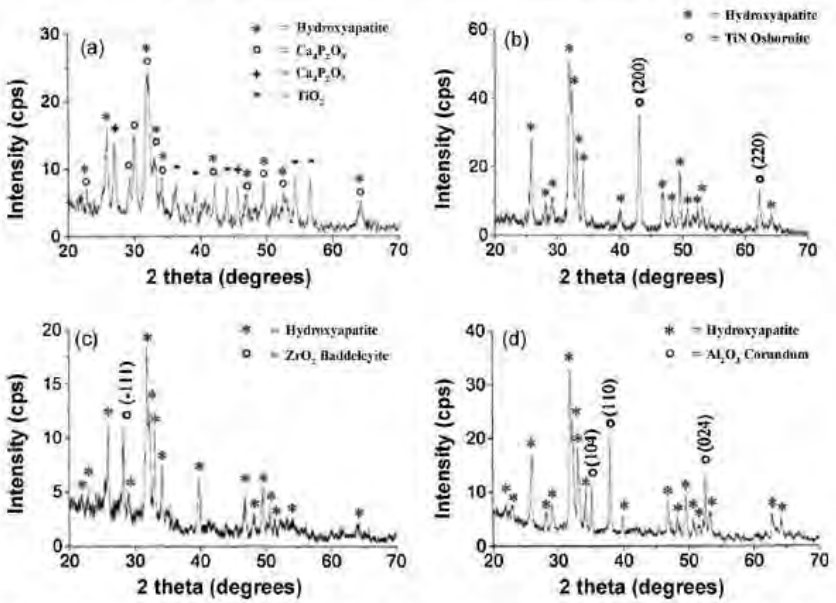


Fig. 87. GIXRD spectra (Cu Kα, λ = 0.154 nm) of the HA thin films without buffer layer (a) and with TiN (b); ZrO_2 (c) or Al_2O_3 and (d) buffer between the HA film and the metallic substrate. (Reprinted from [234] with permission from Elsevier.)

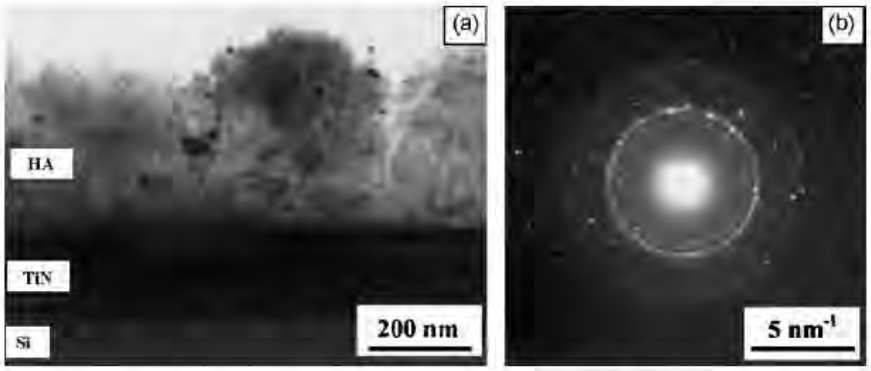


Fig. 88. Cross-section TEM image (a) and the corresponding diffraction pattern (b) of the HA/TiN/Si sample. (Reprinted from [234] with permission from Elsevier.)

hFOB 1.19 cells cultured on OCP coating (Fig. 93(d)) were more flattened, indicating a strong attachment and well spreading across the surface as compared to bare Ti (Fig. 93(b)).

2.5. Micro-arc oxidation

Micro-arc oxidation (MAO), also called plasma electrolytic oxidation, or anodic spark deposition, or micro-arc discharge oxidation, is a plasma-chemical and electrochemical process. The process combines electrochemical oxidation with a high-voltage spark treatment in an aqueous electrolytic bath which also contains modifying elements in the form of dissolved salts (e.g., silicates) to be incorporated into the resulting coatings [249]. A schematic of the MAO system is illustrated in Fig. 94 [249]. During the MAO process, the component is immersed in an aqueous electrolyte bath and connected to a high-voltage power supply. A water-cooled stainless steel vessel serves as the container as well as the counter-electrode. When the applied voltage exceeds a certain critical value, micro-plasma discharge occurs on the surface of the component thereby resulting in a modified surface [250]. This arc thermochemical interaction induced by the high temperature (10^3 to 10^4 K [251]) and high pressures (10^2 to 10^3 MPa [247]) discharge channel can produce high performance, firmly adhered oxide ceramic films on the metals. Thus micro-arc oxidation coating technology is often used for Al, Ti, Zr, Mg and their alloys [252]. Since MAO can be carried out at room temperature for components with complex geometries, it is considered as a simple, economical and environmentally friendly coating technique for producing oxide ceramic coatings on metal surface.

MAO can be a potential coating technique for implants applications as it can produce porous, rough and firmly adherent ceramic coatings on the surface of a metallic material. This porous nature of the ceramic coating can enhance the anchorage of the implant to the new generating bone tissue and open up the possibility for the incorporation and release of antibiotics around

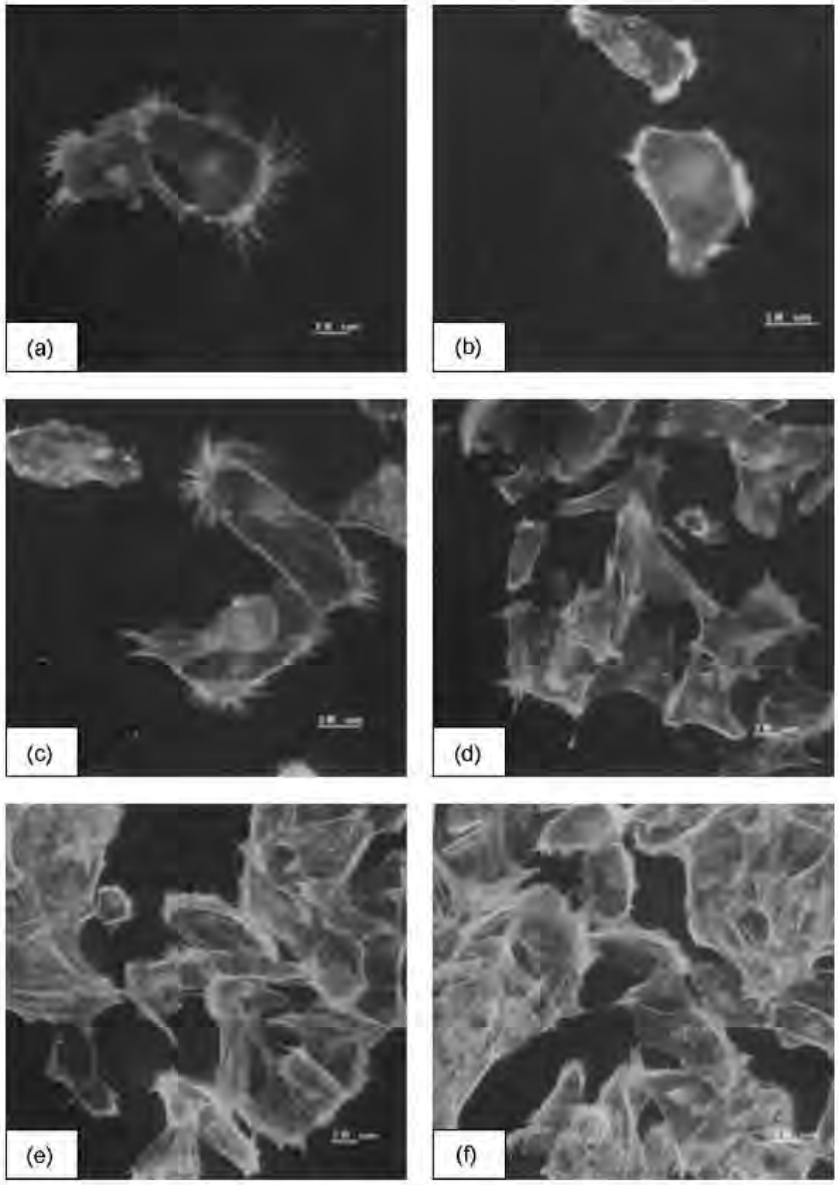


Fig. 89. Confocal laser scanning microscope images of cells attached on HA films deposited on Ti foils using a pulsed laser at various laser processing conditions (a) 3 J/cm^2 (b) 6 J/cm^2 (c) 9 J/cm^2 (d) 3 J/cm^2 annealed (e) 6 J/cm^2 annealed and (f) 9 J/cm^2 annealed. (Reprinted from [235] with permission from Elsevier.)

the implants. Hence several researchers have explored the possibility Ca–P-based coatings on metallic materials by MAO coating technique [253–257].

Song and coauthors [253] synthesized Ca- and P-containing titanium oxide layers on commercially available titanium substrate by MAO coating technique at various applied voltages. The Ti plates were anodized in an electrolyte bath containing 0.04 ml/l β-glycerophosphate disodium salt pentahydrate ($C_3H_7Na_2O_6P{\cdot}5H_2O$, β-GP) and 0.04 ml/l calcium acetate monohydrate ($(CH_3COO)_2{\cdot}Ca{\cdot}H_2O$, CA). MAO was carried out at fixed applied voltages varying in the range of 250–500 V using a pulse power supply, and a pulse frequency, a duty circle, and a duration time set at 1000 Hz, 60%, and 3 min, respectively. XRD patterns (Fig. 95) [253] of the samples oxidized at various voltages demonstrate the presence of anatase (TiO_2) at 250 V and both anatase and rutile (TiO_2) at 350 V. No Ca- and P-containing phases were detected up to 350 V. With further increase in applied voltage (500 V) the Ti peak was significantly reduced and new Ca-, P-, Ti-, and O-containing compounds were formed in addition to rutile and anatase. These dominant phases at 500 V include β-$Ca_2P_2O_7$, $CaTiO_3$, α-$Ca_3(PO_4)_2$, and $Ca_2Ti_5O_{12}$. Surface morphology of the samples synthesized at various voltages is shown in Fig. 96 [253]. At lower voltages the oxide layer exhibited a well-separated and homogeneously distributed porous microstructure (Fig. 96(a)) [253]. The pore size increased with increasing applied voltage (Fig. 96(b)) [253] and at higher voltages (450 V) the oxide layers cracked and the surface became slightly

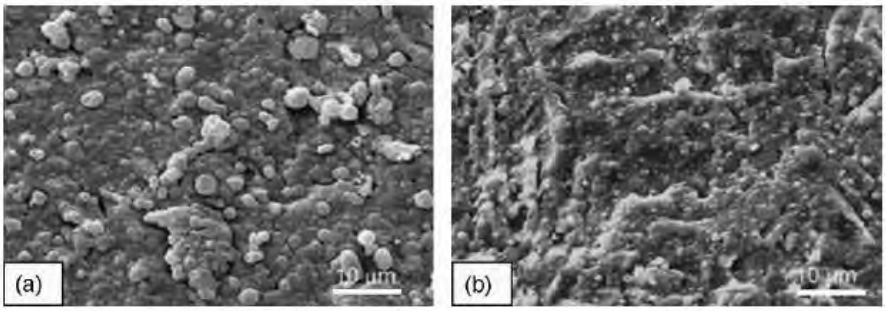


Fig. 90. SEM images showing the morphology of the thin films of (a) OCP, and (b) Mn-CHA deposited by PLD on Ti substrates. (Reprinted from [236] with permission from Elsevier.)

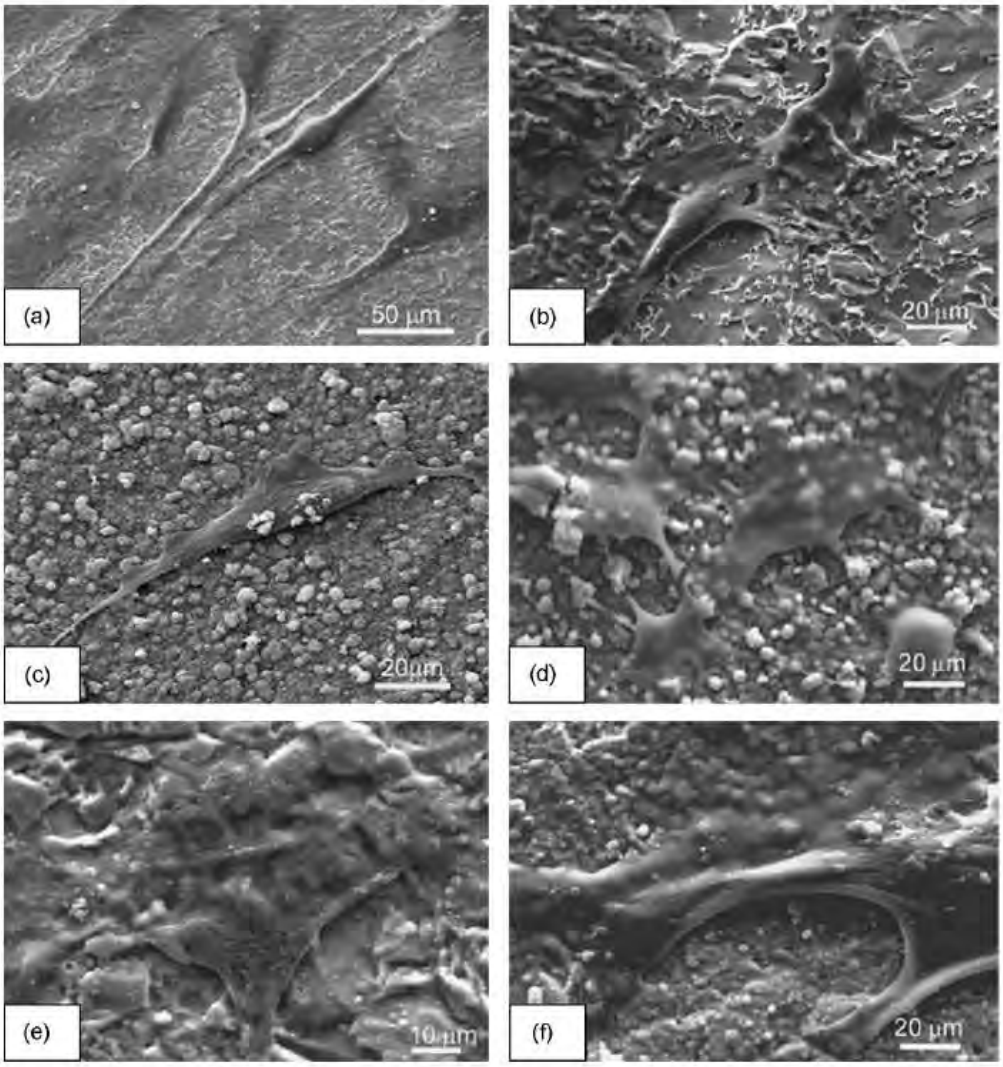


Fig. 91. SEM images of primary osteoblasts on (a and b) Ti, (c and d) OCP coating, and (e and f) Mn-CHA coating. (a, c and e): 7 days of culturing; (b, d and f): 21 days of culturing. (Reprinted from [236] with permission from Elsevier.)

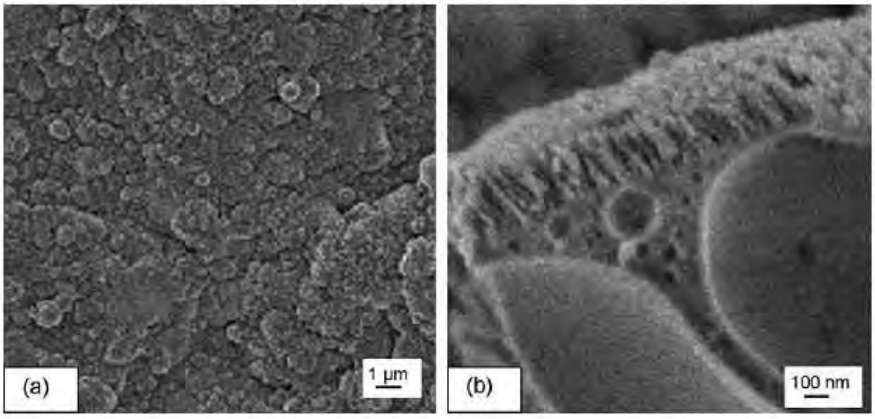


Fig. 92. SEM images showing the morphology of the films deposited by PLD on Ti substrates heated at 150 °C and subjected to post-deposition treatment at 150 °C. (Reprinted from [237] with permission from Elsevier.).

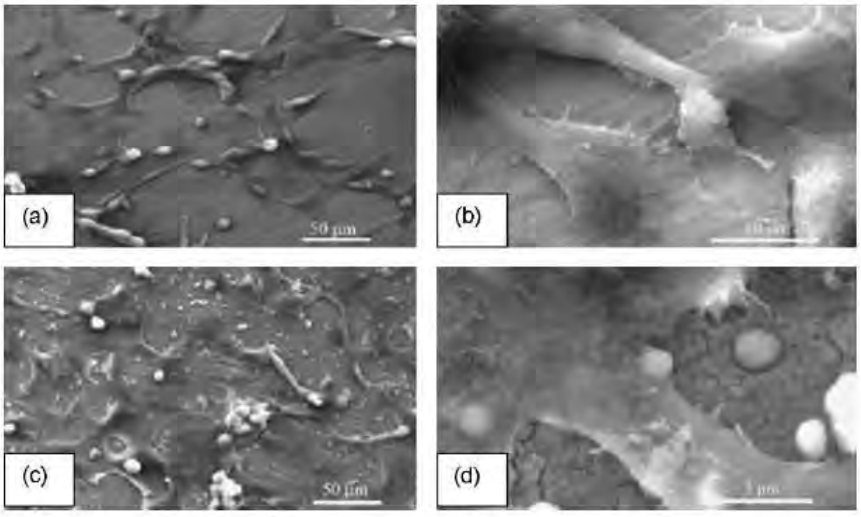


Fig. 93. SEM of hFOB 1.19 cells deposited on bare Ti (a and b), and on OCP coating (c and d). (Reprinted from [237] with permission from Elsevier.)

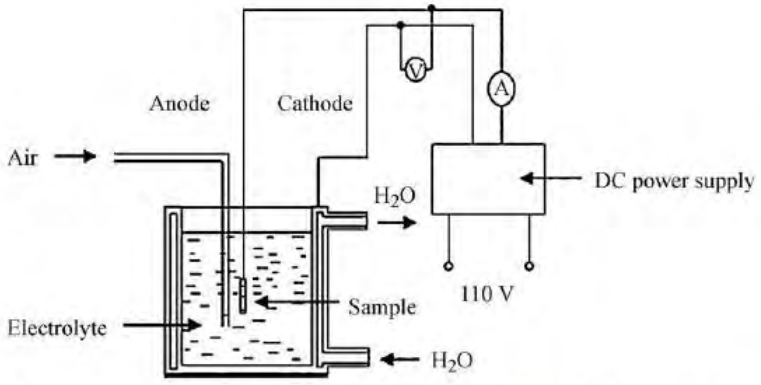


Fig. 94. Schematic representation of micro-arc oxidation setup. (Reprinted from [249] with permission from Elsevier.)

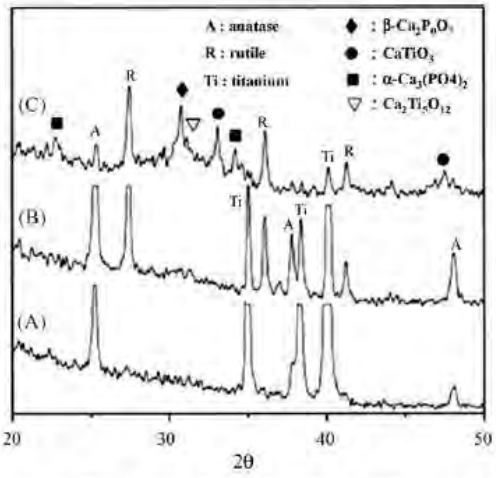


Fig. 95. XRD patterns of the micro-arc oxidized samples obtained at (A) 250, (B) 350, and (C) 450 V. (Reprinted from [253] with permission from Elsevier.)

rough and irregular (Fig. 96(c)) [253]. The cross-sectional view (Fig. 96(d)) [253] demonstrated a highly adherent oxide coating to the substrate and some of the pores extending to the bottom of the substrate were also obvious.

Sun et al. [254] proposed a novel method to directly deposit HA on Ti–6Al–4V by MAO in Ca- and P-containing electrolytic bath. They proposed that the applied voltage and treatment time were two important factors for HA formation. For the MAO process a pulse power supply was employed, Ti–6Al–4V plate was used as an anode, and a stainless steel cylinder container was used as a cathode. The electrolytic solution used for the process is a mixture of 0.2 M acetate monohydrate and 0.02 M β-glycerophosphate disodium salt pentahydrate. Ti–6Al–4V plates were processed with applied voltage in the range of 400–480 V and pulse frequency, duty circle and duration time fixed at 100 Hz, 6%, and 1.5–20 min, respectively. XRD spectra (Fig. 97) [254] of the MAO coatings formed at different applied voltage for 20 min demonstrate the presence of rutile, $CaTiO_3$ and α-TCP peaks for all voltages. The rutile and $CaTiO_3$ peaks reduce with increasing voltage, however, the α-TCP peaks have little or no change. HA and $CaCO_3$ peaks are detected at voltages higher than 430 V, and tend to increase with increasing applied voltage. Further to optimize the treatment time, MAO coatings were formed at a fixed voltage of 480 V and treatment time varying from 1.5 to 20 min. At 1.5 min the authors only detected the presence of Rutile, $CaTiO_3$ and α-TCP and HA and $CaCO_3$ phases appeared only after a treatment time of 3 min. From 1.5 to 20 min, rutile and $CaTiO_3$ phases were reduced, α-TCP phases have little change, and HA and $CaCO_3$ phases gradually increased. The result, therefore, indicates that treatment time is also an important factor for HA formation and at 20 min there are almost only HA and $CaCO_3$ phases left. Surface morphologies of the coatings (Fig. 98) [254] formed at 480 V and varying treatment time (1.5–20 min) demonstrate a reduction in the number of pores with increasing treatment time. It is attributed to the gradual coverage of HA and $CaCO_3$ on the TiO_2 matrix. From the understanding derived from the XRD and SEM results, the authors concluded that HA and $CaCO_3$ are gradually formed on the TiO_2 matrix, and the coatings are a kind of bi-layer HA/TiO_2 coatings, containing α-TCP and $CaCO_3$.

Wei et al. [255] developed a micro-arc oxidized TiO_2-based coatings containing Ca and P on the titanium alloy. The electrolytes used for the MAO process was a mixture of nano-HA, calcium acetate, calcium dihydrogen phosphate ($Ca(H_2PO_4)_2{\cdot}H_2O$), disodium ethylenediaminetetracetate (EDTA-2Na), and sodium hydroxide (NaOH). The authors studied the effects of HA

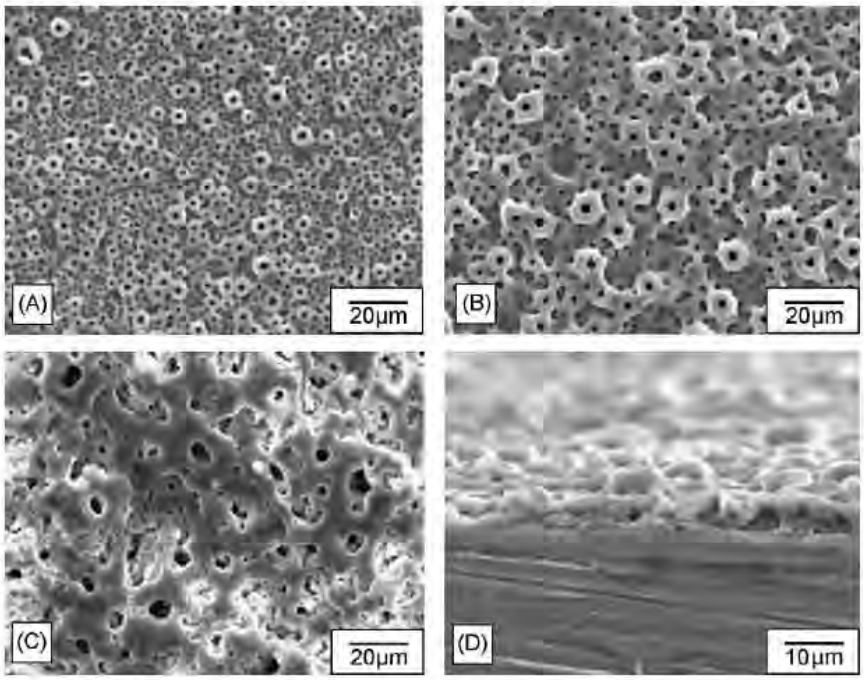


Fig. 96. Surface morphologies of the micro-arc oxidized samples formed at (A) 250 V, (B) 350 V, (C) 450 V, and (D) cross-section view of specimen (B). (Reprinted from [253] with permission from Elsevier.)

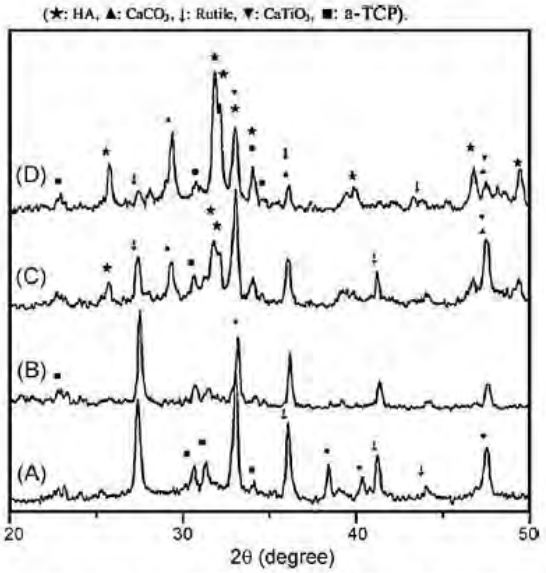


Fig. 97. XRD spectra of the MAO coatings formed at different applied voltages (A) 400 V (B) 430 V (C) 450 V (D) 480 V treated for 20 min. (Reprinted from [254] with permission from Elsevier.).

concentration on the structure and in vitro bioactivity of the MAO coatings. The HA concentration in the electrolyte was varied as 0, 4, 8, 12, and 16 g/l and the MAO samples obtained from such concentrations were labeled as MAO0, MAO4, MAO8, MAO12, and MAO16, respectively. From XRD (Fig. 99) [255] studies it is observed that on the surface of MAO0 coating, there is only the presence of anatase with low crystallinity and amorphous phase. With increase in HA concentration, the presence of rutile was also observed for MAO12 along with anatase. The results indicated an increase in crystallinity of both rutile and anatase with increase in HA concentrations. SEM surface morphologies of the coatings (Fig. 100) [255] show porous structures beneficial for cell attachment, propagation, and bone growth. The micropores were uniformly distributed for all HA concentrations and no major changes in terms of size and amount of the pores were observed with increasing HA concentration. The authors also studied the effects of HA concentration on the Ca and P concentrations and Ca/P ratios of the MAO coatings. Their results indicated that the Ca and P concentrations decreased with increasing HA concentrations and Ca/P ratios of the coatings are about 1 and no pronounced change was observed with increasing HA concentrations.

Apart from the above efforts in processing and synthesizing Ca–P-based coatings by MAO, several researchers also studied its in vitro bioactivity and biocompatibility [258,259]. Han et al. [258] synthesized a multiphase mixture of rutile, $CaTiO_3$, β-$Ca_2P_2O_7$ and α-$Ca_3(PO_4)_2$ on titanium by MAO in an electrolytic bath containing a mixture of acetate monohydrate ($(CH_3COO)_2Ca{\cdot}H_2O$) and β-glycerophosphate disodium salt pentahydrate ($C_3H_7Na_2O_6P{\cdot}5H_2O$) at 500 V. The authors then studied its in vitro bioactivity by immersing the samples in SBF. A SEM image of the surface of the coating obtained at 500 V is shown in Fig. 101(a) [258]. The coated surface indicated a porous morphology with pore size in the range of 3–4 μm. Following immersion in SBF for 50 days a thin apatite-like layer completely covered the surface and no open pores were visible (Fig. 101(b)) [258]. This mineralizing ability of the coating was due to the positively charged surface owing to the presence of rutile and $CaTiO_3$ and its ability to react with water molecules present in SBF as a result of the $CaTiO_3$, β-$Ca_2P_2O_7$ and α-$Ca_3(PO_4)_2$ phases.

Wei and Zhou [259] synthesized TiO_2-based coating containing amorphous Ca–P on titanium alloy by MAO and studied its in vitro biocompatibility. The MAO pre-processed sample were heat treated at 400, 600, 700 and 800 °C in air for 1 h and the affect

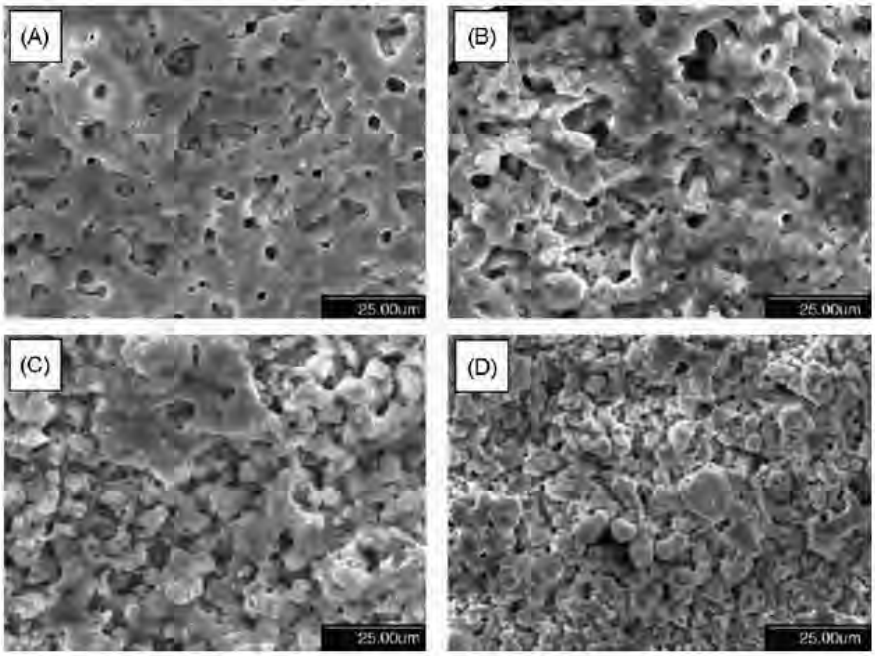


Fig. 98. SEM of the MAO coatings formed at 480 V treated for (A) 1.5 min (B) 3 min (C) 10 min (D) 20 min. (Reprinted from [254] with permission from Elsevier.)

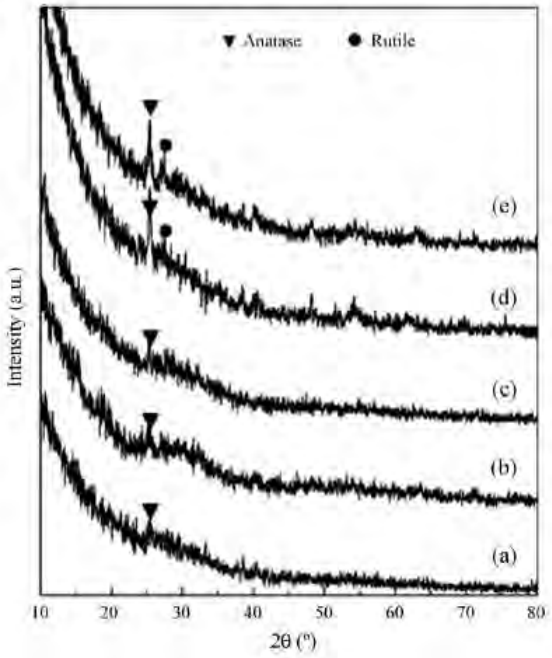


Fig. 99. XRD patterns of (a) MAO0, (b) MAO4, (c) MAO8, (d) MAO12 and (e) MAO16 coatings. (Reprinted from [255] with permission from Elsevier.)

of heat treatment on the biocompatibility of the coatings was studied by the culture of MG63 cells. The heat treatment process altered the surface topography of the coating and the average roughness increased with increasing heat treatment temperature (Fig. 102) [259]. SEM micrographs (Fig. 103) [259] of the MG63 cells following culture for 3, 5 and 7 days on the MAO and the MAO modified surfaces demonstrated increased cell proliferation with increasing culture time. After 7 days the cells on the MAO and 400 °C-treated MAO completely covered the surface with a smooth and flat morphology. In contrast, the other heat-treated samples demonstrated less proliferation of the MG63 cells and seem to be not biocompatible. This improved adhesion and proliferation of the MG63 cells on the MAO and 400 °C-treated MAO coatings as compared to the other heat-treated samples were attributed to its smooth surface with topographical features matching the length scales of the cells.

2.6. Magnetron sputtering deposition

Physical vapor deposition methods for producing coatings in a vacuum environment can be broadly classified into two main groups: (1) those involving thermal evaporation techniques, where a material is heated in vacuum until its vapor pressure is greater than the ambient pressure, and (2) those involving ionic sputtering methods, where a highly energetic ion beam strikes a solid target and knocks of the atoms from the surface [260]. These ionic sputtering techniques include diode sputtering, ion beam sputtering, and magnetron sputtering. We are here specifically concerned about the magnetron sputtering technique to deposit thin films. Magnetron sputtering emerged in 1970s and is considered as a high-rate vacuum coating technique for depositing metals, alloys, and compounds onto a wide range of materials with thickness up to about 5 μm [260]. Some of the advantages associated with magnetron sputtering are [260,261] (1) high deposition rate, (2) ease of sputtering any metal, alloy or compound, (3) high-purity films, (4) extremely high adhesion of films, (5) excellent coverage of steps and small features, (5) ability to coat heat-sensitive substrates, (7) ease of automation, and (8) excellent uniformity on large area substrates.

Sputtering in general is a process where atoms or molecules are ejected from the target by the bombardment of high-energy particles. Material is ejected from the target in a way to obtain usable quantities of material which can be directly deposited onto the substrate. For effective coating using sputtering process two important criteria must be met: (1) ions of sufficient energy must be created and directed towards the surface of the target to eject atoms from the material, and (2) secondly the ejected atoms must be able to move freely towards the object to be coated with little impedance to their movement. Hence sputter coating is a vacuum process where low pressures are required to maintain high ion energies and to prevent too many atom-gas collisions after ejection from the target. At very high-pressure material can also be deflected straight back into the target and which reduces the deposition rates further. Unfortunately, the need to operate at low pressures contrasts with the process required to produce the bombarding ions, namely that of plasma generation. The solution to this problem was the magnetron sputter deposition system as shown in Fig. 104.

A magnetron sputtering system works on the principle of applying a specially shaped magnetic field to a diode sputtering

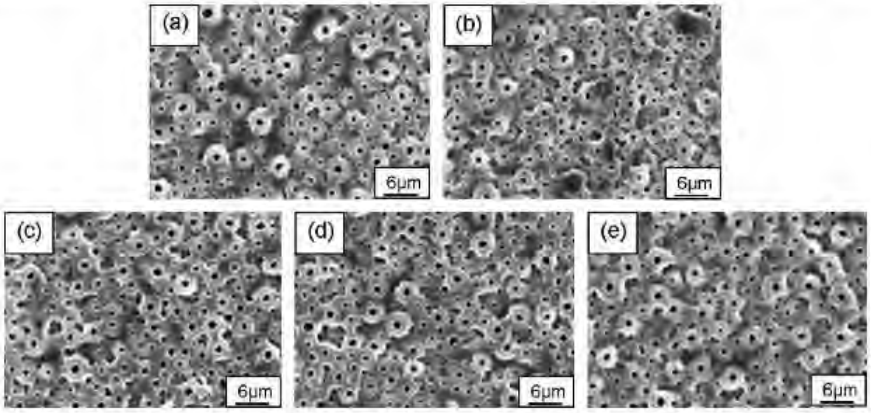


Fig. 100. SEM micrographs of the surfaces of (a) MAO0, (b) MAO4, (c) MAO8, (d) MAO12 and (e) MAO16 coatings. (Reprinted from [255] with permission from Elsevier.)

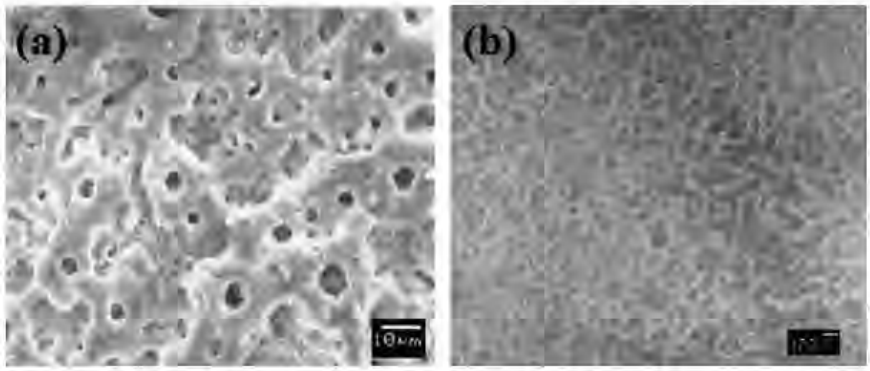


Fig. 101. (a) Surface morphologies of the MAO samples formed in the acetate monohydrate and β-glycerophosphate disodium salt pentahydrate containing solution at 500 V and (b) its morphology following immersion in SBF. (Reprinted from [258] with permission from Elsevier.)

target. This high magnetic field traps the primary and secondary electrons in a localized region close to the cathode into an endless 'race track'. In this manner the chance of experiencing an ionizing collision with a gas atom is vastly increased and the ionization efficiency is increased too. This also reduces the loss and makes an effective usage of some of the secondary electrons that may cause radiation problems. Therefore, the ion current density is vastly increased by an order of magnitude over other conventional sputtering techniques and thereby a faster deposition rate at low pressure. Owing to the several advantages associated with the magnetron sputter deposition technique, many researchers have explored the deposition of Ca–P films on metallic materials for implant applications by this technique [262–270].

Silicon-substituted hydroxyapatite (Si–HA) as a biomaterial has been reported to promote early bonding at the bone/implant interface. Therefore, Si–HA can be used as a coating material on implant surfaces for load-bearing applications such as artificial hip implants and knee implants. Thian et al. [262] studied the biocompatibility of magnetron co-sputtered silicon-containing hydroxyapatite (Si–HA) coatings on Ti substrate. The film deposition was carried out in a custom-built sputter deposition chamber maintained at room temperature and evacuated to a base pressure lower than 10^{-7} Torr. High-purity argon gas was used as a back-filled gas to bring the work pressure to 5×10^{-3} Torr and a constant flow of Ar was supplied into the chamber during the deposition process. Si and HA targets were held onto two water-cooled magnetrons by means of spring clips and the Ti substrate was placed on a circular substrate support facing the targets. The film composition was controlled by the relative power supplied to each target and a total sputter duration of 4 h was used in the process. The sputter deposited films were then heat treated in a tube furnace at 700 °C for 3 h. Fig. 105 shows the surface morphology of the as-deposited and heat-treated Si–HA films. The as-deposited Si–HA films (Fig. 105(a)) [262] appeared dense with an excellent coverage on the substrate surface. No cracks and other surface defects were visible. SEM micrographs of the heat-treated films (Fig. 105(b)) [262] reveal precipitates containing silicon–calcium phosphate (Si–CaP) of sizes approximately 200 nm in length and 75 nm in width. Human osteoblast-like (HOB) cells were used to study the biocompatibility of the uncoated Ti substrates, as-deposited, and heat-treated Si–HA thin films. Confocal laser scanning microscopic images of various specimens cultured with HOB cells for 4 days is shown in Fig. 106 [262]. In all cases results showed that the cells maintained their typical HOB cell morphology. The as-deposited and heat-treated Si–HA films, demonstrated many focal contacts on the surfaces, with well-defined actin cytoskeletal organization and numerous stress fibers throughout the cells. Cells were randomly attached to the as-deposited film, but were selectively oriented along parallel grinding grooves for the heat-treated film.

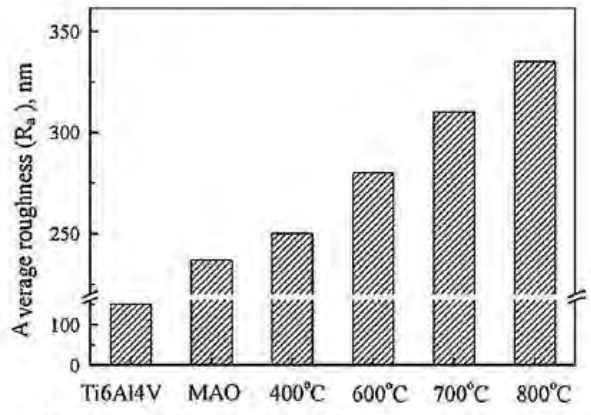


Fig. 102. The average roughness of the surfaces of the Ti6Al4V, MAO coatings before and after heat treatment. (Reprinted from [259] with permission from Elsevier.)

Nelea et al. [263] studied the microstructure and mechanical properties of hydroxyapatite thin films, grown on Ti–5Al–2.5Fe alloy substrates by radio-frequency magnetron sputtering technique. The deposition was performed from pure HA target and in some cases a buffer layer of TiN was introduced by pulsed laser deposition prior to HA coating. The films were deposited in low pressure Ar or Ar–O_2 mixtures at substrate temperatures ranging from 70 to 550 °C. It was observed that the films grown at temperatures below 300 °C were prevalently amorphous and contains a small amount of crystalline material. The films obtained at a substrate temperature of 550 °C or the films grown at room temperature followed by annealing at 550 °C contain the HA phase. Confocal microscopic image (Fig. 107) [263] of the HA/TiN/TiAlFe film demonstrated a smooth and uniform surface having an average roughness of 50 nm. The mechanical behavior of the films grown without and with TiN buffer layer was studied from the load–displacement curves obtained by nanoindentation at a load of 0.5 mN. It can be observed from the load displacement curves (Fig. 108) [263] that the penetration depth is smaller (58 nm) for the films grown with TiN buffer layer as compared to the films grown without TiN buffer (78 nm). One possible reason for this is that TiN is significantly harder as compared to TiAlFe substrate. Thus the introduction of TiN buffer layer pleads for a good structure, uniformity with high quality interfaces.

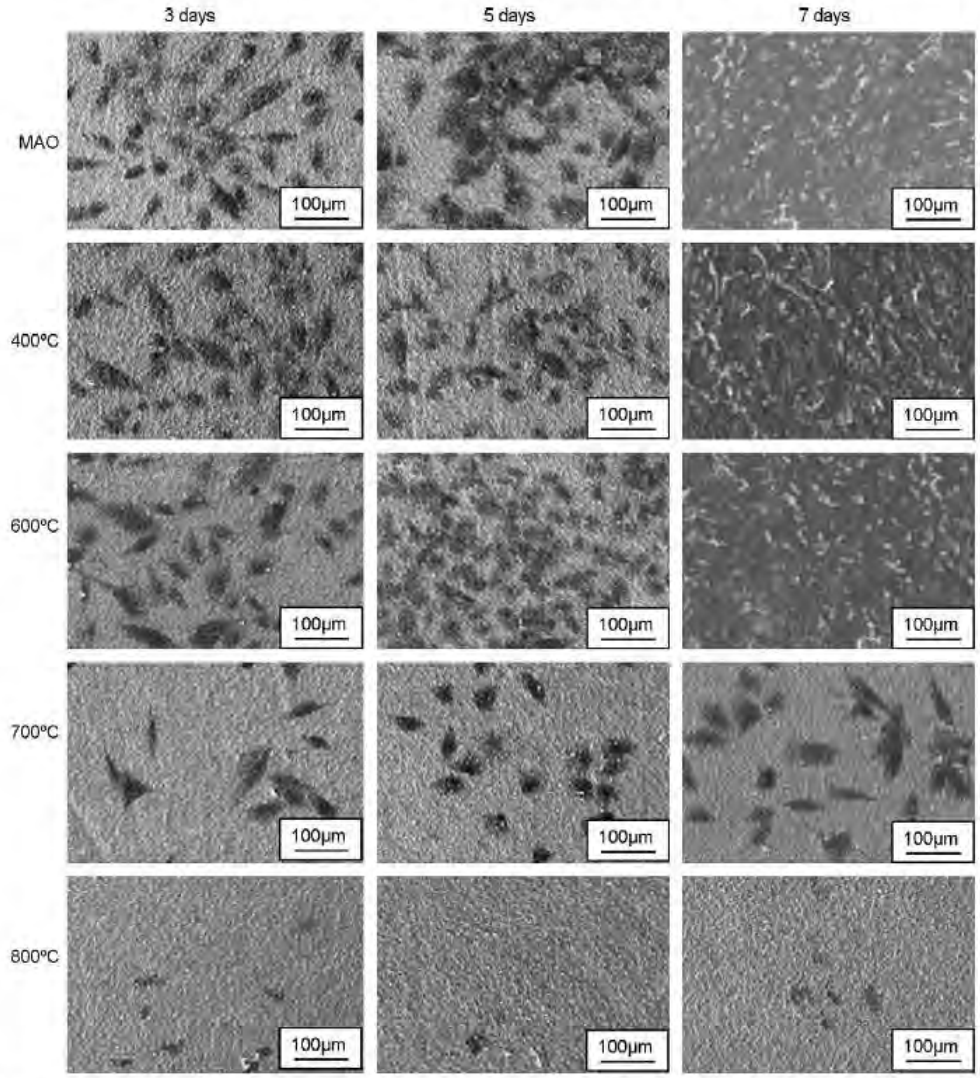


Fig. 103. SEM micrographs of the MG63 cells after culturing for 3, 5 and 7 days on the MAO and heat-treated MAO coatings. (Reprinted from [259] with permission from Elsevier.)

Apart from its favorable mechanical properties and in vitro biocompatibility, Ca–P coatings obtained using this technique also proved for its strong in vivo response by inducing bone growth at the interface. Wolke et al. [267] studied the in vivo dissolution behavior of magnetron sputtered Ca–P coatings on TiO_2-blasted implants, by subcutaneous implantation in rabbits. The implants were subcutaneously placed behind the back of the rabbits by a surgical procedure and after 1, 4 and 12 weeks of implantation they animals were sacrificed and the implants were studied for its histological evolutions using a light optical microscope.

After 1 week of implantation the samples were characterized by a thick loose connective tissue capsule, containing many inflammatory cells and blood vessels surrounding the implant (Fig. 109(a)) [267]. After 4 weeks of implantation the specimens were surrounded by a thin to medium-thin fibrous tissue capsule, which is almost free of inflammatory cells and contained fibroblasts, collagen and blood vessels (Fig. 109(b)) [267]. After 12 weeks of implantation the tissue response became very uniform and a thin connective tissue surrounded all implants. At the interface there was a strong bonding between the capsule and the implant surface and a complete absence of the inflammatory cells (Fig. 109(c)) [267]. Based on the above results the authors demonstrated the efficacy of magnetron sputtering technique to synthesize Ca–P coatings for load bearing implants.

2.7. Sol–gel derived coatings

Sol–gel processing can be broadly defined by a series of experimental steps as mentioned below [271]:

- At the first step it involves the preparation of a sol, generally by the in situ generation of ultrafine particles in a liquid vehicle. This is mostly due to the hydrolysis and condensation reactions occurring when a metal alkoxide is mixed is mixed with water

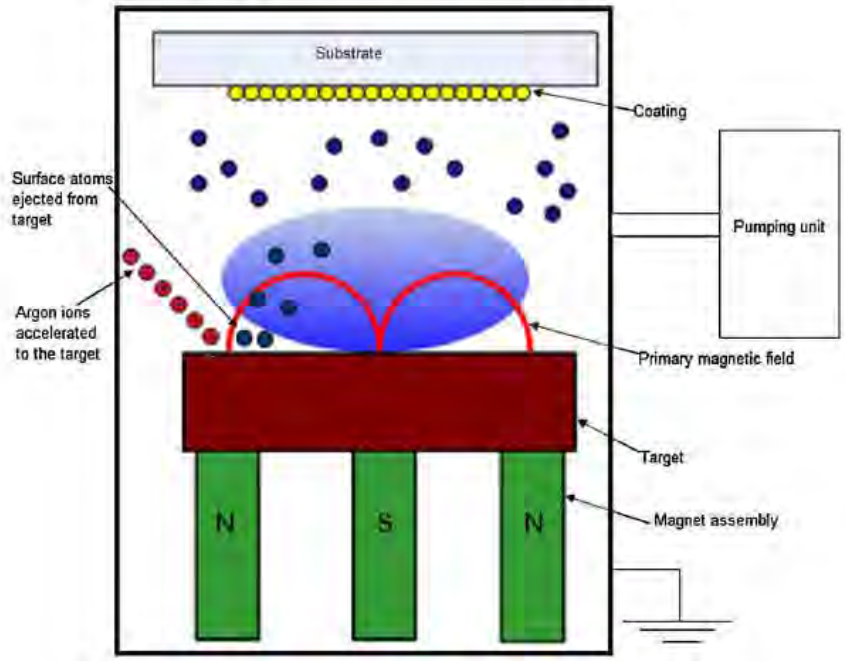


Fig. 104. Schematic of a magnetron sputter deposition system.

and a mutual solvent (mostly alcohol) in the presence of acid or base catalyst (via growth of polymeric molecules or Ostwald ripening).
- This is followed by ageing of the sol at a suitable temperature for arriving at desired properties (e.g., optimum viscosity).
- The sol is then subjected to casting, spinning, drawing, coating, emulsification, dipping, spraying, etc. for obtaining the required gel form coating through sol–gel transition.
- At the final stage the specimen is subjected to drying, followed by heating in most cases to obtain the desired product.

Each step discussed above is guided by a set of experimental parameters (Table 8) [271] which control the chemistry of the process and the quality of the final product. For obtaining reproducibility of the final product and its commercial exploitation all such parameters must be given due attention. Brinker and Scherer have broadly divided these parameters into two categories: the respected and the neglected ones [272]. Respected parameters are important specially in defining the quality of the sol, and consequently, that of the corresponding gel. On the other hand, the neglected parameters probably demand lesser attention, but may affect the properties of the sol and the gel when neglected completely.

Some advantages associated with sol–gel coating technique can be listed as follows [271]:

- Its can produce thin bond-coating to provide excellent adhesion between the metallic substrate and the top coat.
- Can easily shape materials into complex geometries in a gel state.
- It can produce high-purity products as the organo-metallic precursor of the desired ceramic oxides can be mixed, dissolved in a specified solvent and hydrolyzed into a sol, and subsequently a gel. Hence, the composition can be highly controlled.
- Provides an excellent matrix for entrapping a variety of organic and inorganic compounds and biologically important molecules.
- Possesses low temperature sintering capability, usually 200–600 C.
- Sol–gel coating technique is a simple, economic, and effective method to produce high quality coatings.

Due to its ability to produce crystalline films at relatively low temperatures, possibility to tailor the microstructures, and its convenience for complex shape coatings, sol–gel derived coatings are being widely explored to develop Ca–P coatings on metallic materials for implant applications [273–278].

Nguyen et al. [273] synthesized calcium phosphate films by sol–gel coating technique over Ti–6Al–4V implants having a sintered porous surface. The porous region is made by vacuum sintering atomized Ti–6Al–4V powders of 45–150 μm size range. The solution used for the sol–gel dip-coating process was of sufficiently low viscosity to allow complete permeability throughout the porous region. The dip-coated samples were then vacuum annealed (10^{-3} and 10^{-4} Torr) to minimize the oxidation of the Ti alloy substrate. The final annealing temperature for the samples was set at 760 °C (±10 °C) with a 15 min hold time. The samples were

Table 8
Various parameters in sol–gel processing. (Reprinted from [271] with permission from Springer.).

Some respected parameters
1. Choice of precursors
2. Concentration of Precursors (i.e. addition of water, organics)
3. Water/alkoxide mol ratio
4. Type and amount of catalyst
5. Control of hydrolysis reaction etc.
Some neglected parameters
1. Volatile evolution rate in sol
2. Variations in ambient conditions
3. Small impurities in sol
4. Rate of change of viscosity etc

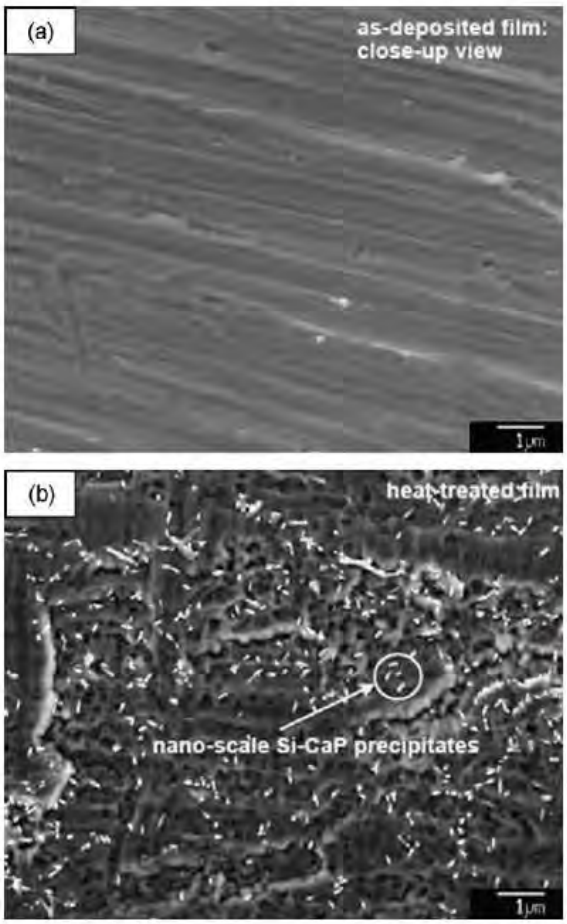


Fig. 105. SEM morphology of the as-deposited and heat-treated Si-HA thin films. (Reprinted from [262] with permission from Elsevier.)

finally furnace cooled in vacuum to room temperature. SEM micrographs (Fig. 110) [273] of the calcium–phosphate coated implant reveals that the sol–gel coating process did not bring any significant change in size and shape of the pores intended for bone ingrowth. However, the deposited film altered the topography of the sintered particles and made the surface more irregular. The coated implants were then placed transversely across the tibiae of 17 New Zealand rabbits to evaluate its in vivo biocompatibility. Implanted sites were allowed to heal for 2 weeks, after which the specimens were retrieved to evaluate their bone regeneration and bone ingrowth ability. SEM micrographs reveal that the calcium phosphate layer was well adapted to the metal substrate (Fig. 111(a and b)) [273] and bone was in direct contact with the calcium phosphate layer (Fig. 111(c and d)) [273]. Numerous osteocytes were also observed through out the bones which were ingrown the surface porosity (Fig. 111(c and d)) [273]. The authors, therefore, demonstrated the effectiveness of sol–gel formed Ca–P films over porous-surfaced structures for enhancing osteoconductivity.

Li and coauthors developed hydroxyapatite thin films on micro-arc oxidized titanium (MAO-Ti) substrate by means of the sol–gel method and studied its biocompatibility by culture of human osteosarcoma cell line [274]. Here, the HA sol was prepared by mixing the precursor phosphorous source (Triethyl phosphate) and calcium source (calcium nitrate). The MAO-

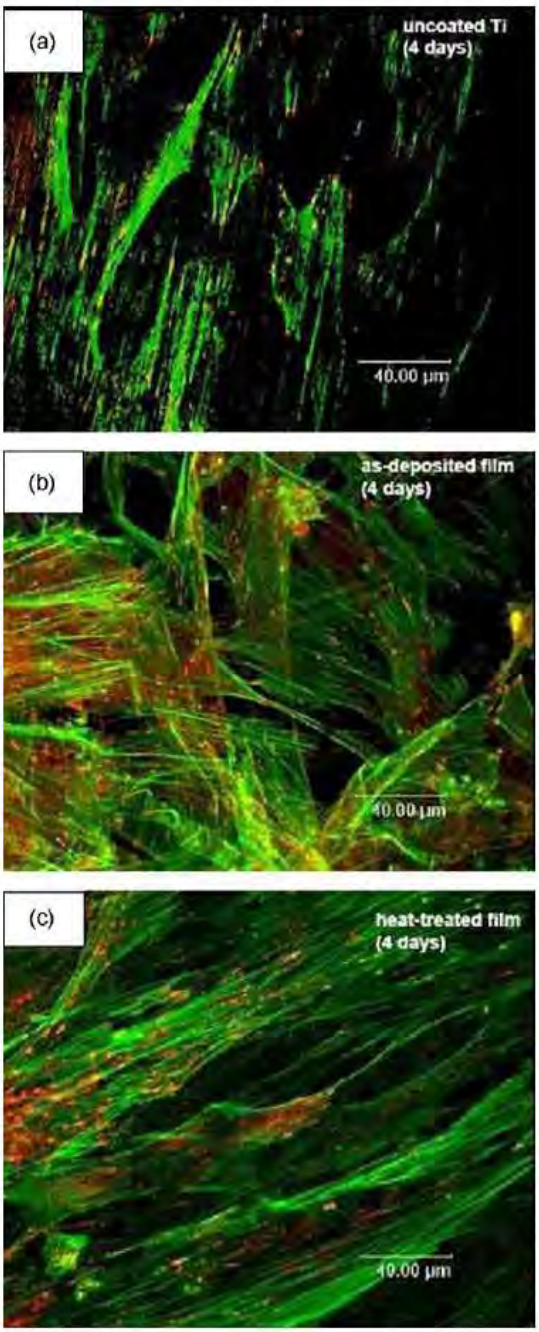


Fig. 106. CLSM images illustrating actin cystoskeleton and vinculin focal contacts on uncoated Ti substrates, as-deposited and heat-treated Si-HA thin films at culture day 4. FITC phalloidin stains the actin sytoskeleton (green) and Texas red stretavidin stains the vinculin focal contacts (red). (Reprinted from [262] with permission from Elsevier.) (For interpretation of the references to color in this figure legend, the reader is referred to the web version of the article.)

treated Ti specimen (MAO-Ti) was spin-coated with the prepared HA sols at a spin rate of 3000 rpm for 40 s. The coated specimens were then dried at 80 °C for 2 h and then heat treated at 550 °C for 2 h at a heating rate of 2 °C/min. Surface morphologies of the

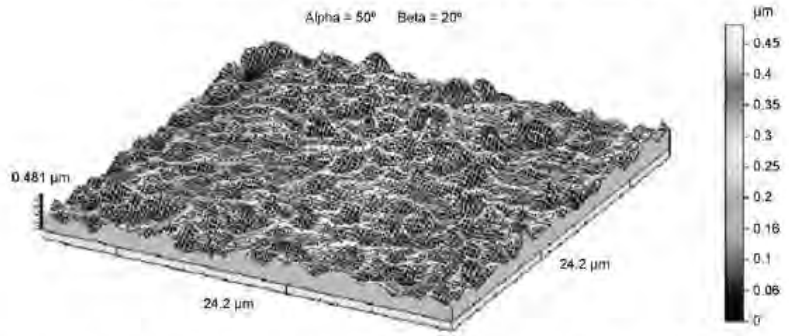


Fig. 107. A white light confocal microscopic image showing the surface aspect of the film grown on TiN/TiAlFe. (Reprinted from [263] with permission from Elsevier.)

coated and uncoated samples are shown in Fig. 112. The pure Ti substrate depicts the machining grooves (Fig. 112(a)) [274] and after MAO treatment at 270 V, a porous oxide layer was formed through out the Ti surface (Fig. 112(b)) [274]. When the MAO-Ti was coated with an HA sol at a concentration of 1.5 M and heat treated at 550 °C, some of the large pores became slightly smaller (Fig. 112(c)) [274]. The porosity continuously decreased with increasing HA concentration (Fig. 112(c–f)) [274]. From the cross-sectional views (Fig. 113(a)) [274] it can be observed, that for the MAO treatment at 270 V, a rough oxide layer (2–3 µm thickness) was formed on Ti. When the MAO-Ti was coated with 1.5 M HA sol, a very thin film of HA (100–200 nm) was formed (Fig. 113(b) [274]. With the HA coating at highest sol concentration (4 M), a much thicker layer (1–1.5 µm) was formed (Fig. 113(c)) [274]. SEM morphologies of the HOS cells proliferated on the specimens during culture for 3 days are shown in Fig. 114. On pure Ti, the cells spread out in an intimate contact with the specimen surface (Fig. 114(a) [274] where as on MAO-Ti the cells appeared to show slightly less extended cell membranes Fig. 114(b)) [274]. On the other hand on HA coated surfaces the cell spread out more actively (Fig. 114(c and d)) [274]. After 5 days of incubation, the cells proliferated on the specimens were counted and presented graphically as shown in Fig. 115. The number of cells on the HA sol–gel coated MAO-Ti substrate was significantly higher as compared to the MAO-Ti without the sol–gel coating and increased with increasing sol concentration. This, therefore, proved the biocompatibility of the sol–gel deposited HA coatings.

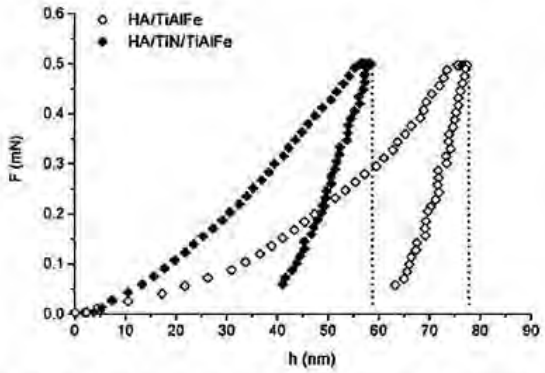


Fig. 108. Load–displacement curves obtained by nanoindentation at a imposed load of 0.5 mN. (Reprinted from [263] with permission from Elsevier.)

2.8. Direct laser melting

In the present section the discussion is only confined to Ca–P coatings obtained by direct laser melting using both continuous wave (CW) and pulsed lasers in our research group [1–9] as almost no work on similar approach is reported in the open literature to date. This technique produces a sound metallurgical bonding between the Ca–P-rich ceramic layer and the metallic substrate. Further with precise control of the laser processing parameters, it simultaneously allows creation of physical textures with multi-phase microstructure within the modified surface layer. The steps followed in direct laser melting can be generalized as follows:

- The starting precursor (calcium phosphate) powder is mixed thoroughly in a water-based organic solvent.
- The precursor solution is sprayed onto the substrate coupons, with an air-pressurized spray gun.
- The samples are then air dried to remove the moisture.
- Finally, the samples are scanned under a laser beam to produce a strong metallurgical bond between the coating and the substrate.

The schematic of the above process is illustrated in Fig. 116.

Some advantages associated with direct laser melting are listed as follows [279–283]:

- High spatial coherence and directionality of the laser beam can permit extreme focusing and directional irradiation at high intensities.
- The monochromaticity of a laser beam allows for a controlled depth of heat treatment without affecting the properties of the bulk.
- Laser light is considered as a sterile tool as there is no direct contact with the material being processed, and, hence, can be effectively utilized for medical and biological specimens.
- Unlike other particle-beam technologies such as ion beam and electron beam lasers are not necessarily required to operate in vacuum.

2.8.1. Continuous wave (CW) and pulsed laser melting

A continuous wave laser is characterized by a temporally constant beam power and hence the beam is more likely to produce a uniform thermal condition within the beam–substrate interaction region. On the other hand, pulsed lasers have short pulse lengths and high peak power at alternatively low average energy and thereby produce a non-uniform thermal condition within the interaction zone. These distinctively different operation modes and the resulting thermo-physical effects are expected to produce completely different physical and chemical effects in the

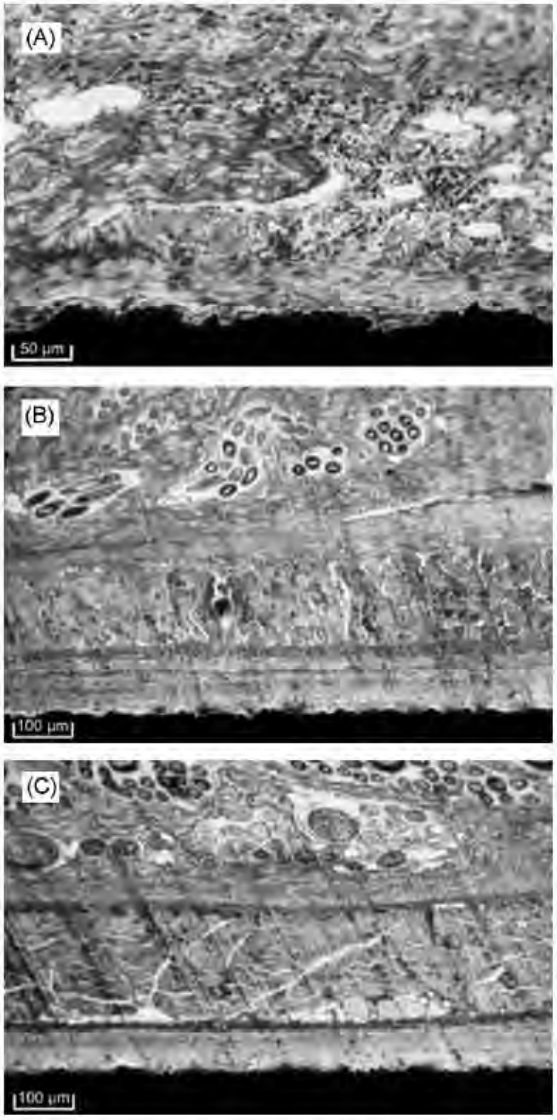


Fig. 109. A light microscopical section of a coated specimen after 1 week of implantation showing a moderately thick loose connective tissue capsule, containing inflammatory cells and blood vessels surrounded by the implant (A). After 4 weeks the capsule was almost free of inflammatory cells (B). At 12 weeks of implantation the implants were surrounded with a thin connective tissue capsule (C). (Reprinted from [267] with permission from Elsevier)

interaction zone. A knowledge of the temperature evolution and cooling rate during laser processing by both pulsed and CW lasers can provide useful information for predicting various phases evolved under a set of laser parameters. The temporal and spatial variation of temperature distribution on material due to laser interaction by a pulsed and CW lasers can be calculated by solving the one dimensional heat conduction equations assuming very narrow or no heat diffusion in other dimensions due to extremely rapid processing speeds. For thermal analysis the material is assumed to be homogeneous, initial temperature of the material is assumed constant and heat input is uniform during the irradiation, and convection and radiation losses are neglected. Under such conditions, the governing equation for heat transfer can be written as [282]

$$\frac{\partial T(z,t)}{\partial t} = \alpha \frac{\partial^2 T(z,t)}{\partial z^2}$$

For a CW laser the variation of temperature ($\Delta T = T(z,0) - T_0$) along the depth (z) of the material during heating and cooling can be written as follows:

During heating ($0 < t < t_p$):

$$\Delta T(z,t)_{t<tp} = \frac{H}{k}(4\alpha t)^{1/2} ier\, fc\left[\frac{z}{(4\alpha t)^{1/2}}\right].$$

During cooling ($t > t_p$):

$$\Delta T(z,t)_{t>tp} \frac{2H\alpha^{1/2}}{k} \times \left[t^{1/2} ier\, fc\left(\frac{z}{(4\alpha t)^{1/2}}\right) - (t-t_p)^{1/2} ier\, fc\left[\frac{z}{(4\alpha(t-t_p))^{1/2}}\right]\right]$$

ierfc is defined as

$$ier\, fc(x) = \frac{1}{\sqrt{\pi}}\{\exp(-x^2) - x(1 - er\, f(x))\} \text{ and } er\, f(x) = \frac{2}{\sqrt{\pi}}\int_0^x e^{\xi^2} d\xi.$$

The temperature at the surface during heating and cooling can be obtained by substituting $z = 0$ in the above two equations. Therefore

$$\Delta T(0,t) t < t_p = \frac{H}{k}\left(\frac{4\alpha t}{\pi}\right)^{1/2},$$

$$\Delta T(0,t) t > t_p = \frac{H}{k}\left[\left(\frac{4\alpha t}{\pi}\right)^{1/2} - \left(\frac{4\alpha(t-t_p)}{\pi}\right)^{1/2}\right].$$

Here α is the thermal diffusivity, k is the thermal conductivity, t_p is the total residence time of the laser pulse during a CW operation, T is the instantaneous temperature and T_0 is the initial constant temperature of the material. H is the absorbed laser energy and is given as $H = AI_0$, where A is the absorptivity of the material and I_0 is the incident laser power density.

Based on the one dimensional heat conduction equations the variation in temperature (ΔT) for a pulsed laser with respect to time (t) and thickness (z) during the pulse-on period ($t_p > t > 0$) is given as [277]

$$T(z,t) == T_0 + \frac{2AI_0}{k}\sqrt{\alpha t}\, ier\, fc\left(\frac{z}{2\sqrt{\alpha t}}\right).$$

The surface temperature at $z = 0$ is

$$T(0,t) = T_0 + \frac{2AI_0}{k}\sqrt{\frac{\alpha t}{\pi}}.$$

After termination of the laser pulse, i.e. ($t > t_p$) variation of temperature with respect to time and thickness is given as

$$T(z,t) = T_0 + \frac{2AI_0}{k} \times \left[\sqrt{\alpha t}\, ier\, fc\left(\frac{z}{2\sqrt{\alpha t}}\right) - \sqrt{\alpha(t-tp)}\, ier\, fc\left(\frac{z}{2\sqrt{\alpha(t-t_p)}}\right)\right]$$

Here t_p is the pulse width or the pulse duration of the laser beam in a pulsed mode operation.

By effectively controlling the thermo-physical interactions of a CW laser, Kurella and Dahotre [2] synthesized a multiphase bioactive Ca–P coating with multiscale organization ranging from the nano- to the meso-scale by direct laser melting technique. SEM micrographs (Fig. 117) [2] of the processed coating demonstrate a hierarchical organization and periodic arrangement of star-like

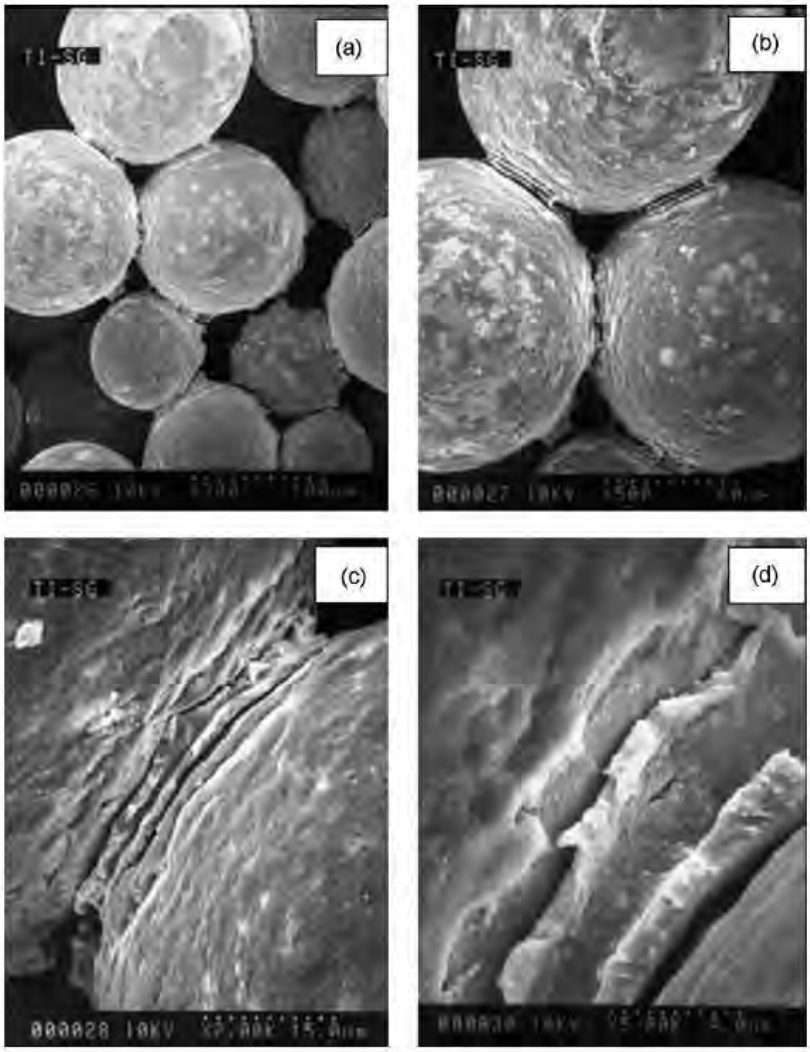


Fig. 110. Scanning electron micrographs depicting the typical appearance of calcium phosphate-coated implants (a = 300×; b = 500×). Higher magnification micrographs of the calcium phosphate coating in a sinter neck region are shown in (c) at 2000× and (d) 5000×. In these regions the HA film appeared thicker and showed signs of delamination in some regions. (Reprinted from [273] with permission from Elsevier.)

phases (A) uniformly distributed inside a self-assembled cellular structure (B). From EDS analysis it was confirmed that the star-like structure 'A' is Ti-rich and Ca–P deficient where as the cellular assembly 'B' is a Ca–P-rich region. The formation of such morphology was attributed to the rapid cooling associated with laser processing which resulted in the formation, organization and controlling of the dimensions of CaP-rich glassy phase into a micron scale cellular morphology and submicron scale clusters of $CaTiO_3$ phase inside these cells. The authors believe that this multiscale organization of bioactive coating on implant may closely mimic the natural organization of the human compact bone and there by aid in protein interaction, cell orientation and tissue integration upon insertion at the defected site.

In a previous work done by our research group [7], the authors demonstrated the feasibility of a porous and geometrically textured Ca–P-based coatings on Ti–6Al–4V substrate by direct melting using a CW Nd:YAG laser. XRD studies of the coated samples demonstrated the existence of TiO_2, Ti, α-TCP and $CaTiO_3$ as the major phases. The formation of all such phases were expected as laser direct melting is an intense process (10^8 to 10^{10} W/cm^2), leading to the melting and mixing of both the precursor calcium phosphate and substrate Ti–6Al–4V to form various solid solutions. The formation of α-TCP is considered as a beneficial bioactive phase as it hydrolyses under physiological conditions to form HA. Cross-sectional view (Fig. 118) [7] of a sample processed at 1006 J cm^{-2} represent a geometrically textured topography with a pit depth of ~150 μm and a pit width of ~600 μm. The formation of a porous coating at the surface is presented as an inset in Fig. 118. The formation of such pores in laser materials processing are attributed to the bubble motion in the molten pool due to thermo-capillary forces in the direction of temperature gradient and pore coalescence due to this bubble motion. The authors believe that a porous coating may help in bone in growth and the physically textured surface may induce certain

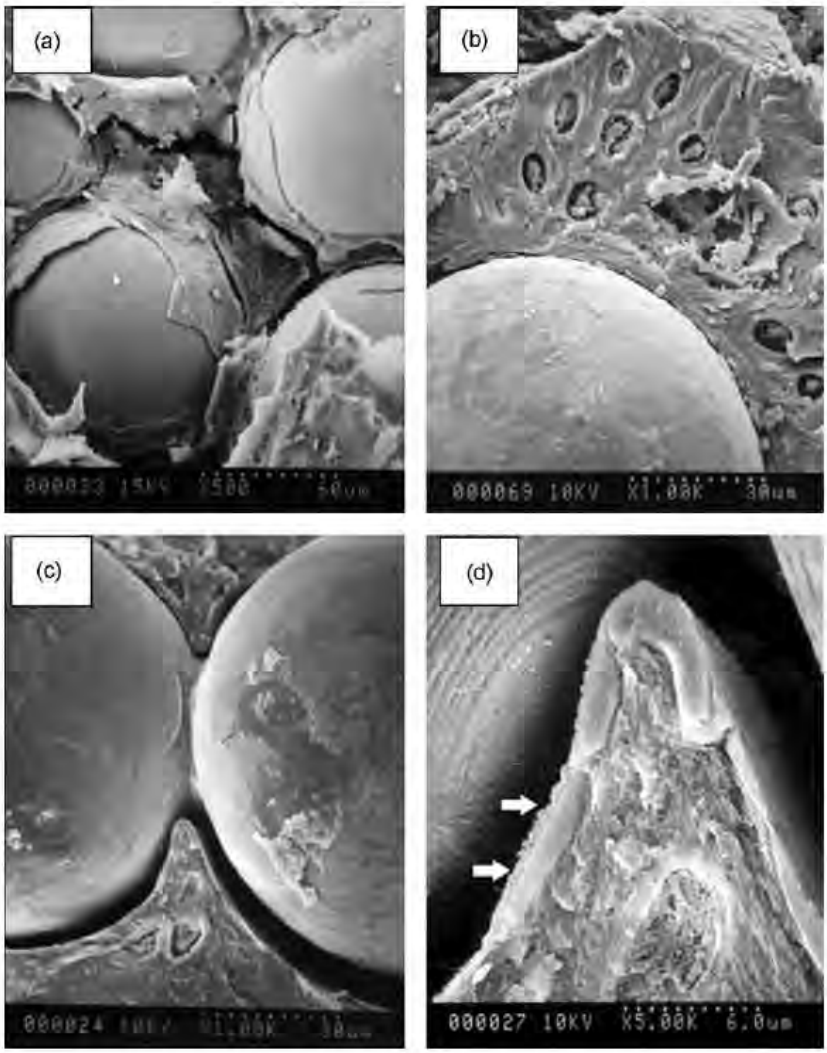


Fig. 111. Scanning electron micrographs of a freeze-fractured specimen showing that the calcium phosphate film is well-adapted to the Ti–6Al–4V particles (a and b). Bone is observed in direct contact with the HA film (b–d) with numerous osteocytes (b–d). In the sinter neck regions where calcium phosphate film delamination, bone had formed between the film and the underlying Ti alloy substrate (arrows—c and d). (Reprinted from [273] with permission from Elsevier.)

amount of mechanical stimulation during the early days of implantation and help in quick fixation. Further, the bioactivity of the coated samples was also proved by the formation of an apatite-like layer following immersion in SBF for 24 h (Fig. 119) [7].

The pulsed mode operation of a pulsed Nd:YAG laser system is also being effectively utilized by the current group [284] to develop Ca–P-based coatings on Ti–6Al–4V substrate by direct laser melting technique. The intermittent delivery of laser pulses at a regular interval allows physical texturing to be achieved by two ways: (1) by varying the spot overlap and (2) by varying the track overlap. The spot overlap can be related to the spot diameter, pulse frequency, and linear scan speed of the laser by the following equation:

$$(\text{spot diameter}) \times (1 - \text{spot overlap}) \times (\text{pulse frequency}) = \text{linear speed}.$$

A schematic of the pulsed laser system used for the coating is shown in Fig. 120 [284]. 2D (Fig. 121(a)) [284,285] and 3D (Fig. 121(b)) [284,285] confocal microscopy images of the surface of the coated samples illustrate the regular texture and corresponding roughness produced using pulse laser direct melting technique. The atoms at the surface of such textured coatings are likely to possess broken and/or unsaturated bonds and as a result they may drive many biological reactions corresponding to cell attachment, cell orientation and cell proliferation. Biomineralization ability of these coated samples was further demonstrated by the formation of an apatite-like phase following immersion in SBF for 48 h (Fig. 122). XRD studies in Fig. 123 compares diffraction patterns obtained before and after immersion in SBF. Before immersion in SBF only a maxima corresponding to α-tricalcium phosphate (α-TCP), $CaTiO_3$, TiO_2 and Ti were observed. After immersion in SBF for 48 h only the diffraction peaks corresponding to HA were observed as a result of the dissolution of α-TCP and $CaTiO_3$.

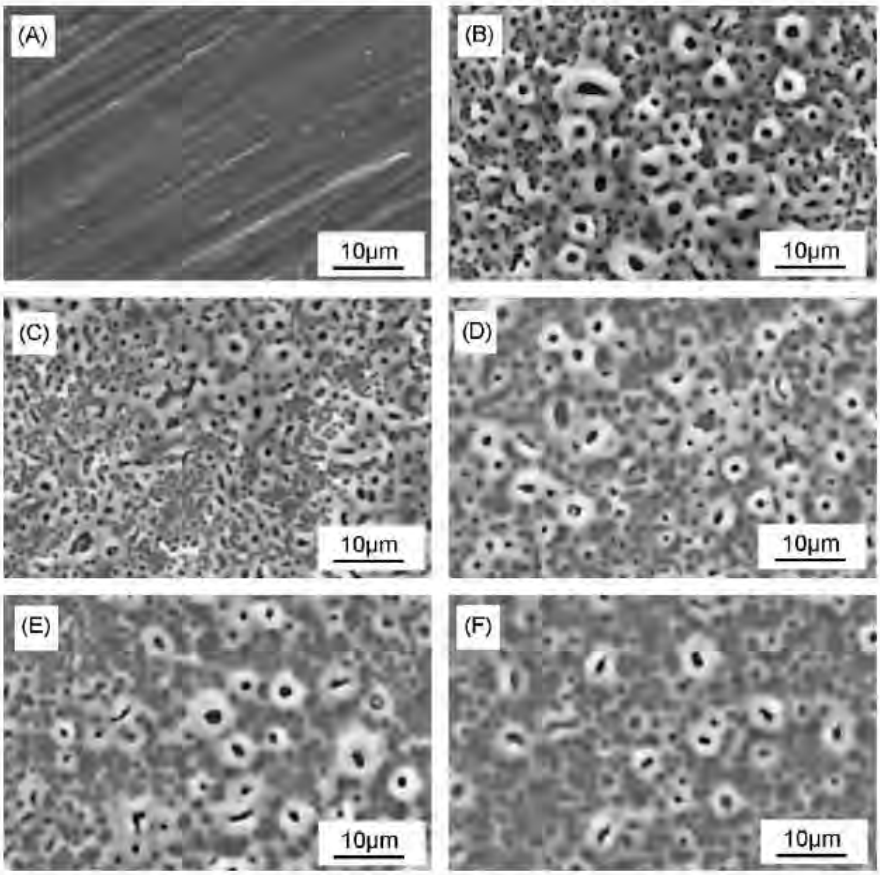


Fig. 112. SEM morphologies of (A) pure Ti, (B) MAO-Ti, and HA sol-gel coating on MAO-Ti with sol concentration of (C) 1.5 M, (D) 2 M, (E) 3 M, and (F) 4 M. (Reprinted from [274] with permissions from Wiley Inter Science.)

3. Performance of Ca–P coatings in body (in vivo) environment

Although several experiments concerning the in vivo studies of Ca–P-based coatings have indicated a stronger and faster fixation, and more bone ingrowth at the interface, the clinical performance of such coatings are still far from being concluded. Hence, most of these in vivo studies are only limited to animal model experiments and nowhere efforts of testing such coatings in an actual human body environment are reported. Some of the major concerns associated with the usage of Ca–P-based coatings in actual body environment, with regard to its long-term stability can be listed as follows [286–292]:

- The degradation and resorption of the Ca–P-based coatings in a biological environment, could lead to disintegration of the coating, resulting in the loss of both coating–substrate bond strength and the implant fixation.
- Coating delamination and disintegration with the formation of particulate debris is also a major concern.
- Ca–P-based coatings may also lead to increased polyethylene wear from the acetabular cup and thereby alleviate the problem of osteolysis.

In this section we intend to highlight the clinical performance of Ca–P-based coatings obtained from animal experiments over the last few years by various authors [286–292].

Hayakawa et al. [286] studied the influence of surface roughness of Ca–P coated Ti implants on bone bonding and bone formation by inserting them in the trabecular bone of rabbits. Four types of Ti implants, i.e. implants blasted with Ti powder, sintered with Ti beads, Ti powder blasted and provided with an additional Ca–P coating, and Ti beads provided with Ca–P coating were prepared to study the effect of surface topography and surface chemistry on bone bonding and bone regeneration. The Ca–P coatings were performed by the ion beam dynamic mixing method. Histological evaluation of the bone–implant interface was carried out following implantation periods of 2, 3, 4and 12 weeks. The authors did not observe any major difference in bone contact to the various implants after an implantation period of 3 and 4 weeks. However, after 12 weeks of implantation the highest percentage of bone contact was found across the Ca–P coated bead implants. Histological appearance of the calcium phosphate coated bead implants following implantation period of 4 and 12 weeks are shown in Figs. 124(a) and 129(b), respectively. After a 4-week implantation period of calcium phosphate coated bead implants new bone was found not only on the implant surface but also inside the Ti beads, whereas, after a 12-week healing period the Ti surface was almost completely covered by new bone. Hence, the authors concluded that both an appropriate geometry and chemical compatibility at the surface can alleviate the bone regeneration and bone bonding to the implant.

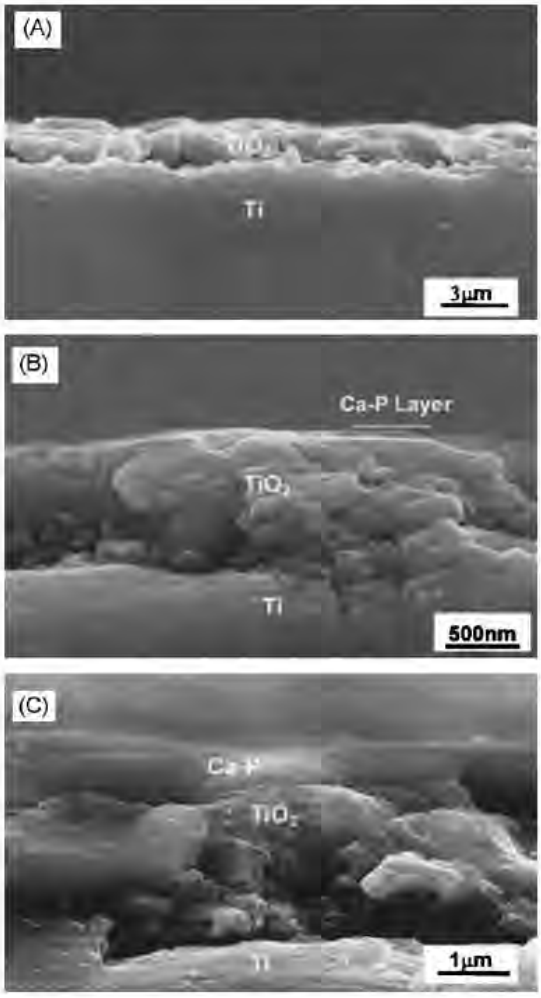


Fig. 113. SEM cross-sectional views of (A) MAO-Ti and HA sol-gel coating on MAO-Ti with sol concentration of (B) 1.5 M and (C) 4 M. (Reprinted from [274] with permissions from Wiley Inter Science.)

Three different types of surface treated Ti implants, i.e.: (1) implants blasted with Ti powder and etched with a solution of 10% HF + 5% HNO_3 (control), (2) Ti-blasted implants modified with a 0.5 μm thick Ca–P coating followed by rapid heat-treatment, and (3) Ti-blasted and Ca–P coated implants immobilized with biophosphonate at the surface were prepared by Yoshinari et al. [287]. The implants were then inserted into the edentulous areas in the mandibular molar region of beagle dogs to study the bone response to the implant surface. After 12 weeks of healing period the authors observed a maximum percentage of bone formation around the biphosphonate-immobilized implants as compared to the other two (Fig. 125) [287]. This is attributed to the fact that the biphosphonates immobilized on the titanium surface can react directly with the surrounding osteoblastic cells, influencing cell differentiation, and thereby promoting hard tissue replacement. Histomorphometrical evaluations of the samples were carried to measure the percentage of bone–implant contact. From Fig. 126 [287] it can be observed that the bone–implant contact percentage was significantly higher for biphosphonate-immobilized implants as compared to the other two surface treated implants.

Ong et al. [288] studied the effect of radio-frequency sputtered Ca–P coatings of Ti implants, on the bond strength at the bone–implant interface, and percentage bone contact length. Cylindrical coated and uncoated samples were implanted for 3–12 weeks in adult male foxhound dogs for these studies. The dogs were sacrificed following an implantation period of 3 and 12 weeks, and the bone–implant blocks were then removed and fabricated for pull test using an Instron tensile testing machine. The mean ultimate interfacial shear strength for the as sputtered Ca–P implant was statistically higher as compared to the bare Ti and as sputtered/heat-treated Ca–P implant (Fig. 127) [288]. This high ultimate interfacial shear strength of as-deposited Ca–P coatings observed just after 3 weeks of implantation suggests rapid bone in growth and is attributed to the amorphous nature of the Ca–P coating. Histological evaluation of the control Ti implants following 12 weeks after implantation reveals new bone growing on preexisting cortical bone and into the implant grooves in direct contact with the implant surface (Fig. 128(a)) [288]. Intense remodeling of the preexisting bone, as well as newly formed bone in contact with the surface of the as-deposited Ca–P coated implant, was also observed 12 weeks after implant placement (Fig. 128(b)) [288]. The authors, therefore, concluded that the sputter deposition process may be an alternative means of coating dental and orthopedic implants with Ca–P, to achieve equivalent or higher bond strengths and percent bone contact at the bone–implant interface.

There are only a limited amount of in vivo studies available in the open literature. The limitations to such experiments may be attributed to any of the following reasons:

- Difficulty in selection of a suitable animal model so as to simulate the actual mechanical loading and unloading conditions the implant might undergo in a human body environment.
- The need to sacrifice a large number of animals, since most of these experiments demands a statistical analysis to validate the results.
- The high cost and long time frame of clinical testing these experiments demand.
- Lack of coordination among material scientists and biologists and thereby an insufficient understanding of this interdisciplinary subject.
- Serious ethical concerns on the use of animals for experimental studies, as they are subjected painful procedures or toxic exposures during the course of test.

Even though importance and need for development of Ca–P coatings for improved bio-implants have been recognized it is still mostly being explored on research level, and after extensive search of open literature these coatings appear to have made limited headway into commercialization. In spite of mention of the commercial products such as hip implants and dental implants by Zimmer Orthopedics, Smith and Nephew and Biomet, the science and technology related to their manufacturing is not disclosed by any one of them due to the proprietary reasons. Hence, at this point it is difficult to bring a detailed discussion on commercialization of Ca–P coatings.

4. Future work

Human compact bone is basically a hierarchical organization at different length scales ranging from nanoscale to mesoscale (Fig. 129) [150]. It essentially consists of 20 wt% collagen, 69 wt% calcium phosphate, 9 wt% water and the rest as organic materials such as proteins, polysaccharides and lipids [15]. At the

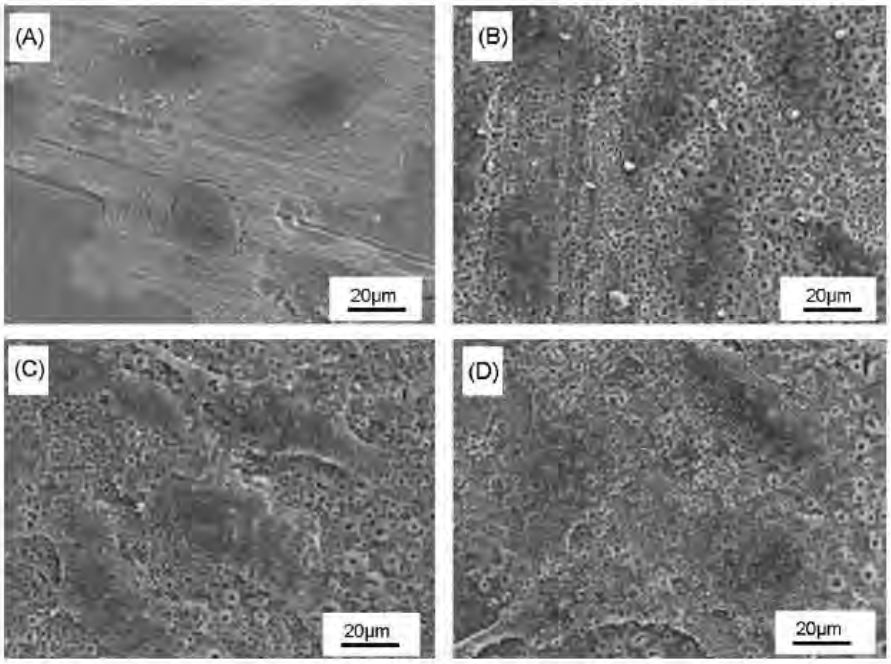


Fig. 114. SEM morphology of the HOS cells after culturing for 3 days on (A) pure Ti, (B) MAO-Ti, and HA sol–gel coating on MAO-Ti at sol concentration with (C) 1.5 M and (d) 3 M. (Reprinted from [274] with permissions from Wiley Inter Science.)

first level in the hierarchy are the collagen filaments which are approximately 1 nm in diameter. Hydroxyapatite crystals are embedded in parallel into these collagen filaments so that the larger dimensions of the crystal are along the long axis of the fiber. These collagen fibrils in turn gets organized into a sheet or woven texture to form the extra-cellular matrix (ECM). Bone cells such as osteocytes resides between these several sheet-like parallel arrays (lamellar bone) or are concentrically arranged into a cylindrical structure known as the osteon. These osteons are then grouped together into long bundles known as Haversian bone, a basic building block of bone microstructure. Finally, at the macroscopic level each bone is made up of a strong calcified outer compact layer [150,293]. Therefore, artificial scaffold biomaterials mimicking this hierarchical organization of the naturally occurring bone in terms of its surface chemistry and surface topography may be the design for the future.

Since cells are sensitive to features ranging from the nanoscale to the mesoscale, a key implant design criterion will be to provide appropriate topographical cues that may stimulate cell differentiation even without the requirement for an appropriate surface chemistry. A laser-based interference patterning technique may be used to manipulate the surface topography in a periodical way. Interference patterning involves irradiating the surface of the sample with two or more overlapping coherent and linearly polarized laser beams of defined geometry [294–298]. This geometry depends on the wavelength and angles between the

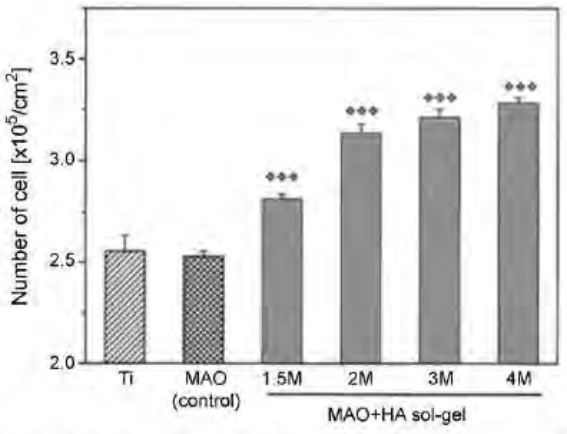


Fig. 115. Number of HOS cells proliferated on samples after culturing for 5 days. The error bars represent means ± 1 SD; $n = 6$; $p < 0.001$ compared to MAO-Ti. (Reprinted from [274] with permissions from Wiley Inter Science.)

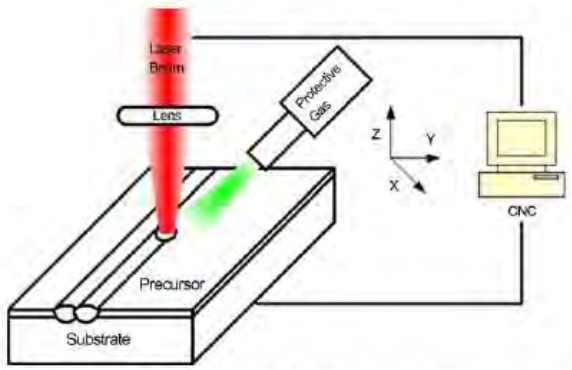


Fig. 116. Schematic of a continuous wave Nd:YAG laser used for the coating process.

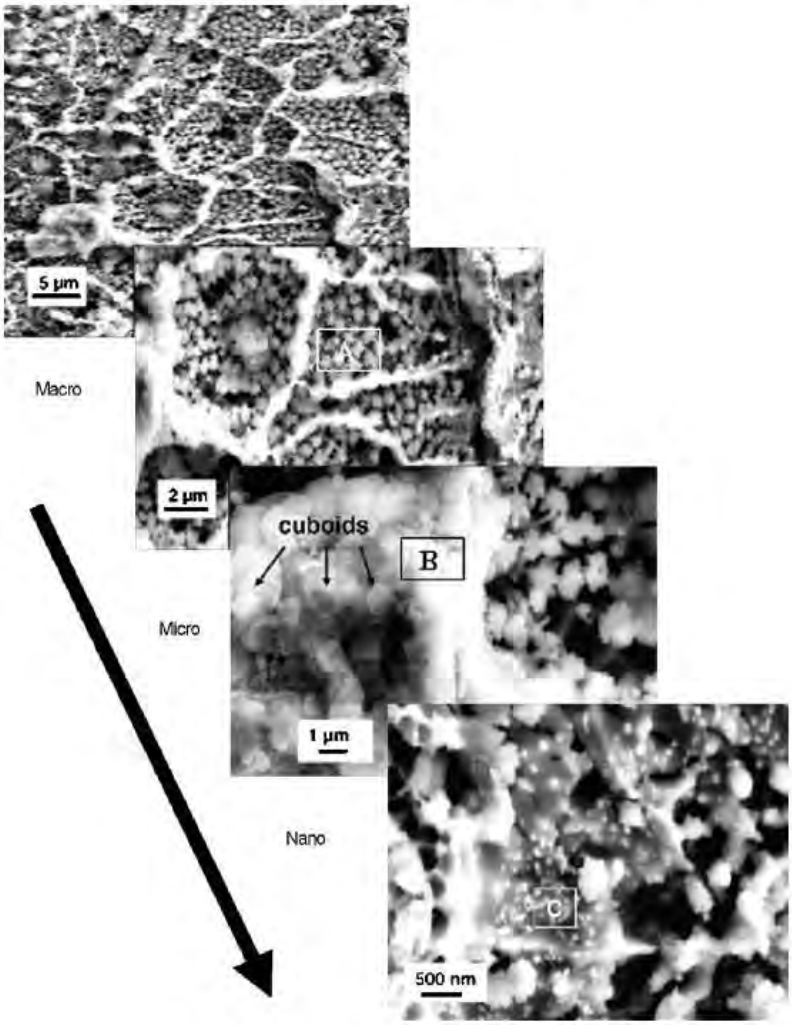


Fig. 117. SEM images of the hierarchical organization of calcium phosphate tribasic coating on Ti alloy substrate obtained by laser melting using a continuous wave Nd:YAG system. (Reprinted from [2] with permission from Elsevier.)

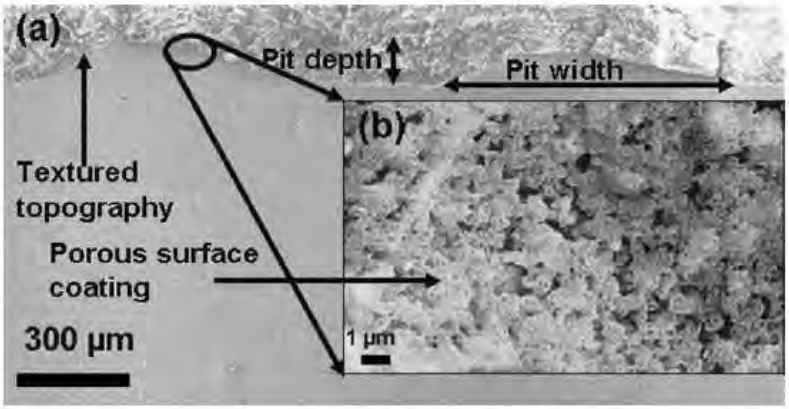


Fig. 118. SEM micrographs of the Ca–P-coated sample processed at a laser fluence of 1006 J cm^{-2}: (a) with a textured topography in the cross-sectioned sample and (b) the inset with multi-scale features at the coating surface. (Reprinted from [7] with permissions from Institute of Physics Publishing (IOP).)

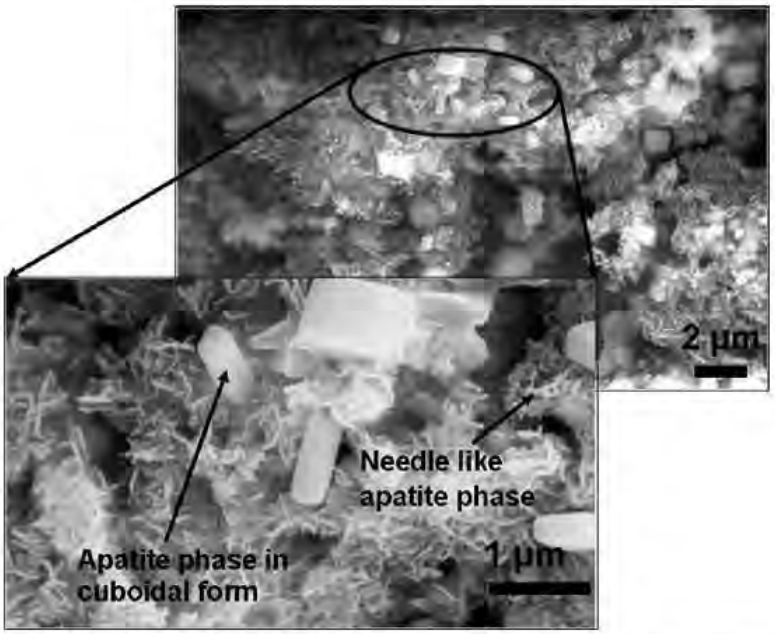


Fig. 119. SEM image of the Ca-P coated sample processed at laser fluence of 1006 J cm^{-2} and after immersion in SBF for 1 day. (Reprinted from [7] with permissions from Institute of Physics Publishing (IOP).).

beams. The two dimensional intensity distribution of the pattern is given by the following equation [296]:

$$I(x) = 2I_0\left\{\cos\left[\frac{4\pi x}{\lambda}\sin\left(\frac{\theta}{2}\right)\right] + 1\right\}$$

where I_0 is the intensity of the laser beam, λ the wavelength and θ the angle in between the beams. The periodicity d of the interference pattern is given as

$$d = \frac{\pi}{2\sin(\theta/2)}$$

A schematic of a laser inter interferometry setup is shown in Fig. 130 [297].

The energy required to produce a single fringe of a particular surface feature size is given as [279]

$$E = \frac{kT_m t_p 10^{-4}}{2\sqrt{\chi t_p} ier\, fc[z/2\sqrt{\chi t_p}]}$$

where E density is the energy in J/cm^2, k is the thermal conductivity in W/m K, T_m is the melting temperature in degrees, t_p is the pulse time in seconds, χ is the thermal diffusivity in m^2/s and z is the

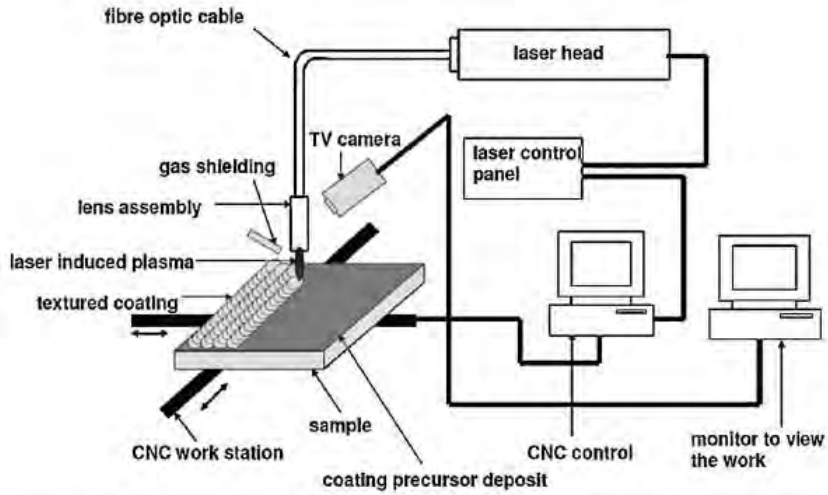


Fig. 120. Schematic of the pulsed Nd:YAG laser system used for the coating process. (Reprinted from [284] with permissions from Institute of Physics Publishing (IOP)

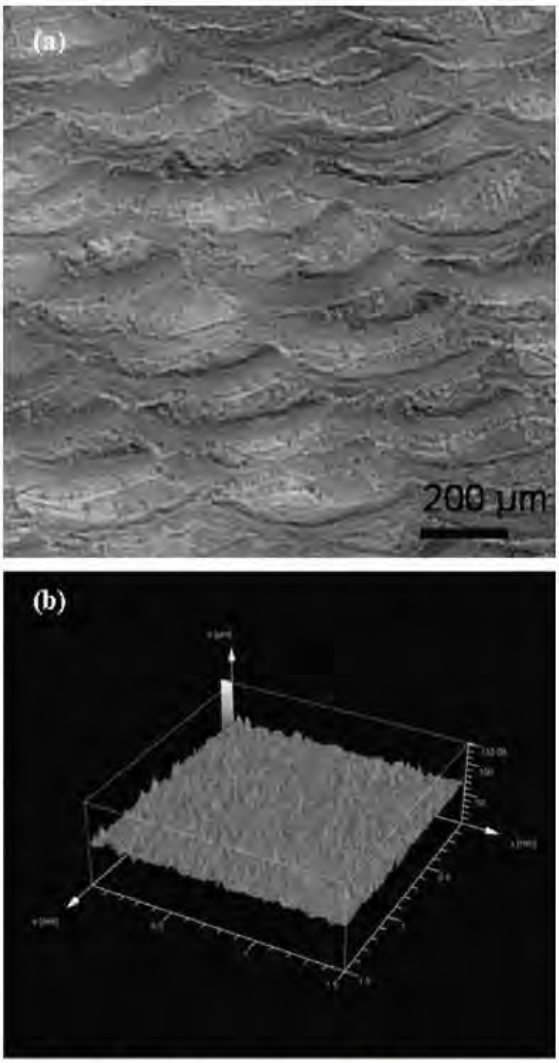


Fig. 121. Figure illustrates (a) a 2-dimensional and (b) 3-dimensional confocal microscopic image of the surface of the Ca–P-coated samples obtained using a pulsed Nd:YAG laser system. (Reprinted from [284,285] with permissions from Maney Publishing.)

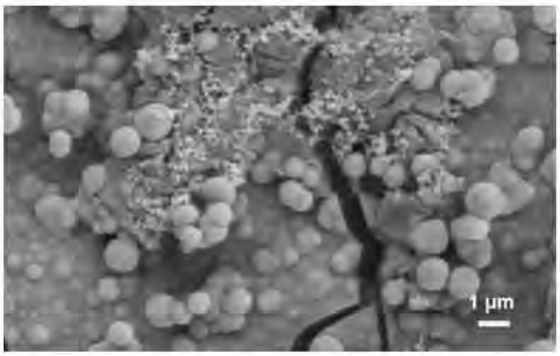


Fig. 122. SEM micrographs revealing the formation of globular apatite like layer following immersion in SBF for 48 h.

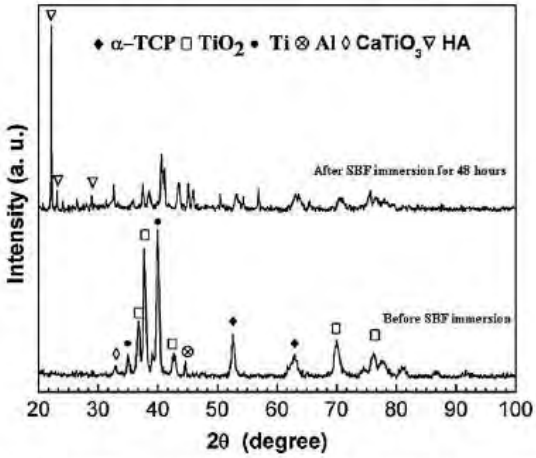


Fig. 123. X-ray diffraction patterns comparing the phases evolved before, and after immersion in SBF for 48 h.

feature size that is assumed to the melt depth in meters. A schematic representation of the interference patterns due to a variation in the interference angle and thermal conductivity of the material is shown in Fig. 131 [297]. Thus, by selecting laser processing parameters in tune with implant material properties, a variety of surface patterns (textures) and microstructures that are suitable for bio-applications can be produced.

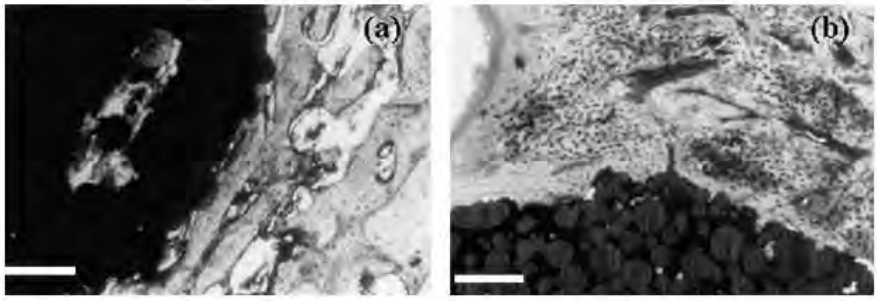


Fig. 124. Histological appearance of Ti–CaP/beads implant after (a) 4 weeks and (b) 12 weeks of implantation (bar = 200 µm). (Reprinted from [286] with permission from Elsevier.)

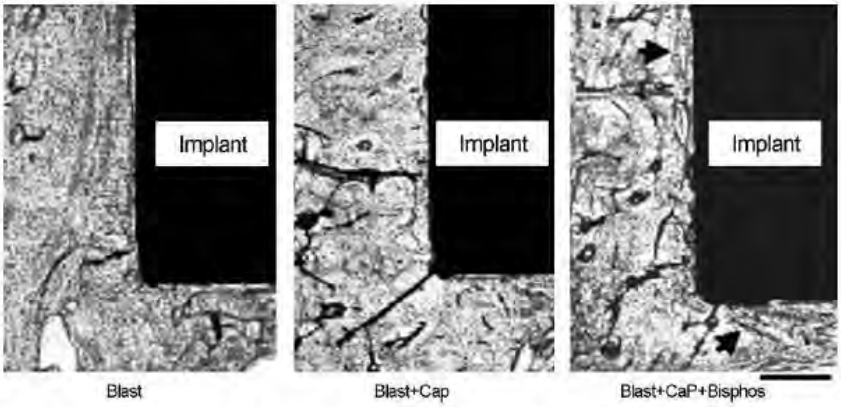


Fig. 125. Light micrographs of implant–bone interface 12 weeks after implantation (bar = 300 μm). (Reprinted from [287] with permission from Elsevier.)

It is well established that organic components such as proteins and bone-derived growth factors, can serve not only to strengthen the hard tissue but also stabilize its mineral contents. Therefore Ca–P coatings incorporated with non-collagenous proteins and bone-derived growth factors may be an alternate design for the regulation of bone formation, absorption, and fracture healing. Since most of the coating techniques involve a high-temperature deposition process, no biological active molecules can be added simultaneously during the preparation of Ca–P layers. Hence, several alternate biomimetic routes such as dip coating, self-

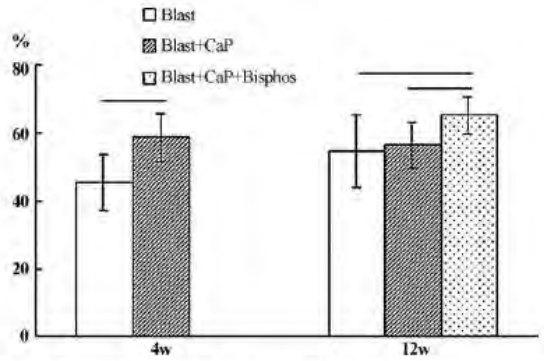


Fig. 126. Percentage of implant–bone contact for different surface treatments. (Reprinted from [287] with permission from Elsevier.)

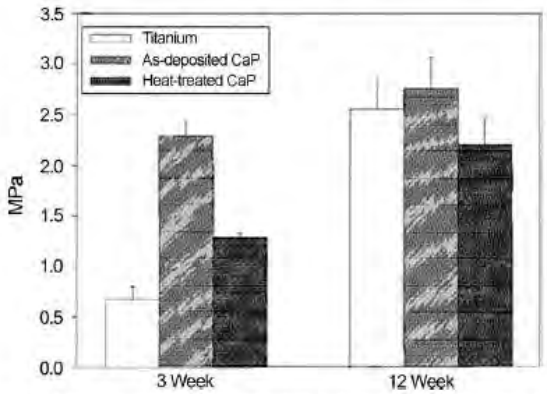


Fig. 127. Mean ultimate interfacial strength of as-deposited CaP, heat-treated CaP, and Ti implants. The error bar represents one standard error. (Reprinted from [288] with permissions from Wiley Inter Science.).

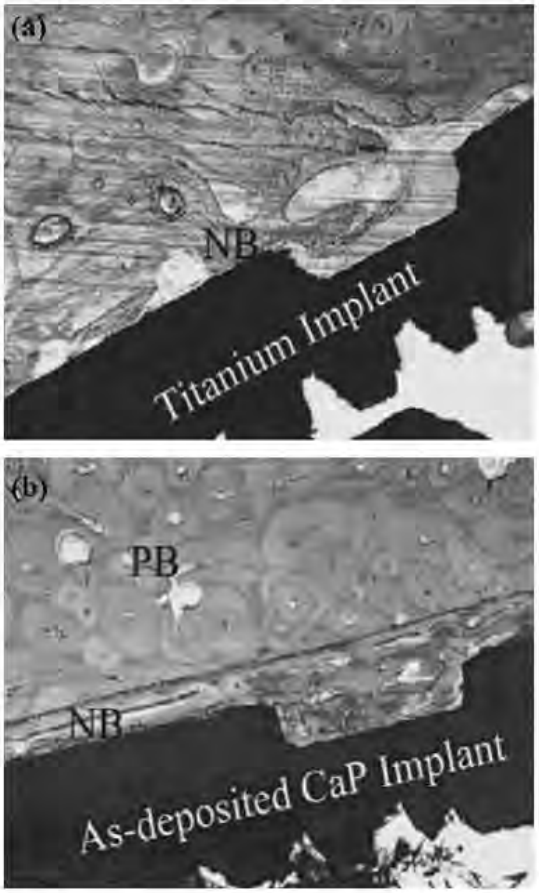


Fig. 128. Histological evaluation of the (a) control Ti implants and (b) Ca–P-coated implant following 12 weeks after implantation. (Reprinted from [288] with permissions from Wiley Inter Science.)

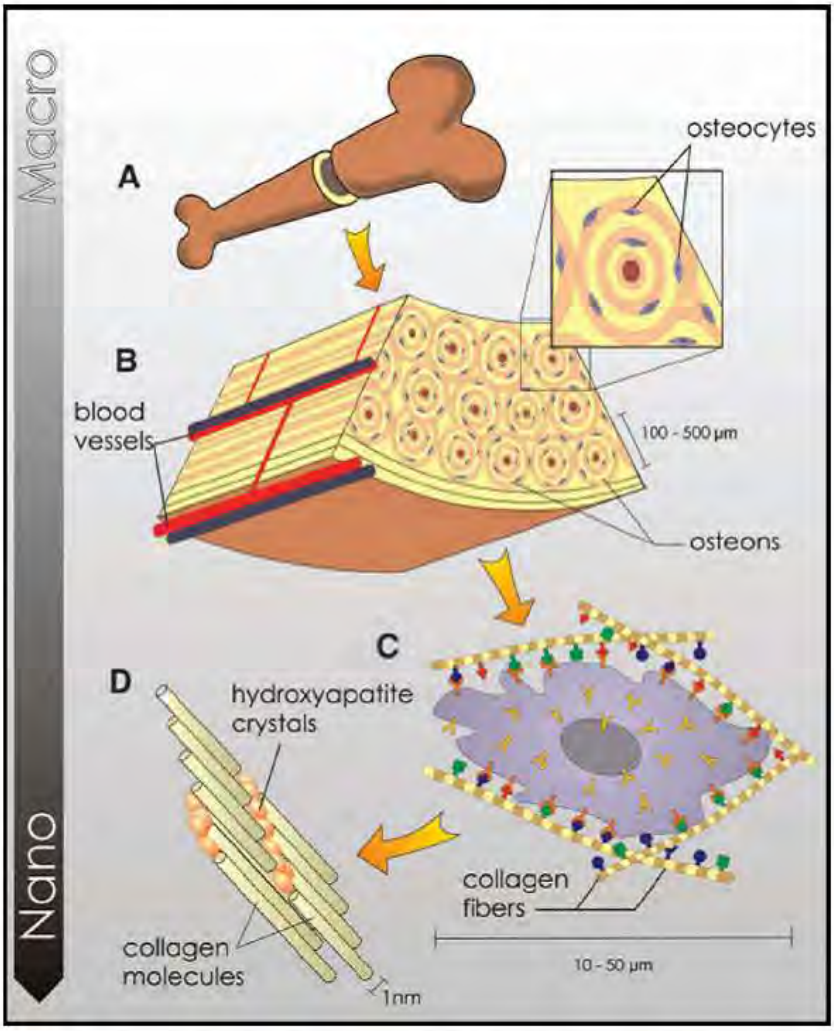


Fig. 129. Schematic representation of the hierarchical organization of bone at different length scales. (Reprinted from [150] with permissions from American Association for the Advancement of Science (AAAS).)

assembled monolayers (SAMs) technique, click chemistry, layer-by-layer assembly (LbL) technique, etc. have been explored to achieve such a coating [299–303].

Another promising and active area of research in this direction is the use of orthopedic implants as drug delivery devices to enhance the fixation of implants [304]. The rationale behind such an approach is to keep the bone intact around the implant without any resorption during the early days implantation. Here a combination of bone cement and antibiotics may be used as a precursor. Work done by various other researchers [305–307] have demonstrated that improved therapy by this technique can be achieved by the use of resorbable calcium phosphates ceramic materials or polymeric materials such as methyl-methacrylate ether as beads or as cements and vancomycin and gentamycin as the antibiotics. Further it is well known that for a normal bone remodeling process, bone formation occurs where the skeleton is mechanically stimulated. Hence, a further advance therapy in this direction would be to correlate the drug delivery with the mechanical situation surrounding the bone. Such an approach by designing controlled release of growth factors in response to mechanical signal has recently been proposed by Lee et al. [308].

In the recent past, however, the "trial-and-error" approach initially taken by the scientists and engineers to develop

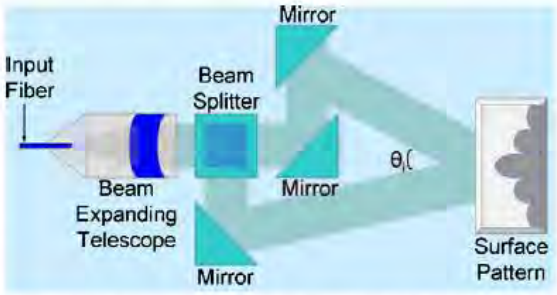


Fig. 130. Schematic setup of laser interferometer. (Reprinted from [297] with permission from Journal of Minerals, Metals and Materials Society (JOM).)

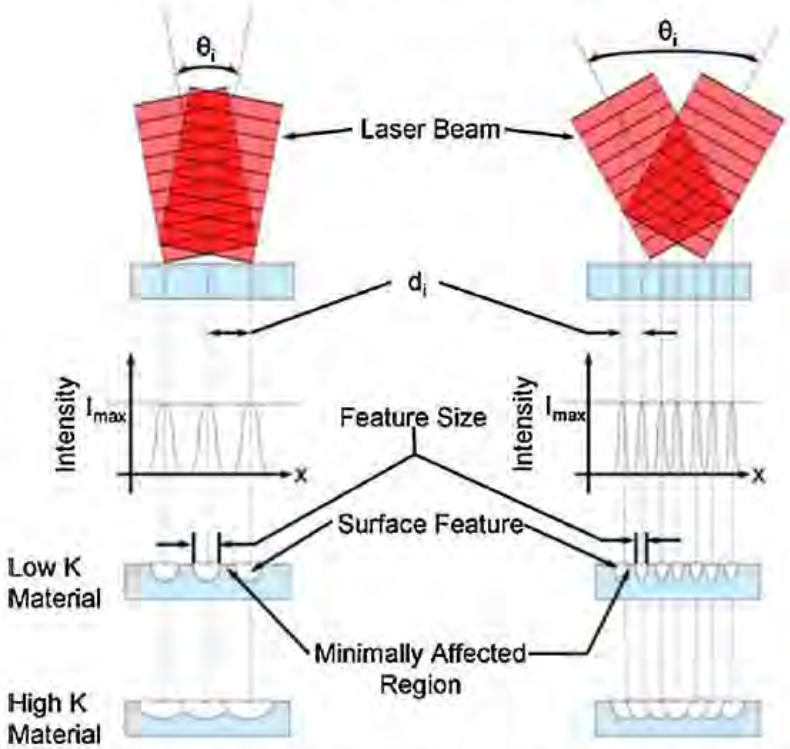


Fig. 131. Schematic representation of interference patterns due to variation in interference angle and thermal conductivity of material. (Reprinted from [297] with permission from Journal of Minerals, Metals and Materials Society (JOM).)

orthopedic implants is not a preferred choice, and people are trying to develop materials with a systematic understanding. At last we strongly believe that a better coordination among various disciplines and a sound understanding of cellular processes that lead to efficient new bone growth may help engineers and scientists to come up with better and efficient implants in the future.

References

[1] A. Kurella, N.B. Dahotre, Journal of Biomedical Applications 20 (2005) 5–50.
[2] A. Kurella, N.B. Dahotre, Acta Biomaterialia 2 (2006) 677–688.
[3] A. Kurella, N.B. Dahotre, Journal of Minerals, Metals and Materials Society (JOM) 58 (2006) 64–66.
[4] A. Kurella, N.B. Dahotre, Journal of Materials Science: Materials in Medicine 17 (2006) 565–572.
[5] P.G. Engleman, A. Kurella, A. Samant, C.A. Blue, N.B. Dahotre, Journal of Minerals, Metals and Materials Society (JOM) 57 (2005) 46–50.
[6] R. Singh, A. Kurella, N.B. Dahotre, Journal of Biomaterials Applications 21 (2006) 46–72.
[7] S.R. Paital, N.B. Dahotre, Biomedical Materials 2 (2007) 274–281.
[8] S.R. Paital, N.B. Dahotre, 2009, Acta Biomaterialia, doi:10.1016/j.actbio.2009.03.004.
[9] R. Singh, N.B. Dahotre, Journal of Materials Science: Material in Medicine 18 (2007) 725–751.
[10] Larry L. Hench, Julia M. Polak, Science 295 (2002) 1014–1017.
[11] J.R. Davis, Hand Book of Materials for Medical Devices, 1st ed., ASM International, 2003.
[12] Valerie Olivier, Nathalie Faucheux, P. Hardouin, Drug Discovery Today 9 (2004) 803–811.
[13] D. Green, D. Walsh, S. Mann, R.O.C. Oreffo, Bone 30 (2002) 810–815.
[14] B. Kasemo, Current opinion in Solid State and Materials Science 3 (1998) 451–459.
[15] Buddy D. Ratner, Allan S. Hoffman, Fredrick J. Schoen, J.E. Lemons, Biomaterials Science, 2nd ed., Elsevier Academic Press, 2004.
[16] Source: www.zimmer.com.
[17] Source: http://www.thehipkneesurgeon.com/jointKnee.php.
[18] Source: http://www.djosurgical.com/products/shoulder/rsp/index.htm.
[19] Source: http://www.ascensionortho.com/Physician_Info/pyrocarbon_info.html.
[20] Suresh K. Pandey, Liliana Werner, David J. Apple, Mahmut Kaskaloglu, American Academy of Ophthalmology 109 (2002) 2042–2051.
[21] David J. Apple, Bulletin of World Health Organization 81 (2003) 756–757.
[22] Source: http://www.lymebaydentistry.co.uk/lbd/jsp/dental_implants.jsp.
[23] MacNeil Sheila, Materials Today 11 (2008) 26–35.
[24] Robert Langer, Nature Reviews 392 (1998) 5–10.
[25] David F. Williams, Biocompatibility of Clinical Implant Materials, 1st ed., CRC Press, 1981.
[26] Chun-Che Shih, Chun-Ming Shih, Yea-Yang Su, Mau-Song Chang, Shin-Jong Lin, Applied Surface Science 219 (2003) 347–362.
[27] I. Ozbek, B.A. Konduk, C. Bindal, A.H. Ucisik, Vacuum 65 (2002) 521–525.
[28] J. Beddoes, K. Bucci, Journal of Materials Science: Materials in Medicine 10 (1999) 389–394.
[29] David R. Haynes, Tania N. Crotti, Michael R. Haywood, Journal of Biomedical Materials Research 49 (2000) 167–175.
[30] Karim Bordji, Jean-Yves Jouzeau, Didier Mainard, Elisabeth Payan, Jean-Pierre Delagoutte, Patrick Netter, Biomaterials 17 (1996) 491–500.
[31] T.M. Sridhar, U. Kamachi Mudali, M. Subbaiyan, Corrosion Science 45 (2003) 237–252.
[32] J. Walczak, F. Shahgaldi, F. Heatley, Biomaterials 19 (1998) 229–237.
[33] Jeong Sik Choi, Duk Yong Yoon, ISIJ International 41 (2001) 478–483.
[34] Chun-Che Shih, Chun-Ming Shih, Yea-Yang Su, Lin Hui Julie Su, Mau-Song Chang, Shin-Jong Lin, Corrosion Science 46 (2004) 427–441.
[35] L.Z. Zhuang, E.W. Langer, Journal of Materials Science 24 (1989) 381–388.
[36] H.S. Dobbs, J.L.M. Robertson, Journal of Materials Science 18 (1983) 391–401.
[37] J.B. Vander Sande, J.R. Coke, J. Wulff, Metallurgical Transactions A 74 (1976) 389–397.
[38] J. Cawley, J.E.P. Metcalf, A.H. Jones, T.J. Band, D.S. Skupien, Wear 255 (2003) 999–1006.
[39] J.-P. Immarigeon, Krishna Rajan, W. Wallace, Metallurgical Transactions A 15A (1984) 339–345.
[40] Mitsuo Niinomi, Metallurgical and Materials Transactions A 33A (2002) 477–486.
[41] F. Conrado Aparicio, Javier Gil, Carlos Fonseca, Mario Barbosa, Josep Anton Planell, Biomaterials 24 (2003) 263–273.
[42] Van R. Noort, Journal of Materials Science 22 (1987) 3801–3811.
[43] Thomas J. Webster, Jeremiah U. Ejiofor, Biomaterials 25 (2004) 4731–4739.
[44] V.M. Frauchiger, F. Schlottig, B. Gasser, M. Textor, Biomaterials (2004) 593–606.

[45] Toshikazu Akahori, Mitsuo Niinomi, Materials Science and Engineering A 243 (1998) 237–243.
[46] D. Scharnweber, R. Beutner, S. Röbler, H. Worch, Journal of Materials Science: Materials in Medicine 13 (2002) 1215–1220.
[47] Sara Bruni, Maria Martinesi, Maria Stio, Cristina Treves, Tibberio Bacci, Francesca Borgioliv, Acta Biomaterialia 1 (2005) 223–234.
[48] Ying Long Zhou, Mitsuo Niinomi, Toshikazu Akahori, Hisao Fukui, Toda S Hiroyuki, Materials Science and Engineering A 398 (2005) 28–36.
[49] P. Linez-Bataillon, F. Monchau, M. Bigerelle, H.F. Hildebrand, Biomolecular Engineering 19 (2002) 133–141.
[50] Jin-Woo Park, Kwang-Bum Park, Jo-Young Suh, Biomaterials 28 (2007) 3306–3313.
[51] Omayra Rivera-Denizard, Nannette Diffoot-Carlo, Vivan Navas, Paul A. Sundaram, Journal of Materials Science: Materials in Medicine 19 (2008) 153–158.
[52] Yu Mi Lee, Eun Jung Lee, Sung Tae Yee, Byung Il Kim, Eun Sang Choe, Hyun Wook Cho, Journal of Materials Science: Materials in Medicine 19 (2008) 1851–1859.
[53] L. Saldaña, N. Vilaboa, G. Vallés, J. González-Cabrero, L. Munuera, Journal of Biomedical Materials Research 73A (2005) 97–107.
[54] Maria Martinesi, Sara Bruni, Maria Stio, Cristina Treves, Francesca Borgioli, Journal of Biomedical Materials Research 74A (2005) 197–207.
[55] T. Seshacharyulu, S.C. Medeiros, W.G. Frazier, Y.V.R.K. Prasad, Materials Science and Engineering A 284 (2000) 184–194.
[56] Y.G. Ko, W.S. Jung, D.H. Shin, C.S. Lee, Scripta Materialia 48 (2003) 197–202.
[57] S.L. Semiatin, V. Seetharaman, I. Weiss, Materials Science and Engineering A 263 (1999) 257–271.
[58] J. Black, Journal of Bone and Joint Surgery 70B (1988) 517–520.
[59] A. Choubey, R. Balasubramaniam, B. Basu, Journals of Alloys and Compounds 381 (2004) 288–294.
[60] M.A. Khan, R.L. Williams, D.F. Williams, Biomaterials 20 (1999) 631–637.
[61] M.C. Bottino, P.G. Coelho, M. Yoshimoto, B. König Jr., V.A.R. Henriques, A.H.A. Bressiani, J.C. Bressiani, Materials Science and Engineering C 28 (2008) 223–227.
[62] Source: http://www.disanto.com/Product%20Pics.htm.
[63] Larry L. Hench, Journal of American Ceramic Society 74 (1991) 1487–1510.
[64] Wanpeng Cao, Larry L. Hench, Ceramics International 22 (1996) 493–507.
[65] Larry L. Hench, Journal of American Ceramic Society 81 (1998) 1705–1728.
[66] J.A. Roether, A.R. Boccaccini, L.L. Hench, V. Maquet, S. Gautier, R. Jérôme, Biomaterials 23 (2002) 3871–3878.
[67] J. Huang, L. Di Silvio, M. Wang, I. Rehman, C. Ohtsuki, W. Bonfield, Journals of Materials Science: Materials in Medicine 8 (1997) 809–813.
[68] Larry L. Hench, Journal of Materials Science: Materials in Medicine 17 (2006) 967–978.
[69] Feng-Huei Lin, Min-Hsiung Hon, Journal of Materials Science 23 (1988) 4295–4299.
[70] Sophie Verrier, Jonny J. Blaker, Maquet Verinique, Larry L. Hench, Aldo R. Boccaccini, Biomaterials 25 (2004) 3013–3021.
[71] Ian A. Silver, Judith Deas, Maria Erecińska, Biomaterials 22 (2001) 175–185.
[72] Q.Z. Chen, J.J. Blaker, A.R. Boccaccini, Journal of Biomedical Materials Research Part B: Applied Biomaterials 76B (2006) 354–363.
[73] A. Balamurugan, G. Balossier, J. Michel, S. Kannan, H. Benhayoune, A.H.S. Rebelo, J.M.F. Ferreira, Journal of Biomedical Materials Research Part B: Applied Biomaterials 83B (2007) 546–553.
[74] Qizhi Z. Chen, Ian D. Thompson, Aldo R. Boccaccini, Biomaterials 27 (2006) 2414–2425.
[75] Edward A. Ross, Christopher D. Batich, William L. Clapp, Judith E. Sallustio, Nadeen C. Lee, Kidney International 63 (2003) 702–708.
[76] K. de Groot, J.G.C. Wolke, J.A. Jansen, Proceedings Institute of Mechanical Engineers 212 (1998) 137–147.
[77] R. Detsch, H. Mayr, G. Ziegler, Acta Biomaterialia 4 (2008) 139–148.
[78] E. Gyorgy, S. Grigorescu, G. Socol, I.N. Mihailescu, D. Janackovic, A. Dindune, Z. Kanepe, E. Palcevskis, E.L. Zdrentu, S.M. Petrescu, Applied Surface Science 253 (2007) 7981–7986.
[79] Hae-Won Kim, Hyoun-E. Kim, Vehid Salih, Jonathan C. Knowles, Journal of Biomedical Materials Research 68A (2004) 522–530.
[80] L. Clèries, J.M. Fernández-Pradas, J.L. Morenza, Journal of Biomedical Materials Research 49 (2000) 43–52.
[81] Manith B. Nair, S. Suresh Babu, H.K. Varma, John Annie, Acta Biomaterialia 4 (2008) 173–181.
[82] Mangal Roy, B. Vamsi Krishna, Amit Bandyopadhyay, Susmita Bose, Acta Biomaterialia 4 (2008) 324–333.
[83] Xuebin Zheng, Minhui Huang, Chuanxian Ding, Biomaterials 21 (2000) 841–849.
[84] Hae-Won Kim, Young-Hag Koh, Long-Hao Li, Sook Lee, Hyoun-Ee Kim, Biomaterials 25 (2004) 2533–2538.
[85] P.A. Ramires, A. Romito, F. Cosentino, E. Milella, Biomaterials 22 (2001) 1467–1474.
[86] L. Chou, B. Marek, W.R. Wagner, Biomaterials 20 (1999) 977–985.
[87] Y.W. Gu, K.A. Khor, P. Cheang, Biomaterials 24 (2003) 1603–1611.
[88] C. Mauli Agrawal, Journal of Materials (1998) 31–35.
[89] Source: www.devicelink.com.
[90] Source: http://www.genesis-tech.ch/company/.
[91] Source: http://tc.engr.wisc.edu/UER/uer01/author1/content.html.
[92] Source: http://www.jri-ltd.co.uk/total_knee_replacement.asp.
[93] Min Wang, Biomaterials 24 (2003) 2133–2151.
[94] S. Ramakrishna, J. Mayer, E. Wintermantel, Kam W. Leong, Composite Science and Technology 61 (2001) 1189–1224.
[95] S.L. Evans, P.J. Gregson, Biomaterials (1998) 1329–1342.
[96] M.S. Abu Bakar, M.H.W. Cheng, S.M. Tang, S.C. Yu, K. Liao, C.T. Tan, K.A. Khor, P. Cheang, Biomaterials 24 (2003) 2245–2250.
[97] Lin-Shu Liu, Andrea Y. Thompson, Mohammad A. Heidaran, James W. Poser, Robert C. Spiro, Biomaterials 20 (1999) 1097–1108.
[98] S.H. Teoh, International Journal of Fatigue 22 (2000) 825–837.
[99] Mitsuo Niinomi, Biomaterials 24 (2003) 2673–2683.
[100] M. Long, H.J. Rack, Biomaterials 19 (1998) 1621–1639.
[101] M. Long, R. Crooks, H.J. Rack, Acta Materialia 47 (1999) 661–669.
[102] Chia-Wei Lin, Chien-Ping Ju, Jiin-Huey Chern Lin, Biomaterials 26 (2005) 2899–2907.
[103] Takao Hanawa, Science and Technology of Advanced Materials 3 (2002) 289–295.
[104] Lissa A. Pruitt, Biomaterials 26 (2005) 905–915.
[105] Joon Park, R.S. Lakes, Biomaterials an introduction, 3rd edition, Springer, 2007.
[106] P. Bills, L. Blunt, X. Jiang, Wear 263 (2007) 1133–1137.
[107] M. Semlitsch, H.G. Willert, Processing Institute of Mechanical Engineers 211 (1997) 73–88.
[108] J. Nevelos, E. Ingham, C. Doyle, R. Streicher, A. Nevelos, W. Walter, J. Fisher, The Journal of Arthroplasty 15 (2000) 793–795.
[109] Manuela Teresa Raimondi, Riccardo Pietrabissa, Biomaterials 21 (2000) 907–913.
[110] E. Ingham, J. Fisher, Processing Institute of Mechanical Engineers 214 (2000) 21–37.
[111] S. Affatato, M. Goldoni, M. Testoni, A. Toni, Biomaterials 22 (2001) 717–723.
[112] M.A.L. Hernández-Rodríguez, R.D. Mercado-Solís, A.J. Pérez-Unzueta, D.I. Martinez-Delgado, M. Cantú-Siuentes, Wear 259 (2005) 958–963.
[113] A. Wang, S. Yue, J.D. Bobyn, F.W. Chan, J.B. Medley, Wear 225–229 (1999) 708–715.
[114] J.A. Ortega-Sáenz, M.A.L. Hernández-Rodríguez, A. Pérez-Unzueta, R. Mercado-Solis, Wear 263 (2007) 1527–1532.
[115] Eriko Kitamura, Roxana Stegaroiu, Clinical Oral Implants Research 15 (2004) 401–412.
[116] H.J. Chun, S.Y. Cheong, J.H. Han, S.J. Heo, J.P. Chung, I.C. Rhyu, Y.C. Choi, H.K. Baik, Y. Ku, M.H. Kim, Journal of Oral Rehabilitation 29 (2002) 565–574.
[117] P.J. Prendergast, Clinical Biomechanics 12 (1997) 343–366.
[118] W. Xu, A.D. Crocombe, S.C. Hughes, Proceedings Institute of Mechanical Engineers 214 (2000) 595–602.
[119] Source: http://www.endolab.de/computer/computersimulation_e.htm.
[120] U. Kamachi Mudali, T.M. Sridhar, Baldev Raj, Sadhana 28 (2003) 601–637.
[121] Marcel Pourbaix, Biomaterials 5 (1984) 122–134.
[122] C. Valero Vidal, A. Igual Muñoz, Corrosion Science 50 (2008) 1954–1961.
[123] J.E. Lemons, R. Venugopal, L.C. Lucas, Handbook of biomaterials evaluation: Scientific, Technical and Critical Testing of Implant Materials, Taylor and Francis, Philadelphia, PA, 1999, pp. 155–170.
[124] R. Venugopal, J. Gaydon, Princeton Applied Research, Technical Note, 99–101.
[125] K. Kieswetter, Z. Schwartz, T.W. Hummert, D.L. Cochran, J. Simpson, D.D. Dean, B.D. Boyan, Journal of Biomedical Materials Research 32 (1996) 55–63.
[126] Ann Wennerberg, International Journal of Machine Tolls and Manufacturing 38 (1998) 657–662.
[127] D.D. Deligianni, N. Katsala, S. Ladas, D. Sotiropoulou, J. Amedee, Y.F. Missirlis, Biomaterials 22 (2001) 1241–1251.
[128] Ricardo Luiz Perez Teixeira, Geralda Cristina Durães de Godoy, Marivalda de Magalhães Pereira, Materials Research 7 (2004) 299–303.
[129] Hwei Ling Khor, Yujun Kuan, Hildegard Kukula, Kaoru Tamada, Wolfgang Knoll, Martin Moeller, Dietmar W. Hutmacher, Biomacromolecules 8 (2007) 1530–1540.
[130] D.J. Wilson, N.P. Rhodes, R.L. Williams, Biomaterials 24 (2003) 5069–5081.
[131] R.G. Richards, M. Wieland, M. Textor, Journal of Microscopy 199 (2000) 115–123.
[132] Yoshiyuki G. Takei, Takashi Aoki, Kohei Sanui, Naoya Ogata, Yasuhisa Sakurai, Teruo Okano, Macromolecules 27 (1994) 6163–6166.
[133] D.Y. Kwok, A.W. Neumann, Advances in Colloid and Interface Science 81 (1999) 167–249.
[134] M. Morra, E. Occhiello, F. Garbassi, Advances in Colloid and Interface Science 32 (1990) 79–116.
[135] E.L. Decker, B. Frank, Y. Suo, S. Garoff, Colloids and surfaces A 156 (1999) 177–189.
[136] Tammar S. Meiron, Journal of Colloid and Interface Science 274 (2004) 637–644.
[137] F.K. Skinner, Y. Rottenberg, A.W. Neumann, Journal of Colloid and Interface Science 130 (1989) 25–34.
[138] T. Yasuda, T. Okuno, Langmuir 10 (1994) 2435–2439.
[139] Source: http://www.labkorea.com/products/cam/tantec/cammicro.html#specs.
[140] Jianhua Wei, Masao Yoshinari, Shinji Takemoto, Masayuki Hattori, Eiji Kawada, Baolin Liu, Yutaka Oda, Journal of Biomedical Materials Research Part B: Applied Biomaterials 81 (2007) 66–75.
[141] Yuehuei H. An, Richard J. Friedman, Journal of Biomedical Materials Research: Applied Biomaterials 43 (1998) 338–348.
[142] M.I. Jones, I.R. McColl, D.M. Grant, K.G. Parker, T.L. Parker, Journal of Biomedical Materials Research 52 (2000) 413–421.
[143] H. Zreiqat, Stella M. Valenzuela, Besim Ben Nissan, Richard Roest, Christine Knabe, Ralf J. Radlanski, Herbert Renz, Peter J. Evans, Biomaterials 26 (2005) 7579–7586.
[144] Colin A. Scotchford, Elaine Cooper, Graham J. Leggett, Sandra Downes, Journal of Biomedical Materials Research 41 (1998) 431–442.
[145] Benjamin G. Keselowsky, David M. Collard, Andrés J. Garcia, Proceedings of the National Academy of Sciences of the United States of America 102 (2005) 5953–5957.

[146] William G. Brodbeck, Matthew S. Shive, Erica Colton, Yasuhide Nakayama, Takehisa Matsuda, Journal of Biomedical Materials Research 55 (2001) 661–668.
[147] Kevin E. Healy, Carson H. Thomas, Alireza Rezania, Jung E. Kim, Patrick J. McKeown, Barbara Lom, Philip E. Hockberger, Biomaterials 17 (1996) 195–208.
[148] K. Anselme, P. Linez, M. Bigerelle, D. Le Maguer, P. Hardouin, H.F. Hildebrand, A. Iost, J.M. Leroy, Biomaterials 21 (2000) 1567–1577.
[149] Kay C. Dee, David A. Puleo, Rena Bizios, Tissue Biomaterial Interactions, John Wiley & Sons Inc., Hoboken, NJ, 2003.
[150] Molly M. Stevens, Julian H. George, Science 310 (2005) 1135–1138.
[151] F.Z. Cui, Z.S. Luo, Surface and Coatings Technology 112 (1999) 278–285.
[152] A. Nanci, J.D. Wuest, L. Peru, P. Brunet, V. Sharma, S. Zalzal, M.D. McKee, Journal of Biomedical Materials Research 40 (1998) 324–335.
[153] Yoshihiro Ito, Biomaterials 20 (1999) 2333–2342.
[154] E. Wintermantel, J. Mayer, J. Blum, K.L. Eckert, P. Lüscher, M. Mathey, Biomaterials 17 (1996) 83–91.
[155] F.H. Jones, Surface Science Reports 42 (2001) 75–205.
[156] Matthew Tirrell, Efrosini Kokkoli, Markus Biesalski, Surface Science 500 (2002) 61–83.
[157] Byung-Ho Yoon, Young-Hag Koh, Chee-Sung Park, Hyoun-Ee Kim, Journal of American Ceramic Society 90 (2007) 1744–1752.
[158] G.A. Dunn, A.F. Brown, Journal of Cell Science 83 (1986) 313–340.
[159] Turchanin Andrey, Tinazli Ali, El-Desawy Mohamed, Großmann Helge, Schnietz Mark, Harun H. Solak, Tampé Robert, Gölzhäuser Armin, Advanced Materials 1–7 (2008).
[160] Hyeongil Kim, Seong-Ho Choi, Jae-Jun Ryu, Seung-Yong Koh, Ju-Han Park, In-Seop Lee, Biomedical Materials 3 (2008) 1–6.
[161] G.P. Reaber, M.P. Lutolf, J.A. Hubbell, Acta Biomaterialia 3 (2007) 615–629.
[162] M. Gutierres, M.A. Lopes, N. Sooraj Hussain, A.F. Lemos, J.M.F. Ferreira, A. Afonso, A.T. Cabral, L. Almeida, J.D. Santos, Acta Biomaterialia 4 (2008) 370–377.
[163] Yaping Guo, Yu Zhou, Dechang Jia, Acta Biomaterialia 4 (2008) 334–342.
[164] Jing Lu, Masaru P. Rao, Noel C. MacDonald, Dongwoo Khang, Thomas J. Webster, Acta Biomaterialia 4 (2008) 192–201.
[165] Faming Zhang, Jiang Chang, Jianxi Lu, Kaili Lin, Congqin Ning, Acta Biomaterialia 3 (2007) 896–904.
[166] Laurent Le Guehennec, Marco-Antonio Lopez-Heredia, Benedicte Enkel, Pierre Weiss, Yves Amouriq, Pierre Layrolle, Acta Biomaterialila 4 (2008) 535–543.
[167] Xuanyong Liu, Xiaobing Zhao, Baoe Li, Cong Cao, Yuqi Dong, Chuanxian Ding, Paul K. Chu, Acta Biomaterialia 4 (2008) 544–552.
[168] Li-Hong He, Owen C. Standard, Tiffany T.Y. Huang, Bruno A. Latella, Michael V. Swain, Acta Biomaterialia 4 (2008) 577–586.
[169] Chang-Hwan Choi, Sepideh H. Hagvall, Benjamin M. Wu, James C.Y. Dunn, Ramin E. Beygui, Chang-Jin, C.J Kim, Biomaterials 28 (2007) 1672–1679.
[170] Darmawati Mohamad Yunos, Oana Bretcanu, Aldo R. Boccaccini, Journal of Materials Science 43 (2008) 4433–4442.
[171] Guobao Wei, Peter X. Ma, Biomaterials 25 (2004) 4749–4757.
[172] B.O. Arronson, J. Lausmaa, B. Kasemo, Journal of Biomedical Materials Research 35 (1997) 49–73.
[173] Takao Hanawa, Materials Science and Engineering A 267 (1999) 260–266.
[174] Qing Zhao, Guang-Jie Zhai, D.H.L. Ng, Xiao-Zhong Zhang, Zhi-Qing Chen, Biomaterials 20 (1999) 595–599.
[175] Zhen-Mei Liu, Zhi-Kang Xu, Jian-Qin Wang, Jian Wu, Jun-Jie Fu, European Polymer Journal 40 (2004) 2077–2087.
[176] Fu Zhang, E.T. Kang, K.G. Neoh, Peng Wang, K.L. Tan, Biomaterials 22 (2001) 1541–1548.
[177] Inn-Kyu Kang, Oh Hyeong Kwon, Young Moo Lee, Yong Kiel Sung, Biomaterials 17 (1996) 841–847.
[178] Joerg C. Tiller, Gary Bonner, Li-Chun Pan, Alexander M. Klibanov, Biotechnology Bioengineering 73 (2001) 246–252.
[179] Daniel Hal Davis, Constantina S. Giannoulis, Robert W. Johnson, Tejal A. Desai, Biomaterials 23 (2002) 4019–4027.
[180] M.P. Lutolf, J.A. Hubbell, Nature Biotechnology 23 (2005) 47–55.
[181] Fiona E. Black, Mark Hartshorne, Martyn C. Davies, Clive J. Roberts, Saul J.B. Tendler, Philip M. Williams, Kevin M. Shakesheff, Langmuir 15 (1999) 3157–3161.
[182] Yasuhiko Iwasaki, Nobuyuki Saito, Colloids and Surfaces B: Biointerfaces 32 (2003) 77–84.
[183] Shuguang Zhang, Lin Yan, Michael Altman, Michael Lassle, Helen Nugent, Felice Frankel, Douglas A. Lauffenberger, George M. Whitesides, Biomaterials 20 (1999) 1213–1220.
[184] A.P. Vander Heiden, G.M. Willems, T. Lindhout, A.P. Pijpers, L.H. Koole, Journal of Biomedical Materials Research 40 (1998) 195–203.
[185] Ying Luo, Molly S. Shoichet, Nature Materials 3 (2004) 249–253.
[186] L.G. Ellies, D.G. Nelson, J.D. Featherstone, Biomaterials 13 (1992) 313–316.
[187] Y. Yang, K.H. Kim, J.L. Ong, Biomaterials 26 (2005) 327–337.
[188] B. LeÔn, J.A. Jansen, Thin Calcium Phosphate Coatings for Medical Implants, 2nd ed., Springer, New York, USA, 2009.
[189] W. Ensinger, Review of Scientific Instruments 63 (1992) 5217–5233.
[190] I.-S. Lee, C.-N. Whang, G.H. Lee, F.-Z. Cui, A. Ito, Nuclear Instruments and Methods in Physics Research B 206 (2003) 522–526.
[191] M. Hamdi, A. Ide-Ektessabi, Surface and Coatings Technology 163–164 (2003) 362–367.
[192] A. Rabiei, B. Thomas, C. Jin, R. Narayan, J. Cuomo, Y. Yang, J.L. Ong, Surface and Coatings Technology 200 (2006) 6111–6116.
[193] Jae-Man Choi, Hyoun-Ee Kim, In-Seop Lee, Biomaterials 21 (2000) 469–473.
[194] Z.S. Luo, F.Z. Cui, W.Z. Li, Journal of Biomedical Materials Research 46 (1999) 80–86.
[195] F.Z. Cui, Z.S. Luo, Q.L. Feng, Journal of Materials Science: Materials in Medicine 8 (1997) 403–405.
[196] B.H. Zhao, I.-S. Lee, W. Bai, F.Z. Cui, H.L. Feng, Surface and Coatings Technology 193 (2005) 366–371.
[197] D.M. Brunette, P. Tengvall, M. Textor, P. Thomsen, Titanium in Medicine: Materials Science, Surface Science, Engineering, Biological Responses and Medical Applications, Springer, 2001.
[198] ASM Handbook, American Society of Materials International, vol. 5, Materials Park, OH, 2004.
[199] E. Lugscheider, C. Barimani, P. Eckert, U. Eritt, Computational Materials Science 7 (1996) 109–114.
[200] R. Suryanarayana, Plasma Spraying Theory and Applications, World Scientific, 1993.
[201] K.A. Khor, Z.L. Dong, C.H. Quek, P. Cheang, Materials Science and Engineering A 281 (2000) 221–228.
[202] Z.L. Dong, K.A. Khor, C.H. Quek, T.J. White, P. Cheang, Biomaterials 24 (2003) 97–105.
[203] K.A. Khor, Y.W. Gu, D. Pan, P. Cheang, Biomaterials 25 (2004) 4009–4017.
[204] Limin Sun, Christopher C. Berndt, Clare P. Grey, Materials Science and Engineering A 360 (2003) 70–84.
[205] S. Dyshlovenko, B. Pateyron, L. Pawlowski, D. Murano, Surface and Coatings technology 179 (2004) 110–117.
[206] Bang-Yen Chou, Edward Chang, Biomaterials 20 (1999) 1823–1832.
[207] N. Clausen, Journal of American Ceramic Society 59 (1976) 49–51.
[208] Ji Huaxia, C.B. Ponton, P.M. Marquis, Journals of Materials Science: Materials in Medicine 3 (1992) 283–287.
[209] Y.C. Tsui, C. Doyle, T.W. Clayne, Biomaterials 19 (1998) 2031–2043.
[210] M. Inagaki, T. Kameyama, Biomaterials 28 (2007) 2923–2931.
[211] C. Lavos-Vaalereto, S. Wolynec, M.C.Z. Deboni, B. Konig Jr, Journal of Biomedical Materials Research (Applied Biomaterials) 58 (2001) 727–733.
[212] C. Massaro, M.A. Baker, F. Cosentino, P.A. Ramires, S. Klose, E. Milella, Journal of Biomedical Materials Research (Applied Biomaterials) 58 (2001) 651–657.
[213] Laxmidhar Besra, Meilin Liu, Progress in Materials Science 52 (2007) 1–61.
[214] Y. Fukada, N. Nagarajan, W. Mekky, Y. Bao, H.S. Kim, Journal of Materials Science 39 (2004) 787–801.
[215] Cong Wang, J. Ma, Wen Cheng, Ruifang Zhang, Materials Letters 57 (2002) 99–105.
[216] I. Zhitomirsky, Materials Letters 42 (2000) 262–271.
[217] J. Ma, C.H. Liang, L.B. Kong, C. Wang, Journal of Materials Science: Materials in Medicine 14 (2003) 797–801.
[218] T.M. Sridhar, U. Kamachi Mudali, M. Subbaiyan, Corrosion Science 45 (2003) 2337–2359.
[219] I. Zhitomirsky, L. Gal-or, Journal of Materials Science: Materials in Medicine 8 (1997) 213–219.
[220] Omer O. Van der Biest, Luc J. Vandeperre, Annual Review of Material Science 29 (1999) 327–352.
[221] J. Ma, C. Wang, K.W. Peng, Biomaterials 24 (2003) 3505–3510.
[222] Lídia Ágata de, Mônica Calixto de Andrade, Alexandre Malta Rossi, Gloria de Almeida Soares, Journal of Biomedical Materials Research 60 (2002) 1–7.
[223] M. Wei, A.J. Ruys, B.K. Milthorpe, C.C. Sorrell, J.H. Evans, Journal of Sol-Gel Science and Technology 21 (2001) 39–48.
[224] M. Wei, A.J. Ruys, B.K Milthorpe, C.C. Sorrell, Journal of Biomedical Materials Research 45 (1999) 11–19.
[225] S.K. Yen, C.M. Lin, Materials Chemistry and Physics 77 (2002) 70–76.
[226] P. Mondragón-Cortez, G. Vargas-Gutiérrez, Materials Letters 58 (2004) 1336–1339.
[227] M. Javidi, S. Javadpour, M.E. Bahrololoom, J. Ma, Materials Science and Engineering C 28 (2008) 1509–1515.
[228] Bauerle Dieter, Laser Processing and Chemistry, 3rd ed., Spriger, 2000.
[229] C. Belouet, Applied Surface Science 96–98 (1996) 630–642.
[230] Rajiv K. Singh, J. Narayan, Physical Review B 41 (1990) 8843–8859.
[231] M. Aden, E.W. Kreutz, A. Voss, Journal of Physics D: Applied Physics 26 (1993) 1545–1553.
[232] P.R. Willmott, J.R. Huber, Reviews of Modern Physics 72 (2000) 315–328.
[233] S.I. Anisimov, D. Bäuerle, B.S. Lukyanchuk, Physical Review B 48 (1993) 12076–12081.
[234] V. Nelea, C. Ristoscu, C. Chiritescu, C. Ghica, I.N. Mihailescu, H. Pelletier, P. Mille, A. Cornet, Applied Surface Science 168 (2000) 127–131.
[235] M.D. Ball, S. Downes, C.A. Scotchford, E.N. Antonov, V.N. Bagratashvili, V.K. Popov, W.-J. Lo, D.M. Grant, S.M. Howdle, Biomaterials 22 (2001) 337–347.
[236] A. Bigi, B. Bracci, F. Cuisinier, R. Elkaim, M. Fini, I. Mayer, I.N. Mihailescu, G. Socol, L. Sturba, P. Torricelli, Biomaterials 26 (2005) 2381–2389.
[237] G. Socol, P. Torricelli, B. Bracci, M. Iliescu, F. Miroiu, A. Bigi, J. Werckmann, I.N. Mihailescu, Biomaterials 25 (2004) 2539–2545.
[238] C.K. Wang, J.H. Chern Lin, C.P. Ju, H.C. Ong, R.P.H. Chang, Biomaterials 18 (1997) 1331–1338.
[239] Rajiv K. Singh, F. Qian, V. Nagabusham, R. Damodaran, B.M. Moudgil, Biomaterials 15 (1994) 522–528.
[240] S. Hontsu, T. Matsumoto, J. Ishii, M. Nakamori, H. Tabata, T. Kawai, Thin Solid Films 295 (1997) 214–217.
[241] J.M. Fernández-Pradas, G. Sardin, L. Clèries, P. Serra, C. Ferrater, J.L. Morenza, Thin Solid Films 317 (1998) 393–396.
[242] V. Nelea, C. Morosanu, M. Iliescu, I.N. Mihailescu, Applied Surface Science 228 (2004) 346–356.
[243] Haitong Zeng, William R. Lacefield, Sergey Mirov, Journal of Biomedical Materials Research 50 (2000) 248–258.

[244] L. Torrisi, R. Setola, Thin Solid Films 227 (1993) 32–36.
[245] Valentin Craciun, Ian W. Boyd, Doina Craciun, Pascal Andreazza, Jacques Perriere, Journal of Applied Physics 85 (1999) 8410–8414.
[246] J.L. Arias, F.J. García-Sanz, M.B. Mayor, S. Chiussi, J. Pou, B. León, M. Pérez-Amor, Biomaterials 19 (1998) 883–888.
[247] B. Mayor, J. Arias, S. Chiussi, F. Garcia, J. Pou, B. León Fong, M. Pérez-Amor, Thin Solid Films 317 (1998) 363–366.
[248] V. Nelea, H. Pelletier, M. Iliescu, J. Werckmann, V. Craciun, I.N. Mihailescu, C. Ristoscu, C. Ghica, Journal of Materials Science: Materials in Medicine 13 (2002) 1167–1173.
[249] H.X. Li, V.S. Rudnev, Z.H. Zheng, T.P. Yarovaya, R.G. Song, Journal of Alloys and Compounds 462 (2008) 99–102.
[250] K. Prasad Rao, G.D. Janaki Ram, B.E. Stucker, Scripta Materialia 58 (2008) 998–1001.
[251] A.L. Yerokhin, X. Nie, A. Leyland, A. Matthews, Surface and Coatings Technology 130 (2000) 195–206.
[252] Fu Liu, Ying Song, Fuping Wang, Tadao Shimizu, Kaoru Igarashi, Liancheng Zhao, Journal of Bioscience and Engineering 100 (2005) 100–104.
[253] Won-Hoon Song, Youn-Ki Jun, Yong Han, Seong-Hyeon Hong, Biomaterials 25 (2004) 3341–3349.
[254] Jifeng Sun, Yong Han, Xin Huang, Surface and Coatings Technology 201 (2007) 5655–5658.
[255] Daqing Wei, Yu Zhou, Yaming Wang, Dechang Jia, Applied Surface Science 253 (2007) 5045–5050.
[256] Huang Yong, Wang Yingjun, Ning Chengyun, Nan Kaihui, Han Yong, Rare Metals 27 (2008) 257–260.
[257] Yong Han, Jifeng Sun, Xin Huang, Electrochemistry Communications 10 (2008) 510–513.
[258] Y. Han, S.H. Hong, K. Xu, Surface and Coatings Technology 168 (2003) 249–258.
[259] D. Wei, Y. Zhou, Applied Surface Science 255 (2009) 6232–6239.
[260] S. Swann, Physics Technology 19 (1988) 67–75.
[261] R.D. Arnell, P.J. Kelly, Surface and Coatings Technology 112 (1999) 170–176.
[262] E.S. Thian, J. Huang, S.M. Best, Z.H. Barber, W. Bonfield, Biomaterials 26 (2005) 2947–2956.
[263] V. Nelea, C. Morosanu, M. Iliescu, I.N. Mihailescu, Surface and Coatings Technology 173 (2003) 315–322.
[264] J.D. Long, S. Xu, J.W. Cai, N. Jiang, J.H. Lu, K.N. Ostrikov, C.H. Diong, Materials Science and Engineering C 20 (2002) 175–180.
[265] K. van Dijk, H.G. Schaeken, J.G.C. Wolke, J.A. Jansen, Biomaterials 17 (1996) 405–410.
[266] J.G.C. Wolke, K. de Groot, J.A. Jansen, Journal of Biomedical Materials Research 39 (1998) 524–530.
[267] J.G.C. Wolke, J.P.C.M. van der Waerden, H.G. Schaeken, J.A. Jansen, Biomaterials 24 (2003) 2623–2629.
[268] B. Feddes, J.G.C. Wolke, J.A. Jansen, A.M. Vredenberg, Journal of Applied Physics 93 (2003) 662–670.
[269] J.G.C. Wolke, J.P.C.M. van der Waerden, K. de Groot, J.A. Jansen, Biomaterials 18 (1997) 483–488.
[270] Shinn-Jyh Ding, Biomaterials 24 (2003) 4233–4238.
[271] D. Ganguli, Bulletin of Materials Science 16 (1993) 523–531.
[272] C.J. Brinker, G.W. Scherer, Sol–gel science: the physics and chemistry of sol–gel processing, Academic Press, San Diego, USA, 1990.
[273] H.Q. Nguyen, D.A. Deporter, R.M. Pilliar, N. Valiquette, R. Yakubovich, Biomaterials 25 (2004) 865–876.
[274] Long-Hao Li, Hae-Won Kim, Su-Hee Lee, Young-Min Kong, Hyoun-Ee Kim, Journal of Biomedical Materials Research 73A (2005) 48–54.
[275] M. Metikoš-Huković, E. Tkalčec, A. Kwokal, J. Piljac, Surface and Coatings Technology 165 (2003) 40–50.
[276] D.B. Haddow, P.F. James, R. Van Noort, Journal of Sol-Gel Science and Technology 13 (1998) 261–265.
[277] Laurent-Dominique Piveteau, Beat Gasser, Louis Schlapbach, Biomaterials 21 (2000) 2193–2201.
[278] E. Tkalcec, M. Sauer, R. Nonninger, H. Schmidt, Journal of Materials Science 36 (2001) 5253–5263.
[279] Dieter Bäuerle, Laser Processing and Chemistry, 3rd ed., Springer, 2000.
[280] F. John, Ready Industrial Applications of Lasers, 2nd ed., 1997.
[281] M. Bass, Laser Materials Processing, vol. 3, 1983.
[282] S.P. Harimkar, N.B. Dahotre, Laser Fabrication and Machining of Materials, 1st ed., 2007.
[283] Schuocker Dieter, High Power Lasers in Production Engineering, 1st ed., Imperial College Press, 1999.
[284] S.R. Paital, Balani Kantesh, Agarwal Arvind, N.B. Dahotre, Biomedical Materials 4 (2009) 1–10.
[285] S.R. Paital, N.B. Dahotre, Materials Science and Technology 24 (2008) 1144–1161.
[286] Tohru Hayakawa, Masao Yoshinari, Hideo Kiba, Hirotsugu Yomamoto, Kimiya Nemoto, John A. Jansen, Biomaterials 23 (2002) 1025–1031.
[287] M. Yoshinari, Y. Oda, T. Inoue, K. Matsuzaka, M. Shimono, Biomaterials 23 (2002) 2879–2885.
[288] J.L. Ong, K. Bessho, R. Cavin, D.L. Carnes, Journal of Biomedical Materials Research 59 (2002) 184–190.
[289] Limin Sun, Christopher C. Berndt, Karlis A. Gross, Ahmet Kuck, Journal of Biomedical Materials Research 58 (2001) 570–592.
[290] J.E.G. Hulshoff, K. Van Dijk, J.P.C.M. Van Der Waerden, W. Kalk, J.A. Jansen, Journal of Materials Science: Materials in Medicine 7 (1996) 603–609.
[291] H. Caulier, J.P.C.M. van der Waerden, J.G.C. Wolke, W. Walk, I. Naert, J.A. Jansen, Journal of Biomedical Materials Research 35 (1997) 19–30.
[292] H. Caulier, T. Hayakawa, I. Naert, J.P.C.M. Van Der Waerden, J.G.C. Wolke, J.A. Jansen, Journal of Materials Science: Materials in Medicine 8 (1997) 531–536.
[293] Jae-Young Rho, Liisa Kuhn-Spearing, Peter Zioupos, Medical Engineering and Physics 20 (1998) 92–102.
[294] A. Lasagni, C. Holzapfel, T. Weirich, F. Mucklich, Applied Surface Science 253 (2007) 8070–8074.
[295] Andres Lasagni, Mohammadreza Nejati, Rolf Clasen, Frank Mucklich, Advanced Engineering Materials 8 (2006) 580–584.
[296] C. Daniel, F. Mucklich, Z. Liu, Applied Surface Science 208-209 (2003) 317–321.
[297] P.G. Engleman, A. Kurella, A. Samant, C.A. Blue, N.B. Dahotre, Journal of Minerals Metals and Materials Society 57 (2005) 46–50.
[298] Claus Daniel, T. John Balk, Thomas Wubben, Frank Mucklich, Advanced Engineering Materials 7 (2005) 823–826.
[299] Jui Chakraborty, Mithlesh K. Sonha, Debrata Basu, Journal of American Ceramic Society 90 (2007) 1258–1261.
[300] D. Becker, U. Geifsler, U. Hempel, S. Bierbaum, D. Scharnweber, H. Worch, K.-W. Wenzel, Journal of Biomedical Materials Research 59 (2002) 516–527.
[301] H.B. Wen, J.R. de Wijn, C.A. van Blitterswijk, K. de Groot, Journal of Biomedical Materials Research 46 (1999) 245–252.
[302] Y. Liu, E.B. Hunziker, N.X. Randall, K. de Groot, P. Layrolle, Biomaterials 24 (2003) 65–70.
[303] Corinne R. Wittmer, Jennifer A. Phelps, W Mark Saltzman, Van Tassel S Paul R., Biomaterials 28 (2007) 851–860.
[304] Dominique##P. Pioletti, Olivier Gauthier, Vincent A. Stadelmann, Bruno Bujoli, Jérôme Guicheux, Pierre-Yves Zambelli, Jean-Michel Bouler, Current Drug Delivery 5 (2008) 59–63.
[305] S. Radin, J.T. Campbell, P. Ducheyne, J.M. Cuckler, Biomaterials 18 (1997) 777–782.
[306] H. Gautier, G. Daculsi, C. Merle, Biomaterials 22 (2001) 2481–2487.
[307] L. Obadia, G. Amador, G. Daculsi, J.-M. Bouler, Biomaterials 24 (2003) 1265–1270.
[308] Kuen Yong Lee, Martin C. Peters, Kenneth W. Anderson, David J. Mooney, Nature 408 (2000) 998–1000.

Review of laser based biomimetic and bioactive Ca–P coatings

S. R. Paital and N. B. Dahotre*

Human bone is typically a hierarchical organisation at different length scales ranging from nanoscale to mesoscale. Synthetic biomaterials mimicking this structural aspect of the bone and thereby facilitating structure and function of damaged or dysfunctional tissues is the current trend in designing of biomaterials. Under such trend artificial biomaterials with biocompatible surface coatings and engineered three-dimensional features ranging from nanoscale to mesosclae to support cells and tissue growth is becoming a reality. In light of this, the present review provides a description of laser induced coating techniques, one of several methods of design and synthesis of biosurfaces. Especially, the laser induced coating technique to produce a bioactive and biomimetic calcium phosphate (Ca–P) based ceramic coating on Ti based alloys is the focus of present discussion. The two common coating methodologies namely, the pulsed laser deposition and direct melting using a pulsed and continuous wave laser are the subject of discussion. The formation of multiscale features, microstructures and phase evolution due to such coatings are discussed. Finally, the concept of laser based interference patterning as a future tool to explore these kinds of coatings is highlighted. Attempts are also made to demonstrate the effectiveness of these coatings in bioenvironment.

Keywords: Laser processing, Calcium phosphate, Ceramic coating, Titanium alloys

Published by Maney Publishing (c) IOM Communications Ltd

Introduction

Surfaces and interfaces for biomedical applications

Biomaterials are synthetic materials intended to replace part of a human body or function appropriately in contact with a living tissue. The three most important factors that can dictate the success of a biomaterial are type of material, design and biocompatibility. The four major different classes of materials used as biomaterials include polymers, metals, ceramics and natural materials. The design of biomaterials and devices are intended to have the appropriate mechanical properties, durability, functionality and biological response. Mechanical properties, durability and functionality are governed by the bulk properties of the material whereas biological response depends on the surface chemistry and structure. Biocompatibility is regarded as the acceptance of the implant material by the surrounding tissues. However, biocompatibility is application specific as a material may be biocompatible for one kind application but may not be for other. Some of the important applications of biomaterials include:

(i) replacement of a diseased or damaged part
(ii) assisting in healing
(iii) improving function
(iv) correcting functional abnormalities
(v) correcting cosmetic problem
(vi) aiding towards diagnosis
(vii) aiding towards treatment.[1]

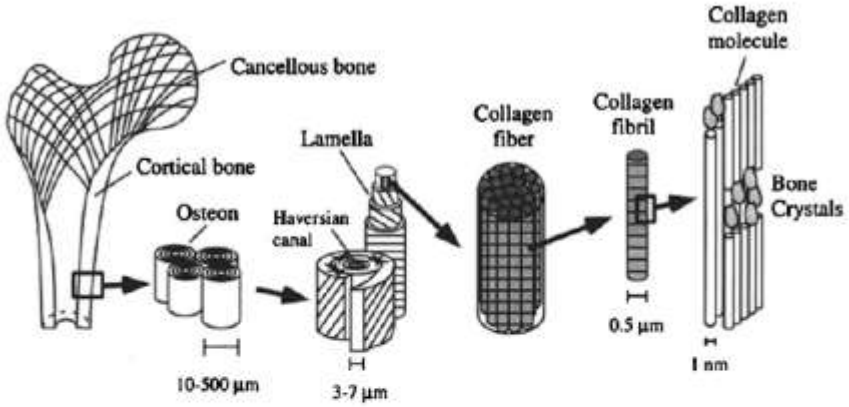
The types of biomaterials devices currently available in the market include replacement heart valve prosthesis, dental implants, hip/knee implants, catheters, pacemakers, oxygenators and vascular grafts.

The various phenomena that occur at the interface after the implantation of a biomaterial into a living system are sequential.[2] Initially the proteins respond to the implant surface and within a few seconds to minutes a monolayer of protein film is adsorbed to the surface. Since cells respond to the proteins this protein film controls the subsequent bioreaction with the implants. These cells then multiply and organise into complex tissues such as bone. Human bone is basically a hierarchical organisation at different length scales ranging from nanoscale to mesoscale.[3] A schematic representation of such an organisation is illustrated in Fig. 1.[4] A compact human bone essentially consists of 20 wt-% collagen, 69 wt-% calcium phosphate, 9 wt-% water and the rest as organic materials such as proteins, polysaccharides and lipids.[2] Collagen filaments array are considered to be at the first level in the hierarchy. These long fibrous structural proteins are $\sim$1 nm in diameter. Calcium phosphates in the form of hydroxyapatite crystals are deposited parallel to the collagen filaments so that the larger dimension of the crystal is along the

Department of Materials Science and Engineering, University of Tennessee, Knoxville, TN 37996, USA

*Corresponding author, email ndahotre@utk.edu

© 2008 Institute of Materials, Minerals and Mining
Published by Maney on behalf of the Institute
Received 25 January 2008; accepted 18 February 2008
DOI 10.1179/174328408X341825



1 Schematic of hierarchical organisation of bone at different length scales (Reprinted from ref. 4 with permission from Elsevier)

Published by Maney Publishing (c) IOM Communications Ltd

long axis of the fibre. These collagen fibrils in turn get organised into a sheet or woven texture. Bone cells such as osteocytes resides between these several sheet like parallel arrays (lamellar bone) or are concentrically arranged into a cylindrical structure known as the osteon. These osteons are grouped together into long bundles known as harvesian bone which becomes the basic building block of bone microstructure. Finally at the macroscopic level each bone is made up of a strong calcified outer compact layer.[4] Therefore the use of artificial biomaterial to mimic these properties of bone is becoming a reality.

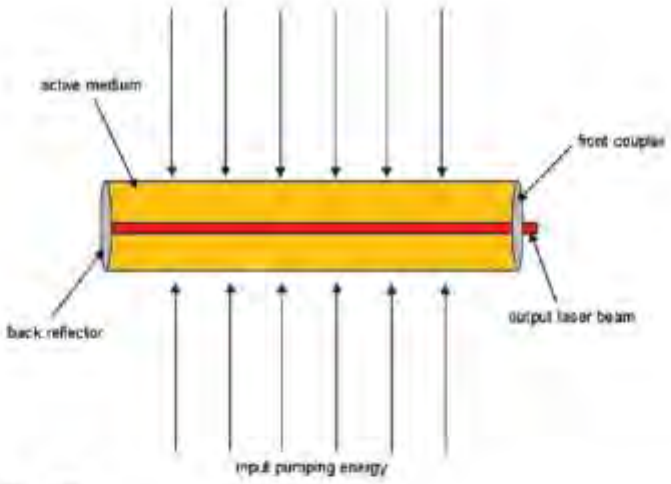
Cells being sensitive to features ranging from nanoscale to microscale, fabrication of three-dimensional (3D) topographies and nanoscale engineering at the implant surface are the current approaches in biomimetics.[4–11] These 3D features are expected to mimic the naturally occurring nanoscale structure of extra cellular matrix (ECM) in the body and thereby support cells and provide an instructive background towards tissue growth. These 3D features, surface irregularities or surface microtexture can be in the form of grooves, hills, pores and pillars. Some of the most commonly used methods to achieve this kind of patterned surfaces are photolithographic technique, deep reactive ion etching, microcontact printing, lithographic, galvanoformung, abformung (LIGA) and scratching.

Apart from this physical modification of the surfaces, biocompatibility and biological responses also strongly depend on the surface chemistry. The surface chemistry can be altered by providing engineered biocoatings such as alumina, zirconia, bioactive glasses (glass ceramics) and calcium phosphate based (Ca–P) ceramics on Ti based alloys. Alumina and zirconia are considered as boinert as they do not induce the formation of a fibrous tissue at the interface and show direct contact with the surrounding tissue. Bioactive glasses and Ca–P based ceramics are considered as bioactive as they form a direct chemical bond with the bone. Ca–P based ceramics are widely used as a bioactive coating as it possess similarity with the mineral phase hydroxyapatite present in the human bone and teeth.[12] Ca–P based ceramics often occur in the nature as geological minerals.[13] The chemical name, mineral name and the composition of various Ca–P based ceramics are summarised in Table 1.[13] Hydroxyapatite (HA) is the most extensively used synthetic Ca–P ceramic for bone graft purposes as it is chemically and crystallographically similar to biological apatite. These kinds of coatings on Ti based alloys for hip joint prosthesis and dental implants are proved to be bioactive and osteoconductive.

In the present paper, the discussion is only confined to Ca–P based bioactive coatings. Various coating methodologies such as ion beam assisted deposition,[14] plasma spray deposition,[15–21] pulsed laser physical vapour deposition,[22–26] magnetron sputtering,[27] sol–gel based coatings,[28,29] electrodeposition[30] and laser induced coatings[31] have been explored for fabrication and synthesis of biocoatings. Among these various techniques, plasma spray coating is the most commercially used method for orthopedics and dental applications. However, it suffers

Table 1 Chemical name, mineral name and composition of various Ca–P based ceramics[13](Adopted from ref. 13 with permission from Institute of Mechanical Engineers (I. MechE))

Ca–P	Formula	Name/mineral	Abbreviation
0·5	$Ca(H_2PO_4)_2.H_2O$	Monocalcium phosphate monohydrate	MCPM
1·0	$CaHPO_4.2H_2O$	Hydrated calcium phosphate/brushite	DCP
1·0	$CaHPO_4$	Anhydrous calcium phosphate/monetite	ADCP
1·33	$Ca_8H_2(PO_4)_6.5H_2O$	Octacalcium phosphate	OCP
1·5	$Ca_3(PO_4)_2$	Tricalcium phosphate/whitlockite	TCP
1·67	$Ca_{10}(PO_4)_6F_2$	Flourapatite	FA
1·67	$Ca_{10}(PO_4)_6(OH)_2$	Hydroxyapatite	HA
2·0	$CaO.Ca_3(PO_4)_2$	Tetracalcium phosphate/hilgenstockite	TTCP



2 Shematic of a laser design

from certain drawbacks such as poor adherence of the coating to the substrate and nonuniformity in morphology and crystallinity.[32] Therefore, in the present paper, an overview of one of the highly promising techniques, laser based Ca–P coating on Ti based alloys for hard tissue replacements is considered.

Materials processing by lasers is enchanting the attention of scientists, engineers and manufacturers world wide due to the following fundamental reasons:[33–35]

(i) the high spatial coherence and directionality of the laser beam permits extreme focusing and directional irradiation at high intensities
(ii) monochromaticity of the laser beam allows for a controlled depth of heat treatment without affecting the properties of bulk
(iii) laser light is considered as a sterile tool as there is no direct contact with the material being processed, and, therefore, can be effectively used for medical and biological applications
(iv) laser beams can also be used to travel at greater speeds making them ideal for industrial production lines
(v) unlike other particle beam technologies such as ion beam and electron beam lasers are not necessarily required to be operated in a vacuum.

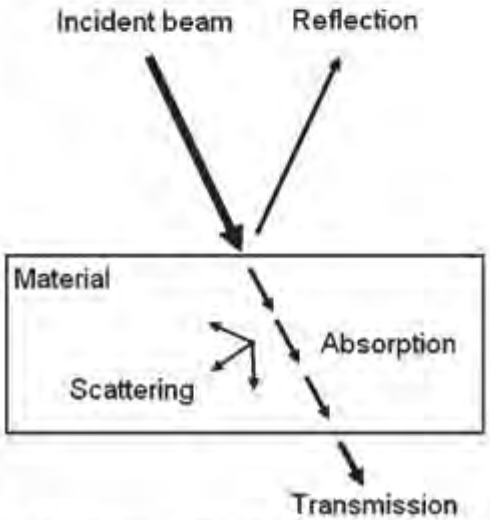
Laser light and laser material interaction

The purpose of this section is to give the readers a basic knowledge regarding mechanism of laser light production, the basic design of a laser and various parameters associated with laser materials processing. The production of laser light is based on three basic mechanisms:

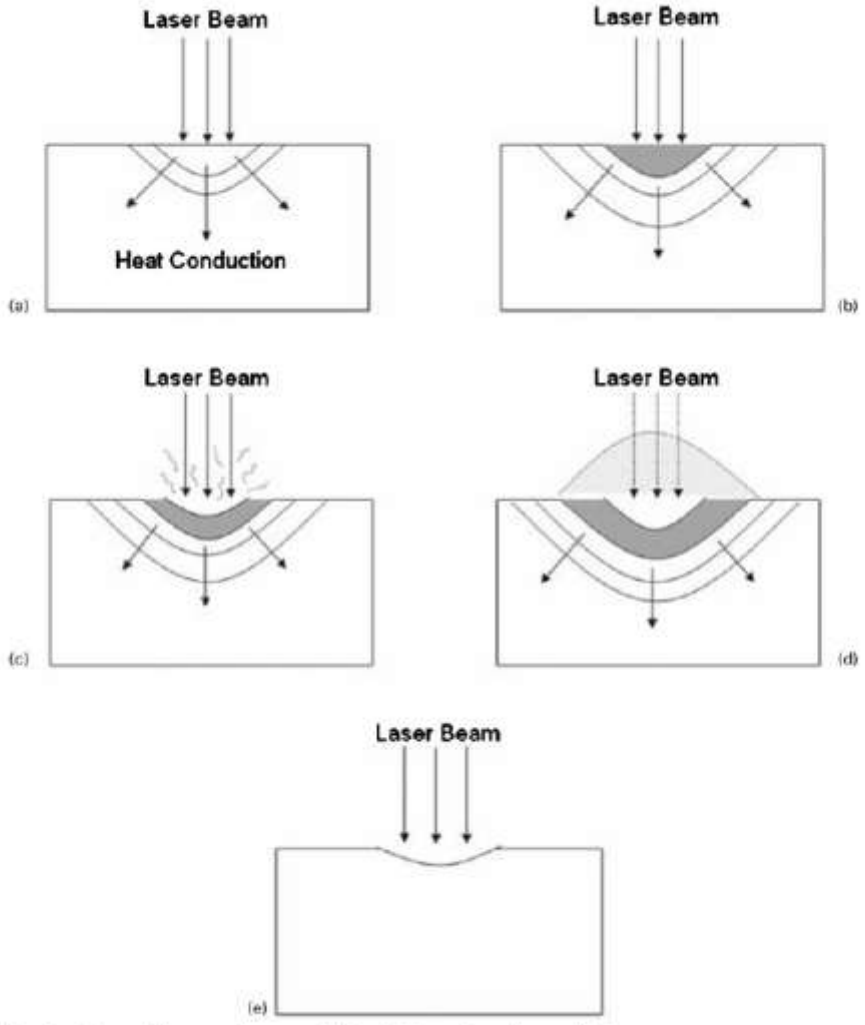
(i) absorption
(ii) spontaneous emission
(iii) stimulated emission.[35–38]

The two essential components of a laser device are an active medium and an optical resonator. The active medium produces the optical gain or the population inversion under proper pumping conditions and the optical resonator consists of a pair of mirrors with specific radii of curvature and reflectivities to provide optical feedback and thereby a amplified output beam. The pumping can be carried out by various mechanisms such as gas discharge, optical pumping or electrical current. A schematic of such a process is shown in Fig. 2. The various laser parameters associated with laser materials processing can be classified as average power, wavelength of the laser beam, beam size, laser peak power, pulse width and its mode structure.

When the electromagnetic radiation of a laser beam interacts with the surface of a material the various phenomena that takes place are reflection, refraction, absorption, scattering and transmission. The schematic representation of such a process is illustrated in Fig. 3.[39] The most desirable phenomena for laser material processing are absorption of the radiation by the material.

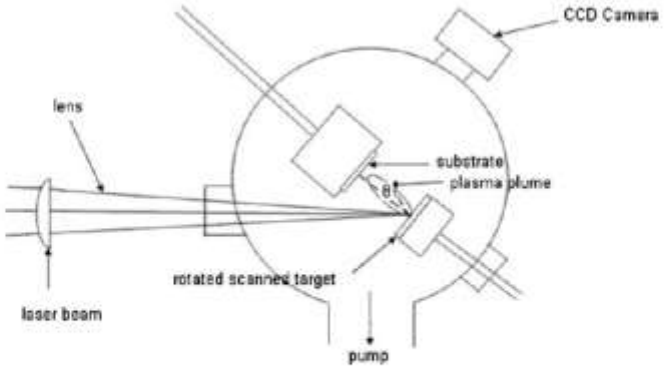


3 Schematic of Laser Material Interaction (Reprinted from ref. 8 with permission from Springer)

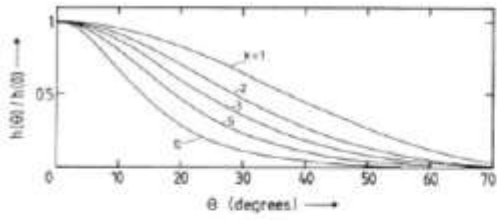


a heating; *b* surface melting; *c* surface vaporisation; *d* plasma formation; *e* ablation

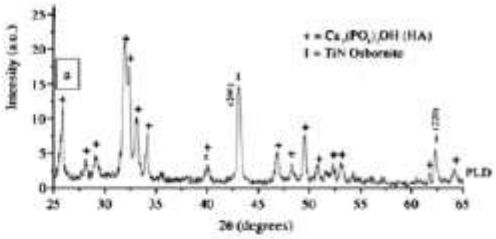
4 Various effects of laser material interaction (Reprinted from ref. 38 with permission from Springer)



5 Schematic of a PLD setup



6 Variation in film thickness profiles at varying radial angles (Reprinted from ref. 41 with permission from American Physical Society (APS))



8 Grazing Incidence angle X-ray Diffraction (GIXRD) of the deposited film (Reprinted from ref. 42 with permission from Springer)

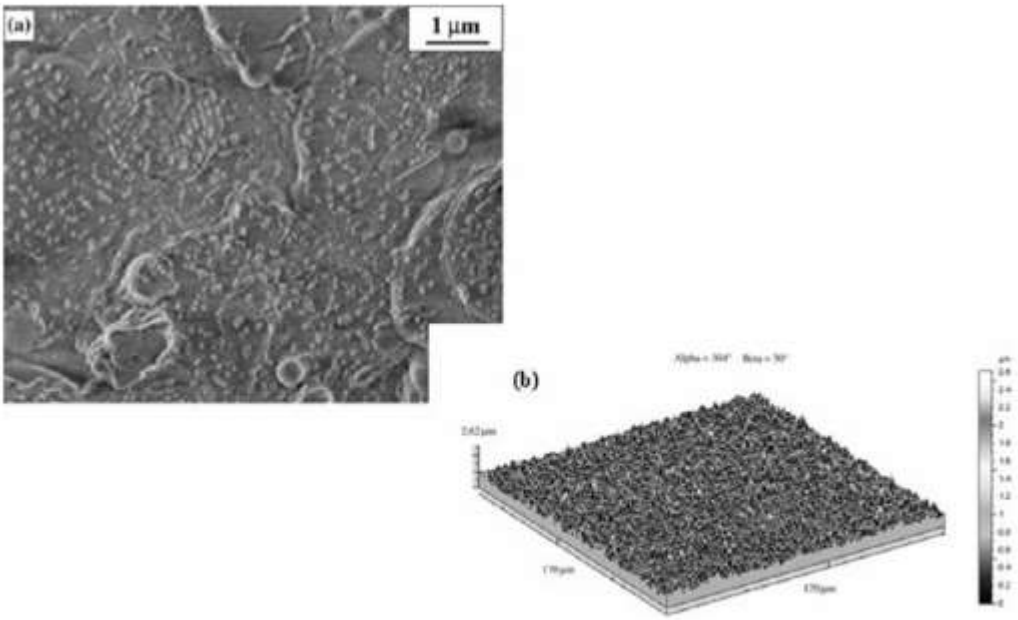
Absorption of the laser beam by the material results in various effects such as heating, melting, vaporisation and plasma formation.[38] The schematic representation of such effects is illustrated in Fig. 4.[38] These effects depend on the laser parameters listed above and the thermophysical properties of the material. Heating a material surface needs high interaction time and intensity of $\sim 10^2$ to 10^3 W cm^{-2}. This is useful for applications such as transformation hardening. For applications such as joining, glazing, cladding, alloying, coating, etc. surface melting is required which can be achieved at intensities of approximately 10^4 to 10^8 W cm^{-2}. In laser machining (drilling, cutting, trimming) and laser vapour deposition technique the material has to be removed from the workpiece as liquid, vapour or plasma. Therefore these need very high laser intensities in the range of 10^{10} to 10^{12} W cm^{-2} in a very short interaction time. As the laser intensities required in these processes are different, the physical phenomena behind their effects are distinctively different. These physical phenomena remain the basis for selection of laser processing parameters during various techniques employed in the coating. The details of such phenomena and governing equations are provided in the following sections on various laser based coating methods.

Appropriate selection of laser parameters and lasers can be, therefore, employed to simultaneously achieve both a bioactive and textured coating. The bioactivity may aid towards protein signalling and the physical texturing may help in differentiation, proliferation, and migration of the cells by responding to the signals from the proteins. Further this textured topography induces minimum stress on the surrounding bone and anchors it firmly. This therefore helps in osseointegration, regeneration, formation and function of the damaged hard tissue such as bone.

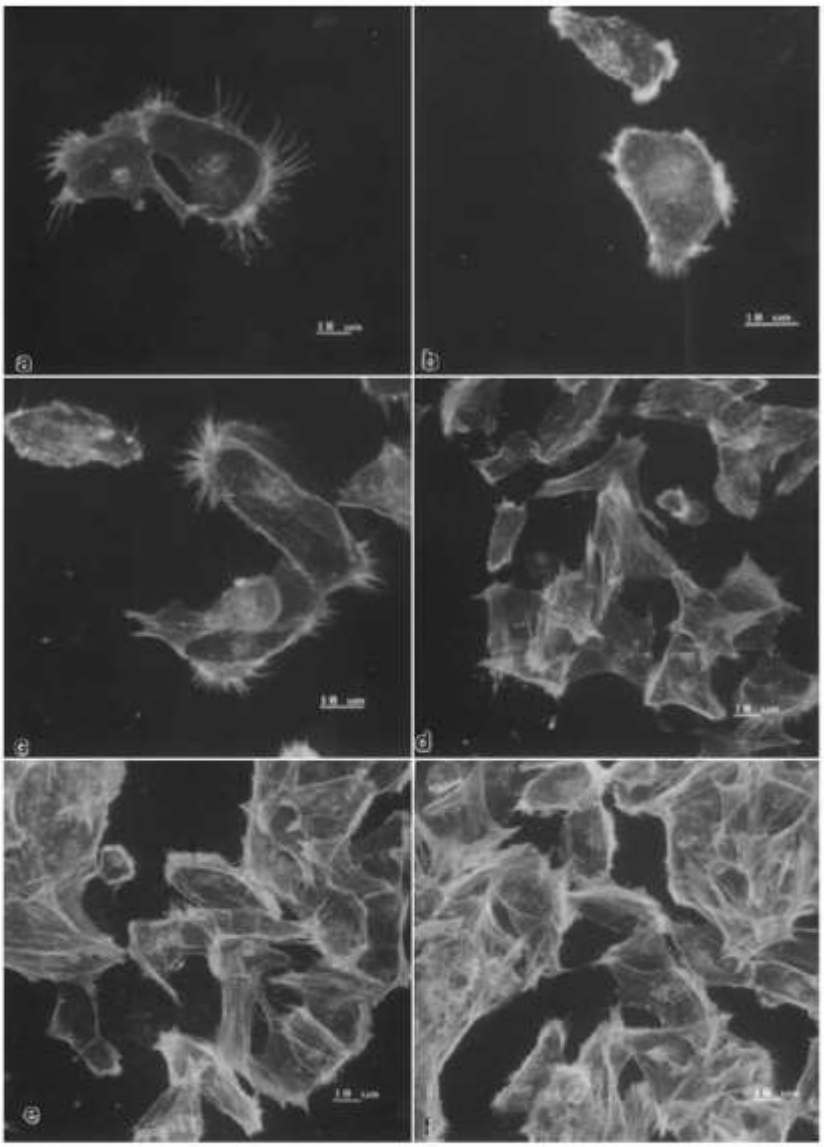
Laser coating of Ca–P

Pulsed laser deposition of thin film

The high intensity of a laser beam can be used to ablate the target material and condense it on the surface of the substrate in the form of a thin film. Thin film formation



7 SEM micrograph of *a* HA film grown by PLD technique and *b* surface topography of this deposited film obtained using white light confocal microscopy (Reprinted from ref. 42 with permission from Springer)



a 3 J cm^{-2}; *b* 6 J cm^{-2}; *c* 9 J cm^{-2}; *d* 3 J cm^{-2} annealed; *e* 6 J cm^{-2} annealed; *f* 9 J cm^{-2} annealed

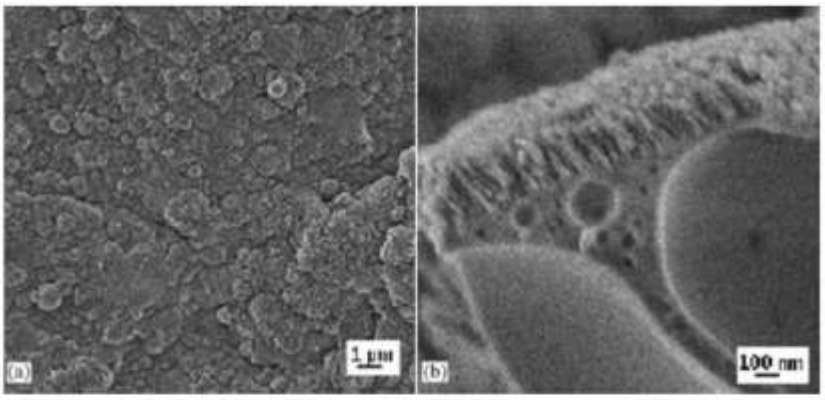
9 Confocal laser scanning microscopy images of cells attached on HA films deposited on Ti foils using pulsed laser at various laser processing conditions (Reprinted from ref. 25 with permission from Elsevier)

by pulsed laser ablation is termed as pulsed laser deposition (PLD). Pulsed laser deposition can also be used to fabricate multicomponent stoichiometric films from a single target.[33] The short duration of the pulses and non-equilibrium processing conditions in PLD has some unique advantages:[33,39,40]

(i) it can be used to synthesise metastable materials which is difficult to be obtained by any standard techniques
(ii) films can also be formed from the species generated during pulsed laser ablation. The physical properties of such films are considered to be superior to conventional evaporation or electron beam evaporation
(iii) nanocrystalline films can also be fabricated
(iv) fabrication of composite films consisting of different materials can also be obtained.

A typical setup for thin film deposition by PLD is schematically shown in Fig. 5. It essentially consists of a laser source, reaction chamber, a target and substrate. The pulsed laser deposition process can be classified into three separate regimes:

Published by Maney Publishing (c) IOM Communications Ltd



a droplet like feature at surface of coating; *b* morphologically homogeneous and brush like layer at inner structure

10 SEM micrographs of octacalcium phosphate $Ca_8H_2(PO_4)_6.5H_2O$ (OCP) thin films on Ti substrate deposited by PLD technique using UV KrF laser source operating at wavelength of 248 nm (Reprinted from ref. 43 with permission from Elsevier)

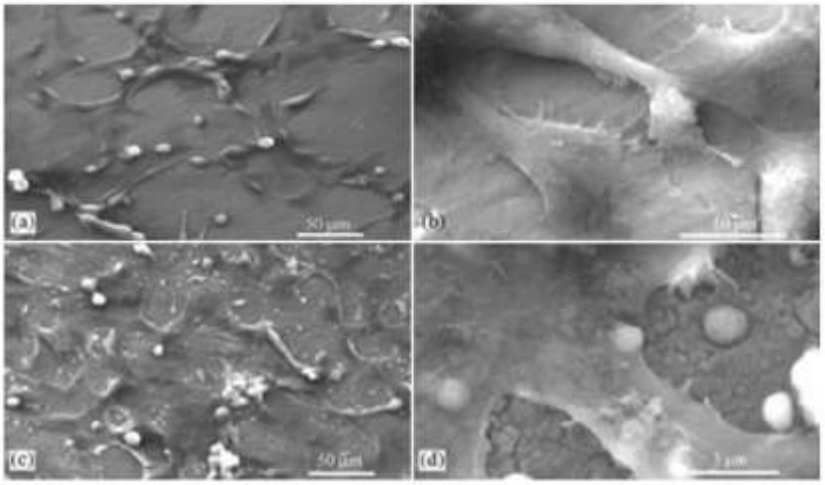
Published by Maney Publishing (c) IOM Communications Ltd

(i) interaction of the laser beam with the bulk target
(ii) plasma formation, heating and 3D isothermal expansion of the plasma
(iii) adiabatic expansion and deposition of thin films.[40]

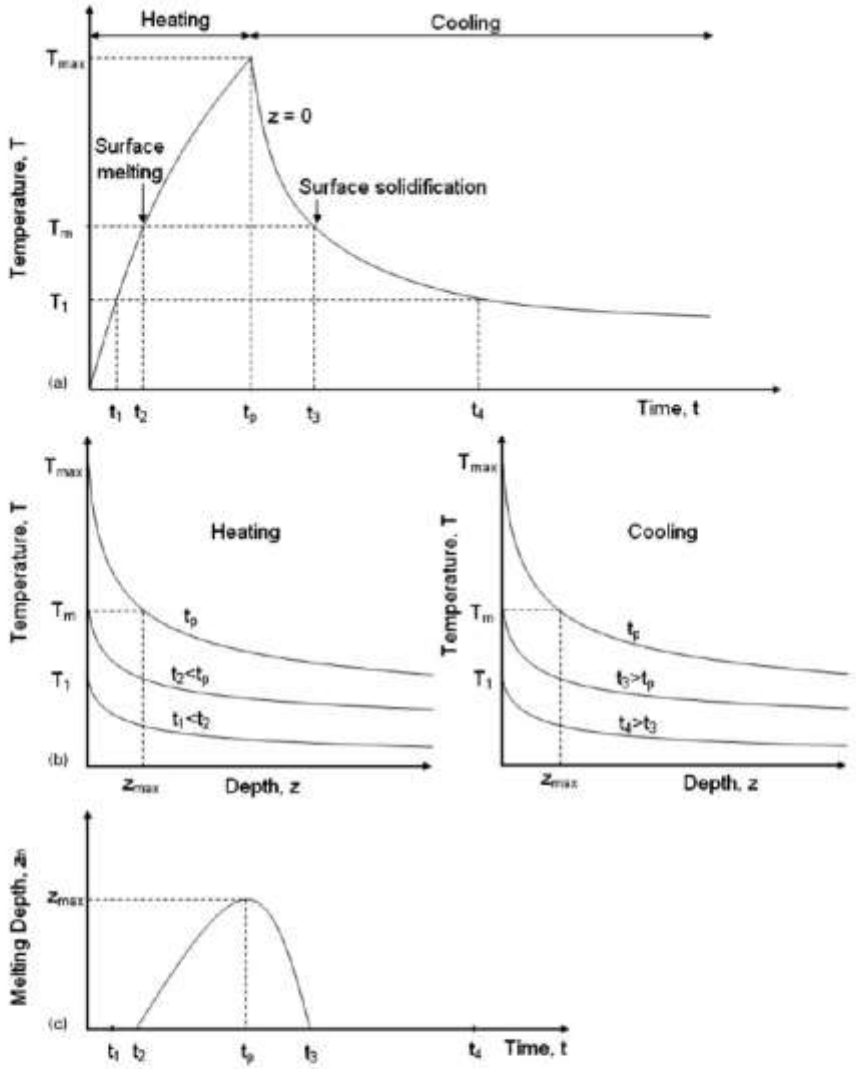
Ablation can take place either in a vacuum chamber or in an inert gas or reactive atmosphere. Typical range of laser fluences needed to generate a plasma plume is approximately in the order of 0·1–10 J cm^{-2}.[33] The distance between the target and the substrate should match the length of the plasma plume which is approximately 3–8 cm. Targets are either in the form of discs or cylinders. The uniformity in film thickness on the substrate can be obtained by moving the substrate relative to the plasma plume. Therefore, the dominant mechanism in PLD that is the formation of hot plasma depends on laser parameters such as energy density (fluence), pulse duration, wavelength, polarisation, pulse repetition rate and the material being irradiated.[40] Anisimov *et al.*[41] made theoretical calculation of the film thickness profiles obtained by PLD, assuming the adiabatic expansion of the plasma plume in vaccum. The film thickness profile is given by the following equation[41]

$$h(\theta)=\frac{Mk^2}{2\pi\rho_s z_s^2}\left(1+k^2\tan^2\theta\right)^{-3/2}$$

where k is a constant which varies with the pulse width of the laser beam, M is the mass of the plasma plume, z_s is the distance at which the substrate is placed with respect to the target and θ is the radial angle and ρ_s is the density of the substrate. The variation in film thickness profiles at varying θ is illustrated in Fig. 6.[41] For a spherical expansion of the plasma $h(\theta)$ can be expressed as[41]



11 Image (SEM) of fibroblasts and osteoblasts adhesion on bare Ti *a*, *b* and on OCP coating *c*, *d* (Reprinted from ref. 38 with permission from Elsevier)



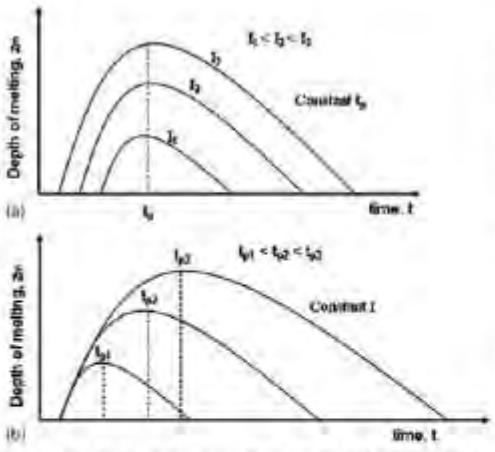
12 Temporal evolution and depth of melting for a continuous wave laser irradiation (Reprinted from ref. 38 with permission from Springer)

$$h(\theta)=\frac{M}{2\pi\rho_s r_s^2}\cos^3\theta$$

A knowledge of the film thickness profile can be used to estimate the kinetic energy of the moving species and thereby the temperature of the expanding plasma plume. This in turn may help us to predict the various phase transformations that may take place for a particular set of parameter employed for the deposition process. Also as the high energetic species bombard the substrate surface it may improve or deteriorate the overall morphology, stoichiometry and microstructure. A knowledge of the thickness profile may help us to predict the distance between the target and the substrate and thereby the energy of the impinging species. Also the initial substrate temperature strongly affects the nature of the film i.e. amorphous, polycrystalline, or single crystalline. For example, higher substrate temperatures in general favour a crystalline phase. Lasers mostly employed to achieve these kind of coatings are excimer lasers, Nd:YAG lasers and Nd:glass lasers.

Nelea *et al.*[42] deposited hydroxyapatite by the PLD technique using a KrF pulsed laser system. Thin films of HA were grown on Ti–5Al–2·5Fe substrate precoated with a buffer layer of TiN. The buffer layer was used to improve the adherence of the film to the substrate. Some of the advantages associated with the PLD were its ability to grow Ca–P coatings with different phases and composition based on the deposition parameters. Figure 7*a* represents the scanning electron micrograph (SEM) of the surface of the film grown by this method.[42] Figure 7*b* shows the surface topography of this film

Published by Maney Publishing (c) IOM Communications Ltd



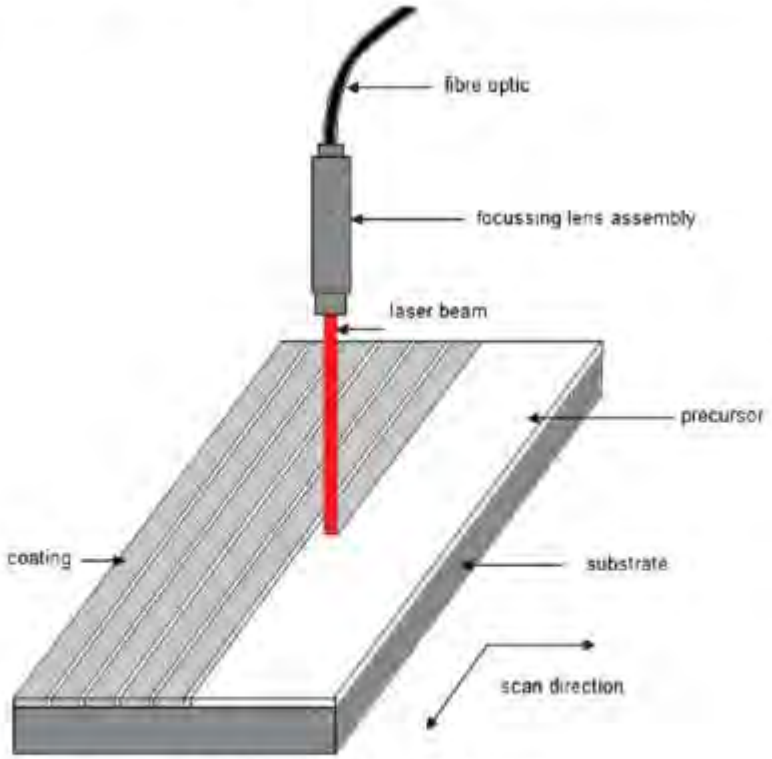
13 Effect of laser parameters such as pulse duration t_p and laser intensity I on the depth of melting (Reprinted from ref. 38 with permission from Springer)

obtained using white light confocal microscopy.[42] Both these images reveal a rough surface of the coating which may be good for adhering the osteoblast cells when exposed to body plasma and thereby provide osseointegration. Grazing incidence angle X-ray diffraction in Fig. 8 shows the characteristic diffraction peaks corresponding to HA phase.[42] This indicates the retention of the HA phase by this method. Ball *et al.*[25] cultured human osteoblast cells on thin films of HA coating on Ti foils obtained by PLD. The effect of crystallinity and laser fluence on cell attachment was studied. It was observed that cell attachment was enhanced with increasing laser fluence and increased crystallinity as represented in Fig. 9.[25]

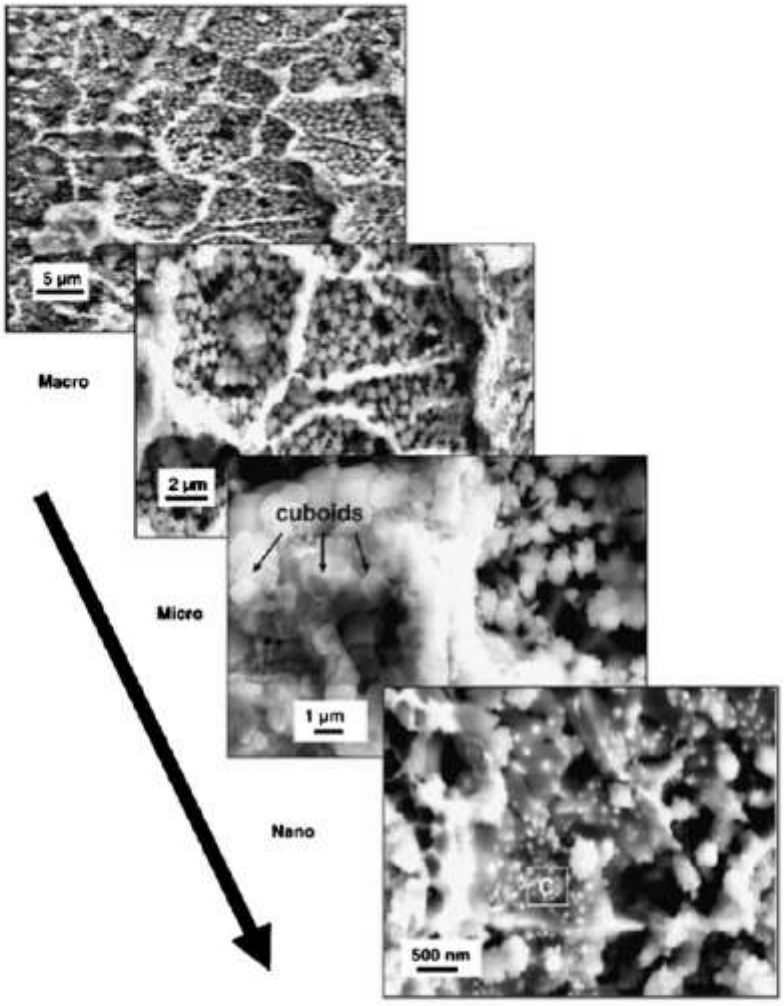
Socol *et al.*[43] deposited nanocrystalline octacalcium phosphate $Ca_8H_2(PO_4)_6.5H_2O$ (OCP) thin films on Ti substrate by PLD technique using a UV KrF laser source operating at a wavelength of 248 nm. OCP due to its structural resemblance to HA, its frequent occurrence in pathological and physiological calcifications and its ability to dissolve more quickly stimulate faster bone growth. Typical SEM images (Fig. 10*a* and *b*)[43] of films deposited by this technique on a Ti substrate heated at 150°C and post-deposition treatment at 150°C reveals a droplet like feature at the surface of the coating (Fig. 10*a*) and a morphologically homogeneous and brush like layer at the inner structure (Fig. 10*b*). *In vitro* tests of the coated samples proved very good adherence and proliferation of both fibroblast and osteoblast like cells as shown in Fig. 11.[43]

Coatings by direct laser melting using a continuous wave and pulsed laser

In a continuous wave (CW) laser, the output power of the laser beam is constant with time. During a continuous wave operation the beam is likely to produce



14 Schematic of a continuous wave Nd:YAG laser used for the coating process



15 Images (SEM) of hierarchical organisation of calcium phosphate tribasic coating on Ti alloy substrate obtained by laser melting using a continuous wave Nd:YAG system (Reprinted from ref. 31 with permission from Elsevier)

Published by Maney Publishing (c) IOM Communications Ltd

more uniform thermal conditions within the beam–substrate interaction region. On the contrary, a pulsed laser may have a short pulse length and high peak power at alternatively low average energy thereby producing a non-uniform thermal conditions within the interaction zone. Such distinctively different thermal conditions are expected to produce completely different physical and chemical effects in the interaction zone (coating). Some types of lasers can be operated both in the pulsed mode and continuous mode. CO_2 lasers are the most commonly used continuous wave lasers. Nd:YAG lasers can be obtained both in the pulsed mode and continuous mode.

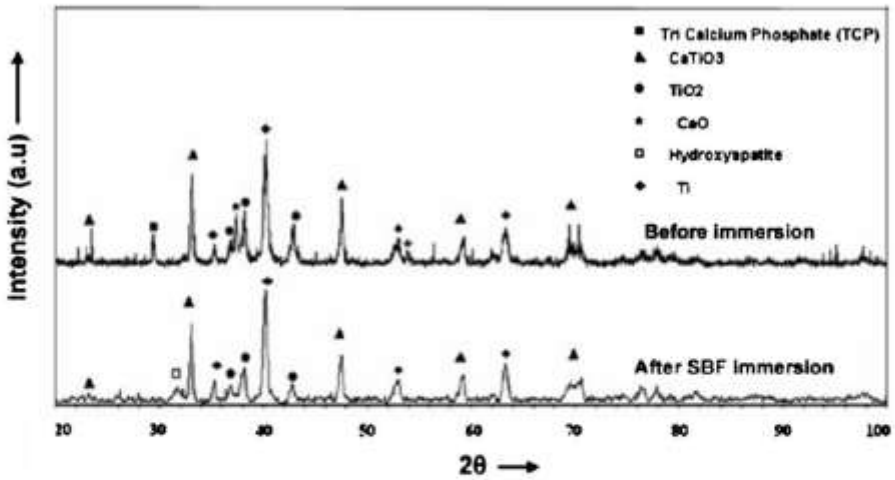
Continuous wave laser

The most desired phenomena for surface coatings by this technique is melting of the substrate and the precursor so that a strong bonding is achieved at the interface. The temporal and spatial variation of temperature distribution on material due to laser irradiation by a continuous wave system can be predicted by one dimensional heat conduction equations. The following assumptions were made for the thermal analysis:

(i) material is homogeneous and the thermophysical properties are independent of temperature
(ii) initial temperature of the material is constant and heat input is uniform during the irradiation time
(iii) convection and radiation losses from the surface are negligible.

The governing equation for the one dimensional heat transfer can be written as[38]

$$\frac{\partial T(z,t)}{\partial t} = \alpha \frac{\partial T^2(z,t)}{\partial z^2}$$



16 XRD diffraction patterns comparing the peaks obtained before and after immersion in SBF (Reprinted from ref. 31 with permission from Elsevier)

where T is the temperature at location z, after time t and α is the thermal diffusivity. Initial boundary conditions can be set as:

$T(z, 0)=T_0$, for $0 \leqslant z \leqslant \infty$, $t=0$, Here T_0 is the initial constant temperature of the material.

Assuming that at the surface ($z=0$) the laser energy absorbed is equal to the energy conducted then

$$-k\frac{\partial T(0,t)}{\partial z} = \delta H$$

where k is the thermal conductivity, and H the absorbed laser energy.

$$H = AI_0$$

where A is the absorptivity of the material and I_0 is the incident laser power density. If t_p is the pulse duration then:

$\delta=1$ for $0 \leqslant t \leqslant t_p$, and $\delta=0$ for $t \geqslant t_p$.

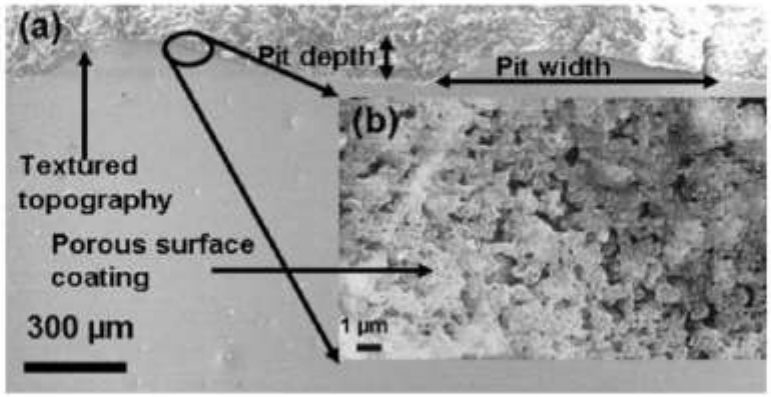
The variation of temperature along the depth (z) of the material during heating and cooling can be written as follows

during heating ($0<t<t_p$)

$$\Delta T(z,t)_{t>t_p} = \frac{H}{K}(4\alpha t)^{1/2}\,\mathrm{ierfc}\left[\frac{z}{(4\alpha t)^{1/2}}\right]$$

During cooling ($t>t_p$)

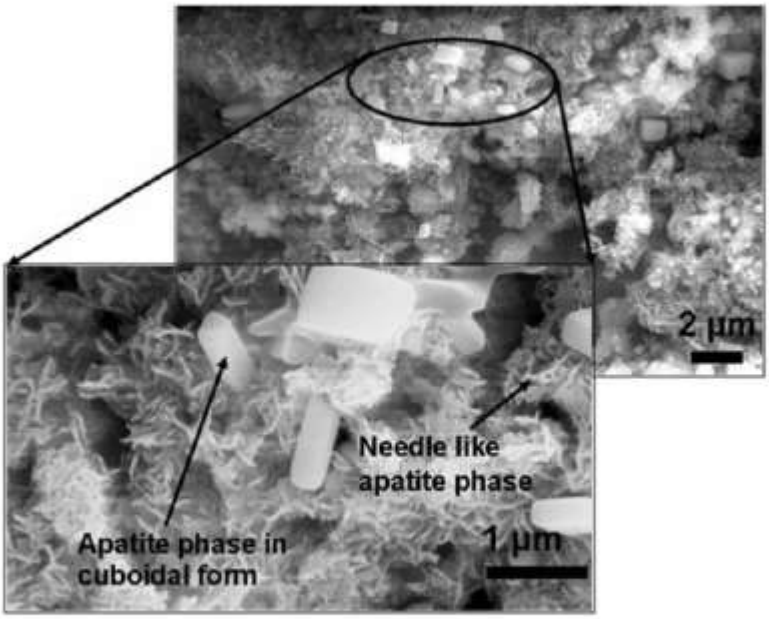
$$\Delta T(z,t)_{t>t_p} = \frac{2H\alpha^{1/2}}{k}\left\langle t^{1/2}\mathrm{ierfc}\left[\frac{z}{(4\alpha t)^{1/2}}\right] - (t-t_p)^{1/2}\,\mathrm{ierfc}\left\{\frac{z}{[4\alpha(t-t_p)]^{1/2}}\right\}\right\rangle$$



a textured topography in cross-sectioned sample; b inset revealing porous morphology of coating

17 SEM micrograph of calcium phosphate tribasic coating on Ti alloy substrate obtained using 2·5 kW Hobart Continuous wave Nd:YAG laser (Reprinted from ref. 45 with permission from Institute of Physics Publishing (IOP))

Published by Maney Publishing (c) IOM Communications Ltd



18 SEM micrograph of coated sample processed at 1006 J/cm^{-2} and after immersion in SBF for one day (Reprinted from ref. 45 with permission from Institute of Physics Publishing (IOP))

ierfc is defined as

$$\text{ierfc}(x)=\frac{1}{\pi^{1/2}}\{\exp(-x^2)-x[1-\text{erf}(x)]\}$$

and

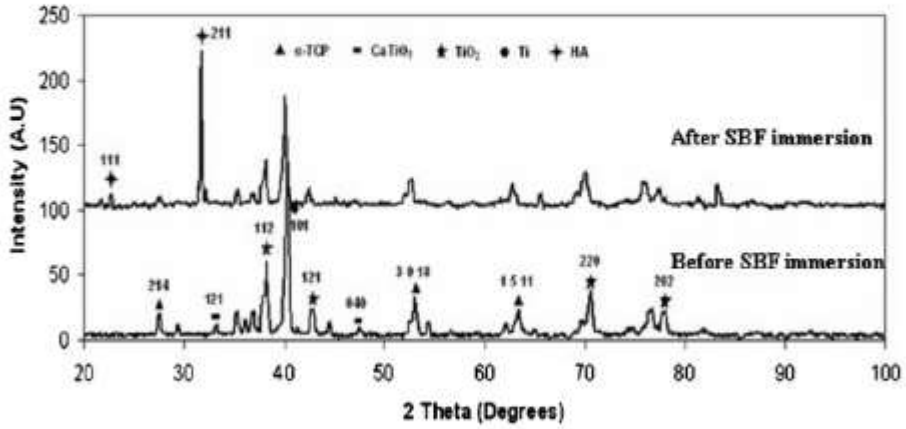
$$\text{erf}(x)=\frac{2}{\pi^{1/2}}\int_0^x e^{\xi^2}\text{d}\xi$$

The temperature at the surface during heating and cooling can be obtained by substituting $z=0$ in the above two equations. Therefore

$$\Delta T(0,t)_{t<t_p}=\frac{H}{k}\left(\frac{4\alpha t}{\pi}\right)^{1/2}$$

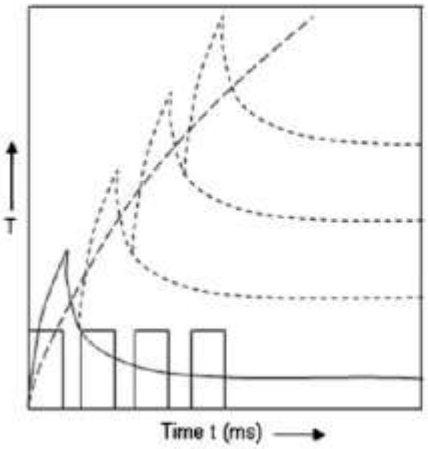
$$\Delta T(0,t)_{t>t_p}=\frac{H}{k}\left\{\left(\frac{4\alpha t}{\pi}\right)^{1/2}-\left[\frac{4\alpha(t-t_p)}{\pi}\right]^{1/2}\right\}$$

Figure 12 represents the temporal evolution and depth of melting for a continuous wave laser irradiation.[38] The effect of laser parameters such as pulse duration t_p and laser intensity I on the depth of melting can be schematically shown in Fig. 13.[38] The above information may be helpful in estimating the various phases that

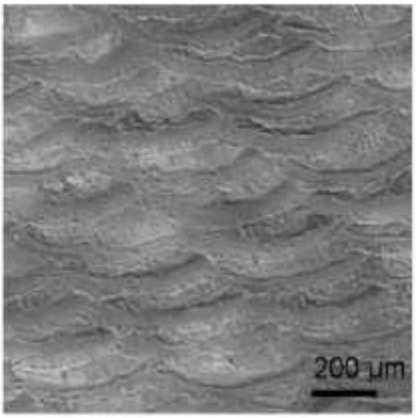


19 XRD patterns comparing phases evolved before and after immersion in SBF for 5 days

Published by Maney Publishing (c) IOM Communications Ltd



20 Temporal variation of the surface temperature with increasing rectangular pulses



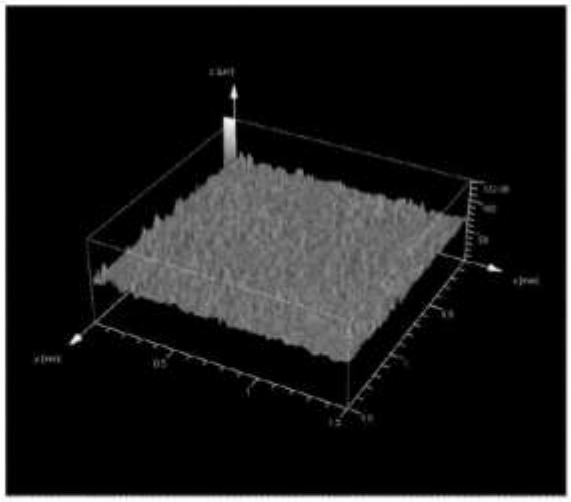
21 Two-dimensional white light confocal microscopy image of the coating surface revealing features obtained due to laser spot overlap and track overlap

Published by Maney Publishing (c) IOM Communications Ltd

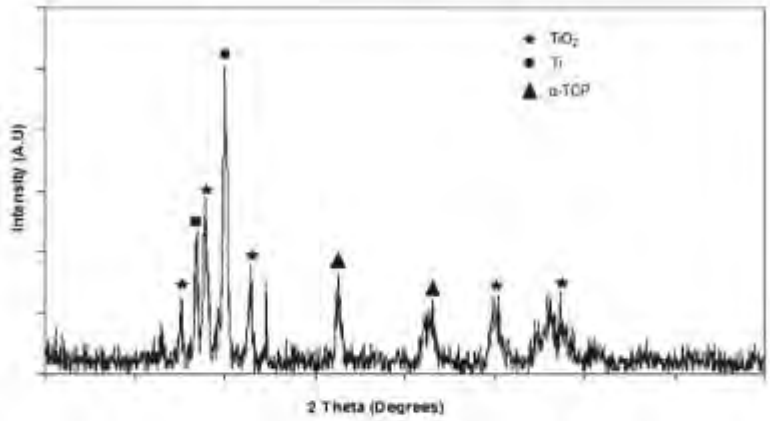
are formed under the processing parameters such as energy and power of the laser beam.

Kurella *et al.*[31,44] used a continuous wave Nd:YAG laser operating at 1064 nm wavelength to develop calcium phosphate coatings on Ti based alloys. In this technique, the starting powder of calcium phosphate was mixed in water based organic solvent and was sprayed onto the Ti–6Al–4V plate using an air spray gun. The samples were then dried to remove the moisture. The sample is then scanned under a laser beam to produce a strong bond between the coat and the substrate. The schematic of the above process is illustrated in Fig. 14. The formation of mutiscale features ranging from nano to mesoscale was obtained by controlling the thermophysical interactions during laser processing. Scanning electron images in Fig. 15 illustrate the hierarchical organisation of such coatings at the surface.[31] It was explained that the formation of such a morphology is mostly due to the rapid cooling associated with laser processing which resulted in the formation, organisation and controlling of the dimensions of Ca–P rich glassy phase into a micrometre scale cellular morphology and submicrometre scale clusters of $CaTiO_3$ phase inside these cells. The biocompatibility of the coatings were proved by the formation of an HA phase after immersion in a simulated biofluid (SBF) for 14 days. X-ray diffraction (XRD) patterns in Fig. 16 compares diffraction patterns obtained before and after immersion in SBF.[31] Before immersion in SBF only the diffraction peaks corresponding to CaO, α-tricalcium phosphate (TCP), $CaTiO_3$, TiO_2 and Ti were observed. After immersion in SBF for 14 days only the diffraction peaks corresponding to HA were observed as a result of the dissolution of CaO.

The work performed by the authors also developed a porous and textured Ca–P bioceramic coating on Ti–6Al–4V substrate using a 2·5 kW Hobart continuous wave Nd:YAG laser following the same technique as



22 Three-dimensional white light confocal microscopy image of the coating surface indicating a rough surface of the coating



23 XRD pattern of the coated surface

above.[45] The beam was transferred from the source to the work piece using a fibre optic cable. The formation of such a porous and textured coating obtained at a laser fluence of 1006 J cm^{-2} and scan speed of 200 cm min^{-1} is represented in Fig. 17.[45] These pores are considered to be formed by bubble motion in the molten pool due to thermocapillary forces in the direction of temperature gradient and pore coalescence due to this bubble motion.[46] The formation of such a porous and geometrically textured bioactive coating is aimed at triggering protein interactions at the interface and thereby promoting the subsequent reactions beneficial for hard tissue replacement. The waviness or the physical texturing is also aimed at inducing certain amount of mechanical stimulation on the surrounding bone during the early days of implantation so that a quick fixation takes place.[47] Furthermore, the bioactivity of the coatings was proved by the formation of an apatite like layer on the surface of the sample after being immersed in an SBF. Figure 18 reveals cuboids and needle like apatite phase formed just after 1 day immersion in SBF.[45] X-ray diffraction patterns in Fig. 19 compares the phases evolved before and after immersion in SBF for 5 days. After immersion in SBF for 5 days a strong HA peak corresponding to 2θ=37·713° and (211) plane is confirmed from the XRD pattern.

Pulsed laser

In pulsed mode operation, short duration pulses of very high peak power are delivered periodically. In normal pulse operation, the pulse durations are in the range of few microseconds to milliseconds. Most of the solid state lasers such as the Nd:glass and Nd:YAG lasers are operated in the pulsed mode. The pulse duration is manipulated by controlling the inductance and capacitance of the power supply for the flash lamp.[34] Based on the one dimensional heat conduction equations the variation in temperature T with respect to time t and thickness z during the pulse on period ($\tau > t > 0$) is given as[37]

$$T(z,t) = \mathrm{To} + \frac{2\mathrm{A_o I_o}}{\mathrm{K}}(\alpha t)^{1/2}\mathrm{ierfc}\left[\frac{z}{2(\alpha t)^{1/2}}\right]$$

The surface temperature at $z=0$ is

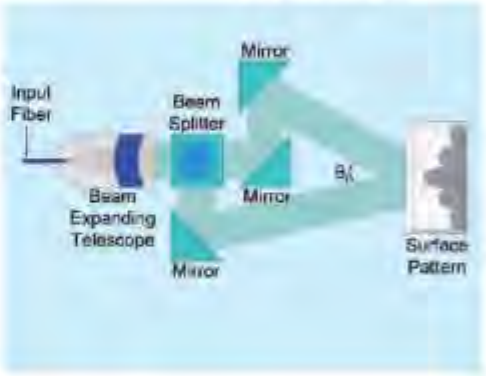
$$T(0,t) = \mathrm{To} + \frac{2\mathrm{A_o I_o}}{\mathrm{K}}\left(\frac{\alpha t}{\pi}\right)^{1/2}$$

After termination of the laser pulse i.e. ($t > \tau$) variation of temperature with respect to time and thickness is given as

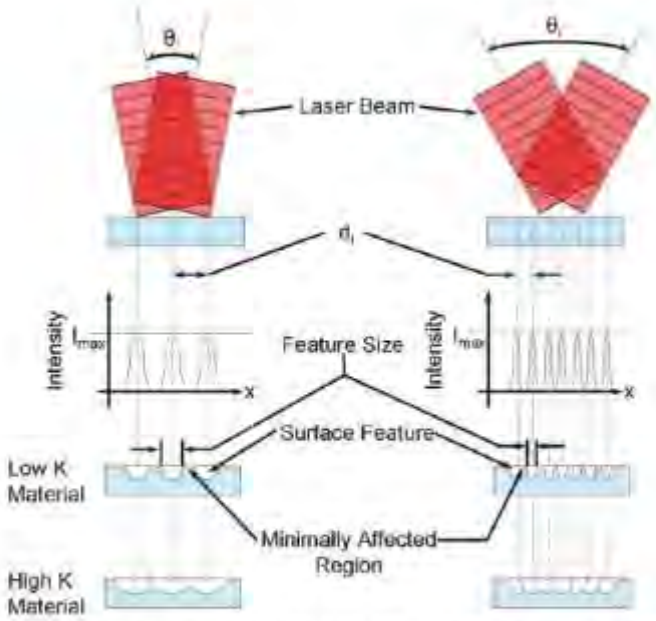
$$T(z,t) = \mathrm{To} + \frac{2\mathrm{A_o I_o}}{\mathrm{K}}\left\langle (\alpha t)^{1/2}\mathrm{ierfc}\left[\frac{z}{2(\alpha t)^{1/2}}\right] - [\alpha(t-t_p)]^{1/2}\,\mathrm{ierfc}\left\{\frac{z}{2[\alpha(t-t_p)]^{1/2}}\right\}\right\rangle$$



24 Image (SEM) indicating a rough and hierarchical organisation of the coating surface



25 Schematic setup of a laser interferometer (Reprinted from ref. 51 with permission from Journal of Minerals, Metals and Materials Society (JOM))



26 Schematic representation of the interference patterns due to the variation in the interference angle and thermal conductivity of the material (Reprinted from ref. 51 with permission from Journal of Minerals, Metals and Materials Society (JOM))

The temporal evolution with increasing rectangular pulses for a particular thickness of the sample is illustrated in Fig. 20. This helps us in understanding the maximum temperature rise and drop during the beam-on and beam-off situations respectively. An understanding of this may help us in predicting the various phase evolution due to a particular pulse width and pulse frequency.

As the beam is delivered in a pulsed mode, overlapping of the pulses can be obtained by varying the scan speed for a given pulse frequency. This in turn may be helpful in creating physically textured coating beneficial for bio applications. The spot overlap is related to the spot diameter, pulse frequency and linear speed by the following equation: (spot diameter) × (1−spot overlap) × (pulse frequency)=linear speed

Also in the pulsed mode operation due to shorter pulse widths the associated cooling rate is extremely high as compared to a continuous wave operation. This may be helpful in retaining some metastable or amorphous phases of Ca–P beneficial for biosapplication.

Based on this concept, the present authors have developed a Ca–P based coating on Ti–6Al–4V substrate using a pulsed Nd:YAG system. The precursor calcium phosphate tribasic powder was coated to the substrate in the same fashion as described earlier, and after which it was scanned using the pulsed Nd:YAG system. Unlike CW lasers with a pulsed laser physical texturing can be achieved by two ways:

(i) by varying the spot overlap
(ii) by varying the track overlap.

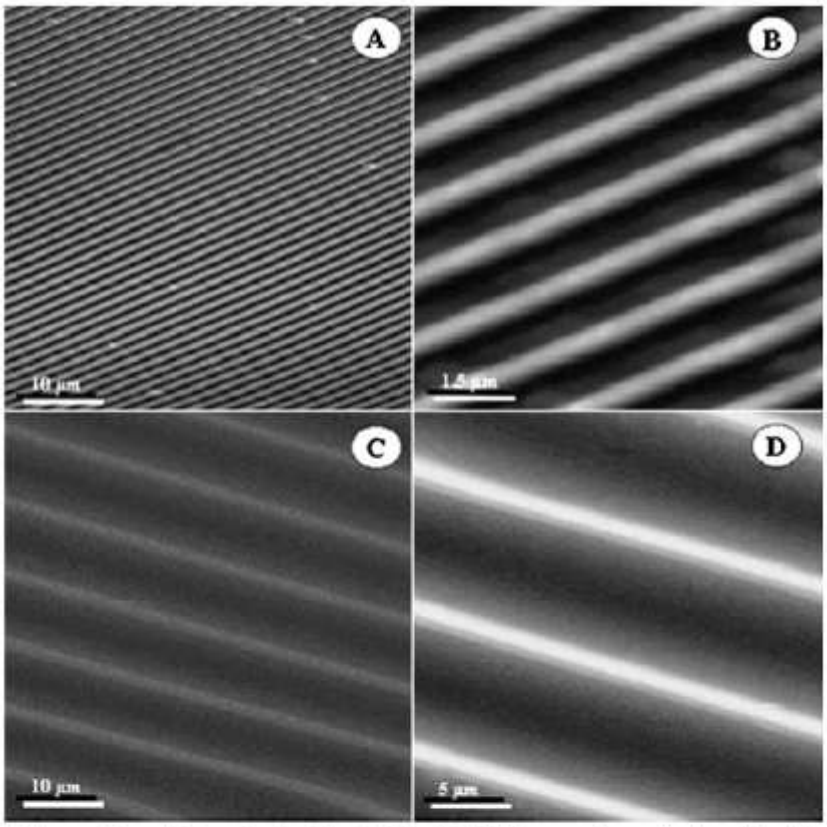
Figures 21 and 22 reveal 2D and 3D white light confocal microscopy images of the surface of the coating obtained by this technique. The 3D morphology of the coating indicates a rough surface of the coating. The atoms at the surface are highly unstable due to lack of bonding to the neighbouring atoms and as a result may drive many biological reactions corresponding to cell adsorption, cell adhesion, cell growth and blood compatibility. The XRD pattern of the coated surface in Fig. 23 reveals the presence of beneficial phases such as TiO_2, Ti and α-tricalcium–phosphate. Scanning electron image in Fig. 24 reveals a rough organisation of the coating surface. The synthesis of such multiscale textured coating using a pulsed Nd:YAG system is first by this group.

Surface modification by laser induced interference patterning

Interference patterning is used to manipulate the topography and phase microstructure of various compositions in a periodical way. A patterned biomaterial surface may provide contact guidance for cells and thereby aid cell growth in a particular orientation. Lasers are more attracted in these kinds of applications because of its available high power and monochromaticity. Laser interference patterning involves irradiating the surface of the sample with two or more overlapping coherent and linearly polarised laser beams of defined geometry.[49–52] This geometry depends on the wavelength and angles between the beams. The 2D intensity distribution of the pattern is given by the following equation[50]

$$I(x) = 2I_0\left\{\cos\left[\frac{4\pi x}{\lambda}\sin\left(\frac{\theta}{2}\right)\right] + 1\right\}$$

where I_0 is the intensity of the laser beam, λ is the



(A), (B) AFM images of laser patterning on hydrophobic side of film; (C), (D) AFM images of laser patterning on hydrophiliic side of film

27 Surface morphology of laser patterned Thermanox film (Reprinted from ref. 53 with permission from Institute of Electrical and Electronics Engineers (IEEE))

Published by Maney Publishing (c) IOM Communications Ltd

wavelength and θ is the angle in between the beams. The periodicity d of the interference pattern is given as

$$d = \frac{\pi}{2\sin\left(\frac{\theta}{2}\right)}$$

Unlike more common lithography techniques which involves a number of elements such as a pre design set of masks, replications of patterns and choice of resist, laser interference patterning has the advantage of creating patterns in a single step.[48] The schematic setup of a laser interferometry is shown in Fig. 25.[51] This basic design can be divided into three parts:

(i) the laser beam which has to be coherent
(ii) the beam expanding telescope (BET), the beam splitters and mirrors
(iii) the sample on which the pattern has to be developed.

The temperature evolution in such a process can be analytically derived using the heat transfer equation based on the fourier's law of heat conduction.

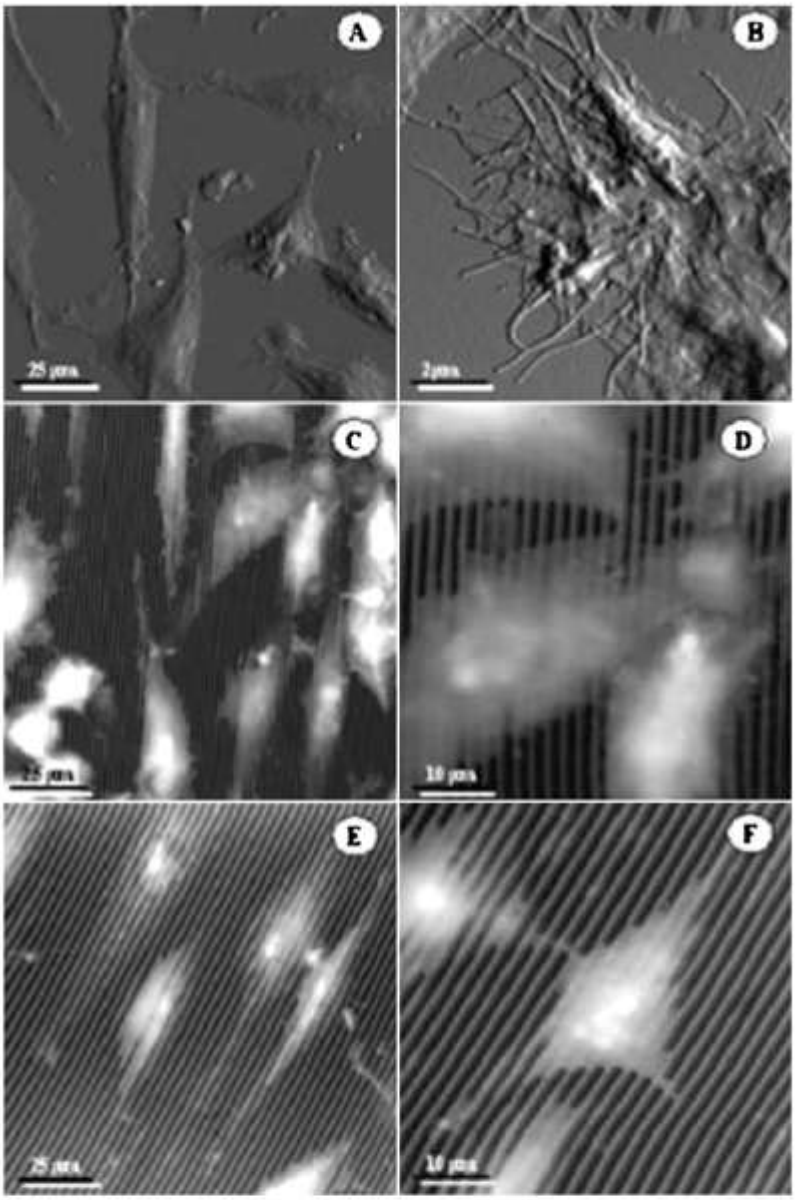
$$\rho C_p \frac{\partial T}{\partial t} = q_a - q_m - q_v + \nabla(k\nabla T)$$

where ρ is the density of the material, C_p is the specific heat, $T = T(x,z,t)$ is the temperature at position (x,z) and time t, q_a, q_m and q_v are the heat added, the heat of melting and the heat of vaporisation. The energy required to produce a single fringe of a particular surface feature size is given as[50]

$$E = \frac{kT_m t_p 10^{-4}}{2(\chi t_p)^{1/2}\,\mathrm{ierfc}\left[\frac{z}{2(\chi t_p)^{1/2}}\right]}$$

where E density is the energy in J cm^{-2}, k is the thermal conductivity in W mK^{-1}, T_m is the melting temperature in degrees, t_p is the pulse time in seconds, χ is the thermal diffusivity in m^2 s^{-1} and z is the feature size that is assumed to the melt depth in metres. A schematic representation of the interference patterns due to a variation in the interference angle and thermal conductivity of the material is shown in Fig. 26.[51]

As of now the search of open literature did not reveal any work related to Ca–P based coatings on Ti obtained by this technique. However, extensive work has been carried out on polymeric biomaterials so as to produce various patterns by this technique.[53–55] Li *et al.*[53] used a *Q*-switch Nd:YAG laser operating at 266 nm wavelength to obtain micropatterned features on hydrophilic and hydrophobic surface of a thermanox film. Figure 27



(A), (B) L929 cells growing on unmodified hydrophilic surface; (C), (D) L929 cells growing on modified hydrophobic surface; (E), (F) L929 cells growing on modified hydrophilic surface

28 **Images (AFM) of L929 cells growing on laser patterned surface (Reprinted from ref. 53 with permission from Institute of Electrical and Electronics Engineers (IEEE))**

shows the AFM images of a micropatterned surface obtained by this technique.[53] Furthermore, these patterns also proved their biocompatibility by inducing a directional cell growth of L929 cells as shown in Fig. 28.[53] Therefore, the above laser based interference patterning technique may be a promising tool to produce various micropatterned Ca–P based coatings on Ti substrates for hard tissue replacement.

Conclusions

The present paper discussed four different types of laser based coating techniques and its implementation for Ca–P based coatings on Ti based alloys. A special emphasis was given on Ca–P based coatings obtained by direct melting using a continuous wave and pulsed Nd:YAG systems obtained by the present group. The formation of

Published by Maney Publishing (c) IOM Communications Ltd

various phases and their bioactivity were discussed. Finally the laser based interference patterning is proposed as a future and highly promising technique to obtain various patterned Ca–P coatings at different length scales suitable for this kind of applications.

References

1. J. B. Park and J. D. Bronzino: 'Biomaterials: principles and applications', 10th edn; 2003, Boca Raton, FL, CRC Press.
2. B. D. Ratner, A. S. Hoffman, F. J. Schoen and J. E. Lemons: 'Biomaterials science', 2nd edn; 2004, San Diego, CA, Elsevier Academic Press.
3. M. M. Stevens and J. H. George: *Science*, 2005, **310**, 1135–1138.
4. J.-Y. Rho, L. Kuhn-Spearing and P. Zioupos: *Med. Eng. Phys.*, 1998, **20**, 92–102.
5. M. P. Lutolf and J. A. Hubbell: *Nature Biotechnol.*, 2005, **23**, 47–55.
6. H. Assender, V. Bliznyuk and K. Porfyrakis: *Science*, 2002, **297**, 973–976.
7. E. Cukierman, R. Pankov, D. R. Stevens and K. M. Yamada: *Science*, 2001, **294**, 1708–1712.
8. E. Cukierman, R. Pankov and K. M. Yamada: *Curr. Opin. Cell Biol.*, 2002, **14**, 633–639.
9. C. S. Chen, J. Tan and J. Tien: *Ann. Rev. Biomed. Eng.*, 2004, **6**, 275–302.
10. E. Dujardin and S. Mann: *Adv. Mater.*, 2002, **14**, 775–788.
11. B. Kasemo: *Surf. Sci.*, 2002, **500**, 656–677.
12. S. Mann: 'Biomineralization: principles and concepts in bioinorganic materials chemistry', 1st edn; 2001, Oxford, Oxford University Press.
13. K. de Groot, J. G. C. Wolke and J. A. Jansen: *Proc. Inst. Mech. Eng.*, 1998, **212**, 137–147.
14. T. Bialock, X. Bai and A. Rabon: *Surf. Coat. Technol.*, 2007, **201**, 5850–5858.
15. H. X. Ji, C. B. Ponton and P. M. Marquis: *J. Mater. Sci. Mater. Med.*, 1992, **3**, 283–287.
16. Y. C. Tsui, C. Doyle and T. W. Clyne: *Biomaterials*, 1998, **19**, 2031–2043.
17. M. Inagaki and T. Kameyama: *Biomaterials*, 2007, **28**, 2923–2931.
18. Z. L. Dong, K. A. Khor, C. H. Quek, T. J. White and P. Cheang: *Biomaterials*, 2003, **24**, 97–105.
19. K. A. Khor, Z. L. Dong, C. H. Quek and P. Cheang: *Mater. Sci. Eng. A*, 2000, **A281**, 221–228.
20. B.-Y. Chou and E. Chang: *Biomaterials*, 1999, **20**, 1823–1832.
21. L. M. Sun, C. C. Berndt and C. P. Grey: *Mater. Sci. Eng. A*, 2003, **A360**, 70–84.
22. V. Nelea, C. Ristoscu, C. Chiritescu, C. Ghica, I. N. Mihailescu, H. Pelletier, P. Mille and A. Cornet: *Appl. Surf. Sci.*, 2000, **168**, 127–131.
23. C. K. Wang, J. H. Chern Lin, C. P. Ju, H. C. Ong and R. P. H. Chang: *Biomaterials*, 1997, **18**, 1331–1338.
24. J. M. Fernandez-Pradas, G. Sardin, L. Clavia, P. Serra, C. Ferrater and J. L. Morenza: *Thin Solid Films*, 1998, **317**, 393–396.
25. M. D. Ball, S. Downes, C. A. Scotchford, E. N. Antonov, V. N. Bagratashvili, V. K. Popov, W. J. Lo, D. M. Grant and S. M. Howdle: *Biomaterials*, 2001, **22**, 337–347.
26. H. T. Zeng, W. R. Lacefield and S. Miser: *J. Biomed. Mater. Res.*, 2000, **50**, 348–358.
27. A. R. Boyd, B. J. Meenan and N. S. Leyland: *Surf. Coat. Technol.*, 2006, **200**, 6002–6013.
28. M. Metikos-Hukovic, E. Tkalcec, A. Kwokal and J. Piljac: *Surf. Coat. Technol.*, 2003, **165**, 40–50.
29. D. B. Haddow, P. F. James and R. Vannoort: *J. Sol-gel Sci. Technol.*, 1998, **13**, 261–265.
30. M. Shirkhanzadeh: *J. Mater. Sci. Lett.*, 1991, **10**, 1415–1417.
31. A. Kurella abd N. B. Dahotre: *Acta Biomater.*, 2006, **2**, 677–683.
32. F. J. Gracia-Sanz, M. B. Mayor, J. L. Arias, J. Pou, B. Leon and M. Perez-Amor: *J. Mater. Sci. Mater. Med.*, 1997, **8**, 861–865.
33. D. Bäuerle: 'Laser processing and chemistry', 3rd edn; 2000, Berlin, Springer.
34. J. F. Ready: 'Industrial applications of lasers', 2nd edn; 1997, New York, Academic Press.
35. M. Bass (ed.): 'Laser materials processing', Vol. 3; 1983, Amsterdam, North-Holland.
36. S. O. Kasap: 'Principles of electronic materials and devices', 3rd edn; 2006, Boston, McGraw Hill.
37. D. Schuocker: 'High power lasers in production engineering'; 1999, London, Imperial college press.
38. S. P. Harimkar and N. B. Dahotre: 'Laser fabrication and machining of materials', 1st edn; 2008, Berlin, Springer.
39. P. R. Willmott and J. R. Huber: 'Pulsed laser vaporization and deposition, Reviews of Modern Physics, 2000, 72, (1), 315–328.
40. R. K. Singh and J. Narayan: *Phys. Rev. B*, 1990, **41B**, 8843–8859.
41. S. I. Anisimov, D. Bäuerle and B. S. Lukyanchuk: *Phys. Rev. B*, 1993, **48B**, 12076–12081.
42. V. Nelea, H. Pelletier, M. Iliescu, J. Werckmann, V. Craciun, I. N. Mihailescu, C. Ristoscu and C. Ghica: *J. Mater. Sci. Mater. Med.*, 2002, **13**, 1167–1173.
43. G. Socol, P. Torricelli, B. Bracci, M. Iliescu, F. Mirescu, A. Bigi, J. Werckmann and I. N. Mihailescu: *Biomaterials*, 2004, **25**, 2539–2545.
44. A. Kurella and N. B. Dahotre: *JOM*, 2006, 64–66.
45. S. R. Paital and N. B. Dahotre: *Biomed. Mater.*, 2007, **2**, 274–281.
46. D. Triantafyllidis, L. Li and F. H. Stott: *Appl. Surf. Sci.*, 2003, **208**, 458–462.
47. S. Hansson and M. Norton: *J. Biomech.*, 1999, **32**, 829–836.
48. A. Lasagni, C. Holzapfel, T. Weirich and F. Mucklich: *Appl. Surf. Sci.*, 2007, **253**, 8070–8074.
49. A. Lasagni, M. Nejati, R. Clasen and F. Mucklich: *Adv. Eng. Mater.*, 2006, **8**, 580–584.
50. C. Daniel, F. Mucklich and Z. Liu: *Appl. Surf. Sci.*, 2003, **208–209**, 317–321.
51. P. Gregory Engleman, A. Kurella, A. Samant, C. A. Blue and N. B. Dahotre: *JOM*, 2005, **57**, (12), 46–50.
52. C. Daniel, T. J. Balk, T. Wubben and F. Mucklich: *Adv. Eng. Mater.*, 2005, **7**, 823–826.
53. P. Li, U. Bakowsky, F. Yu, C. Luchbuch, F. Muecklich and C.-M. Lehr: *IEEE Trans. Nano Biosci.*, 2003, **2**, 138–145.
54. F. Yu, F. Mucklich, P. Li, H. Shen, S. Mathur, C.-M. Lehr and U. Bakowsky: *Biomacromolecules*, 2005, **6**, 1160–1167.
55. F. Yu, P. Li, H. Shen, S. Mathur, C.-M. Lehr, U. Bakowsky and F. Mucklich: *Biomaterials*, 2005, **26**, 2307–2312.

VITA

Sameer Ranjan Paital did his Bachelors in Metallurgical Engineering from Andhra University College of Engineering, Visakhapatnam, India in 2004. He graduated with first class distinction and was among the top 1% of the students in his graduating year. Sameer later worked as a research fellow at International Advanced Research Center (ARCI) on laser drilling of IN718 superalloys for aero engine applications. After a 2 year stint at ARCI he came to University of Tennessee, Knoxville (UTK) to join the graduate program in Materials Science and Engineering in fall 2006. During the past 4 years Sameer has published 16 papers in the area of materials science and engineering in peer reviewed journals and presented his work at 5 international conferences. He is still active in writing his research results and at least 4 more papers are under review or preparation for journal publication. Apart from his duties as a graduate student researcher, he also was the reviewer for three international journals (1) Biomedical Materials, (2) Journal of Biomedical Materials Research: Part B - Applied Biomaterials, and (3) Journal of Materials Engineering and Performance. For his accomplishments during his graduate PhD programme at UTK, Sameer was honored with several awards and recognitions. Among them are the Materials Science and Engineering graduate student award for excellence in research, Chancellors Honors Award for Outstanding Professional Promise and 1st Place award for the Biological Materials Science Poster Symposium at The Minerals Metals and Materials Society Conference held at Seattle in 2010. He is an active member of ASM, TMS, ACers and AIST. Sameer's research interests include laser materials processing, surface modification, and Biomaterials processing.